CERN Yellow Reports: Conference Proceedings CERN-2020-007

ECLOUD'18

Proceedings of the Joint INFN-CERN-ARIES Workshop on Electron-Cloud Effects

3–7 June 2018, La Biodola, Isola d'Elba, Italy

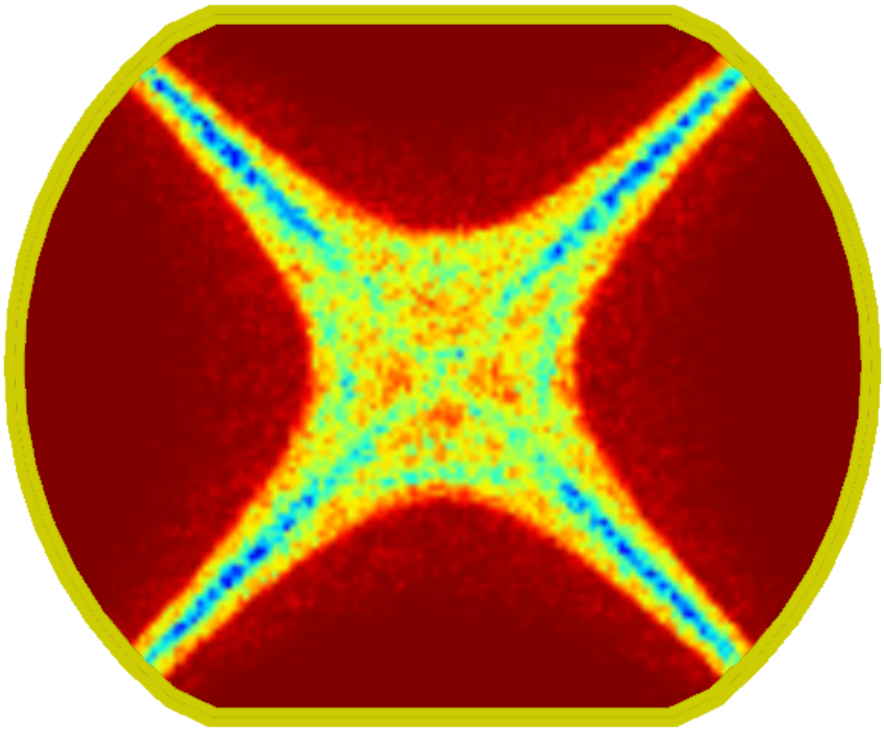

Editors:
R. Cimino
G. Rumolo
F. Zimmermann

CERN

CERN Yellow Reports: Conference Proceedings
Published by CERN, CH-1211 Geneva 23, Switzerland

ISBN 978-92-9083-581-3 (paperback)
ISBN 978-92-9083-582-0 (PDF)
ISSN 2519-8084 (Print)
ISSN 2519-8092 (Online)
DOI https://doi.org/10.23732/CYRCP-2020-007

This volume should be cited as:
ECLOUD'18: Proceedings of the Joint INFN-CERN-ARIES Workshop on Electron-Cloud Effects, 3–7 June 2018, La Biodola, Isola d'Elba, Italy, Eds. R. Cimino, G. Rumolo, F. Zimmermann, CERN Yellow Reports: Conference Proceedings, CERN-2020-007 (CERN, Geneva, 2020), doi:10.23731/CYRM-2020-007.

A contribution in this report should be cited as:
[Author name(s)], in ECLOUD'18: Proceedings of the Joint INFN-CERN-ARIES Workshop on Electron-Cloud Effects, 3–7 June 2018, La Biodola, Isola d'Elba, Italy, Eds. R. Cimino, G. Rumolo, F. Zimmermann, CERN-2020-007 (CERN, Geneva, 2020), pp. [first page]–[last page], http://doi.org/10.23732/CYRCP-2020-007.[first page].

Corresponding editor: Giovanni.Rumolo@cern.ch.
Accepted by the CERN Reports Editorial Board (contact Carlos.Lourenco@cern.ch) in September 2020.
Published by the CERN Scientific Information Service (contact Jens.Vigen@cern.ch).
Indexed in the CERN Document Server and in INSPIRE.
Published Open Access to permit its wide dissemination, as knowledge transfer is an integral part of the mission of CERN.

Abstract

This report contains the proceedings of the sixth electron-cloud workshop, ECLOUD'18, held, from 3 to 7 June 2018 at La Biodola (Isola d'Elba) Italy. The ECLOUD'18 workshop reviewed many recent electron-cloud (EC) observations at existing storage rings, EC predictions for future accelerators, and various advanced electron-cloud studies. The existence of EC effects in many frontier accelerators has by now been firmly established. It is a consequence of the strong coupling between a positively charged particle beam and a cloud of electrons that almost inevitably builds up inside the vacuum chamber. The EC causes various effects limiting accelerator performance, such as beam instabilities, beam losses, emittance growth, increases in vacuum pressure, additional heat load on the vacuum chamber walls inside cold magnets, and interference with certain types of beam diagnostics.

At ECLOUD'18, recent EC studies were presented, discussed and compared: electron-cloud observations at the LHC, SuperKEKB, CESR-TA and DAFNE; electron-cloud predictions for FAIR, NICA, EIC and for the FCC and other machines; electron-cloud mitigation measures, such as clearing electrodes, graphite/carbon coatings, and chemically or laser treated surfaces; modeling of incoherent electron-cloud effects; self-consistent simulations including ionized molecules; synergies with other communities like the Valencia Space Consortium and the European Space Agency, surface science experts and specialists for conventional accelerator impedance.

ECLOUD'18 identified a number of open questions and defined future R&D needs.

Preface

Electron clouds—abundantly generated in accelerator vacuum chambers by residual-gas ionization, photoemission and secondary emission—can affect the operation and performance of hadron and lepton accelerators in a variety of ways. They can induce increases in vacuum pressure, beam instabilities, beam losses, emittance growth, reductions in the beam lifetime, or additional heat loads on a (cold) chamber wall.

Electron clouds were recognized as a potential problem for the LHC in the second half of the 1990s (*CERN Courier* July/August 1999, p. 29) and the first workshop to focus on the phenomenon, ECLOUD'02, was held at CERN in 2002 (*CERN Courier* July/August 2002, p. 15).

The sixth electron-cloud workshop, ECLOUD'18 took place at La Biodola, Elba, Italy, from 3 to 7 June 2018. The Workshop gathered 60 physicists and engineers from around the world to discuss the state of the art and to review the recent electron-cloud experience.

Many electron-cloud signatures have been recorded and a great deal of data accumulated, not only at the LHC, but also at the CESR Damping Ring Test Accelerator (CesrTA) at Cornell, DAΦNE at Frascati, the Japan Proton Research Complex (J-PARC), SuperKEKB in Japan, and PETRA III at DESY. These machines all serve as valuable test beds for simulations of electron-cloud build up, instabilities and heat load, as well as for new diagnostics methods. The latter include measurements of synchronous phase-shift and cryogenic effects at the LHC, as well as microwave transmission studies, coded-aperture images and time-resolved shielded pick-ups at CesrTA. The impressive resemblance between simulation and measurement suggests that the existing electron-cloud models correctly describe the phenomenon. The workshop also analysed the means of mitigating electron-cloud effects affecting future projects, such as the High-Luminosity LHC, HE-LHC, FCC-hh, the IEC and Project-X in the US, CSNS in China, the upgrade of the ISIS machine in the UK, and the International Linear Collider (ILC) proposed for construction in Japan.

An International Advisory Committee (IAC) had assembled an exceptional programme for ECLOUD'18. Noteworthily, several members of the spacecraft community had participated in this IAC, ranging from the Val Space consortium based in Valencia, over the French aerospace laboratory Onera, the Instituto de Ciencia de Materiales de Madrid, the Princeton Plasma Physics Laboratory, to the École Polytechnique Fédérale de Lausanne (EPFL). Indeed, satellites in space suffer from problems that greatly resemble the electron cloud in accelerators and that can be modelled and cured by similar countermeasures. These problems include the motion of the satellites through electron clouds in outer space, the relative charging of satellite components under the influence of sunlight, and the loss of performance of high-power microwave devices on space satellites. Intriguingly, the "Furman formula" parameterizing the secondary emission yield, which was first introduced around 1996 to analyse electron-cloud build-up for the PEP-II B factory, then under construction at SLAC, is now widely used to describe secondary emission on the surface of space satellites. Common mitigation measures for both accelerators and satellites include clearing electrodes, graphite/carbon coatings, and chemically or laser treated surfaces. The accelerator and spacecraft communities now also share, or link, some of their simulation codes such as BI-RME/ECLOUD and FEST3D. A second community strongly involved in the ECLOUD workshop series is surface scientists, who, at this meeting, elucidated the chemistry and secrets of secondary emission, conditioning, and photon reflections. A new, third community contributing to the ECLOUD'18 workshop is experts in impedance issues: all mitigation methods to suppress the EC should comply with the stringent requirements imposed by the available impedance budget. In addition, also the engineering community studying cryogenic aspects in accelerator facilities and astrophysicists examining desorption properties in interstellar media were contributing to ECLOUD'18, in order to obtain the widest possible view on most of the EC related issues. In this respect, yet another important theme at ECLOUD'18 was the adaptation and use of Gabor lenses, e.g. at the University of Frankfurt, to study incoherent electron-cloud effects in a laboratory set-up.

Several powerful new simulations and simulation codes were presented at ECLOUD'18. These codes include: SYNRAD3D from Cornell and SYNRAD+ from CERN for photon tracking, modelling surface properties and 3D geometries; OSMOSEE from ONERA and an advanced Monte Carlo method to model the secondary emission yield developed at ECT-FBK and TIFPA-INFN in Trento, to compute the secondary emission yield, including at low primary energies; PyECLOUD from CERN to perform improved and faster build-up simulations; the latest version of WARP-POSINST from Lawrence Berkeley National Laboratory,

which allows for self-consistent simulations that combine build up, instability and emittance growth, and which is deployed to study beam-cloud behaviour over hundreds of turns through the Super Proton Synchrotron (SPS); a new 2D simulation tool "openECLOUD" for electron cloud studies was developed in Darmstadt; the application of Tech-X's VSim code for modelling the geometric suppression of secondary electron yield; and the combination BI-RME/ECLOUD resulting from a collaborative effort of EPFL and CERN to study various aspects of the interaction of microwaves with an electron cloud.

ECLOUD'18 could not solve all of the puzzles and numerous open questions remain. For example: How can we explain the different behaviour in different LHC sectors which have experienced the same amount of beam time and beam-induced "scrubbing"? Why does the surface conditioning with electrons and photons differ? How can the complex nature of the intricate incoherent effects, and their impact on Landau damping, be fully described? Which ingredients are missing for correctly modelling the electron-cloud behaviour for electron beams (e.g. the existence of a certain fraction of high-energy photoelectrons)? Can the secondary-emission yield change over a time scale of seconds during the accelerator cycle (a suspicion based on evidence from the Main Injector at Fermilab, and from microwave transmission studies at the CERN SPS)? Can the surface conditioning be speeded up by the controlled injection of carbon monoxide gas? How important is the effect of positive ions for the survival and build-up of an electron cloud, for the resulting beam instabilities and for beam loss? Can anti-EC coatings be applied in situ on an already existing or operating machine? How helpful are cleaning electrodes and how can they be optimized?

As for the "electron-cloud safety" of future machines, ECLOUD'18 concluded that the design mitigations the LHC and its upgrades or successors (HL-LHC, HE-LHC FCC-hh, FCC-ee, etc.) should also be safe regarding electron cloud if proper mitigation strategies are chosen. Further optimization is still required. Certainly, new challenges will be encountered when integrating electron-cloud solutions with the many other design requirements for a new machine.

ECLOUD'18 was jointly organized and co-sponsored by INFN-Frascati, INFN-Pisa, CERN, EuroCirCol and ARIES-APEC. The participants also enjoyed a one-hour soccer match between theoretical and experimental electron-cloud experts—this time the latter outnumbered by the former—as well as post-dinner discussions until well after midnight.

ECLOUD'18 presented a superb overview of the present state-of-the-art in electron-cloud modelling and understanding. The remaining challenges, outstanding open questions, and several new approaches were carved out. Electron cloud remains important for the LHC and its upgrade HL-LHC, for SuperKEKB, for the US EIC, and for all future high-energy colliders including HE-LHC, FCC-hh, FCC-ee and CEPC. An ECLOUD'21 workshop would surely be warranted, extending over up to 5 days, given the growing cross-fields and interdisciplinary R&D related to electron cloud issues, and La Biodola (Isola d'Elba) again seems to be a strong candidate site to host this event in late summer or early fall 2021.

All ECLOUD'18 presentations are available on the web site https://agenda.infn.it/event/13351/overview . These proceedings are structured according to the thirteen workshop sessions and one opening seminar:

- Special opening seminar on "Electron cloud effects (ECEs) in accelerators" by F. Zimmermann
- Session 1: ECE on beam dynamics: observations and prediction (I) (chair F. Zimmermann)
- Session 2: ECE on beam dynamics: observations and prediction (II) (chair G. Iadarola)
- Session 3: ECE effects on vacuum and heat load (I) (chair G. Rumolo)
- Session 4: ECE effects on vacuum and heat load (II) (chair M.R. Masullo)
- Session 5: Surface properties, coating and experimental studies (I) (chair R. Larciprete)
- Session 6: Surface properties, coating and experimental studies (II) (chair M. Taborelli)
- Session 7: Multipactoring and related effects (chair V. Baglin)
- Session 8: Electron and photon interaction with low temperature surfaces (chair L. Mether)
- Session 9: Simulations and diagnostics (I) (chair J. Crittenden)
- Session 10: Simulations and diagnostics (II) (chair M. Tobiyama)
- Session 11: Mitigation (I) (chair K. Ohmi)
- Session 12: Mitigation (II) (chair O. Malyshev)
- Session 13: Outlook and conclusion (chair A. Ghigo)

These proceedings have been published in paper and electronic form. The paper copy is in black and white; the electronic version contains colour pictures.

The compilation of these proceedings would not have been possible without the help of the chairpersons and speakers of all the sessions. In particular, we would like to warmly thank all the participants for their stimulating contributions. The exceptional workshop programme has been made possible by the IAC.[1] Finally, we would like to extend our warm thanks to the Organizing Committee, consisting of: Marco Angelucci (INFN-LNF); Maria Giuseppina Bisogni (University of Pisa and INFN Pisa); Roberto Cimino (INFN-LNF), Chair; Maria Rita Ferrazza (INFN-LNF); Lucia Lilli (INFN Pisa); Riccardo Paoletti (University of Siena, and INFN Pisa) and Giovanni Rumolo (CERN), for the wonderful preparation and excellent support.

Geneva and Frascati, 30 March 2020

Roberto Cimino, LNF-INFN, and Frank Zimmermann, CERN
ECLOUD'18 Chairs

[1] Members of the IAC: Gianluigi Arduini (CERN); Vincent Baglin (CERN); Riccardo Bartolini (University of Oxford); Mohamed Belhaj (ONERA); Michael Benedikt (CERN); Oliver Brüning (CERN); Paolo Chiggiato (CERN); Roberto Cimino (INFN), Chair; Jim Crittenden (Cornell University); Stefano De Santis (LBL); Wolfram Fischer (BNL); Giuliano Franchetti (GSI); John Fox (SLAC and Stanford University); Miguel Furman (LBL); Benito Gimeno Martinez (VSC and University of Valencia); Susanna Guiducci (INFN); Chen Hesheng (IHEP); Giovanni Iadarola (CERN); Ubaldo Iriso (ALBA/CELLS); José Miguel Jimenez (CERN); Alexander Krasnov (BINP); Rosanna Larciprete (CNR); Oleg Malishev (ASTEC); Oliver Meusel (Goethe University Frankfurt); Mauro Migliorati (Sapienza University of Rome); Catia Milardi (INFN); Kazuhito Ohmi (KEK); Katsunobu Oide (KEK); Ioannis Papaphilippou (CERN); Eugene Perevedentsev (BINP); Mauro Pivi (MedAustrom); Qing Qin (IHEP); David Raboso (ESA-ESTECH); Tor Raubenheimer (SLAC); Giovanni Rumolo (CERN); Daniel Schulte (CERN); Elena Shaposhnikova (CERN); Vladimir Shiltsev (FNAL); Yusuke Suetsugu (KEK); Mauro Taborelli (CERN); Jiuqing Wang (IHEP); Rainer Wanzenberg (DESY); Seiya Yamaguchi (KEK) and Frank Zimmermann (CERN), Chair.

CONTENTS

[1] Paper not submitted to the proceedings. For your convenience, the slides presented are available in electronic form at the URL: https://agenda.infn.it/event/13351/timetable/#20180603

[1] Paper not submitted to the proceedings. For your convenience, the slides presented are available in electronic form at the URL: https://agenda.infn.it/event/13351/timetable/#20180603

[1] Paper not submitted to the proceedings. For your convenience, the slides presented are available in electronic form at the URL: https://agenda.infn.it/event/13351/timetable/#20180603

[1] Paper not submitted to the proceedings. For your convenience, the slides presented are available in electronic form at the URL: https://agenda.infn.it/event/13351/timetable/#20180603

[1] Paper not submitted to the proceedings. For your convenience, the slides presented are available in electronic form at the URL: https://agenda.infn.it/event/13351/timetable/#20180603

ELECTRON CLOUD EFFECTS IN ACCELERATORS*

F. Zimmermann†, CERN, Geneva, Switzerland

Abstract

This article presents a brief overview of the electron-cloud problem in charged-particle accelerators. It covers first and historical observations, simulation efforts, past challenges, modelling achievements, recent successes, objectives and future challenges.

PREHISTORY

In 1977, during operation with bunched proton beams at the Intersecting Storage Rings (ISR) a strong pressure rise was experienced in a 7-m long Al chamber in a resonance-like manner at certain combinations of bunch charge and bunch spacing; see Fig. 1. Realizing that an aluminium surface was likely to have a large seconday emission yield, O. Gröbner explained this observation by the new mechanism of "bunch-induced multipactoring" [1].

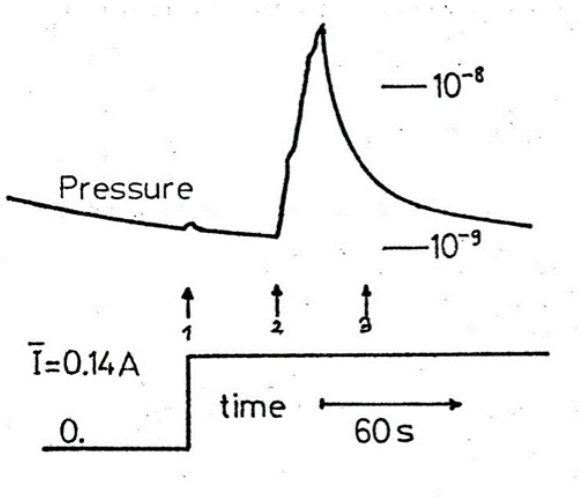

Figure 1: Pressure size observed during slow horizontal displacement of a bunched proton beam across the aperture of an aluminium vacuum chamber at the CERN ISR [1]. The numbered arrows indicate different horizontal beam positions.

In the late 1980, a vertical instability with a peculiar frequency spectrum was seen at the KEK Photon Factory when operated with multi-bunch positron beams. The same type of instability did not occur for electron beams. M. Izawa and co-workers proposed that the positron beam instability was driven by electrons, and applied a simple analytical model, with a wake-field coupling affecting several successive bunches, to explain the frequency spectrum observed [2].

* This work was supported in part by the European Commission under the HORIZON 2020 project ARIES no. 730871.

† frank.zimmermann@cern.ch

Developing the first ever electron-cloud simulation code, PEI, to model the effect of photoelectrons, in the early 1990s, K. Ohmi showed that a simulated multi-bunch instability driven by photoelectrons could indeed explain the observations at the KEK Photon Factory [3]. Figure 2 compares experimental frequency spectra of the positron-beam instability with the analytical model of M. Izawa and with a simulation result from K. Ohmi.

Inspired by K. Ohmi's work, in 1996, M. Furman and G. Lambertson performed electron-cloud simulations for PEP-II, using their new code POSINST, which in addition to the photoelectrons also included the effect of secondary emission [4].

In early 1997, using a separately developed, similar code, ECLOUD, the author performed first electron-cloud simulations for the LHC, revealing a significant electron cloud build up due to both (or either) photo-electrons and secondary electrons [5]. As a result, F. Ruggiero launched a CERN electron-cloud crash program for the LHC [6].

LHC ELECTRON CLOUD

In 1999, the first "LHC beams" stored in the LHC injector, the SPS, experienced electron-cloud driven beam instabilities with different characteristics in the horizontal and vertical plane [7, 8] that could be explained by the electron motion in a vertical magnetic field. From 2000 to 2002, a large number of novel, specialized diagnostics was developed and installed in the SPS [9], such as in situ SEY measurements (for conditioning or "scrubbing" studies) [N. Hilleret], pick-up calorimeters (measuring heat load and energy spectrum) [B. Henrist], strip detectors (spatial distribution) [9], a warm calorimeter (heat) [10] and a cold LHC-prototype vacuum chamber COLDEX [11]. Many of these experimental observations were reviewed in Ref. [9].

As an outcome from these studies and the crash program, an LHC mitigation strategy was defined, consisting of beam screen with (1) sawtooth chamber [13] in proper orientation [14, 15], (2) pumping slot shields [16], and (3) "scrubbing" or the conditioning/decrease of the secondary emission yield as a function of incident electron dose [12, 17–19]. Figure 3 shows the final version of the LHC beam screen; sawtooth and shields are indicated.

The behaviour of the secondary emission yield for low primary electron energies attracted quite some attention, as it greatly affects the survival of secondary electrons before the next bunch arrives. Different models were proposed to describe the low-energy character of the secondary emission yield and fitted to experimental data [12, 18, 19], including data at cryogenic temperature [12].

A few days of "scrubbing" are now routinely scheduled during every LHC start-up. The reconditioning is particularly needed after thermal cycle and venting of a sector. In

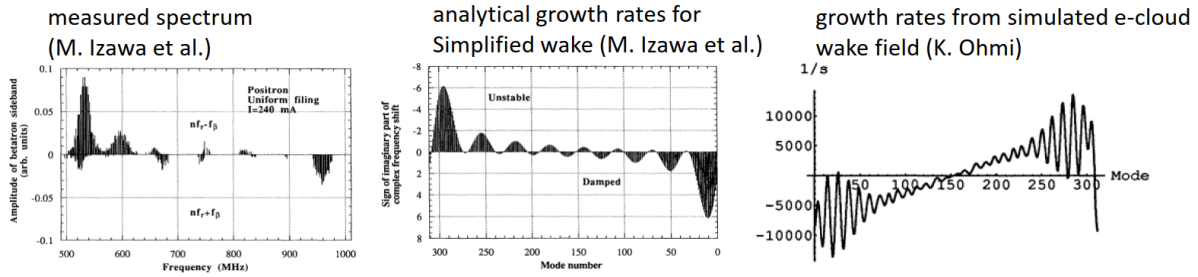

Figure 2: Measured frequency spectrum of unstable positron beam in the KEK Photon Factory [2], growth rates from a simple analytical model with a constant wake field extending over 8 successive bunches [2], and growth rates expected using a more realistic wake field obtained from the simulated photo-electron motion [3].

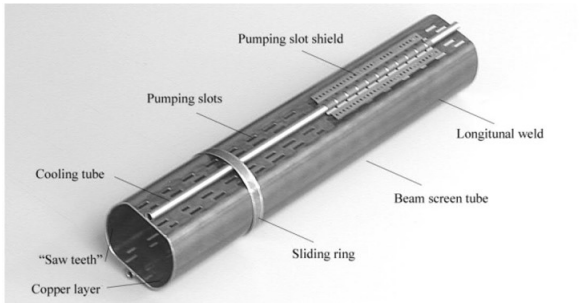

Figure 3: LHC beam screen with sawtooth surface and pumping-slot shields for electron-cloud mitigation [16].

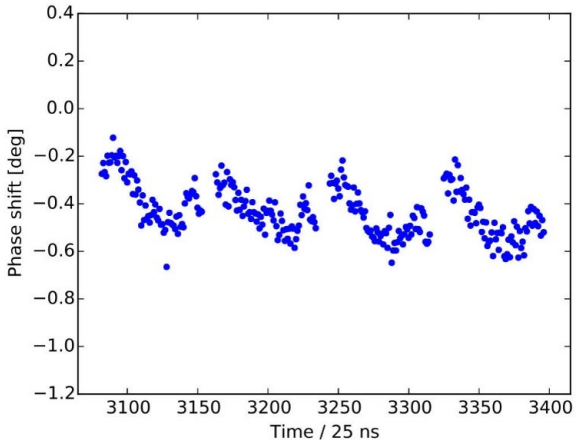

Figure 4: Synchronous phase shift due to electron cloud measured along several bunch trains in the LHC [22].

2017 this reconditioning required about 1 week with standard 25 ns beam. A single day of scrubbing suffices to recondition sectors that were not vented in the preceding shutdown [20, 21].

DIAGNOSTICS

In addition to using pressure rise, heat load and beam instabilities as signals of the electron cloud in the LHC, other diagnostics techniques were also developed. Energy loss of the beam to the electron cloud leads to a synchronous phase shift along a bunch train (see Fig. 4) which can be used to estimate the average electron cloud density around the ring [22]. The energy loss deduced in this way is consistent with the heat load detected by the LHC cryogenics system.

Microwaves can interact with electron clouds in various ways [23, 24]. When electromagnetic waves are transmitted through a not-too-dense electron plasma, they experience a phase shift and possibly a small attenuation. Therefore, another technique to detect the presence of an electron cloud in beam-pipe section of interest relies on an electron-induced modulation of a microwave signal sent through this section [25–29]. This method was tested in the SPS [26], PEP-II [28, 29], the LHC [26], the FNAL Main Injector [30] and the FNAL Recycler [30, 31]. Figure 5 shows an example result from PEP-II, Fig. 6 an example from the FNAL Recycler.

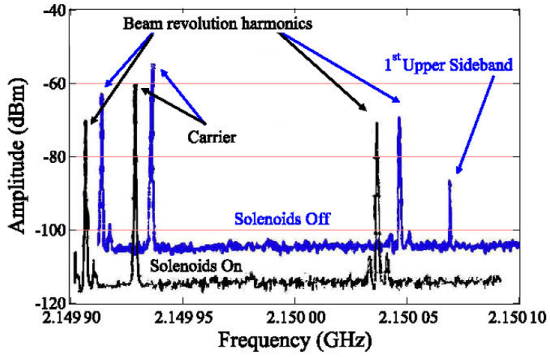

Figure 5: Phase modulated microwave signal at PEP-II [28].

COLLABORATIONS

Collaborations and exchanges with other communities facing similar problems were launched. For example, space satellites with high-power RF systems can be strongly affected by multipacting processes, which depend on the wavelengths and dimensions of the devices in question and on the secondary emission yields. With multifrequency operation the beating field evolution highly resembles the electric field

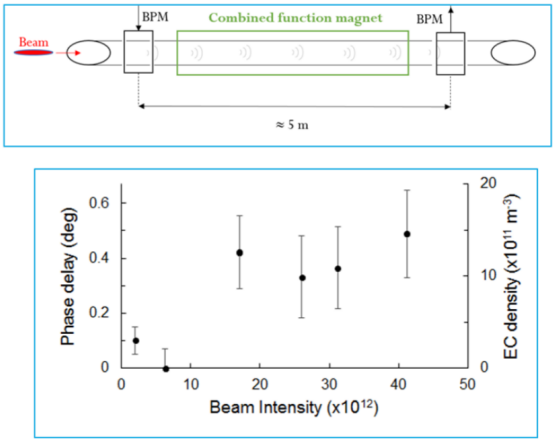

Figure 6: Microwave transmission results at the FNAL Recycler [30, 31].

of successive LHC bunches. The European Space Agency's ESTECH and its partners develop advanced surface coatings and have their own models for the secondary emission yields and its dependence on various parameters. Figure 7 shows F. Caspers and the author during a visit at ESA-ESTECH in Norwijk.

Figure 7: F. Caspers and F. Zimmermann during a 2009 visit at ESA/ESTECH in Norwijk.

ELECTRON-CLOUD DRIVEN INSTABILITY AND EMITTANCE GROWTH

Around 2001/2002, detailed simulation studies revealed that the unstable multi-bunch mode spectrum strongly depends on the magnetic field to which the moving electrons are subjected [32, 33]. At KEKB the installation and activation of weak solenoid fields in the previously field-free regions dramatically altered the mode spectrum of the electron-cloud driven coupled-bunch instability [32, 33].

Simulations and experiments revealed that the electron cloud can be trapped for longer periods of time, not only in the fields of solenoids, but also in the fields of quadrupoles, sextupoles and combined function magnets [31, 34, 35]; see Figs. 8 and 9.

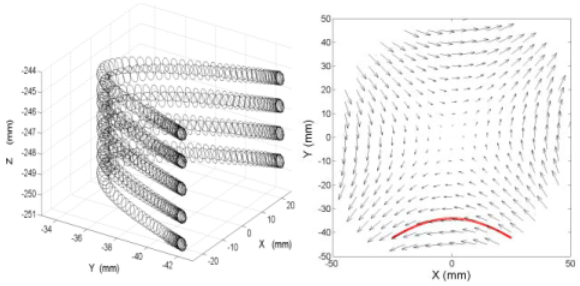

Figure 8: Photoelectron trapping in a magnetic quadrupole field during the bunch train gap at KEKB, simulated by the code CLOUDLAND. Left: 3D orbit; Right: 2D orbit (red line) and quadrupole field (black arrow) [34].

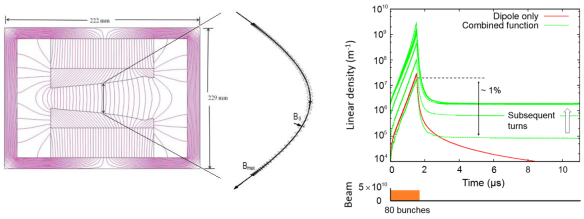

Figure 9: Cross-section of a permanent combined function dipole, at the FNAL Recycler, with indicated trapped electron trajectory (left), and comparison of simulated electron-cloud decay following a bunch-train passage in a pure dipole field and a combined function magnet (right) [31, 35].

At KEKB a strong vertical blow-up was observed above a certain beam current, as is illustrated in Fig. 10. The current threshold value depended on the bunch spacing. The threshold was increased by adding weak solenoid windings in otherwise field-free regions [36]. The synchrotron light diagnostics also indicated a possible residual slow beam size growth below the threshold (Fig. 10).

The fast vertical blow up of the KEKB LER positron beam above the "threshold" could be explained by single-bunch electron-cloud instability, using a 2-particle model [37], simulations [37], and a more refined analytical model based on an approximation through a conventional resonator impedance and interpretation in terms of a TMCI-like instability [38].

For SuperKEKB many countermeasures for electron-cloud suppression were adopted, such as an antechamber for photon capture, TiN coating of the vacuum chamber, grooved surfaces and clearing electrodes inside the wiggler magnets [39]. Figure 11 shows the vertical beam size blow up versus beam current In commissioning phase 1, after the installation of permanent magnets in the uncoated bellows sections. Up to a current of 0.9 A no strong blow up was observed. The design beam current is 3.6 A.

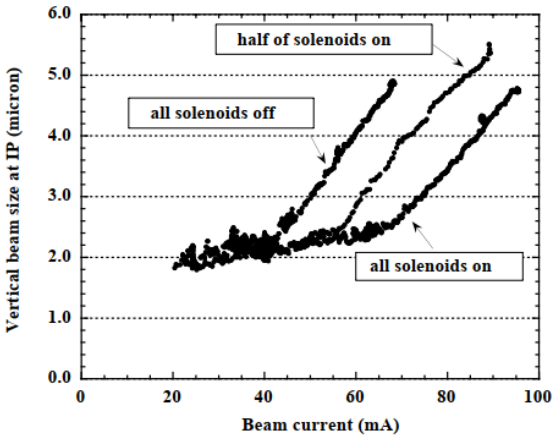

Figure 10: Vertical beam size, measured by the interferometer, versus beam current at the KEKB Low Energy (positron) Ring without and with partial or full solenoid fields in otherwise field-free regions. In the measurement two trains were injected on opposite sides in the ring. Each train contained 60 bunches. The bunch spacing was 4 RF buckets [36].

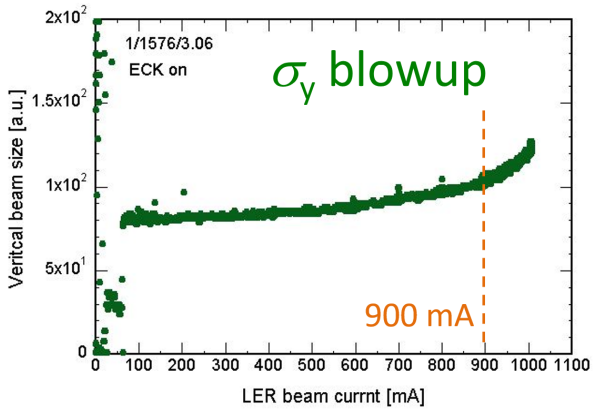

Figure 11: Vertical beam size versus beam current at the SuperKEKB Low Energy (positron) Ring in the commissioning phase 1 after installing permanent magnets at the bellows. In the measurement one long train was injected; the average bunch spacing was 3.06 RF buckets [39, 40].

For proton beams, the electron cloud can drive a similar single-bunch instability. Contrary to conventional instabilities, due to the smaller beam sizes at higher energy and strong electron cloud pinch, at higher proton energies the electron-driven proton beam instability can exhibit a lower threshold, roughly decreasing as $1/\sqrt{\gamma}$. This unfavourable scaling with energy was predicted analytically in 2005 [41, 42], and confirmed three years later in detailed simulations and experiments [43]. Approximating the threshold density as $\rho_{e,\mathrm{thr}} \approx 2\gamma Q_s/(\pi\beta r_p C)/H$ [37], where the pinch enhancement factor H is roughly modelled as increasing in proportion to the number of (small-amplitude) electron oscillations with angular frequency ω_e inside the beam potential, $H \approx 1 + 4\sigma_z\omega_e/(\pi c) \approx 4\sqrt{N_b r_e \sigma_z \gamma/(\sqrt{2\pi}\beta\varepsilon_{\mathrm{N}})}$, the threshold electron density can be estimated as [41, 42]

$$\rho_{e,\mathrm{thr}} \approx \frac{\left(\alpha_c - \frac{1}{\gamma^2}\right)\varepsilon_{||,\mathrm{rms,N}} f_{\mathrm{rf}}}{4\pi^2\sigma_z^2 r_p}\sqrt{\frac{\sqrt{2\pi}\varepsilon_{\mathrm{N}}}{\beta\sigma_z N_b r_e}}\frac{1}{\sqrt{\gamma}} \qquad (1)$$

where f_{rf} denotes the RF frequency, α_c the momentum compaction factor, C the circumference, β the average transverse beta function, σ_z the rms bunch length, N_b the bunch population, r_e the classical electron radius, r_p the classical proton radius, ε_{N} the normalized transverse rms emittance, $\varepsilon_{||,\mathrm{rms,N}}$ the longitudinal normalized rms emittance in units of metre, γ the relativistic Lorentz factor. Eq. (1) assumes $4\sigma_z\omega_e/(\pi c) \gg 1$. The emittances and beta functions of the proton beam were taken to be approximately equal in the horizontal and vertical plane ($\varepsilon_{\mathrm{N}} \approx \varepsilon_{x,\mathrm{N}} \approx \varepsilon_{y,\mathrm{N}}$, $\beta \approx \beta_x \approx \beta_y$).

Figure 12 shows a simulation example [43], which indicates the predicted $1/\sqrt{\gamma}$ behavior [41].

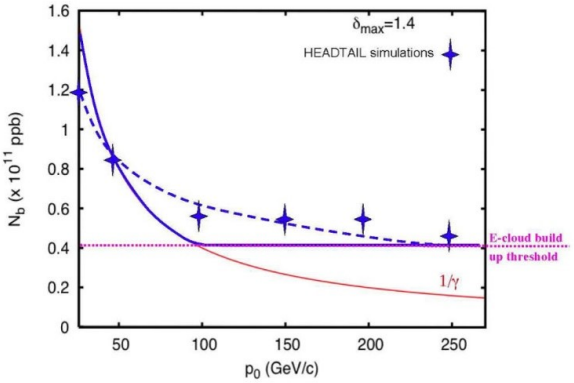

Figure 12: Simulated ECI thresholds at different momenta, study done with quasi-self-consistent e-cloud distribution [43].

If the electron cloud is generated by beam-induced multipacting inside magnets, the electron cloud also shows an unusual dependence on the bunch intensity. At highest proton intensities electrons receive too much energy from a passing bunch, so that the secondary emission yield is no longer maximum, but decreasing with higher incident electron energy. As the bunch intensity decays during a physics store the multipacting region moves closer to the center of the beam pipe, and the central electron-cloud density increases. if the electrons are close to the beam, they can drive a single-bunch instability [37]. Figure 13 shows an example from the LHC [45, 46]. This prediction is consistent with LHC beam observation, where the onset of instability often occurs after a significant decay in the beam intensity.

In addition to coherent beam motion, below the instability threshold the electron cloud can give rise to an incoherent emittance growth [47]. Evidence for such incoherent emittance driven by an electron cloud has been reported from various postron and proton storage rings. At the KEKB B factory already below the instability threshold the measured beam size increased with beam current, though much more

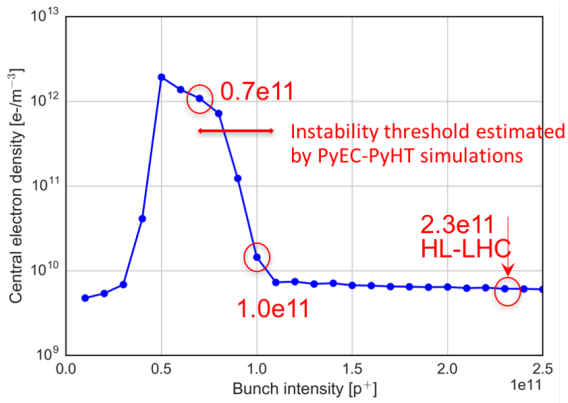

Figure 13: Simulated central electron-cloud density in an LHC dipole magnet as a function of bunch population; also indicated is the expected single-bunch instability threshold (red arrow) obtained from a separate simulation [43].

gradually than above the threshold [36]. Also at RHIC an electron cloud caused emittance growth and beam loss [48]. Similar effects were seen at the Tevatron for 19-ns bunch spacing, without any sign of coherent beam motion [49]. Figure 16 presents the simulated effect of clearing bunches for the FNAL recycler.

MITIGATION METHODS

Proposed techniques of beam manipulations to combat electron cloud build up include the satellites and clearing bunches. Figure 14 shows the concept of satellite bunches for electron-cloud mitigation in the LHC. The simulated effect of satellite bunches for the LHC is illustrated in Fig. 15 [50]. Figure 16 presents similar results for clearing bunches in the FNAL Recycler [35].

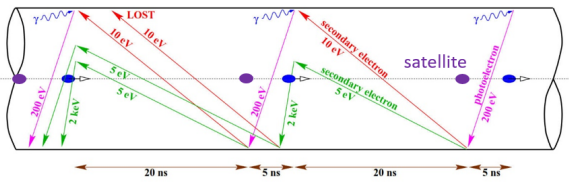

Figure 14: Illustration of intermediate low-intensity satellite bunch deployed for electron-cloud clearing [50] (F. Ruggiero).

A well established standard procedure for electron-cloud suppression is beam scrubbing, that is the operation at the limit of acceptable vacuum pressure or cryogenic heat load for extended periods of time with highest sustainable electron-cloud intensities in order to reduce the secondary emission yield of the vacuum chamber surface, allowing for subsequent safe and electron-free operation at lower beam intensity. Figure 15 illustrates the application of this concept at the LHC, where bunch spacing is a key parameter, determining the strength of the electron cloud. In the LHC, shorter bunch separations lead to enhanced electron-cloud formation, and better surface conditioning. Figure 17 illustrates how, at the LHC "scrubbing" with 25 ns spacing allows for subsequent electron-cloud free operation at 50 ns [51]. Similarly, for fully eliminating electron cloud at a bunch spacing of 25 ns, beam conditioning with a special "doublet" beam — a beam with alternatingly 5 ns and 20 ns spacing — has been considered [51].

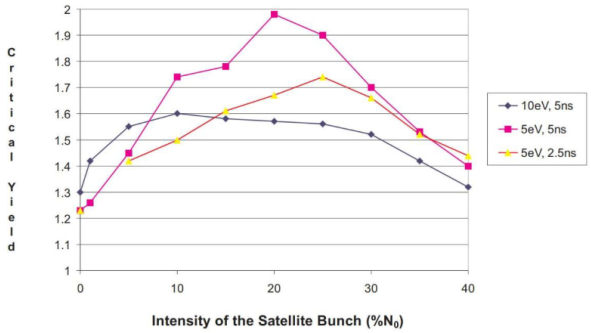

Figure 15: Critical value of the maximum secondary electron yield $\delta_{\max}$ versus the relative intensity of satellite bunches following the nominal bunches at a spacing of 2.5 ns (one LHC RF bucket) or 5 ns (two LHC RF buckets). A highly reflective beam screen surface is assumed, with a surface photon reflectivity $R \simeq 1$, and a half-Gaussian secondary electron energy distribution with 5 eV or 10 eV r.m.s. width [50].

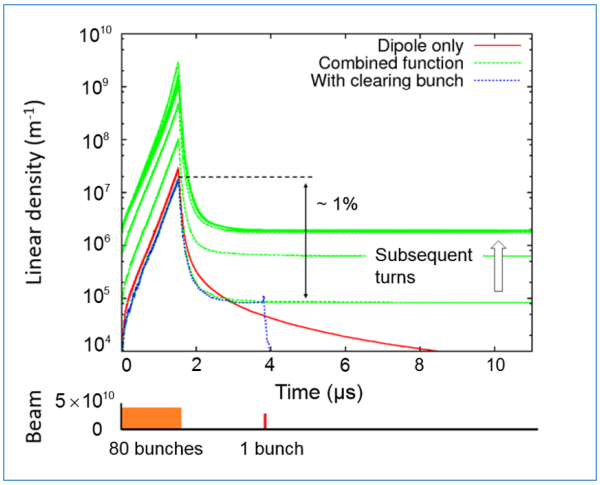

Figure 16: Simulated electron line density in a combined function magnet of the FNAL Recycler as a function of time; a clearing bunch removes the trapped cloud (blue dashed line), preventing the long-term accumulation of electrons [35].

Amorphous carbon (a-C) coating [52] and Laser Ablation Surface Engineering (LASE) [53, 54] of the vacuum chamber surface prior to beam operation are two further, highly efficient schemes for electron-cloud mitigation Both methods dramatically reduce the secondary emission yield. With LASE a maximum secondary emission yield below 1 can be achieved on Cu, Al and stainless steel surfaces;

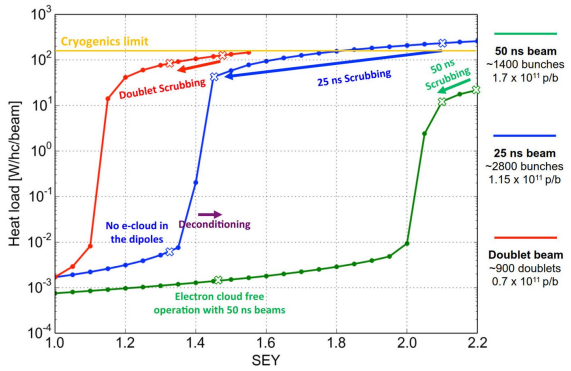

Figure 17: Recipe and effect of LHC beam scrubbing, to prepare for subsequent LHC operation not affected by the electron cloud. The simulated heat load on the LHC dipole beam screen is shown as a function of the SEY for 50 ns (1400 bunches, green line), 25 ns (2800 bunches, blue line) and doublet beams (900 doublets, red line) [51].

see Figs. 18 and 19. The positive effect of LASE has been demonstrated experimentally, with beam in the SPS [55].

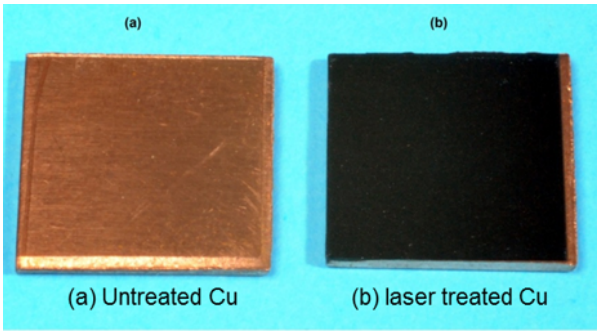

Figure 18: Untreated and laser-treated copper surface [53].

In 2005 an in-situ installation of clearing electrodes was proposed for the LHC [56], as is illustrated in Fig. 20. Presently, another technique for in-situ coating is under development for eRHIC [57, 58]; see Fig. 21. This system could be used to apply various types of coating: Cu, TiN, NEG, and a-C.

MODELLING EFFORTS

Modelling efforts have been discussed and reviewed, among others, at several past two-stream-instability and electron-cloud workshops [59–63]. Figure 22 shows the dream of the CARE-HHH-2004 workshop [64], a complete electron-cloud simulation. We have since come quite a bit closer towards this goal.

Since a few years already, the Warp-Posinst code allows fully self-consistent simulations (many bunches, many turns): of the e-cloud build-up and associated beam dynamics [66]. In particular, Warp-Posinst enabled the first direct simulation of a train of 3×72 LHC-type bunches — using 9,600 CPUs on the Franklin supercomputer (NERSC, U.S.A.). In Fig. 23, we present an example simulation result,

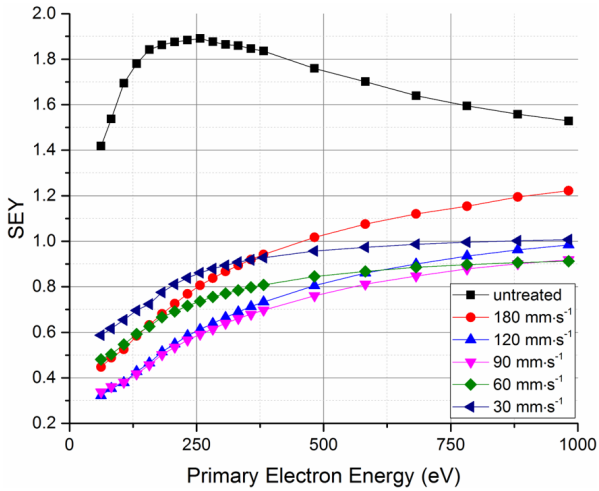

Figure 19: Secondary emission of copper as a function of primary electron energy, without any treatment, and with laser treatment at different processing speeds [54].

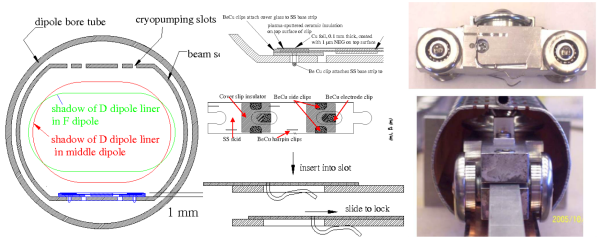

Figure 20: Illustrations of the proposed in-situ installation of LHC clearing electrodes [56].

for the injection of an LHC proton beam into the SPS. A substantial density rise in the tails of the batches is noticeable from turn 0 to turn 800.

LANDAU DAMPING WITH A PINCHING ELECTRON CLOUD

An analytical Landau-damping stability diagram has been constructed for the pinched electron cloud [67]. The model

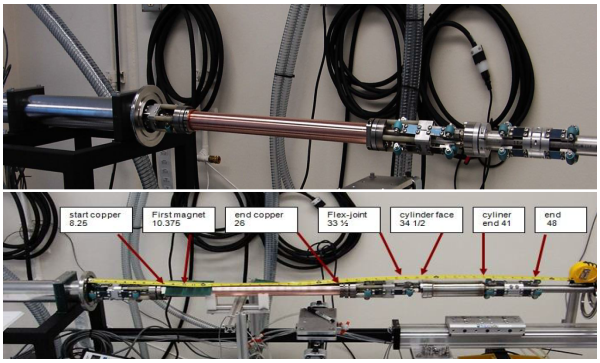

Figure 21: A 50-cm long cathode magnetron mole assembly for in-situ coating of the RHIC vacuum chamber [57, 58].

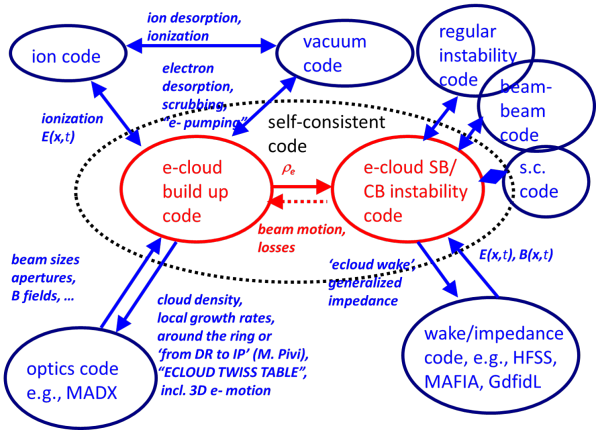

Figure 22: Schematic of the 'ultimate' electron-cloud code sketched in 2004 [65].

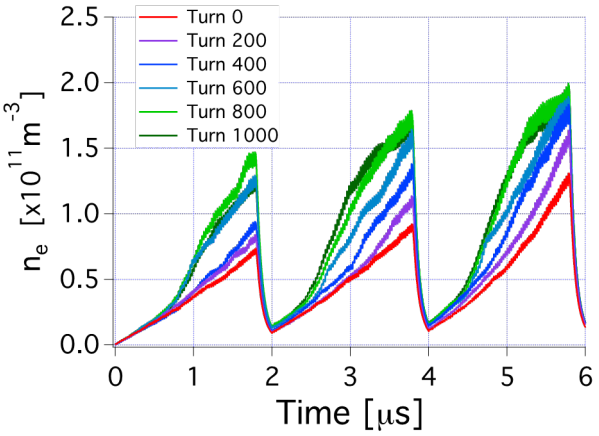

Figure 23: Average electron cloud density history seen at a fixed station [66].

assumes a quasi-parabolic profile (Fig. 24 left)

$$\rho_b(z) = \frac{15}{16\sqrt{7}\sigma_z}\left(1 - \frac{y^2}{7\sigma_z^2}\right)^2 , \qquad (2)$$

and a linear tune shift along the bunch, as a first order approximation of the effect of the electron-cloud pinch,

$$\Delta Q_{ec}(z) = \frac{z - \sqrt{7}\sigma_z}{\sqrt{7}\sigma_z}\Delta Q_{ec,max} ; \qquad (3)$$

see the right picture of Fig. 24. The latter can be converted to

$$z = \frac{\sqrt{7}(2\Delta Q_{ec} + \Delta Q_{ec,max})\sigma_z}{\Delta Q_{ec,max}} . \qquad (4)$$

Together with (2), this yields

$$\rho_b(\Delta Q_{ec}) = \frac{15}{8\Delta Q_{ec,max}}\left(1 - \left(\frac{2\Delta Q_{ec} - \Delta Q_{ec,max}}{\Delta Q_{ec,max}}\right)^2\right)^2 . \qquad (5)$$

Combining formalisms and recipes from H.G. Hereward [68], D. Möhl and H. Schönauer [69], A.E. Chao [70],

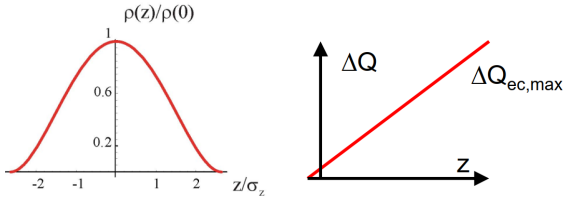

Figure 24: Bunch profile (left) and approximate tune shift along the bunch due to the pinching electron cloud (right), as assumed in the analytical Landau damping model [67].

J.S. Berg [71], E. Métral and F. Ruggiero [72], and assuming a synchrotron period is long compared with the instability rise time leads to the dispersion relation

$$\begin{aligned} 1 &= -\int_0^{\Delta Q_{ec,max}} dQ_{ec}\, \frac{\rho(\Delta Q_{ec})\,[\Delta Q_{coh} - \Delta Q_{ec}]}{Q_0 + \Delta Q_{ec} - Q} \\ &= -\left[P.V.\int_0^{\Delta Q_{ec,max}} dQ_{ec}\, \frac{\rho(\Delta Q_{ec})\,[\Delta Q_{coh} - \Delta Q_{ec}]}{Q_0 + \Delta Q_{ec} - Q}\right. \\ &\quad \left. + i\pi\rho(Q - Q_0)\,[\Delta Q_{coh} - Q + Q_0]\right] , \end{aligned} \qquad (6)$$

which can be rewritten as

$$\Delta Q_{coh} = -\frac{P.V.\int_0^{\Delta Q_{ec,max}} dQ_{ec}\, \frac{\rho(\Delta Q_{ec})\Delta Q_{ec}}{\Delta Q_{ec} - \Delta Q} + i\pi\rho(\Delta Q)\Delta Q - 1}{P.V.\int_0^{\Delta Q_{ec,max}} dQ_{ec}\, \frac{\rho(\Delta Q_{ec})}{\Delta Q_{ec} - \Delta Q} + i\pi\rho(\Delta Q)} . \qquad (7)$$

where $\Delta Q \equiv Q - Q_0$ is the net physical tune shift, and ΔQ_{coh} is the coherent tune shift due to an external machine impedance. We can now plot the trace when ΔQ runs along the real axes (border of stability) in the complex ΔQ_{coh} plane. The result is displayed in Fig. 25. Though the electron potential moves with the beam, the electron cloud alone creates non-trivial stability diagram. We note that $\Delta Q_{ec,max}$ can be huge, of order 0.1–0.2.

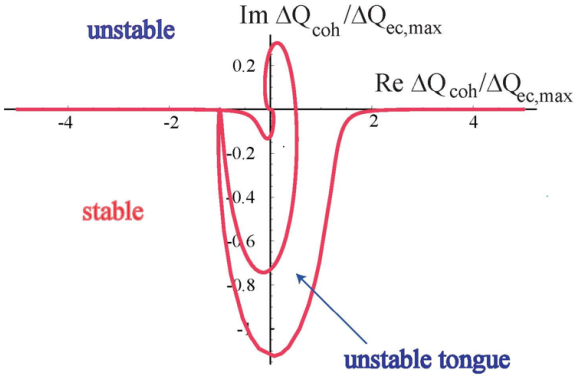

Figure 25: Stability diagram in the presence of a pinching electron cloud [67].

16L2

An interesting effect was seen at the LHC in 2017/18. Apparently limited to a short region "16L2" of the LHC ring,

this phenomenon was marked by loss spikes and fast beam instabilities. The 16L2 problem was mitigated by introducing groups of empty buckets inside the bunch trains and by locally adding weak magnets fields, both cures characteristic of an "electron cloud". The 16L2 was finally explained by a local electron cloud (plus, possibly, an accompanying ion cloud) of high density. The local electron-cloud activity was later attributed to a frozen layer of air and/or water on the surface extending over a few meters length, which had been caused by an accidental air inlet through an adjacent pumping port; see Fig. 26.

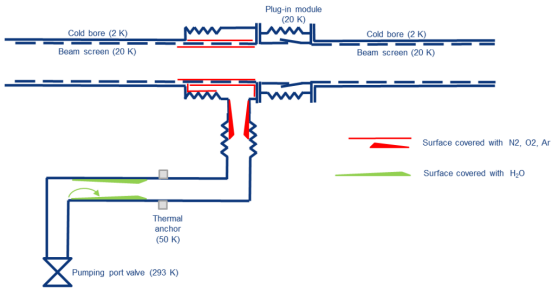

Figure 26: A frozen layer of water and/or air at the LHC's 16L2 location [73].

ELECTRON CLOUD IN THE FCC

Electron cloud is a concern for the proton rings of the proposed 100 TeV hadron collider, FCC-hh [74], with much enhanced synchrotron radiation compared with the LHC, and also for the positron ring of the future circular electron-positron collider, FCC-ee [75]. The FCC hadron-collider beam screen and the lepton-collider vacuum system are illustrated in Fig. 27. Different types of antechambers and advanced surface treatments like LASE, for FCC-hh, and a novel (ultrathin) NEG coating developed for FCC-ee [76,77], will help suppress electron-cloud buildup without a noticeable increase in the machine impedance.

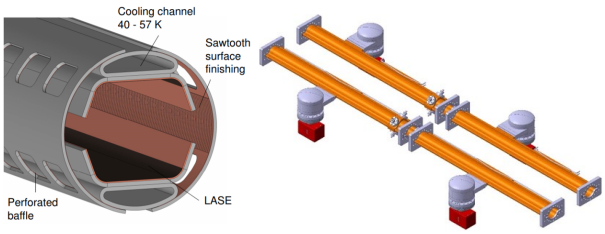

Figure 27: Beam screen for the FCC-hh arcs, with a "folded" integrated antechamber and LASE surface treatment [74] (left), and FCC-ee vacuum chambers with an antechamber, discrete local photon stops, adjacent or opposite pumping domes, and ultra0thin NEG coating [75] (right). Vacuum-chamber optimisation for both FCC-hh hand FCC-ee took into account the need for electron-cloud suppression.

The superiority of the new FCC-hh beam screen design compared with the LHC beam screen is apparent from a comparison of the respective simulated heat load and central electron-density for the HE-LHC [78] (an LHC energy doubler based on FCC-hh magnet technology); see Fig. 28.

The modelling for FCC-ee brings forth new challenges, e.g., related to the energy of the synchrotron-radiation photons. At FCC-ee, photo-electrons are generated via classical photo-effects, but additional, energetic electrons are emitted after an atomic de-excitation [79, 80]. The threshold value for the second process is about 1 keV; for comparison the critical photon energy in the FCC-ee arcs at the $t\bar{t}$ threshold is of order 1 MeV. The atomic deexcitation phenomenon has been integrated with the photon tracking code, SYNRAD3D [81].

Finally, it is interesting to note that the electron cloud itself may interact with the propagating synchrotron radiation [82]. If such effect proved important, this would require yet another level of self-consistency in the electron-cloud modelling effort, where photons and electrons are so far treated fully independently.

FROM LHC TO HL-LHC

The arc heat loads have already been a challenge for LHC Run 2 (2015–2018) with 25 ns bunch spacing, where the LHC operated close to cryogenics limits in some of the arcs. In these arcs the heat load was much larger than expected from impedance and synchrotron radiation. A large differences was observed between sectors; see Fig. 29. A corresponding difference in the electron-cloud behavior between sectors is (or was) the most plausible explanation. The extrapolated HL-LHC heat loads for the high-load sectors would not be acceptable [83, 84].

The highest heat has been found in the sectors around the ATLAS experiment. There has been much speculation as to what was different in the high-load sectors, causing the difference in heat load. Possible explanations included shielding from cosmic rays by the Jura mountains, the changes which may have occurred during the installation/production sequence, or the effect of an inverted, missing or differently shaped sawtooth surface on the beam screen (Fig. 30).

EPILOGUE

In January 2018, the Chair of the LHC Machine Advisory Committee stressed that "LHC electron cloud is a top priority for the LHC and for CERN!" [88]. The same statement, of course, applies to any other future accelerator operating with positively charged particle beams.

ACKNOWLEDGEMENTS

I would like to thank G. Arduini, E. Belli, M. Benedikt, R. Cimino, G. Franchetti, M. Giovannozzi, G. Iadarola, K. Oide, L. Mether, E. Métral, M. Migliorati, G. Rumolo, D. Schulte, and M. Vretenar for helpful discussions and continuous encouragement.

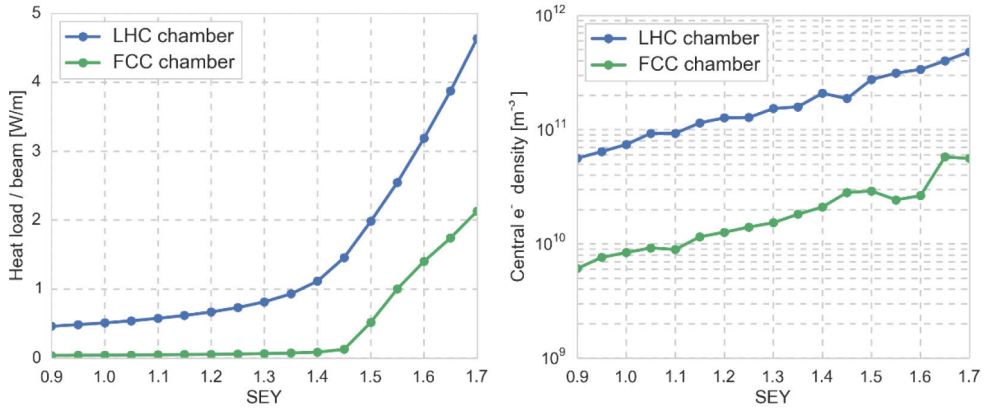

Figure 28: Simulated heat load (left) and central electron density (right) for the HE-LHC [78], comparing an LHC-type beam screen (blue) and the beamscreen designed for FCC-hh (green) (L. Mether).

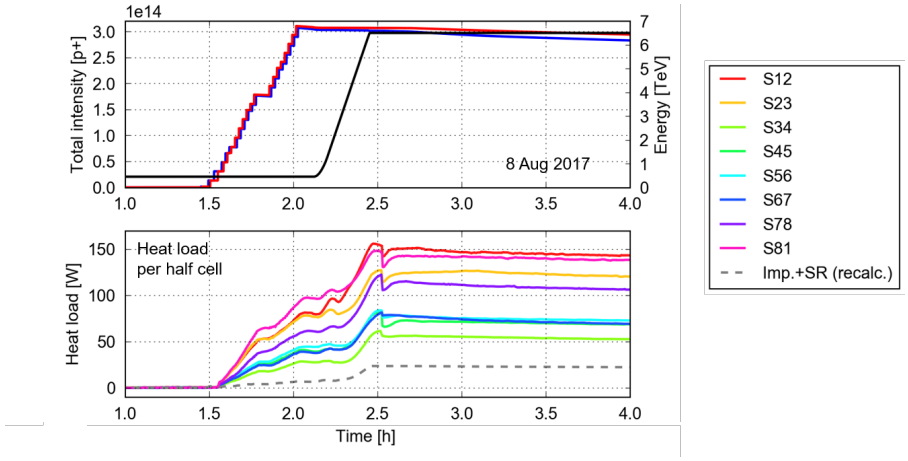

Figure 29: Total beam intensity (top) and heat load per half cell in each of the 8 LHC sectors (bottom) during 4 hours in 2017 [83, 84].

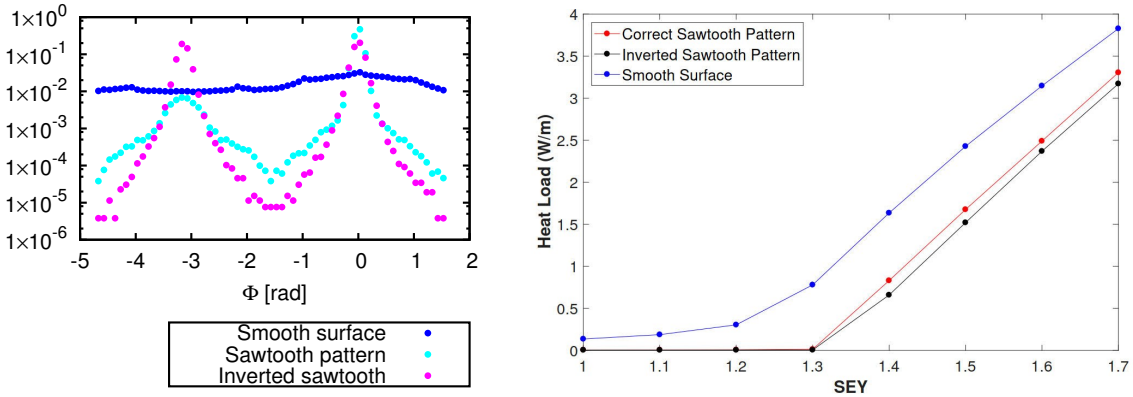

Figure 30: Azimuthal distribution of absorbed synchrotron-radiation photons [85] simulated with the code SYNRAD3D (left) and heat load per metre as a function of the maximum secondary emission yield for different sawtooth configurations [86] simulated by using the SYNRAD3D results as input for the code PyECLOUD [87] (right).

REFERENCES

[1] O. Gröbner,"Bunch Induced Multipactoring", presented at the International Conference on High Energy Accelerators, Serpukhov 1977, CERN-ISR-VA 77-38 (1977).

[2] M. Izawa, Y. Sato, and T. Toyomasu, "The Vertical Instabiity in a Positron Bunched Beam," Phys. Rev. Lett. 74, 25 (1995) 5044.

[3] K. Ohmi, "Beam-Photoelectron Interactions in Positron Storage Rings," Phys. Rev. Lett. 75, 8 (1995) 1526.

[4] M.A. Furman and G.R. Lambertson, "The Electron-Cloud Instability in PEP-II," Proc. EPAC'96 Sitges, LBNL 38220 (1996).

[5] F. Zimmermann, "A simulation study of electron-cloud instability and beam-induced multipacting in the LHC," CERN LHC-Project-Report-95, SLAC-PUB-7425 (1997).

[6] LHC Electron Cloud Crash Programme, web site `http://ab-abp-rlc.web.cern.ch/ab-abp-rlc-ecloud/`

[7] G. Arduini et al., "Transverse Instabilities of the LHC Proton Beam in the SPS," Proc. 7th European Particle Accelerator Conference, Vienna, Austria (2000) 341.

[8] K. Cornelis, "The Electron Cloud Instability in the SPS," Proc. Mini Workshop on Electron Cloud Simulations for Proton and Positron Beams, CERN, Geneva, Switzerland, 15–18 April 2002, CERN-2002-001 (2002) pp. 11–16.

[9] J.M. Jimenez et al., "Electron Cloud with LHC-Type Beams in the SPS: A Review of Three Years of Measurements,âĂİ LHC Project Report 632 (2002).

[10] V. Baglin, B. Jenninger, "SPS electron cloud heat load measurements with WAMPAC and simulations," Proc. ini Workshop on Electron Cloud Simulations for Proton and Positron Beams, CERN, Geneva, Switzerland, 15–18 April 2002, CERN-2002-001 (2002) pp. 79–85.

[11] V. Baglin, I.R. Collins, B. Jenninger, "Performance of a Cryogenic Vacuum System (COLDEX) with a LHC Type Proton Beam," CERN-LHC-Project-Report-667

[12] R. Cimino, I.R. Collins et al., "Can Low-Energy Electrons Affect High-Energy Physics Accelerators?," Phys. Rev.'Lett.'93, 014801 (2004).

[13] I. Collins, "Electron cloud investigations," CERN SL Seminar, Thursday 11 November 1999 (1999) `https://indico.cern.ch/event/413583`.

[14] N. Kos, Engineering Change Order - Class I "Change of Beam screen Types in CryoDipoles for Sector 3-4," LHC-VSS-EC-0010 ver. 1.0, EDMS Document no. 985318, June 2009.

[15] G. Guillermo, D. Sagan, and F. Zimmermann, "Examining mitigation schemes for synchrotron radiation in high-energy hadron colliders," Phys. Rev. Accel. Beams 21, 021001 (2018).

[16] O.S. Brüning et al., "LHC Design Report vol. 1", CERN Yellow Report CERN-2004-003-V-1, Section 12.3.1. (2004).

[17] O.S. Brüning et al., "Electron Cloud and Beam Scrubbing in the LHC," Proc. 18th Biennial Particle Accelerator Conference, New York, NY, USA, 29 March – 2 April 1999 (1999) 2629. and CERN LHC-Project-Report-290

[18] V. Baglin et al., "A Summary of Main Experimental Results Concerning the Secondary Electron Emission of Copper," CERN LHC-Project-Report-472 (2001).

[19] R.E. Kirby, F.K. King, "Secondary electron emission yields from PEP-II accelerator materials," Nucl. Instr. Meth. A 469 (2001) 1–12.

[20] G. Iadarola, L. Mether, G. Rumolo, "Filling schemes and e-cloud constraints for 2017," Proc. 7th Evian Workshop on LHC beam operation, Evian Les Bains, France, 13–15 Dec. 2016 (2016) pp. 239–244.

[21] M. Solfaroli, "Machine configuration and parameters," 8th LHC Operations Evian Workshop, Evian, 12–14 December 2017 `https://indico.cern.ch/event/663598/`.

[22] J. F. Esteban Müller, P. Baudrenghien, T. Mastoridis, E. Shaposhnikova, and D. Valuch, "High-accuracy diagnostic tool for electron cloud observation in the LHC based on synchronous phase measurements," Phys. Rev. ST Accel. Beams 18, 112801 (2015)

[23] F.J. Decker, F. Caspers, F. Zimmermann, "Impact of Microwaves on the Electron Cloud and Incoherent Effects," Proc. Mini Workshop on Electron Cloud Simulations for Proton and Positron Beams, CERN, Geneva, Switzerland, 15–18 April 2002 (2002) pp. 87–90.

[24] M. Mattes, E. Sorolla, F. Zimmermann, arXiv:1310.0212 Proc. Joint INFN-CERN-EuCARD-AccNet Workshop on Electron-Cloud Effects: ECLOUD'12; 5–9 June 2012, La Biodola, Isola d'Elba, Italy, CERN-2013-002 (2012) pp. 177–180.

[25] F. Caspers, F. Zimmermann, "Interactions of Microwaves and Electron Clouds," Proc. Particle Accelerator Conference 2009, Vancouver, Canada, 04–08 May 2009 (2009) pp. WE1PBI02

[26] T. Kroyer et al., "Unexpected results on microwave waveguide mode transmission measurements in the SPS beam pipe," in Proc. 31st Advanced ICFA Beam Dynamics Workshop on Electron-Cloud Effects, Napa, CA, USA, 19–23 April 2004 (2004) pp. 89–94

[27] T. Kroyer, F. Caspers, E. Mahner, "The CERN-SPS Experiment on Microwave Transmission through the Beam Pipe," Proc. 21st IEEE Particle Accelerator Conference, Knoxville, TN, USA, 16–20 May 2005 (2005) pp. 2212

[28] M. T. F. Pivi et al., "Microwave Transmission Measurement of the Electron Cloud Density in the Positron Ring of PEP-II," in Proc. 11th European Particle Accelerator Conference, Genoa, Italy, 23 - 27 Jun 2008 (2008) pp. MOPP065

[29] S. De Santis et al., "Measurement of Electron Clouds in Large Accelerators by Microwave Dispersion," Phys. Rev. Lett. 100 (2008) 094801

[30] J. S. Eldred et al., "Electron Cloud Measurements in Fermilab Main Injector and Recycler," Proc. IPAC2015 (2015) MOPMA027

[31] S. A. Antipov, "Fast Transverse Beam Instability Caused by Electron Cloud Trapped in Combined Function Magnets," Springer Theses (2018) ISBN 3030024083, 9783030024086

[32] S. S. Win, H. Fukuma, S. Kurokawa, K. Ohmi, "Study Of Coupled Bunch Instability Caused By Electron Cloud In Kekb Positron Ring," Proc. 8th European Particle Accelerator Conference, Paris, France, 3–7 June 2002 (2002) pp. 1592

[33] S. S. Win et al., "Numerical study of coupled-bunch instability caused by an electron cloud," Phys. Rev. ST Accel. Beams 8, 094401 (2005).

[34] L. Wang, H. Fukuma, S. Kurokawa, K. Ohmi, K. Oide, "Photoelectron Trapping in Electric and Magetic Field," in Proc. 8th European Particle Accelerator Conference, Paris, France, 3–7 June 2002 (2002) pp. 1586.

[35] S. A. Antipov, S. Nagaitsev, "Electron Cloud Trapping In Recycler Combined Function Dipole Magnets," PoS ICHEP2016 (2017) 773, doi: 10.22323/1.282.0773.

[36] H. Fukuma, "Electron Cloud Effects at KEKB," Proc. Mini Workshop on Electron Cloud Simulations for Proton and Positron Beams, CERN, Geneva, Switzerland, 15–18 April 2002, CERN-2002-001 (2002) pp. 1–9; doi: 10.5170/CERN-2002-001.1

[37] K. Ohmi, F. Zimmermann, "Head-tail instability caused by electron cloud in positron storage rings," Phys. Rev. Lett. 85 (2000) 3821–3824.

[38] K. Ohmi, F. Zimmermann, E. A. Perevedentsev, "Wake-field and fast head-tail instability caused by an electron cloud," Phys. Rev. E 65 (2001) 016502.

[39] Y. Suetsugu et al., "Mitigating the electron cloud effect in the SuperKEKB positron ring," Phys. Rev. Accel. Beams 22, 023201 (2019).

[40] Y. Suetsugu, "Updates of SKEKB MR Vacuum System," 22nd KEKB Review, 14 Match 2018.

[41] F. Zimmermann, "Scaling the Electron Cloud Instability Threshold to Higher SPS Energy," presented at CERN ABP-RLC Meeting, 18 Nov. 2005 http://ab-abp-rlc.web.cern.ch/ab-abp-rlc/Meetings/2005/2005.11.18/ScalingWithEnergy-FZ.pdf

[42] F. Zimmermann, "Overview of Electron-Cloud Effects in the LHC and Present Understanding," CERN-GSI bi-lateral working meeting on Collective EffectsâĂŞCoordination of Theory and Experiments, 30 March 2006 http://care-hhh.web.cern.ch/care-hhh/Collective\%20Effects-GSI-March-2006/default.html

[43] G. Rumolo, G. Arduini, E. Métral, E. Shaposhnikova, E. Benedetto, R. Calaga, G. Papotti, and B. Salvant, "Dependence of the Electron-Cloud Instability on the Beam Energy," Phys. Rev. Lett. 100, 144801 (2008).

[44] O. Domínguez, K. Li, G. Arduini, E. Métral, G. Rumolo, F. Zimmermann, and H. Maury Cuna, "First electron-cloud studies at the Large Hadron Collider," Phys. Rev. ST Accel.'Beams 16, 011003 (2013).

[45] A. Romano et al., "Electron cloud buildup driving spontaneous vertical instabilities of stored beams in the Large Hadron Collider," Phys. Rev. Accel. Beams 21, 061002 (2018).

[46] R. D'Agnolo et al, "Strategy for Extreme Beam Facilities," CERN-ACC-2017-0033, ARIES Monograph XLIV, Institute of Electronic Systems, Warsaw University of Technology, Warsaw, 2017, edited by F. Zimmermann (2017).

[47] E. Benedetto, G. Franchetti, F. Zimmermann, "Incoherent effects of electron cloud in proton storage rings," Phys. Rev. Lett. 97 (2006) 034801.

[48] J. Wei et al., "Observation of Electron-Ion Effects at RHIC Transition," in Proc. 2005 Particle Accelerator Conference (PAC), Knoxville, Tennessee, 2005, edited by C. Horak (2005) p. 4087.

[49] Xiaolong Zhang, email to Francesco Ruggiero, October 2005

[50] Francesco Ruggiero and Xiaolong Zhang, "Collective Instabilities in the LHC: Electron Cloud and Satellite Bunches," in Proc. Workshop on Instabilities of High Intensity Hadron Beams in Rings, Upton, NY, USA, 28 June – 1 July 1999, edited by T. Roser and S.Y. Zhang, Amer. Inst. Phys., AIP Conference Proceedings 496 (1999) pp. 40–48.

[51] G. Iadarola, G. Rumolo, "Electron Cloud and Scrubbing: Perspective and Requirements for 25 ns Operation in 2015," in Proc. 5th Evian Workshop on LHC beam operation, Evian-les-Bains, France, 2–4 June 2014, CERN-ACC-2014-0319 (2014) pp. 81–92.

[52] C. Yin Vallgren et al., "Amorphous Carbon Coatings for Mitigation of Electron Cloud in the CERN SPS," in Proc. 1st International Particle Accelerator Conference, Kyoto, Japan, 23–28 May 2010 (2010) pp. TUPD048

[53] O Malyshev, "Laser Ablation Surface Engineered (LASE) surfaces for e-cloud mitigation," FCC-hh impedance and beam screen workshop, CERN, 30–31 March 2017 (2017).

[54] R. Valizadeh et al., "Reduction of secondary electron yield for E-cloud mitigation by laser ablation surface engineering," Applied Surface Science, Vol. 404, 15 (2017) 370–379 doi: 10.1016/j.apsusc.2017.02.013.

[55] S. Calatroni et al., "First accelerator test of vacuum components with laser-engineered surfaces for electron-cloud mitigation," Phys. Rev. Accel. Beams 20 (2017) 113201

[56] P. M. McIntyre, A. Sattarov, "illing the Electron Cloud Effect in the LHC Arcs," Proc. 21st IEEE Particle Accelerator Conference, Knoxville, TN, USA, 16–20 May 2005 (2005) pp. 2971

[57] A. Hershcovitch et al., "Recent RHIC in-situ coating technology developments," Proc. Joint INFN-CERN-EuCARD-AccNet Workshop on Electron-Cloud Effects, La Biodola, Isola d'Elba, Italy, 5–9 Jun 2012, CERN-2013-002 (2013) pp. 251–258

[58] A. Hershcovitch et al., "Device and Technique for In-situ Coating of the RHIC Cold Bore Vacuum Tubes with Thick OFHC," Proc. 4th International Particle Accelerator Conference, Shanghai, China, 12–17 May 2013 (2013) pp. 3508

[59] Workshop on Two-Stream Instabilities - Two-Stream Instabilities, KEK, Tsukuba, Japan, 11—14 September 2001; http://conference.kek.jp/two-stream/.

[60] Mini Workshop on Electron Cloud Simulations for Proton and Positron Beams — ECLOUD'02, CERN, 15 –18 April 2002. Proc. edited by G. Rumolo and F. Zimmermann, CERN-2002-001 (2002).

[61] 31st Advanced ICFA Beam Dynamics Workshop on Electron-Cloud Effects — ECLOUD'04, Napa, CA, USA, 19–23 April 2004. Proc. edited by M. Furman, S. Henderson, and F. Zimmermann, CERN-2005-001 (2005).

[62] International Workshop on Electron-Cloud Effects — ECLOUD'07, Daegu, Korea, April 9–12, 2007. Proc. edited by H. Fukuma, K. Ohmi, and E.-S. Kim, KEK Proceedings 2007-10 (2007).

[63] Joint INFN-CERN-EuCARD-AccNet Workshop on Electron-Cloud Effects — ECLOUD'12, La Biodola, Isola d'Elba, Italy. Proc. edited by R. Cimino, G. Rumolo, and F. Zimmermann, CERN-2013-002 (2013).

[64] 1st CARE-HHH-APD Workshop on Beam Dynamics in Future Hadron Colliders and Rapidly Cycling High-Intensity Synchrotrons — "HHH 2004", CERN, Geneva, Switzerland, 8–11 November 2004. Proc. edited by F. Ruggiero, W. Scandale, and F. Zimmermann, CERN-2005-006 (2005).

[65] F. Zimmermann, "Summary of Panel Discussion on Electron-Cloud Simulation Codes", in Proc. HHH-2004 [64] (2005) p. 297

[66] M.A. Furman, J.-L. Vay, M. Venturini, "Direct Numerical Modeling of E-Cloud Driven Instability of Three Consecutive Batches in the CERN SPS," Proc. IPAC 2012, New Orleans, USA (2012) 1125-1127

[67] F. Zimmermann, "Stability Diagram with Electron Cloud," presented at CERN ABP-RLC Meeting, 7 July 2006 http://ab-abp-rlc.web.cern.ch/ab-abp-rlc/Meetings/2006/2006.07.07/stability\%20diagram\%20with\%20e-cloud.ppt

[68] H. G. Hereward, "Landau damping by non-linearity," CERN-MPS-DL-69-11 (1969).

[69] D. Möhl and H. Schönauer, "Landau damping by non-linear space-charge forces and octupoles," in Proc. 9th International Conference on High-energy Accelerators, SLAC, Stanford, CA, USA, 2–7 May 1974 (1974) pp. 380–384

[70] A. W. Chao, Physics of collective beam instabilities in high energy accelerators, published by Wiley, New York, USA (1993).

[71] J. Scott Berg and F. Ruggiero, "Landau Damping with two-dimensional betatron tune spread", CERN SL-AP-96-71 (AP) (1996).

[72] E. Métral and F. Ruggiero, "Landau damping with two-dimensional betatron tune spread from both octupoles and non-linear space charge," in Proc. 9th European Particle Accelerator Conference, Lucerne, Switzerland, 5–9 July 2004 (2004) pp. 1897

[73] F. Bordry, "LHC Performance Workshop (Chamonix'18) Summary," CERN, 7 March 2018.

[74] M. Benedikt et al., "FCC-hh: The Hadron Collider", The European Physical Journal Special Topics 228, 4 (2019) 755–1107; 10.1140/epjst/e2019-900087-0

[75] M. Benedikt et al., "FCC-ee: The Lepton Collider", The European Physical Journal Special Topics 228, 2 (2019) 261–623; 10.1140/epjst/e2019-900045-4

[76] E. Belli et al., "Electron cloud buildup and impedance effects on beam dynamics in the Future Circular e+e- Collider and experimental characterization of thin TiZrV vacuum chamber coatings," Phys. Rev. Accel. Beams 21 (2018) 111002

[77] E. Belli, "Coupling Impedance and Single Beam Collective Effects for the Future Circular Collider (Lepton Option)," PhD Thesis Sapienza, CERN-THESIS-2018-381 (2018).

[78] F. Zimmermann et al., "HE-LHC: The High-Energy Large Hadron Collider", The European Physical Journal Special Topics 228, 5 (2019) 1109–1382; 10.1140/epjst/e2019-900088-6

[79] S. Poprocki, J. A. Crittenden, D. L. Rubin, D. Sagan, "Modeling Studies for Synchrotron-Radiation-Induced Electron Producyion in the Vacuum Chamber Walls at CesrTA," Proc. 9th International Particle Accelerator Conference IPAC2018, Vancouver, BC, Canada (2018) 3011.

[80] S. Poprocki et al., "Measurement and modeling of electron-cloud-induced betatron tune shifts at the Cornell Electron-Positron Storage Ring test accelerator," Phys. Rev. Accel. Beams 22, 081001 (2019).

[81] G. Dugan and D. Sagan, "Simulating synchrotron radiation in accelerators including diffuse and specular reflections," Phys. Rev. Accel. Beams 20, 020708 (2017).

[82] D. I. Kaltchev and F. Zimmermann, "On the Transparency of the Electron Cloud to Synchrotron Radiation," Proc. Mini Workshop on Electron Cloud Simulations for Proton and Positron Beams, CERN, Geneva, Switzerland, 15–18 April 2002, CERN-2002-001 (2002) pp. 243–250.

[83] G. Iadarola, "Digesting the LIU high brightness beam: is this an issue for HL-LHC?", Chamonix'18 LHC Performance Workshop (2018).

[84] L. Tavian,' "Report from the task force on beam induced heat load", Chamonix'18 LHC Performance Workshop (2018).

[85] G. Guillermo, D. Sagan, and F. Zimmermann, "Examining mitigation schemes for synchrotron radiation in high-energy hadron colliders," Phys. Rev. Accel. Beams 21, 021001 (2018).

[86] G. Guillermo Canton, G.H.I. Maury Cuna, E. Ocampo, F. Zimmermann, "Electron Cloud Build Up for LHC Sawtooth Vacuum Chamber," in Proc. 9th International Particle Accelerator Conference, Vancouver, Canada, 29 April – 4 May 2018 (2018) TUPAF030

[87] G. Iadarola, E. Belli, K. Li, L. Mether, A. Romano, and G. Rumolo, "Evolution of Python Tools for the Simulation of Electron Cloud Effects," CERN-ACC-2017-240 (2017).

[88] N. Holtkamp, private communication, 18 January 2018.

ELECTRON CLOUD EFFECTS AT THE CERN ACCELERATORS

G. Rumolo*, H. Bartosik, E. Belli, G. Iadarola, K. Li, L. Mether, A. Romano, F. Zimmermann,
CERN, Geneva, Switzerland
P Dijkstal, PSI, Villigen, Switzerland
M. Schenk, EPFL, Lausanne, Switzerland

Abstract

Electron cloud effects have been identified as one of the main performance limitations for some of the synchrotrons of the CERN accelerator complex. The tools for the simulation of the electron cloud build-up and its effects on beam stability have significantly evolved in recent years, leading to a much better understanding of all machine observations. At the same time, electron cloud mitigation measures have been tested (e.g. surface treatments) and implemented in operation (e.g. beam induced scrubbing). The combination of a deeper understanding of the electron cloud and a handle on its mitigation has been the key to reach and exceed the nominal luminosity in the LHC during Run 2 as well as to define strategies to cope with the High Luminosity (HL) operation of the LHC as from 2026.

INTRODUCTION AND HISTORY

General concept and early studies

Electron production in a closed environment with an oscillating electromagnetic field can lead under certain circumstances to multipacting, i.e. avalanche multiplication of the number of electrons due to their acceleration in the electromagnetic field and subsequent impact against high Secondary Electron Yield (SEY) surfaces. This phenomenon can significantly degrade the performance of RF devices (e.g. in applications for space satellites [1]) as well as that of accelerator (or storage) rings operating with closely spaced positron or proton bunches [2].
Figure 1 illustrates schematically how an electron cloud (e-cloud) builds up at a certain location (transversal cut) in the vacuum chamber of an accelerator ring.

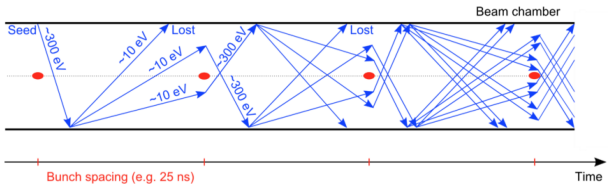

Figure 1: Sketch of electron cloud formation in the vacuum chamber of an accelerator ring.

Each passing bunch generates a number of primary electrons (e.g. photoelectrons), which are accelerated by the beam field and fly across the chamber cross section. Each electron produces secondaries when it hits the inner wall of the vacuum chamber, provided that the SEY is greater than unity at the impact energies. The number of electrons in the vacuum chamber thus increases by the arrival of the next bunch, and eventually grows exponentially as more bunches go through. The e-cloud build up stops when a dynamical steady state is reached, at which the space charge repulsion of the e-cloud itself prevents the electrons newly emitted at the surface from being accelerated in the beam field, and the net electron production and loss rates become equal. E-cloud build up in an accelerator is associated to pressure rise, heat load in cryogenic regions, stable phase shift, beam instability and emittance growth.
Observations and first studies of beam-induced multipacting at CERN date back to 1977, when a pressure rise at the Intersection Storage Ring (ISR) after installation of an aluminum test chamber was ascribed to electron accumulation [3]. Based on the ISR experience, concerns about the Large Hadron Collider (LHC) operation already started at the very first design stages in the 1980's. These worries were then reinforced over the next two decades, when beam instabilities due to photoelectrons were observed at the KEK Photon Factory [4,5] and a series of e-cloud studies including both simulations and experiments were launched both at the Beijing Electron Positron Collider [6] and for the positron ring (LER) of the PEP-II B Factory [7].

E-cloud studies at CERN before LHC (1996-2009)

In the second half of the 90's first estimates were published, predicting a serious effect on heat load and beam stability for LHC (e.g. [8–11]). The existence of conditions for beam-induced multipacting in the LHC was first mentioned in 1996 [8]. About the same time, mainly motivated by the e-cloud observations in e^+ storage rings, the e-cloud build up code ECLOUD was developed [9]. The code gradually grew and new features were added over the years to improve its modelling [10] and reproduce different observables (e.g. heat load on chamber, effect on pick up electrodes [12]) as well as to explore possible mitigation techniques (e.g. satellite bunches). In parallel to the numerical effort, advanced analytical models were also developed to describe the e-cloud formation and evolution as well as the effects of its interaction with a particle beam [13–15].
After 1998, e-cloud effects were directly and systematically observed at the CERN Super Protron Synchrotron (SPS) with the LHC beam (25 ns bunch spacing) [16].
In the early 2000's, the e-cloud was observed also in the upstream injector, the Proton Synchrotron (PS) in its late stages of the preparation of the 25 ns spaced beams [17–19]. At the same time, since beam stability and lifetime turned

* Giovanni.Rumolo@cern.ch

out to be significantly affected by the presence of an e-cloud in the CERN accelerator rings, the HEADTAIL code was developed in order to study the interaction of an e-cloud with a bunch of positively charged particles [12,20]. As a novelty with respect to existing codes (e.g. the one described in [21]), the HEADTAIL code had several distinctive features:

- It could model both the e-cloud and the particle bunch as ensembles of macroparticles with a finite transverse size (strong-strong approach), such that the emittance growth due to e-cloud could also be studied alongside with coherent beam stability;
- Although the code was originally intended to only model the interaction of a particle bunch with an e-cloud, its scope was soon extended to include other types of sources of collective interactions, like beam coupling impedances and space charge, which in turn benefited from the slice modeling. The study of the interplay between any of these effects became possible;
- HEADTAIL was also interfaced with ECLOUD to receive the electron distribution just before a bunch passage in the saturation stage of the electron cloud build up, to be used as initial distribution for the interaction with the bunch.

The beam transport in the transverse planes and the longitudinal motion, which had been initially modelled through simple decoupled one-turn linear transfer matrices, were upgraded over the years to include more detailed lattices, nonlinearities (multipoles, different RF systems), coupling between transverse planes and damping. The ECLOUD and HEADTAIL codes were intensively used over the first decade of the 2000's not only to interpret the observed e-cloud effects in the SPS [22–24], but also to study future upgrade scenarios and mitigation techniques [25–27]. The data recorded during the SPS experimental studies also served as a benchmark for the validation of the simulation tools, steering the assessment of the models to be used for the LHC predictions. It also became increasingly clear that the electron cloud was a potential danger for the LHC operation in terms of heat load on the cold beam screen, beam stability and beam quality degradation [28–30]. Extensive simulation studies showed that the heat load in the beam screen of the dipoles would exceed the cryogenic capacity already for a maximum SEY of 1.3 with nominal beam parameters (much lower value than the known SEY of "as received" Cu, but considered attainable through conditioning). Furthermore, while it was found that the e-cloud driven instability could be efficiently controlled with transverse feedback and/or high chromaticity, the e-cloud was also identified as responsible for a slow emittance growth induced by periodic crossing of resonances, leading to an intolerable degradation of the beams in collision also in the absence of a strong instability. However, a reliable assessment of the impact of all these predictions on the future LHC operation was made very difficult by the sensitivity of the results to the model parameters and the numerical accuracy [28]. The following strategy was therefore laid out and applied to the LHC (fully detailed in the LHC Technical Design Report [31]):

- Use sawtooth pattern in the beam screen of the dipoles to reduce photon reflectivity and photoemission yield;
- Shield the pumping slots on top and bottom of the beam screen in the cryogenic regions in order to avoid multipacting (and heat deposition) on the cold bore;
- Coat all warm sections with Non-Evaporable Getter material (NEG) having low SEY;
- Rely on surface scrubbing (from electron bombardment while running within the limits of the cryogenic system) to eventually lower the maximum SEY close enough to its estimated e-cloud build up threshold value;
- Keep the back-up options to run with larger bunch spacing (50 ns) or to use cleaning satellite bunches, if they can be produced in a clean manner in the injectors, compatibly with the requirements from the experiments.

The LHC era

After the LHC was fully installed and commissioned, and its regular operation started as of November 2009, the years 2010 – 2013 (Run 1) and 2015 – 2018 (Run 2) were characterised by the following main facts:

- **SPS**: The LHC beams with 25 ns bunch spacing were successfully produced within specifications (i.e. without visible degradation from e-cloud even for the lower transverse emittances achieved in the pre-injectors) [32]. The future operation with double intensity and brightness was extensively investigated by means of both experimental and numerical studies [33, 34]. It was concluded that beam induced scrubbing would be the baseline choice also for operation in the new beam parameter range, while making sure that all the logistics for a-C coating would be fully developed in case of need for post-LS2 implementation due to persisting e-cloud issues in Run 3;
- **LHC**: Apart from some cases of localised pressure rise in the common beam chambers, operation in presence of e-cloud in the LHC was first experienced when the bunch spacing was reduced from 150 ns to 75 and then 50 ns, which required the first LHC scrubbing run in 2011. As first tests of injection of 25 ns spaced beams revealed severe e-cloud effects, which required further understanding and scrubbing, the 50 ns bunch spacing was kept for operation throughout Run 1. After a successful scrubbing run and a pilot physics run with 25 ns beams at the end of 2012, operation eventually switched to 25 ns in Run 2 (2015-2018) [35–39]. Run 2 was characterised by the progress in the understanding of the observed heat loads and beam instabilities, the arising of puzzling observations like the difference of

heat loads between the LHC sectors, and the establishment of predictions for the HL-LHC operation beyond 2025 [40–42].

The simulation tools used over the previous decade underwent an important upgrade and re-write, evolving into the modular Python based codes PyECLOUD and PyHEADTAIL [43, 44] – more robust, performant, reliable and flexible. These codes have been eventually merged into a common set of accelerator library modules that can be combined to provide simulations of e-cloud build up and multi-bunch beam dynamics under collective effects (including e-cloud and ions) [45, 46]. This development was necessary, and turned out to be instrumental to interpret and explain all the SPS and LHC observations, steer their current operation and make all the required extrapolations for the future operation of both machines in the HL-LHC era. The success of this project was the result of a long standing effort and, unlike previous attempts to modernise and speed up the e-cloud tools (both in-house and through external collaborations), has produced a maintainable and durable set of tools.

THE ELECTRON CLOUD IN THE CERN ACCELERATORS

The Proton Synchrotron (PS)

The production scheme of the LHC beams in the PS is based on two or three steps of bunch splitting in order to obtain at the exit of the PS bunch trains with 50 ns or 25 ns spacing, respectively. In either case, the final stage of bunch splitting takes place at top energy (26 GeV) and is followed by adiabatic bunch shortening and fast bunch rotation shortly before extraction [47]. These two processes are meant to reduce the bunch length from the initial 15 ns after the last splitting to 12 and then 4 ns, respectively, and make the bunches fit into the 5 ns long SPS buckets. The beam parameters are summarized in Table 1.

Table 1: PS beam parameters at 26 GeV for 50 and 25 ns beams

	50 ns	**25 ns**
Bunch intensity ($\times 10^{11}$ ppb)	1.3-2.0	1.3-2.0
Bunch length (ns)	$15 \rightarrow 12 \rightarrow 4$	
Number of bunches	36	72
Transv. rms emittances (μm)	1-2	2-3

The LHC beams in the PS are prone to e-cloud formation only during the last few tens of milliseconds of the production cycle, as was confirmed in several observations and dedicated studies conducted between 2000 and 2009 [19,48–50]. A measurement campaign to reveal e-cloud at 26 GeV and the related beam instabilities was conducted right before LS1 to assess the possible impact of the e-cloud on future beams [34]. To clearly observe the instability rising, the flat top had to be extended by several ms with respect to an operational cycle. Figure 2, upper plot, shows for example the amplitude of the horizontal oscillation as a function of the bunch and turn number for a typical train of 72 bunches with 25 ns spacing right after the bunch rotation. It is possible to see that the bunches at the end of the train are the first to become unstable, and then the instability appears with lower rise times to the middle of the train. The unstable motion propagates in a correlated fashion between bunches, while the head of the train remains stable. The bottom plot shows the horizontal cut of the upper picture, where one can see the exponential rise.

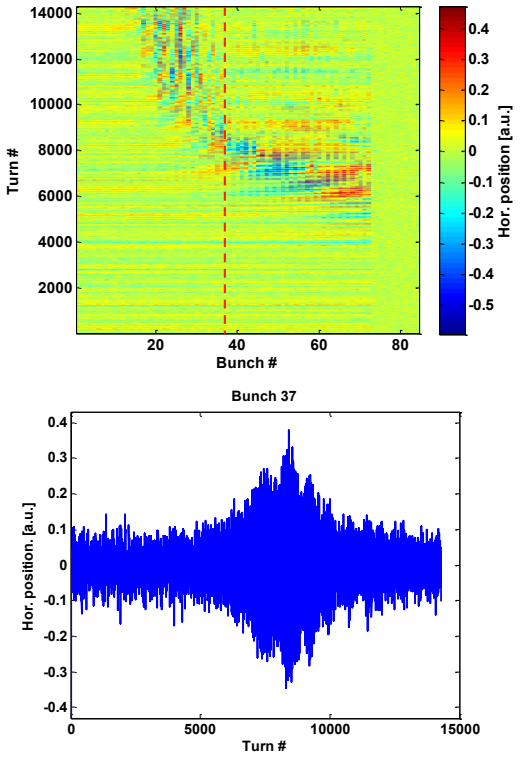

Figure 2: Instability along a 72 bunch train in the CERN PS. The evolution of the horizontal oscillation amplitude is plotted as a function of bunch and turn number (top) and the horizontal cut displayed with a red dashed line in the top plot is shown in the bottom plot.

However, during Run 2 (2014-2018), thanks to already installed LIU hardware, the PS has successfully produced trains of 72 bunches with 2.6e11 p/b at the PS extraction, which represent the beam structure and bunch intensity targeted for post-LS2. Although no problem of transverse beam stability has emerged for these beams at 26 GeV, it must be noticed that their transverse emittance was still about twice lower than the future post-LS2 beams.

The Super Proton Synchrotron (SPS)

Since the early 2000's, observations of pressure rise, beam instability and emittance growth in the SPS pointed to the presence of an e-cloud limiting the capability of this accelerator of handling LHC-type beams [51]. Stabilising the beam with the transverse damper and sufficiently high chromaticity, regular scrubbing runs (lasting from few days to

two weeks) took place at the beginning of almost every operational year between 2002 and 2010 to achieve the necessary reduction of the SEY of the vacuum chambers. The strategy has proved successful, as the e-cloud indicators (e.g. emittance growth along the bunch train) gradually disappeared and the nominal LHC beams could be produced in the SPS with no significant e-cloud degradation as from 2011. The achieved parameters are summarised in Table 2. The three values of bunch length quoted are the injected value, that after filamentation at flat bottom (RF voltage to 4 MV), and at flat top (after controlled longitudinal emittance blow up during the accelerating ramp, if needed – usually not applied with Q20 optics).

Table 2: SPS beam parameters for 50 and 25 ns beams

	50 ns	**25 ns**
Beam energy (GeV)	26 → 450	
Bunch intensity ($\times 10^{11}$ ppb)	1.2-1.8	1.3
Full bunch length 4σ (ns)	4 → 2.8 → 1.5	
Number of bunches	144	288
Transv. rms emittances (μm)	1-2	1.5-2.5

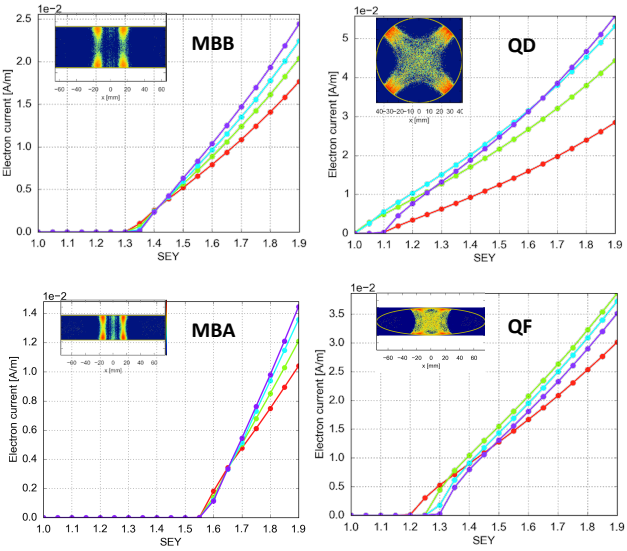

Figure 3: SEY curves for e-cloud formation for four types of SPS chambers and four different bunch intensities (red 1.0×10^{11} p/b, green 1.5×10^{11} p/b, turquoise 2.0×10^{11} p/b, purple 2.5×10^{11} p/b).

Many studies were conducted in the SPS, both as a test-bench for LHC [22, 23] and in the framework of the LHC injector upgrade (LIU) program [26, 27, 32]. During LS1, the SPS was opened and the vented surfaces of the beam chambers were expected to return to high values of SEY. However, the post-LS1 experience showed that scrubbing can be recovered fairly quickly (1 week) for the nominal intensity, while higher intensities, like those required in the HL-LHC era, are still affected by losses and further scrubbing will be needed [33].
A key point to be addressed for the SPS was to determine the values of SEY thresholds for e-cloud formation in the different beam chambers and define what parts are critical for present and future LHC beams. Figure 3 shows the electron flux to the wall as a function of the SEY for four different values of bunch current and for the main types of SPS chambers, i.e. MBA and MBB-type for dipoles plus QD and QF for quadrupoles (shapes and sizes of these chambers can be found in [43]). The following features can be observed:

- The e-cloud build up is fairly insensitive to bunch intensity for dipoles (though the position of the stripes changes), while thresholds in quadrupoles exhibit a non-monotonic behaviour with bunch intensity;
- Above the SEY threshold, the electron flux always becomes quickly larger for larger bunch currents;
- MBA-type chambers have higher SEY threshold value and therefore are the easiest to scrub, while MBB-type and quadrupole chambers have lower SEY threshold (comparable or lower values than those to which StSt potentially scrubs) and might suffer from large e-cloud build up even after extensive scrubbing.

Considering all the results of the above study as well as the encouraging results from the scrubbing campaigns in 2014 and 2015 with larger bunch currents than nominal (2.0×10^{11} p/b), it was decided to apply a-C coating [27] only to the quadrupole chambers and some of the drift chambers during the Long Shutdown 2 (LS2), while relying on scrubbing for the long term operation of the SPS with HL-LHC beam intensities. Further experience with high intensity beams in the SPS (>2e11 p/b) has shown that scrubbing is indeed effective to reduce the emittance growth, however a horizontal instability has been also observed to limit the bunch intensity to about 1.8e11 p/b and a stabilisation strategy has to be laid out. While the source of this instability has not yet been pinned down, its features might point to e-cloud to play a role in its onset. Coating of the MBB chambers in LS3 is kept as an option if scrubbing will turn out not to be sufficient to guarantee the desired beam quality during Run 3 [33].

The Large Hadron Collider (LHC)

In mid 2010 LHC started operating with 150 ns spaced bunches for physics. During this period of operation, a pressure rise was observed in uncoated parts of the common vacuum chamber, which could be suppressed by installation of solenoids. Injection of 75 ns and 50 ns beams showed initially strong e-cloud effects [35]. At the beginning of 2011, a ten day scrubbing run with 50 ns beams took place in order to prepare the machine to operate with this type of beams and thus extend the luminosity reach for the 2011 run. The scrubbing run was successful and by end June the number of bunches collided in the LHC reached its maximum value of 1380 per beam, while the intensity per bunch and the transverse emittances remained constant at their nominal values

(i.e., 1.15×10^{11} ppb and 2.5 μm). Over 2011 and 2012, the 50 ns beams were gradually made brighter (to about (10^{11}p/b)/(1 μm)) and more intense (up to 1.7×10^{11} p/b at collision) without causing any significant recrudescence of the e-cloud effects. Experience with 25 ns beams prior to LS1 was only limited to few MD sessions in 2011 and 2012, and a scrubbing run followed by a pilot physics run at the end of 2012. The 25 ns beams appeared to suffer from strong instabilities at injection (damped with transverse damper and high chromaticity) and exhibited poor lifetime and blown up emittances. Using the heat load measurements, the SEY on the beam screen in the arcs was estimated to decrease from an initial value above 2.0 to about 1.4 [36, 37], with little deconditioning between 2011 and 2012.

During LS1, the LHC chambers were vented and the SEY was reset to its initial values. That's why an extended scrubbing of four weeks with 25 beams, with very gradual intensity ramp up, was necessary to reach the stage at which the LHC could start producing physics with 25 ns beams. After several cycles of deconditioning/reconditioning, 2242 bunches per beam were successfully put in collision by October 2015. The filling pattern used was relaxed (injection of trains of 36 bunches from SPS) in order to keep the heat load in the beam screen of the arcs below the limit (135 W per half cell (W/hc) for one of the sectors). In 2016, after a 24 hour scrubbing run, the LHC went into physics production. With 2040 bunches per beam (in trains of 72 bunches) and nominal beam parameters, the LHC reached its nominal peak luminosity of 10^{34} cm^{-2} s^{-1}. At this point, the heat load in the beam screen of the arcs was very close to its limit (160 W/hc) and only exhibited a slow decrease thanks to scrubbing accumulated during the physics stores. Finally, the brightness of the beams was increased by switching to the BCMS scheme (trains of twice 48 bunches spaced by 225 ns) [52] and the final fills with 2220 bunches could comfortably exceed the nominal luminosity by up to 40% with heat load within the capacity of the cryogenic system. During this year it was not possible to increase further the number of bunches in LHC, because the SPS could not produce LHC beams in longer trains than 2x 48 bunches, due to a vacuum leak in the internal dump. During the winter shutdown between 2016 and 2017, Sector 12 of LHC had to be opened to exchange a faulty dipole. That's why at the beginning of 2017 a longer scrubbing (about a week) was needed to recondition Sector 12 before moving to physics production. In 2017, the number of bunches injected quickly got to the maximum of about 2600 per beam, and in this configuration the LHC ran during the first part of the year. Unfortunately, in the second part, due to air condensation in both chambers in the cell 16L2, which probably took place while pumping after the shutdown, it was necessary to move to a low e-cloud variant of the 25 ns beam, i.e. the so-called 8b+4e. This beam had the advantage to limit the probability of occurrence of UFO-like events at 16L2, which caused strong beam losses and premature dumps with the standard 25 ns beam. In spite of a partial warm up of the Sector 12, which had been believed to be sufficient to degas the condensed air and pump it out, the 16L2 persisted in 2018 and limited the intensity per bunch in LHC (1e11 p/b).

The general evolution during 2015-18 can be seen in Fig. 4, which displays the bunch number in the top plot and the heat load measured at high energy in the eight arcs for all physics fills in the bottom one. Two puzzling features can be noticed, which are potentially unsettling for future operation:

- While the normalised heat load decreased by a factor two in 2015 (due to both scrubbing and filling pattern relaxation), the evolution in 2016 shows only a limited decrease at the beginning and then it levels off in the second part of the year and throughout 2017-18 (excluding the 8b+4e run at the end 2017, which was intrinsically low e-cloud). This suggests that scrubbing has saturated, even while running at high heat load. Running with trains of doublets (pairs of bunches 5 ns) [52] could perhaps lead to additional scrubbing in the future, but it was not tested again after 2015 due to the SPS dump in 2016 and to 16L2 in 2017-18;
- There is a constant offset between the values of the normalised heat load in different sectors and the "asymptotic" values differ by a factor three. The heat load in the "best" sectors landed to about twice the value expected from impedance and synchrotron radiation, suggesting that the e-cloud is still playing a role everywhere in LHC. In this situation, the sectors with the highest heat load are a limit for the total intensity that can be collided in LHC. The reason of this spread is still under investigation, and it is hoped that the surface analysis of some bad beam screens extracted in LS2 can clarify its origin.

Table 3 shows the achieved LHC beam parameters.

Table 3: LHC beam parameters for 50 and 25 ns beams

	50 ns	**25 ns**
Beam energy (TeV)	0.45 → 3.5/4 → 6.5	
Bunch intensity ($\times10^{11}$ ppb)	1.1-1.7	1.0-1.2
Bunch length (ns)	1.0-1.5	
Number of bunches	1376	2800
Transv. rms emittances (μm)	1.1-1.7	1.5-2.5

In high e-cloud operation, i.e. with 25 ns beams, the beam stability at injection and along the cycle is usually preserved with large chromaticity values, relatively high octupole currents and a fully functional transverse feedback system [53]. Due to the tune footprint in presence of large chromaticity and strong e-cloud, this also implies that the tunes must be carefully placed to be far enough from any dangerous resonance line. The incoherent losses observed when the vertical tune of the LHC was 0.31 at injection (due to the proximity to the third order resonance) could be easily avoided by lowering the vertical tune at injection to values around 0.29.

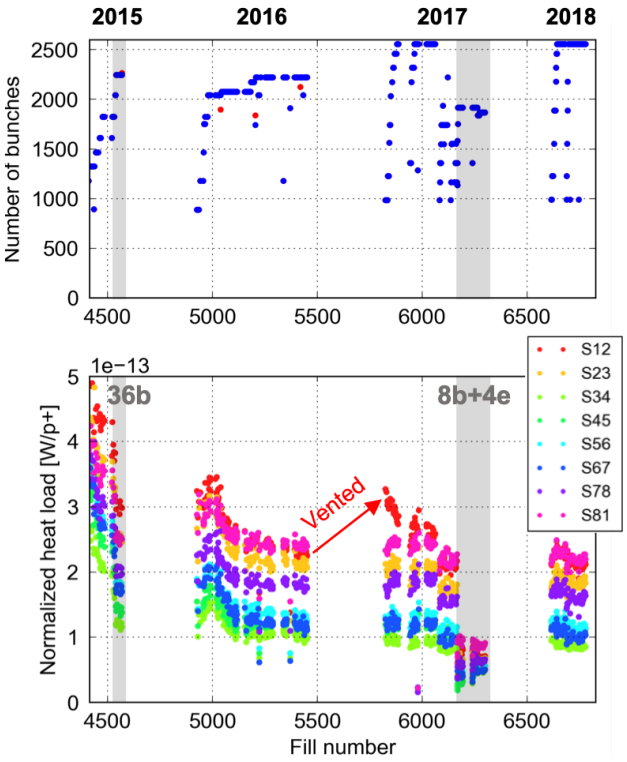

Figure 4: Top: evolution of number of bunches in LHC during Run 2. Bottom: heat load at 6.5 TeV in the eight sectors (as labeled) for all fills with 25 ns bunch spacing normalized to the total intensity of the circulating beam.

The horizontal tune had to be also lowered to keep a safe distance from the vertical one not to trigger instabilities from coupling [54]. Extensive simulation studies were carried out to try to disentangle the role of the e-cloud in the different LHC regions (dipoles, quadrupoles/multipoles, drift chambers) [53]. At nominal intensity it is believed that the two-stripe structure of the e-cloud in the dipoles makes it basically "harmless" for the beam stability (due to the very low central density of electrons) and the beam instability is caused by the e-cloud in the quadrupoles. Conversely, for lower bunch currents a third stripe develops at the center of the chamber and the region around the beam gets quickly densely populated with electrons. This range of bunch intensities is explored, while the beam intensity decreases during the phase of "stable beams", i.e. when the beams are colliding at 6.5 TeV to provide data for the experiments. In practice, this situation resulted in single bunches at the ends of the trains becoming vertically unstable at some advanced point of the store, which was observed systematically in the LHC during the first phase of the 2016 run in spite of the high chromaticity, the current in the octupoles close to its maximum and the presence of the beam-beam head-on tune spread [55]. This instability, which was kept under control by increasing further the chromaticity in stable beams, disappeared during the second part of the run, even with low chromaticity, probably thanks to the scrubbing of the central region of the beam screen accumulated with physics.

For HL-LHC operation, it is essential that the e-cloud with the future beam parameters will: 1) produce heat load in the cold regions that is compatible with the capacity of the cryogenic system; and 2) not cause beam degradation due to instability or incoherent effects. The dependence of the e-cloud with bunch intensity has been found to be favourable in simulations (central density and heat load level off or even drop for higher intensities than the present nominal), and this has been partially experimentally verified up to bunch intensities of 2e11 p/b, but only in trains of 12 bunches. It has been envisaged to make a low SEY treatment of the beam screens of the twin and single bore magnets in the interaction regions, including triplets and matching sections [41] to minimise the impact of these regions on the total load on the cryogenic system. For the arcs, future operation will rely on both the predicted dependence of e-cloud with intensity and efficiency of scrubbing, while keeping the back up option of running with low e-cloud filling patterns, like full or mixed 8b+4e [56], in case of need. The option of adding a 200 MHz RF system to lengthen the bunches, which could make operation possible if the heat load is still limited by the e-cloud in the dipoles [42], is presently not in the baseline of the upgrade project.

ACKNOWLEDGMENTS

The authors would like to thank G. Arduini, V. Baglin, B. Bradu, G. Bregliozzi, K. Brodzinski, X. Buffat, R. Cappi, L. Carver, F. Caspers, P. Chiggiato, S. Claudet, P. Costa-Pinto, J. Esteban-Müller, M. Giovannozzi, B. Goddard, M. Jimenez, E. Mahner, E. Métral, H. Neupert, S. Rioja-Fuentelsaz, E. Rogez, B. Salvant, E. Shaposhnikova, G. Skripka, M. Taborelli, L. Tavian, C. Yin-Vallgren, M. Van Gompel, C. Zannini for their contributions.

REFERENCES

[1] MULCOPIM Conference, 5-7 April, 2017, Noordwijk, The Netherlands, http://esaconferencebureau.com/2017-events/mulcopim2017/home (2017)

[2] ECLOUD12 Workshop, 5-9 June, 2012, Isola d'Elba, Italy, https://agenda.infn.it/conferenceDisplay.py?confId=4303 (2012)

[3] O. Gröbner, in *Proceedings of the 10th International Conference on High Energy Accelerators*, Protvino, Russia, 1977, Inspire CNUM: C77-07-11.1 (1977)

[4] M. Izawa, Y. Sato, and T. Toyomasu, Phys. Rev. Lett. **74**, 5044 (1995)

[5] K. Ohmi, Phys. Rev. Lett. **75**, 1526 (1995)

[6] Z.Y. Guo *et al.*, in *Proceedings of the 1st Asian Particle Accelerator Conference (APAC 98)*, Tsukuba, Japan, 1998, KEK Report No. 98-23 (1998)

[7] M. A. Furman and G. R. Lambertson, in *Proceedings of the 17th IEEE Particle Accelerator Conference (PAC 97)*, Vancouver, Canada, Inspire CNUM: C97-05-12 (1998)

[8] O. Gröbner, Vacuum, **47**, 591 (1996)

[9] F. Zimmermann, CERN-LHC-PROJECT-REPORT-95, SLAC Report No. SLAC-PUB-7425 (1997)

[10] O. Brüning, CERN-LHC-PROJECT-REPORT-158, (1997)

[11] M. Furman, CERN-LHC-PROJECT-REPORT-180 (1998)

[12] G. Rumolo, F. Ruggiero and F. Zimmermann, Phys. Rev. ST Accel. Beams **4** 012801 (2001)

[13] G. Stupakov, CERN-LHC-PROJECT-REPORT-141 (1997)

[14] F. Ruggiero, CERN-LHC-PROJECT-REPORT-166 (1997)

[15] L. Vos, CERN-LHC-PROJECT-NOTE-150 (1998)

[16] Proceedings of the Workshop on LEP-SPS Performance, Chamonix X, Chamonix, 2000, edited by P. Le Roux, J. Poole, and M. Truchet, Yellow Report CERN-SL-2000-007 DI, pp. 110-157 (2000)

[17] G. Arduini, in *Proceedings of Chamonix XI, 2001*, Yellow Report CERN-SL-2001-003 DI , pp. 125-134 (2001)

[18] J. M. Jimenez *et al.*, LHC-PROJECT-REPORT-632 (2003)

[19] R. Cappi, *et al.*, Phys. Rev. ST Accel. Beams **5**, 094401 (2002)

[20] G. Rumolo and F. Zimmermann, Phys. Rev. ST Accel. Beams **5**, 121002 (2002)

[21] K. Ohmi and F. Zimmermann, Phys. Rev. Lett. **85**, 3821 (2000)

[22] V. Baglin, A. Rossi, *et al.* in *Proceedings of ECLOUD'04, Napa, CA, 2004*, http://icfa-ecloud04.web.cern.ch/icfa-ecloud04/; Yellow Report CERN-2005-001 pp. 113-118 and pp. 123-138 (2005)

[23] D. Schulte, G. Arduini, V. Baglin, J. M. Jimenez, F. Ruggiero, and F. Zimmermann , in *Proceedings of PAC2005, 16-20 May 2005, Knoxville Tennessee, USA*, LHC-PROJECT-REPORT 847 (2005)

[24] G. Rumolo, CERN-BE-Note-2009-029 (2009)

[25] G. Rumolo, E. Métral and E. Shaposhnikova, in *Proceedings of LHC LUMI 2006, 16-20 October, Valencia, Spain*, Yellow Report CERN-2007-002, pp. 129-134 (2007)

[26] G. Rumolo *et al.*, Phys. Rev. Letters **100** 144801 (2008)

[27] C. Yin Vallgren *et al.*, Phys. Rev. ST Accel. Beams **14**, 071001 (2006)

[28] F. Zimmermann and E. Benedetto, ICFA Newsletter no. 32 (2004)

[29] E. Benedetto, G. Rumolo, D. Schulte and F. Zimmermann, Phys. Rev. ST Accel. Beams **8**, 124402 (2005)

[30] E. Benedetto, G. Franchetti and F. Zimmermann, Phys. Rev. Lett. **97**, 034801 (2006)

[31] LHC Design Report, edited by O. Brüning *et al.*, CERN-2004-003-V-1 (2004)

[32] H. Bartosik *et al.*, CERN-ATS-Note-2013-019 (2013)

[33] "LIU-SPS Scrubbing Review: Conclusions and Recommendations", W. Fischer (BNL), Y. Suetsugu (KEK), K. Cornelis, J. M. Jimenez, M. Meddahi and F. Zimmermann, CERN, 8-9 September 2015, EDMS LIU-PM-RPT-0023 (2015)

[34] "LIU Technical Design Report - Volume I: Protons", edited by J. Coupard *et al.*, CERN-ACC-2014-0337 (2015)

[35] G. Arduini *et al.*, CERN-ATS-Note-2011-046 MD (2011)

[36] G. Rumolo *et al.*, in *Proceedings of the LHC Beam Operation Workshop - Evian 2011, 12-14 December, 2011, Evian, France*, CERN-ATS-2012-083 pp. 165-175 (2012)

[37] G. Iadarola, G. Arduini, H. Bartosik and G. Rumolo, in *Proceedings of the LHC Beam Operation Workshop - Evian 2012, 17-20 December, 2012, Evian, France*, CERN-ATS-2013-045 pp. 119-128 (2013)

[38] G. Iadarola and G. Rumolo, in *Proceedings of the LHC Beam Operation Workshop - Evian 2015, 15-17 December, 2015, Evian, France*, CERN-ACC-2015-0376 pp.101-110 (2015)

[39] L. Mether, P. Dijkstal, G. Iadarola, G. Rumolo, "Electron Cloud in 2016: Cloudy or clear?", in *Proceedings of the LHC Beam Operation Workshop - Evian 2016, 13-15 December, 2016, Evian, France*, to be published

[40] G. Arduini *et al.*, J. Instrum. **11** C12081 (2016)

[41] G. Iadarola, E. Métral and G. Rumolo, CERN-ACC-2016-0112 (2016)

[42] G. Iadarola and G. Rumolo, "200 MHz option for HL-LHC: e-cloud considerations (heat load aspects)", presentation at the 68th HiLumi WP2 meeting, 3 May 2016, https://indico.cern.ch/event/523881/, CERN, Geneva (2016)

[43] G. Iadarola and G. Rumolo, in *Proceedings of ECLOUD'12, 5-9 June, 2012, Isola d'Elba, Italy*, Yellow Report CERN-2013-002 pp. 19-26 and pp. 189-194 (2013)

[44] K. Li *et al.*, in *Proceedings of ICFA Advanced Beam Dynamics Workshop on High-Intensity and High-Brightness Hadron Beams (HB'16), Malmö, Sweden, July 3-8, 2016*, pp. 363-367, doi:10.18429/JACoW-HB2016-WEAM3X01 (2016)

[45] L. Mether, G. Iadarola and G. Rumolo, n *Proceedings of ICFA Advanced Beam Dynamics Workshop on High-Intensity and High-Brightness Hadron Beams (HB'16), Malmö, Sweden, July 3-8, 2016*, pp. 368-372, doi:10.18429/JACoW-HB2016-WEAM4X01 (2016)

[46] G. Iadarola *et al.*, "Evolution of the Python tools for the simulation of electron cloud effects", THPAB043, elsewhere in these proceedings

[47] R. Garoby, CERN/PS 99-13 (RF) (1999)

[48] E. Mahner, T. Kroyer and F. Caspers, Phys. Rev. ST Accel. Beams **11**, 094401 (2008)

[49] S. Fuentelsaz Rioja, CERN-THESIS-2014-298 (2014)

[50] A. Romano, CERN-THESIS-2014-286 (2014)

[51] G. Arduini, K. Cornelis, W. Höfle, G. Rumolo, and F. Zimmermann, in *Proceedings of PAC 2001, 18-23 June 2001, Chicago, USA*, pp. 685-687, CERN-SL-2001-0050 (2001)

[52] H. Bartosik and G. Rumolo, in in Proceedings of the LHC Beam Operation Workshop - Evian 2014, 2-4 June, 2014, Evian, France , CERN-ACC-2014-0319, pp. 93-97 (2014)

[53] A. Romano, G. Iadarola, K. Li and G. Rumolo, "Macroparticle simulation studies of the LHC beam dynamics in the presence of electron cloud", TUPVA018, elsewhere in these proceedings

[54] E. Métral, *et al.*, in *Proceedings of ICFA Advanced Beam Dynamics Workshop on High-Intensity and High-Brightness Hadron Beams (HB'16), Malmö, Sweden, July 3-8, 2016*, pp. 254-259, doi:10.18429/JACoW-HB2016-TUAM2X01 (2016)

[55] A. Romano, G. Iadarola and G. Rumolo, "Electron cloud instability studies for the LHC", presentation at the Electron Cloud meeting 40, https://indico.cern.ch/event/605497/, 31 March 2017, CERN, Geneva (2017)

[56] G. Iadarola *et al.*, CERN-ACC-NOTE-2017-0013 (2017)

COUPLED-BUNCH INSTABILITIES AND RELATED EFFECTS DUE TO ELECTRON CLOUD IN SuperKEKB LER

Makoto Tobiyama, KEK Accelerator Laboratory and SOKENDAI, 1-1 Oho, Tsukuba 305-0801, Japan

Abstract

Coupled-bunch instabilities due to electron cloud effect have been observed in KEKB LER. The effect was clearly explained by the electron cloud effect (ECE) in the drift space by the numerical simulations. For SuperKEKB collider which is the upgrade of the KEKB collider, several methods to mitigate the ECE have been applied. The effectiveness of those methods has been evaluated using the beam in Phase 1 and Phase 2 operation of SuperKEKB. Preliminary experimental results will be shown.

INTRODUCTION

The KEKB collider has been upgraded to the SuperKEKB collider with a final target of 40 times higher luminosity than that of KEKB. It consists of a 7 GeV high energy ring (HER, electrons) and a 4 GeV low energy ring (LER, positrons). About 2500 bunches per ring will be stored at total beam currents of 2.6 A (HER) and 3.6 A (LER) in the final design goal. After the first stage of commissioning (Phase 1) without the Belle-II detector, which started in Feb. 2016 and continued until the end of June [1, 2], we have installed the superconducting final quadrupoles (QCS) and the Belle-II detector, without innermost detectors vertex detectors such as Pixel detectors nor Silicon Vertex Detectors (VXD) [3,4].

In KEKB LER, we have observed unexpected strong transverse coupled-bunch instabilities (CBI) and an increase of the vertical beam size with beam current. Both the unstable modes and the growth time had strong dependence of the bunch filling patterns. Though the CBI had been suppressed by the transverse bunch-by-bunch feedback systems, the increase of the vertical beam size still remained which strongly reduced the luminosity.

To suppress the beam blow-up and the coupled-bunch instabilities, we wound solenoid magnets in almost all the straight sections (>95%) with magnetic field of 4.5 mT.

The solenoid had worked well to suppress the increase of the vertical beam size and to achieve high luminosity, though the growth rate of the unstable modes had not changed too much. The result of the transient-domain analysis of the CBI with the several conditions of the solenoid magnets such as turning-on, turning-off, partly activated, agreed with the numerical simulations very well.

For SuperKEKB, we had employed several mitigation methods to suppress the electron cloud effects [5]. The bunch feedback systems have also improved with improved digital signal processing technique to have faster feedback damping with less noise effect in the systems. The effectiveness of the methods has been evaluated with the beam during the Phase 1 operation and the Phase 2 operation of the SuperKEKB LER where Phase 2 operation have been performed from March 2018 to middle of June 2018. In this paper we describe the results of the electron cloud effect in LER in the view point of the coupled bunch instabilities. The main parameters of the SuperKEKB rings in the Phase 2 operation are shown in Table 1.

Table 1: Main Parameters of SuperKEKB HER/LER/DR in Phase 2 Operation

	HER	LER	DR
Energy (GeV)	7	4	1.1
Circumference(m)	3016		135
Max. current (mA)	800	860	12
Bunch length (mm)	5	6	6.6
RF frequency (MHz)	508.887		
Harmonic number (h)	5120		230
Betatron tune(H/V)	44.54/ 46.56	45.54/ 43.56	8.24/ 7.17
Synchrotron tune	0.02	0.018	0.025
T. rad. damp time (ms)	58	43	12
x-y coupling (%)	0.27	0.28	10
Emittance (nm)	3.2	4.6	29
Peak luminosity	$5.5 \times 10^{33}/cm^2/s$		
Beam position monitor	486	444	83
Turn by turn monitor	69	70	83
Trans. FB system	2	2	1
Visible SR monitor	1	1	1
X-ray size monitor	1	1	0
Beta. tune monitor	1	1	1
DCCT	1	1	1
Bunch current mon.	1	1	1
Beam loss monitor	105(IC)/101(PIN)		34

TRANSVERSE BUNCH-BY-BUNCH FEEDBACK SYSTEMS

Figure 1 shows the block diagram of the bunch-by-bunch feedback systems installed in SuperKEKB rings [6]. The system consists of position detection systems, high-speed digital signal processing systems with a base clock of 509

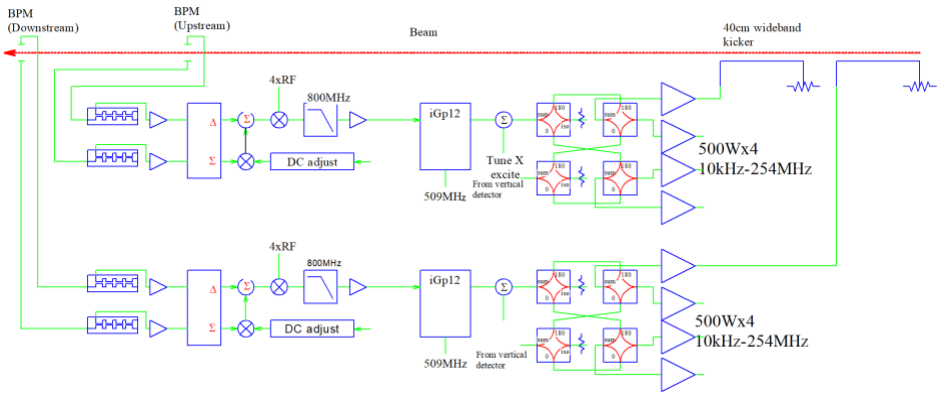

Figure 1. Block diagram of the transverse bunch feedback systems.

MHz (iGp12 [7]), and wide-band kickers fed by wide-band, high-power amplifiers.

For SuperKEKB rings, we have changed the button electrodes with better time response using feedthroughs with glass-type sealing, developed bunch position detection circuits with better bunch separation and lower electrical noise, employed iGp12 feedback signal processors with larger FPGA, exchanged the wideband high-power amplifiers with higher maximum power and with much better time-domain response than before. Finally, we have doubled the transverse feedback loop to cope with the lower fractional betatron tune around 0.52.

In the early stage of the commissioning of both rings we encountered very strong transverse coupled-bunch instabilities which limited the maximum beam currents. After the tuning of the timing and phase of the transverse feedback systems, we successfully suppressed the coupled-bunch instabilities up to the maximum beam current of around 1000 mA with the minimum bunch separation of 4 ns.

The transient behaviour of the beam just after closing or opening of the feedback loop reveals many important characteristics of the coupled-bunch motions as well as the performance of the feedback systems [8,9]. The iGp12 has intrinsic functions to initiate and record the grow-damp measurement. Since we are using two iGp12s on one transverse plane, we triggered both iGp12s with a hardware line simultaneously.

In the transient-domain analysis, we at first open the transverse (horizontal or vertical) feedback loop, which means to change the feedback gain to be zero, and start recording each bunch position observed in the iGp12 feedback processors. As the maximum recording length without down-sampling in the iGp12 processor is around 23 ms, we have set the nominal growth time of iGp12s, which is the "Feedback OFF period", to be around 4 ms to 10 ms depending on the growth rate. After the growth time, we close the feedback loop again before losing beam.

In the analysis, we at first make FFT of base 5 for the oscillation data of 256 turns (5120 bunches × 256 data points) to obtain the whole spectrum. Then extract amplitude of the spectrum that corresponds to the betatron frequencies (f_b+m × f_{rev}), where f_b, m and f_{rev} represent the betatron frequency, mode of the oscillation and revolution frequency, respectively, and align the amplitude by increasing order of the mode IDs. By repeating the above procedure while advancing the starting point of the data by 128 turn, we obtain the growth or damp of the instabilities in the view of unstable modes. Figure 2 shows an example of the grow-damp experiment on SuperKEKB HER of by 3 filling patterns with the beam current of around 730 mA. The unstable modes are concentrated around the lower (negative) modes and the amplitudes of the growing unstable modes are out of the exponential growth with the progress of the unstable modes. In this case the growth rate was around 1/0.9 ms^{-1} while the feedback damping rate without the correction of grow rate was faster than 1/0.5 ms^{-1}.

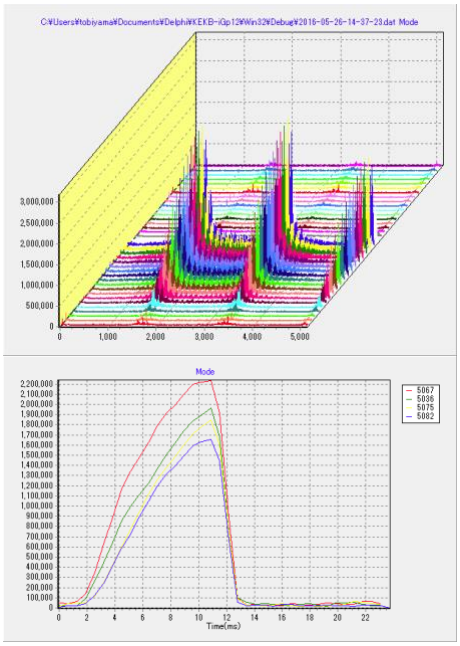

Figure 2. An example of transient-domain analysis at SuperKEKB HER (electron ring) at by 3 filling patterns with the beam current of around 730 mA. (Upper): Change of unstable modes (horizontal, from 0 to 5119) with time (depth, from 0 to 24 ms). (Lower): Growth and damp of some unstable modes. The growth time was around 0.9 ms.

ELECTRON CLOUD EFFECT AND ITS MITIGATION

KEKB LER

In KEKB LER, we have performed many experiments to measure the electron cloud effect with changing the filling patterns and strength of the solenoid magnets including the excitation pattern of magnets, which have been installed mainly at the drift space. The results have shown good agreements with the numerical simulation with the assumption of the electron cloud at the drift space mainly contributing the ECE [10]. In this case, coupled-bunch instabilities due to ECE behaves as follows:

- Rather broad unstable modes appear which reflect the cloud distributions. Modes around higher part come from the natural electron clouds in the drift space region. The modes around lower part come from the electron clouds near the chamber surface due to the higher solenoidal field (>few mT).
- The growth rate of the unstable modes has relation to the strength of the applied solenoid magnetic fields. Intermediate field levels actually enhance the growth rate, which result in a more severe situation for the bunch feedback systems. On the contrary, no solenoid field and enough solenoid field case show similar growth rate of the instabilities. Therefore, adding external solenoid field might suppress the vertical beam size blow-up but does not suppress the coupled-bunch instabilities.

Figures 3 and 4 show examples of measured unstable modes without a solenoid field and with full field at KEKB LER with by 4 patterns [9]. The unstable modes have changed drastically from the higher modes (without solenoid field) to the lower modes (with fully applied solenoid field).

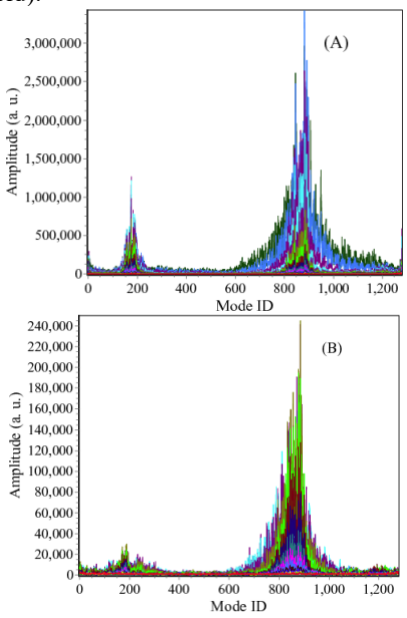

Figure 3. Unstable modes without a solenoid field for the horizontal plane (A) and vertical plane (B) with by 4 filling patterns.

In Fig. 5, the measured growth rates of the instabilities with various solenoid field are shown. As seen in the figure, a large enhancement of the growth rate for both the horizontal and vertical planes has been seen at lower (insufficient) solenoid fields. It was concluded that insufficient solenoid field made the coupled-bunch situation much worse than no-solenoid case.

Mitigation for SuperKEKB

The main bending magnets of LER have been replaced with much longer ones with lower magnetic field. To fit the modified lattice and to mitigate the ECE for SuperKEKB, most of the vacuum chambers of LER have been replaced with the antechamber made of aluminium alloy with TiN coating with a thickness of around 200 nm. In addition, vacuum chambers for bending magnets have been processed with a grooved surface around the top and bottom of the chamber. In the wiggler straight section to increase synchrotron radiation loss, we have prepared vacuum chambers made of copper alloy with clearing electrodes which are capable to sustain external DC electrical field up to 1 kV with maximum current of 100 mA. The detailed discussion of the mitigation of ECE and the experimental results on the Phase 1 and Phase 2 operation are shown in another the document of theses proceedings [5].

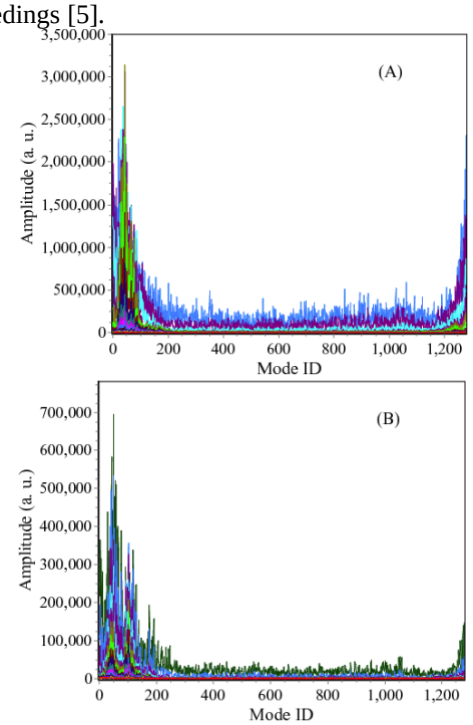

Figure 4. Unstable modes with a full (~4.5 mT) solenoid field for the horizontal plane (A) and the vertical plane (B).

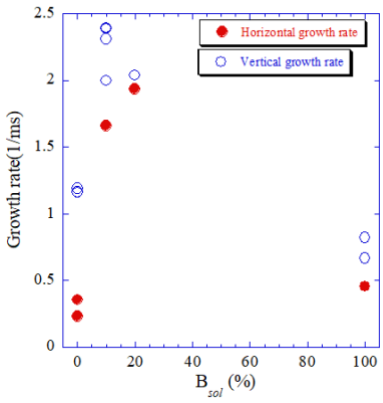

Figure 5. Measured growth rates against the magnetic field strength of the solenoid magnets where total number of bunches was 1154 (600 mA) with by 4 (=8 ns) spacing.

MEASUREMENTS OF ELECTRON CLOUD EFFECT

Phase 1 operation

During the Phase 1 operation of SuperKEKB, we have found the vertical beam size blow-up starting at 0.6 A with the filling pattern of 3.06, which means the repeating by 3 filling of 15 buckets and 4 RF bucket spacing. Figure 6 shows the measured vertical beam size increase with the beam current.

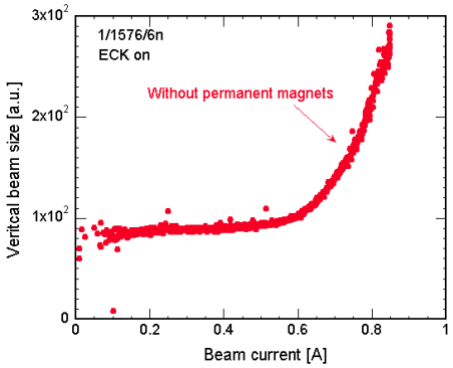

Figure 6. Vertical beam size blow-up with beam current at Phase 1 operation of SuperKEKB LER.

The measurements have been examined with by 2, by 3, by 4 and by 6 RF bucket patterns with 150 bunches per bunch train, 4 or 8 bunch trains, up to 600 mA. The grow-damp measurements have been also performed with several beam currents. Note for some filling patterns with much faster growth rate, the re-capture of the oscillation was not easy, which meant the growth of the coupled-bunch oscillation had caused the beam loss, especially for the vertical plane. Figure 7 and 8 show examples of grow-damp experiment with by 2 filling patterns (300 mA).

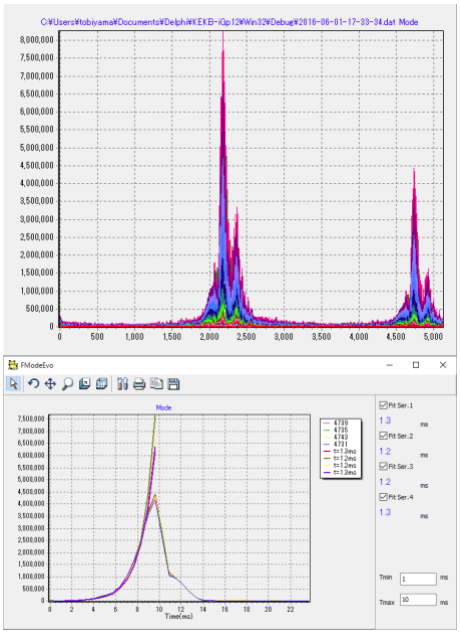

Figure 7. Unstable modes and growth behaviours of major modes on vertical plane with total number of bunches of 600 (300 mA) with by 2 (=4 ns) filling parttren.

The growth time of the unstable modes are around 0.6 ms and 1.2 ms for horizontal and vertical plane, respectively. The feedback damping time for both planes were less than 0.5 ms in this case. Figure 9 shows the summary of the unstable modes.

The main unstable modes are concentrated around mode numbers 400 and 500 modes far from zero mode for horizontal and vertical planes, respectively. Those higher modes strongly support the coupled-bunch instabilities has been caused by the electron clouds around the drift space of the ring.

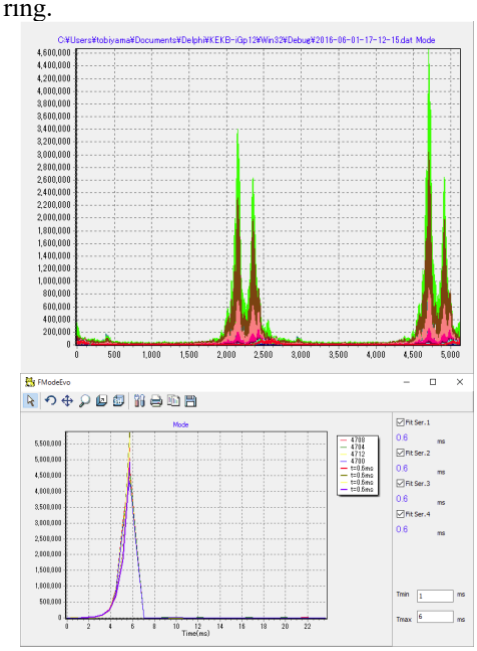

Figure 8. Unstable modes and growth behaviours of major modes on horizontal plane.

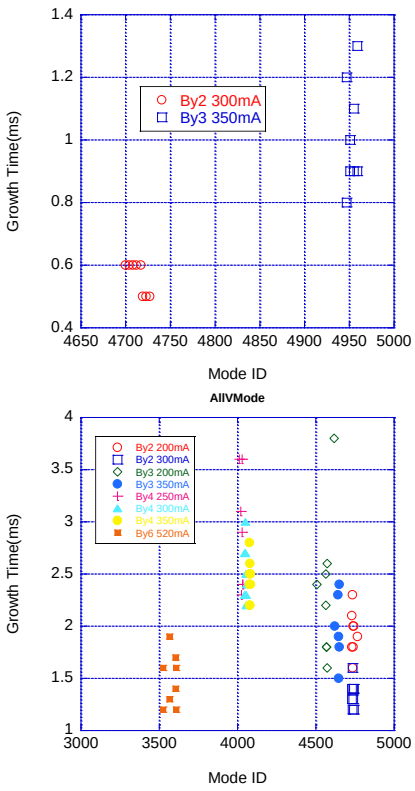

Figure 9. Summary of unstable modes for horizontal (upper) and vertical (lower) plane with various filling patterns.

At the same time, a non-linear pressure rise against the beam current around the bellows made of aluminium alloy without TiN coating was found. As a test, we applied solenoid magnetic field with 40 to 100 G near the inner wall at the center of bellows. As a result, the rate of pressure rise at the section was relaxed which confirmed the pressure rise was caused by the electron cloud effect.

After installing solenoidal-field made of permanent magnets and return yokes all the bellows section, we have made the measurements of the vertical beam size with grow-damp measurements. As seen in Fig. 10, typical unstable modes caused by the electrons in solenoid field (lower modes) on both horizontal and vertical planes have appeared at the lower to middle beam current. Also the growth rate of the horizontal plane has been reduced around 4 times, though in the vertical plane the rate was not too much affected. Nevertheless, at higher beam current unstable modes of higher mode region appeared again. According to the numerical simulation, magnetic field at the bellows section should be enough to suppress the cloud effect. Therefore the higher-unstable modes with high beam current were suspected to be caused by the electron clouds at normal drift spaces with antechamber structure and with TiN coating.

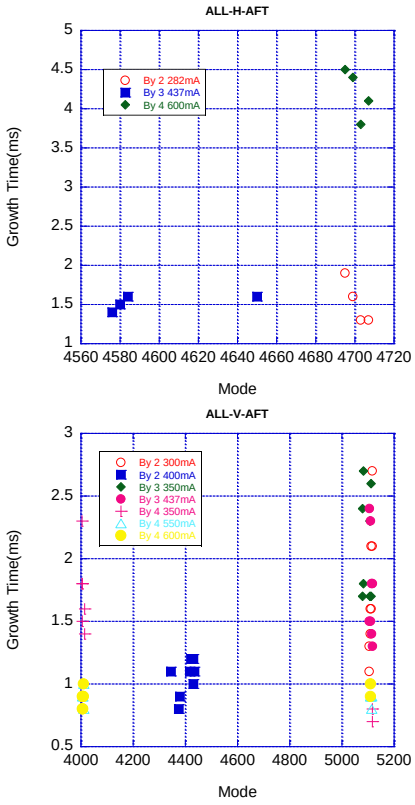

Figure 10. Summary of unstable modes for horizontal (upper) and vertical (lower) plane with various filling patterns after installing the solenoid magnets around bellows.

In measurements of vertical beam size, a beam size blow-up as a function of beam current was observed for several filling patterns, though the threshold line density of a bunch train of blow-up has increased up to 1.5 times higher than before installing the solenoid magnets.

As a countermeasure against the ECE difficulties, 'quasi-solenoid' magnets consist of permanent magnets and iron yokes have been attached to most of the drift space of the ring. For drift space near to existing electro-magnets the units without iron yokes have been installed.

Phase 2 operation

In the Phase 2 operation, we have measured the vertical beam size and the grow-damp behaviours of the coupled-bunch instabilities with similar conditions as Phase 1 experiments. Up to the maximum beam current, no vertical beam size blow-up has been observed. Figure 11 shows the summary of vertical unstable modes. Note for horizontal plane, the typical growth rates were much slower than that of Phase 1 cases and was not easy to analyse with enough accuracy. The growth rates of the vertical unstable modes have further reduced around the factor of two or three. As seen in Fig 12, the distribution of unstable modes has also changed to be narrower than that of Phase 1, which suggest the contribution of electron cloud effects to the unstable mode might not be so large now. Further study including numerical simulations to investigate the cause will be needed.

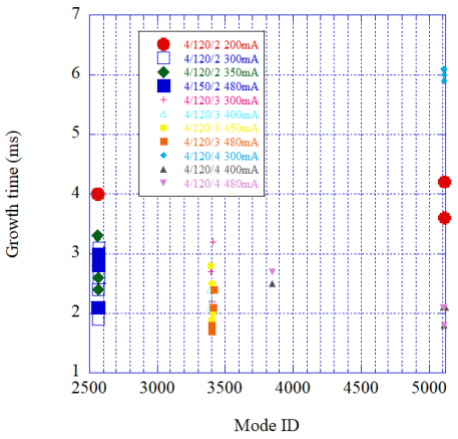

Figure 11. Summary of unstable modes for vertical plane with various filling patterns and beam currents on the Phase 2 operation of SuperKEKB LER.

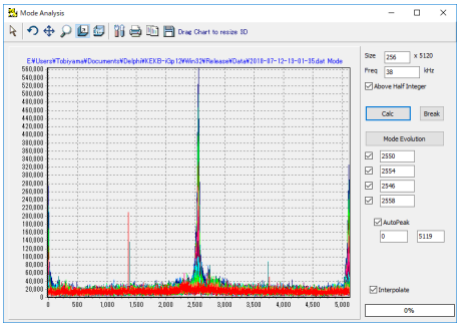

Figure 12. Vertical unstable modes of by 2 filling pattern at Phase 2 operation. The mode distribution is narrower than that of phase 1.

SUMMARY

Coupled-bunch instabilities caused by electron cloud effect have been observed in SuperKEKB Phase 1 operation, which were mainly caused by the vacuum bellows made of aluminium alloy without TiN coating. Mode analysis of trasient-domain measurements show the typical behavior of electron cloud effect coming from the drift electrons. By adding weak solenoid field at bellows section, the increase of vacuum pressure and the vertical beam size blow-ups have been sucessfully suppressed. The unstable modes have changed to those from solenoid field electrons. For higher beam current, drift electron pattern appeared again which suggest mitigation at normal drift space might be needed. After adding solenoid magnet around most of the drift space for the Phase 2 operation of SuperKEKB LER, no vertical blow-up has been observed up to the maximum beam current. On the transient-domain analysis, the unstable modes pattern has changed and much slower growth rates have been observed. The mitigations applied during Phase 1 to Phase 2 have been confirmed to work well up to now.

The author would like to express sincere appreciation to Prof. Y. Suetugu, Prof. H. Fukuma, Prof. K. Ohmi and Prof. J. Flanagan for their strong collaboration and furutiful discussions on the electron cloud effect measurments. The commissiong group of SuperKEKB ring are acknowledged for their strong support of the accelerator study of electron cloud effects.

This work is partly supported by the US-Japan collaboration in High Energy Physics (R&D for SuperKEKB and the next generation high luminosity colliders).

REFERENCES

[1] Y. Funakoshi *et al.*, in *Proc. of IPAC'16*, Korea, Busan, 2016, paper TUOBA01.

[2] M. Tobiyama *et al.*, in *Proc. of IBIC'16*, Spain, Barcelona, 2016, paper MOAL03.

[3] Y. Onishi *et al*, in *Proc. of IPAC'18*, 2018, Vancouver, BC, Canada.

[4] A. Morita *et al.*, in *Proc of ICHEP'18*, Korea, Seoul, 2018, paper TUOBA01.

[5] Y. Suetsugu *et. al.* presented in Ecloud2018, Elba, Italy, 2018, this workshop.

[6] M. Tobiyama *et al.*, in *Proc. of PASJ'16*, Japan, Chiba, 2016, paper TUOM06.

[7] DimTel. http://www.dimtel.com/

[8] J. D. Fox, *et al.*, in *Proc. of PAC'99*, New York, 1999, p.636.

[9] M. Tobiyama, *et al.*, Phys. Rev. ST ACCL. Beams **9**, 012801 (2006).

[10] S. S. Win, *et al.*, Phys. Rev. ST ACCL. Beams **8**, 094401 (2005).

MEASUREMENTS AND SIMULATIONS OF ELECTRON-CLOUD-INDUCED TUNE SHIFTS AND EMITTANCE GROWTH AT CESRTA

S. Poprocki, J.A. Crittenden, D.L. Rubin, and S.T. Wang
CLASSE, Cornell University, Ithaca NY 14853

Abstract

Extensive measurements of electron-cloud-induced betatron tune shifts and emittance growth are presented for trains of positron and electron bunches at 2.1 and 5.3 GeV at various bunch populations. Measurements using a witness bunch with variable distance from the end of the train and variable bunch population inform the study of cloud decay and the pinch effect. Improved electron cloud buildup modeling using detailed information on photoelectron production properties obtained from recently developed simulations successfully describes the tune shift measurements after determining ring-wide secondary-yield properties of the vacuum chamber by fitting the model to data. Space-charge electric field maps of the cloud from the validated model are then incorporated into a multiparticle tracking simulation of the beam through the lattice with electron cloud elements in the dipoles and field-free regions. The simulations predict emittance growth in agreement with the measurements.

INTRODUCTION

The buildup of low-energy electrons in the vacuum chamber along a train of positron bunches (See Fig. 1) can cause tune shifts, beam instabilities, and incoherent emittance growth. These electron cloud (EC) effects have been observed in many positron and proton storage rings [1], and can be a limiting factor in accelerator performance. Electron cloud effects have been observed and studied at the Cornell Electron-Positron Storage Ring (CESR) Test Accelerator (CESRTA) since 2008. Figure 2 shows a schematic of the CESR synchrotron and storage ring. A comprehensive summary of these studies which include mitigation methods can be found in [2].

First, we present measurements of vertical and horizontal emittance growth along a train of positron bunches followed by a witness bunch, with comparison to corresponding measurements using electron bunches, at 2.1 GeV. The bunch current and distance of the witness bunch beyond the end of the train are varied to study the pinch effect and the decay of the cloud, respectively.

Next, methods of betatron tune shift measurement are discussed and compared. A comprehensive set of measurements along trains of positron bunches at 2.1 GeV and 5.3 GeV are shown.

Lastly, we describe the full procedure of electron cloud simulation starting with the generation of photons from synchrotron radiation, tracking of the photons in a 3D model of the vacuum chamber including reflections, absorption of the photons and their production of primary electrons, the buildup of cloud along a train of bunches, calculation of betatron tunes, and ultimately particle tracking of a beam through the CESR lattice with electron cloud elements in dipoles and field-free regions. Although electron cloud buildup models have been successful in simulating tune shifts [3, 4] and vertical emittance growth [5] in general agreement with measurements, their predictive power has been limited by the large number of free parameters. Furthermore, no single set of parameters could reproduce in simulation, measurements of horizontal and vertical tune shifts over a wide range of bunch currents and beam energies.

In an effort to improve the predictive power of the model for tune shifts and emittance growth, we have recently employed the Synrad3D [6] and Geant4 [7] codes to calculate azimuthal distributions of absorbed photons, quantum efficiencies, and photoelectron energy distributions around the vacuum chamber throughout the circumference of the CESR ring [8]. Secondary yield parameters are fit to the large dataset of betatron tune shift measurements collected at CESR. The validated model is then used in improved simulations of vertical emittance growth, achieving good agreement with the measurements.

EMITTANCE GROWTH MEASUREMENTS

Bunch-by-bunch, turn-by-turn vertical beam size measurements were taken with an X-ray-based beam size monitor [9]. Additionally, single-shot bunch-by-bunch horizontal beam size measurements were collected using a gated camera [10]. Bunch-by-bunch feedback is used on all bunches for size measurements, to minimize centroid motion and associated coherent emittance growth. All measurements of emittance growth are done at 2.1 GeV and 14 ns bunch spacing. Figure 3 shows vertical emittance growth along a 30-bunch train of positron bunches for values of the bunch current ranging between 0.36 and 0.72 mA/b. No vertical beam size blowup is observed for bunch currents below 0.5 mA/b, and a current of 0.7 mA/b produced a blowup of a factor of four of the initial bunch size. For this reason, we focus on measurements (and simulations) at two currents: 0.4 mA (0.64×10^{10} bunch population) which is below the vertical blowup threshold, and 0.7 mA (1.12×10^{10}) which produces significant blowup. Measurements at these currents were repeated for trains of electrons, and the results are shown in Fig. 4 for both the vertical and horizontal bunch sizes. Emittance growth along the bunch train is observed only for positron bunches with currents exceeding the threshold current, and is seen in both the vertical and horizontal planes.

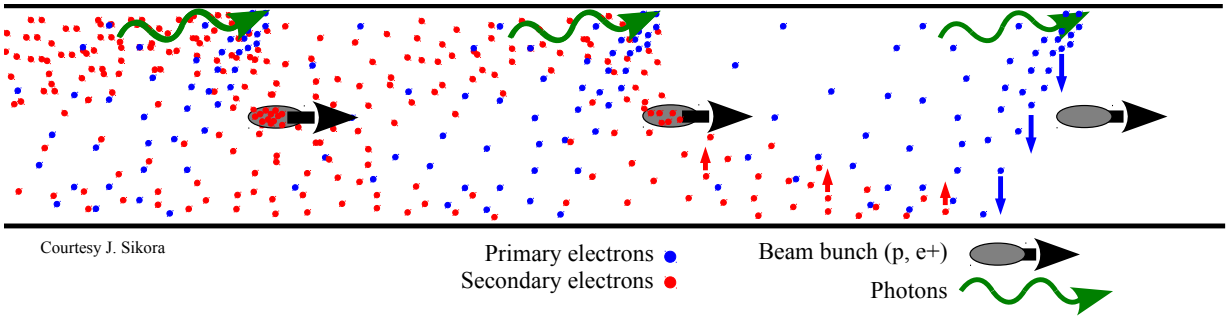

Figure 1: Depiction of electron cloud build-up in the vacuum chamber along a train of positively charged bunches moving left to right, at a specific point in time. Photons emitted via synchrotron radiation (caused by an upstream bending magnet) strike the outside wall of the vacuum chamber and produce electrons via the photoelectric effect or atomic de-excitation processes. These primary electrons (blue dots) may hit the vacuum chamber wall and produce secondary electrons (red dots). Electrons are accelerated by the passage of trailing bunches and produce more secondary electrons. The attraction of electrons into the bunch, known as the pinch effect, is also depicted.

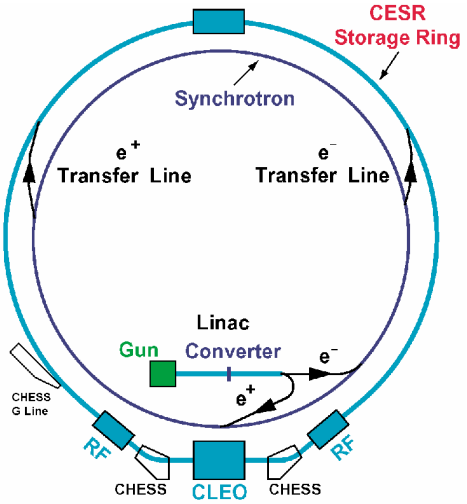

Figure 2: Schematic diagram of the CESR linac, synchrotron, and storage ring. Positrons circulate in the clockwise direction (top-down) and electrons anti-clockwise. The storage ring circumference is 768 m.

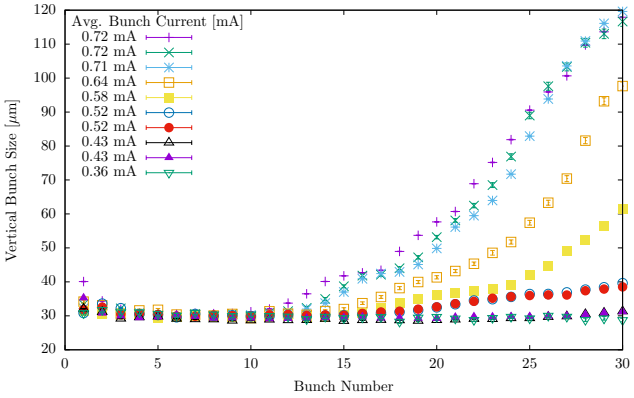

Figure 3: Vertical emittance growth along a 30 bunch train of positrons at 2.1 GeV, for a range of bunch currents. A bunch current of 1 mA corresponds to a bunch population of 1.6×10^{10} particles. Vertical blowup is observed for bunch currents above 0.5 mA/b.

Electron bunches did not show emittance growth at either current, which suggests the mechanism for the observed emittance growth is due to the attraction of the positron bunches and cloud electrons.

Measurements of vertical bunch size for a witness bunch are shown in Fig. 5. A single positron witness bunch follows a 30 bunch train of positrons at 0.7 mA/b. The witness bunch is initially injected into bunch position 60 at a current of 0.25 mA. Note that the ring can fit 183 bunches at a bunch spacing of 14 ns. The witness bunch size is measured, and its current increased to 0.5 mA. This process is repeated until the witness bunch has been measured at 1.0 mA, at which time it is ejected by disabling its feedback and giving it a kick via the feedback system. The witness bunch is then injected closer to the end of the train and measurements repeated until the witness bunch reaches the end of the train. By way of this back to front procedure, measurements of emittance growth are insensitive to residual charge that may be left in buckets where the charge is not completely ejected.

Vertical emittance growth is seen to depend on both the distance of the witness bunch to the train, which determines the cloud density seen by the witness bunch, and the bunch current of the witness bunch, which determines the strength of the pinch effect (*i.e.* cloud electrons being pulled into the positively charged bunch).

TUNE SHIFT MEASUREMENTS

Tune shifts have been measured in a number of ways at CESRTA. Coherently kicking the bunch train once ("pinging") and measuring the bunch-by-bunch, turn-by-turn bunch positions yields a fast measurement of the tune shift after peak-fitting the FFTs [2, 11]. However, multiple peaks from coupled-bunch motion contaminate the signal. In addition, only vertical tune shift measurements using vertical pinger kicks are reliable with this method. The development of a vertical band of electron cloud density in dipole mag-

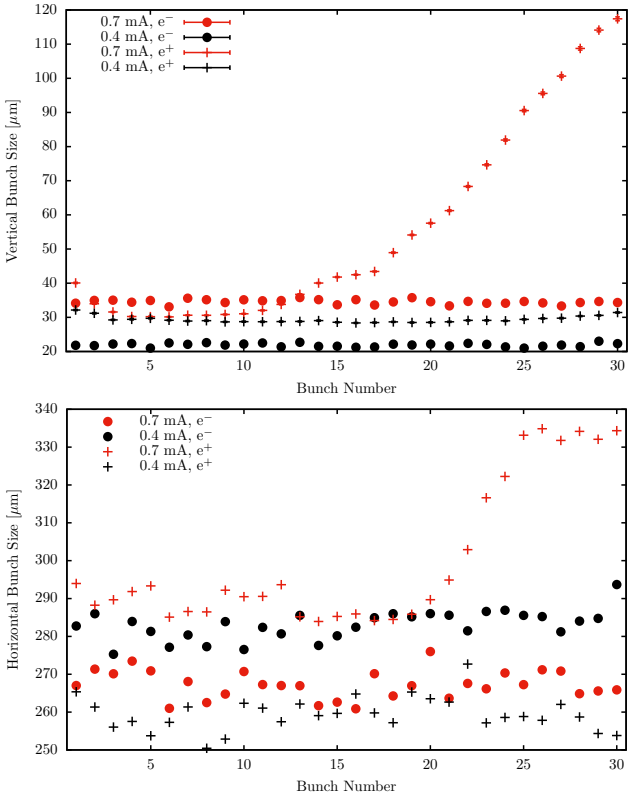

Figure 4: Vertical (top) and horizontal (bottom) bunch size along a 30 bunch train of positrons (+) and electrons (•) at 2.1 GeV for two different bunch currents: 0.4 mA/b (0.64×10^{10} particles) (black) and 0.7 mA/b (1.12×10^{10} particles) (red).

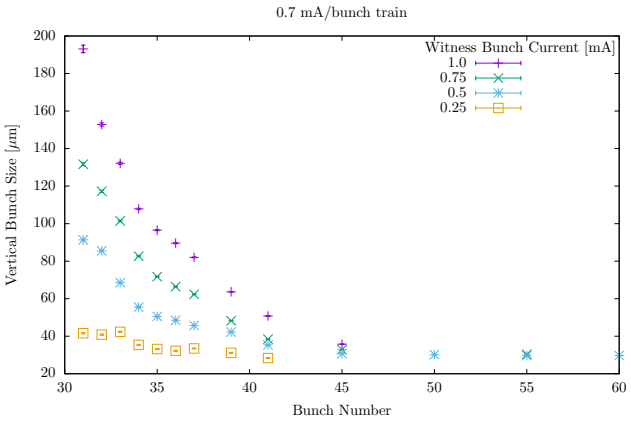

Figure 5: Vertical bunch size of a positron witness bunch at four different bunch currents (0.25, 0.5, 0.75, and 1.0 mA) trailing a 30 bunch train of 0.7 mA/b positrons at 2.1 GeV. Note that a single witness bunch is present for each measurement. The witness bunch current, which controls the strength of the pinch effect, is seen to have a large effect on the vertical bunch size.

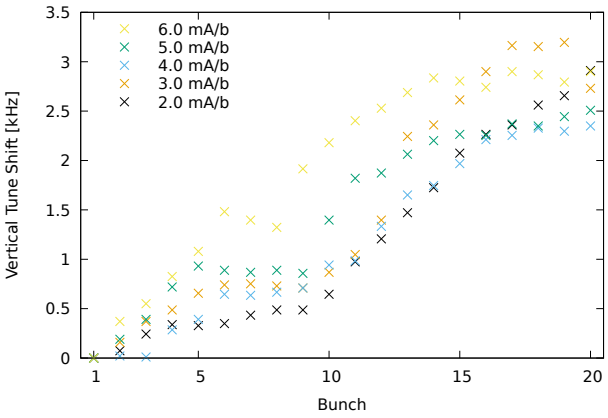

Figure 6: Vertical betatron tune shifts in kHz (to be compared to the revolution frequency of 390 kHz), measured using the "pinging" method, along a 20-bunch train of positrons at 5.3 GeV for values of the bunch current ranging from 2 to 6 mA/b ($3.2–9.6 \times 10^{10}$ bunch populations).

nets (see next section), *i.e.* a strong horizontal asymmetry on the scale of the beam size, is an important contribution to the tune shifts. A horizontal ping kick moves the bunch train coherently, and thus the cloud as well, so the measured horizontal tune shifts are suppressed by this measurement technique, since the test bunch receives no coherent kick from a cloud symmetric about its position. Better results are obtained by enabling bunch-by-bunch feedback on the train, disabling it one bunch at a time and measuring the tune of that bunch. The self-excitation (no external kick applied) is enough to get a signal, but the precision can be improved by kicking the single bunch with a gated stripline kicker. In the latest measurements we improve on this technique further by utilizing a digital tune tracker which excites the bunch via a transverse kicker in a phase-locked loop with a beam position monitor.

Tune shifts using the pinging method for 20 bunch trains of positrons at 5.3 GeV at various bunch currents are shown in Fig. 6. Large bunch-to-bunch fluctuations as well as overlap of data are seen compared to the same measurements obtained using the digital tune tracker, shown in Fig. 7, wherein the vertical tune shift increases monotonically with bunch current. However, the horizontal tune shift shows a remarkable behavior whereby the tune shift along the train decreases with later bunches and higher currents. Our modeling shows this effect to be due to the "cloud splitting" behavior in dipoles where the vertical stripe of cloud splits into two stripes due to cloud electron energies surpassing the peak energy of the secondary emission yield (SEY) curve due to the greater kicks from higher bunch populations.

Tune shift measurements taken with the digital tune tracker for positrons at 2.1 GeV are shown in Fig. 8. The horizontal tune shift shows a significant sensitivity to the bunch current, wherein the total horizontal tune shift increases by more than a factor of 5 when increasing the bunch current from 0.4 to 0.7 mA/b.

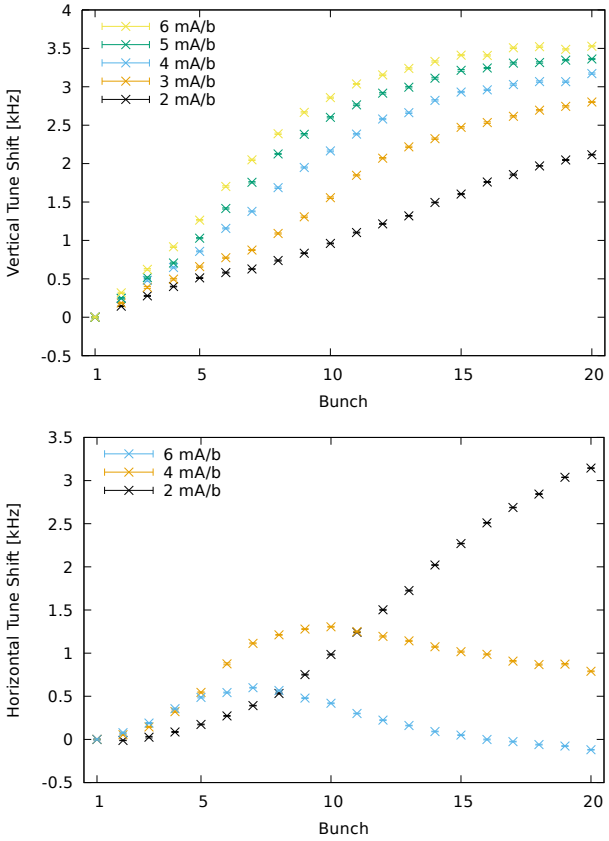

Figure 7: Vertical (top) and horizontal (bottom) tune shifts in kHz (to be compared to the revolution frequency of 390 kHz), measured using the digital tune tracker, for a 20 bunch train of positrons with values for the bunch current ranging between 2 and 6 mA/b (3.2–9.6×10^{10} bunch populations) at 5.3 GeV. Data were taken in each plane separately, and only at 2, 4, and 6 mA/b in the horizontal plane. These measurements are more reliable than those obtained via the pinging method (Fig. 6).

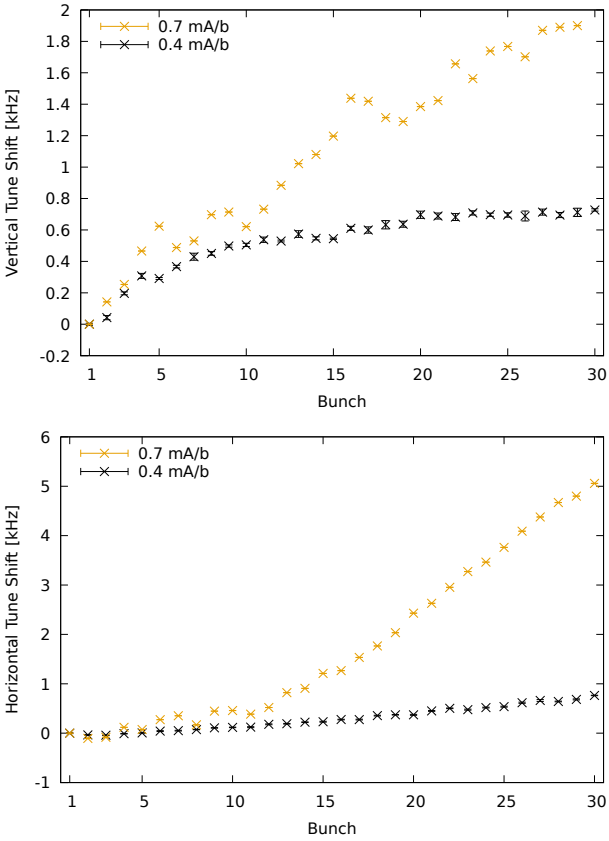

Figure 8: Vertical (top) and horizontal (bottom) tune shifts in kHz (to be compared to the revolution frequency of 390 kHz), measured using the digital tune tracker, for a 30 bunch train of positrons at 0.4 and 0.7 mA/b (0.64×10^{10} and 1.12×10^{10} bunch populations) at 2.1 GeV. The fluctuations in the vertical tune shift measurements at 0.7 mA/b were avoided for the other measurements by using an improved averaging method.

SIMULATIONS

The simulation pipeline involves running four different codes which feed into each other. The first step is simulation of photon generation from synchrotron radiation, and the subsequent tracking of photons including reflections in a detailed 3D vacuum chamber model of the entire CESR ring. This simulation results in information on individual photons absorbed in the vacuum chamber wall. The interaction of those absorbed photons with the vacuum chamber wall is then modeled in a Geant4-based simulation of electron production via the photoelectric and Auger effects. Quantum efficiencies and photoelectron energy distributions are obtained differentially in absorption site location both tranversely and around the ring. These first two steps are described in detail in Ref. [8]. The resulting data is then input into the electron cloud buildup simulation to model the generation of primary electrons. Time-dependent space-charge electric field maps from the cloud are obtained and used to calculate tune shifts. Finally, the field maps are incorporated into a particle tracking simulation of the beam through the full CESR lattice with EC elements overlaid on each dipole and field-free element. This allows for simulation of the equilibrium beam sizes.

These four simulation steps, along with a method of SEY parameter determination, will be discussed in more detail below.

Tracking photons from synchrotron radiation

This simulation is done using the Synrad3D code developed at Cornell University. Individual photons are generated according to a synchrotron radiation analysis of the lattice using the Bmad library [12]. A three dimensional description of the vacuum chamber geometry as well as the vacuum chamber materials is also supplied. A 5 nm layer of carbon monoxide on aluminum was found to be most consistent with photon reflectivity measurements of our vacuum chamber [6]. Photon scattering off the vacuum chamber walls is simulated using both smooth surface specular re-

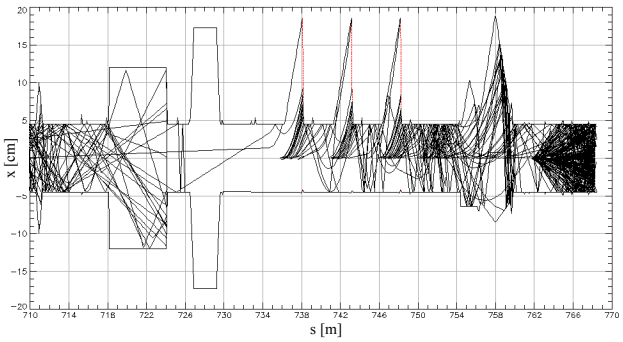

Figure 9: Top down view (x vs. s) for a portion of the CESR ring, showing photon tracks (black lines). The red vertical lines represent X-ray beam line exit ports, and any photon hitting those surfaces are terminated and not included in the calculation of photon absorption rates.

flections, according to the X-ray absorption data from the LBNL database [13] for the local material definition, as well as diffuse scattering via an analytic model for a finite surface roughness.

Figure 9 shows a plan view of photon trajectories in a region of the CESR ring which includes X-ray beamline exit windows, where incident photons are not included in the tally of electron-producing photon strikes.

Examples of the type of output data obtained from these simulations is shown in Fig. 10. In particular, for the subsequent simulation step, we obtain for each absorbed photon its azimuthal angle, energy, and grazing angle with the vacuum chamber wall.

Photoelectron production

The simulation of electron production from the photoelectric and Auger effects was performed using the Geant4 simulation toolkit [7, 14]. The absorbed photon data is split into 720 azimuthal bins, and for each bin, individual photons with the given energy and grazing angle are simulated to strike the vacuum chamber, which is modeled as a 5 nm layer of CO on aluminum. The number of electrons produced which come back into the vacuum (see Fig. 11), as well as their energies, are stored. The result is quantum efficiencies in each of the 720 azimuthal bins, as well as electron energy distributions in three azimuthal regions. Since the quantum efficiency depends on both photon energy and grazing angle, and these vary greatly azimuthally for the absorbed photons, so too does the quantum efficiency. Taking this into account in the EC buildup simulations, rather than assuming a single number for quantum efficiency, is a crucial improvement to the model and its predictive ability. Similarly, using the electron energy distributions from these simulations reduces the number of free parameters and assumptions. The simulations are done separately for dipole and field-free regions. See Ref. [8] for details.

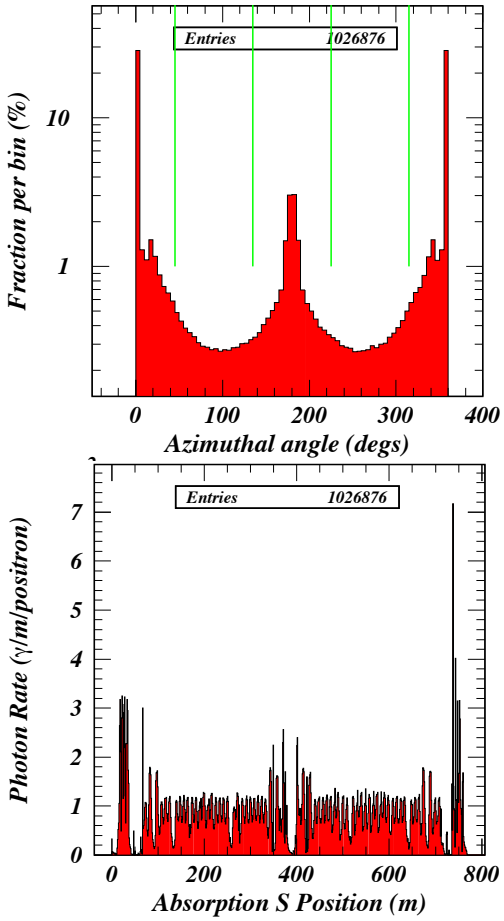

Figure 10: A sample of the information output by the Synrad3D simulation of photons from synchrotron radiation. Top: transverse azimuthal distribution of absorbed photons, where the angle origin is in the horizontal midplane on the outer wall of the beampipe. Note the log scale. Photons typically are absorbed on the outer wall with no prior reflections, or the inner wall after reflecting once, or, more rarely, absorbed on the top/bottom of the vacuum chamber after multiple reflections. Bottom: Photon absorption rate vs. s position around the ring.

Electron cloud buildup

The EC buildup simulation is based on extensions [11] to the ECLOUD [15] code. The beam size used in these simulations for the 2.1 GeV beam is ring-averaged and weighted by the element lengths for either the 800 Gauss dipole magnets or the field-free drift regions, and roughly 730 (830) microns horizontally for dipoles (drifts) and 20 microns vertically. The large ring-averaged horizontal size is dominated by dispersion effects. In these simulations we clearly see the pinch effect of the beam attracting the EC (Fig. 12). Electric field maps on a 15×15 grid of $\pm 5\sigma$ of the transverse beam size are obtained for 11 time slices as the bunch passes through the cloud. The time between slices is 20 ps. Figure 13 shows these field maps in a dipole for bunch number 30 in the 0.7 mA/b train during the central time slice. Since only a

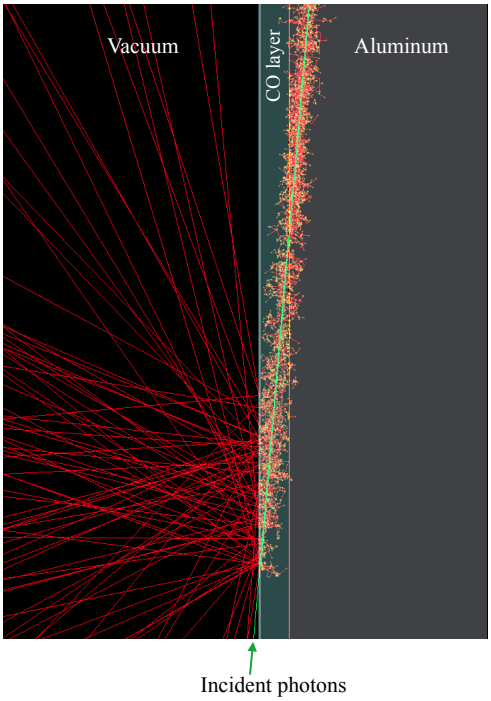

Figure 11: Tracks from incident 300 eV photons (green) and subsequently generated electrons (red) from Geant4. The outgoing angular distribution of electrons is normal to the surface on average.

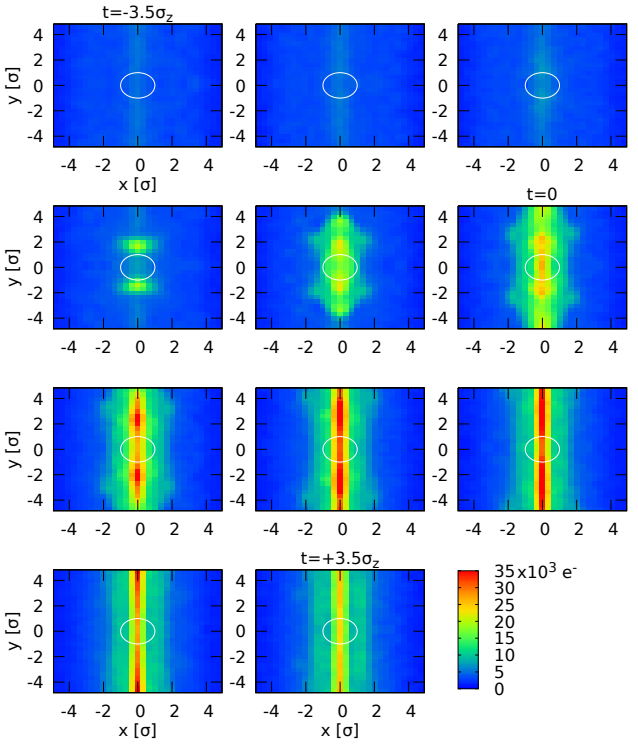

Figure 12: Transverse charge distributions of the electron cloud in an 800 Gauss dipole field during the passage of the last bunch of the 30 bunch train at 0.7 mA/b at 2.1 GeV, in the central region ($\pm 5\sigma$ of the beam size) for 11 time slices spanning $\pm 3.5\sigma_z$. One sigma of the beam size is shown as a white circle. Time increases from left to right, top to bottom. The time between slices is 20 ps.

small fraction (~0.1%) of photoelectrons are within the $\pm 5\sigma$ region around the beam, it is necessary to combine the results of many ECLOUD simulations to minimize statistical uncertainty in the calculation of the electric field.

The modeled tune shifts are calculated from the cloud space-charge electric field gradients. They can also be obtained from the tracking simulation described in the next section, and are found to be in agreement, but calculating them directly from the field gradients saves a step. The pinch effect, wherein the bunch attracts the nearby cloud as it passes, can be clearly seen in Figs. 14 and 15 as a dramatic increase in electric field gradients. However, since the bunch length is a mere 9 mm (16 mm) long at 2.1 mm (5.3 GeV), it hardly perturbs the built-up cloud during its passage. Additionally, for an offset bunch (the one being excited) in an on-axis train, the pinched cloud is found to be centered on the offset bunch, even in the presence of a dipole field (as shown in Fig. 16). Thus the kick on the offset bunch due to the pinched cloud can be neglected, and does not contribute to the coherent tune shift, as confirmed by the witness bunch betatron tune measurements shown in Fig. 17. The pinched cloud can however contribute to incoherent tune spread and emittance growth as demonstrated in the witness bunch measurements (Fig. 5). For this reason, the space-charge electric field gradients immediately prior to the bunch arrival are used when calculating the tune shifts.

SEY parameter determination

Tune shifts from simulation are found to depend strongly on a number of secondary electron yield parameters. Moreover, the effects of these parameters on the tune shifts can be highly correlated. Direct SEY measurements can provide a good starting point, but it is difficult to accurately measure all of the parameters. Furthermore, the ring-wide averaged SEY in the ring may be different than an external measurement of one piece of vacuum chamber. We use the model of secondary emission developed by Furman and Pivi and the SEY parameters determined for copper in [16] as a starting point. To improve agreement between the model and the various tune shift measurements, an optimizer is used to fit the SEY parameters to the tune shift measurements. At each iteration, the EC buildup simulations are run in parallel with the current best SEY parameters, and each parameter varied up and down by an adaptive increment. The tune shifts from these simulations are obtained, and the Jacobian is calculated and provided to the optimizer. The optimized input parameters are, in the notation of Furman and Pivi,

- $\hat{E}_{\mathrm{ts}}$: incident electron energy at which the true secondary yield is maximum for perpendicular incidence,
- s: true secondary SEY energy dependence parameter,

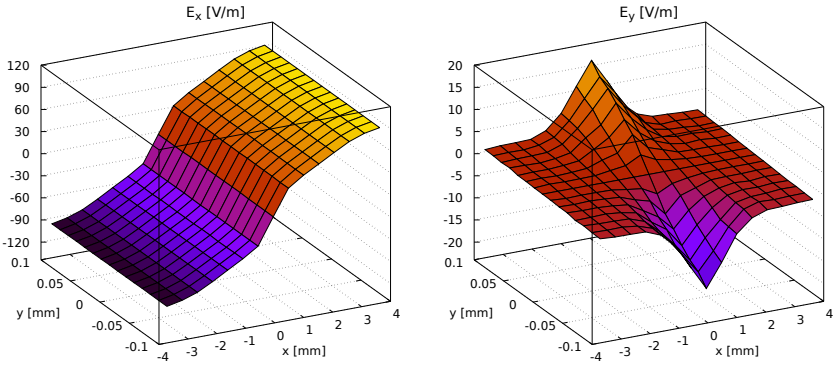

Figure 13: Space-charge electric field maps in a region of $\pm 5\sigma$ of the transverse beam size for the central time slice of the last bunch of the 30 bunch train at 0.7 mA/b at 2.1 GeV (see Fig. 12).

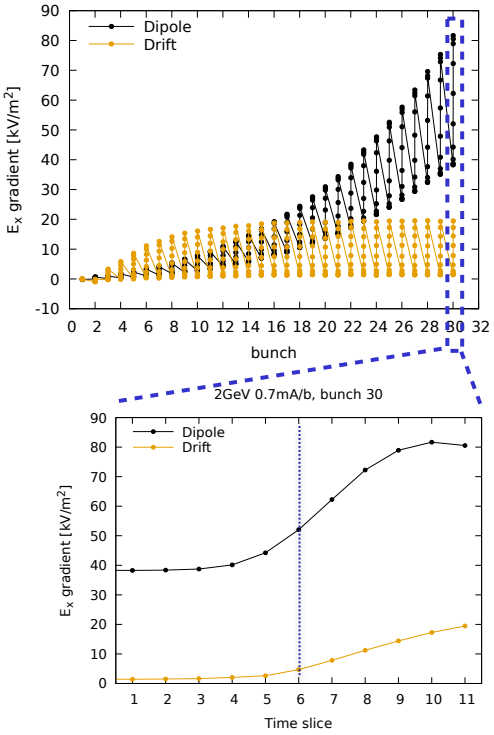

Figure 14: Top: horizontal electron cloud space-charge electric field gradients for the 11 time slices within each of 30 bunches, for dipoles and drifts. Bottom: electric field gradients for the 11 time slices in bunch 30, showing the center of the bunch at time slice 6.

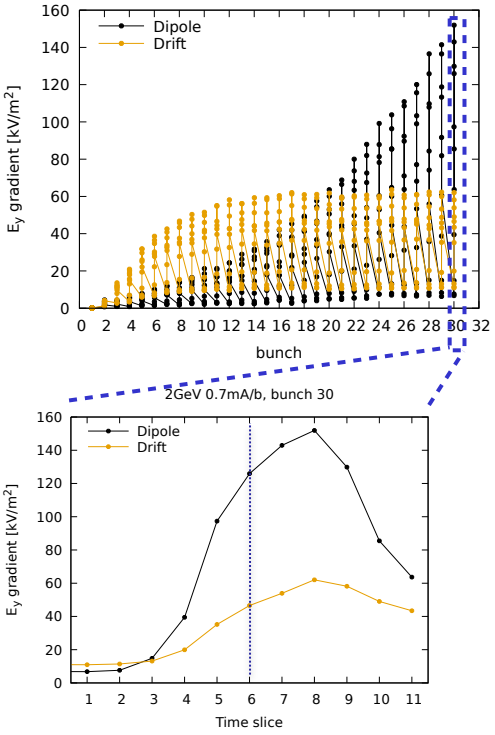

Figure 15: Top: vertical electron cloud space-charge electric field gradients for the 11 time slices within each of 30 bunches, for dipoles and drifts. Bottom: electric field gradients for the 11 time slices in bunch 30, showing the center of the bunch at time slice 6.

- $P_{\mathrm{l,r}}(\infty)$: rediffused secondary yield at high incident electron energy,
- $\hat{\delta}_{\mathrm{ts}}$: true secondary yield at perpendicular incidence,
- t_1 and t_2 : amplitude of the cosine dependence and power of the cosine in the true secondary yield: $\delta_{\mathrm{ts}}(\theta_{\mathrm{e}}) = \hat{\delta}_{\mathrm{ts}}[1 + t_1(1 - \cos^{t_2}\theta_{\mathrm{e}})]$, where $\theta_{\mathrm{e}} = 0$ for perpendicular electron incidence,
- t_3 and t_4 : amplitude of the cosine dependence and power of the cosine in true secondary peak energy: $E_{\mathrm{ts}}(\theta_{\mathrm{e}}) = \hat{E}_{\mathrm{ts}}[1 + t_3(1 - \cos^{t_4}\theta_{\mathrm{e}})]$,
- $\hat{P}_{\mathrm{l,e}}$: elastic yield in the low-energy limit, and
- ϵ and p : parameters for the energy distribution of the secondaries:

$$\frac{\mathrm{d}N}{\mathrm{d}E_{\mathrm{sec}}}(E_{\mathrm{sec}}) \propto \begin{cases} \dfrac{(E_{\mathrm{sec}}/\epsilon)^{p-1} e^{-E_{\mathrm{sec}}/\epsilon}}{\epsilon} & \text{for } E_{\mathrm{sec}} \leq 5\epsilon \\ 0 & \text{for } E_{\mathrm{sec}} > 5\epsilon \end{cases}.$$

Some of these parameters are highly correlated and could be removed from the optimization. The fits are performed simultaneously over all tune shift data at 2.1 and 5.3 GeV shown in Figs. 7 and 8.

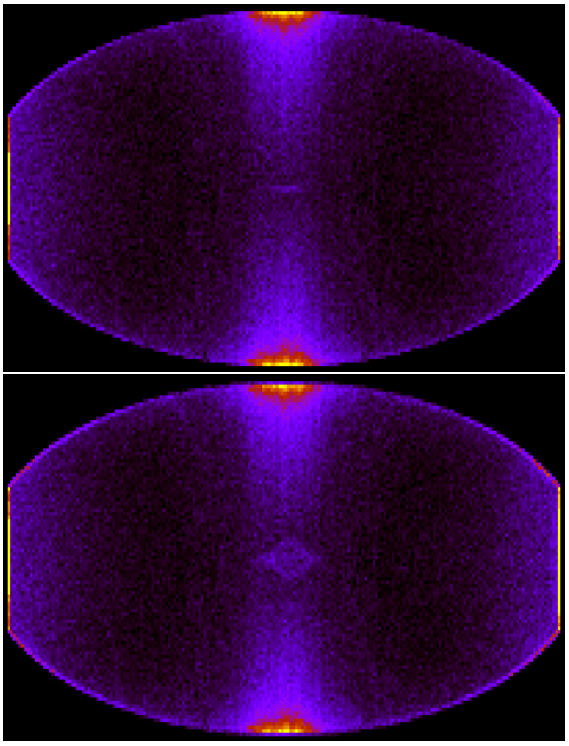

Figure 16: Simulated electron cloud density during the 3rd (top) and 6th (bottom) of 11 time slices during of the passage of bunch 15 (arbitrary), which has been offset from the centered bunch train by 1 mm horizontally to simulate the effect of kicking a single bunch when measuring its tune. The "pinched" cloud is found to be centered on the offset bunch position. The short bunch length (16 mm) bunch hardly modifies the larger built-up cloud. The simulated bunch current is 2 mA/b. At higher currents, the vertical band widens (4 mA/b) and splits into two (6 mA/b).

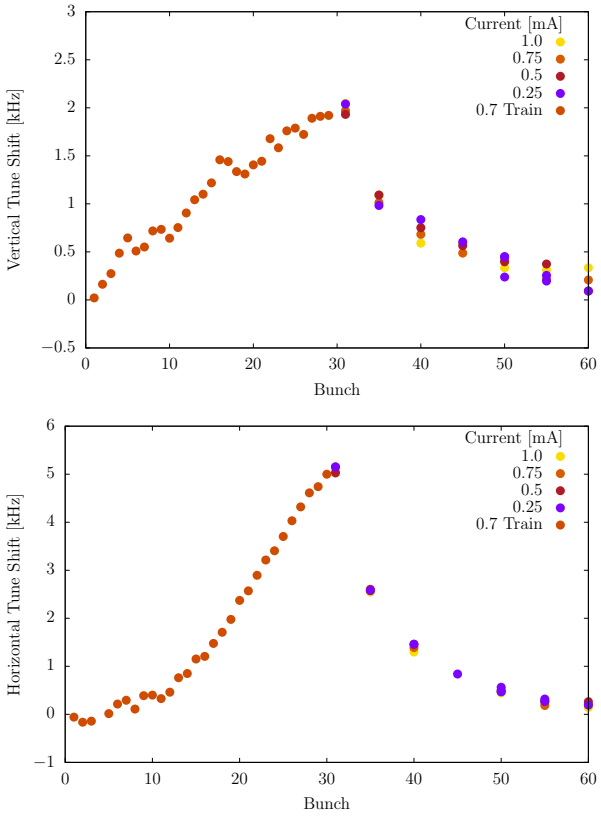

Figure 17: Vertical (top) and horizontal (bottom) tune shifts in kHz (to be compared to the revolution frequency of 390 kHz), measured using the digital tune tracker, for a 30 bunch train of positrons at 0.7 mA/b (1.12×10^{10} bunch population) at 2.1 GeV, followed by a witness bunch in bunch positions 31–60 at currents of 0.25, 0.5, 0.75, and 1.0 mA. The vertical tune shift from impedance (~1.0 kHz/mA) has been subtracted to show just the effects from EC. No dependence of the tune of the witness bunch on the witness bunch current is seen.

Beam particle tracking

The particle tracking simulations use a custom beam-cloud interaction element in Bmad overlaid on the dipole or drift elements and use the full CESR lattice. The electric fields from the different time slices are linearly interpolated to give the value of the fields at the x, y, and t of each particle. To include the effect of uncorrected vertical dispersion and its contribution to the vertical emittance, we give random Gaussian-distributed offset errors to the lattice so as to match the measured single-bunch vertical bunch size in simulation.

RESULTS

The comparison of tune shifts from simulation to measurements is shown in Figs. 18 and 19. After fine adjustment of the SEY parameters from the optimizer, excellent agreement is found over a range of bunch currents and energies.

Vertical bunch size growth in the tracking simulations over 100,000 turns is shown in Fig. 20. Equilibrium bunch size is calculated by averaging over the last 20,000 turns and is also shown in Fig. 20 with comparison to data. We see no bunch size growth in simulations or data for the 0.4 mA/b trains, but the growth is evident in both for the 0.7 mA/b positron train. Figure 21 shows the measurements for witness bunches for a 0.7 mA/b train where the witness bunch current is varied from 0.25 mA to 1.0 mA in 0.25 mA steps. We see that the witness bunch current has a strong effect on the bunch size, indicating a contribution by the pinch effect to the equilibrium emittance. This effect is also seen in the simulations.

SUMMARY

Vertical and horizontal emittance growth measurements along a train of positron bunches including a witness bunch were shown. Measurements of the vertical bunch size of the witness bunch varying its bunch population and distance from the train show emittance growth which scales both with shorter distances from the train (more cloud), and witness bunch current (more pinch effect).

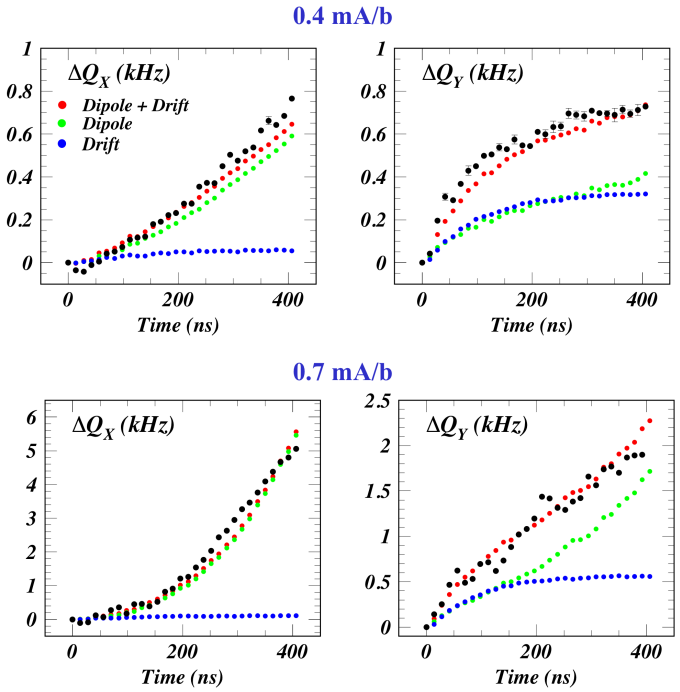

Figure 18: Horizontal (left) and vertical (right) tune shifts from data (black) and simulations (red: sum of dipoles (green) and drifts (blue)) for 30 bunch trains of positrons at 0.4 and 0.7 mA/b (0.64×10^{10} and 1.12×10^{10} bunch populations) at 2.1 GeV.

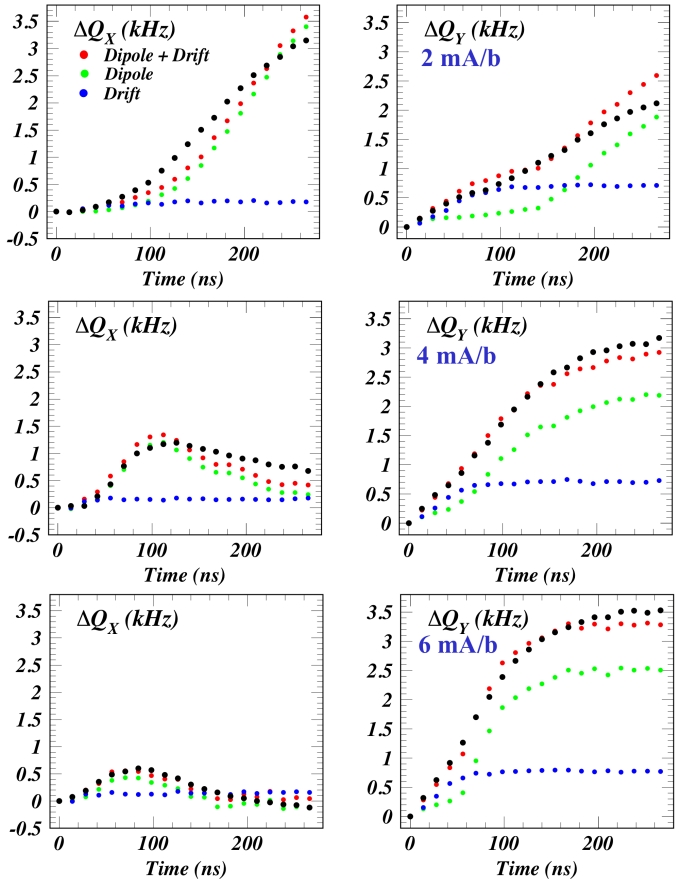

Figure 19: Horizontal (left) and vertical (right) tune shifts from data (black) and simulations (red: sum of dipoles (green) and drifts (blue)) for 20 bunch trains of positrons at 2, 4, and 6 mA/b ($3.2–9.6 \times 10^{10}$ bunch populations) at 5.3 GeV.

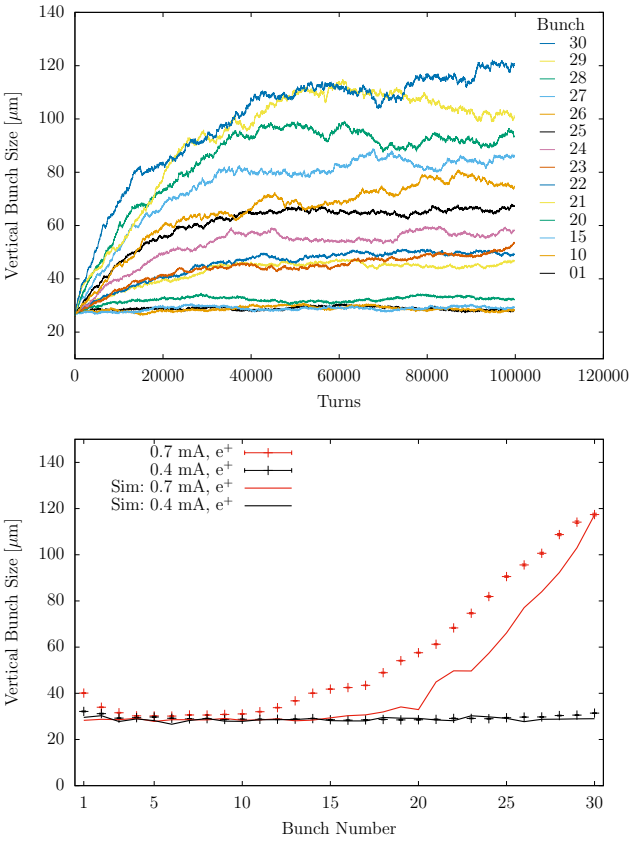

Figure 20: Top: vertical bunch size versus turn number from tracking simulations for 30 bunches of positrons at 0.7 mA/b (1.12×10^{10} bunch population) at 2.1 GeV. Bottom: Equilibrium vertical bunch size, obtained as the average of the last 20,000 turns, versus bunch number in simulations (lines) compared to measurements (points).

We have obtained improved measurements of betatron tune shifts along trains of positron bunches in the horizontal and vertical planes for a range of bunch populations, enabling advances in the predictive power of electron cloud buildup modeling. The Synrad3D and Geant4 simulation codes were employed to eliminate ad hoc assumptions in photoelectron production rates and kinematics characteristic of prior buildup simulations (see Ref. [8] for details). Electron cloud model parameters for secondary electron yield processes were determined through tune shift modeling optimized to the measurements. Excellent agreement in tune shifts were obtained over a range of beam currents and energies. The validated model was then used in a tracking simulation of the beam particles over many radiation damping times with electron cloud elements overlaid on the dipole and field-free regions. The simulations predict vertical emittance growth in agreement with the measurements. These results show that emittance growth due to electron cloud, modeled as an incoherent phenomenon is in good agreement with measurements when centroid bunch motion is damped with turn-by-turn feedback.

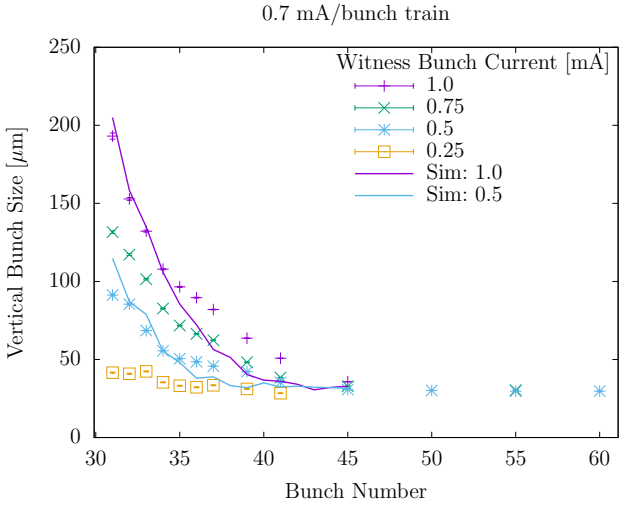

Figure 21: Vertical bunch size from tracking simulations (lines) compared to measurements (points) for witness bunches at various bunch currents following a 30 bunch train of positrons at 0.7 mA/b at 2.1 GeV.

ACKNOWLEDGMENTS

The authors wish to acknowledge important contributions from the technical staffs of the Wilson Laboratory. This work is supported by National Science Foundation and by the US Department of Energy under contract numbers PHY-0734867, PHY-1002467 and DE-FC02-08ER41538 and DE-SC0006505.

REFERENCES

[1] F. Zimmermann, "Electron-Cloud Effects in Past & Future Machines—Walk through 50 Years of Electron-Cloud Studies," in *Proceedings of ECLOUD 2012: Joint INFN-CERN-EuCARD-AccNet Workshop on Electron-Cloud Effects, La Biodola, Elba, Italy*, R. Cimino, G. Rumolo & F. Zimmermann, Eds., CERN, Geneva, Switzerland (2013), CERN-2013-002, p. 9–17.

[2] "The CESR Test Accelerator Electron Cloud Research Program: Phase I Report," Tech. Rep. CLNS-12-2084, LEPP, Cornell University, Ithaca, NY (Jan. 2013).

[3] S. Poprocki *et al.*, "Incoherent Vertical Emittance Growth from Electron Cloud at CesrTA," in *IPAC2016: Proceedings of the 7th International Particle Accelerator Conference, Busan, Korea* (2016), Paper TUPOR021.

[4] J. Crittenden *et al.*, "Electron Cloud Simulations for the Low-Emittance Upgrade at the Cornell Electron Storage Ring," in *NAPAC2016: Proceedings of the North American Particle Accelerator Conference, Chicago, IL* (2016), Paper TUPOB23.

[5] S. Poprocki *et al.*, "Incoherent Vertical Emittance Growth from Electron Cloud at CesrTA," in *NAPAC2016: Proceedings of the North American Particle Accelerator Conference, Chicago, IL* (2016), Paper WEA2CO03.

[6] G. Dugan & D. Sagan, "Simulating synchrotron radiation in accelerators including diffuse and specular reflections," *Phys. Rev. Accel. Beams* **20**, 020708 (Feb. 2017).

[7] S. Agostinelli *et al.*, "Geant4—a simulation toolkit," *Nuclear Instruments and Methods in Physics Research Section A: Accelerators, Spectrometers, Detectors and Associated Equipment* **506**, p. 250 – 303 (2003).

[8] J. Crittenden *et al.*, "Simulations of synchrotron-radiation-induced electron production in the CESR vacuum chamber wall," in *Proceedings of ECLOUD 2018: Joint INFN-CERN-EuroCirCol-ARIES-APEC Workshop on Electron-Cloud Effects, La Biodola, Elba, Italy*.

[9] J. P. Alexander *et al.*, "Vertical Beam Size Measurement in the CESR-TA e^+e^- Storage Ring Using X-Rays from Synchrotron Radiation," *Nucl. Instrum. Methods Phys. Res.* **A748**, p. 96–125 (Jun. 2014).

[10] S. Wang & R. Holtzapple, "Single-shot Bunch-by-Bunch Horizontal Beam Size Measurements using a Gated Camera at CesrTA," in *IPAC2016: Proceedings of the 7th International Particle Accelerator Conference, Busan, Korea* (2016), Paper MOPMR052.

[11] J. A. Crittenden *et al.*, "Progress in Studies of Electron-cloud-induced Optics Distortions at CesrTA," in *Proceedings of the 2010 International Particle Accelerator Conference, Kyoto, Japan*, ACFA (2010), p. 1976–1978.

[12] D. Sagan, "Bmad: A Relativistic Charged Particle Simulation Library," *Nucl. Instrum. Methods Phys. Res.* **A558**, p. 356–359 (Mar. 2006).

[13] B. L. Henke, E. M. Gullikson & J. C. Davis, "X-Ray Interactions: Photoabsorption, Scattering, Transmission, and Reflection at E = 50–30,000 eV, Z = 1–92," *At. Data Nucl. Data Tables* **54**, p. 181–342 (Jul. 1993).

[14] J. Allison *et al.*, "Recent developments in Geant4," *Nuclear Instruments and Methods in Physics Research Section A: Accelerators, Spectrometers, Detectors and Associated Equipment* **835**, p. 186 – 225 (2016).

[15] F. Zimmermann, G. Rumolo & K. Ohmi, "Electron Cloud Build Up in Machines with Short Bunches," in *ICFA Beam Dynamics Newsletter*, K. Ohmi & M. Furman, Eds., International Committee on Future Accelerators, No. 33, p. 14–24 (Apr. 2004).

[16] M. A. Furman & M. T. F. Pivi, "Probabilistic Model for the Simulation of Secondary Electron Emission," *Phys. Rev. ST Accel. Beams* **5**, 124404 (Dec. 2002).

INVESTIGATING THE ROLE OF PHOTOEMISSION IN THE E-CLOUD FORMATION AT THE LHC

P. Dijkstal*, G. Iadarola†, L. Mether, G. Rumolo
CERN, CH-1211 Geneva 23, Switzerland

Abstract

The presence of electron clouds at the LHC gives rise to several problems, among them is the heat deposited by the electrons on the beam screens of the superconducting magnets, which constitutes a significant load for the cooling system. To improve the understanding of this phenomenon, simulation studies of the e-cloud build-up are performed using the dedicated simulation tool PyECLOUD. Photoelectrons generated by synchrotron radiation can significantly enhance the e-cloud formation. In this contribution, the available literature on photoelectric properties of the material used for the LHC beam screens is reviewed, and the number of photons emitted by the beam is calculated. This allows the definition of suitable simulation parameters for modeling the electrons from photoemission within the PyECLOUD code. The simulations with photoemission seeding are compared to those that neglect photoemitted electrons. The predicted heat loads are compared against measurements from LHC cryogenic cells. Since these cells include several kinds of magnets, simulations with different configurations of the externally applied magnetic field had to be combined. Furthermore a sensitivity study on the modeling of synchrotron radiation is presented.

INTRODUCTION

The formation of electron clouds in the arcs of the Large Hadron Collider (LHC) has been identified as one of the main limitations for the performance of the machine, especially when operating with the nominal bunch spacing of 25 ns [1–4].

Electron clouds can in particular induce severe beam degradation through beam losses, emittance growth and instabilities. Furthermore, the impacting electrons can deposit a significant power on the cold beam screens of the LHC superconducting magnets, which translates into a significant heat load for the cryogenic system. Heat load management will be even more critical in the HL-LHC era, also because the increased bunch intensity will entail a larger heat load from impedance and synchrotron radiation, reducing the available margin for e-cloud heat loads [5].

In order to understand in detail these effects and make reliable predictions for the future, we developed a detailed model of the e-cloud formation in the different elements of the LHC arc half-cell using the PyECLOUD simulation code [6, 7]. The model includes the main dipole and quadrupole magnets, shorter corrector magnets and drift spaces.

Particular care is taken to correctly model the impact of the photoelectrons. For this purpose, we reviewed the available literature on the characterization of the LHC beam screen surface in terms of reflectivity and photoelectron yield and we defined the necessary steps to obtain the photoemission model in the format required by the PyECLOUD code.

The number of photons that is capable of producing photoelectrons is calculated from basic electrodynamics equations. The photoelectric properties of the copper surface of the LHC beam screens have been measured at CERN and other laboratories, mainly in the late 90s and early 2000s [8–11]. The results are summarized and compared in this report, and the corresponding input parameters for PyECLOUD are defined.

Simulations of the magnetic elements that are part of the cryogenic cell of the LHC arcs, such as dipoles, quadrupoles and drift spaces, were performed. In this contribution, the estimated heat loads are compared to measurements collected during LHC operation. The impact of the photoelectrons on the simulation results is investigated. More information about these studies can be found in [12].

EMISSION OF PHOTOELECTRONS FROM THE LHC BEAM SCREENS

Photons are generated by the beam that follows a curved trajectory within dipole magnets. These photons hit the beam chamber surfaces where they are eventually absorbed, possibly after being reflected once or multiple times. We analyze this problem in several steps to finally obtain the model parameters required for e-cloud simulation studies.

Emission of photons by a proton beam in the LHC

The amount of photons generated by a proton having a relativistic parameter γ_{rel} and following a circular trajectory with bending radius ρ has to be calculated. The problem can be solved analytically following the treatment explained in [14].

The following equation describes the power spectrum $\frac{\mathrm{d}P}{\mathrm{d}\omega}$ of the radiation emitted by a highly relativistic charged particle ($\beta_{\mathrm{rel}} \approx 1$) on a circular trajectory:

$$\frac{\mathrm{d}P}{\mathrm{d}\omega} = \frac{P_s}{\omega_c} S_s \left(\frac{\omega}{\omega_c} \right) \tag{1}$$

* Current address: Paul Scherrer Institut, CH-5232 Villigen PSI, Switzerland
† Correspondence e-mail: giovanni.iadarola@cern.ch

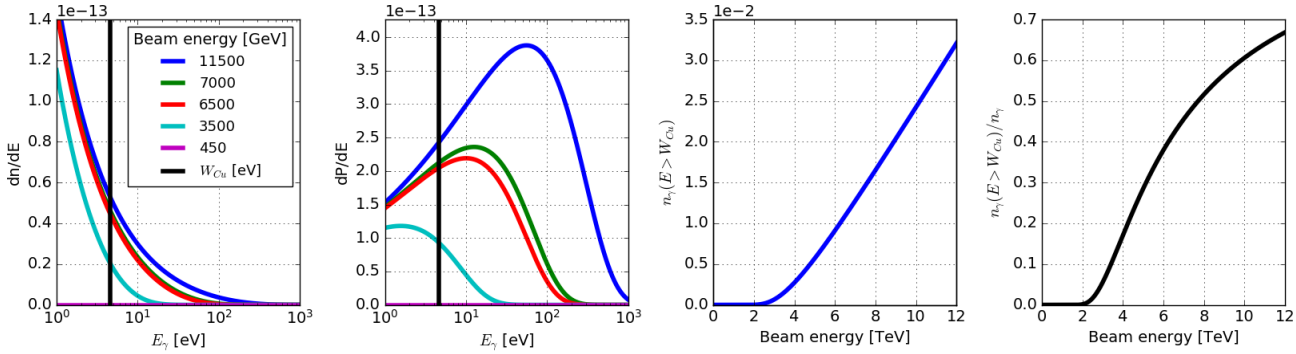

Figure 1: Left: the photon energy distribution of the synchrotron radiation emitted by a proton travelling in an LHC dipole with different kinetic energies. Middle left: the corresponding emitted power spectrum. Middle right: the number of photons above the work function of copper W_{Cu} (4.6 eV [13]) as a function of the proton energy. Right: the fraction of photons with an energy above W_{Cu} as a function of the proton energy.

where P_s is the total emitted power,

$$P_s = \frac{e^2}{4\pi\epsilon_0}\frac{2c\gamma_{\mathrm{rel}}^4}{3\rho^2} \tag{2}$$

and ω_c the critical frequency of the radiation:

$$\omega_c = \frac{E_c}{\hbar} = \frac{3c\gamma_{\mathrm{rel}}^3}{2\rho} \tag{3}$$

The function S_s is an integral of the modified Bessel function $K_{5/3}$:

$$S_s(x) = \frac{9\sqrt{3}}{8\pi}x\int_x^\infty K_{5/3}(z)\mathrm{d}z \tag{4}$$

The photon energy is related to the radiation frequency by:

$$E_\gamma(\omega) = \hbar\omega \tag{5}$$

The emitted power spectrum is related to the spectrum of emitted photons per unit time $\frac{\mathrm{d}\dot{n}_\gamma}{\mathrm{d}\omega}$:

$$\frac{\mathrm{d}P}{\mathrm{d}\omega} = \hbar\omega\frac{\mathrm{d}\dot{n}_\gamma}{\mathrm{d}\omega} \tag{6}$$

Using Eq. 1 we obtain:

$$\frac{\mathrm{d}\dot{n}_\gamma}{\mathrm{d}\omega} = \frac{1}{\hbar\omega}\frac{\mathrm{d}P}{\mathrm{d}\omega} = \frac{1}{\hbar\omega}\frac{P_s}{\omega_c}S_s\left(\frac{\omega}{\omega_c}\right) \tag{7}$$

Figure 1 shows the photon spectrum in Eq. 7 as a function of the photon energy for different energies of the LHC proton beam, together with the corresponding power spectrum of the radiation.

The number of photons above a certain frequency per unit path length is given by (see [12]):

$$n_\gamma(\omega > \omega_{\mathrm{min}}) = \frac{\sqrt{3}}{8\pi^2}\frac{e^2\gamma_{\mathrm{rel}}}{\hbar c\epsilon_0\rho}\cdot\int_{\frac{\omega_{\mathrm{min}}}{\omega_c}}^\infty K_{5/3}(x)\left(x-\frac{\omega_{\mathrm{min}}}{\omega_c}\right)\mathrm{d}x \tag{8}$$

Note that also ω_c depends on γ_{rel}, with the effect that $n_\gamma(\omega > \omega_{\mathrm{min}})$ depends non-linearly on the beam energy as shown in Fig. 1.

Due to the photoelectric effect, electrons can be extracted from the beam chamber surface. The work function of a metal is the energy gap between the Fermi and vacuum energy levels, which is 4.6 eV in the case of copper [13], the material of the LHC beam screen surface. Only photons with energy sufficient to overcome this gap can contribute to the photoelectron generation process. The plots in Fig. 1 show the number of such photons per unit length and per proton, as well as their ratio with respect to all photons.

Another interesting feature is the angular distribution of photons. Far above the critical angle θ_c, emission of synchrotron radiation is negligible. The critical angle can be written as:

$$\theta_c(\omega) = \frac{1}{\gamma_{\mathrm{rel}}}\left(\frac{2\omega_c}{\omega}\right)^{1/3} = \left(\frac{3c}{\rho\omega}\right)^{1/3} \tag{9}$$

For energies corresponding to the copper work function, the critical angle is about 0.36 mrad. It is even smaller for higher energies.

Beam screen photoemission properties from past measurement campaigns

The beam screen that is installed in the cryogenic magnets of the LHC has the purpose of absorbing the heat load caused by the beam through impedance, synchrotron radiation and electron cloud effects. This beam screen is made of stainless steel with a surface of co-laminated copper. It is thermally isolated from the liquid helium and kept at a temperature between 4.6 and 20 K, which allows for more efficient cooling compared to 1.9 K, the temperature of the superconducting coils of the magnets [15]. The beam screen is cooled by a flow of weakly supercritical helium through two small attached tubes (see Fig. 2) and is perforated to enable the vacuum pumping of the volume inside. The pumping slots are covered by shields that intercept electrons before they can reach the cold bore [16].

The majority of the beam screens at the LHC are installed within strong dipolar magnetic fields. Photoelectrons generated at the side of the chamber are confined there by the magnetic field and cannot move to the center of the pipe where the beam is located. Compared to those electrons that are generated at the top and bottom parts of the beam chamber, they receive a much weaker kick from the beam in the direction in which they are free to move, and therefore have a limited impact on heat loads and beam stability.

For these reasons, at the side of the beam screen that is exposed to direct synchrotron radiation, the surface exhibits a sawtooth structure (Fig. 2 - bottom). Its purpose is to avoid a grazing impact of the photons and thereby provide a smaller probability of reflection. This results in a large fraction of photoelectrons being generated at the side of the chamber where they are less harmful.

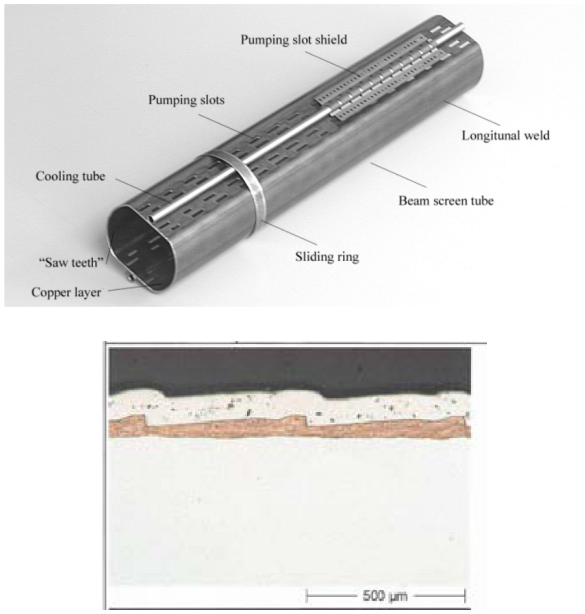

Figure 2: Top: the beam screen used at the LHC [16]. Bottom: the sawtooth structure present on the side where the synchrotron radiation first impacts, in order to have a low probability of photon reflection [17].

Photoemission from the LHC beam screens was extensively studied with dedicated measurements between 1998 and 2004 [8–11]. The present section summarizes the main results of these studies that are relevant for the simulation of the electron cloud formation in the LHC arcs. The following notation is used in most of them: R is the photon reflectivity of the material, and Y, Y^* are respectively the photoelectron yields per incident and absorbed photon. They are defined as follows, where N_e and n_γ are the number of photoelectrons and the number of photons, respectively:

$$n_{\gamma,\text{incident}} = n_{\gamma,\text{absorbed}} + n_{\gamma,\text{reflected}} \tag{10}$$

$$R = \frac{n_{\gamma,\text{reflected}}}{n_{\gamma,\text{incident}}} \tag{11}$$

$$Y = \frac{N_e}{n_{\gamma,\text{incident}}} \tag{12}$$

$$Y^* = \frac{N_e}{n_{\gamma,\text{absorbed}}} = \frac{Y}{1-R} \tag{13}$$

Table 1: Photoemission properties for different materials when irradiated by synchrotron radiation with different critical photon energy [8].

		45 eV		194 eV	
Surface	Status	R (%)	Y* (e/ph)	R (%)	Y* (e/ph)
Cu co-lam.	as-received	80.9	0.114	77.0	0.318
	air baked	21.7	0.096	18.2	0.180
Cu elect.	as-received	5.0	0.084	6.9	0.078
Cu sawtooth	as-received	1.8	0.053	-	-
	150°C, 9h	1.3	0.053	1.2	0.052
	150°C, 24h	1.3	0.040	1.2	0.040

In [8], the properties of several materials were studied using synchrotron radiation from the EPA ring, including co-laminated copper with and without the sawtooth structure. It was possible to measure the reflectivity R (only in the forward direction), as well as the photoelectron yield Y^*. The main results of this article are provided in Table 1.

	45 eV		**194 eV**	
Dose (ph/m)	R (%)	Y* (e/ph)	R (%)	Y* (e/ph)
~ 2 10^{19}	8	0.029	7	0.040
1.5 10^{22}		0.015		0.022

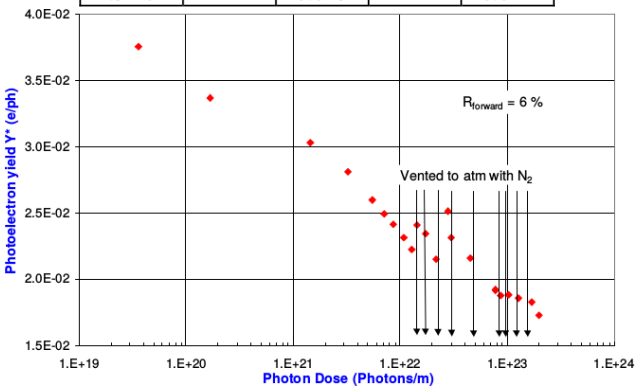

Figure 3: Top: reflectivity and photoelectron yield from measurements of copper samples with sawtooth structure on the surface. Bottom: the impact of photon-induced conditioning on the photoelectron yield. Both results were published in [9].

A different experiment [9] quantified the effect of photon-induced conditioning ("scrubbing") on the photoelectron yield of co-laminated copper with sawtooth. Figure 3 shows

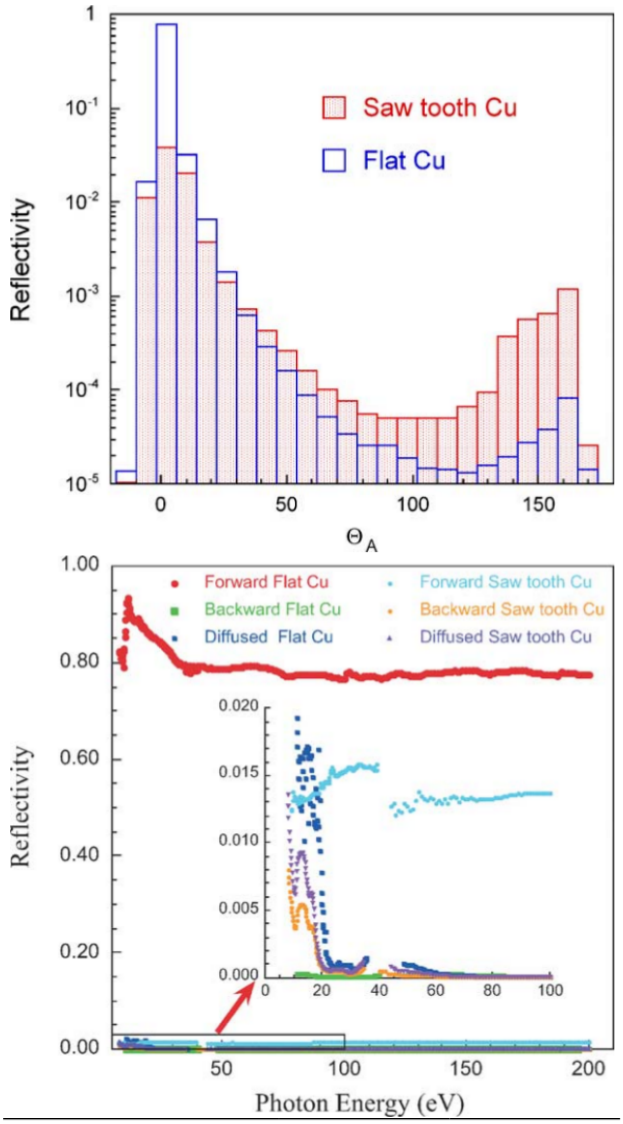

	Flat sample	Saw-tooth sample
Forward scattering (%)	80	4
Back scattering (%)	0	2
Diffused (%)	2	4
Total	82	10

Figure 4: Top: Measured reflectivity of Cu samples for different angles with respect to grazing incidence. Middle: Measured reflectivities for different photon energies and material configurations. Bottom: Summary of reflectivities for LHC-type photon spectrum. These results were published in [10].

the results. Photon "scrubbing" with a dose of $1.5 \cdot 10^{22}$ photons, corresponding to about 600 hours of nominal LHC operation, caused a decrease of the photoelectron yield by roughly 50%. The results indicate that this process had not saturated and that the yield could possibly have decreased even further with additional photon dose. No effect of photon "scrubbing" is observed on the photon reflectivities. One can note that this experiment measured larger photon reflectivities with respect to the results reported in [8].

The angular distribution of the reflected photons is studied in detail in [10]. Copper samples with and without sawtooth structures were irradiated with synchrotron light between 8 eV and 200 eV, and the reflectivities in different directions were measured. The main results of this article are shown in Fig. 4. The reflectivity as a function of the angle is shown for synchrotron radiation with a critical energy of 44 eV. In addition, the measured total reflectivity as a function of the photon energy is provided. In case of the sawtooth, the reflectivity is reported as 10%, which is larger than in [8] and [9] (1.8% and 8%, respectively). It was also found that R depends on the photon energy.

The comprehensive paper [11] covers many photoemission properties of different materials. Among these are the kinetic energy spectra of photoelectrons, the angular spectra of photoemission and the dependency of photoelectron yields on photon energy (see also Fig. 12). Furthermore, also the total photoemission yields and how these are affected by photon-induced conditioning are reported (see Table 2). Copper is among the studied materials, although only without a sawtooth-shaped surface. One has to note that, unlike in the previously mentioned measurement campaigns, the reflectivities were not measured. The photoelectron yields therefore correspond to yield per incident photon Y. It is notable that these tend to be higher than those presented in [8, 9]. However, the incident angle of photons was 45°, compared to a 11 mrad grazing incidence in case of [8, 9].

Parameters for photoemission simulations

In this section we will use the calculations and measurement results presented in the previous sections to model the generation of photoelectrons in PyECLOUD build-up simulations. For this purpose, we will use the notation defined in Tab. 3.

The PyECLOUD code [18] does not model photons directly. Instead, the photoemission process is described through the number of photoelectrons emitted per proton and per meter (**k_pe_st**), and the fraction of photoelectrons (**refl_frac**) not emitted from a narrow region in one specific part of the chamber, which corresponds to photons that are reflected at least once. This means that the quantity (1-**refl_frac**) is the fraction of photoelectrons generated at the part of the beam screen where the synchrotron radiation first impacts. The calculation of **k_pe_st** requires knowledge of the beam energy, since the number of photons with sufficient energy to generate photoelectrons ($n_\gamma(E > W_{\mathrm{Cu}})$) depends on the beam energy (see Eq. 8). In the following, $n_\gamma(E > W_{\mathrm{Cu}})$ is computed for the operational LHC beam energy, which is 6.5 TeV.

In the case of a uniform beam pipe surface, **k_pe_st** is simply computed as follows:

$$\mathbf{k\_pe\_st} = n_\gamma(E > W_{\mathrm{Cu}})Y^* \tag{14}$$

The reflection coefficient is not needed since all photons are eventually absorbed, either on direct impact or after an arbitrary number of reflections.

Table 2: Measured white light (WL) photoelectron yields for Au and Cu [11] before (low dose WL yield) and after (WL yield) conditioning with synchrotron radiation with a spectrum similar to that emitted by LHC beams. The yield decreased by about 40% as a consequence of this conditioning. The other columns that are labeled "energy window" only take into account those electrons that have been emitted with a kinetic energy between 1 and 6 eV.

Sample	Low dose WL yield (electrons/photon)	Energy window low dose WL yield (electrons/photon)	WL yield (electrons/photon)	Energy window WL yield (electrons/photon)
Au	0.047 ± 0.020	0.022 ± 0.020	0.041 ± 0.002	0.023 ± 0.002
Cu	0.103 ± 0.020	0.051 ± 0.020	0.063 ± 0.002	0.042 ± 0.002

Table 3: The notation used to describe the surface materials.

Y_i, Y_i^*	Photoelectron yields per incident and per absorbed electron (defined by Eq. 12 and Eq. 13) in the region of direct impact of the synchrotron radiation (i.e. sawtooth region)
Y_r, Y_r^*	Photoelectron yields per incident and per absorbed electron in the remaining part of the chamber
R_i, R_r	Reflection rates in the region of direct synchrotron radiation impact and in the remaining part of the chamber
N_i, N_r	Photoelectrons emitted in the region of direct impact of the synchrotron radiation and in the remaining part of the chamber
N_t	Total number of emitted photoelectrons
$n_\gamma(E > W_{\mathrm{Cu}})$	Number of photons with an energy above the copper work function, emitted per proton and per m in the LHC arc bending magnets (Eq. 8)

However, if the region of initial impact has special properties, e.g. the LHC beam screen with its sawtooth structure, the properties of both surface types must be taken into account. The photon numbers that are absorbed at the sawtooth part and after initial reflection are weighted with the respective photoelectron yields Y^* and the probability of initial reflection:

$$\begin{aligned} \textbf{k\_pe\_st} &= N_i + N_r && (15)\\ &= n_\gamma(E > W_{\mathrm{Cu}}) \left((1 - R_i)Y_i^* + R_i Y_r^*\right) && (16)\\ &= n_\gamma(E > W_{\mathrm{Cu}}) \left(Y_i + R_i Y_r^*\right) && (17) \end{aligned}$$

Here we ignore the effect of photons that are reflected back to the sawtooth material, as it covers only a small fraction of the total beam screen surface.

The quantity **refl_frac** is computed as follows:

$$\textbf{refl\_frac} = \frac{N_r}{N_t} = \frac{N_r}{N_i + N_r} = \frac{R_i Y_r^*}{(1 - R_i)Y_i^* + R_i Y_r^*} \quad (18)$$

Table 4 provides an overview of the results from the papers reviewed in the previous section. Y was not specified in [11] but can be calculated from Y^* and R. Since only the references [8, 9] include results for sawtooth materials, these publications are used to extract the parameters for electron cloud simulations. The reflectivities from [10] are chosen as they also include backward scattering of photons. The parameters (**refl_frac**) and (**k_pe_st**) are thus calculated from a combination of quantities that are not part of the same publication.

Two types of beam screens are considered, one with a sawtooth structure at the location where the synchrotron radiation directly impacts and another one with flat copper everywhere. The effect of photon-induced conditioning was not studied in each reference publication.

For a **conservative estimate** (Tab. 5), we do not take into account possible conditioning of the surfaces and we use the high photoelectron yields Y from [8].

An **optimistic estimate** (Tab. 6) includes the lowest yields that can be obtained from the published results that were summarized in the previous section. Photon conditioning effects need to be included for both the material in the sawtooth and elsewhere. This is quantified in [8, 9] for copper with sawtooth structures, in which case a reduction of the yield by a factor of 4.7 was observed ($Y = 0.052$ was measured in [8] before conditioning and $Y = 0.011$ was measured in [9] after conditioning). In the absence of published measurement results for smooth Cu after photon "scrubbing", we apply the same factor as for the sawtooth material, obtaining for the surface after conditioning: $Y = \frac{2.2 \cdot 10^{-2}}{4.7} = 4.6 \cdot 10^{-3}$.

Here the beam energy is only considered in the calculation of n_γ (Eq. 8). It shall be noted that the references [8–11] all used a synchrotron radiation spectrum that is very similar to the one from the LHC running at 7 TeV. In the absence of data that corresponds to a LHC at 6.5 TeV, we resort to using the available results for 7 TeV. However one should note that results corresponding to a 11.5 TeV beam (see Fig. **??** and 4) are significantly different from those corresponding to a 7 TeV beam.

Table 4: Different published experimental results on photoelectron yields and reflectivities. If two values are stated for a photoelectron yield, they correspond to measurements before and after photon "scrubbing". All other values are measured before photon conditioning. The reflectivities colored in red only include the forward reflectivity. The yields in blue were not published but could be retrieved with the simple relation between R, Y and Y^* (Eq. 13).

Source	Cu co-lam.			with sawtooth		
	R [%]	Y	Y^*	R [%]	Y	Y^*
Baglin et al. 1998 [8]	80.9	0.022	0.114	1.8	0.052	0.053
Cimino et al. 1999 [11]	-	0.103/0.063	-	-	-	-
Baglin et al. 2001 [9]	-	-	-	8	0.021/0.011	0.029/0.015
Mahne et al. 2004 [10]	82	-	-	10	-	-

Table 5: The yields and reflectivities from Tab. 4, together with the number of photons from Eq. 8, lead to a **conservative estimate** of the PyECLOUD input parameters refl_frac and k_pe_st.

Chamber type	R_i	R_r	Y_i	Y_r	Y_i^*	Y_r^*
Cu co-lam. with sawtooth	10.0	82.0	5.2e-02	2.2e-02	5.8e-02	1.2e-01
Cu co-lam.	82.0	82.0	2.3e-02	2.3e-02	1.3e-01	1.3e-01

Chamber type	N_i	N_r	N_t	n_γ	refl_frac	k_pe_st
Cu co-lam. with sawtooth	5.2e-02	1.2e-02	6.4e-02	1.1e-02	1.89e-01	7.00e-04
Cu co-lam.	2.3e-02	1.0e-01	1.3e-01	1.1e-02	8.20e-01	1.38e-03

Table 6: Photon "scrubbing" effects are considered to arrive at a more **optimistic estimate** with lower electron yields with respect to the values in Tab. 5.

Chamber type	R_i	R_r	Y_i	Y_r	Y_i^*	Y_r^*
Cu co-lam. with sawtooth	10.0	82.0	1.0e-02	4.6e-03	1.1e-02	2.6e-02
Cu co-lam.	82.0	82.0	4.6e-03	4.6e-03	2.6e-02	2.6e-02

Chamber type	N_i	N_r	N_t	n_γ	refl_frac	k_pe_st
Cu co-lam. with sawtooth	1.0e-02	2.6e-03	1.3e-02	1.1e-02	2.03e-01	1.39e-04
Cu co-lam.	4.6e-03	2.1e-02	2.6e-02	1.1e-02	8.20e-01	2.81e-04

PYECLOUD SIMULATIONS AND COMPARISON AGAINST HEAT LOAD MEASUREMENTS

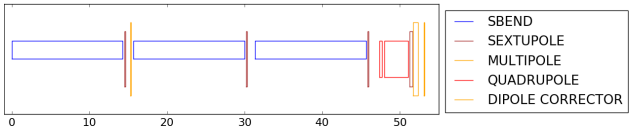

Figure 5: All cryogenic cells (half-cells in terms of beam optics) in the LHC arcs contain three main dipoles and one main quadrupole, interleaved by corrector magnets in different configurations. In this plot, one of the most common types of half-cells is sketched, showing only the magnetic elements.

The arcs of the LHC are divided in cryogenic cells, each of which contains three main dipoles, a main quadrupole and several corrector magnets, as shown in Fig. 5. Because two cryogenic cells correspond to a FODO cell in terms of beam optics, these are often called half-cells. The beam screen inside each of these cryogenic cells is cooled by a flow of weakly supercritical helium. Pressures and temperatures of the helium are measured at different points in each cell and allow a computation of the heat loads deposited on the corresponding beam screen [15]. The contributions of impedance and synchrotron radiation can be estimated starting from measured beam properties [19]. The remaining heat loads are attributed to electron cloud effects.

In this section, this heat load is compared to predictions based on electron cloud simulation results obtained with the PyECLOUD code. During such simulations, the cloud is modeled with macroparticles that are tracked through the electro-magnetic fields from three sources: the beam, the space-charge of the cloud itself and externally applied magnetic fields. Whenever particles hit the surface of the beam pipe, the multipacting process model [6] is sumulated. Furthermore, the impact energy is recorded. The main parameter of the secondary emission model is the SEY parameter. Snapshots of the electron distributions in various magnetic elements are shown in Fig. 6.

Simulation studies

PyECLOUD build-up simulation studies have been performed for all relevant magnetic elements and for the drift sections of the LHC arcs. Each of these magnets is simulated either with photoemission seeding or starting with a uniform initial distribution of 10^7 electrons per meter. Such an initial population is small with respect to the densities that are reached in simulations above the multipacting threshold.

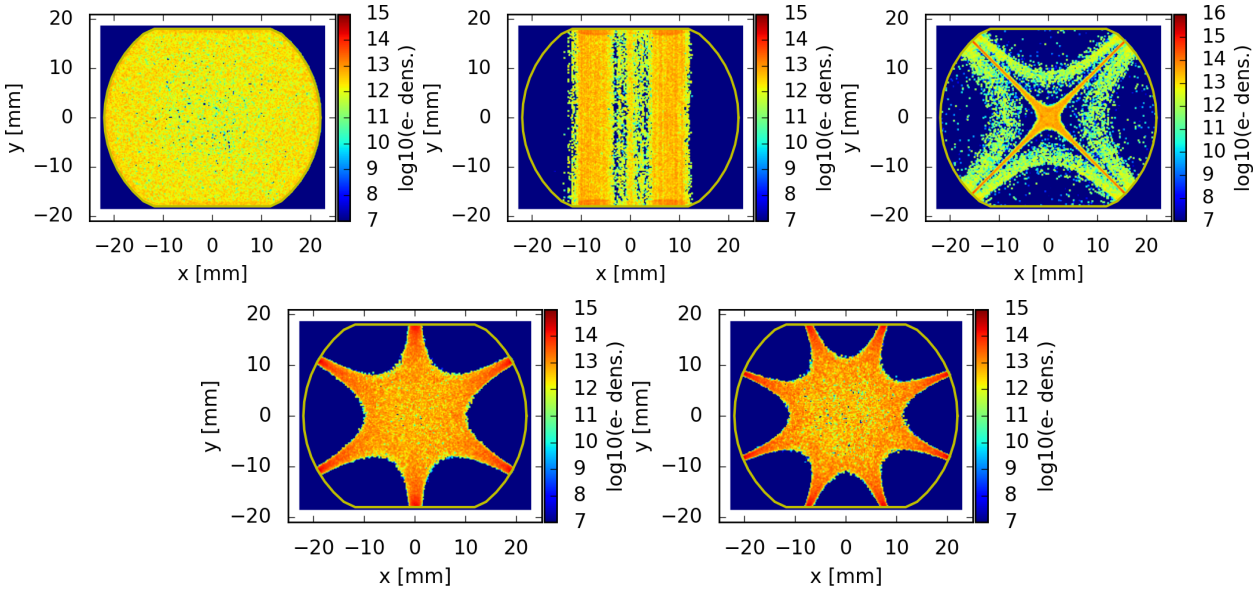

Figure 6: Electron density distributions of drifts, dipoles, quadrupoles, sextupoles and octupoles as obtained from PyECLOUD simulations.

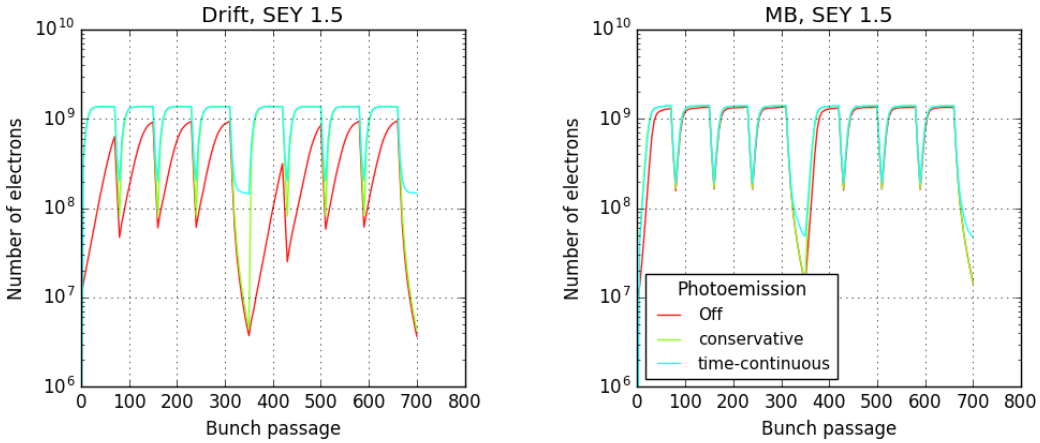

Figure 7: The evolution of the number of electrons per meter in the chamber of a drift and a dipole as obtained from PyECLOUD simulations with an SEY parameter of 1.2. The different electron cloud seeding mechanisms are compared.

The magnetic lengths and the operational magnetic field parameters of the simulated devices operating at a beam energy of 6.5 TeV are shown in Tab. 7. The length of a single magnet is given in the first column. There is no cell that contains all corrector magnets at once. The average length per half cell was found by taking all cryogenic cells in the arcs into account.

For all considered magnetic elements, simulations have been performed. The simulated beam consists of two trains of 288 bunches, each formed by four batches which in turn consist of 72 bunches. The two trains are interleaved with 30 empty bunch slots, and the consecutive batches are interleaved with eight empty slots. The heat load from the second train is rescaled in order to obtain the heat load that corresponds to a filled LHC machine with 2800 bunches in total, without having to simulate each train. This procedure is chosen since the electron cloud in the second and later trains are identical in case the electron density is saturated by the end of the train, a condition that is usually satisfied as shown in Fig. 7. The bunch intensity is set to $1.1{\cdot}10^{11}$ p/bunch.

Figure 8 shows heat loads as a function of the SEY parameter for different external magnetic field configurations. Simulations performed with and without photoelectrons are compared. A significant difference between the two is observed only for the drift spaces, and for the dipole magnets. In these cases both the conservative and optimistic photoemission parameters (as defined in Tabs. 5 and 6 respectively) have been simulated.

The multipacting threshold is significantly altered by the photoelectrons in the case of the drift space and of the vertical dipole corrector (MCBV). In these particular cases the photoelectrons generated by the direct impact of the synchrotron radiation at the side of the beam screen are not trapped by the magnetic field lines and can directly contribute to the multi-

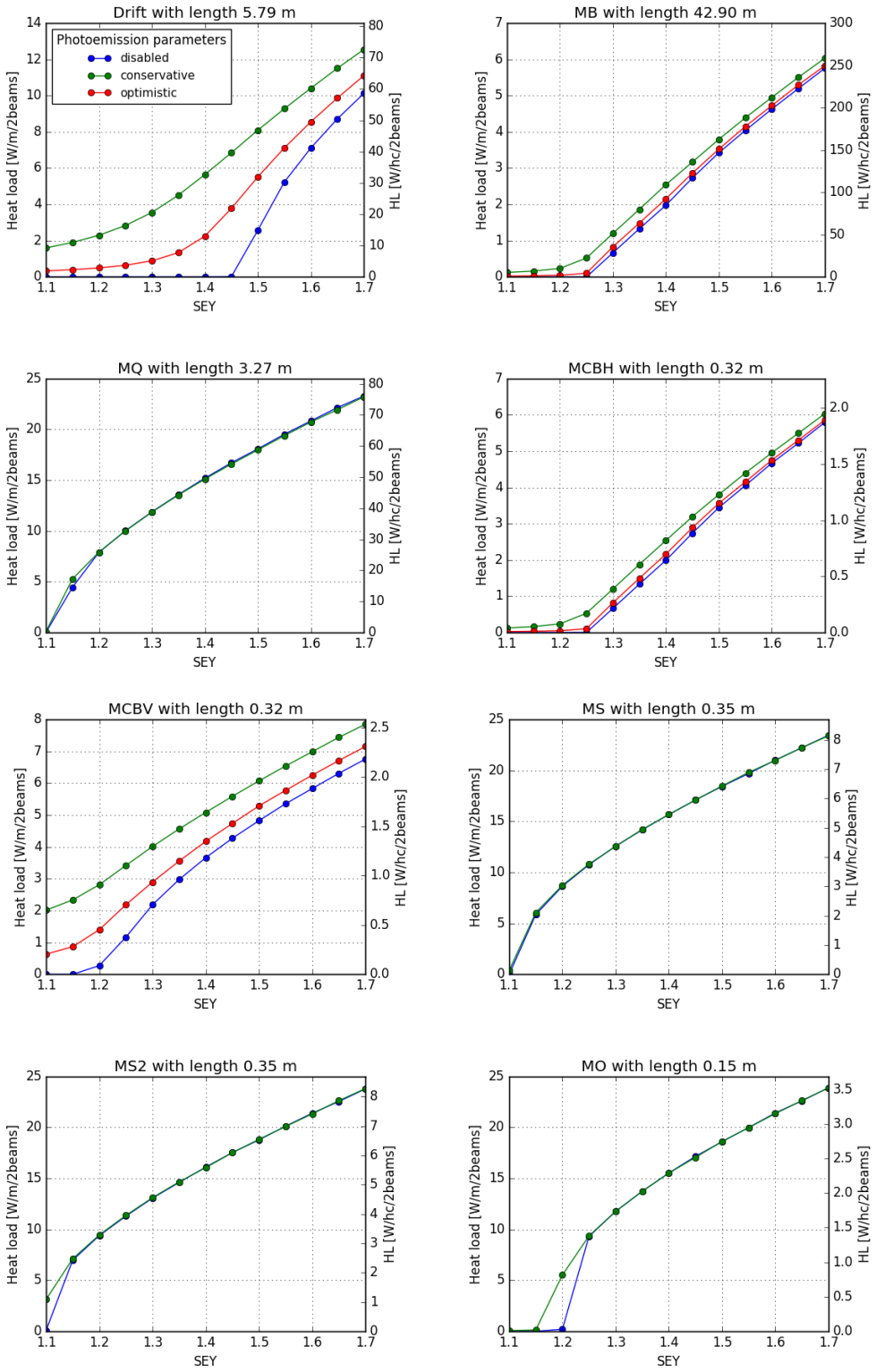

Figure 8: Heat loads from PyECLOUD simulationswithout photoelectron emission and with "conservative" photoemission parameters. In the case of the drifts and dipole magnets (MB, MCBH, MCBV), also the "optimistic" parameters have been simulated. The left axes correspond to the heat load per meter, the right axes to the heat load in the average cryogenic cell.

Table 7: Magnetic field strengths and gradients used in the simulation study. The lengths correspond to the average cryogenic cell in the LHC arcs.

Magnet	**Length per half cell** [m]	**Magnetic field**	**Skew mag. field**
Drift	5.79	-	-
Main Bend (MB)	42.90	7.73 T	-
Horizontal corrector (MCBH)	0.32	2.72 T	-
Vertical corrector (MCBV)	0.32	-	2.32 T
Main quadrupole (MQ)	3.27	$1.75{\cdot}10^2$ T/m	-
Main sextupole (MS)	0.35	$1.52{\cdot}10^3$ T/m^2	-
Main sextupole (MS2)	0.35	$-2.60{\cdot}10^3$ T/m^2	-
Main octupole (MO)	0.15	$3.47{\cdot}10^5$ T/m^3	-

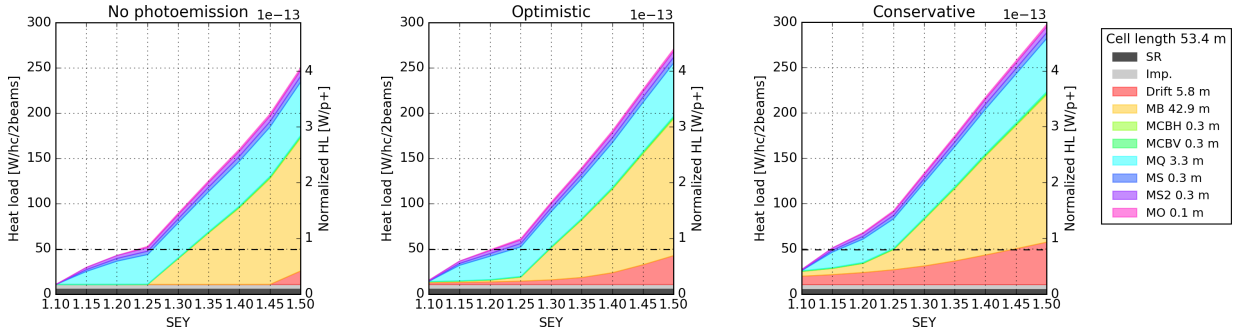

Figure 9: Total heat load in the average LHC half cell as a function of the SEY parameter of the beam-screen surface (assumed to be the same over the entire half-cell). The different contributions are shown in different colors. Three configurations for the photoemission are considered as indicated on top of the plots. The horizontal dashed line corresponds to the value measured in low heat load cells.

pacting. For all other magnet types, only the photoelectrons generated by reflected photons can contribute significantly (see Fig. 6) .

Comparison to the measured heat loads in the LHC

For each of the LHC arc half-cells the heat load deposited on the beam screens can be estimated from the measured thermodynamic parameters of the cooling fluid (e.g. temperatures, pressures). For standard arc cells, the installed sensors only allow measuring the total heat load over the two beam screens of the 53-m long half-cell, hence it is not possible to disentangle the effect of the single magnets nor of a single beam.

In order to compare these data with the simulations presented in the previous section, we have calculated the total heat load expected for the average arc half-cell, summing up the calculated contributions from impedance and synchrotron radiation [19] and the simulated e-cloud contribution from the different elements. This is done by assuming that all beam screen surfaces in the half-cell exhibit the same SEY parameter. As before, three configurations for the photoemission are considered: uniform initial seeding with no photoemission, conservative and optimistic surface parameters as described in the previous section. The results are shown in Fig. 9. The dashed lines indicate the heat load measured in a low-load cryogenic cell during a typical LHC fill [12, 20].

SENSITIVITY OF PHOTOEMISSION MODELING

Photoelectron yields and reflectivities are only a part of the information needed to model the effect of photoelectron seeding on the electron cloud build-up simulations. In this section we investigate the impact of the more implicit properties of the photoemission modeling. Changes to the simulation code have been introduced that vary the initial energy of photoelectrons and the times and locations at which they are generated in the chamber. The influence of these changes on the simulations is presented in the following subsections. More information can be founds in [12].

Delayed photoelectron production

In PyECLOUD, photoelectrons are generated with the same time structure as the longitudinal beam profile. In reality however, the two are not exactly synchronized due to the fact that the protons are bent by the magnetic field while the photons are not, as illustrated in Fig. 10. The difference is calculated in the following equations the bending radius (R) of the LHC main dipoles is 2803.9 m and the radius of the chamber (r) is 22 mm). A beam travelling at the speed

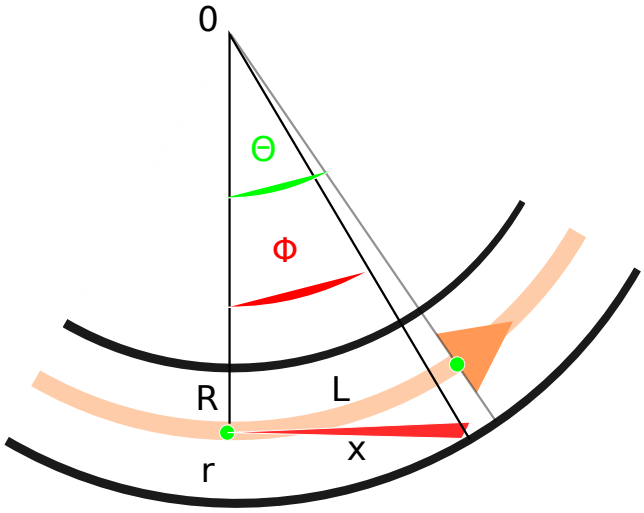

Figure 10: The path difference between protons (green) and photons(red). R and r are the bending and chamber radii, while L and x are respectively the paths the protons and the photons travel until the photon hits the chamber walls.

of light is assumed, therefore L and x are equally long by definition:

$$(R + r)^2 = R^2 + x^2 \tag{19}$$

$$x = \sqrt{2Rr + r^2} = 11.1 \text{ m} \tag{20}$$

$$\Phi = \tan^{-1} \frac{x}{R} \tag{21}$$

$$\Theta = \frac{L}{R} = \frac{x}{R} \tag{22}$$

$$\tag{23}$$

The time-delay between the beam and the synchrotron radiation is given by:

$$\Delta t = \frac{R(\Theta - \Psi)}{c} = 1.938 \cdot 10^{-13}\ s \tag{24}$$

This difference is negligible as it is much smaller than a time step of the simulation, which is normally around 10^{-11} s.

However, photons that are absorbed only after several reflections (note that the reflection coefficient for grazing incident photons on copper without sawtooth was measured to be larger than 80%) are delayed significantly with respect to the originating beam particle. One reflection to the opposite side of the chamber causes a delay of $\Delta t = \frac{2r}{c} = 1.48 \cdot 10^{-10}$ s, which is already longer than a time step in the simulations, but much shorter than the bunch spacing. Backward reflections, which are expected for sawtooth surfaces, lead to delays that can be of the order of the bunch spacing of 25 ns, for which a distance of travel of 7.5 m is required. This acts as an e-cloud seeding mechanism that extends to the bunch gaps, and could in principle alter the way the electron cloud decays.

To investigate the impact of the time structure of the photoelectron generation, a modified version of PyECLOUD

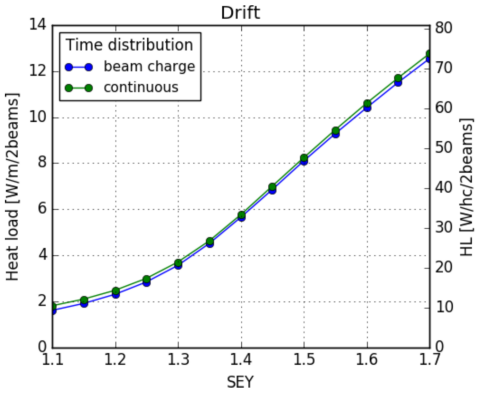

Figure 11: The effect of a generation of photoelectrons that is continuous in time is compared to the usual assumption, where the generation coincides with the beam charge profile. The case of a drift section is considered.

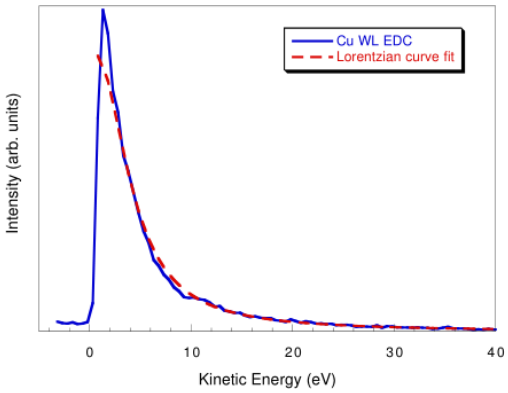

Figure 12: Photoemission spectra for 30 eV photons on copper together with Lorentzian fit to the low-dose WL spectrum centered at 0.64 eV and 3.7 eV wide [11].

has been utilized, in which photoelectrons are generated uniformly in time. The results for the case of a drift section are presented in Fig. 11 and compared to the usual PyECLOUD modeling. The heat loads are practically unaffected by the changes. Similar results are found also for the case of the dipole magnet. Therefore, changes to the code concerning the time structure of the emission are not deemed necessary.

Energy of generated photoelectrons

By default a truncated Gaussian is used for the energy distribution in PyECLOUD simulations. According to laboratory measurements [11], different distributions are more realistic (see Fig. 12). Therefore, other distributions have been optionally introduced in the simulation code. These are specified by the new input parameter **energy_distribution**, which allows to choose from the following options (see Fig. 13):

- a truncated Gaussian, which is the standard in PyECLOUD:

$$p(E) = \frac{1}{\sqrt{2\pi\sigma^2}} e^{-\frac{(E-\mu)^2}{2\sigma^2}} \tag{25}$$

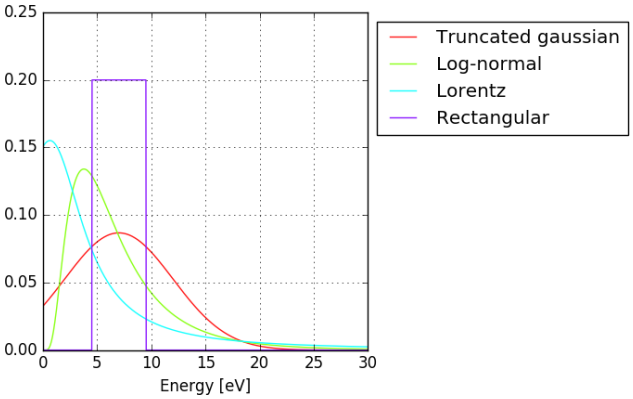

Figure 13: This plot shows a truncated normal distribution, as well as a log-normal distribution with the same mean and variance as the undistorted Gaussian distribution. In addition, also a Lorentzian and a rectangular distribution are shown.

- a Lorentzian, truncated to positive values as indicated by Fig. 12 (however it only fits well for the low-dose sample, otherwise the low-energy part is greatly reduced):

$$p(E) = \frac{1}{\pi} \frac{\sigma}{\sigma^2 + (E-\mu)^2} \tag{26}$$

- a log-normal distribution, which could probably also be fitted to the data in Fig. 12:

$$p(E) = \frac{1}{E\sigma\sqrt{2\pi}} e^{-\frac{(\ln E - \mu)^2}{2\sigma^2}} \tag{27}$$

  It shall be noted that μ and σ are simply parameters and not the mean and standard deviations of the distribution.

- a rectangular or a mono-energetic distribution (unphysical) for sensitivity studies.

Four different energy distributions shown in Fig. 13 were simulated. Figure 14 shows a comparison of the resulting e-cloud buildup. The simulations were performed with a generation of photoelectrons that is uniform in time. It is evident that the initial energy of the photoelectrons does not have any impact on the resulting heat loads.

SUMMARY

Electron cloud build-up simulations were performed for the main elements of the LHC arc half-cell (main dipoles and quadrupoles, corrector magnets, multipoles and drift spaces). Different assumptions on the photoelectron yield were made based on laboratory measurements of the LHC beam screen materials. Simulations performed with different models were compared against the simple case in which the e-cloud formation is seeded with a uniform initial electron distribution. The presence of photoelectrons has a significant impact on the e-cloud formation only in the cases of the drift spaces and of the dipole magnets. The effect of the photoelectrons

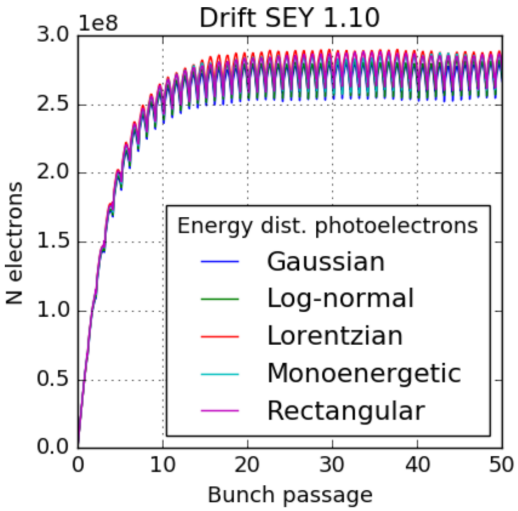

Figure 14: The impact of several different energy distributions of emitted photoelectrons is investigated by simulating a drift with different energy distribution functions.

is practically negligible for the quadrupoles and for higher order multipoles, in which the multipacting is stronger due to electrons trapped by the field gradient.

The simulation results were compared against measured heat load data from the LHC cryogenic system. Taking into account the effect of photoelectrons we can conclude that measurements for the cells with the lowest heat loads are compatible with a low SEY parameter (SEY<1.2, corresponding to a full surface conditioning).

The sensitivity of the simulation results on different characteristics of the photoemission process was also investigated. In particular we addressed the impact of the time structure of the photoemission production, and of the energy spectrum of the photoelectrons. None of these features was found to have a significant impact on the e-cloud buildup and, in particular, on the estimated heat loads.

ACKNOWLEDGEMENTS

The authors would like to thank G. Arduini, V. Baglin, O. Boine-Frankenheim, B. Bradu, E. Métral, A. Perin and A. Romano for their important input and support to the presented work.

REFERENCES

[1] G. Rumolo, F. Ruggiero, and F. Zimmermann, "Simulation of the electron-cloud build up and its consequences on heat load, beam stability, and diagnostics," *Physical Review Special Topics-Accelerators and Beams*, vol. 4, no. 1, p. 012801, 2001.

[2] L. Mether, "Electron cloud in 2016: cloudy or clear?," in *Proc. of the 7th Evian Workshop, Evian 13-15 Dec 2016*, 2016. `https://indico.cern.ch/event/578001/`.

[3] G. Iadarola, L. Mether, and G. Rumolo, "Filling schemes and e-cloud contraints for 2017," in *7th Evian Workshop on LHC beam operation*, pp. 239–244, 2017.

[4] G. Rumolo *et al.*, "Electron Cloud Effects at the LHC and LHC Injectors," in *Proc. of International Particle Accelerator Conference (IPAC'17), Copenhagen, Denmark*, May 2017.

[5] G. Apollinari, I. B. Alonso, O. Brüning, M. Lamont, and L. Rossi, *High-Luminosity Large Hadron Collider (HL-LHC)*. Geneva: CERN, 2015. Preliminary Design Report.

[6] G. Iadarola, *Electron Cloud studies for CERN particle accelerators and simulation code development*. PhD thesis, University of Naples Federico II, 2014.

[7] G. Iadarola, E. Belli, K. Li, L. Mether, A. Romano, and G. Rumolo, "Evolution of Python Tools for the Simulation of Electron Cloud Effects," in *Proc. of International Particle Accelerator Conference (IPAC'17), Copenhagen, Denmark, May, 2017*, JACoW.

[8] V. Baglin, I. R. Collins, and O. Gröbner, "Photoelectron yield and photon reflectivity from candidate LHC vacuum chamber materials with implications to the vacuum chamber design," in *Particle accelerator. Proceedings, 6th European conference, EPAC'98, 1998.*, 1998.

[9] V. Baglin, I. R. Collins, O. Gröbner, C. Grünhagel, B. Henrist, N. Hilleret, and B. Jenninger, "Measurements At EPA Of Vacuum And Electron-Cloud Related Effects," in *11th Chamonix - LHC Workshop*, 2001.

[10] N. Mahne, V. Baglin, I. Collins, A. Giglia, L. Pasquali, M. Pedio, S. Nannarone, and R. Cimino, "Photon reflectivity distributions from the LHC beam screen and their implications on the arc beam vacuum system," *Applied Surface Science*, vol. 235, no. 1–2, pp. 221 – 226, 2004. 8th European Vacuum Conference and 2nd Annual Conference of the German Vacuum Society.

[11] R. Cimino, V. Baglin, and I. Collins, "VUV synchrotron radiation studies of candidate LHC vacuum chamber materials," *Vacuum*, vol. 53, no. 1, pp. 273 – 276, 1999.

[12] P. Dijkstal, G. Iadarola, L. Mether, and G. Rumolo, "Simulation studies on the electron cloud build-up in the elements of the LHC Arcs at 6.5 TeV," tech. rep., Oct 2017.

[13] K. Jakobi, "Work function data: Datasheet from Landolt-Börnstein - Group III Condensed Matter · Volume 24B: "Electronic and Vibrational Properties" in SpringerMaterials."

[14] A. Hofmann, *The Physics of Synchrotron Radiation*. Cambridge: Cambridge University Press, 2004.

[15] E. Hatchadourian, P. Lebrun, and L. Tavian, "Supercritical Helium Cooling of the LHC Beam Screens," LHC Project Report 212, CERN, Geneva, 1998.

[16] O. Brüning, P. Collier, P. Lebrun, S. Myers, R. Ostojic, J. Poole, and P. Proudlock, *LHC Design Report*. Geneva: CERN, 2004.

[17] F. Zimmermann, "Electron-Cloud Effects in past and future machines - walk through 50 years of Electron-Cloud studies," in *Proceedings, 5th Workshop on Electron-Cloud Effects (ECLOUD'12): La Biodola, Isola d'Elba, Italy, June 5-9, 2012*, 2013.

[18] G. Iadarola, G. Rumolo and collaborators, "PyECLOUD Reference Manual." `https://github.com/PyCOMPLETE/PyECLOUD/wiki`.

[19] G. Iadarola, G. Rumolo, P. Dijkstal, and L. Mether, "Analysis of the beam induced heat loads on the LHC arc beam screens during Run 2," tech. rep., Dec 2017. `https://cds.cern.ch/record/2298915`.

[20] G. Iadarola, "Overview on heat loads in the LHC." These proceedings.

OVERVIEW OF HEAT LOADS IN THE LHC

G. Iadarola*, B. Bradu, P. Dijkstal, L. Mether, G. Rumolo, G. Skripka, L. Tavian
CERN, Geneva, Switzerland

Abstract

A consequence of the formation of electron cloud in beam chambers is the deposition of energy on their walls due to electron impacts. In cryogenic devices this can cause a significant heat load for the cryogenics system, posing constraints on machine design and operation

At the LHC this effect is found to be quite strong and needs to be addressed to avoid performance limitations in view of the planned HL-LHC upgrade. Unexpectedly the eight LHC arcs show very different heat loads. These differences, which appeared after the 2013-14 shut-down period, are still unexplained and have been the subject of thorough investigations and characterizations.

This contribution describes the main observations on the heat loads deposited on the arc beam screens with different beam conditions and in different moments of the LHC operational experience.

INTRODUCTION

The Large Hadron Collider (LHC) is a 27-km synchrotron and particle collider in operation at CERN since 2008 [1]. The machine mostly operates with two proton beams, injected with a beam kinetic energy of 450 GeV and then accelerated to collision energy. The design collision energy is 7 TeV but so far only beam energies up to 6.5 TeV have been reached. The beam structure consists of several trains of 25 ns spaced bunches, allowing a maximum of about 2800 circulating bunches per beam. The nominal bunch population is 1.15×10^{11} p/bunch.

The LHC has an eight-fold symmetric structure, with eight Long Straight Sections (LSS) that host the physics detectors and other equipment, and eight arcs (or sectors). Each arc is 2.5 km long and is made of 23 regular FODO cells, each made of two "half-cells". Each half-cell is 53 m long and is made of one 3.1 m long superconducting quadrupole and three superconducting dipoles, each 14.3 m long, together with much shorter corrector magnets.

Figure 1 shows a cross section of the LHC main dipole. To avoid too large power deposition on the superconducting coils, a beam screen is inserted inside the 1.9 K cold bore, in order to intercept beam-induced heat loads due to RF heating, synchrotron radiation and e-cloud. The beam screen is made of stainless steel with a thin co-laminated copper layer needed to minimize the beam-coupling impedance. It is held by low-conductivity supports and is actively cooled with a helium flow to operate in the range 5-20 K [2]. By measuring the thermodynamic properties of the helium, it is possible to know the heat load deposited on the screen [3]. Magnets in each half-cell share the same cooling circuit, therefore in general only the total heat load on each half-cell can be measured, not the load on individual magnets.

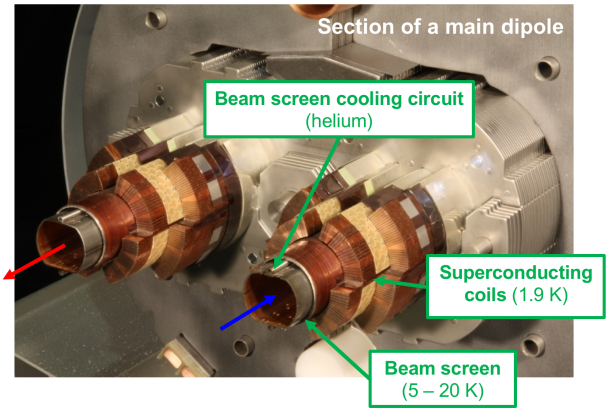

Figure 1: A cut of an LHC dipole magnet.

HEAT LOAD OBSERVATIONS

The history of the LHC operation can be divided in three main periods [4]:

- **Run 1** (2010-2013) was first physics data-taking period. The beam energy was limited to 4 TeV, the bunch spacing was 50 ns, the maximum number of bunches in collision was 1380, the bunch population was gradually increased up to 1.7×10^{11} p/bunch.
- **Long Shutdown 1** (LS1, 2013-2015). In this period no beam operation took place, in order to allow for consolidation and maintenance of the machine equipment. All arcs were warmed up to room temperature and all their beam screens were exposed to air.
- **Run 2** (2015-2018) was second physics data-taking period. The beam energy was increased to 6.5 TeV, the bunch spacing was 25 ns, the maximum number of bunches in collision was 2556, the bunch population was around 1.2×10^{11} p/bunch.

The heat loads observed on the arc beam screens during typical physics runs were very different between Run 1 and Run 2. In Run 1 heat loads were very modest, in the order of 10 W/half-cell, which is compatible with what is expected from impedance and synchrotron radiation heating. Moreover in this period the heat loads in the eight arcs were very similar.

During Run 2, instead, the heat loads became much larger, exceeding 100 W/half-cell. This required the implementation of dedicated feed-forward controls on the cryogenic system regulations [5,6]. The measured heat load were much

* Giovanni.Iadarola@cern.ch

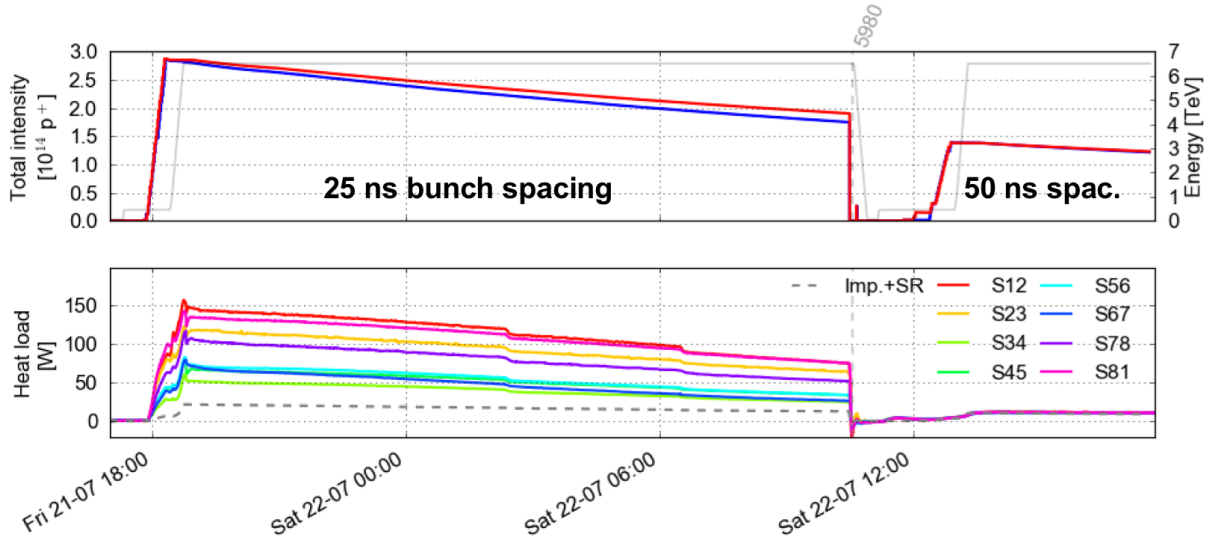

Figure 2: Intensities of the two LHC beams (top) and evolution of the heat load in the eight arcs (bottom) during two consecutive fills with different bunch spacing. Heat load values are in Watts per half-cell. The expected load from impedance and synchrotron radiation is indicated by the dashed curve.

larger than estimated from impedance and synchrotron radiation, suggesting a significant contribution from e-cloud effects. Unexpectedly, very large differences (up to a factor of 3) are observed among the eight arcs (as it is visible in Fig. 2), in spite of the fact that they are by design identical. A detailed description of the heat load observations during Run 2 can be found in [7].

Dedicated tests showed that, as expected from e-cloud simulations [8], such a radical change was caused by the reduction of the bunch spacing from 50 ns to 25 ns. Figure 2 shows two consecutive fills conducted during Run 2. The first is a regular physics production fill performed with 25 ns bunch spacing while the second is a test fill performed with 50 ns bunch spacing. For the 25 ns fill, the heat loads are much larger than expected from impedance and synchrotron radiation heating and large differences are observed among the arcs. For the 50 ns fill instead, the measurements are compatible with the model including only the impedance and the synchrotron radiation contributions and no significant differences among sectors are observed.

The evolution of the heat loads has been closely monitored during the entire Run 2. Figure 3 shows the average heat load measured in the eight arcs at 450 GeV normalized to the circulating beam intensity, for all p-p physics fills of Run 2 performed with more than 800 bunches. A reduction of the heat loads due to beam conditioning is visible mainly in 2015 and in the first part of 2016. After that, practically no further evolution took place. Remarkably, large differences among the arcs remained very visible and were not affected by beam-conditioning accumulated in the period 2016-2018.

The heat loads are distributed very unevenly along the machine. It is possible to identify two families: a group of high-load sectors (including S12, S23, S78, S81) and a group of low-load sectors (including S34, S45, S56, S67). Interestingly, the high-load sectors are contiguous: in fact the machine is practically split in two parts. Especially in the high-load sectors, large differences are observed also among half-cells [9].

It is possible to show that the power deposited in the form of the heat load ultimately comes from the beam. To do so the power lost by the beam can be inferred from RF stable phase measurements and it is found to be consistent with heat load measurements from the cryogenics. RF stable phase measurements also provide the bunch-by-bunch power loss. The characteristic pattern from the e-cloud is clearly visible: the heat load is generated mainly by bunches at the tail of the trains [7, 9].

These observations pose significant concerns in view of the planned upgrade of the LHC (High Luminosity LHC project - HL-LHC), which foresees, together with several hardware upgrades, a twofold increase of the bunch population. The cooling capacity from the cryogenic system available for the arc beam screens in the HL-LHC era is expected to be the same as for the present operation [10]. The present and the HL-LHC operation scenarios are compared in Fig. 4. In the present configuration, the heat loads from impedance and synchrotron radiation are relatively small (in the order of 1 kW per arc), leaving a large fraction of the cooling capacity available to cope with the additional heating from the e-cloud. In the high-load sectors, this available margin is almost fully utilized (as illustrated in Fig. 4 for the Sector 12), while in the low-load sectors less than half of the available capacity is required (as illustrated in Fig. 4 for the Sector 34). The situation is significantly different for the HL-LHC case in which, mainly due to the increase in bunch population, the expected heating from impedance and synchrotron radiation is much larger (almost 4 kW) leaving much less margin to cope with the e-cloud.

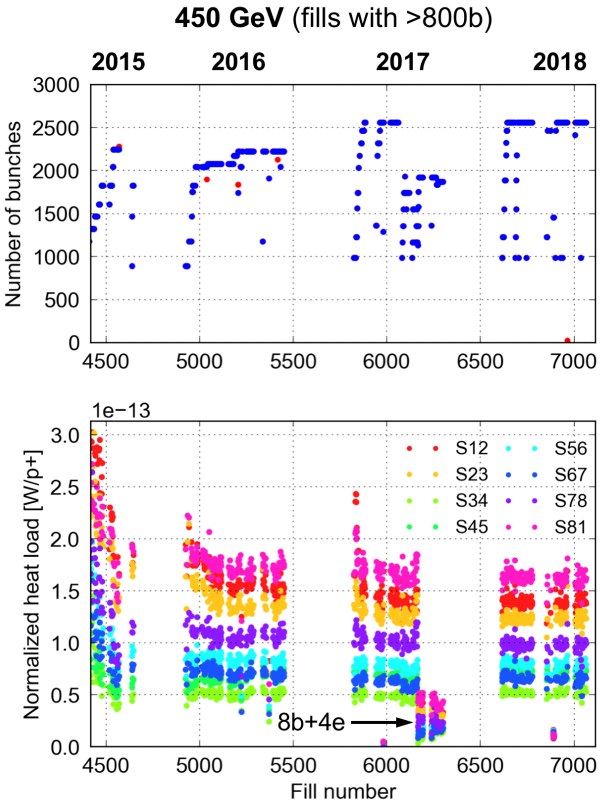

Figure 3: Evolution of the heat loads in the eight LHC arcs during Run 2. Values are in Watts per half-cell and normalized with the circulating beam intensity. The period at the end of 2017 showing lower heat loads was conducted with a special bunch pattern consisting in short trains of eight bunches interleaved with gaps made of four empty slots.

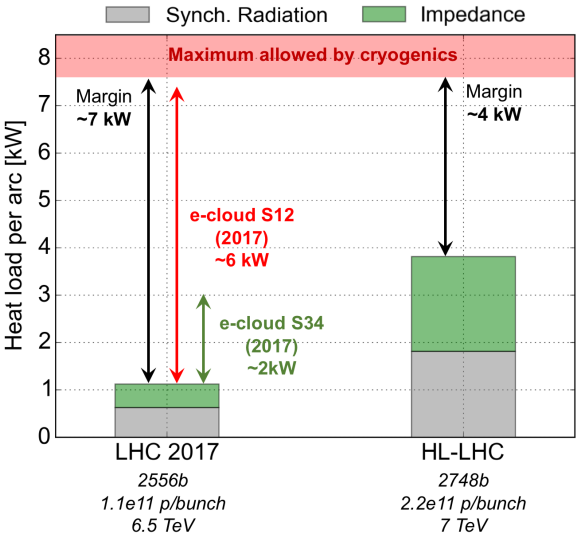

Figure 4: Expected heat loads in the LHC arcs in the present configuration and for the HL-LHC upgrade. The black arrows represent the available margin with respect to the available cooling capacity from the cryogenic system. The red and green arrows represent the heat loads from e-cloud presently observed in a low-load and in a high-load sector respectively.

EFFECT OF VENTING AND THERMAL CYCLES

The observed differences among LHC sectors were not always present.

A test period with 25 ns beams took place at the end of Run 1, in 2012. The heat loads measured during this period can be directly compared against Run 2 data, as the measurement system was largely unchanged and the beam conditions were very similar [11].

A comparison between two very similar fills performed before and after LS1 is shown in Fig. 5. The differences among sectors appeared only after the LS1, during which all arcs were warmed up to room temperature and exposed to air. It is possible to notice that still in 2018, after multiple years of conditioning of the beam chambers, the heat load in the worse sectors is four times larger than before LS1. So far, no difference in the activities conducted during LS1 in the eight sectors could be identified, which could explain this different behaviour in terms of heat load.

During Run 2, in particular during the 2016-17 winter shutdown, the sector 12 had to be warmed-up to room temperature and exposed to air in order to replace a faulty main magnet. The immediate effect of this operation is visible in Fig. 6. As expected a large de-conditioning was observed in Sector 12, which is visible in all half-cells (see Fig. 7 - top). In Fig. 6 one can also notice that the heat loads in the other sectors, which remained under vacuum and at cryogenic temperature, stayed practically unchanged.

Seven days were allocated at the beginning of 2017 for a dedicated scrubbing run at injection energy with the main objective of re-conditioning Sector 12. The evolution of the heat loads during this period is illustrated in Fig. 8, which also shows how the bunch number and the length of the bunch-trains were increased during the scrubbing period. A clear conditioning effect is visible on Sector 12 over the first four days, after which the heat loads had reached levels similar to end-2016, i.e. before the warm-up (as it can be seen at a cell-by-cell level in Fig. 7 - bottom). No further evolution was observed thereafter, and in particular it was not possible to reduce the heat loads to levels similar to 2012.

Comparing these observations with those made before and after LS1, we notice that the effect of LS1 was somehow more permanent than the effect of the 2016-17 venting. The reasons of this behaviour are presently under investigation [12, 13].

COMPARISON OF THE MEASUREMENTS AGAINST MODELS AND SIMULATIONS

Electron cloud is the only identified heating mechanism that is found to be compatible with the observations [9]. The most characteristic features are the following:

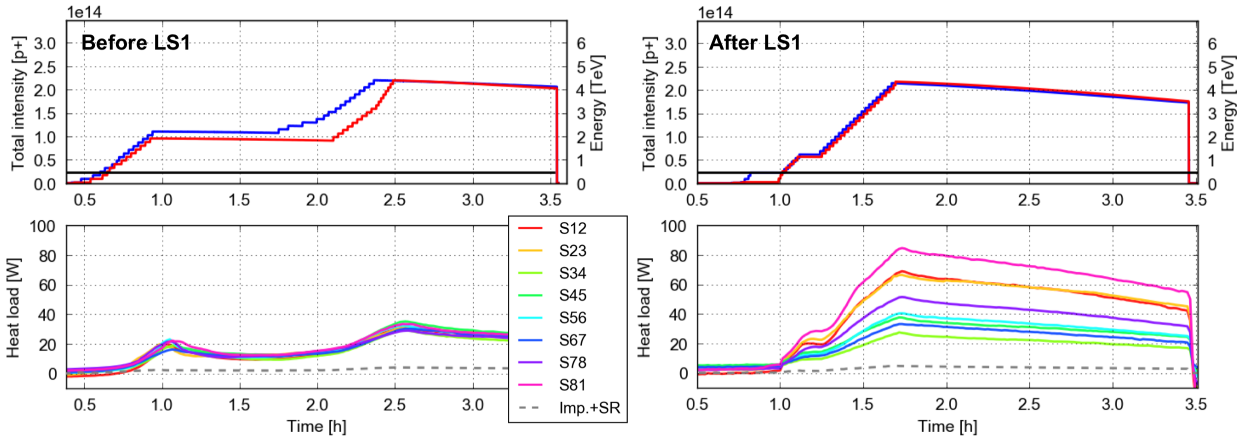

Figure 5: Beam intensities (top) and heat loads measured in the eight LHC arcs (bottom) measured during two fills conducted with the same filling pattern in 2012 (left) and in 2018 (right). Heat load values are in Watts per half-cell.

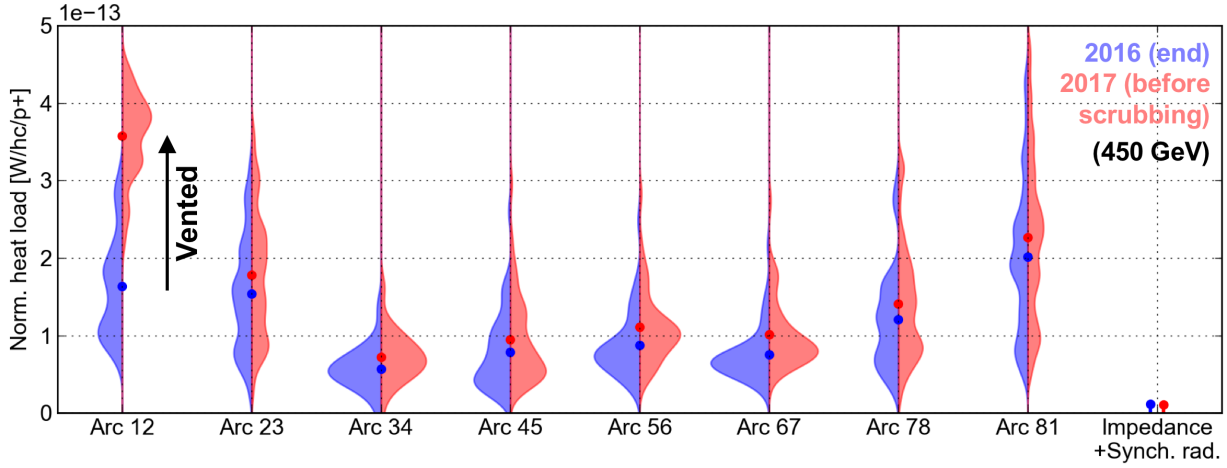

Figure 6: Average (dots) and cell-by-cell distribution in the eight arcs before and after the 2016-17 winter shut-down. The effect of the air exposure for the beam screens in sector 12 is clearly visible. Heat load values are in Watts per half-cell and normalized by the circulating beam intensity.

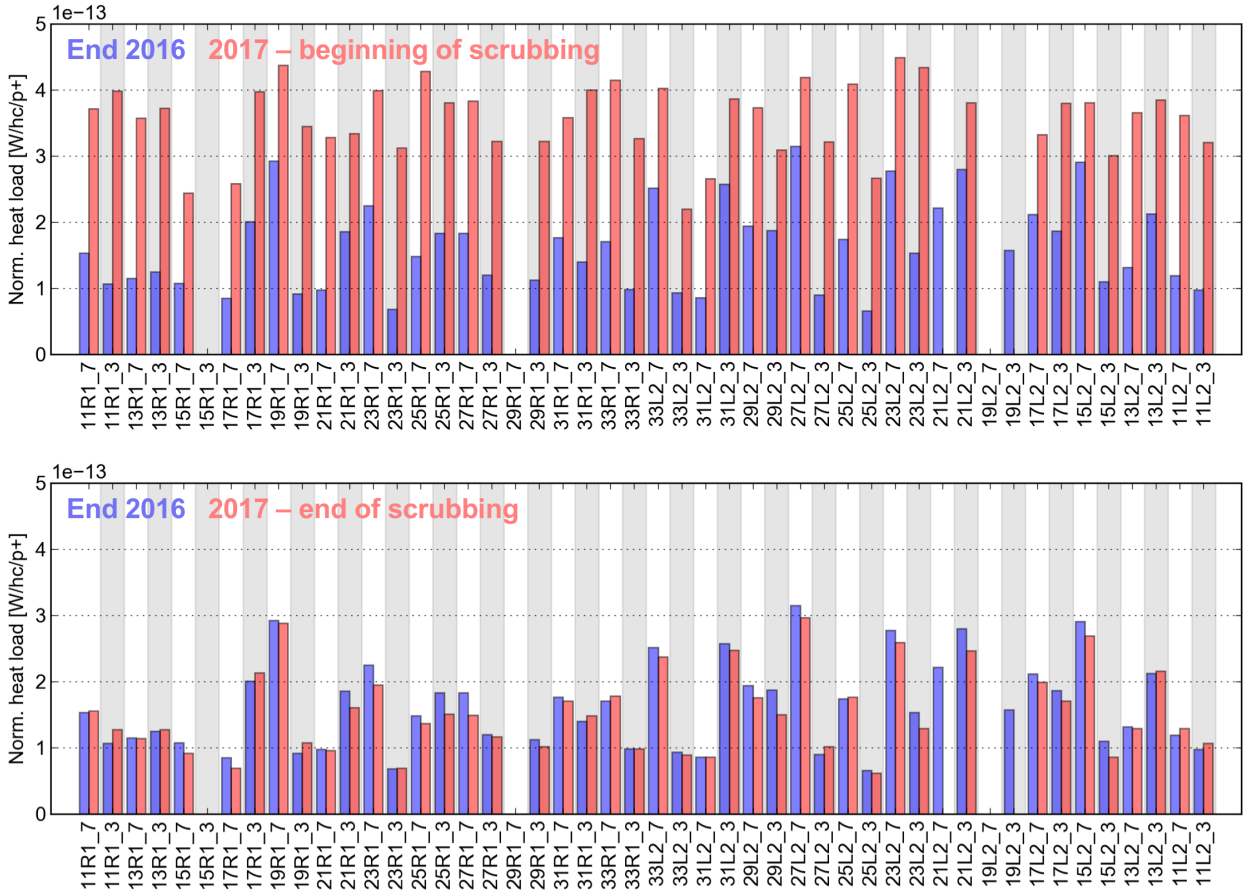

Figure 7: Heat loads in all half-cells of sector 12 as measured at the end of 2016 (in blue) and at the beginning and end of the 2017 scrubbing run (in red in the top and bottom plots respectively). Heat load values are in Watts per half-cell and normalized by the circulating beam intensity.

- Heat loads significantly larger than impedance and synchrotron radiation estimates are visible only with the 25 ns bunch spacing;
- Measurements taken with 25 ns beams and different bunch intensity show the existence of an intensity threshold around 0.4×10^{11} p/bunch;
- Large heat loads and heat load differences among sectors are already present at injection energy (450 GeV) and increase only moderately during the energy ramp. It is unlikely that photoelectrons from synchrotron radiation play a major role in generating the observed differences, as they should show a very strong dependence on the beam energy.

In Fig. 9 we compare the measured heat loads (on the right) against the result of e-cloud buildup simulations performed with the PyECLOUD code [14], for different $\mathrm{SEY}_{\mathrm{max}}$ parameters. The model used for these simulations is described in detail in [15, 16].

Assuming that the differences in heat load are caused by differences in SEY, we observe that the average heat load measured in the low-load sectors is compatible with $\mathrm{SEY}_{\mathrm{max}}$=1.25 while the average heat load measured in the high-load sectors is compatible with $\mathrm{SEY}_{\mathrm{max}}$=1.35. We also observe that for the half-cells showing the highest load the estimated $\mathrm{SEY}_{\mathrm{max}}$ can be as high as 1.50.

INFORMATION FROM SPECIAL INSTRUMENTED CELLS

As already mentioned, in most of the LHC arc half-cells temperature sensors on the beam screen cooling circuit are available only at the entrance and at the exit of the half-cell, therefore only the total load deposited over the entire half-cell length is known.

A small selection of arc half-cells have been equipped with additional thermometers to allow measuring the heat load on each magnet:

- Three half-cells in sector 45 were instrumented during LS1 and they always showed relatively low heat loads during Run 2.
- One half-cell in sector 12, the half-cell 31L2 which was showing higher heat loads in 2015-16, was instrumented during the 2016-17 winter shut-down, when one of its magnets had to be exchanged.

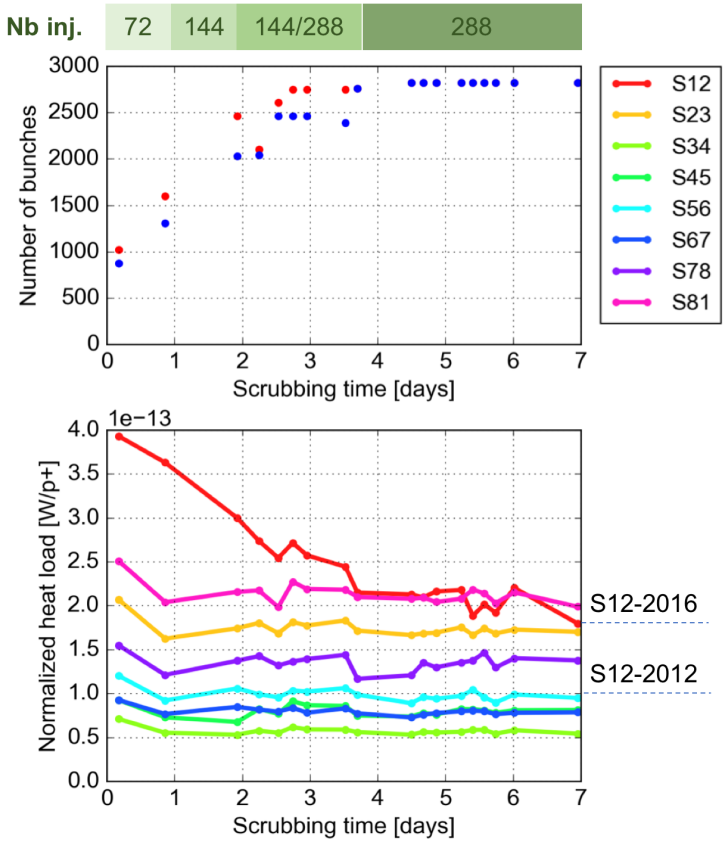

Figure 8: Evolution of beam configuration (top) and heat loads in the LHC arcs (bottom) during the 2017 scrubbing run. Heat load values are in Watts per half-cell and normalized by the circulating beam intensity. The values that had been measured for sector 12 in 2012 and in 2018 are marked on the side of the plot.

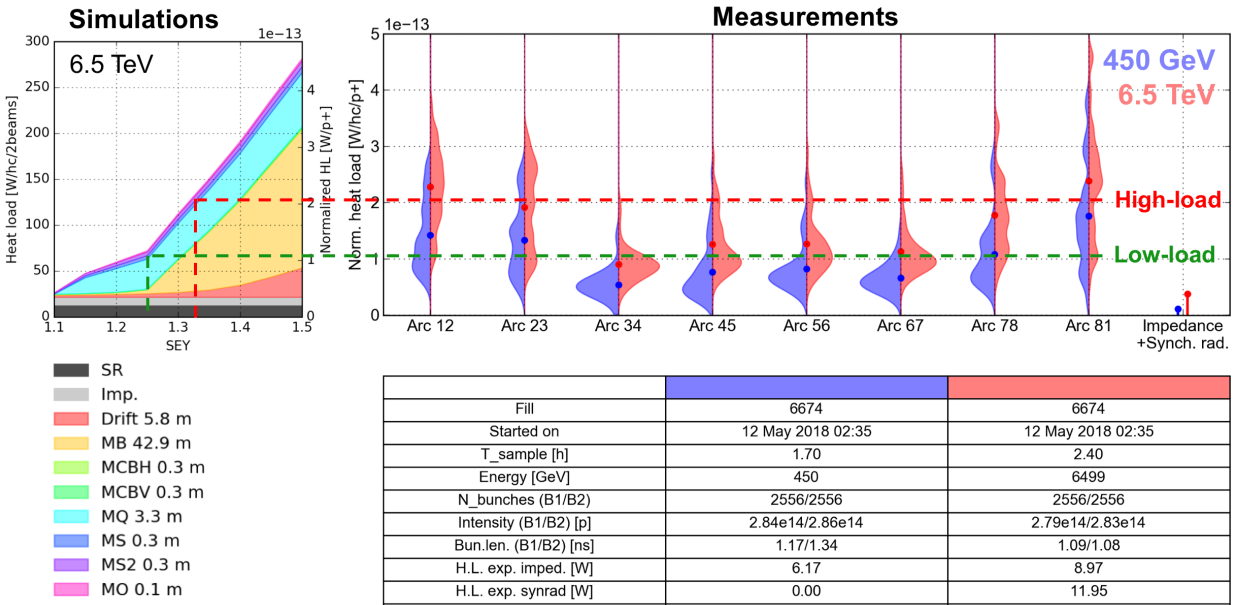

Fill	6674	6674
Started on	12 May 2018 02:35	12 May 2018 02:35
T_sample [h]	1.70	2.40
Energy [GeV]	450	6499
N_bunches (B1/B2)	2556/2556	2556/2556
Intensity (B1/B2) [p]	2.84e14/2.86e14	2.79e14/2.83e14
Bun.len. (B1/B2) [ns]	1.17/1.34	1.09/1.08
H.L. exp. imped. [W]	6.17	8.97
H.L. exp. synrad [W]	0.00	11.95
H.L. exp. imp.+SR [W/p+]	1.08e-14	3.72e-14
T_nobeam [h]	1.15	1.15

Figure 9: Heat loads from PyECLOUD simulations (left) compared against measurements from a typical fill of the 2018 run (right).

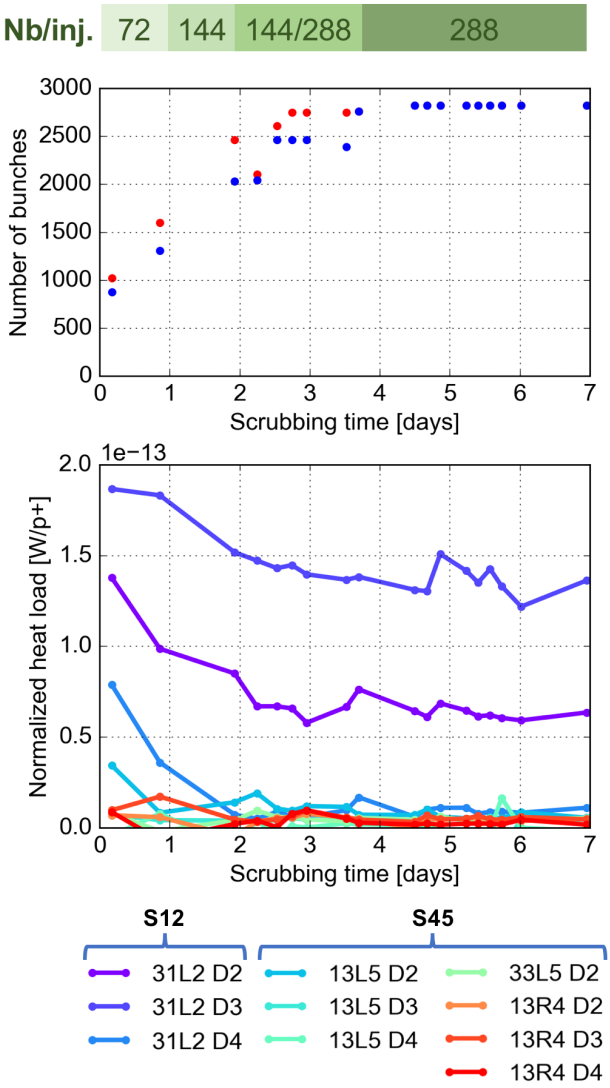

Figure 10: Evolution of beam configuration (top) and heat loads in the instrumented dipoles (bottom) during the 2017 scrubbing run. Heat load values are in Watts per half-cell and normalized by the circulating beam intensity.

It is particularly interesting to look at the evolution of the heat loads in the magnets of the cell 31L2 right after the thermal cycle and air exposure which took place in the 2016-17 winter shut-down, when the dipole "31L2-D4" was exchanged.

As shown in Fig. 10, very low heat loads were measured on the dipoles in sector 45 which had not been exposed to air during the winter shut-down. The newly installed dipole "31L2-D4" conditioned very rapidly to the same level as those in S45. The other two dipoles in the same half-cell ("31L2-D2" and "31L2-D3"), which are installed since the time of the LHC construction, surprisingly show much larger heat loads even after a long period of conditioning. Most likely magnets with a similar behaviour are present also in the other high-load half-cells.

SUMMARY AND FUTURE PLANS

During Run 2, large heat loads are observed on the arc beam screens of the LHC when operating with 25 ns bunch space spacing, which are worrisome for the HL-LHC upgrade.

These heat loads are very different from arc to arc, from cell to cell and from magnet to magnet. The origin of these differences is still unknown and is the subject of several investigations.

Such large differences appeared only after the 2013-14 shut-down, in which the beam screens of all the arcs were warmed-up and exposed to air, but no further change was observed when the air exposure was repeated on one of the sectors in the 2016-17 winter shutdown.

Electron cloud effects are the only identified mechanism that is compatible with experimental observations like the dependence on the bunch spacing, the dependence on the bunch intensity, the bunch-by-bunch pattern on beam power loss (measured by the RF system).

Efforts are ongoing to further localize the heat load within the magnet length, using the temperature evolution observed in the instrumented half-cells at the re-cooldown after a beam dump. For this purpose during the upcoming Long Shutdown 2 (LS2) mass flow-meters will be installed to reduce the uncertainty on the measurement of the helium flow. During LS2 magnets extracted from the LHC will undergo extensive analysis aiming at identifying the origin of the observed heat load differences. Moreover, additional half-cells will be instrumented in preparation for the 2021-23 run.

ACKNOWLEDGMENTS

The authors would like to thank all members of the CERN Beam-Induced Heat Loads Task Force, G. Arduini, F. Giordano, E. Metral, and B. Salvant for their important input to the present contribution.

REFERENCES

[1] O. Bruning, P. Collier, P. Lebrun, S. Myers, R. Ostojic, J. Poole, and P. Proudlock (editors), "LHC Design Report, Volume 1." CERN-2004-003-V-1, 2004.

[2] E. Hatchadourian, P. Lebrun, and L. Tavian, "Supercritical Helium Cooling of the LHC Beam Screens," *LHC Project Report*, vol. 212, 1998.

[3] K. Brodzinski and L. Tavian, "First Measurements of Beam-Induced Heating on the LHC Cryogenic System," Tech. Rep. CERN-ATS-2013-009, CERN, Geneva, Jan 2013.

[4] J. Wenninger, "LHC status and performance," *PoS*, vol. CHARGED2018, p. 001, 2019.

[5] B. Bradu, A. Tovar González, E. Blanco Viñuela, P. Plutecki, E. Rogez, G. Iadarola, G. Ferlin, and B. Fernández Adiego, "Compensation of beam induced effects in LHC cryogenic systems," in *Proc. of International Particle Accelerator Conference (IPAC'16), Busan, Korea, May 8-13, 2016*, 2016.

[6] B. Bradu, "How does a cryogenic system cope with e-cloud induced heat load? what can we learn from heat load measurements?." These proceedings.

[7] G. Iadarola, G. Rumolo, P. Dijkstal, and L. Mether, "Analysis of the beam induced heat loads on the LHC arc beam screens during Run 2," *CERN-ACC-NOTE-2017-0066*, Dec 2017.

[8] O. Domínguez, K. Li, G. Arduini, E. Métral, G. Rumolo, F. Zimmermann, and H. M. Cuna, "First electron-cloud studies at the large hadron collider," *Phys. Rev. ST Accel. Beams*, vol. 16, p. 011003, Jan 2013.

[9] G. Iadarola, "Electron cloud and heat loads in the LHC arcs." Accelerator and beam physics forum, CERN, 12 Jul 2018 https://indico.cern.ch/event/740046.

[10] G. Apollinari, I. Bejar Alonso, O. Bruning, P. Fessia, M. Lamont, L. Rossi, and L. Tavian, *High-Luminosity Large Hadron Collider (HL-LHC): Technical Design Report V. 0.1*. CERN Yellow Reports: Monographs, Geneva: CERN, 2017.

[11] G. Iadarola, "Head loads in run 1 and run 2." Presentation at the LHC Machine Committee, CERN, 12 Sep 2018 , available at https://indico.cern.ch/event/756722/.

[12] L. Tavian, "Report from the task force on beam induced heat load." Presentation at the LHC Performance Workshop 2018, Chamonix, Jan 2018.

[13] V. Petit, "Characterisation of beam screens extracted from lhc magnets." These proceedings.

[14] G. Iadarola, E. Belli, K. Li, L. Mether, A. Romano, and G. Rumolo, "Evolution of Python Tools for the Simulation of Electron Cloud Effects," in *Proc. of International Particle Accelerator Conference (IPAC'17), Copenhagen, Denmark, May, 2017*, JACoW.

[15] P. Dijkstal, G. Iadarola, L. Mether, and G. Rumolo, "Simulation studies on the electron cloud build-up in the elements of the LHC Arcs at 6.5 TeV," *CERN-ACC-NOTE-2017-0057*, Oct 2017.

[16] P. Dijkstal, "Investigating the role of photoemission in the e-cloud formation at the lhc." These proceedings.

ELECTRON CLOUD BUILD-UP IN TWO-BEAM REGIONS FOR HL-LHC: HEAT LOAD AND VACUUM ASPECTS

G. Skripka*, G. Iadarola, CERN, 1211 Geneva, Switzerland

Abstract

Electron cloud in particle accelerators is known to have a detrimental effect on the vacuum pressure and can cause a large heat deposition on a vacuum chamber surface. In a particle collider, in the presence of two beams in the same chamber, the build-up of the electron cloud becomes more complicated and the electron density cannot be simply scaled from the case of a single beam. The build-up process in the devices with common chambers can be modeled by correctly accounting for the arrival times of the two beams, the beam positions and their sizes. Numerical studies were made to estimate the electron flux on the internal surfaces of two common chamber devices of the future High Luminosity Large Hadron Collider: the triplet assemblies in the four experimental insertion regions and the injection protection absorber (TDIS). Different possible coating options in both devices were investigated aiming at a reduction of the electron current and of the deposited heat load.

INTRODUCTION

The operation of the Large Hadron Collider (LHC) with 25 ns bunch spacing during Run 2 has shown that beam induced heat loads can pose serious limitations on the achievable machine performance [1, 2]. One of the main sources of the beam-induced heat loads in the LHC is known to be electron cloud (e-cloud). Electrons impacting on the vacuum chamber surface introduce a thermal load additional to the one induced by the impedance and the synchrotron radiation emitted by the circulating beam. The heat loads induced by e-cloud can pose serious limitations for operation of cryogenic devices. Another limitation posed by the e-cloud is the rapid increase of the vacuum pressure above the acceptable level due to electron-stimulated gas desorption. It is therefore important to assess the potential limitations for the High Luminosity LHC (HL-LHC) era [3] when the machine will operate with the 25 ns bunch spacing and double bunch intensity with respect to the present configuration. In the studies presented here we used the PyECLOUD code, which allows simulating the e-cloud build-up in the presence of one or multiple circulating beams in one chamber [4]. The employed modelling of the secondary emission process is described in [5]. In the following we will call "SEY parameter" the maximum of the SEY curve.

Simulating the e-cloud buildup with two beams in the same chamber

Numerical simulations of the e-cloud build-up in devices with a common chamber require special care [5–7]. The arrival time of bunches from the two beams depends on the position along the device, hence, there is not a simple bunch spacing describing the time structure of the beams.

Due to the non-linearity in the e-cloud build-up mechanism, the electron density cannot be simply scaled from the case of the single beam and the build-up process in the devices with common chambers has to be modelled correctly accounting for the arrival times of the two beams, their position and their size at different location along the device.

For the case of two beams in a common chamber the e-cloud densities from beam 1 and beam 2 separately do not add up to the total density for the two beams simultaneously in the chamber and that also the multipacting threshold is different. When simulating the two beams together, the delay in the arrival time plays a significant role. In particular, we should point out that the multipacting is not always stronger in the presence of two beams compared to the single beam case [8].

The PyECLOUD code used for this simulation study is 2D code. Therefore in order to get the longitudinal e-cloud profile, slices along the device at given longitudinal positions have to be simulated, correctly accounting for the difference in the arrival time of the two beams as well as the other beam properties at each section. The LREs, where the counter-rotating beams pass simultaneously occur at evenly spaced locations along the machine. In between LREs the delay between bunch passages from the two beams range between -12.5 ns to +12.5 ns (for the nominal bunch spacing of 25 ns). We have simulated two "LHC batches" each made of 4 train of 72 bunches separated by gaps of 225 ns for both beam 1 and 2. The spacing between the batches is 800 ns.

Common chamber devices for HL-LHC

One type of the common chamber device in the current LHC and future HL-LHC are the Inner Triplets installed on each side of the four experimental interaction points. The triplet assembly consists of superconducting quadrupole magnets (Q1, Q2, Q3), one separation/recombination superconducting dipole (D1), a corrector package (including sextupoles, octupoles, decapoles, dodecapoles in both normal and skew orientations) and drift spaces as sketched in Fig. 1. The reduction of the heat deposition on the cold magnets is of high importance. Therefore, the heat load was estimated for all elements of the new Inner Triplets in points 1 and 5 which are being designed for the HL-LHC project, taking into account the presence of a surface treatment (coatings) for the reduction of the SEY.

Another critical common chamber device in the HL-LHC is the TDIS injection protection absorber (Fig. 2), designed to absorb the beam injected into the LHC, in case of injection kicker malfunctions and timing errors.Two such devices will be installed: one in the common region at point 2 and one

* galina.skripka@cern.ch

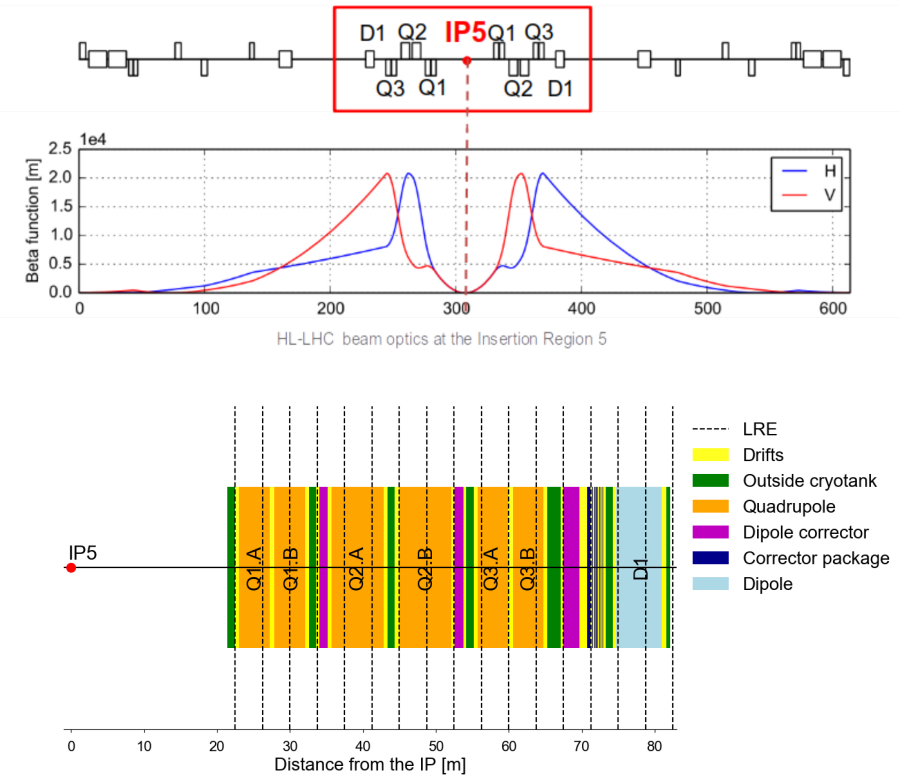

Figure 1: HL-LHC beam optics at insertion region 5 (top) and a detailed layout for the right hand side of the interaction point 5, with the LREs in the triplet marked by dashed lines(bottom).

at point 8. TDIS is designed to have three segments with movable absorbing jaws on the top and the bottom of one beam (the one that is injected right upstream of the device) and a single beam screen surrounding the second circulating beam. During the LHC operation, a similar injection protection absorber TDI has suffered from vacuum issues observed when retracting the jaws after the beam injection, as well as heating and other issues [9–11].

E-CLOUD BUILD-UP SIMULATIONS

The main beam parameters used in the build-up simulations are reported in Table 1. The triplets were simulated with the beams at 7 TeV energy since the multipacting is expected to be stronger. For the TDIS absorber we have studied the build-up process with the 450 GeV beams, when the jaws are moved closer to the beam. After the beam injection the TDIS jaws are retracted and stay parked far from the beams.

To correctly model the two counter-rotating beams in the same chamber, we simulate different slices along the device, accounting for the different arrival times, the transverse sizes and the transverse positions of the two beams at each section. A sufficiently long portion of the beam has been simulated in order to reach the equilibrium number of electrons at all sections where multipacting occurs. All results presented in the following are re-scaled to the full number of bunches for HL-LHC.

Table 1: Simulation parameters

Energy, GeV	7000 (triplets) / 450 (TDIS)
Intensity, p/bunch	2.2×10^{11}
RMS bunch length (Gaussian), m	0.09
Bunch spacing, ns	25
Optics	HL-LHC v1.2 (β^*=15 cm)

Inner Triplets

We present the study for the Inner Triplets on the right side of the interaction point 5 (IP5) of the HL-LHC. Due to the symmetry considerations, the results are applicable to the identical devices installed on the other side and at the IP1. Also the Inner Triplets at the low-luminosity interaction points (IP2 and IP8) were simulated. The results of the study can be found in [12]. Coating with amorphous carbon (*a-C*) is foreseen for all HL-LHC Inner Triplets to reduce the heat load and avoid e-cloud-induced instabilities.

Simulations were performed for a number of sections along the triplet assembly and for different values of the SEY parameter assuming SEY=1.3 for the *uncoated case* and SEY=1.1 when the *a-C* coating of the beam screen is present. For these two cases, the heat load distributions along the Inner Triplet are compared in the left plot in Fig. 3. The dashed vertical lines mark the locations of the LREs. The heat load tends to be larger at locations between the LREs where the beams are not synchronized (effective bunch spacing of 12.5 ns). The largest peaks are observed at the

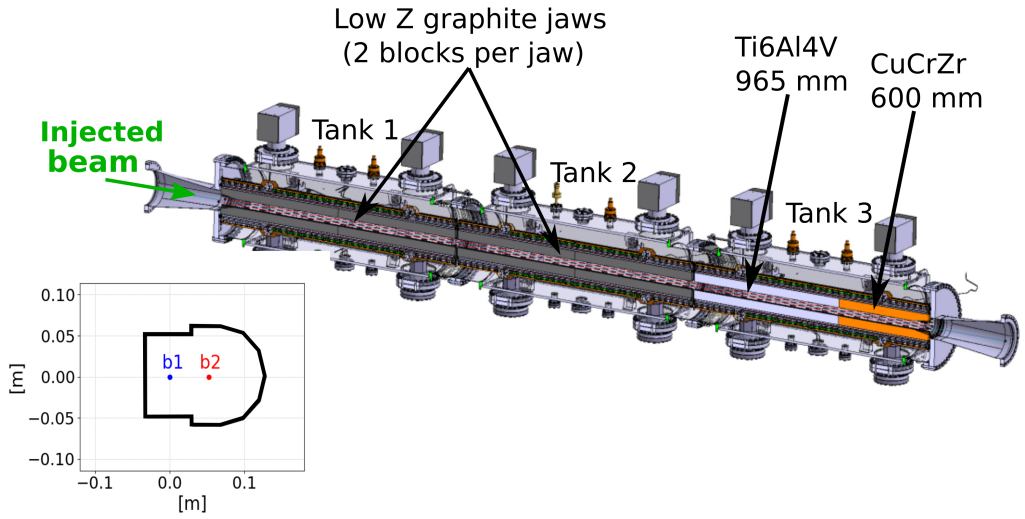

Figure 2: TDIS model with indicated the materials of the jaws (from [13]). The 2D chamber cross-section used in PyECLOUD simulations is shown in the corner. The injected and circulating beams are indicated in blue and red respectively.

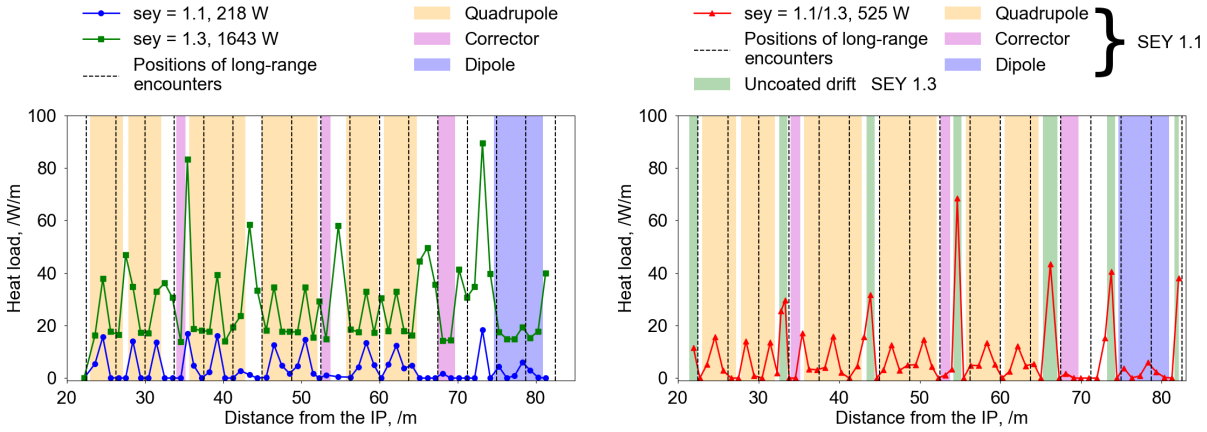

Figure 3: Heat load along one of the IR5 triplets for two uniform SEY cases (left) and a nonuniform SEY case (right) where the drift spaces outside the cold masses are not coated. The colored areas mark different magnetic field configurations as indicated in the legend.

drift sections. The heat load expected in absence of surface treatment is very high, in the order of 1.5 kW, but a strong reduction is observed when *a-C* coating is applied.

Due to technical difficulties, the coating might not be applied for some components in the drift sections located outside the cold masses, like the beam position monitors and the bellows. For this reason, the case of a non-uniform SEY along the triplet was studied, assuming that all the drifts between the cold masses are not coated and have SEY=1.3. The right plot in Fig. 3 shows the heat load distribution along the triplet under these assumptions. The uncoated drifts are indicated with the green background color. One can notice that the heat load density in these regions is significantly larger compared to the coated sections. The heat load from uncoated drifts constitutes more than a half of the total heat load in the triplet. This needs to be taken into account in the cryogenics design. More details on the e-cloud studies for the Inner Triplets of the HL-LHC can be found in [12].

TDIS absorber

The 3D model of the TDIS absorber is shown in Fig. 2. By design it will have three segments in separate tanks, allowing for better alignment of the device with respect to the beam [13]. The jaws in the first two segments will be made of graphite, which has a low SEY parameter, close to 1.0, whereas the jaws in the third tank will be metallic with a section in aluminum coated with titanium and a section in copper.

A first set of simulation was performed assuming the same SEY parameter for all surfaces exposed to the beam. The e-cloud buildup was simulated for the different jaw configurations. It was found that the electron current is increasing with the jaw opening. The most critical half-gap size was found at about 40 mm. Similarly to the case of the Inner Triplets, the current tends to be larger at locations between LREs as can be seen in Fig. 5. Interestingly, the dependence of the e-cloud on the distance from the LREs

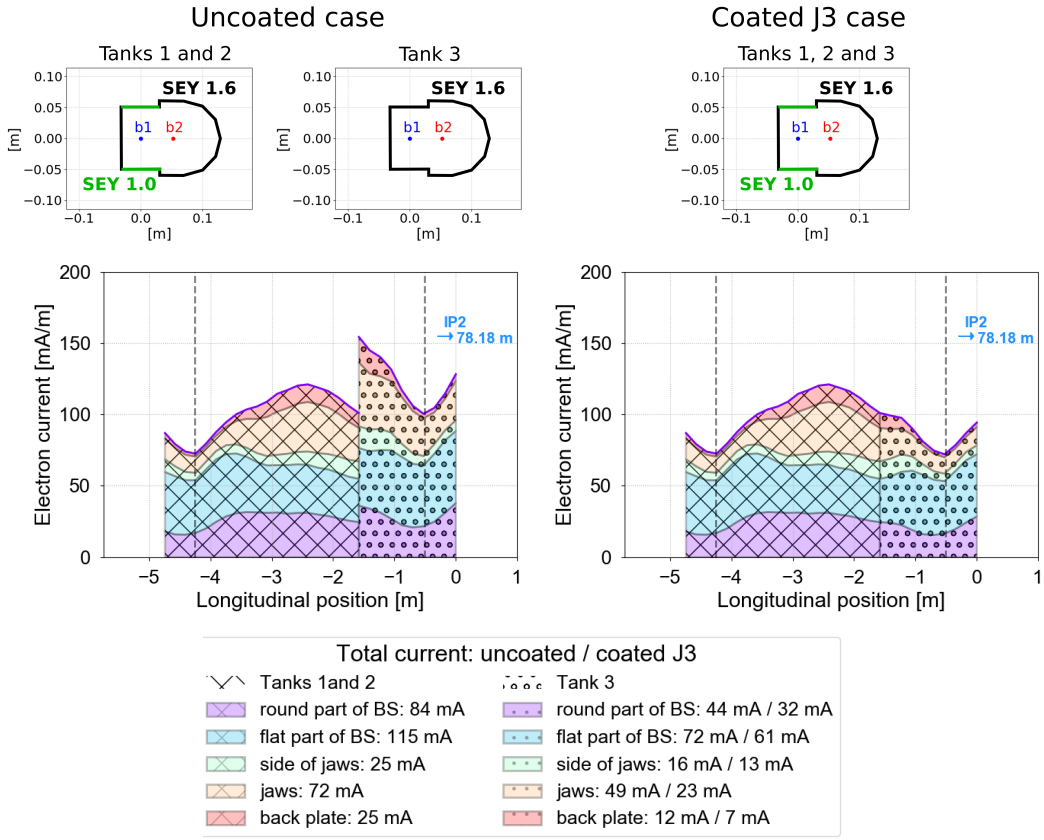

Figure 4: Contributions to the total electron current from different surfaces for *the uncoated* (left) and *the coated* (right) SEY distributions.

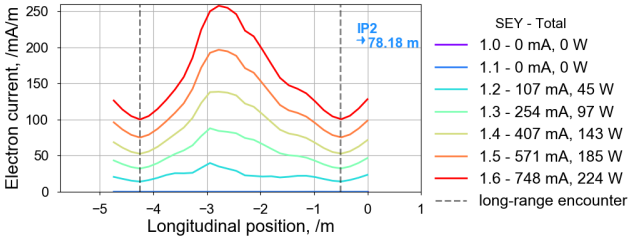

Figure 5: Longitudinal profile of the electron current in the TDIS for the 40 mm half-gap and different SEY (uniform over the chamber). The total current for each SEY is indicated in the legend. The positions of LREs are marked with dashed vertical lines.

was found to change significnatly with the bunch population (for details see [8]).

More advanced simulations were performed to assess the detailed electron current distribution along the device assuming a realistic non-uniform SEY profile. We assumed SEY=1.6 for the metallic parts, corresponding to the partially conditioned surface. Since the metallic jaws in tank three are expected to have high SEY, the possibility of coating them with *a-C* was studied. Figure 4 (top) shows the SEY distributions in the TDIS chamber along the three tanks without coating and with the coating applied on the jaws in tank three (*coated J3*). The two corresponding longitudinal electron current profiles are shown in Fig. 4 (bottom). Different colors mark contributions from different surfaces of the chamber. The effect of *a-C* coating on the jaws in tank three is clearly visible. However, it is evident that a large contribution comes from the surface of the beam screen (blue and purple) in both cases. The portion of electrons impacting on the surface of the beam screen, including round and flat parts, constitutes more than half of the total number of electrons.

Based on these results the effect of *a-C* coating on the beam screen was also studied. The e-cloud in the TDIS was simulated assuming the SEY configuration shown in Fig. 6. Simulations have shown that if both the beam screen and the jaws in tank three are coated with *a-C* (SEY=1.0), the electron current can be fully suppressed.

The results of these simulations were used as an input for dynamic pressure studies [14]. It was shown that by suppressing the multipacting on the beam-screen the target pressure of less than 5×10^{-9} mbar can be achieved even without coating of the metallic jaws. More details on the e-cloud studies for the TDIS absorber can be found in [8].

CONCLUSIONS

E-cloud build-up simulations with two beams in a common chamber require particular care. Due to the nonlinearities of the e-cloud, the single beam case cannot be simply scaled to describe the situation when multiple beams

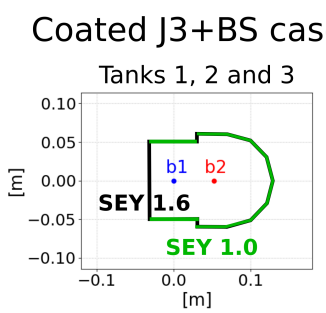

Figure 6: SEY distribution in the TDIS in the case when a-C coating is applied to both the jaws in tank three and the beam screen.

are present in one chamber. The dependence on the location due to changing hybrid bunch spacing along the device needs to be taken into account.

The e-cloud build-up was studied in the main elements of the Inner Triplets of the HL-LHC considering different coating scenarios. Simulations have shown that if all the triplet elements will be coated with *a-C* except for the drifts between the cold masses, the total heat load could be reduced by factor of three.

E-cloud build-up simulations for the TDIS absorber have shown that the *a-C* coating can significantly reduce the electron current. Most of the electrons were found to be produced on the beam screen surface. Simulations with *a-C* applied on both the metallic jaws and the beam screen have shown that the e-cloud in this scenario can be fully suppressed.

ACKNOWLEDGEMENTS

Authors would like to thank C. Bracco, R. De Maria, P. Dijkstal, L. Gentini, G. Mazzacano, A. Perillo-Marcone, P. Ribes Metidieri, A. Romano, G. Rumolo, M. Taborelli and C. Yin-Vallgren for their valuable input. Research supported by the HL-LHC project.

REFERENCES

[1] G. Iadarola, G. Rumolo, P. Dijkstal, and L. Mether, "Analysis of the beam induced heat loads on the LHC arc beam screens during Run 2," December 2017, CERN (CERN-ACC-NOTE-2017-0066).

[2] G. Iadarola, "Digesting the LIU high brightness beam: is this an issue for HL-LHC?", unpublished. Presentation at the LHC Performance Workshop 2018, 31 January 2018, Chamonix.

[3] G. Apollinari *et al.*, "High-Luminosity Large Hadron Collider (HL-LHC): Technical Design Report V. 0.1". CERN Yellow Reports: Monographs 4/2017, Geneva: CERN,2017.

[4] "PyECLOUD code" https://github.com/PyCOMPLETE/PyECLOUD/wiki

[5] G. Iadarola, "Electron Cloud Studies for CERN Particle Accelerators and Simulation Code Development", CERN-THESIS-2014-047, March 2014.

[6] F. Zimmermann, "Electron-cloud Simulations for the LHC Straight Sections," LHC-PROJECT-NOTE-201, Geneva, CERN, 1999.

[7] A. Rossi *et al.*, "A simulation study of the electron cloud in the experimental regions of the LHC", in Proc. 8th European Particle Accelerator Conference, Paris, France, 3 - 7 Jun 2002, pp.2583.

[8] G. Skripka, G. Iadarola, "Electron cloud studies for the LHC TDI and HL-LHC TDIS", August 2018, CERN (CERN-ACC-NOTE-2018-0060).

[9] D. Carbajo Perez *et al.*, "Operational Feedback and Analysis of Current and Future Designs of the Injection Protection Absorbers in the Large Hadron Collider at CERN", in Proceedings of the 8th International Particle Accelerator Conference (IPAC 2017): Copenhagen, Denmark, May 14-19, 2017, 2017 (WEPVA108).

[10] A. Lechner et al., "TDI - Past observations and improvements for 2016", in Proceedings of the 2015 Evian Workshop on LHC beam operation, p. 123, September 2015.

[11] A. Lechner, "Summary of issues with the present TDI – the TDI history in a nutshell", unpublished. Presented at TDIS Internal Review Meeting 2016, CERN, 2016.

[12] G. Skripka, G. Iadarola, "Beam-induced heat loads on the beam screens of the inner triplets for the HL-LHC", February 2018, CERN (CERN-ACC-NOTE-2018-0009).

[13] L. Gentini, "Updates on detailed TDIS mechanical design", unpublished. Presented at WP14 Coordination meeting: TDIS updates, D1 FLUKA calculations, CERN, 2017.

[14] P. Ribes Metidieri et al., "TDIS pressure profile simulations after LS2", CERN-ACC-NOTE-2018-0075.

BEAM INDUCED DYNAMIC PRESSURE DURING RUN 2 (2015-2018) MACHINE OPERATION IN THE LHC

C. Yin Vallgren*, P. Ribes Metidieri
G. Bregliozzi†, CERN, Geneva, Switzerland

Abstract

The LHC successfully returned to operation in April 2015 after almost 2 years of Long Shutdown 1 (LS1) for various upgrade and consolidation programs. During Run 2 (2015 - 2018) the LHC operated for more than 3600 fills and it has reached a total integrated luminosity of more than 150 fb^{-1}.

This paper summarizes the dynamic vacuum observations in different locations along the LHC during the dedicated fills as well as during the physics runs with different beam parameters. The beam-induced dynamic pressure rise in presence of synchrotron radiation and electron multipacting have been investigated and are presented here. A clear beam conditioning effect has been observed in Run 2.

INTRODUCTION

The LHC vacuum system includes 48 km of cryogenic beam pipes and 6 km of room temperature vacuum system, which were designed to cope with beam dynamic effects, such as electron cloud, synchrotron radiation, impedance heating and ion-induced desorption. The main vacuum pumping system is comprised of cryo-surface pumping, NEG coating pumping and sputteration pumps [1].

In this paper, an overview of the evolution of the beam induced pressure rise during Run 2 is given. Run 2 period is considered from April 2015, when the LHC resumed operation after a 2-year period of maintenance (Long Shutdown 1 - LS1), to December 2018, when the LHC operation will be stopped for Long Shutdown 2 - LS2.

Figure 1 shows the schedule for the LHC operation during Run 2 and the upcoming Long Shutdown 2. The different years of operation comprised by Run 2 are separated by 3-month long maintenance closures of the LHC at the end of each year called Year End Technical Stops - YETS (Extended Year End Technical Stops - EYETS if the closure time is 5 months). Each of these periods is followed by a period of recommissioning with beam.

OVERVIEW OF LHC BEAM OPERATION DURING RUN 2 (2015 - OCT 2018)

Figure 2 shows the integrated luminosity during the different years comprised by Run 1 and Run 2 as a function of the date in the corresponding year. In 2015, the integrated luminosity was visibly smaller than in the other operation years mainly due to the shorter operation period after LS1, and an integrated luminosity of 4.24 fb^{-1} and 4.25 fb^{-1} were achieved in ATLAS and CMS,resspectively. At the end of 2016 and 2017, integrated luminosities of 38.48 fb^{-1} and 50.82 fb^{-1} were achieved in ATLAS, while luminosities of 40.96 fb^{-1} and 50.58 fb^{-1} were achieved in CMS, respectively at the end of those years. Even though the integrated luminosity during 2018 has only been recorded until October, the curve of integrated luminosity with time shows a steeper slope than previous years and it has already successfully reached a total integrated luminosity of more than 150 fb^{-1}, the set achievement of Run 2.

Table 1 summarizes the achievements and limitations found in during the different years of Run 2.

OVERVIEW OF LHC BEAM PARAMETERS IN RUN 2

LHC beam parameters overview during 2015

The 2015 operations successfully started on the 5th of April under the status of recommissioning with beam. The overview of the LHC beam schedule along the year is summarized in Fig. 3. During 2015 operation, the LHC operated for more than 1000 fills. The 2015 LHC proton physics started with beam of low intensity at 6.5 TeV, followed by two scrubbing runs of high intensity beams at 450 GeV for about 3 weeks, finally ended with 2244 bunches per beam circulating with 25 ns bunch spacing at top energy of 6.5 TeV. The last month of the LHC physics run in 2015 was dedicated to lead ions.

The first scrubbing run started with 50 ns @ 450 GeV on June 24 and finished on July 3. Just after about 24 hours from the start, the 25 ns beam was immediately injected in the LHC. After some struggling with the setting-up of the beams, the LHC was successfully filled with both Beam 1 and Beam 2 consisting of 1020 bunches in trains of 72 bunches with bunch spacing of 25 ns. Beam 2 was strongly limited by the MKI8D degassing leading to pressure close to the interlock's level (5×10^{-8} mbar set by the equipment owner). Measureable vacuum conditioning along most of the LHC was observed. The pressure along the machine did not increase with increasing intensity and were all well below the sector valve interlock thresholds (2×10^{-6} mbar).

Intensity Ramp-up 1, with 50 ns @ 6.5 TeV, was in the end limited to about 450 bunches due to radiation induced faults in Quench Protection System (QPS) electronic boards [2].

The Scrubbing Run 2 continued with the same strategy as the Scrubbing Run 1: inject as many protons as possible into the LHC, in order to create as high as possible electron flux on the inner surfaces of the vacuum chamber and in that way reduce the Secondary Electron Yield (SEY). The first three days were focused on the intensity ramp-up with trains of 72 bunches, followed by 144 bunches from the SPS

* christina.yin.vallgren@cern.ch
† giuseppe.bregliozzi@cern.ch

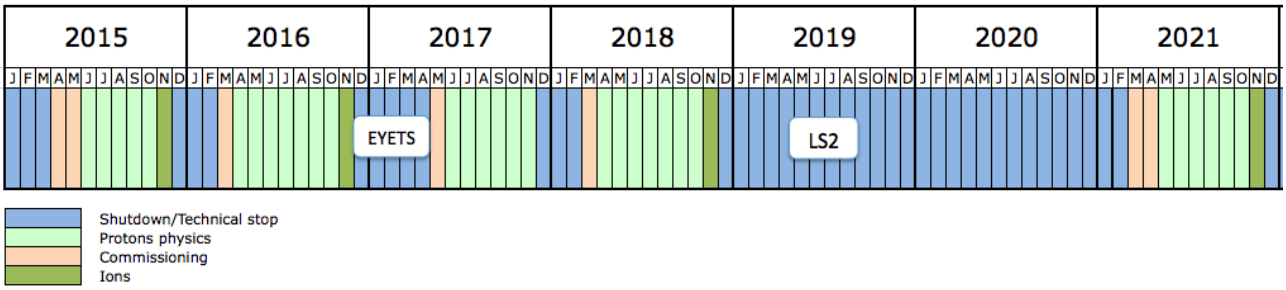

Figure 1: Overview of the LHC beam schedule during Run 2 and LS2.

Table 1: Overview of the operation of the LHC during Run 2.

Year	Top achieved beam intensity [b]	Filling scheme bpi	Limitations
2015	2244	trains of 4x36b	- Limited to 450b by radiation induced faults in QPS electronic boards until TS2. - 144bpi up to 1450b, limited of the available cooling capacity on ARC BS
2016	2220	trains of 96b	Technical issue in the SPS and LHC dumps
2017	2556	trains of 144b	2556b until early August,stable operation with 1900b of 8b4e due to 16L2
2018	2556	trains of 144b	-

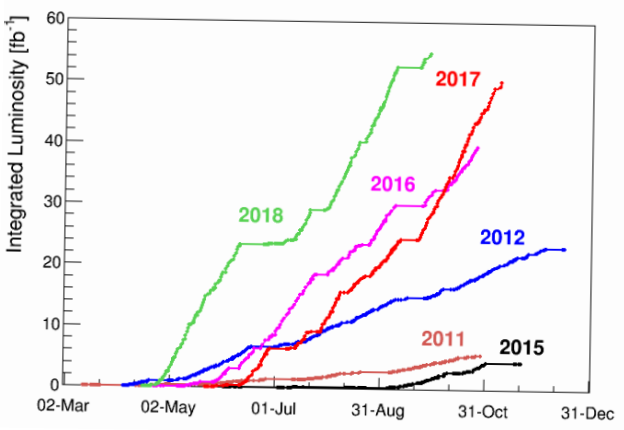

Figure 2: Integrated luminosity during Run 2 (until 01.10.2018).

Figure 3: Overview of the LHC beam schedule during 2015.

already on Day 4. The injection process was, in general, slowed down by the cryogenic limitations (to avoid loss of the cryoplant) [3].

In Intensity Ramp-up 3 which was the last physics run with protons before the end of the year, there was one week physics run with high β^* from Oct 12.

The 2015 LHC proton physics ended with 2244 bunches per beam circulating with 25 ns bunch spacing at top energy of 6.5TeV. The first fills consisted of injecting bunch trains of 144 bunches. However, around 1450 bunches, we started approaching the limit of the available cooling capacity on the arc beam screens. The filling schemes changed from 144 bunches train to 72 bunches trains and later 36 bunch trains. The beams with 2244 bunches in total were injected by using the trains of 36 bunches in order not to reach the limitation of the cryoplant. The heat load per bunch significantly decreased by using this strategy.

LHC beam parameters overview during 2016

The 2016 operation successfully started on the 29th March under the status of recommissioning with beam. The overview of the LHC beam schedule along the year is summarized in Fig.4. During 2016 operation, the LHC operated for more than 800 fills. The 2016 LHC proton physics started with beams of low intensity at 6.5 TeV, without dedicated scrubbing runs. In less than 2 weeks, the LHC already reached 1177 bunches in both beams. Due to the technical limitation in both the SPS and LHC dumps, the beams were limited to 2220 bunches, with 96 bunch train injected from the SPS.The last month of the LHC physics run in 2016 was dedicated to lead ions.

The 2016 LHC proton physics ended with 2220 bunches per beam circulating with 25 ns bunch spacing at top energy of 6.5TeV.

LHC beam parameters overview during 2017

The 2017 operations successfully started on the 1st May under status of recommissioning with beam, after a 5 months'

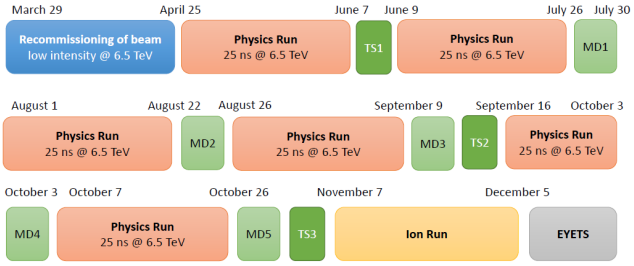

Figure 4: Overview of the LHC beam schedule during 2016.

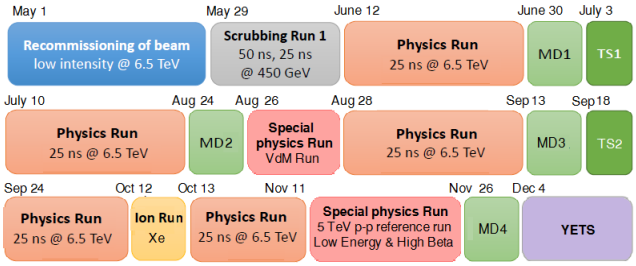

Figure 5: Overview of the LHC beam schedule during 2017.

period of closure (EYETS). The overview of the LHC beam schedule along the year is summarized in Fig. 5. Even thought 2017 was a shorter operational year due to the EYETS, around 150 days of proton physics (including intensity ramp-up) could be ensured, and the LHC operated for more than 800 fills.

The 2017 operation LHC proton physics started with beams of low intensity at 6.5 TeV, after 7 days of dedicated scrubbing at 450 GeV and high intensity. In less than 2 weeks, the LHC already reached 2556 bunches in both beams.

During the last months of operation, a day was dedicated to xenon ions, another day to the VdM run and 16 days were dedicated to a special physics run at 5 TeV and high β^* physics run.

The 2017 LHC proton physics ended with 1868 bunches per beam circulating with 25 ns bunch spacing at top energy of 6.5 TeV due to the so-called *16L2* issue [4] and the special filling scheme with 8b4e type of beam was introduced to avoid the high heat load in some parts of the ARCs.

LHC beam parameters overview during 2018

The 2018 operation started on the 30th of March under the status of recommissioning with beam. The overview of the LHC beam schedule along the year is summarized in Fig.6. During the period from March to July of the 2018 operational year, the LHC has operated for more than 1300 fills.

The 2018 operation LHC proton physics started with beams of low intensity at 6.5 TeV, after 17 days of interleaved commissioning and one day of dedicated scrubbing run.

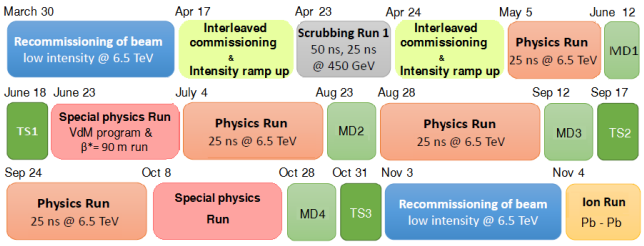

Figure 6: Overview of the LHC beam schedule during 2018.

LHC PRESSURE EVOLUTION DURING RUN 2

In this section, an overview of the average dynamic pressure rise for several specific locations in the LHC with physics beam of 25 ns at 6.5 TeV at stable beam during Run 2 is presented.

LHC Long Straight Sections pressure evolution

Figure 7 shows the average reading of Bayard-Alpert gauges installed ± 100-120 m from the Interaction Points (IP) in the Combination Chambers (CC) of each Long Straight Section (LSS), where both beams circulate in the same beam pipe and the vacuum chambers are mostly Non-Evaporable Getter (NEG) coated. Because the two beams come from both directions, the effective bunch spacing in these regions can be as low as half of 25 ns. It can be appreciated that during Run 2 the pressure in the studied regions doesn't exceed in any case a value of 10^{-8} mbar, a clear proof for the electron cloud mitigation efficiency of the NEG coatings.

Figure 8 shows the normalized average pressure reading of the same Bayard-Alpert gauges. Between the different operation years in Run 2, it can be observed a pressure *deconditioning* effect, followed by a fast conditioning. It is also interesting to point out that a slight pressure increase in LSS1 (where the experiment ATLAS is located) and LSS5 (where the experiment CMS is located) can be appreciated in Fig. 8, which could be explained by a partial saturation of NEG in these regions.

Figure 9 summarizes the overview of the average dynamic pressures for special sectors in the LHC, such as for the NEG pilot sectors (dedicated NEG coated sections for studies in IP7, A5R2, A6L8), the cold-warm transitions, where the synchrotron radiation is strongly present, and at the cold-warm transitions, where the synchrotron radiation is negligible, i.e. at injection energy.

It is interesting to notice that as shown in Fig. 9, the pressure in a cold-warm transition in the presence of synchrotron radiation is approximately twice as large as the pressure in the same location at the end of injection, i.e., in the absence of synchrotron radiation.

Figure 10 displays the average dynamic normalized pressures for the NEG pilot sector, for the cold-warm transition with and without the presence of synchrotron radiation. Figure 10 shows a very low pressure in the dedicated NEG

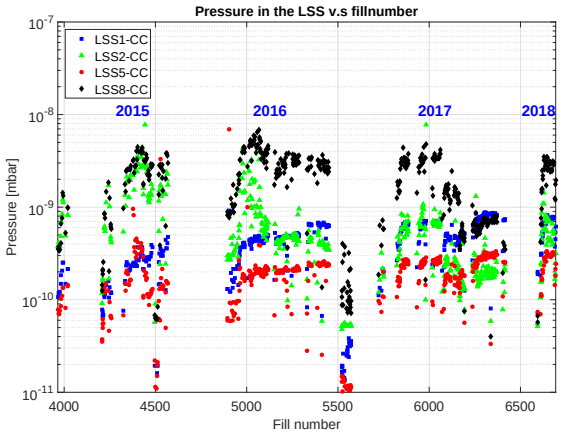

Figure 7: Average reading of Bayard Alpert gauges ± 100-120 m from IP in the combination chambers (CC) of each LSS.

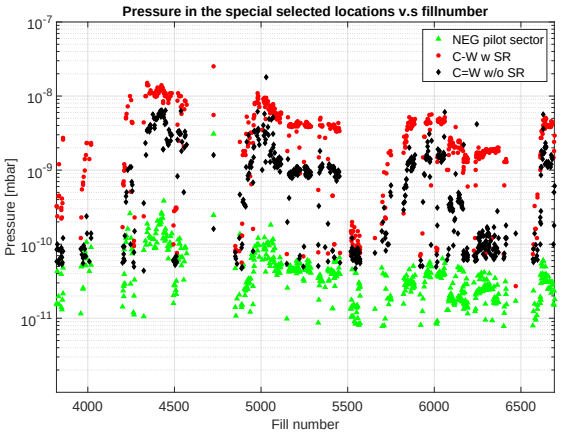

Figure 9: Average dynamic pressure evolution in the NEG pilot sectors, in a cold-warm transitions in the presence and absence of synchrotron radiation.

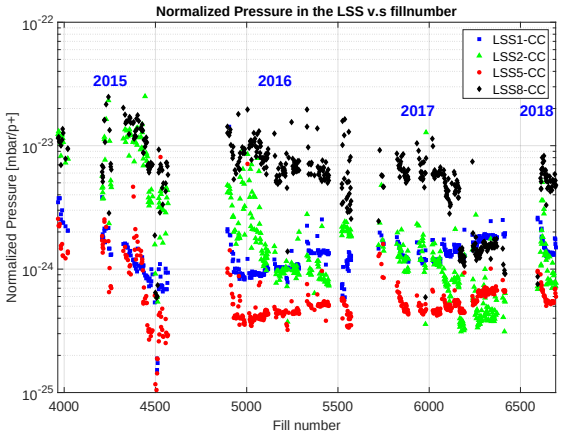

Figure 8: Average reading of Bayard Alpert gauges installed ± 100-120 m from IP in the combination chambers (CC) of each LSS normalized by the beam intensity.

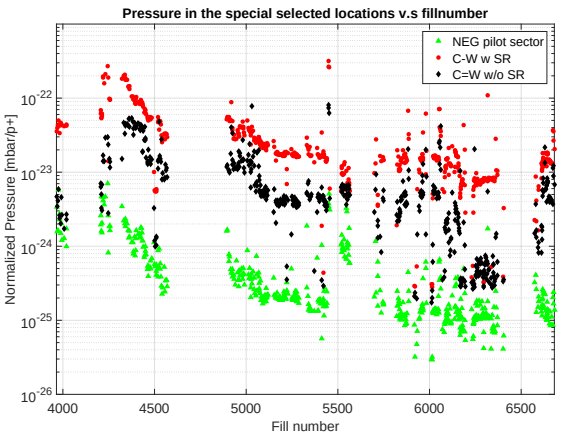

Figure 10: Normalized average dynamic pressure evolution in the NEG pilot sectors, in a cold-warm transitions in the presence and absence of synchrotron radiation.

pilot sector during all Run 2 and no real pressure increase in-between the operation years.

LHC experimental areas' dynamic pressure rise

In this section, pressure as a function of time for a typical physics fill is plotted for ATLAS and CMS experiments and shown in Fig. 11, 12 and 13. A correlation between the dynamic pressure and the beam intensity, beam energies and luminosity is clearly visible. The typical curve in pressure can be divided into three main pressure rise peaks, with a typical example of ATLAS detailed in Fig. 11. The first pressure peak with the maximum at the end of injection indicates the dynamic pressure rise due to electron cloud in the beam pipe. The second pressure peak at the maximum of the beam energy ramp-up indicates the effect of synchrotron radiation from the Inner triplets (IT). The third one well correlates with the luminosity, the same as seen in the case of CMS (Fig. 12). However, the reason for the sudden pressure rise right after the start of collision is not yet clear. This could be a result of particle lost during or generated by collisions, that desorb gas molecules from the walls. Or this could also be ionization in the cables for the gauges close to the IP area. However, it is worth mentioning that the pressure seems to increase with increasing luminosity. More studies in this area are ongoing. On the other hand, since the collision rate for ALICE and LHCb are comparably smaller, no visible pressure rise is detected after the start of collisions in those experiments (Fig. 14) and Fig. 15).

Figures 12 and 13 show the pressure evolution for two selected fills in CMS. The main difference between the two selected fills is that in fill 4532 the CMS detector solenoid was on and during fill 4536 it was turned off. With and without CMS detector solenoid on, a clear difference in the pressure induced by electron cloud is shown in Fig. 12 and 13, when the beams were injected. The detector seems to have a clear effect on suppressing of the electron cloud in the interaction point of the CMS detector. It is also noted that

the CMS gauge seem to be very sensitive to the electronics interference.

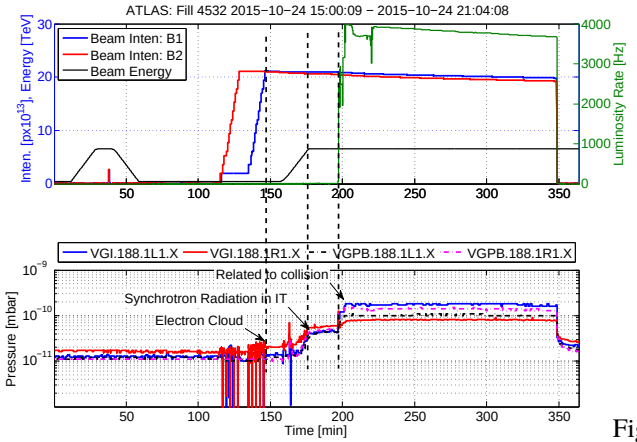

Figure 11: ATLAS Experiment, fill 4532 (1825b).

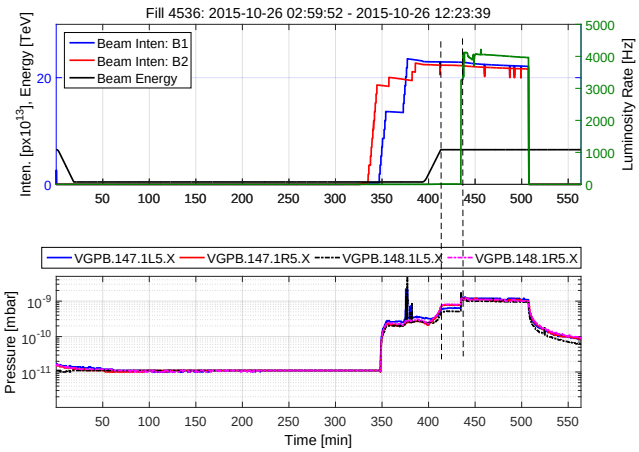

Figure 13: CMS Experiment, fill 4536 (2041b). The CMS detector solenoid was turned off.

LHC ARC pressure evolution

The average of the dynamic pressure in the different ARCs as a function of the fill number is shown in Figs. 16 and 18 for beam 1 and 2, respectively. Figure 17 and 19 exhibit the normalized dynamic pressure in the different ARCs as a function of the fill number for beam 1 and 2 respectively.

At the beginning of each operation year of Run 2, the scrubbing runs provided sufficient mitigation against beam-induced pressure rise at 450 GeV. As a consequence, a fast decrease of the dynamic average pressure in the ARCs due to the conditioning effect can be appreciated.

During the physics runs of Run 2, the cooling capacity on the ARC beam screen approached its pre-defined design limit (160 W/half cell). During 2015, sectors 12 and 23 presented the highest heat load, while in 2016 and 2017 the sectors with the highest heat load were 81 and 12. The abrupt

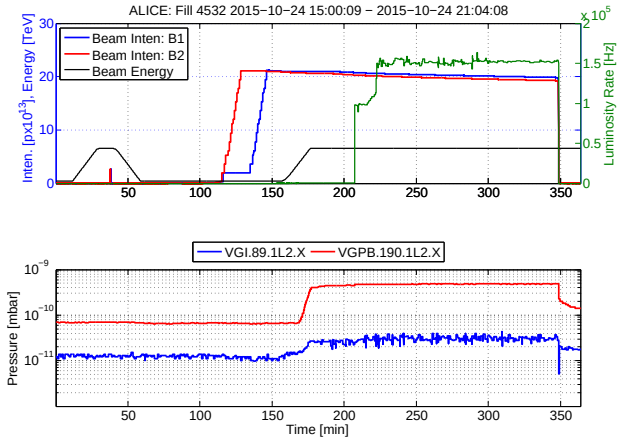

Figure 14: ALICE Experiment, fill 4532 (1825b).

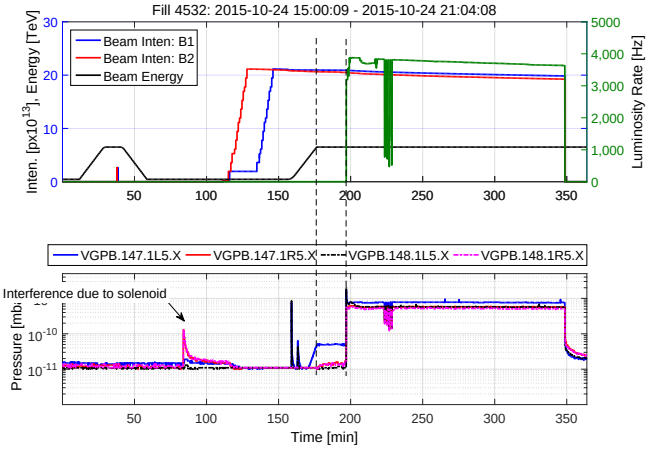

Figure 12: CMS Experiment, fill 4532 (1825b).

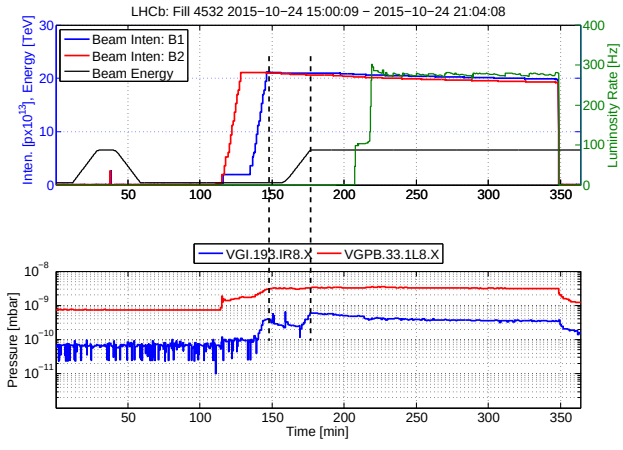

Figure 15: LHCb Experiment, fill 4532 (1825b).

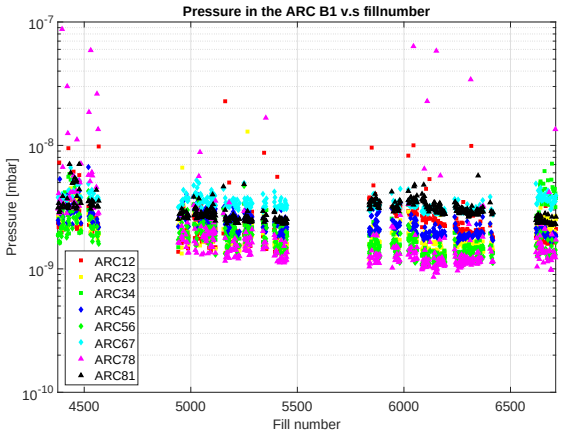

Figure 16: Average of the dynamic pressure in the different ARCs as a function of the fill number for beam 1.

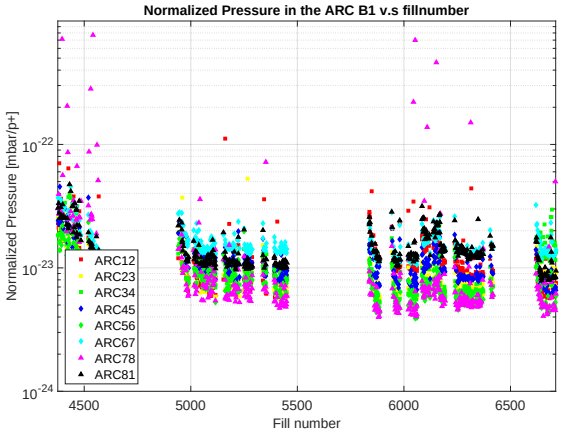

Figure 17: Normalized average dynamic pressure in the different ARCs as a function of the fill number for beam 1.

reduction of the heat load at the end of 2017 corresponds to the introduction of the filling scheme 8b4e.

In term of pressure, different sectors exhibit the highest pressure rise during the operation years of Run2. For beam 1, the sectors with the highest pressure rise during 2015 were ARC 12 and 78, while during 2016, 2017 and 2018, the sectors with the highest pressure rise were ARC 12 and 81. For beam 2, the sector with the highest pressure rise during the entire run was ARC 12. It can also be noted that from the beginning of 2016 , the sector with the lower pressure corresponds to ARC 78, whilst the smallest heat load contribution comes from ARC34. For this reason, we can conclude that a clear correlation between high pressure and high heat load can not directly be extracted from these observations.

The scrubbing in the ARCs during the scrubbing run for both 50 ns and 25 ns is sufficient to reduce the pressure rise due to electron cloud, as confirmed in Fig. 22a and 22b. However, after the Technical Stop 2 in 2015 (TS2, a maintenance shutdown for about 5 days), a clear increase

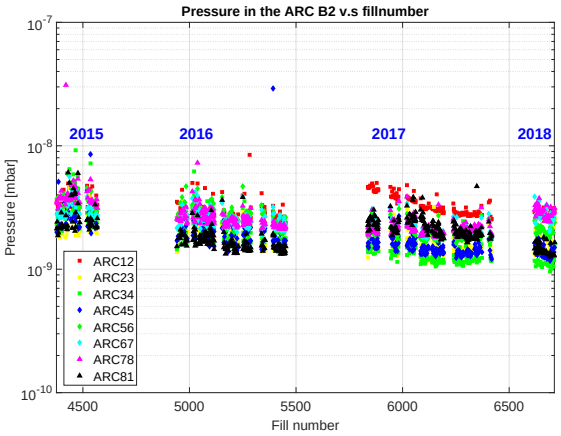

Figure 18: Average of the dynamic pressure in the different ARCs as a function of the fill number for beam 2.

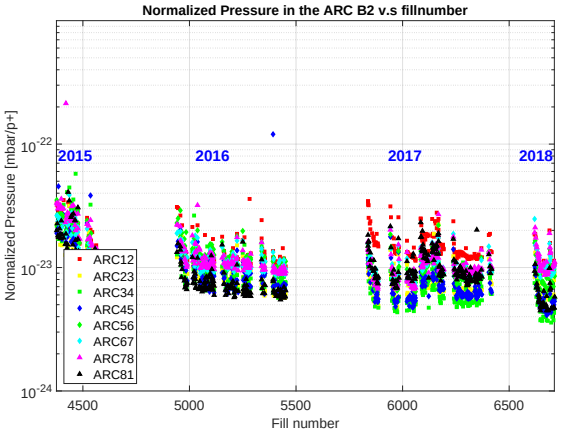

Figure 19: Normalized average dynamic pressure in the different ARCs as a function of the fill number for beam 2.

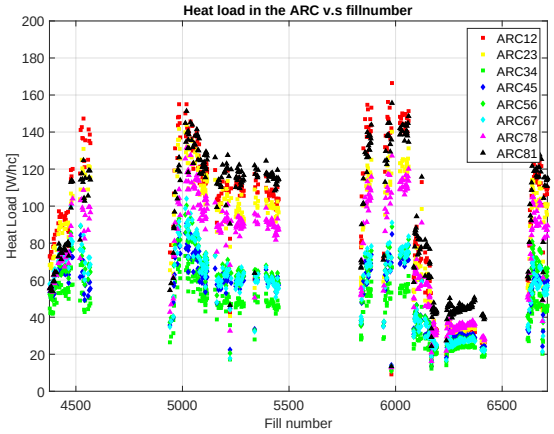

Figure 20: Average heat load in the different ARCs as a function of the fill number.

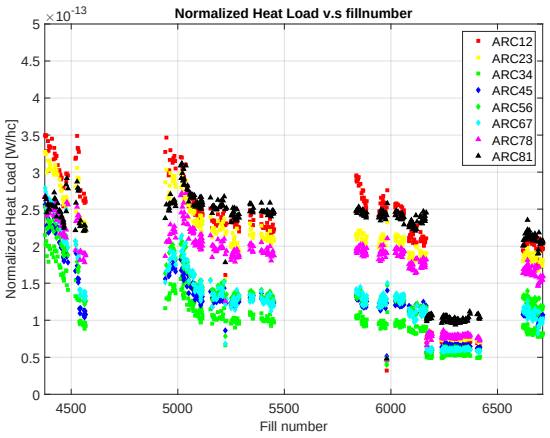

Figure 21: Average normalized heat load in the different ARCs as a function of the fill number.

in pressure was also observed in the ARCs, as shown in Fig. 22c.

Figure 22c clearly shows the loss of conditioning effect accumulated during Scrubbing Run 2 and Physics Run 2. The reduction of the pressure rise seemed to be reset completely. It is more likely that the loss of conditioning was rather due to the low energy beams circulated in the machine after TS2 than long term in-activities of the beam. De-conditioning was observed mainly when running with low e-cloud filling schemes (Physics Run 2, MD combined with TS, High β^*). Recovery of conditioning was achieved quickly, as shown in Fig. 23.

In order to study the causes of the de-conditioning observed in the LHC, the evolution of the Electron Stimulated Desorption (ESD) yield and of the Secondary Electron Yield (SEY) of fully conditioned copper left under ultra high vacuum (UHV) have been studied and are presented in Fig. 24 and 25, respectively.

As shown in Fig. 24, after leaving a sample of fully-conditioned copper under ultra high vacuum (UHV) for a week, a noticeable increase of its ESD as a function of the electron dose could not be observed. Similarly, a significant increase in the SEY of fully-conditioned copper left for 16 days under UHV could not be observed either. These results arouse new questions on how the observed pressure rise after a prolonged TS are generated. More studies are ongoing in this topic.

CONCLUSIONS

In conclusion, the LHC vacuum performance in Run 2 is overall successful after all the upgrades made during the LS1. The LHC operation was mainly characterized by high heat load in four ARCs and the so-called *16L2* issue, which gives more than 50 unexpected dumps. Understanding the cause of the high heat load in some of the ARC sectors is extremely important for the future operation runs.

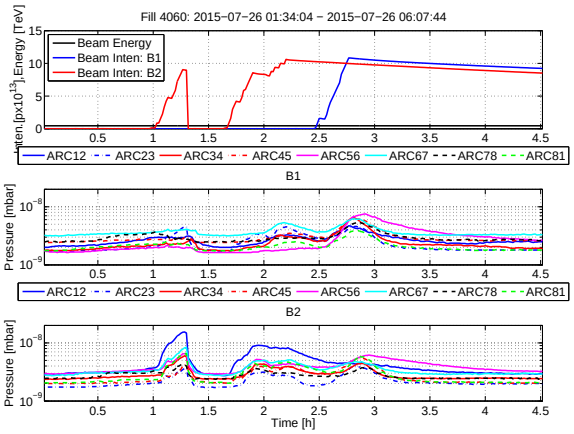

(a)

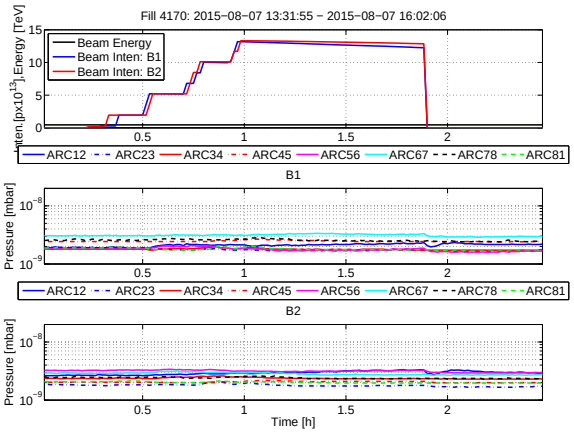

(b)

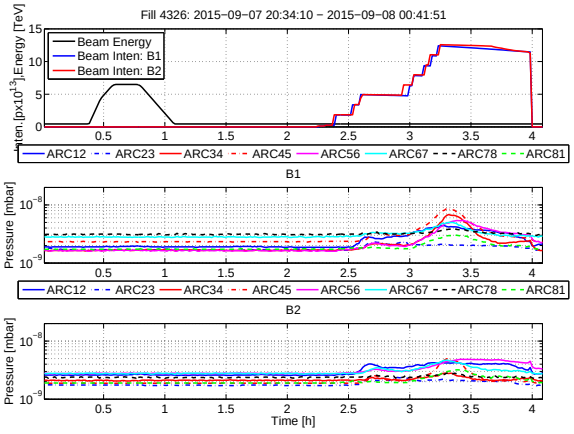

(c)

Figure 22: 25 ns scrubbing run validation and de-conditioning. Average pressure for each of the ARCs for Beam 1 and 2. (a): Fill 4060, 25 ns, B1:1236b and B2: 1236b. Pressure increase in the ARCs before the 25 ns scrubbing run. (b): Fill 4170, 25 ns, B1: 1176b B2: 1176b. No pressure increase. (c): Fill 4326: same filling scheme as Fill 4170, 25 ns, B1: 1176b B2: 1176b after TS2.

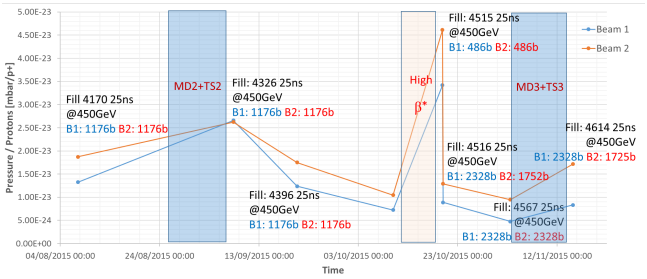

Figure 23: Observed loss of the conditioning effect in pressure in ARCs during the technical stops. Average maximum pressure of each of the ARCs for the selected scrubbing checks @450 GeV.

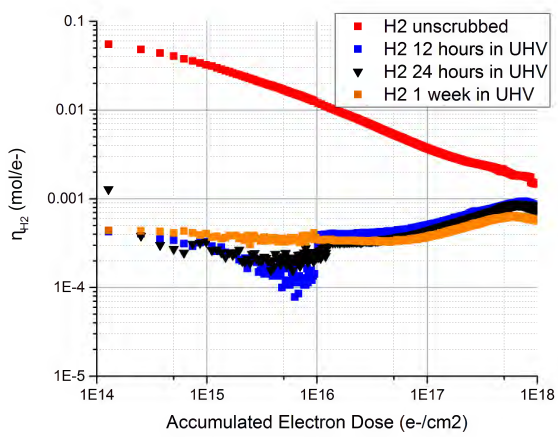

Figure 24: Electron Stimulated desorption (ESD) of backed copper as a function of the accumulated electron dose (courtesy by S. Callegari [5]).

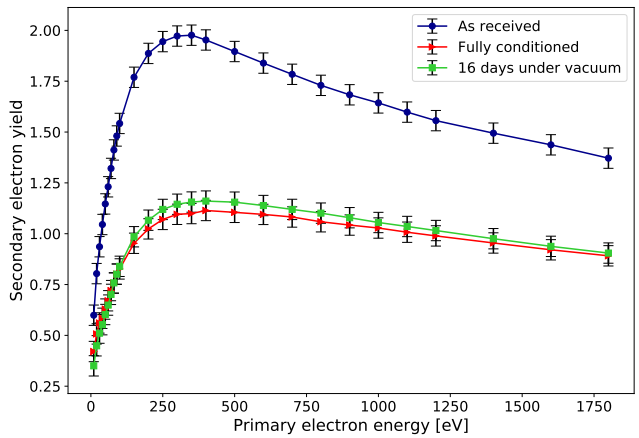

Figure 25: Secondary Electron Yield (SEY) of unbacked copper as a function of the primary electron energy (courtesy by V. Petit).

ACKNOWLEDGMENTS

Special thanks to Simone Callegari and Valentine Petit for contributing with the experimental ESD curves and SEY curves, respectively.

REFERENCES

[1] J. Jimenez and et al, "Vacuum and cryogenics observations for different bunch spacing," 2011. Proceddins of Chamonix 2011 workshop on LHC Performance.

[2] J. Uythoven, "Machine protection at 6.5 TeV." in Chamonix 2016.

[3] G. Ferlin, "Cryogenics." in Chamonix 2016.

[4] L. Mether, "16L2: Operation, observations and physics aspects." in Evian 2017.

[5] S. Callegari and et al, "Electron Stimulated Desorption Studies on Copper After Bake-Out in Ultra-High Vacuum and with Different Venting Conditions." EVC-15, 2018.

HOW DOES A CRYOGENIC SYSTEM COPE WITH E-CLOUD INDUCED HEAT LOAD ?

B. Bradu, K. Brodzinski, G. Ferlin, CERN, Geneva, Switzerland

Abstract

Since 2012, the e-clouds produced by LHC beams are inducing significant dynamic heat loads on the LHC cryogenic system. These additional heat loads are deposited on beam screens where they must be properly extracted by the cryogenic system between 4.6 K and 20 K in order to ensure a stable beam vacuum and a good thermal barrier for superconducting magnets operated at 1.9 K. First, this paper describes how the cryogenic instrumentation located in the surrounding of the beam screens allows to measure the amount of power deposited by the beam and then to estimate the e-cloud contribution. Then, as this dynamic heat load induces fast transients on the cryogenic system, the standard feedback regulation techniques cannot be used anymore due to the slow response time of the cryogenic systems. Consequently, feed-forward controls based on beam information have been successfully setup from 2015 over the 485 beam screen regulation loops to guarantee optimal transients during the beam operation where significant heat load differences are observed all around the machine.

INTRODUCTION: LHC CRYOGENICS

LHC cryogenics is a large, complex and distributed system along the 27 km ring. Cryogenics must provide cryogenic conditions for many equipment in the LHC tunnel such as superconducting magnets, Distribution Feed Boxes (DFB) with their current leads, superconducting Radio-Frequency cavities, thermal shields and beam screens.

To fulfill all these requirements, eight cryoplants are installed around the LHC, sitting at points 18,2,4,6,8, see Fig. 1. Each cryogenic point is equipped with two cryoplants (except in P18/P2 where the two cryoplants are split for geographical reasons) to provide the cryogenic conditions to the two adjacent sectors [1].

One characteristic of the LHC cryogenics is its size and its access constraints. The cold mass is about 37000 $tons$ with an helium inventory of about 120 $tons$ stored in the magnets and in the cryogenic distribution line. Moreover, LHC is located in a confined area (tunnel) and the cryogenic distribution lines are long (3.5 km).

As the thermal transients mainly depends on the cold mass, the coolant mass, the surface of thermal exchange and the pipe diameters and lengths, the LHC cryogenic system response can be very slow and delayed. For instance, the time of flight for the helium supply at 4.5 K and 3 bar between the refrigerator and the end of the sector is about 8 hr, the time of flight for the helium return (3 K and 16 $mbar$) is about 20 min and the time of flight of beam screen helium return (20 K and 1.2 bar) is about 1 hr.

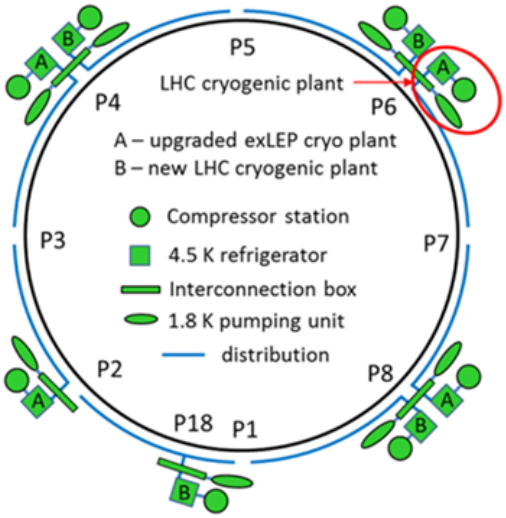

Figure 1: LHC cryogenics overview

All these considerations makes the LHC cryogenics very sensitive to the transients. Fortunately, most of the heat loads are static, but it remains significant dynamic heat loads which must be properly handled by the cryogenic system during the standard LHC operation (no beam - injection - ramp - stable beams - dump).

LHC dynamic heat loads

The main dynamic heat loads are either deposited in magnets at 1.9 K, either in beam screens between 4.6 K and 20 K. As the refrigeration power is not comparable for these two temperature levels, we will use equivalent isothermal power at 4.5 K as reference to be able to fairly compare the heat loads. The dynamic heat loads for the ultimate operation defined in the LHC design report are reported in Table 1 for a typical high-load sector as sector 1-2 [1].

As we can notice in Table 1, the main contributor in the dynamic heat loads is the electron-cloud component. Note that the Eddy current is also a large contributor but this heat load is present only during a short period of about 20 min during the magnet ramping and deramping. It is also important to note that dynamic heat loads applied on the 1.9 K magnet helium bath can benefit from the large superfluid helium heat capacity to smooth efficiently the transient whereas the transient is much more difficult to manage between 4.6 K and 20 K. Consequently, the dynamic heat load inducing the most significant impact on the cryogenic system is the electron-cloud, far away beyond other contributions.

Table 1: Equivalent isothermal dynamic heat loads at 4.5 K for one typical high load sector for ultimate operation.

Heat Load	Temperature	Cause	Heat Load Eq. @ 4.5 K	Remark
Resistive heating	1.9 K	Current in magnet splices	0.75 kW	Rise in 20 min
Eddy current	1.9 K	Current in magnet coils	2.5 kW	Only during ramp
Beam induced on magnets*	1.9 K	Beam and collisions	2.2 kW	Instantaneous
Synchrotron radiation	4.6 K – 20 K	Beam	0.8 kW	Instantaneous
Image current	4.6 K – 20 K	Beam	1.3 kW	Instantaneous
Electron-cloud	4.6 K – 20 K	Beam	5.0 kW	Instantaneous

*include beam gas scattering, photo e-cloud, collision debris in triplets, particle losses in DS.

Cryogenic beam screen circuits

Beam screens are located inside beam pipes and they are cooled by conduction via two cooling pipes of 3.7 mm diameter each, see Fig. 2. Beam screen cooling circuits are supplied by the Cryogenic Distribution Line (QRL) header C with supercritical helium at 3 bar and 4.6 K. After the the thermalisation of the magnet supports (magnet cold feet), an electrical heater (EH) is used to warm-up the helium in case of no beam-screen heat load when there is no beam-induced heating. Two helium circuits are then cooling in parallel the two beam screens in each aperture and the circuits are crossed at each magnet interconnection in order to homogenize the temperatures in case of asymmetrical heat loads between the two apertures. Finally, a control valve (CV) is managing the total flow at the outlet, ending to the QRL header D at 1.2 bar. The complete flow scheme and nominal temperatures and pressures are presented in Fig. 3 for a standard half-cell of 53 m which is repeated 485 times over the LHC ring.

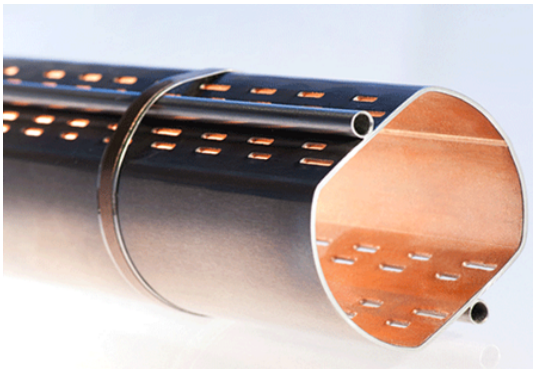

Figure 2: Beam screen with the associated cooling tubes

The temperature limits of the beam screen are defined to avoid thermo-hydraulic oscillations along the cooling pipes, to maintain stable vacuum in the beam pipe, to thermalize the current leads of the corrector magnets and to reduce beam-induced heat loads to the cold mass [2]. The minimum temperature is established between 6 K and 13 K, depending on the flow, to avoid thermo-hydraulic oscillations and the maximum allowed temperature is 40 K for 30 minutes to ensure ultra high vacuum conditions.

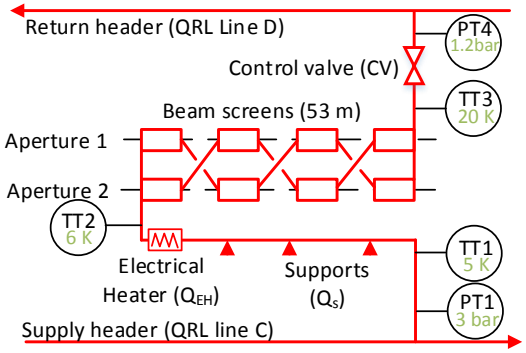

Figure 3: Beam screen cooling scheme with its associated instrumentation and typical values during beam operation

HEAT LOAD MEASUREMENTS

Standard half-cell heat load measurements

The beam screen heat load Q_{BS} can be simply calculated via an enthalpy balance on the beam screen cooling circuit as described in [8] using Eq. 1. Note that the sensor TT_2 is not reliable due to its proximity with the electrical heater and it is more accurate to perform the enthalpy balance on the complete cooling circuit betweeen the header C and the header D of the QRL, deducing the electrical heater power Q_{EH} and the static heat load $Q_s = 5\ W$. The enthalpies h are calculated using appropriated thermodynamic tables and the massflow $\dot{m}$ passing by the valve is computed using the Samson valve Eq. 2 where K_{vmax} represents the valve coefficient at maximum opening, R is the rangeability of the valve and CV is the valve position.

$$Q_{BS} = \dot{m} \cdot (h(P_3, TT_3) - h(PT_1, TT_1)) - Q_s - Q_{EH} \quad (1)$$

$$\dot{m} = 1.25 \cdot 10^{-5} \cdot \sqrt{P_3 \cdot \rho(P_3, TT_3)} \cdot \frac{K_{vmax}}{R} \cdot e^{CV \cdot \ln(R)} \quad (2)$$

The pressure before the valve P_3 is unknown and the pressure drop P induced by the frictions in the cooling tubes has to be computed using Eq. 3 ($P_3 = PT_1 - P$). fr is the friction coefficient computed using a valid correlation based on the Reynolds number, n_c is the total number of

cooling tubes in the circuits ($n_c = 4$ in the ARC), L is the circuit lentgh ($L = 53\ m$ in ARC), ρ is the helium average density in the circuit, D is the cooling tube diameter ($D = 3.7\ mm$) and S is the cooling tube cross section area.

$$P = fr \cdot \left(\frac{\dot{m}}{n_c}\right)^2 \cdot \frac{L}{\rho \cdot D \cdot S^2} \tag{3}$$

In this case, an algebraic loop is created as the massflow and the pressure drop are inter-dependent. This numerical problem can be easily solved by performing few iterations converging to the correct result.

Valve calibrations

The main source of error in the heat load calculation is coming from the valve massflow calculation in Eq. 2 in which the valve rangeability R is rarely well known. Consequently, some calibration measurements have to be done in order to estimate this parameter using the beam screen electrical heaters. The following sequence has been applied when there is no beam in the LHC on each beam screen valve:

- Open the valve at its usual opening when there is no beam ($\approx$ 30 %) and regulate the beam screen inlet temperature at 20 K using the electrical heater. The heater should be around 50 W.
- Open the valve at its maximal opening when there is beam ($\approx$ 65 %) and regulate the beam screen inlet temperature at 20 K using the electrical heater. The heater should be around 150 W.

Then, the rangeabilities for these two measurements are calculated to obtain $Q_{BS} = 0.0\ W$ from Eq. 1 and the average rangeability value R is taken to minimize the error over the valve opening range. The root mean square error ϵ_{rms} is then computed from Eq. 4 using the two errors ϵ_1 and ϵ_2 made when calculating Q_{BS} using Eq.1 with the average rangeability.

$$\epsilon_{rms} = \sqrt{1/2 \cdot (\epsilon_1^2 \quad \epsilon_2^2)} \tag{4}$$

Without calibration, taking the manufacturer rangeability, an rms error of about 15 % is observed whereas after the calibration process, the rms error is reduced to about 5 %.

Heat load measurement results

Once the valve calibration is achieved to reduce the error on the valve massflow computations, the different beam screen heat loads Q_{BS} can be calculated during beam operation. Fig. 4 and 5 show the results on the 485 beam screen circuits around the LHC for a typical beam operation at 50 ns and 25 ns.

At 50 ns, e-cloud heat loads are supposed negligible due to the significant bunch spacing and the heat loads are coming only from the synchrotron radiations and the image current. We observe an average of about 8 W per half-cell around the machine with a dispersion of about 1 W, which correspond precisely to the expected heat load for synchrotron radiations and image current for this fill using the usual scaling laws represented in Eq. 6 and 7.

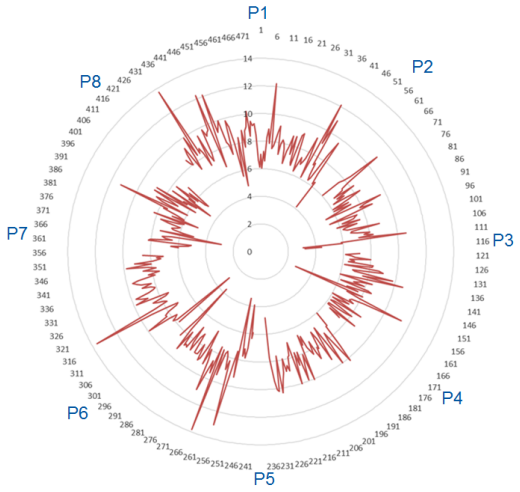

Figure 4: Beam screen heat load measurements at 50 ns during fill 5980 the 22nd July 2017. $nb = 1284\ bunches$; $I = 1.4 \cdot 10^{14}\ p\ /beam$; $E = 6.5\ TeV$.

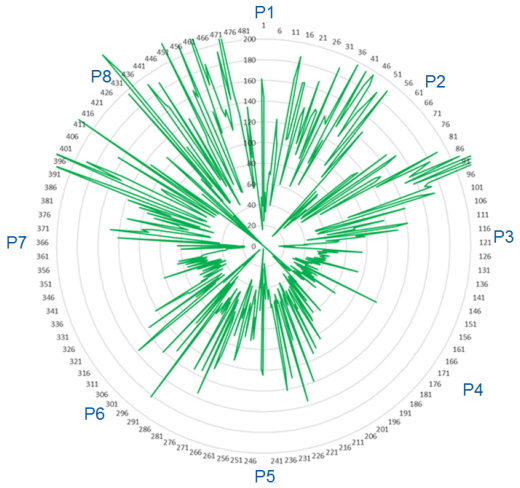

Figure 5: Beam screen heat load measurements at 25 ns during fill 6675 the 12th May 2018 (after scrubbing). $nb = 2556\ bunches$; $I = 3.0 \cdot 10^{14}\ p\ /beam$; $E = 6.5\ TeV$.

At 25 ns, e-cloud is expected to be the main contributor in the beam screen heat loads. We observe in this fill high heat load values along the machine, up to 200 W per half-cell but also a very high dispersion between half-cells and between sectors. A factor three can be observed between two sectors with a factor four between two adjacent half-cells whereas theoretically, all half-cells should show the same heat loads.

Instrumented half-cell heat load measurements

Four half-cells have been equipped with additional thermometers on the two beam screen cooling circuits between

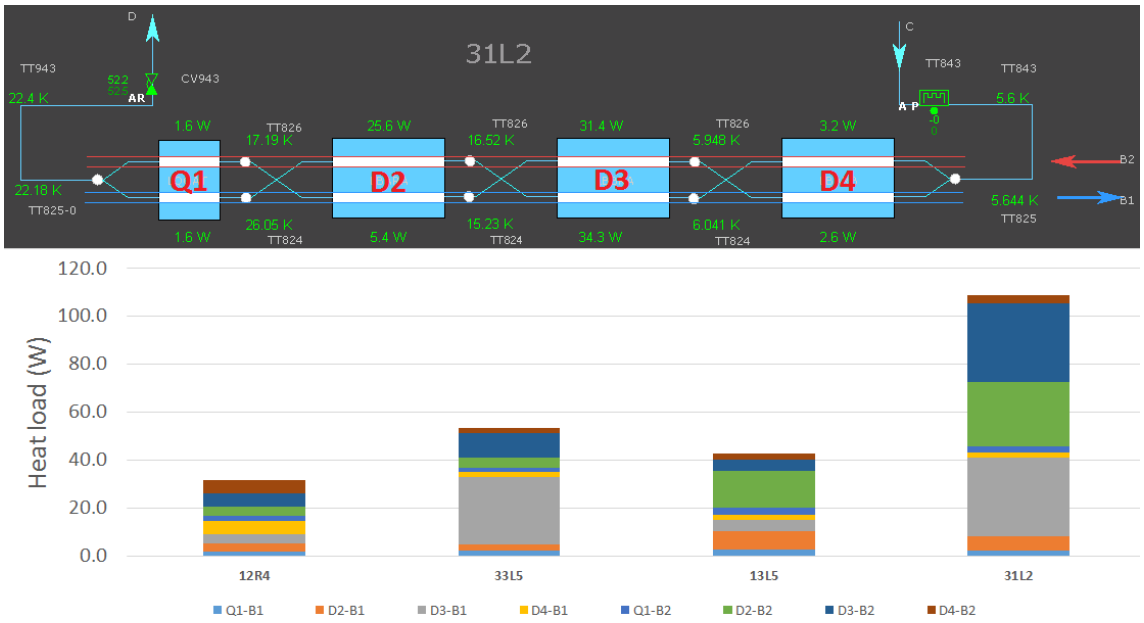

Figure 6: Typical scheme of an instrumented half-cell composed by one quadrupole $Q1$ and three dipoles $D2$, $D3$ and $D4$ (top). Summary of heat loads measured in each aperture ($B1$ and $B2$) of the four instrumented half-cells during Fill 6737 the 28^{th} May 2018 (bottom).

each magnets. These additional temperature sensors can be then used to perform independent enthalpy balances on each aperture for each magnet, giving a total of eight heat load measurements over the 53 m (two apertures on the four magnets), see Fig. 6 where one instrumented half-cell is represented with corresponding heat load measurements.

In the case of the instrumented half-cells, the thermal transients occurring on the beam screen after beam dumps when the heat load disappears can give useful information to estimate the possible heat load profiles along each aperture, see [9] for details. This analysis has been successfully done and is giving asymmetrical heat load distributions in the high load apertures.

HOW TO COPE WITH E-CLOUD TRANSIENTS ?

As described in the above sections, heat load transients induced by e-cloud can be a major issue for the LHC cryogenic system because of their high amplitude, their fast induced transient and their high versatility around the machine. In order to cope with e-cloud transients, two main paradigms have been established in the LHC cryogenic system management: *be prepared* and *start on time*.

Be prepared: pre-loading

The first intuitive action to be setup is the pre-loading of the cryogenic system using electrical heaters at appropriated power and locations when there is no beam. As the expected beam induced heat loads over the beam screens are about 3 kW @ 4.5 K on each LHC sector, such an equivalent power should be pre-loaded using different available electrical heaters when there is no beam. Two pre-loadings are performed in the machine:

- Pre-loading in the 4.5 K refrigerators with about 1.5 kW @ 4.5 K in the cold-box helium phase separator.
- Pre-loading in each of the individual beam screen cooling loop with about 50 W in each half-cell every 53 m. This pre-loading represent a total of about 1.5 kW @ 4.5 K on each sector.

Once this pre-loading is performed over the machine when there is no beam, the cryogenic control system has to remove progressively this pre-loading as function of the beam induced heat loads. The difficulty is then to perform this action in a synchronous manner with the beam parameters changes and the solution consists in starting on time.

Start on time: feed-forward control

First of all, the beam screen control scheme is composed by two independent feedback loops using two PID controllers as depicted in blue in Fig. 7:

- an outlet temperature controller (*PID1*) regulates the outlet temperature of the beam screen at 20 K using the control valve when there is no beam and at 22 K when there is beam with more than 600 bunches.
- an inlet temperature controller (*PID2*) regulates the beam screen inlet temperature at 13 K using the electrical heater located at the circuit entrance when there is no beam and at 6 K when there is a beam with more than 600 bunches;

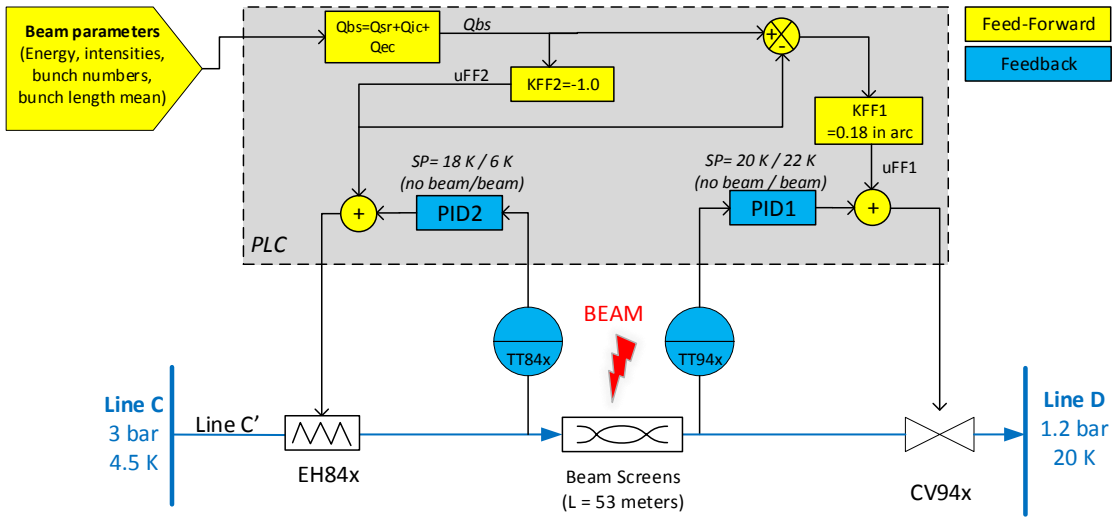

Figure 7: Beam screen control scheme embedding feedback and feed-forward control loops

These two feedback loops ensure a correct temperature distribution over the beam screen in steady-state with and without beams but they cannot manage properly the transients due to the large delays and time constants. Consequently, to start on time and to avoid over-shoots during fast transients, two feed-forward control loops have been setup in addition to the feedback loops as depicted in the yellow boxes of Fig. 7:

- First, the beam screen heat load Q_{BS} is estimated in real-time within the PLC, directly from the beam parameters (energy, intensities, bunch numbers and mean bunch length), see the next section for details.
- The electrical heater is then reduced proportionally with the estimated heat load until reaching 0.0 W.
- Then, if the estimated heat load becomes larger than the initial electrical heater value, the valve is opening proportionally with the additional estimated heat load to be compensated knowing the valve size.

As the delay between the beam-induced heat load and its effects on the beam screen outlet temperature is of the same order of magnitude than the effect of the valve action (around 10 minutes), this feed-forward action allows actuators to cancel the beam-induced heat load before any temperature overshoot happens. This feed-forward architecture is then optimal as all possible actuators are used to compensate the heat loads with shutting off completely the electrical heater when the heat load is maximum.

Beam induced heat load estimation

The deposited heat load on the beam screens Q_{BS} can be estimated from beam parameters doing the sum of the different contributions: synchrotron radiations Q_{sr}, image current Q_{ic} and electron cloud Q_{ec}, see Eqs. 5, 6, 7 and 8 where E is the beam energy, nb the number of bunches, Nb the number of protons per bunch, σ the mean bunch length and the different constants are summarized in Tab. 2.

$$Q_{BS} = Q_{sr} \quad Q_{ic} \quad Q_{ec} \tag{5}$$

$$Q_{sr} = Q_{sr0} \cdot L \cdot \left(\frac{E}{E_0}\right)^4 \cdot \left(\frac{Nb}{Nb_0}\right) \cdot \left(\frac{nb}{nb_0}\right) \tag{6}$$

$$Q_{ic} = Q_{ic0} \cdot L \cdot \sqrt{\frac{0.6 \cdot E \quad 2800}{E_0}} \cdot \left(\frac{Nb}{Nb_0}\right)^2 \cdot \left(\frac{nb}{nb_0}\right) \cdot \left(\frac{\sigma}{\sigma_0}\right)^p \tag{7}$$

$$Q_{ec} = \left[K_{eci} \cdot q_{eci} \cdot \left(1 - \frac{E - E_{inj}}{E_{ramp} - E_{inj}}\right) K_{ecr} \cdot q_{ecr} \cdot \left(\frac{E - E_{inj}}{E_{ramp} - E_{inj}}\right)\right] \cdot n_b \cdot \frac{Nb - Nb_t}{Nb_0 - Nb_t} \tag{8}$$

Due to the different electron cloud heat load values along the machine, three tuning parameters per half-cell are used in Eq. 8. q_{eci} and q_{ecr} represent respectively the electron cloud heat load value per bunch at injection energy (450 GeV) and after the ramp (6.5 TeV), and Nb_t represents the number of protons per bunch threshold where the electron cloud phenomenon appears. This parametrization is performed once a year using an automatic script with a reference fill to setup the 1455 parameters for all beam screen half-cells. Then, the two gains K_{eci} and K_{ecr} are initially

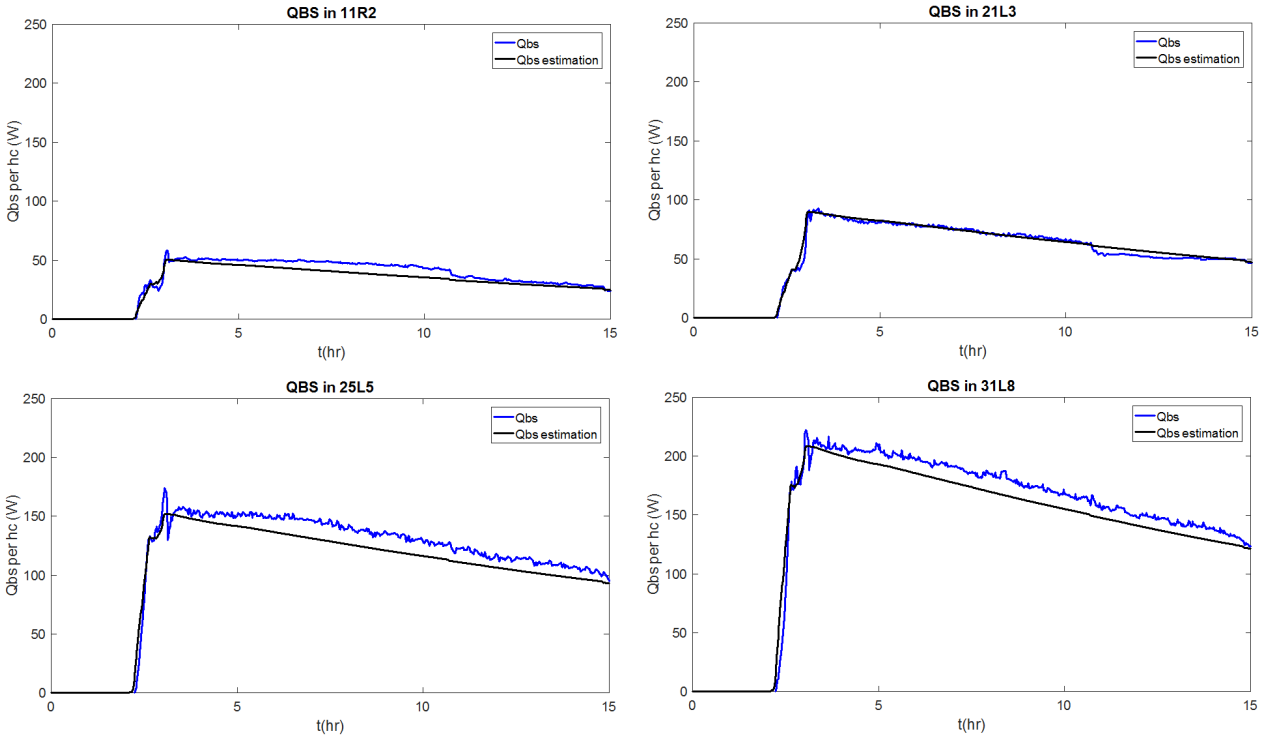

Figure 8: Beam screen heat load estimation compared to measurements on four different half-cells around the machine

equal to 1.0 and they can be tuned by cryogenic operators during the conditioning period in order to adjust easily and massively the electron cloud heat load estimations.

These equations allow us to reasonably estimate the deposited heat loads on the beam screens in all half-cells as we can see in Fig. 8 where a comparison between this model and measurements is shown on four different half-cells with different heat load values.

Table 2: LHC Beam screen heat load constants

Name	Description	Value
L	Beam screen length	53 m
E_0	Nominal energy	7 TeV
E_{inj}	Injection energy	0.45 TeV
E_{ramp}	Final energy after ramp	6.5 TeV
Nb_0	Nominal protons per bunch	$1.15 \cdot 10^{11}$
nb_0	Nominal bunch number	2808
σ_0	Nominal bunch length mean	1.06 ns
Q_{sr0}	Nominal synch. rad. load	0.165 W/m
Q_{ic0}	Nominal image current load	0.135 W/m
p	Bunch dependence factor	-1.5

Validation with dynamic simulations

In order to validate this control scheme including feedback and feed-forward control loops, several dynamical simulations were performed for the extreme cases, validating the different transient responses around the machine. To perform such simulations, a dynamic model of the cryogenic beam screen circuits developed on Ecosimpro some years ago have been re-used [6].

Fig. 9 and 10 show the simulation results for beam screen half-cells under high heat loads (peak of 230 W) and low heat loads (peak of 50 W) using only feedback loops (blue curves) and using feedback with feed-forward loops (red curves). The control scheme is perfectly fitting the requirements in both situations when the feed-forward loops are used, with a very small overshoot on the temperature outlet at 23 K during a short time and minimizing the necessary refrigeration power during the whole fill.

Results during LHC Run 2

Once the dynamic simulations proved the efficiency of the new proposed control scheme using feed-forward loops, the LHC cryogenic control system has been updated accordingly with a progressive deployment over the 485 beam screen cooling loops around the machine.

Fig. 11 is presenting the measurements over one high-load half-cell during a LHC nominal fill in May 2018. Results are very similar to the simulation performed for similar heat loads and the control scheme reacts as expected, correctly controlling the beam screen temperature and minimizing the refrigeration power variation.

Fig. 12 shows the same measurements but for a low-load half-cell during the same fill and the results are again in agreement with simulations demonstrating the efficiency on this control scheme for small heat loads as well.

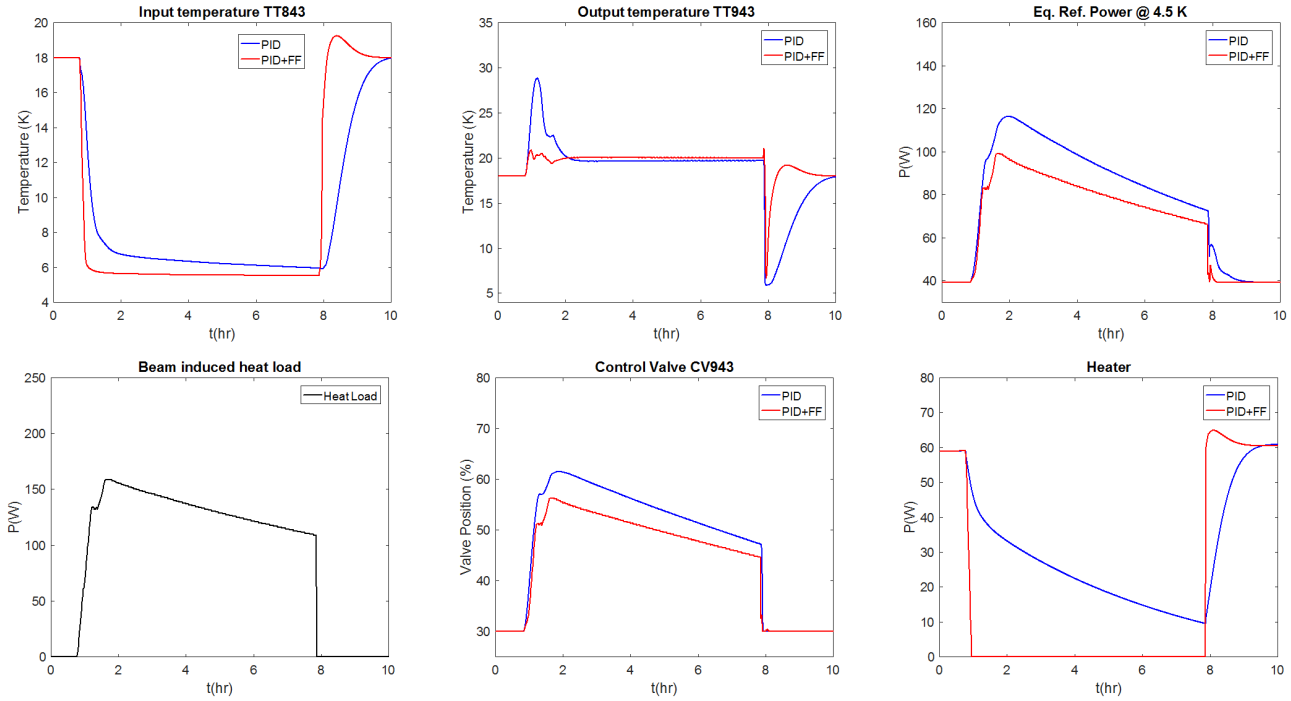

Figure 9: Beam screen dynamic simulation during a fill for a high heat load half-cell

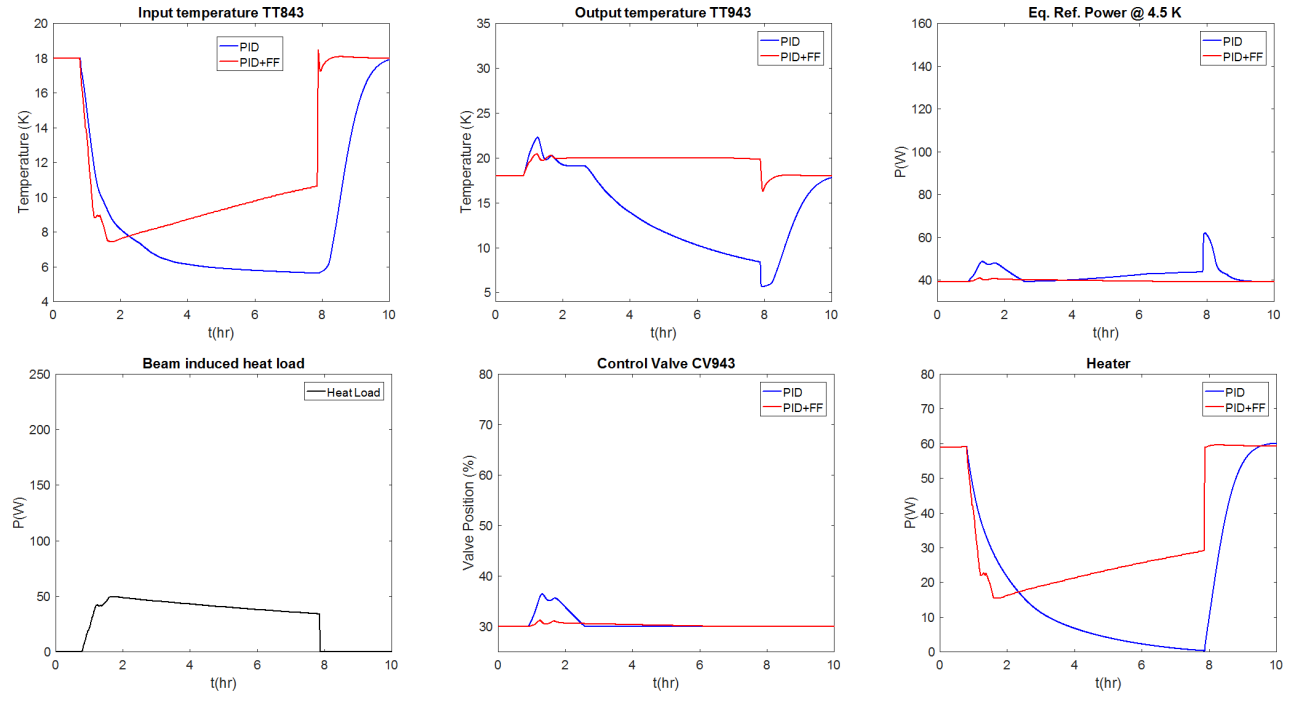

Figure 10: Beam screen dynamic simulation during a fill for a low heat load half-cell

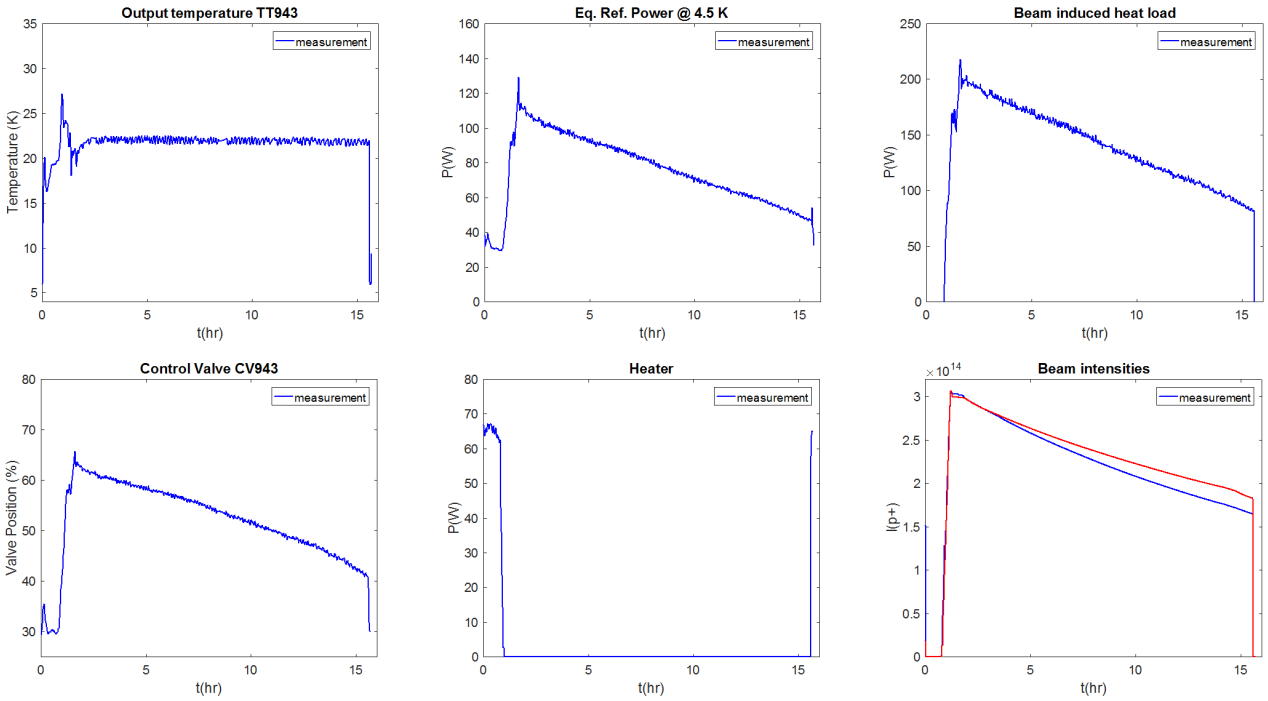

Figure 11: Beam screen measurements during the fill 6675 the 12th May 2018 for a high heat load half-cell

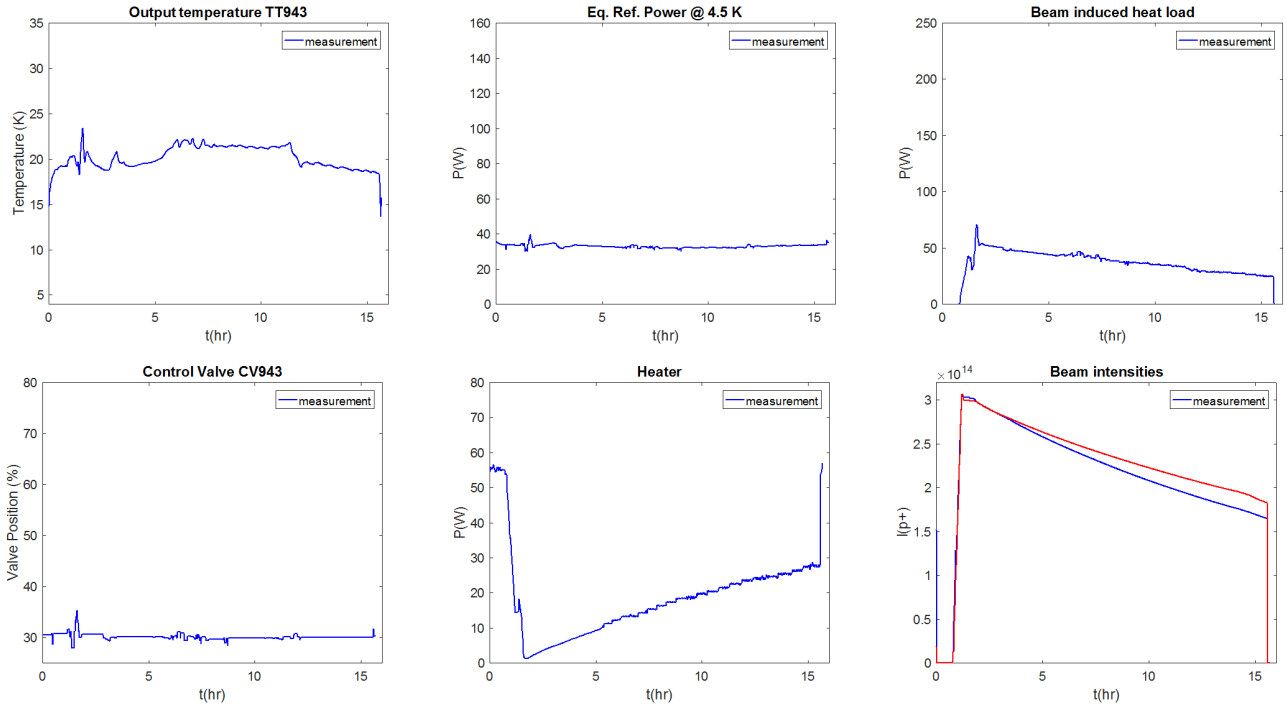

Figure 12: Beam screen measurements during the fill 6675 the 12th May 2018 for a low heat load half-cell

CONCLUSION

Since 2016, the Feed-Forward control scheme has been deployed and tuned over the 485 beam screen loops. This new control scheme proved its efficiency during the LHC Run 2, obtaining a cryogenic system able to cope with the important e-cloud induced heat loads. LHC cryogenic system is close to the optimal operation and it is not limiting the daily LHC operation as far as the total beam-induced heat loads are compatible with the available cooling power of refrigerators.

Nevertheless, LHC cryogenics is now approaching its hardware cryogenic capacity limit and heat loads cannot significantly increase in the coming years.

ACKNOWLEDGMENTS

This work has been possible tanks to the help of the cryogenics operation team, the control support teams, the CERN e-cloud experts and the collaboration of the LHC beam operation team.

REFERENCES

[1] O. Bruning et al., "LHC Design Report", CERN, Geneva (2004).

[2] V. Baglin, Ph. Lebrun, L. Tavian, R. van Weelderen, "Cryogenic Beam Screens for High-Energy Particle Accelerators", ICEC 24, Fukuoka, Japan (2012).

[3] G. Iadarola , G. Arduini, V. Baglin, H. Bartosik, J. Esteban Muller, G. Rumolo, E. Shaposhnikova, L. Tavian, F. Zimmermann , O. Domínguez "Electron Cloud and Scrubbing Studies for the LHC", IPAC 13, Shanghai, China (2013).

[4] K. Li, H. Bartosik, G. Iadarola, L. Mether, A. Romano, G. Rumolo, M. Schenk, "Electron cloud observations during LHC operation with 25 ns beams", IPAC 16, Busan, Korea (2016).

[5] B. Bradu, E. Rogez, E. Blanco, G. Ferlin, A. Tovar, " Beam screen cryogenic control improvements for the LHC run 2", ICEC 26, New-Delhi, India (2016).

[6] B. Bradu, E. Blanco, P. Gayet, "Example of cryogenic process simulation using EcosimPro: LHC beam screens cooling circuits", Cryogenics, 53:45-50 (2013).

[7] L. Tavian, "Performance limitations of the LHC cryogenics: 2012 review and 2015 outlook", LHC Beam Operation workshop, Evian, France (2012).

[8] K. Brodzinski, L. Tavian, "First Measurements of Beam-Induced Heating on the LHC Cryogenic System", ICEC 24, Fukuoka, Japan (2012).

[9] B. Bradu, K. Brodzinski, D. Delikaris, C. Garion, L. Tavian, "Heat load profile estimates on LHC beam screens by thermal transient analysis", ICEC 26, Oxford, United Kingdom (2018).

[10] E. Hatchadourian and Ph. Lebrun and L. Tavian, "Supercritical Helium Cooling of the LHC Beam Screens", ICEC 17, Bournemouth, United Kingdom (1998).

SUB-THz EM CHARACTERIZATION OF COATED MATERIALS

A. Passarelli†, H. Bartosik, G. Rumolo, CERN, 1211 Geneva 24, Switzerland
V. G. Vaccaro, M. R. Masullo, C. Koral, INFN Naples Unit, 80126 Napoli, Italy
A. Andreone, Physics Department, University of Naples Federico II, 80126 Napoli, Italy
O. Boine-Frankenheim, T.U. Darmstadt, Schlossgartenstrasse 8, 64289 Darmstadt, Germany

Abstract

The electromagnetic characterization of coating materials is fundamental to build a reliable impedance model of any accelerator. In particular, since the CLIC (Compact LInear Collider) necessitates bunches with short longitudinal length, a full electromagnetic characterization of the coating material surface impedance is needed at high frequencies in the millimetric wave length and beyond. The goal of this paper is to develop a measurement method to characterize the coating materials in the sub-THz frequency range. The electromagnetic characterization of the material is performed using a time domain coherent THz spectrometer. The method is based on the attenuation measurement of the signal passing through a waveguide specifically designed, having a very thin central layer where the coating material is deposited on both sides. The guide is equipped with two "horn" antennas integrated on both sides of the device to enhance the electromagnetic signal collection. This novel technique is tested on slabs coated with a Non-Evaporable Getter (NEG) and allows evaluating the surface impedance in the frequency range from 0.1 to 0.3 THz.

INTRODUCTION

The main goal of this paper is to develop a measurement method for the electromagnetic characterization of the coating material used in accelerator beam pipes. The coating materials requiring a characterization of their surface impedance are the amorphous Carbon (a-C), used for electron cloud mitigation [1] and the Non-Evaporated Getter (NEG), used to reach the ultra-high vacuum condition in the accelerator chambers [2]. The electron cloud in positron rings is a mechanism that starts when the synchrotron radiation photons, emitted by the beam, create a large number of photo-electrons at the inner chamber wall surface. These primary electrons, after being accelerated in the electric field of a passing bunch, may again hit the inner wall of the beam pipe, causing secondary emission or being elastically reflected [3]. If the secondary electron yield (SEY) of the surface material is greater than unity, the number of electrons grows exponentially leading to dynamic instabilities and many other side effects [4, 5].

In order to lower the value of SEY of the pipe walls, a-C coatings have been extensively tested [1] and used [6] at the CERN SPS accelerator and in other experiments [7] with very effective results.

The Ultra-High Vacuum is needed in particle accelerators to reduce the gas-beam scattering, the risk of high voltage discharge and to improve the thermal insulation [8]. The application of NEG coatings allows a distributed and continuous pumping in large accelerator vacuum chambers even in very narrow beam pipes. CERN was the pioneer in NEG thin film coating technology [9], these coatings are currently used in the LHC warm vacuum pipes. Furthermore, other accelerators like ESRF, ELETTRA, SOLEIL, MAX IV and Sirius widely employ NEG pumps in their chambers.

These coatings used for the reduction of SEY or for the improvement of the pumping processes, change the vacuum chamber surface impedance. A reliable impedance model, including a resistive wall contribution, requires an accurate electromagnetic characterization of these materials [10].

Among the NEG alloys, the alloy made from titanium (Ti), zirconium (Zr) and vanadium (V) has the lowest activation temperature at 180 degrees [11]. The surface impedance of samples coated with this NEG alloy has been evaluated for our study. We decided to test our methodology with NEG deposition whose production, with the desired thickness of 5μm, is simpler compared to a-C. Therefore, the investigation on the a-C has been postponed. As described above, there is the need to create a reliable system for measuring the surface impedance of the materials used on the coating sample. The NEG characterization of different samples has already been carried out in another paper [12, 13] by comparing numerical simulations and experimental measurements in the sub-THz frequency range.

The methodology presented in this work was studied with the idea of overcoming some of the inconveniences of the method reported in [12]:

- non-homogeneous deposition with unpredictable thickness and relevant peel-off and blistering;
- the impossibility to reuse the system for further measurements.

It has to be underlined that the NEG properties vary with the parameters of the specific coating process, like pressure in the vacuum chamber and/or voltage applied to the cathode. This means that any measurement will be not valid for NEG in general but relevant to the coating process.

This work is the first step to develop a reliable, manageable and inexpensive system for measuring the surface impedance in the sub-THz region.

METHOD

As mentioned above, the resistive wall impedance is an essential contributor for a detailed machine impedance model. In this evaluation, the EM characterization of the vacuum chamber coatings up to high frequencies may be

† andrea.passarelli@cern.ch

crucial as for CLIC DRs because of their 1.8 mm rms bunch length [14].

The goal of this work is to develop a new method to give a reliable estimation of the surface impedance of the coated material as a function of frequency. This method proposes to measure the attenuation of the signal passing through a waveguide (see Fig.1) with coated material placed on a copper foil interposed between the two shells of the waveguide. The conductivity value of the material is estimated by inspecting and comparing the theoretical and measured behavior of the attenuation due to the presence of the coating. From that value and from the measured coating thickness we may infer the surface impedance.

The waveguide is placed in the optical path of a time-resolved coherent THz spectrometer, described in detail in the next subsection.

The evaluation of the signal attenuation due to the presence of the sample allows to retrieve the conductivity by using a reference signal passing through the waveguide with copper slab without coating.

The analytical evaluation has been performed by studying the mode propagation in the Device Under Test (DUT). The analytical results are compared with Frequency domain CST simulations [15]. In the second subsection, we show the waveguide used for the experiment and the longitudinal cut where the foil is placed. To avoid coating inhomogeneity, the thickness cannot be bigger than 5-6 μm.

The measurement setup

Tera K15 of the Menlo Systems is the device used for measurements. It is a Time Domain THz spectrometer. The opto-mechanical setup used for our experiment is shown in Fig. 1.

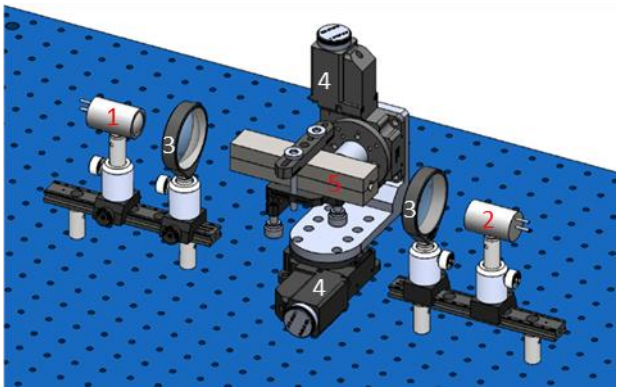

Figure 1: Sketch of the opto-mechanical setup utilized for the measurements: 1)Emitter, 2)Detector, 3)TPX collimating lenses, 4)Micrometric alignment systems, 5)DUT.

The system is based on a 1064 nm fiber laser with 120 fs pulse width and 60 MHz repetition rate. In the standard setup, the laser output splits in 2 beams.

The pump beam generates an electromagnetic transient (THz pulse, ≈ ps) through the excitation of a low-temperature grown GaAs based photoconductive antenna (PCA) emitter, whereas the probe beam is used to detect the THz pulse using a similar PCA receiver. A mechanical optical line (Delay Line) is used to control the delay between probe and pump beams.

This method of detection provides the waveform, that is the electric field amplitude of the THz pulse as a function of the timing difference (see the nominal time domain signal in Fig. 2). For our evaluation, the signal is then converted into the frequency domain using a standard Discrete Fourier Transform (DFT). In the experiment, the maximum frequency resolution is about 4 GHz, limited by the scanning range of the delay line only.

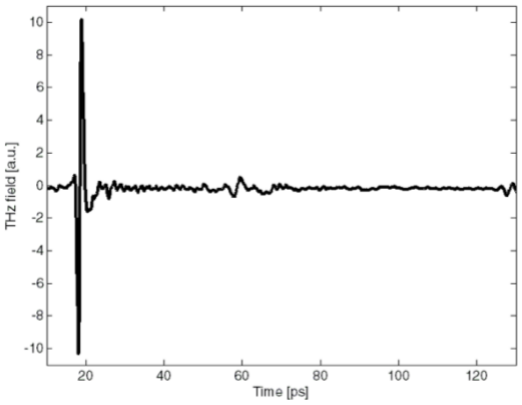

Figure 2: THz time domain signal propagation in free space.

The device under test

The device used for our experiment is shown in Fig. 3. It is a circular waveguide connected to two pyramidal horn antennas on both sides in order to enhance the electromagnetic signal collection and radiation [16]. Likely, this shape has been chosen because it is easier to mill a pyramidal horn than to machine a conical one. Conversely, to drill a cylindrical waveguide is easier to mill a rectangular one.

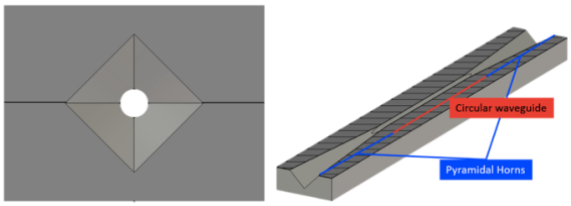

Figure 3: Circular waveguide with two pyramidal horns. Left: Front view. Right: Perspective view of longitudinal cut.

Furthermore, the transition from the horn to the waveguide is smoother than the one obtainable in case of waveguides with a conical-cylindrical or pyramidal-square transition. This can be understood by looking at the magnified stretch of transition in Fig. 4

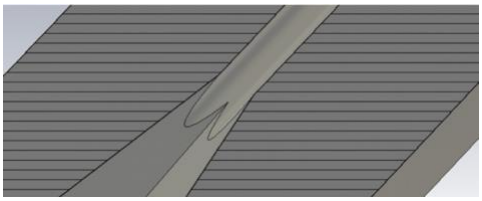

Figure 4: Magnification of the transition between the pyramidal horns and the cylindrical waveguide.

The transition curves are branches of very flat ellipses, which are the intersection between a plane and a circular cylinder. They are very flat since the plane is almost parallel to the axes of the ellipses. Therefore, this behavior smoothes the transition from the pyramidal mode to the cylindrical one. In the analytical evaluation, without affecting the results [17], we assume an abrupt transition where the pyramidal horn stops and the cylindrical waveguide starts at a plane orthogonal to the axis. The distance of this plane from the apexes of the ellipses is the double of the one to the cusp made by two ellipses. The external shape of the device under test is a parallelepiped of size *16×12×120* mm. The internal dimensions are reported in table I.

The slab has the same length as the DUT and is 50 μm thick. During the deposition process, in order to prevent the deformation, the slab is held in an aluminum frame (see Fig. 5).

Table 1: Waveguide internal dimensions.

[mm]	Length	Radius/Side (ext→int)
Cylindrical waveguide	42	0.9
Pyramidal horn	39	6→1.2728

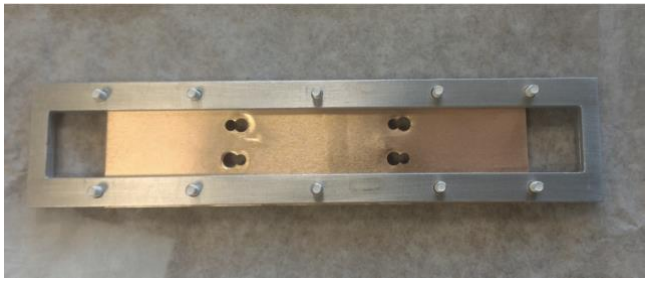

Figure 5: Slab placed in the frame for the deposition.

The TE-VSC-SCC section at CERN performed the deposition process on both sides of two different copper slabs by using a DC magnetron sputtering technique. X-ray fluorescence (XRF) test were performed along the median line of the slab to check the thickness of the coating deposition (see Fig. 6). The slab has been placed between the two shells in such a way that the median line of the slab coincides with the center of the waveguide.

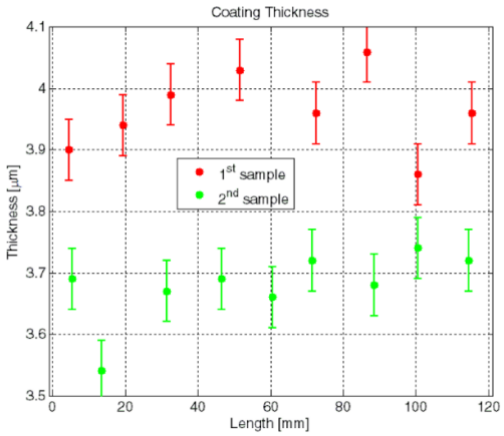

Figure 6: NEG coating deposition thickness on two slabs used for the experiments.

Modes propagating in the waveguide

In order to simplify the analysis, we decided to work with a single mode propagating in the waveguide. The first mode $TE_{1,1}$ propagating inside the circular waveguide is shown in Fig. 7 [18].

The presence of a slab placed in the median plane together with the incident wave conformation (quasi-plane wave) select the modes that can propagate inside the waveguide. The electric field must be orthogonal and continuous (above-below) to the slab surface. Furthermore, some symmetries have to be satisfied (left-right). The above sentence can be condensed in the statement: the projection of the incident plane wave on the mode must be non-null. The second mode that is allowed to propagate is the $TE_{1,2}$, all the other modes in between cannot propagate. Therefore, the allowed bandwidth is defined by the cut-off frequencies of $f_{TE1,1}$ = 97.6 GHz and $f_{TE1,2}$ = 282.6GHz. In sum, we may work in a bandwidth of about 200 GHz.

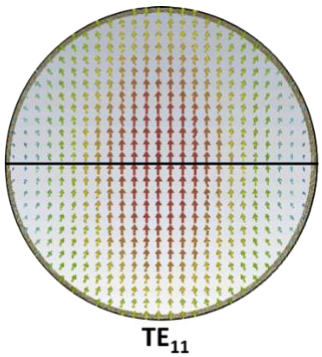

Figure 7: First mode propagating inside the cylindrical waveguide with a foil placed on the center.

Since the semi-aperture of the pyramidal horn is < 5 deg we may consider the modes which propagate in a locally uniform square waveguide and take the relevant lower modes. The first two modes, having the same cut-off frequency, are two degenerate modes. If their excitation coefficient has the same amplitude, their sum will exhibit an electric field everywhere orthogonal to the horizontal diagonal as shown in Fig. 8

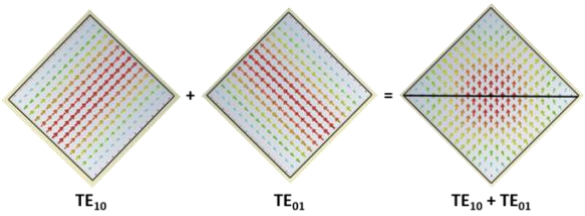

Figure 8: Electric field of the first two degenerate modes inside the square waveguide and sum (right) of the first two modes propagating inside the waveguide with a foil placed on the center.

Doing the same considerations we did for the cylindrical waveguide and considering a waveguide of side of 1.2728 mm, the sum of the first two modes allowed to pass have a cut off frequency of $f_{TE1,0} = f_{TE0,1} = 117.8$ GHz. The other two modes allowed to pass start their propagation from $f_{TE2,1} = f_{TE1,2} = 263.3$ GHz.
Considering negligible the attenuation contribution given by the transitions between the pyramidal horns and the central cylindrical waveguide, the frequency range goes from 118 GHz to 283 GHz.

THE ATTENUATION

We look for a simple and flexible tool able to yield numerical values of the signal attenuation occurring in the waveguide with the slab.

General formulation

In this section we give the general definition of attenuation in a waveguide and we evaluate it in the specific case of the waveguide used for measurements.
The definition of the attenuation constant is expressed by the formula [19, 20]:

$$\alpha = -\frac{1}{2P(z)}\frac{dP}{dz} \tag{1}$$

where P is the total power flow at z and -dP is the power dissipated in a section of waveguide of length dz.
From Eq. 1 follows that the attenuation constant due to losses on guide walls is [19]:

$$\alpha = \frac{1}{2}\frac{\mathrm{Re}[Z_S(z)]}{\mathrm{Re}[Z(z)]}\frac{\int|H_{tan}|^2 ds}{\iint|H_t|^2 dS} \tag{2}$$

where Z_S is the equivalent surface impedance, Z is the characteristic impedance of the propagating mode and H_{tan} and H_t are the nondissipative values of the magnetic field tangential to the guide periphery and transverse to the guide cross section, respectively. The line integral with respect to ds extends over the guide periphery, and the surface integral with respect to dS extends over the guide cross section. We consider the propagation of the sole $TE_{1,1}$ mode in the cylindrical waveguide. The attenuation of this single mode in a generic waveguide is:

$$A_{cyl} = \frac{1}{2}\frac{Re(Z_S)}{Re(Z_{1,1})}\frac{\int_l |n \times H_{1,1}|^2 dl}{|I_{1,1}|^2} \tag{3}$$

where $Z_{i,j}$ is the i,j mode impedance and $I_{i,j}$ is the relevant excitation current. To evaluate the attenuation in the pyramidal transition we consider the sum of two modes, the formula in this case is:

$$A_{pyr} = \frac{1}{2}Re(Z_S)\frac{\int_l |n \times (H_{1,0}+H_{0,1})|^2 dl}{Re(Z_{1,0})|I_{1,0}|^2 + Re(Z_{0,1})|I_{0,1}|^2} \tag{4}$$

Z_S of the formulas 3 and 4, in case of coating, is:

$$Z_s = Z_{coat}\frac{Z_{cu} + jZ_{coat}tan(k_{NEG}d)}{Z_{coat} + jZ_{cu}tan(k_{NEG}d)} \tag{5}$$

where d is the coating thickness. When d = 0 there is no coating and $Z_S = Z_{cu}$.
The characteristic impedance in the Leontovich approximation for a metallic case ($\varepsilon'' \gg \varepsilon'$) is [17]:

$$Z = (1+j)\sqrt{\frac{\omega\mu}{2\sigma}} = \frac{1+j}{\sigma\delta} \tag{6}$$

and the propagation constant in the same condition is:

$$k = (1-j)\sqrt{\frac{\sigma\omega\mu}{2}} = \frac{1-j}{\delta} \tag{7}$$

where δ is the skin-depth defined as:

$$\delta = \sqrt{\frac{2}{\sigma\omega\mu}} \tag{8}$$

and $\mu = \mu_r\mu_0$ is the total permeability, μ_r the relative magnetic permeability, μ_0 the permeability of free space, $\omega = 2\pi f$ and σ the material conductivity.
As stated in the introduction, the procedure consists in the measurement and/or in the analytical evaluation of the relative attenuation defined as:

$$RA \triangleq A^{coat} - A^{cu} \tag{9}$$

This means that the attenuation on the wall is simplified in the above formula and we have to analytically evaluate only the attenuation on the slabs.

Estimation on the foil in the cylindrical waveguide

The first mode in the cylindrical waveguide with a foil placed in the center is shown in Fig. 7.
The constant of attenuation on the foil placed in the center of a cylindrical waveguide is:

$$\alpha_{cyl} = 4Re(Z_S)\frac{\chi'_{1,1}k_{z_{1,1}}}{\pi a_0 Z_0 k_0\left(\chi'^2_{1,1}-1\right)J_1^2(\chi'_{1,1})}$$

$$\left[\frac{k^2_{t_{1,1}}}{k^2_{z_{1,1}}}\oint_0^{\chi'_{1,1}}|J_1(\mathrm{u})|^2du + \oint_0^{\chi'_{1,1}}|J'_1(\mathrm{u})|^2du\right] \quad (10)$$

were Z_0 is the characteristic impedance in the free space, a_0 is the radius of the waveguide. J_1 and J'_1 are the first order Bessel function and its respective derivative. $\chi'_{1,1}$ is the first non-vanishing root of the equation:

$$J'_1(x) = 0$$

and

$$k_0 = \frac{\omega}{c};\quad k_{t_{1,1}} = \frac{\chi'_{1,1}}{a_0};\quad k_{z_{1,1}} = \sqrt{k_0^2 - k_{t_{1,1}}^2}$$

The total attenuation along the foil of length l_g is described by the formula:

$$A_{cyl} = \int_0^{l_g}\alpha_{cyl}dz = \alpha_{cyl}l_g \quad (11)$$

where l_g is the length of the waveguide.
To check our analytical tool, we evaluate the agreement between a numerical code and our formula for various coating thickness with a NEG conductivity value of $\sigma_{coat} = 3.5\ 10^5\ S/m$, which is one of the estimated values in the already quoted paper [12].
We evaluate the relative attenuation (see Eq.9) for the cylindrical waveguide as:

$$RA_{cyl} \triangleq A^{cu}_{cyl} - A^{coat}_{cyl} \quad (12)$$

The comparison between our analytical evaluation (Eq. 12) and CST Frequency Domain simulation is shown in Fig.9.

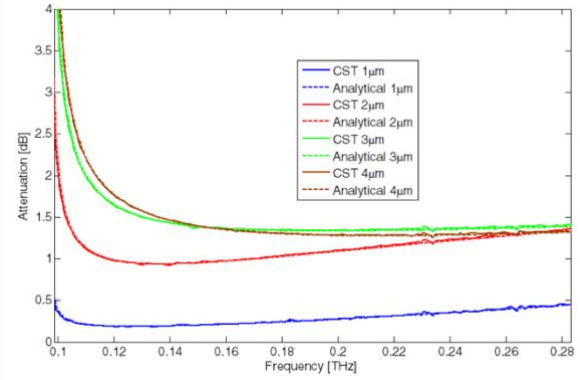

Figure 9: Relative attenuation of the first mode on the foil for different coating thickness with $\sigma_{coat} = 3.5\ 10^5\ S/m$. Comparison between analytical formulas and CST Frequency Domain simulations.

The excellent agreement makes it hard to detect any discrepancies between CST simulations and our theory.

Estimation on the foil in the pyramidal transition

The attenuation on the foil interposed on the center of the pyramidal transition is due to the sum of two degenerate modes. The foil forces the propagation of the first two modes because of the boundary conditions on the metallic foil as visible in Fig. 7.
The total attenuation per unit length is:

$$\alpha_{pyr}(z) = \sqrt{2}\frac{Re(Z_s)k_{z_{sum}}(z)}{a(z)Z_0k_0}\left[1 + \frac{2k^2_{t_{sum}}(z)}{k^2_{z_{sum}}(z)}\right] \quad (13)$$

The total attenuation on the foil in the two transitions is not anymore a constant, because the side is changing along the waveguide, this means that the attenuation of two modes on the pyramidal walls is given by the resolution of the integral:

$$A_{pyr} = 2\int_0^{l_t}\alpha_{pyr}(z)dz =$$
$$\sqrt{2}\frac{Re(Z_s)}{Z_0}\left[-\frac{1}{2\mathrm{d}}log\left[\frac{\sqrt{1-\left(\frac{\pi}{k_0B}\right)^2}-1}{\sqrt{1-\left(\frac{\pi}{k_0B}\right)^2}+1}\frac{\sqrt{1-\left(\frac{\pi}{k_0a}\right)^2}+1}{\sqrt{1-\left(\frac{\pi}{k_0a}\right)^2}-1}\right]+\right.$$
$$\left.\frac{2}{\mathrm{d}}\left[\sqrt{1-\left(\frac{\pi}{k_0B}\right)^2}-\sqrt{1-\left(\frac{\pi}{k_0a}\right)^2}\right]\right] \quad (14)$$

Where

$$a(z) = b + zd = b + \frac{z(B-b)}{l_t}$$

is formula of the side of the waveguide that changes along the transition, l_t is the longitudinal length of the transition and B is the side of the entrance of the pyramidal horn transition and

$$k_{t_{sum}}(z) = \frac{\pi}{a(z)};\quad k_{z_{sum}}(z) = \sqrt{k_0^2 - k^2_{t_{sum}}}$$

We evaluate the relative attenuation (see Eq.9) for the Pyramidal transition as:

$$RA_{pyr} \triangleq A^{cu}_{pyr} - A^{coat}_{pyr} \quad (15)$$

The comparison between this analytical evaluation and the CST Frequency domain solver is in Fig. 10 for $\sigma_{coat} = 3.5\ 10^5\ S/m$.

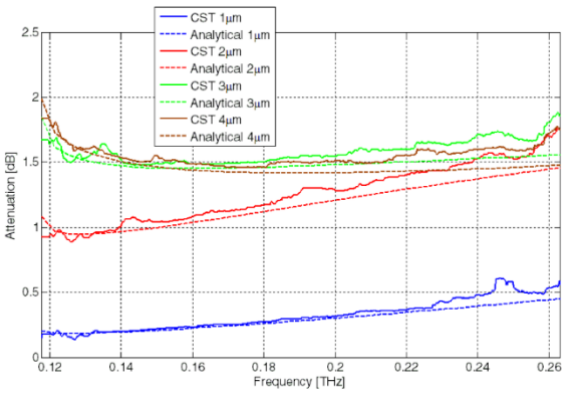

Figure 10: Attenuation of two modes on foil in pyramidal transition for different coating thickness with $\sigma_{coat} = 3.5\ 10^5\ S/m$. Comparison between analytical formulas and CST Frequency Domain simulations.

THE MEASUREMENT CAMPAIGN

Before starting the measurements with the coated slabs, the symmetry of the waveguide has been tested without any slab. The time domain signal passing through the waveguide has been compared with the one passing in the same waveguide rotated by 90 degrees, keeping constant the direction of the electric field. The two signals in Fig. 11 are almost superimposed. This verifies that the waveguide is top-bottom and left-right symmetric.

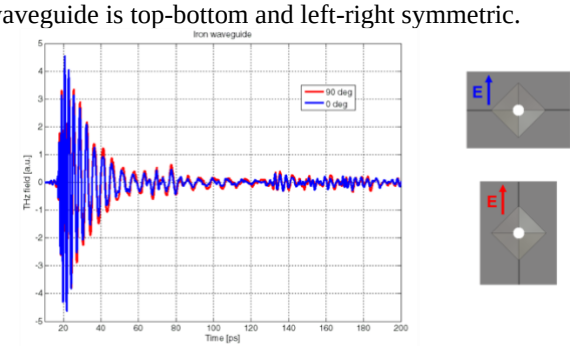

Figure 11: Test of the top-bottom left-right symmetries. The waveguide is 90 degree rotated (red) with respect to the normal use (blue). The polarization of the incident wave is taken constant.

After this check, the measurements have been performed on a waveguide with copper slab placed in the center as reference and then two different NEG coated copper slabs with 3.9 μm and 3.7 μm of coating thickness.
The spectrum of the first set of measurements in the frequency range of our interest is shown in Fig. 12

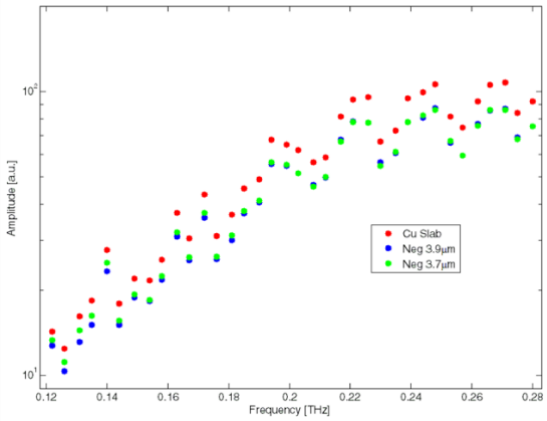

Figure 12: Fourier transform of three different measurements. Waveguide with copper slab (red), waveguide with NEG coated slab of 3.9 μm (blue) and waveguide with NEG coated slab of 3.7 μm (green)

The pattern shows the attenuation due to the presence of the coating on the two different slabs with the respect to the copper one. After preliminary settings of the lens and the maximization and symmetrization of the signal in the waveguide, we carried out 5 repeated measurements to evaluate the attenuation.
Furthermore, at the lowest frequencies, the noise distorts the signal and can introduce artificial phase discontinuities, making the phase unwrapping difficult and producing artifacts in the data spectrum [21]. For this reason, we discarded the data below 160 GHz, and in the following, all results are presented in the range 160 - 283 GHz.
The Fig.13 shows the conductivity evaluation for the NEG coating of 3.9 μm. The signal is compared with theoretical curves with different conductivity of the coating. The best fit, evaluated with the least square method, estimates $\sigma_{coat} = 7.9\ 10^5\ S/m$ with an error of 7%.

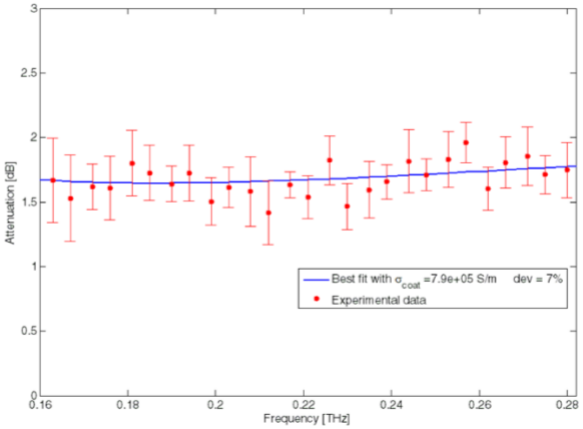

Figure 13: Attenuation on the NEG coated slab of 3.9 μm: averaged experimental data (red dots) and best fit curve (blue).

The measurements have been also performed with a different copper slab with a NEG coating of 3.7 μm.

In Fig.14 σ_{coat} is estimated to be 8.2 10^5 S/m. In this case the error is in the order of 10%, this high value could be caused by a peel-off on the extremal part of the foil.

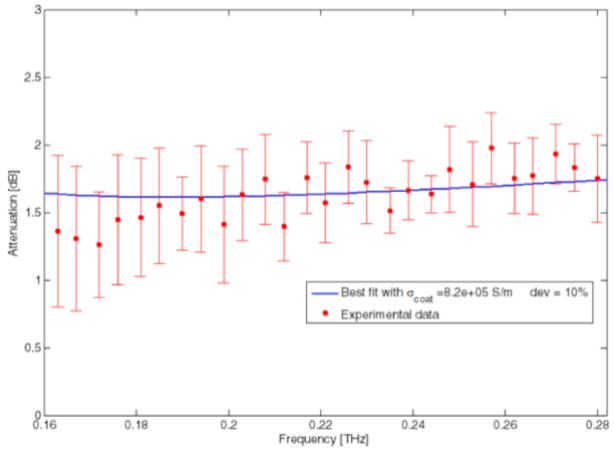

Figure 14: Attenuation on the NEG coated slab of 3.7 μm: averaged experimental data (red dots) and best fit curve (blue).

CONCLUSIONS

The comparison between the analytical evaluation and the numerical solution shows a good agreement. The developed analytical method is reliable. The advantages of the setup with the central coated slab are both intrinsic simplification of the manipulation of all the setup and the possibility to have a uniform deposition on the flat slab. The evaluated coating of the NEG sample for the two different slab goes from 7.9 10^5 S/m to 8.2 10^5 S/m with a maximum error in the estimation of the 10%.

The surface impedance is estimated in figures 15 and 16. That value is derived both from the performed measurements and from the best fit value of conductivity.

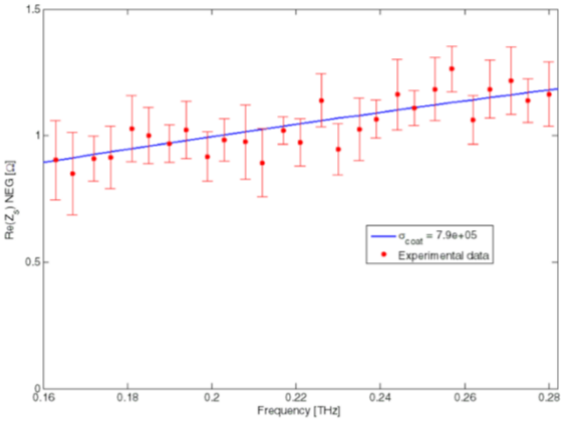

Figure 15: Surface impedance estimation of the 3.9 μm NEG coated slab: from averaged experimental data (red dots) and from best fit curve conductivity (blue).

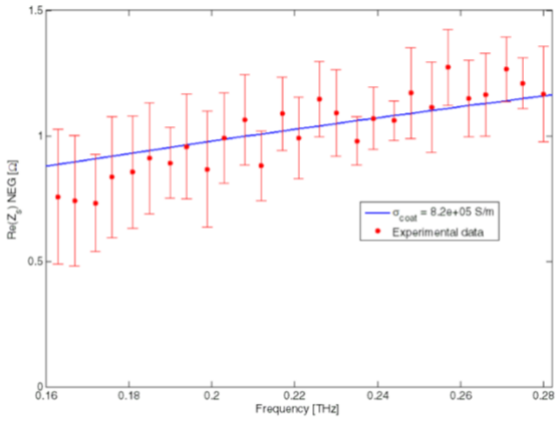

Figure 16: Surface impedance estimation of the 3.7 μm NEG coated slab: from averaged experimental data (red dots) and from best fit curve conductivity (blue).

After the Ecloud'18 workshop where this paper has been presented, a more complete version of the article and following studies on the methodology have been published in [22, 23].

ACKNOWLEDGEMENTS

This research was supported by CLIC project. The authors are deeply grateful to R. Corsini and Y. Papaphilippou for the opportunity given.

REFERENCES

[1] C. Yin Vallgren et al., Amorphous carbon coatings for the mitigation of electron cloud in the CERN Super Proton Synchrotron. Phys. Rev. ST Accel. Beams 14, 071001 (2011).

[2] C. Benvenuti, P. Chiggiato, F. Cicoira, and V. Ruzinov, Decreasing surface outgassing by thin film getter coatings Vacuum, 50, 57 (1998).

[3] M.A. Furman, Electron Cloud Effects in Accelerators, arXiv:1310.1706, Oct 2013, https://cds.cern.ch/record/1606733.

[4] G. Rumolo, F. Ruggiero and F. Zimmermann, Simulation of the electron-cloud build up and its consequences on heat load, beam stability, and diagnostics,Phys. Rev. ST Accel. Beams, 4, 012801, Jan 2001, 10.1103/Phys-RevSTAB.4.012801.

[5] R. Cimino, L.A. Gonzalez, R. Larciprete A. Di Gaspare, G. Iadarola and G. Rumolo, Detailed investigation of the low energy secondary electron yield of technical Cu and its relevance for the LHC, Phys. Rev. Spec. Top. Accel. Beams, 2015, https://cds.cern.ch/record/2136495

[6] M. Taborelli, P. Chiggiato, P.C. Pinto, P. Cruikshank, Nine years of carbon coating development for the SPS upgrade: achievements and heritage. CDS: CERN-ACC-2016-0010.

[7] M. A. Palmer, J. P. Alexander, M. G. Billing , J. R. Calvey & et al. in Proc. 1st Int. Particle Accelerator Conf., 23-28 May 2010, Kyoto, Japan (2010), 12511255.

[8] C. Benvenuti,R. Calder and O. Grobner, Vacuum for particle accelerators and storage rings, Vacuum, 37(6):699 - 707, 1987.

[9] C. Benvenuti, P. Chiggiato, F. Cicoira, and V. Ruzinov, Decreasing surface outgassing by thin film getter coatings, Vacuum 50, 57 (1998), electronic Properties of Metal/Non-Metal Microsystems.

[10] M. Migliorati, E. Belli and M. Zobov, Impact of the resistive wall impedance on beam dynamics in the Future Circular e+e- Collider, Apr 2018, American Physical Society, 10.1103/PhysRevAccelBeams.21.041001, https://link.aps.org/doi/10.1103/PhysRevAccelBeams.21.041001

[11] C. Benvenuti, P. Chiggiato, P. C. Pinto, A. Prodromides, and V. Ruzinov, Influence of the substrate coating temperature on the vacuum properties of TiZrV nonevaporable getter films, Vacuum 71, 307 (2003).

[12] E. Koukovini-Platia, G. Rumolo and C. Zannini Electromagnetic characterization of nonevaporable getter properties between 220330 and 500750 GHz for the Compact Linear Collider damping rings Phys. Rev. ST Accel. Beams 20, 011002 (2017)

[13] E. Koukovini Platia, L. Rivkin and G. Rumolo, High Frequency effects of Impedances and Coatings in the CLIC Damping Rings, 2015, https://cds.cern.ch/record/2056739

[14] M. Aicheler, P. Burrows, M. Draper, T. Garvey, P. Lebrun, K. Peach, N. Phinney, H. Schmickler, D. Schulte and N. Toge, A Multi-TeV Linear Collider Based on CLIC Technology: CLIC Conceptual Design Report, Geneva, CERN-2012-007, 2012, https://cds.cern.ch/record/1500095

[15] CST Microwave Studio - Getting started (2003)

[16] J. F. Johansson and N. D. Whyborn, The diagonal horn as a sub-millimeter wave antenna, May 1992, IEEE Transactions on Microwave Theory and Techniques

[17] S. Silver , Microwave antenna theory and design, IET, Stevenage, Electromagnetic waves, 1983, https://cds.cern.ch/record/212162

[18] C. S. Lee, and S. W. Lee, and S. L. Chuang, Plot of Modal Field Distribution in Rectangular and Circular Waveguides, Microwave Theory and Techniques, IEEE Transactions on Microwave Theory Techniques, Mar 1985, 10.1109/TMTT.1985.1132998.

[19] N. Marcuvitz, Waveguide Handbook, 1986

[20] G. Franceschetti, Electromagnetics: Theory, Techniques, and Engineering Paradigms, 1997, Springer US

[21] W. Withayachumnankul and M. Naftaly, Journal of Infrared, Millimeter, and Terahertz Waves 35, 610 (2014).

[22] Passarelli, A.; Bartosik, H.; Rumolo, G.; Vaccaro, V.G.; Masullo, M.R.; Koral, C.; Papari, G.P.; Andreone, A.; Boine-Frankenheim, O. Novel measurement technique for the electromagnetic characterization of coating materials in the sub-THz frequency range. Phys. Rev. Accel. Beams 2018, 21, 103101, doi:10.1103/PhysRevAccelBeams.21.103101.

[23] Passarelli, A.; Koral, C.; Masullo, M.R.; Vollenberg, W.; Lain Amador, L.; Andreone, A. Sub-THz Waveguide Spectroscopy of Coating Materials for Particle Accelerators. Condens. Matter 2020, 5, 9.

INSTABILITY CAUSED BY ELECTRON CLOUD IN COMBINED FUNCTION MAGNETS: THE FERMILAB EXPERIENCE

S. A. Antipov, CERN, Geneva, Switzerland

Abstract

Electron cloud can lead to a fast instability in intense proton and positron beams in circular accelerators. In the Fermilab Recycler the electron cloud is confined within its combined function magnets. We show that the field of combined function magnets traps the electron cloud, present the results of analytical estimates of trapping, and compare them to numerical simulations of electron cloud formation. The electron cloud is located at the beam center and up to 1% of the particles can be trapped by the magnetic field. Since the process of electron cloud build-up is exponential, once trapped this amount of electrons significantly increases the density of the cloud on the next revolution. In a Recycler combined function dipole this multi-turn accumulation allows the electron cloud reaching final intensities orders of magnitude greater than in a pure dipole. The multi-turn build-up can be stopped by injection of a clearing bunch of 10^{10} p at any position in the ring.

FAST INSTABILITY

In 2014 a fast transverse instability was observed in the proton beam of the Fermilab Recycler. The instability acts only in the horizontal plane and typically develops in about 20-30 revolutions. It also has the unusual feature of selectively impacting the first batch above the threshold intensity of $\sim 4\times10^{10}$ ppb (Fig. 1). The instability is triggered by longitudinal bunch compression (Fig. 2) that occurs due to bunch rotation at injection. These peculiar features suggest that a possible cause of the instability is electron cloud.

Early studies [1,2] indicated the presence of electron cloud in the ring and suggested the possibility of its trapping in Recycler combined function magnets. The presence of the cloud has also been observed in the Main Injector (MI) [3], which operates with similar beams, but it has never caused stability issues. The major difference between the MI (at the injection energy) and the Recycler seems to be the choice of technology for their dipole magnets: separate function (MI) vs combined function (Recycler).

The fast instability seems to be severe only during the start-up phase after a shutdown, with significant reduction being observed after beam pipe conditioning during beam scrubbing runs [4]. It does not limit the current operation with slip-stacking up 700 kW of beam power, but may pose a challenge for a future PIP-II intensity upgrade.

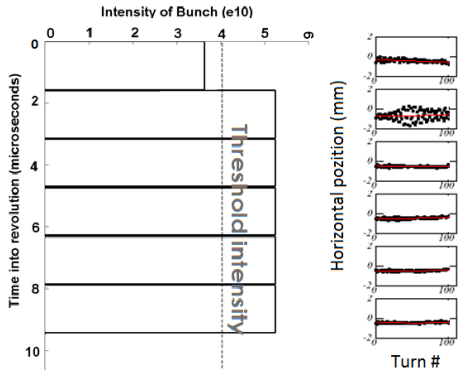

Figure 1: The first batch above the threshold intensity suffers the blow-up after injection into the ring [4].

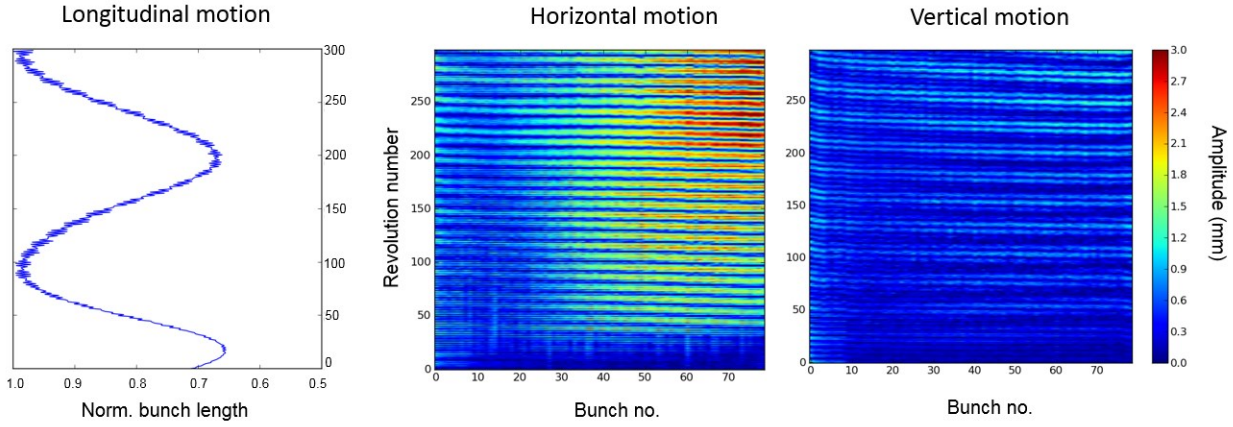

Figure 2: The instability mostly affects the last bunches in the train. It starts after the beam compresses longitudinally (left) and then becomes more severe after it compresses again, half a synchrotron period later. The color depicts the amplitude of the horizontal betatron oscillations of the beam center of mass as a function revolution number and position within the batch. The horizontal stripes are caused by our sampling of beam position once a revolution and appear at twice the betatron frequency: $2Q_x = 0.9$ or 1/10 turns. The data was gathered over 300 revolutions with the transverse dampers off. Beam: 1 batch, 80 bunches, 5×10^{10} ppb.

ELECTRON CLOUD TRAPPING

In a combined function dipole the electrons of the cloud move along the vertical field lines. This motion conserves their energy E and magnetic moment

$$\mu = \frac{mv_\perp^2}{2B} = const, \quad (1)$$

where $v_\perp$ is the component of the velocity normal to the magnetic field B. As an electron moves closer to a magnet pole it sees a higher B (Fig. 2) and it can reflect back if

$$E - \mu B = 0 \quad (2)$$

Alternatively, the electron will reflect back at the point of maximum magnetic field if the angle between the electron's velocity and the field lines is greater than:

$$\theta > \theta_{\max} = \cos^{-1}(\sqrt{B_0 / B_{\max}}). \quad (3)$$

Particles with angles $\theta_{\max} < \theta \le \pi/2$ are trapped by magnetic field. For Recycler magnets (Table 1), Eq. (3) gives a capture of ~10^{-2} particles of electron cloud, assuming uniform distribution.

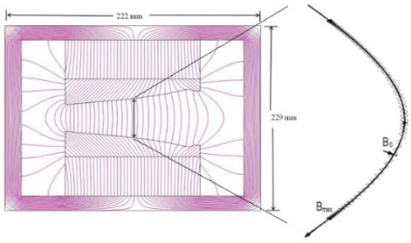

Figure 3: Electron cloud can get trapped by magnetic field of a combined function magnet.

Lifetime of the trapped cloud

Long-term confinement of the electron cloud can be affected by two effects: longitudinal drift and scattering. The drift is caused by the absence of magnetic field gradient in the longitudinal direction. The longitudinal drift velocity can be estimated as

$$v_d = \frac{1}{2}\omega_c r_c^2 \frac{B'}{B_0}, \quad (5)$$

where ω_c is the cyclotron frequency and r_c – the radius of the orbit. In the Fermilab Recylcer an electron cloud particle travels less than 2 cm during on beam revolution, much smaller than the length of its magnets. The drift can therefore be neglected.

The Coulomb scattering cross-section is

$$\sigma_C = \frac{4\pi}{9}\frac{e^4 \ln\Lambda}{(\mathrm{kT})^2} \sim 10^{-15}\,\mathrm{cm}^2 \quad (6)$$

The inelastic scattering cross-section for the energies in question is also of the order of 10^{-15}cm^2 [5]. Combining the two effects we obtain a lifetime ~ 10 ms for the electron cloud density n_e < 10^7 cm^{-3} and the residual gas pressure p ~ 10^{-8} Torr. Since the resulting lifetime of the electron cloud is much larger than the revolution period of 11 μs, all the trapped cloud will be present on the next turn.

Electron cloud clearing with a witness bunch

As mentioned above, the trapping requires at least two bunches: the first to kick the cloud and create the secondaries; and the second to stop a fraction of those. Therefore, a single bunch of high enough intensity does not trap the cloud but clears the aperture instead. This clearing bunch can be used to indicate the presence of the trapped electron cloud and measure its density [6] or to bring the electron cloud density below the threshold, stabilizing the beam.

NUMERICAL SIMULATION OF ELECTRON CLOUD BUILD-UP

We simulated electron cloud build-up over multiple revolutions in a Recycler dipole using the PEI code [7]. For a pure dipole field, the cloud rapidly builds up during the passage of the bunch train and then decays back to the initial ionization electron density in about 300 RF buckets, or ~ 6 μs (Fig. 6). When the field gradient is added, up to 1% of the electron cloud stays trapped, increasing the initial density on the next revolution. The final density, which the cloud reaches after ~ 10 revolutions, is two orders of magnitude greater than in the pure dipole case (Fig. 4). The resulting cloud distribution is a stripe along the magnetic field lines, with higher particle density being closer to the walls of the vacuum chamber (Fig. 5). The width of the stripe is approximately equal to the size of the beam and its intensity increases from turn to turn as the cloud builds up.

At lower densities ~10^{-2} of particles are trapped, which agrees with the analytic estimate (Fig. 4); as the density of electron cloud increases the trapping ratio goes down to ~10^{-3}, probably due to the space charge of electron cloud.

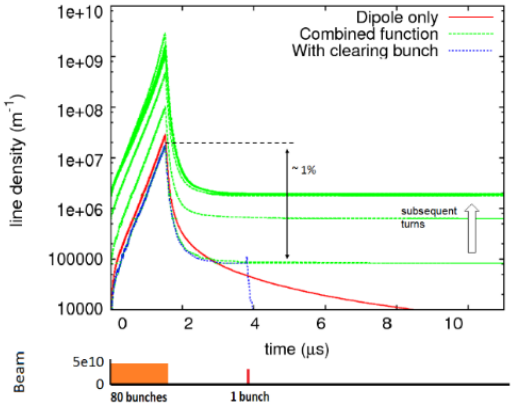

Figure 4: In a combined function magnet the electron cloud accumulates over many revolutions, reaching much higher line density, than in a dipole. A clearing bunch destroys the trapped cloud, preventing the accumulation.

A bunch of 5×10^{10} protons, added 120 RF buckets after the main batch, destroys the trapped cloud, preventing the multi-turn build-up (Fig. 4). First, one can see a small increase in the cloud density as the clearing bunch kicks the cloud and it reaches the vacuum chamber, producing the secondary electrons. Then, the density rapidly drops as these secondaries reach the aperture.

Table 1: Recycler parameters for simulation in PEI

Beam energy	8 GeV
Machine circumference	3.3 km
Batch structure	80 bunches, 5×10^{10} p
Tunes: x, y, z	25.45, 24.40, 0.003
RF harmonic, period	588; 18.9 ns
RMS bunch size: x, y, z	0.3, 0.3, 60 cm
Secondary emission yield	2.1 @ 250 eV
Density of ionization e^-	10^4 m^{-1} (at 10^{-8} Torr)
B-field and its gradient	1.38 kG, 3.4 kG/m
Magnet length	5 m
Beampipe	Elliptical, 100 x 44 mm

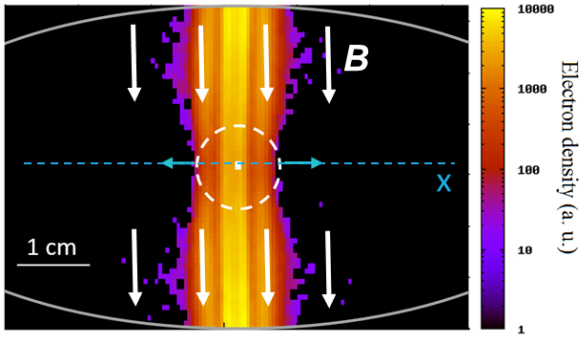

Figure 5: Electron cloud forms a stripe inside the vacuum chamber and its intensity increases with the number of turns. Its horizontal position – beam center (white dot). White circles represent 2 rms beam size.

ANALYTICAL MODEL

As a reactive medium, the electron cloud interacts with the beam similarly to a low-Q impedance [8-10]. Electron cloud instability in the presence of a strong magnetic field can also be calculated using assumptions about the shape of the wake as in [11]. Here we study the beam-cloud motion in a strong dipole field, modelling the motion of the cloud 'stripe' as the mobility term, similar to the work [12]. This approach does not require making initial assumptions about the form of the electron cloud wake or its impedance.

First, consider a round coasting proton beam travelling in a ring with the beam centroid position at an azimuthal angle θ and time t being $X_p(t, \theta)$. Further, assume that the beam travels at a constant azimuthal velocity around the ring ω_0 and use a smooth focusing approximation with a betatron frequency ω_β. For simplicity, one can assume that the ring is uniformly filled with electron cloud of a constant density n_e, which forms a column of the same transverse size as the proton beam, and is located at a horizontal position X_e. Because of the vertical dipole field, the individual electrons of the cloud cannot drift horizontally, but the position X_e can change as some regions build up and others decay, following the transverse motion of the proton beam (Fig. 5). The characteristic rate of this slow motion of the electron cloud λ is then the rate of its build-up: $\lambda \sim 1/\tau_{buildup}$.

For small oscillation amplitudes we can assume the electron-proton interaction force to be linear in displacement. Then the coupled collective motion of the beam and the electron cloud is described by the following system of equations:

$$\begin{cases} \dfrac{d^2}{dt^2}X_p + \Gamma\dfrac{d}{dt}X_p = -\omega_\beta^2 X_p + \omega_p^2(X_e - X_p), \\ \dfrac{\partial}{\partial t}X_e = \lambda(X_e - X_p), \end{cases} \tag{7}$$

where d/dt stands for $(\partial/\partial t + \omega_0\partial/\partial\theta)$, Γ is the rate of Landau damping defined below and the coupling frequency ω_p is approximated as

$$\omega_p^2 = 2\pi n_e r_p c^2/\gamma \tag{8}$$

where r_p is the classical proton radius and γ – the relativistic factor. The linear damping term Γ in Eq. (7) arises from the spread in betatron frequencies for particles oscillating with different amplitudes. The characteristic rate of the Landau damping can be estimated as

$$\Gamma \sim \omega_\beta \Delta Q_x / Q_x, \tag{9}$$

where Q_x is the horizontal tune and ΔQ_x is its rms spread.

Looking for solutions of Eq. (7) in a form $X_{e,p} \propto \exp[-i(\omega t - k\theta)]$, where $\omega = k\omega_0 + \omega_\beta + \Delta\omega$ and k is an integer mode number, one obtains an equation for the complex mode frequency shift:

$$\Delta\omega \approx \frac{1}{2}\left[-i\Gamma + \frac{\omega_p^2}{\omega_\beta}\frac{\omega(\omega - i\lambda)}{\lambda^2 + \omega^2}\right] \tag{10}$$

The most unstable mode with the largest growth rate $\gamma = \mathrm{Im}(\Delta\omega)$, corresponds to a wave number

$$k_{\max} = \lambda/\omega_0 - Q_x. \tag{11}$$

The tune shift of this mode is

$$\Delta Q_{\max} \approx \frac{1}{4Q_x}\frac{\omega_p^2}{\omega_0^2}. \tag{12}$$

The threshold electron cloud density $n_{e,thr}$ can be found from the condition $\gamma_{max} = 0$, which yields

$$n_{e,thr} = \gamma\omega_\beta\Gamma/\pi r_p c^2. \tag{13}$$

Note that in this simple model we do not consider the electron cloud's contribution to Landau damping, which may arise from the nonlinear spread of the betatron tunes, created by the cloud.

Knowing the complex frequency shift $\Delta\omega$ we can find the impedance of the cloud as (see for example [13] Eq. (6.262)):

$$Z(\omega) = iZ_0\frac{\gamma T_0^2\omega_\beta}{2\pi N r_p}\Delta\omega, \tag{14}$$

where N is the number of protons in the ring and Z_0 is the vacuum impedance.

In the case of a bunched beam, in a rigid bunch approximation with the bunch spacing of τ_{rf}, one can use the impedance of the most unstable mode $Z_{\max} = \mathrm{Re}[Z(\omega_{\max})]$ to compute its growth rate (for derivation see [14]):

$$\gamma_{b,\max} \approx \frac{L}{C}\frac{8\pi r_p N_b \beta_x}{\gamma c \tau_{rf}}\frac{Z_{\max}}{Z_0} - \frac{\Gamma}{2}, \qquad (15)$$

where C is the ring circumference and L is the total length of the magnets. For the Recycler $L/C \approx 1/2$.

Instability in Recycler

In order to use the model and estimate the parameters of the fast instability in Recycler one needs to know the density of the electron cloud and the rate of its build-up. We obtained these quantitative parameters by measuring the betatron frequency shift and comparing it with the build-up simulations. We injected one batch of 80 proton bunches of 5×10^{10} ppb and measured the shift of the horizontal tune as a function of bunch number. Because the positive horizontal tune shift is a distinctive feature of the electron cloud, it allowed us an estimation of the cloud density. In order to check with the simulation the cloud density both within the high-intensity batch and after its passage we put a witness bunch of low intensity -0.8×10^{10} p, insufficient to clear the electron cloud, at different positions behind the main batch.

The experimental results are in good agreement with the simulation (Fig. 6) and the small discrepancies may come from the multiple assumptions used in Eq. (15). The resulting dependence allows the estimation of the maximum density of electron cloud $n_e \sim 6\times10^{11}$ m^{-3}. The density increases by an order of magnitude in 40 bunches (800 ns) and falls after the beam has passed in 10 bunches (200 ns). The characteristic rate of the exponential build-up is 2.65×10^{6} s^{-1}.

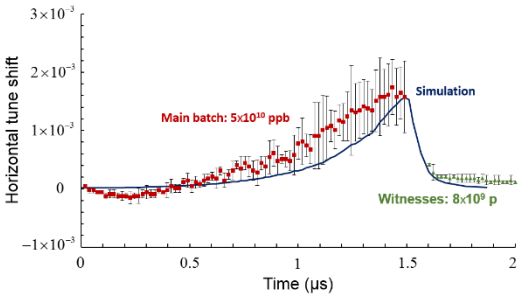

Figure 6: Results the of electron cloud simulation agree with the measured horizontal tune shift. Beam: 5×10^{10} ppb, 80 bunches, followed by one witness bunch of 0.8×10^{10} p at various positions. The gap between the high-intensity batch and the witness is due to the rise-time of the injection kickers.

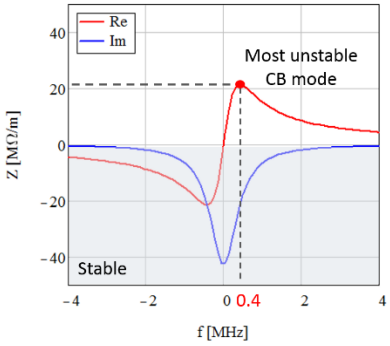

Figure 7: Real and imaginary parts of impedance as a function of a mode angular frequency ω.

Figure 7 shows an effective electron cloud impedance corresponding to the estimated cloud density, estimated using Eq. (14). Using Eq. (15) we obtain the growth rate of 3.3×10^{-2} and the characteristic time of the instability of around 30 turns for a bunch intensity of 5×10^{10} ppb. The threshold electron cloud density, calculated using Eq. (13), $n_{e,thr} = 8.2\times10^{10}$ m^{-3}. According to numerical build-up simulations, this density is achieved at the proton intensity of about 4.5×10^{10} ppb, which is also consistent with experimental observations.

CONCLUSION AND OUTLOOK

Combined function magnets are widely used in the present day machines. Because of the gradient of the magnetic field (which provides the focusing) the electron cloud can be trapped in the magnetic field of such magnets. These trapped particles make it possible for the cloud to accumulate over multiple revolutions, possibly leading to a fast transverse instability.

We have created an analytical model that allows the estimation of the amount of the cloud captured in the magnet. We have shown that up to 1% of the electron cloud can be trapped in the magnetic field of combined function magnets of FNAL Recycler. This fraction of trapped particles will go down for higher intensities in Recycler.

Numerical simulation in PEI agrees with the analytical estimate and confirms that the trapping significantly affects the density of the electron could. It allows the cloud to accumulate over multiple revolutions reaching a density much higher than in a pure dipole. For the parameters of Fermilab Recycler with one batch of normal intensity the cloud reaches ~ 10^9 m^{-1} in a combined function magnet compared to ~ 10^7 m^{-1} in a dipole of the same field strength. An addition of a clearing bunch destroys the trapped cloud, preventing the multi-turn accumulation.

An instability similar to Recycler one occurs in the CERN PS, which also utilizes combined function magnets. The instability was observed in operation before extraction when bunch length is compressed from 11 to 4 ns and in a dedicated study where the beam was stored for a long time – 100 ms at 11 ns bunch length [15,16]. The instability does

not limit the operational performance since normally the beam does not interact with the cloud for a sufficiently long time. Although the trapped cloud might play a minor role in the PS role thanks to the fact that nearly all machine is full, leaving little time for the cloud to decay before the next revolution. A thorough analysis may be needed to identify at which parameters the trapped cloud can pose a limitation.

ACKNOWLEDGMENT

This work was performed as a part of PhD thesis research at Fermilab. The author is grateful numerous members of Fermilab Accelerator Division for their contribution t they study and especially to the PhD advisor S. Nagaitsev, and would also like to thank K. Ohmi (KEK) for his help with PEI code. Fermilab is operated by Fermi Research Alliance, LLC under Contract No. DE-AC02-07CH11359 with the United States Department of Energy.

REFERENCES

[1] J. Eldred, *et al*., in *Proc. HB'14,* pp. 419-427, 2014
[2] S. A. Antipov, et al., in *Proc. IPAC'16*, pp. 1728-1730
[3] N. Eddy *et al.*, in *Proc. PAC'09,* 2009
[4] J. Eldred, "The High-Power Recycler: Slip-stacking & Electron Cloud", Fermilab, Nov. 2015
[5] A. D. MacDonald, *Microwave Breakdown in Gases*, New York, NY: Wiley, 1966
[6] M. Billing *et al., Phys. Rev. ST Accel. Beams* vol. 18, p. 041001, Apr. 2015
[7] K. Ohmi, CERN Rep. CERN-2013-002, pp.219-224
[8] K. Ohmi and F. Zimmermann, *Phys. Rev. Lett.* vol. 85, pp. 3821–3824, 2000
[9] K. Ohmi, F. Zimmermann, and E. Perevedentsev, *Phys. Rev. E* vol. 65, p. 016502, 2001
[10] A. Burov, FERMILAB-PUB-13-005-AD, 2013
[11] V. Balbekov, FERMILAB-FN-1001-APC, 2015
[12] G. Arduini *et al.*, in *Proc. PAC'03*, pp. 3038-3040, 2003
[13] A. Chao, *Physics of Collective Beam Instabilities in High Energy Accelerators*, Ney York, NY: Wiley, 1993
[14] Yu. Alexahin, FNAL Beams-doc-4863-v1, 2015
[15] R. Cappi *et al., Phys. Rev. ST Accel. Beams* vol. 5, 2002
[16] G. Iadarola *et al.*, in *Proc. IPAC'13*, 2013

SECONDARY ELECTRON YIELD OF SURFACES: WHAT WE KNOW AND WHAT WE STILL NEED TO KNOW

M.Taborelli, CERN European Organization of Nuclear Research, Geneva, Switzerland

Abstract

The electron cloud phenomenon in particle accelerators is related to the secondary electron yield of the surfaces in line of sight of the beam. At present, advanced models to predict electron cloud through simulation codes are available and they rely either on experimental data or on parametrizations of the various quantities and dependencies describing the behaviour of electrons impinging on and emitted from the surface. In the present contribution, we review what is well established about these dependencies and which measurements should still be performed.

INTRODUCTION

It is well accepted that the Total or the Secondary Electron Yield (TEY, SEY) of the exposed surfaces is one of the main quantities governing electron cloud and multipacting. Powerful simulation algorithms have been developed with the aim of predicting the maximum operating power of RF devices [1] or the maximum stable particle beam intensity [2]. The algorithms must rely on the physics of the generation and emission of secondary electrons from solids. Ideally for a simulation, the quantity $I(E_s, \theta_{emis}, E_p, \theta_{inc})$ is necessary for the relevant range of energies and angles, where I is the emitted electron intensity for a fixed impinging intensity, E_p is the kinetic energy of the impinging electrons with respect to the vacuum level of the surface, θ_{inc} is the angle if incidence, E_s the energy of emission and θ_{emis} the angle of emission.

Even if the fundamental principles of electron scattering are known, there are no simple exact analytical expressions for the various energy and angle dependencies. Only recently calculations of the yields based for instance on dielectric theory [3, 4, 5], can predict the absolute TEY(E_p) of ideally clean and pure surfaces including a basic model of surface roughness [3]. These are different from the air exposed oxidised and contaminated surface of real devices. The values and shapes of the curve of TEY for a material can change markedly depending on its surface state. For instance for OFE copper the TEY curve can change over a wide range: a typical as-received (air exposed and chemically cleaned for UHV applications) surface of technical copper will have a δ_{max} around 2.0 [6], a freshly electropolished surface has a value of 1.6 [7], but a rough surface can [8] exhibit a δ_{max} as low as 1.0. These values differ significantly from the value of 1.4 [6] for a sputter cleaned surface in vacuum. It is interesting to remark that the range of values mentioned just above cover the range of δ_{max} including those leading to severe e-cloud down to those which suppress e-cloud in accelerators.
Therefore, the electron cloud simulations use experimental data, when available, or parametrizations based on the experimental data, which are in some cases supported by phenomenological models. Typically, parametrizations are used for the primary electron energy dependence of the TEY, for its dependence on impinging electron angle and for the energy and angle distribution of the emitted electrons. Another variable, which influences the TEY, is the history of the surface in terms of received electron or photon irradiation dose and this cannot be directly included in a parametrization.

The present contribution is a tentative to illustrate what is available and how well it describes the real situation. Only metal surfaces will be discussed, since they are the most relevant in the case of particle accelerators.

TEY, PARAMETRIZATION AND MEASUREMENT

1. TEY parametrization:

The TEY(E_p, θ_{inc}) is the ratio between the total number of electrons emitted by the surface and the number of electrons impinging at an angle θ_{inc} and energy E_p. For the emitted electrons the simplest distinction can be made between elastically scattered electrons, El(E_p), emitted at the same energy as E_p, and those emitted at lower energy, which were excited or scattered inelastically, SEY(E_p) (some authors introduce in addition the backscattered electrons, which are in the present case included in the SEY for simplicity). This leads to (we skip in the following of this section θ_{inc} taken as fixed, for instance as zero for normal incidence):

$$TEY(E_p) = SEY(E_p) + El(E_p) \quad (1)$$

In several phenomenological models the values of the maximum of the TEY(E_p), δ_{max} and the energy at which the maximum occurs, E_{max}, are used to fully characterize the curve and enable a scaling of the SEY(E_p) curve (examples in [9, 10]) with respect to normalised variables:

$$\frac{SEY(E_p)}{\delta_{max}} = g\left(\frac{E_p}{E_{max}}\right) \quad (2)$$

However, $g(x)$ depends on the surface condition (chemistry, roughness) and a technical surface of an accelerator component is composed of several layers (the underlying metal, an oxide layer, some surface contamination….). In practice the parametrization of the experimental SEY curve with more variables is used, as for instance [11]:

$$\frac{SEY(E_p)}{\delta_{max}} = \frac{s\frac{E_p}{E_{max}}}{s-1+\left(\frac{E_p}{E_{max}}\right)^s} \quad (3)$$

Where *s* is a fit parameter, often chosen in the range 1.35-1.45.

The relevant range of E_p is limited to about 1keV, corresponding to the maximum energy of the electrons impinging on the beampipe, except for machines which very short and highly charged pulses as the J-Parc accelerator, where the relevant range rises up to some keV [12]. On the other side, at low primary energy, below some tens of eV, the possible excitation channels for secondary electrons decrease and the elastic electrons contribution *El(Ep)* plays an important role. They must therefore be added to the SEY(*Ep*) to get the curve TEY(*Ep*).

Two approaches are common [13, 14] for the parametrization of *El(Ep)*. The first approach starts from the reflectivity of a free electron wave function at a one-dimensional step-like barrier (the surface). In order to match experimental data, the barrier height E_0 must assume values, which are very high (as 150eV) compared with typical work function values. A further coefficient R_0 is added to tune the reflectivity at zero kinetic energy. So, the resulting yield of elastic electrons is:

$$El(E_p) = R_0 \left(\frac{\sqrt{E_p} - \sqrt{E_p + E_0}}{\sqrt{E_p} + \sqrt{E_p + E_0}} \right)^2 \qquad (4)$$

Where R_0 and E_0 are fit parameters. In a second approach the experimental data are fitted with a multi-parameter development in powers of ln(E_p):

$$\ln f = \\ = 1.59 + 3.75 \ln E_p - 1.37(lnE_p)^2 + 0.12(lnE_p)^3 \qquad (5)$$

Where the numerical coefficients are those reported in the reference [14] for "universal function" and *f* is the fraction of elastic electrons:

$$E_l(E_p) = f \cdot TEY(E_p) \qquad (6)$$

or in an equivalent way:

$$TEY(E_p) = \frac{SEY(E_p)}{1-f} \qquad (7)$$

In fact the coefficients in (5) are material dependent and different values were used for instance for copper [15].

The importance of acquiring experimental data on a specific individual sample is clear when considering the difficulties to extrapolate from first principle calculations or parametrization. At present there is no model, which can deliver the correct TEY curve starting from a given surface composition, roughness and received dose.

2. TEY measurements:

In experimental measurements the TEY(E_p) and SEY(E_p) are often used with equivalent meaning, since above a primary energy of some 100 eV the main contribution to the yield is given by secondary electrons and only recently measurements are common below 100eV. In particular, since the maximum, δ_{max}, is generally above 200 eV, we can consider that the maximum of TEY and SEY is the same within a negligible error. In principle, the aim of the experiments is to measure the primary energy dependence of all emitted electrons, the TEY, since all of them contribute to the multipacting effects.

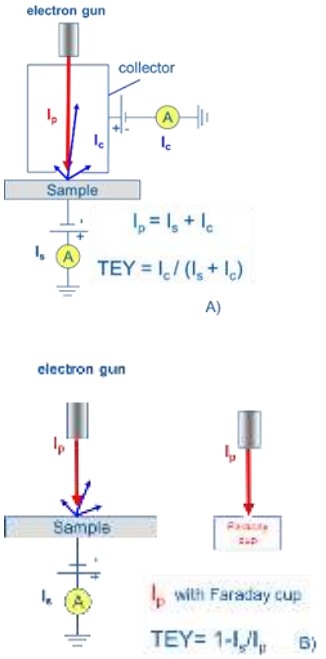

Figure 1: Sketch of the most common measuring modes for the electron yield: A) With a collector, to measure simultaneously the absorbed and emitted current. B) Without collector and with the total impinging current measured either by a Faraday cup or by reversing the bias. The symbols represent total primary current I_p, sample current I_s, collector current I_c and electron yield TEY.

Most of the measurements for simplicity are performed at normal incidence (θ_{inc} =0). TEY curves are acquired routinely in several laboratories for primary energies above 100eV. Recently the measurements of the very low primary energy part of the TEY curve in several labs have achieved reliability down to few eV (measuring in this range is made difficult by the sensitivity of slow electrons to parasitic electric and magnetic fields). The instruments measuring the TEY are based on an electron gun at variable energy and a sample facing the gun. They can be divided in two main categories: a) those measuring simultaneously the current absorbed by the sample and the current emitted by the surface in a collector [6] and b) those measuring in separate runs the current absorbed by the sample and the total current from the electron gun. In the first method a negative bias of few volts constantly applied on the sample helps to avoid recollection of the slow secondary electrons on the sample. The total emitted current is measured simultaneously in a collector, which is

mounted between gun and sample and is coaxial to the gun. In the second method the absorbed current is measured in the same way as in the first case, but the total current is obtained separately, either through a Faraday cup or by applying a sufficiently high positive bias to attract all the electrons on the sample. The two methods are sketched in figure 1. The method of measurement without collector sacrifices the advantage of measuring simultaneously the necessary currents, but gains the advantage of enabling measurements at very low primary energy by placing the electron source close to the sample surface [16], which is important for measurements at low kinetic energy. A more complex scheme based on time-of-flight is presently under development for measurements in a magnetic field [17]. In the case of air exposed samples, which is the initial typical condition for components installed in an accelerator, it is important to keep a low dose of irradiation on the sample. It is well known that for air exposed samples the TEY value starts to decrease for doses above 10^{-6} C/mm^2 at impinging energies above 50eV [18]. In order to limit the delivered dose during measurements the beam is pulsed or deviated away from the surface before and after each point of data acquisition. The methods of measurement described above provide a precise, but not accurate value of the absolute yield, as explained in the following. The typical relative error, generated by the relative error on the measured currents, on a single curve is of few % of TEY (typically better than 0.05 for a yield in the usual range, namely below 2). This means that the reproducibility (precision) on a sample spot is very high and this enables for instance to identify weak differences in SEY of about 0.1 in neighbouring regions of the same sample [19]. However, the absolute value of the TEY cannot be measured with the same accuracy and depends slightly on the geometry of the measuring device, which influences the efficiency of the collection of electrons at the various energies. The accuracy in this case is rather around 10% , depending on the considered E_p. An example of the difference between two measuring devices is shown in figure 2.

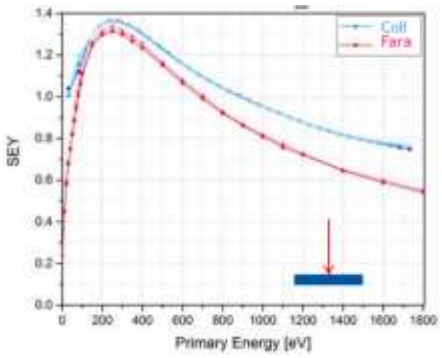

Figure 2: Secondary electron yield curves for a thin film of carbon as a function of primary energy for the same sample measured with a collector system and a Faraday cup system.

For this reason comparison between different laboratories should be taken with care. Even defining a suitable reference sample to compare devices is not a simple task, possible candidates being amorphous carbon coatings, which are rather insensitive to air exposure or surfaces prepared in situ in vacuum with a very well defined procedure.

The vacuum system of several modern accelerators, as for example the beamscreeen of the arcs of LHC (5-20 K), operates at cryogenic temperature, because of the use of superconducting magnets. The SEY of a copper surface at low temperatures has been shown to have the same value as at room temperature [7, 20]. Indeed, no intrinsic dependence on temperature is expected on metals, since the excitations producing secondary electrons involve energies of several eV and are not affected by changes in electron band occupancy within a range of K_BT. Moreover, the scattering governing the mean free path of secondary electrons, at energies where they can escape the solid, are dominated by electron-electron and electron-plasmon interactions and phonons can be almost neglected.

3. Scrubbing and conditioning:

The decrease of δ_{max} with increasing electron irradiation dose [18,21] on an as received surface is well established from laboratory measurements. This phenomenon is called conditioning or beam scrubbing and for copper it can decrease the δ_{max} down to 1.15 for a dose above 10^{-3} C/mm^2 [19]. The kinetics of the decrease and the ultimate value of δ_{max} depend on the impinging electron energy [18]. The effectiveness of the conditioning depends on materials. For copper surfaces the essential ingredients of conditioning are the electron stimulated desorption (ESD) and the modification of the carbon species on the surface, from hydrocarbon-like to graphitic-like [18, 22, 23]. For stainless steel, scrubbing has been observed in accelerators [24] and in the lab, however with a marked scattering in the dose necessary to reach the lowest SEY [25]. For aluminium and its alloys, the conditioning has a minimum as a function of dose, with a δ_{max} which remains far above 1 [26]. The influence of the surface contamination, the importance of the carbon from air exposure and the origin of the carbon, which is observed to grow in some cases are still topics under investigation.

From the few measurements of conditioning of copper at cryogenic temperatures in the laboratory there are no indications that the mechanism differs intrinsically from the room temperature case [27]. This is plausible considering that the processes inducing conditioning have thresholds of some tens of eV (for the kinetic energy of the impinging electron), like ESD and molecule cracking. The only possible influence of the temperature might come from the most effective physisorption compared to room temperature. At such low temperature (5-20 K) most of the residual gas species condense on the surface, except helium and hydrogen, the latter forming only sub-monolayer coverages. On one hand adsorbates can strongly modify the SEY [7, 20] of the surface. On the other hand the longer sojourn time of the molecules, compared with room temperature, could increase the amount of adsorbates available for interaction with the impinging electrons and therefore modify the surface chemical composition as a function of

dose. The comparison of laboratory measurements with the real case of a cryogenic accelerator vacuum system is difficult from this point of view. In the laboratory in most of the configurations a small cold sample is acting as a cryopump in a room temperature vessel, whose walls are source of gases, whereas in an accelerator cryogenic vacuum system the entire environment is cold and gases can come only from particle induced desorption. The domain of conditioning at low temperature in presence of gases is still under investigation [28]

ENERGY SPECTRUM OF EMITTED ELECTRONS

In a calculation of the electron multiplication in a beampipe it is necessary to know the detailed energy distribution of the emitted electrons, in order to recalculate their impact energy on the opposite surface. There is no simple theory describing the shape of the spectrum. For the low E_s energy part including the secondary electrons, various parametrizations have been proposed [29, 14, 30]. The simplest one is a decay with a power law of the energy corrected with the work function [29], which was derived from a phenomenological model. To obtain a better matching with data Maxwell-Boltzmann distribution was proposed, which evolved in a Gaussian distribution [14, 11] with energy and finally with the logarithm of energy [30]. This gives the following expression (total integral spectrum normalized to 1):

$$I(E_p, E_s) = \frac{2}{E_s \sigma\sqrt{2\pi}} e^{-\frac{(\ln(E_s-\mu))^2}{2\sigma^2}}$$

Where μ and σ are defining the maximum and the width of the curve, without further physics meaning. We remark that there is no dependence from E_p, which is a reasonable approximation when the secondary electrons are produced with a large number of collisions, as for E_p above some hundredths of eV (confirmed experimentally above 1keV for instance for Si [31]).

The measurement of I(E_s, E_p) can be carried out in principle in any surface analysis system with an electron gun and an energy analyser, but three aspects should be considered. First, the angle of collection depends on the type of energy analyser. In the case of a retarding field analysers (RFA) a large collection angle is available, ideally 180 degrees (in practice some 110 degrees), whereas hemispherical analysers collect a small solid angle. Therefore, in the latter case the total number of emitted secondary electrons must be extracted by assuming a cosine distribution (see next section: Angle dependence) of the secondary electron emission. There is no such simple scaling for elastically scattered electrons. Second, the electron energy analysers have an energy dependent transmission function, which should be calibrated or calculated. Only in this way the spectrum will be weighted with a constant amplification factor or sensitivity. Third, the acquisition of a spectrum or of many spectra for different *Ep* values, shall be done by limiting the irradiation dose to the surface to avoid conditioning. This last point is not relevant for a sputter cleaned surface, but is particularly important for an as-received surface.

For copper only few measurements of this spectrum I(E_s, E_p) for normal incidence and a calibrated transmission function exist. A set of data obtained with a RFA for a fully conditioned copper surface at cold are presented in [32]. Other measurements on a larger series of as-recieved metals were taken, for E_p=1keV and E_s up to 50eV, with a cylindrical mirror analyser (the intensity is multiplied by the kinetic energy to compensate for transmission) [31] show that the shape of the intensity decrease as a function of E_s strongly depend on the material (see steel vs other metals). Obviously, the spectrum for a specific surface should be measured on purpose.

ANGLE DEPENDENCE

1. Incidence angle dependence of the SEY :

For a flat surface a more grazing incidence angle increases the SEY. An off-normal angle of incidence reduces the depth at which the primary electrons excite the secondary electrons in the solid and therefore the latter can more easily escape than for normal incidence. Compared with the normal emission case, the energy of the maximum, E_{max}, shifts to higher energy, since the secondary electrons still manage to escape the solid even when excited by higher primary energies. This effect can be strongly reduced on a rough surface, since at microscopic level electrons encounter a wide distribution of angles of incidence. For an as received and air exposed metallic surface the change of depth of the excitation of secondary electrons translates also in a different balance in the number of electrons excited in the metal, in the oxide and in the overlayer of airborne contamination.

In a parametrization of the SEY(E_p) curve like (3) one can introduce an incident angle dependence for $\delta_{max}(\theta_{inc})$ and $E_{max}(\theta_{inc})$ to obtain the full curve for any angle. Empirical formulas for such dependences can be found with the introduction of more [11] or less parameters, some including also the possibility to tune for the surface roughness [33]. They are based on available experimental data of SEY measured on different materials, as TiN in the case of [11] and metallic molybdenum [34] in the case of [33]. In another approach the angle dependence is included in an empirical model of SEY(E_p), by considering that the range of the incident beam changes with the cosine of the angle [35]: the scaling of the SEY(E_p) curve is a little more complex in this case. The influence of the different parametrization of the θ_{inc} angle dependence in the electron cloud simulation is partly illustrated in reference [36, 37].

The amount of experimental data of $\delta_{max}(\theta_{inc})$ is scarce. Some are collected in figure 3, where the maximum yield measured at various incidence angles is normalised by the δ_{max} at normal incidence (data quoted as belonging to rough surfaces were excluded). This illustrates the possible error when extrapolating from normal incidence data: the angle dependence of reference 33 for a smooth surface

seems to be too weak in most of the cases. The spread increases by increasing the incident angle.

In the electron cloud case the secondary electrons emitted from the wall are accelerated toward the opposite surface of the beampipe by the beam potential. For sufficiently strong dipole magnets the trajectory of the electrons is a cyclotron rotation with the axis parallel to the magnetic field and the speed component parallel to this axis is accelerated. In such a way the impact angles are restricted to a cone close to normal incidence and only the SEY dependence at small angles is important for the e-cloud simulations. This is obviously not true for drift spaces and quadrupoles.

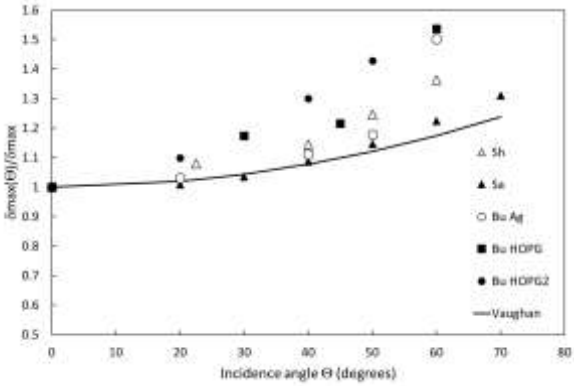

Figure 3: Relative maximum yield as a function of incidence angle. The line corresponds to the model of reference 33, for a smooth surface. The dots are data taken from references 34, 35, 38

In principle a measurement of the SEY(E_p) is possible in most of the set-ups by tilting the sample, but the result should be evaluated with care. In most of the experimental set-ups the sample is biased (either to collect the electrons, or to slow them down, or to avoid recollection of the secondaries) and the electrons do not move in a free field region between gun and sample or between collector and sample.

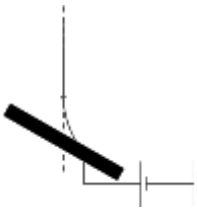

Figure 4: Deviation from straight line for electrons impinging on a sample with a negative bias voltage.

The electric field configuration changes when the sample is rotated with respect to the electron beam. As shown in figure 4 for a sample at negative bias, this situation affects the effective impinging angle of the beam. A suitable correction should be introduced in the measured dependence based on trajectory calculation, which is in practice complicated by the shape of the sample holder. It is evident that such an effect is more marked for electrons, which are slow compared to the applied bias potential.

2. Incidence and emission angle dependence of the distribution of emitted electrons:

The TEY includes the secondary and elastically scattered electrons, as defined in (2). The secondary electrons are emitted along a distribution, which is very close to a cosine law [10]. This is intuitive if one considers a large amount of collisions, so that the memory of the impinging beam is lost and electrons arrive at the surface from the bulk without preferential direction. The angle dependence of the elastic electrons, $El(E_p, \theta_{inc})$, is not the same as for inelastically scattered. No scaling or simple parametrization exists for this quantity. Elastic scattering as a function of incidence and emission angle at energies above about 100 eV can be calculated from the electron atom scattering cross section [3, 4, 5] in a Monte Carlo calculation, or assuming a single large angle scattering [39] or up to double scattering [40]. A single atomic scattering depends only on the scattering angle between impinging beam and emitted electrons, and is independent of the orientation of the surface. In this sense for angles not too far from normal incidence one can take this approximation [figure 1 d) and e) in 5]. The angular distribution is clearly energy dependent (as visible in all the references just quoted above) and, being related to the atomic structure, it is strongly element dependent. Unfortunately, the extrapolation of the atomic cross sections to energies below 100 eV is no longer meaningful, since the electron wavelength approaches the interatomic distance, atoms cannot be treated as being isolated and band structure and diffraction effects play a role. Measurements of $El(E_p, \theta_{inc})$ are rare and $El(E_p, \theta_{inc}, \theta_{emis})$ are difficult, since they require to change independently the angle between primary beam and electron analyser. A nice solution is adopted in [41] where the relative (arbitrary units) distribution of elastically reflected electrons as a function of primary energy and emission angle is extracted from the fluorescence intensity on a LEED screen. The dataset shows the θ_{emis} angle and E_p dependence for clean polycrystalline Al, Cu , Pt and Au [fig 3 in 41] for normal incidence. The intensity does not exhibit a monotonic behaviour with respect to E_p and the increase below 100eV is not a general feature. Moreover, for normal incidence the scattered intensity is generally stronger at small θ_{emis} angles close to surface normal (backscattering). Also for elastic scattering the presence of adsorbates or oxides on the surface can change the picture completely, since the elastic mean free path is limited to few atomic layers.

MAGNETIC FIELD

The question about the influence of the magnetic field on TEY is motivated by the presence of dipole and quadrupole fields in most of the regions of circular accelerators. Axial magnetic fields (solenoids or permanent magnets) are often exploited to eliminate the electron cloud effect, since they avoid that emitted secondary electrons cross the

vacuum chamber and promote multiplication [42, 43]. For dipole fields we can consider the case of a uniform field perpendicular to the surface. In this case, the electrons cross the vacuum chamber on a helical trajectory with the axis perpendicular to the surface. Only the direction of the speed component parallel to the surface is modified and the speed vectors rotates on a cone (figure 5) for a cyclotron orbit (we neglect here for simplicity the effect of the acceleration by the field of the beam, but the argument does not change). Thus, the angle of incidence with respect to the surface normal is not modified by such a magnetic field. For this reason also the depth of excitation of secondary electrons is not modified: the penetration of the primary electron is just the time between scattering events times the speed component perpendicular to the surface and both quantities are not modified by the magnetic field.

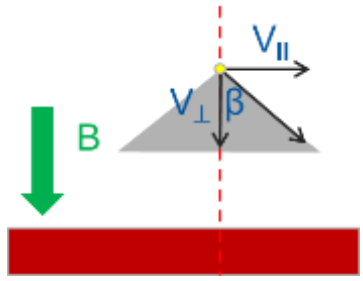

Figure 5 Effect of a magnetic field perpendicular to the surface on the speed of an impinging electron

For quadrupole fields the situation is different, since the field is not uniform in space. As resulting from a calculation in the guiding centre (adiabatic) approximation [44], this can provoke a modification of the relative intensities of the perpendicular and parallel components of the speed. As a consequence the impinging angle changes toward a more grazing direction and in the extreme case the electron can even be reflected by the surface, so that it will remain long time travelling in the field (magnetic bottle). In such case the knowledge of the TEY(E_p, θ_{inc}) is important up to large θ_{inc} . A strong magnetic field, as the 9 T intensity of the LHC dipoles strongly reduces the Larmor radius and one could imagine that it affects the secondary electron cascade. Relevant secondary electrons, which can escape the solid, have a kinetic energy above the work function level. In the solid they have therefore at least a kinetic energy corresponding to the sum of work function and Fermi energy, in total more than 10eV. The corresponding Larmor radius is of the order of microns whereas the mean free path of electrons between two inelastic scattering events is of the order of nanometers [45]. It is clear that the trajectory deviation due to the magnetic field between two scattering events is negligible and therefore there is no intrinsic dependence of the SEY for a flat metal in the mentioned range of field. Measurements of TEY in a magnetic field are very difficult due to deviation induced on the secondary electrons escaping in vacuum. There are only few measurements at low magnetic field [17, 46]. The results up to fields of few tens of mT [46] on a smooth sample confirm that there is no intrinsic dependence, however even the minor roughness on a laminated sample is sufficient to induce a decrease of TEY as a function of the field strength.

CONCLUSIONS

As illustrated above the dependence of the intensity and distribution of the emitted electrons on the energy and direction of the impinging electrons is influenced by surface and material properties. Only few aspects can be generalised and expressed with sufficient reliability through a parametrization. In most of the cases, a measurement is the most reliable approach even if it is not always easy and straightforward. In particular, measurements should be done by taking into account the dose received by the surface, the transmission function of the analysers in case of angle and energy resolved experiments and the influence of the geometry of the measuring system.

ACKNOWLEDGMENTS

It is a pleasure for the author to acknowledge fruitful discussions with V.Petit, G.Iadarola, H.Neupert, D.Zanin and M.Himmerlich as well as with many participants of the ECLOUD 18 workshop.

REFERENCES

[1] ESA multipactor tool from ESA/ESTEC, http://multipactor.esa.int/

[2] G. Iadarola, E. Belli, K. Li, L. Mether, A. Romano, G. Rumolo,Evolution of PYTHON tools for the simulation of electron cloud effects, proceedings IPAC 2017, p. 3803, Copenhagen Denmark

[3] J. Pierron, PhD thesis Université de Toulouse France, Modèle de transport d'électrons à basse énergie pour applications spatiales, 2017

[4] M. Azzolini, M. Angelucci, R. Cimino, R. Larciprete, N. M. Pugno, S. Taioli, M. Dapor: "Secondary electron emission and yield spectra of metals from Monte Carlo simulations and experiments", J.Phys. Cond. Mat. 31 (5) Art. No. 055901 (2019)

[5] E.Kieft, E.Bosch, Refinement of Monte Carlo simulations of electron-specimen interaction in low-voltage SEM, J.Phys. D, Appl.Phys 41 (2008) 215310

[6] I. Bojko, N.Hilleret, C. Scheuerlein, Influence of air exposures and thermal treatments on the secondary electron yield of copper, J.Vac. Sci.Technol. A18, 972 (2000)

[7] A. Kuzucan, H.Neupert, M.Taborelli, H. Störi, Secondary electron yield on cryogenic surfaces as a function of physisorbed gases, J.Vac. Sci.Technol. A30, 051401 (2012)

[8] S. Calatroni, E. Garcia-Tabares Valdivieso, H.r Neupert, V. Nistor, A. T. Perez Fontenla, M. Taborelli, P. Chiggiato, O. Malyshev, R. Valizadeh, S. Wackerow, S. A. Zolotovskaya, W. A. Gillespie, A. Abdolvand, First accelerator test of vacuum components with laser-engineered surfaces for electron-cloud mitigation, PRST AB 20, (2017) 113201

[9] A.J. Dekker, Solid State Physics, ed. F. Seitz, D. Turnbull, H. Ehrenreich, Academic Press, NY, **VI**, 251 (1958).

[10] H.Seiler, Secondary emission in the scanning electron microscope, J.Appl.Phys, 54 R1 (1983)

[11] M.Furman, M.T.F. Pivi, Probabilistic model for the simulation of secondary electron emission PRST AB, 5, 124404 (2002)

[12] Yee-Rendon∗, R. Muto, K. Ohmi, M. Okada, K. Satou, M. Tomizawa and T. Toyama, PYecloud simulations of the electron cloud for the J-Parc main ring, Proc. 14th Annual Meeting of Particle Accel. Soc. Japan, Sapporo (2017) p. 197 https://www.pasj.jp/web_publish/pasj2017/proceedings/PDF/THOM/THOM07.pdf

[13] R. Cimino, I.R.Collins, M.A.Furman, M.Pivi, F.Ruggiero, G.Rumolo and F.Zimmermann, Can low-energy electrons affect high-energy physics accelerators, Phys.Rev.Lett, 93, 014801, (2004)

[14] Scholtz, J.J., D. Dijkkamp, and R.W.A. Schmitz, Philips Journal of Research, 1996. 50(3-4), 375

[15] V.Baglin, I. Collins, B.Henrist, N.Hilleret and G.Vorlaufer, A summary of main experimental results concenring the secondary electron emission of copper, LHC project report 472, CERN, Geneva (2002)

[16] R. Cimino, A. Di Gaspare, L. Gonzalez, and R. Larciprete, Detailed investigation of the low-energy secondary electron yield, IEEE Trans. Plasma Sci., 43, 2015, 2954

[17] V. V. Anashin, A. A. Krasnov. V.K. Ovchar, V.V.Smaluk, D.P.Sukharov, Installation for measurement of secondary emission yield and electron cloud lifetime in magnetic field, DIPAC 2011, Hamburg

[18] R.Cimino, M.Commisso, D.R.Grosso, T.Demma, V.Baglin, R.Flammini and R. Larciprete, Nature of the decrease of the secondary electron yield by electron bombardment and its energy dependence, Phys.Rev.Lett, 109, 064801 (2012)

[19] V.Petit, ECLOUD 18 workshop, 3-7 June 2018, La Biodola, Elba Island, Italy

[20] L. A. Gonzalez, M. Angelucci, R. Larciprete and R. Cimino, "The secondary electron yield of noble metal surfaces," *AIP Advances*, vol. 7, p. 115203, 2017

[21] V.Baglin, I. Collins, B.Henrist, N.Hilleret and G.Vorlaufer, A summary of main experimental results concenring the secondary electron emission of copper, LHC project report 472, CERN, Geneva (2002)

[22] C. Scheuerlein and M. Taborelli, "Electron stimulated adsorption in ultrahigh vacuum manitored by Auger electron spectroscopy," Journal of vacuum science & technology A, vol. 20, no. 1, pp. 93-101, 2002

[23] M. Nishiwaki and S. Kato, "Graphitization of inner surface of copper beam duct of KEKB positron ring," Vacuum, vol. 84, pp. 743-746, 2010

[24] Yin Vallgren, G. Arduini, J. Bauche, S. Calatroni, P. Chiggiato, K. Cornelis, P. Costa Pinto, B. Henrist, E. Métral, H. Neupert, G. Rumolo, E. Shaposhnikova, and M. Taborelli, Amorphous carbon coatings for the mitigation of electron cloud in the CERN Super Proton Synchrotron, Phys Rev. ST Accel Beams **14**, 071001 (2011)

[25] R.Cimino, ECLOUD 18 workshop, 3-7 June 2018, La Biodola, Elba Island, Italy

[26] F.Le Pimpec F.King, R.E.Kirby and M.Pivi, Electron condition26ing of technical aluminium surfaces: effect on secondary electron yield, J. Vac. Sci. Technol. A **23**, 1610 (2005)

[27] V. Baglin, The LHC vacuum system: Commissioning up to nominal luminosity, Vacuum 138 (2017) 112

[28] B.Henrist, ECLOUD 18 workshop, 3-7 June 2018, La Biodola, Elba Island, Italy

[29] M.S.Chung, T.E.Everhart, Simple calculation of energy distribution of low energy secondary emission from metals, J.Appl.Phy 45 (1974), 707

[30] G.Rumolo, F.Zimmermann, E-cloud simulations: build up and related effects, Proceedings of ECLOUD02, CERN, Geneva (2002), p 97

[31] D.C.Joy, M.S.Prasad, H.M.Meyer, Experimental secondary electron spectra under SEM conditions, Journal of Microscopy, 215 (2004) 77

[32] R. Cimino, I.R.Collins, Vacuum chamber surface electronic properties, Appl. Surf. Sci. 235 (2004) 231–235

[33] J.R.M. Vaughan, IEEE Trans El Dev 40, 830, (1993) and 36, 1963, (1989)

[34] A.Shih and C.Hor, Secondary emission properties as a function of the electron emission angle IEEE Trans. El. Electron Dev, 40, (1993) 824

[35] N.Bundaleski, M.Belhaj, T.Gineste, O.Teodoro, Calculation of the angular dependence of the total electron yield, 122 (2015) 255

[36] D. Astapovych, ECLOUD 18 workshop, 3-7 June 2018, La Biodola, Elba Island, Italy

[37] L.Sabato, ECLOUD 18 workshop, 3-7 June 2018, La Biodola, Elba Island, Italy

[38] M.Salehi, E.A.Flinn, Dependence of secondary electron emission from amorphous materials on primary angle of incidence, J.Appl. Phys. 52 (1981) 994

[39] A.Jablonski, Analytical theory of elastic electron backscattering from elements alloys and compounds: comparison with experimental data, J. Electr. Spectr. Rel.Phenom. 206 (2016), 24

[40] W.Werner, I.Tilinin, M.Hayek, Anggular distribution of electrons reflected elastically from nanocrystalline solid surfaces Phys. Rev.B, 50 (1994) 4819

[41] A.Jablonski, P.Jiricek Elastic Electron Backscattering from surfaces at low energies, Surf. Interf.Analysis 24, (1996) 781

[42] Y. Suetsugu, K. Shibata, T. Ishibashi, K. Kanazawa, M. Shirai, S. Terui, and H. Hisamatsu, First commissioning of Super KEKB vacuum system, PRST AB, 19, 121001 (2016)

[43] R.J. Macek, Possible cures for electron cloud problems, proceedings of ECLOUD02, CERN, Geneva (2002), p 259

[44] M. Moisan, J. Pelletier, Individual Motion of a Charged Particle in Electric and Magnetic Fields. Physics of Collisional Plasmas. Springer (2012) Dordrecht

[45] M.P.Seah, W.A.Dench, Quantitative electron spectroscopy ofsurfaces: a standards database for electron inelastic mean free paths in solids, Surf. Interf. Anal. 1, (1979), 2

[46] N.Fil, PhD thesis Université de Toulouse France, Caractérisation et modélisation des propriétés d'émission électronique sous champ magnétique pour des systèmes RF hautes puissances sujets à l'effet multipactor, 2017

SURFACE CHARACTERIZATION OF VACUUM COMPONENTS EXTRACTED FROM LHC DIPOLE MAGNET

V. Petit[†1], H. Neupert, E. Garcia-Tabares, M. Taborelli, CERN, 1211 Geneva 23, Switzerland
M. Belhaj, ONERA, 31055, Toulouse, France
[1]also at ONERA, 31055, Toulouse, France

Abstract

Vacuum components of a dipole magnet exposed to the proton beam in the LHC at CERN were extracted from the LHC ring during the technical stop 2016 – 2017. Chemical analysis as well as Secondary Electron Yield (SEY) measurements were performed on their surface after a month of air exposure, to study possible surface modifications induced by the electron cloud bombardment during operation. The study shows that surfaces exposed to the cloud exhibit a lower maximum SEY and a lower copper hydroxide contribution than the same surface, never exposed to the beam. In addition, carbon graphitization could be detected on one of the LHC extracted components. These three features were previously identified as main characteristics of a copper surface conditioned by electron irradiation. This demonstrates that the LHC extracted components were at least partially conditioned in the accelerator under the effect of electron cloud.

INTRODUCTION

In the last decades, conditioning of surfaces by electron bombardment has been extensively studied in the laboratory, in particular to understand and foreseen the behaviour of particle accelerators with respect to the electron cloud effect [1-3]. However, only few studies on surface modifications induced by electron irradiation could be directly performed on accelerator components [4-7], leading to a lack of understanding regarding the conditioning state of some accelerators [8].

During the extended year-end technical stop (EYETS) 2016-2017, a faulty dipole magnet was exchanged in the LHC ring at CERN. After warming up and venting of a full LHC sector, the magnet was removed from its position in the tunnel and brought to the surface. Two vacuum components exposed to the beam, namely a beam screen and a pumping slot shield, were extracted from the magnet and their surface was analysed in the laboratory by X-Ray Photoelectron Spectroscopy (XPS) and Secondary Electron Yield (SEY) measurements to investigate surface modifications induced by the electron cloud exposure inside the LHC. To interpret the observations, a laboratory study has been performed in parallel to understand the mechanisms and the characteristics of the conditioning process of copper, the material of the LHC beam screen which is exposed to the beams.

† email address valentine.petit@cern.ch

In this paper, the chemical surface analysis as well as SEY measurements performed on the LHC extracted components are reported and compared with results from the laboratory conditioning study.

EXPERIMENTS

Laboratory study

The experiments were carried out in a baked UHV system (base pressure 6 x 10^{-10} mbar) made out of µ-metal. The setup is equipped for XPS analysis at normal emission angle (monochromatic Al Kα source, hν = 1486.7 eV) and SEY measurement. An electron flood gun allows sample irradiation for the conditioning study. The SEY δ is defined as the ratio of the total number of emitted (true secondary and backscattered) electrons I_s and the number of impinging electrons I_p. SEY measurements were carried out at normal incidence, between 10 and 1800 eV electron landing energy. The primary current I_p was first measured applying a positive bias on the sample (V_{sa} = +40 V). The bias was then switched to negative value (V_{sa} = -40V) and the sample current $I_{sa} = I_p - I_s$ was measured. The SEY was then computed: $\delta = 1 - I_{sa}/I_p$. The primary current was kept below 2.5 nA to limit the sample conditioning during the SEY measurement (estimated corresponding dose: 4 x 10^{-7} C/mm²). The reproducibility of the SEY measurement is estimated to be ±0.05 for two subsequent measurements at the same position. Conditioning was carried out using a flood gun at E = 250 eV at normal incidence. The sample current during irradiation was about 150 µA (measured with V_{sa} = +32V) for an irradiated area estimated to 1000 mm². The samples used for the laboratory study were 15x20 mm² copper pieces cut in a spare LHC beam screen and were cleaned in a commercial detergent, following the procedure applied for cleaning the beam screens and pumping slot shields installed in the LHC.

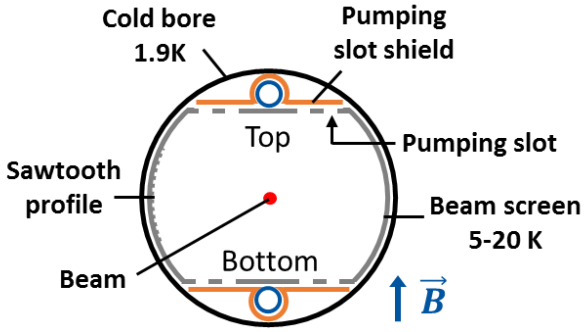

Figure 1: Schematic of the LHC beam vacuum system in the arcs

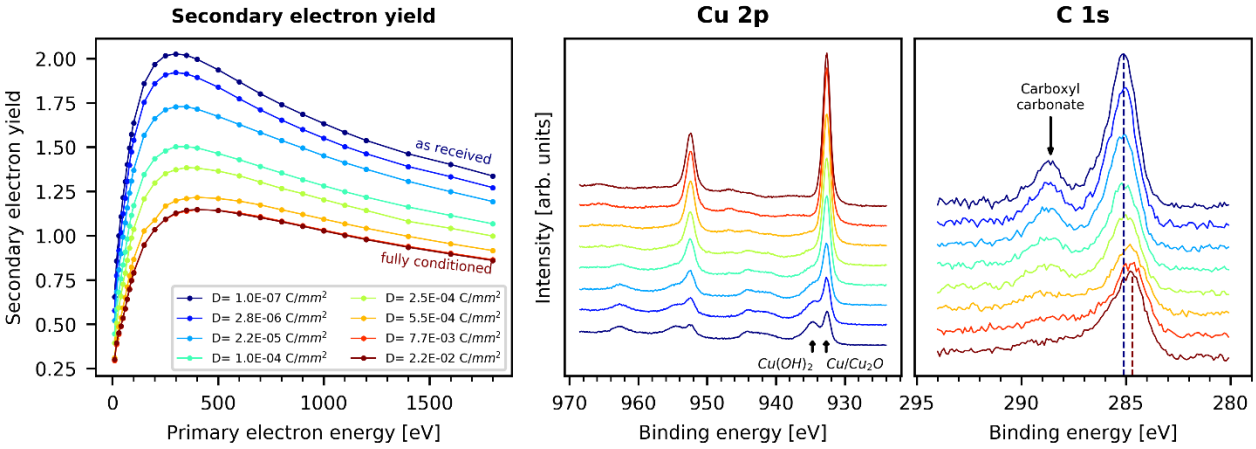

Figure 2: Laboratory conditioning of copper: secondary electron yield curves, Cu 2p and C 1s XPS lines

LHC extracted components

Two vacuum components exposed to the electron cloud during the LHC operation were removed from the LHC dipole magnet (see Figure 1).

A 16 m long beam screen made of colaminated copper (inner face) on stainless steel (outer face) was extracted from the cold bore and slices were cut at different positions along the magnet. For each slice, SEY curves and XPS spectra were acquired in different points with respect to the azimuthal position in the laboratory setup described above. Because of the confinement of the electron cloud by the dipole field, the two flat sides of the beam screen (normal to the field) are expected to receive most of the electron irradiation dose. On the external lateral side, a sawtooth profile is machined to absorb synchrotron radiation (see Figure 1).

The pumping slot shield, made of copper beryllium alloy (UNS C17200) passivated with chromic acid after detergent cleaning and located on top and bottom of the beam screen, was also analysed. In particular, longitudinal SEY profiles and XPS analysis were performed along the beam axis in order to investigate differences in conditioning states between areas which were exposed to the electron cloud through the beam screen pumping slots and areas which remained masked by the beam screen (see Figure 1).

For both components the analysis were performed after 1 to 2 months of air exposure, a venting of a full LHC sector being required to exchange the magnet. Thus, deconditioning of the surface and loss of the *in-situ* conditioning state are expected.

RESULTS AND DISCUSSION

Laboratory conditioning of copper

The SEY curves as well as the Cu 2p and C 1s XPS core spectra acquired during the conditioning of a copper beam screen sample are shown in Figure 2. In the as received state, the sample exhibits a usual airborne contamination layer including copper hydroxide $Cu(OH)_2$ and carbon species. The maximum SEY of such a surface is about 2 and is found at a primary energy of 300 eV. During conditioning, two phenomena occur, leading to a global decrease of the SEY down to 1.15 at a primary energy of 400 eV for a dose of 10^{-2} C/mm². In the first stages of irradiation, a surface cleaning effect by electron stimulated desorption is observed through the vanishing of the $Cu(OH)_2$ and the carboxyl/carbonate components on the Cu 2p and C 1s lines respectively. For an electron dose greater than 2.5 x 10^{-4} C/mm², a shift of the C 1s line towards lower

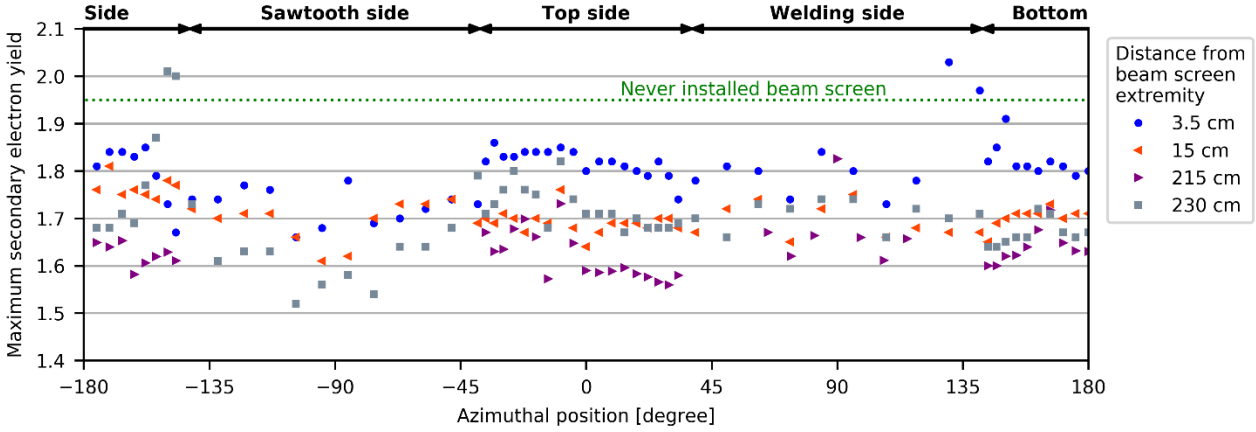

Figure 3: Maximum SEY with respect to azimuthal position for four slices cut in the LHC extracted beam screen

binding energies occurs, corresponding to graphitization of the adventitious carbon layer, as already reported [2].

LHC extracted components

Beam screen

Four slices of beam screen, cut at different positions along the magnet, were analysed. The maximum SEY with respect to the azimuthal position for the 4 slices is shown in Figure 3. Despite the electron confinement by the dipole field, no significant difference of maximum SEY is observed between the flat (top and bottom) sides and the welding side. The maximum SEY of those samples ranges from 1.5 to 1.85, which is well below the value of 1.95 measured on a beam screen never installed in the LHC. This observation is compatible with at least a partial conditioning state of the beam screen inside the LHC.

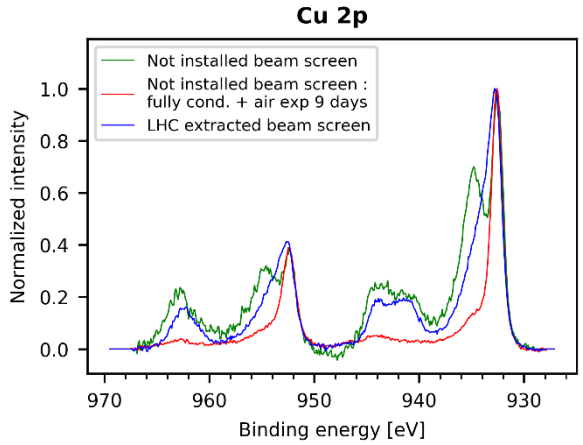

Figure 4: Cu 2p lines acquired on the bottom side of the LHC extracted sample located at 230 cm from beam screen extremity, on a never installed beam screen and on a never installed beam screen fully conditioned in the lab and stored for 9 days in air

XPS analysis performed on the four slices revealed the presence of carbon, oxygen and nitrogen on top of copper, as well as traces of usual contaminants (S, Cl, Si). The Cu 2p line acquired on the bottom side of the slice located at 230 cm from the beam screen extremity is shown in Figure 4. For comparison, the Cu 2p lines acquired on a never installed beam screen before and after a full conditioning process in the lab followed by 9 days of air exposure are also shown. As expected from the laboratory study of copper conditioning reported above, the hydroxide contribution at 934.8 eV of the never installed beam screen is strongly decreased by the lab conditioning and remains low even after 9 days of air exposure. It is clear that the shape of the Cu 2p line of the LHC extracted sample is different from the never installed beam screen one, pointing again towards an electron cloud induced surface modification during LHC operation. No clear difference in the C 1s line is observed between LHC extracted and never installed (before conditioning) beam screens. The amount of carbon varies between 20 and 40% for all the points measured on the four slices and no correlation was found between the carbon concentration and the azimuthal position.

Pumping slot shield

A visual inspection of the pumping slot shield side facing the beam screen revealed the presence of dark traces corresponding exactly to the pumping slot shape and spacing, and thus to the areas exposed to the electron cloud in the LHC (see Figure 1). An air baking at 120°C for 26h enhanced the colour contrast as shown in Figure 5. The origin of the coloration is not yet understood and is currently under investigation.

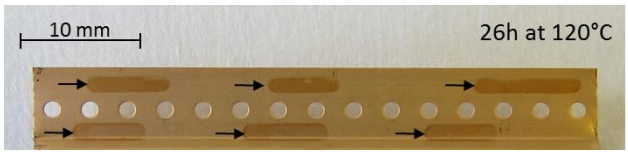

Figure 5: Dark traces corresponding to the pumping slots on the pumping slot shield side facing the beam screen

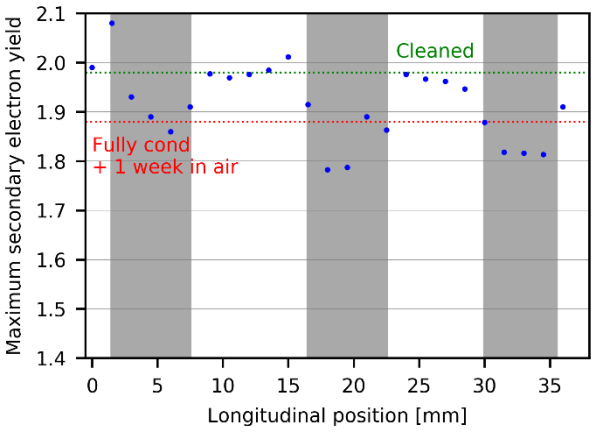

Figure 6: Maximum SEY with respect to longitudinal position for a LHC extracted pumping slot shield. The maximum SEY value for a cleaned (never installed) pumping slot shield before and after a full conditioning process in the lab followed by a week of air exposure

The SEY was measured on the sample as extracted (no baking in air) in different points along the beam axis and the corresponding maximum SEY profile is given in Figure 6 where the grey stripes represent the position of the dark traces. A clear and systematic step pattern is visible with low SEY regions corresponding to dark (irradiated) areas and high SEY regions in the non-irradiated areas. As for the beam screen, a reference sample (same component, but never installed in the LHC) was analysed for comparison. After the cleaning and passivation procedure, the never installed pumping slot shield exhibits a maximum SEY of about 2, corresponding to the value measured in the non-irradiated areas of the LHC extracted component. After full conditioning in the lab and 1 week of air storage, the maximum SEY of the never installed sample is below 1.9 and is compatible, within the experimental accuracy, with the maximum SEY observed in the irradiated areas.

XPS spectra were acquired in both irradiated and non-irradiated areas of the LHC extracted pumping slot shield. In addition to the elements found on the LHC extracted

beam screen, beryllium and chromium could be detected on this component. The Cu 2p and C 1s lines are shown in Figure 7. As expected from the laboratory study reported above, the $Cu(OH)_2$ contribution is strongly decreased in the irradiated areas with respect to the non-irradiated ones. In addition, in the irradiated zones, the C 1s line is shifted to lower binding energy demonstrating a graphitization of the adventitious carbon layer. These two observations are compatible with a conditioning of the dark areas induced by the electron cloud. It is worth mentioning that no difference of carbon concentration is observed whether the material was irradiated or not, contrary to analysis performed on components extracted from the SPS at CERN [9].

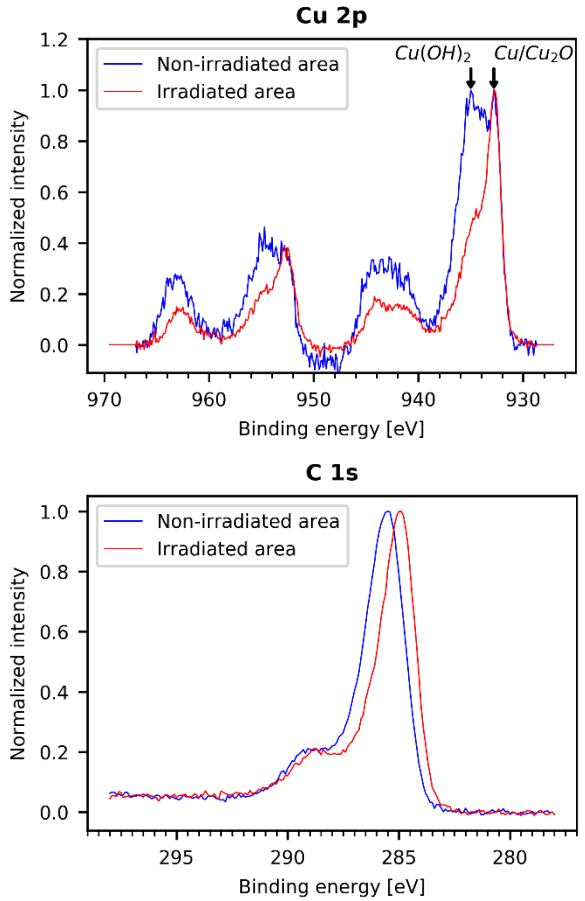

Figure 7: Cu 2p and C 1s lines acquired on the LHC extracted pumping slot shield, in irradiated and non-irradiated areas

CONCLUSION

A laboratory study allowed the identification of different features of the copper conditioning process. During electron irradiation, a decrease of the SEY induced by the cleaning of the surface ($Cu(OH)_2$ and carboxyls/carbonates removal) and carbon graphitization is observed.

In a second time, a beam screen and a pumping slot shield exposed to the beam in the LHC and extracted during the EYETS 2016-2017 were analysed after 1 to 2 months of air exposure. The beam screen as well as the pumping slot shield, in its irradiated areas, exhibit a lower SEY as well as a lower $Cu(OH)_2$ signal than the reference component which was never installed in the LHC. In addition, carbon in a graphitic form is observed in the irradiated areas of the LHC extracted pumping slot shield. These observations, identified in the laboratory study as characteristic features of the conditioning, prove that the LHC extracted components were at least partially conditioned by the electron cloud in the LHC. However, due to venting induced deconditioning, this study does not allow to deduce the conditioning level in terms of SEY of the components during the machine operation.

Furthermore, no carbon growth was observed for the LHC extracted components contrary to previous observations on SPS extracted components, proving that the conditioning does not rely on carbon growth.

More investigations are ongoing to understand the mechanisms of deconditioning in order to prepare the analysis of new components to be extracted from the LHC during the Long Shutdown 2.

ACKNOWLEDGEMENTS

The authors would like to thank all members of the TE-VSC group of CERN involved in this study.

REFERENCES

[1] V. Baglin *et al.*, "A summary of main experimental results concerning the secondary electron emission of copper", CERN, Geneva, Switzerland, Rep. LHC Project Report 472, 2002.

[2] R. Cimino *et al.*, "Nature of the decrease of the secondary electron yield by electron bombardment and its energy dependence", *Phys. Rev. Lett.,* vol. 109, no.16, p. 064801, 2012.

[3] M. Nishiwaki and S. Kato, "Graphitization of inner surface of copper beam duct of KEKB positron ring", *Vacuum,* vol. 84, pp. 743-746, 2010.

[4] S. Kato and M. Nishiwaki, "In-situ measurements at KEKB positron ring and comparison with laboratory experiments" in *Proc. ECLOUD'07*, Daegu, Korea, 2007, pp. 72-75.

[5] W. Hartung *et al.*, "Measurements of secondary electron yield of metal surfaces and films with exposure to a realistic accelerator environment", in *Proc. IPAC2013*, Shanghai, China, 2013, pp. 3493-3495.

[6] J. M. Jimenez *et al.*, "Electron cloud studies and beam scrubbing effect in the SPS", CERN, Geneva, Switzerland, Rep. LHC Project Report 634, 2003.

[7] V. Baglin *et al.* "Measurements at EPA of vacuum and electron-cloud related effects" in *Proc. 11th Workshop of the LHC*, Chamonix, France, 2001.

[8] G. Iadarola, "Overview on heat loads in the LHC," these proceedings.

[9] C. Yin Vallgren *et al.*, "Amorphous carbon coatings for the mitigation of electron cloud in the CERN Super Proton Synchrotron" *Phys. Rev. ST Accel. Beams,* vol. 14, no.17, p. 071001, 2011.

EXPERIMENTAL STUDIES ON SECONDARY ELECTRON EMISSION CHARACTERISTICS OF ACCELERATOR CHAMBER MATERIALS*

S. Liu, Y. Liu†, W. Liu, G. Pei, Institute of High Energy Physics (IHEP),Chinese Academy of Sciences (CAS), [100049] Beijing, China
P. Wang†, L. Zeng, X. Sun, at Dongguan Institute of Neutron Science (DINS), [523803] Dongguan, China

Abstract

The electron multipacting effect that occurs in the accelerator vacuum tubes and radio frequency cavity has a significant impact on beam quality and normal operation of the accelerator. The multipacting effect and electron cloud effect are closely related to secondary electron emission (SEE) characteristics. In this paper, secondary electron yield (SEY), its dependence on incidence angle, spatial and energy distribution of secondary emission electrons and SEY depression as a function of deposited electron dose for Cu are measured. And the SEY of ceramic samples are successfully measured by effective charge neutralization.

INTRODUCTION

During the operation of an accelerator, the electron cloud effect in the vacuum pipe can cause beam instability and emittance growth [1-3]. The secondary electron multipacting effect occurring in the radio-frequency cavity will promote serious ignition in RF cavity, which severely limits the electromagnetic field intensity and even causes the break-up of the RF system [4]. The power deposition from secondary electron multipacting in beam screen may even lead to a quench of the entire superconductor system [5, 6]. Over the past decades, many international accelerator laboratories, such as KEK, FERMILAB, and CERN have set up an experimental apparatus to measure SEY for different materials [7-9].

In order to improve the stability on high current beam , it is necessary to select suitable material with a lower SEY to reduce the secondary electron emission. SEY can be defined as the ratio of the number of secondary electron current I_s to the number of primary electron current I_p. To study the electron cloud effect in the accelerator, a complete measurement and theoretical analysis of the SEE characteristic parameters of the accelerator vacuum chamber materials are required. The complete SEE parameters include SEY and its dependence on the incidence angle of the primary electrons, and the spatial and spectrum distribution of secondary electrons, However, there are many studies focusing on SEY and not on the other SEE parametershave been set u. So a high efficiency SEE characteristics experimental platform based on a new detector and sample holder design has been set up to measure the complete characteristic parameters of various accelerator chamber materials.

The ceramic vacuum pipe in Rapid Cycling Synchrotron of China Spallation Neutron Source (RCS/CSNS) is chosen to suppress eddy current effect produced by the rapidly changing magnetic field in dipole and quadrupole magnets of the RCS ring, but the SEY of the ceramic is so high that a TiN film is plated onto the inner wall of the ceramic vacuum pipe for suppression of SEY [10]. During the measurements on SEY for ceramics, single pulse method [11] is used to solve charge accumulation on the surface of the insulating material. The measurement results were compared with the existing experimental references which verified the reliability and practicality of the measurement method and the platform. The measurement and theoretical results of the secondary electron emission characteristics for various materials can provide a reference for selecting vacuum chamber materials with lower SEY. The measurement results can be used to improve TiN coating process and simulations of the electron cloud.

MEASUREMENT PRINCIPLE AND APPARATUS

Our measurement of the SEE characteristics is explained in Figs. 1-3. A photograph and partial view ground electrodes of the apparatus are shown in Fig. 4. As shown in Fig. 1(a), the sample holder can move up and down and even rotate from 0º to 90º within a retarding field analyser (RFA) [12]. The RFA is composed of a cap detector (connected with terminal A) and a cylindrical wall detector (connected with terminal B) with meshed grid (connected with terminal C) and meshed grid ground electrodes (connected with terminal E) inside. As shown in Fig. 3(a), there is an insulating ring between the cap detector and the wall detector for spatial distribution measurement. In order to obtain the SEY more accurately, the sample (connected with terminal D) is connected with a DC bias source. During the measurement of spectrum, the grid electrode is also connected with a DC bias source. The grounded electrode is used to shield the electrostatic field and to avoid its impact on the electron motion. SEY and its dependence on incidence angle

Because of different conductivity, there are different measuring methods for metallic conductive materials and dielectric samples as below.

High conductivity sample As shown in Fig. 1, there are two ways to measure the SEY of highly conductive metallic: sample method and collector method [13-15]. For the sample method in Fig. 1(a), when -20 V bias is set on

* Work supported by Foundation of Key Laboratory of Particle Acceleration Physics and Technology, IHEP, CAS (JSQ2016ZZ02); National Natural Science Foundation of China (U1832132, 11375215);
† email address:liuyd@ihep.ac.cn;wangpc@ihep.ac.cn

the sample, the SEs are allowed to escape from the sample surface fully and the sample current I_s is measured by picoammeter. By regulating the bias voltage to +100 V which is high enough to prevent SEs from escaping from the sample surface, the primary electron current I_p is obtained. Then the SEY is calculated by the formula δ=1-I/I_p. With correction on the energy of primary beam (E_p) from bias voltage 20 V, the energy calibration is included in the final results. For the collector method in Fig. 1(b), when 50 V bias is added on the detector (close K_A, and K_B connected to the ground), then the SEs are fully collected by the detector and the SE current I_c is measured. When connect the detector and the sample together with DC voltage source (Close K_A and K_B), the primary electron current I_p is obtained. Then the SEY is calculated by the formula δ=I/I_p. As shown in Fig. 1(a), the sample holder can be rotated axially from 0 to 180 degrees for the sake of SEY dependence on the incident angle.

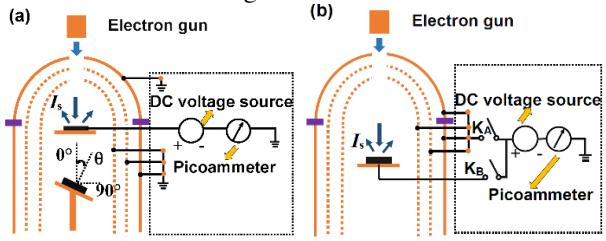

Figure 1: The schematic diagram of SEY measurement for conductive sample (a: sample method; b: collector method)

Dielectric sample Due to the poor electrical conductivity, the charge can be accumulated on the surface of dielectric sample. Therefore the key to measure the SEY of dielectric sample accurately is to eliminate the surface charge accumulation. The method based on negatively biased collector is used to neutralize the secondary electrons accumulation on the surface [11]. A pulse generator can trigger the electron gun to produce a single pulse beam with duration time 150 μs or a periodic pulse beam with repetition frequency 25 Hz, respectively for SEY measurement and charge neutralization. The schematic diagram of measurement is shown in Fig. 2. The measurement procedure is quite complex comparing to the conductive sample: firstly rotate Faraday cage up and set +45 V bias on the Faraday cup, tuning the electron gun to single pulse mode for measurement and obtain incident current I_p; secondly, rotate sample up and set +45 V bias on detector, tuning the electron gun to single pulse mode for measurement and get the secondary electron current I_c. It should be noted that before the next measurement, full neutralization procedure is required: input -45V bias on collector and then switch the electron gun to the periodic pulse mode with the pulse duration 1~ 5s to make the secondary electron return to the sample surface fully.

Spatial distribution of secondary emission electrons

For the measurement on electrons spatial distribution, the picoammeter was connected with terminal B. The experimental principle is to move the sample holder to different vertical positions and measure current variations on the cylindrical wall detector, as shown in Fig. 3(a). Assuming that the sample's initial vertical position is M and the half flare angle of the sample, the measured current on the cylindrical wall detector is I_α; after slightly moving the sample to another position N, the measured current on the wall collector is $I_{\alpha+\Delta\alpha}$ and the angle and current variation are $\Delta\alpha$ and ΔI_α= I_α- $I_{\alpha+\Delta\alpha}$, respectively. Varying the sample position step by step, the secondary electron azimuthal distribution is achieved. Using the cylindrical wall detector for obtaining the secondary electron (SE) current ΔI_α can avoid the measured electrons leakage from the aperture on the top of the cap detector.

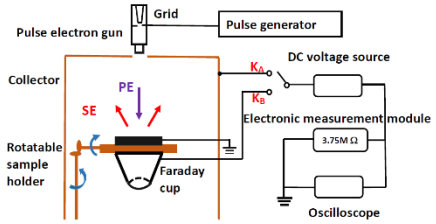

Figure 2: The schematic diagram of measurement for dielectric sample

Energy Spectrum of secondary emission electrons

The RFA which is the capped cylindrical wall detector with two meshed grid layers inside is used for scanning the secondary electron energy spectrum. By scanning the voltage on the grid layer with a DC voltage source, the energy spectrum can be obtained, as shown in Fig. 3(b). Because of the aperture on the top of the cap detector, there is some missing SE current, but these missed secondary electrons only have effect on the measured current amplitude. The secondary electrons' energy distribution will not be altered. During the measurement, the sample holder is placed at the center of the hemispherical detector. By changing the grid voltage U, the secondary electrons with energy less than eU are prevented. Then E(eU)-ΔI_s curve as energy spectrum distribution can be obtained.

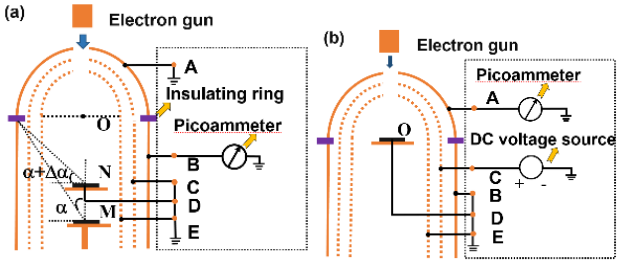

Figure 3: The schematic diagram of spatial and energy distribution measurement

SEY depression with beam deposition

The bombardment from primary beam can clean some contaminants and oxide on the surface of the sample which can cause material surface changes. Longer bombardment by primary electrons with proper energy, the surface graphitization may be produced and the presence of the carbon film can lower the measured SEY [16].

Experimental apparatus

The SEE experimental platform is composed of a vacuum system, electron gun, removable sample holder, and RFA for measuring secondary electrons. The vacuum system can keep the sample in a high vacuum environment with pressure about 10^6 Pa. The Kimball Physics EGL-7 electron gun was installed and directed toward the sample vertically, and the electron beam energy ranges from 100 eV to 5 keV with the emission current span from 1 *n*A to 100 μA. The maximum movable vertical distance of the sample holder is about 150 mm which corresponds to the spatial angle 10°–80°. The sample with an area of 2× 2 cm^2 and thickness of 1.5 mm can be fixed on the sample holder. The grid and ground electrodes in RFA are made of stainless steel wire cage with mesh size about 1 ×1 mm^2. An photograph and partial view of the apparatus are shown in Fig. 4.

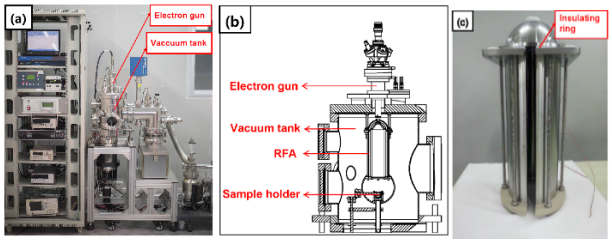

Figure 4: The partial view and photograph of the apparatus and RFA: ((a) schematic of the experimental setup, (b) partial view of experimental setup, (c) structure of RFA.)

MEASUREMENT RESULT AND THEORETICAL ANALYSIS

SEY and its dependence on incidence angle

As described before, there are two ways to measure SEY on conductive sample, such as Cu. As can be seen from Fig. 5 and Table 1, the SEYs of Cu by two methods at normal incidence are similar. Comparing the experimental results with Ref. 17, the similarity is that the primary energy E_{pm} corresponding to the maximum secondary electron are all around 300 eV. However the SEY measured by the sample method was 1.8, slightly lower than the result of Ref. 17.

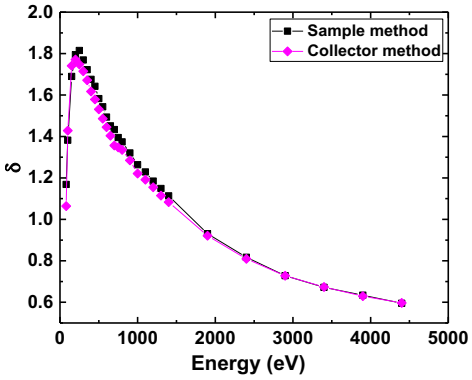

Figure 5: Primary energy and SEY of Cu measured by sample method and collector method.

Table 1: SEY of Cu measured by sample method and collector method

Cu	E_{pm} (eV)	δ_m
sample method	300	1.80
collector method	300	1.70
Valizadeh, Reza, et al.2014	300	1.90

Including conductive samples, the SEY of ceramics was measured by single pulse method in the paper. With confirmation on the SEY supression for ceramics with TiN coating, SEY of ceramics was depressed from 5.97 to 1.66 after coated with TiN and the corresponding energy E_{pm} turned from 775 eV to 230 eV as shown in Fig. 6. Therefore the SEY of untreated ceramic is high and the secondary electron yield can be effectively reduced by the TiN film plated on its inner wall.

However experimental results proved the SEY increasement (SEY~2.15) of ceramic sample with TiN after its exposure in air for 3 months as shown in Fig. 6(b). The results of SLAC show that δ_m of TiN deposited on Al and SS substrate with different impurity types were 1.5–2.4 [18]. The study in SNS indicated that δ_m of TiN plated under high and low vacuum were 1.5–1.6 and 2.0–2.7 [19], respectively; At J-PARC, δ_m was about about 1.6 [20]. According to reference [21], δ_m of ceramic was about 6.4. Therefore, the measured results in the CSNS shown in Table. 1 basically agree with the value of the references.

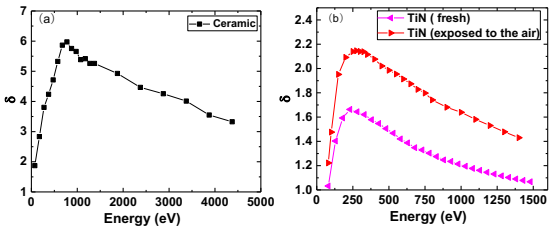

Figure 6: SEY of ceramic sample before and after coated with TiN.

The secondary electron yield under oblique incidence can be measured by rotating the sample holder. As shown in Fig. 7, the SEY gradually increases with the increase of the incident angle θ in the range of 0-60°, with a cosine relationship on incident angle θ, which is consistent with the reference [22]. However, the SEY begins to decrease after the incident angle increased to 60°, which is because the measurement error increases with the increase of the incident angle θ. The result above 60° is not shown in Fig. 7 because of measurement error .

$$y = \cos(\theta)^{-n} \quad (1)$$

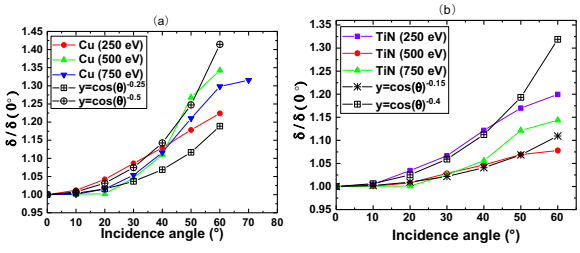

Figure 7: SEY at different incident angle

Table 2: E_{pm} and δ_m of ceramic with and without TiN

Sample	E_{pm}(eV)	δ_m	E_p (reference)	δ_m (reference)
ceramic	775	5.97	650	6.4
coated with TiN (fresh)	230	1.66	300	1.5~2.4

In Eq. 1, n is the coefficient related to the energy of the material and the incident beam, y is a cosine function of θ and n. Comparing the measurement results with calculation results of the cosine function formula, it can be seen that the corresponding coefficients n of several materials ranges from about 0.16 to 0.80.The corresponding values of n for different materials are shown in Table 2.

Spatial distribution of secondary emission electrons

According to the theory [23], the number of true secondary electrons per polar angle is described by following formula:

$$f(\theta) = \cos\theta(1 + a\sin^2\theta + b\sin^4\theta + ...) \quad (2)$$

where a, b, and c are the coefficients decided by the smallest momentum which electrons need to escape the sample. According to Eq. 2, the parameters obtained by fitting the measurement results of Cu and TiN using Eq. 2 are shown in Figure 8 and Table. 3. Therefore the secondary electrons' spatial distribution measured in the experiment is consistent with the theoretical results and Ref. 24. The difference is that the elastic scattering electrons are unconcerned in the theoretical formula, while all kinds of the secondary electrons are included in the experimental data.

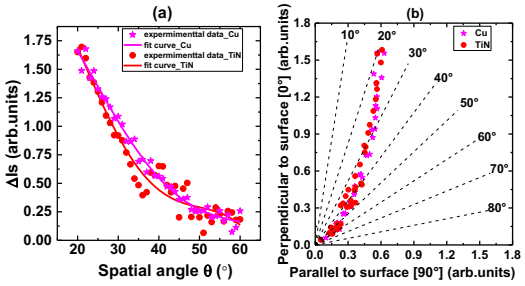

Figure 8: SE spatial distribution in cartesian and polar coordinate systems

Table 3: Fitting parameters spatial distribution

	a	b
Cu	-2.10	1.63
TiN(ceramic substrate)	-1.24	1.91

Energy Spectrum of secondary emission electrons

The SE energy spectrum is measured by RFA [25] and the results are shown in Fig. 9-11. According to the normal secondary electron emission model [26], the SEs are composed of three portions: "true" secondary electron (SE) with the lower energy range 0-50 eV; elastic reflected secondary electron (ERSE) which are emitted with almost the same energy as the incident particles; and inelastic reflected secondary electron (IRSE) or "rediffused" electrons with a uniform energy spectrum from 50 eV to the incident particle energy. For this experiment on the Cu sample, the "true" secondary electron energy ranged from 0 to 50 eV with peak at about 1.5-2.5 eV which does not change with the energy of incident electrons. Because of the aperture on the top of the cap detector for the primary beam passing through, which corresponds to a vertical azimuth about 25°, much of the "elastic" electrons can escape from the aperture which leads to the lower measured current of "elastic" electrons in Fig. 10. Comparing the measured energy spectrum with Ref. 27, it is clear that the "elastic" electrons whose energy is the same with that of primary electrons are also confirmed in our experiments. But due to strict experimental requirements in Ref. 27 such as lower energy primary electrons (3.17 eV–312 eV), accurate energy analyzer, and cryogenic environment (9 K), the portion of reflected electrons and its dependency on low primary energy are less accurately measured in our experiments.

As shown in Table. 4, we can conclude that the percentage for true SE is more than 80% of the total emission electrons. The position of the true secondary electron peak changes very little with the change of the energy of the incident electron as shown in Fig. 11, but the position of the elastic scattering peak increases with the increase of the energy of the incident electron as shown in Fig. 10. This is because of different generation mechanism. The true SE come from extranuclear electrons and the elastic electron come from primary electrons [26].

The width at half maximum (FWHM) [12] of the true secondary electron peak and the elastic reflected electron peak are fitted in Table. 5 and marked in the Fig. 10. In the Ref. [28], FWHM for the secondary electron spectra of polycrystalline Cu is 5.1 eV and the position of the peak is 1.3 eV when the incidence energy is 1.5 keV which is consisitent with the measurement results.

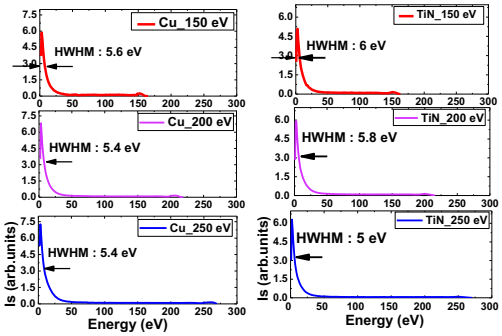

Figure 9: Total secondary electron energy spectrum of Cu and TiN on ceramic.

Table 4: The proportion of secondary electrons composition.

Sample	E_p(eV)	SE	ERSE	IRSE
Cu	150	80.2%	4.8%	15.0%
	200	79.9%	3.1%	17.0%
	250	76.8%	2.9%	20.3%
TiN	150	81.8%	3.3%	14.9%
	200	78.7%	3.5%	17.8%
	250	78.5%	3.0%	18.5%

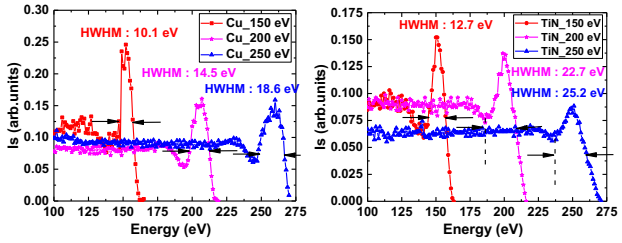

Figure 10: ERSE energy spectrum of Cu and TiN on ceramic.

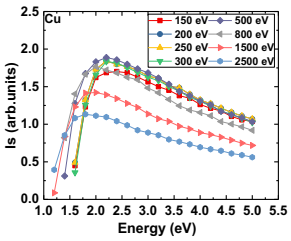

Figure 11: SE energy spectrum of Cu

Table 5: FWHM of the true secondary electron peak and the elastic reflected electron peak

Sample	E_p (eV)	SE (eV)	ERSE (eV)
Cu	150	5.6	10.1
	200	5.4	14.5
	250	5.4	18.6
TiN	150	6.0	12.7
	200	5.8	22.7
	250	5.0	25.2

SEY depression as electron dose deposition

According to Refs. 16 and 29-31, incident electron bombardment can cause surface changes of the material, such as clearance of some contaminants and oxide. In order to understand the "dose" effect, the SEY is measured for different depositions of primary beam. Fixing the primary beam energy and current with continuous bombardment on the sample for 10 hours, the maximum SEY decreases with the increase of incident electron dose and finally stabilizes as shown in Fig. 12. As shown in Table. 6, the charge deposition of 3.13×10^{-3} C/mm^2, the maximum SEY of Cu and TiN drops from 1.81 to 1.46 .Therefore bombardment reducing SEY is an effective secondary electron suppression measure [16].

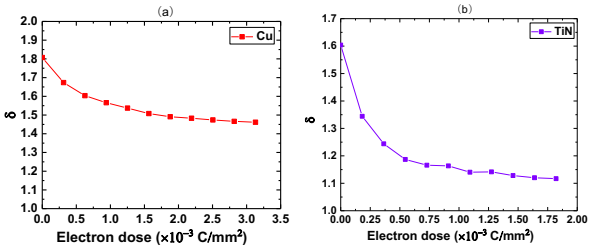

Figure 12: SEY as a function of electron dose

Table. 6: SEY before and after electron bombardment

Sample	δ_0	δ	Dose ($\times10^{-3}$C/mm^2)
Cu	1.81	1.46	3.13
TiN	1.60	1.12	1.82

CONCLUSION

In order to study the SEE characteristics of accelerator vacuum chamber materials, a novel experimental apparatus for SEE measurements was set up in CSNS. SEY, spatial distribution, energy spectrum, and "dose" effect were obtained by this device. SEY on conductive samples measured by sample method and collector method at normal incidence are coincident. Due to the poor electrical conductivity, single pulse method is used for measurement on SEY of dielectric sample to reduce charge accumulation phenomenon on the surfaces. The negative bias collector method can be used to neutralize the secondary electrons accumulation on the surface of insulating sample effectively. The measurement results proved the SEY dependence on incidence angle and spatial angle SE spatial distribution can be parametrized with a cosine relation. The "true" secondary electron energy range (<50 eV) for different materials have been verified in energy distribution measurements. The experimental results demonstrated the availability of measurement methds and validated the the apparatis structure.

REFERENCES

[1] K. Ohmi, F. Zimmermann, "Head-Tail Instability Caused by Electron Clouds in Positron Storage Rings," Phys. Rev. Lett. 85, 3821 (2000).

[2] M. Tobiyama, J. W. Flanagan, H. Fukuma, S. Kurokawa, K. Ohmi, and S. S. Win, "Coupled bunch instability caused by an electron cloud," Phys. Rev. ST Accel. Beams 9, 012801 (2006).

[3] C. M. Lyneis, H. A. Schwettman, J. P..Turneaure, "Elimination on electron multipacting in superconducting structures for electron accelerators". Applied Physics Letters, 1977, 31(8): 541-543.

[4] R. Prakash, A. R. Jana, V. Kumar. "Multipacting studies in elliptic SRF cavities". Nuclear Instruments and Methods in Physics Research Section A: Accelerators, Spectrometers, Detectors and Associated Equipment, 2017, 867: 128-138.

[5] R. Cimino and T. Demma, "Electron cloud in accelerators", Int. Journal of Modern Phys. A, vol. 29, no. 17, p. 1430023, 2014.

[6] R. Cimino, V. Baglin and F. Schäfers. Potential remedies for the high synchrotron-radiation-induced heat load for future highest-energy-proton circular colliders. Physical review letters, 2015, 115(26): 264804.

[7] R. Cimino et al., "Detailed investigation of the low energy secondary electron yield of technical Cu and its relevance for the LHC", Physical Review Special Topics-Accelerators and Beams, vol. 18, no. 5, p. 051002, 2015

[8] K. Yamamoto et al., "Secondary electron emission yields from the J-PARC RCS vacuum components", Vacuum, vol.81, no. 6, pp 788-792, 2007.

[9] Y. Ji, L. Spentzouris and R. Zwaska, "Update of the SEY Measurement at Fermilab Main Injector", in Proc. NAPAC' 16, Chicago, IL, USA, Oct. 2016.doi:10.18429/JACOW-NA-PAC2016-THPOA45

[10] H. Dong, H. Song, Q. Li et al., The vacuum system of the China spallation neutron source. Vacuum, 2018, 154: 75-81.

[11] M. Weng, M. Cao, H. J. Zhao et al. Note: A simple charge neutralization method for measuring the secondary electron yield of insulators. Review of Scientific Instruments, 2014, 85(3): 036108.

[12] P. Staib, U. Dinklage. "Recent developments on an improved retarding-field analyser". Journal of Physics E: Scientific Instruments, 1977, 10(9): 914.

[13] Ji. Yichen, Linda Spentzouris and Robert Zwaska. "Secondary electron yield measurement and electron cloud simulation at Fermilab". (2015): MOPMA039.

[14] K. Yamamoto, T. Shibata, N. Ogiwara et al., "Secondary electron emission yields from the J-PARC RCS vacuum components". Vacuum, 2007, 81(6): 788-792.

[15] H. Miyake, K. Nitta, Michizono S, et al. "Secondary electron emission on degradation sample and development of new measurement system with low electron energy". Discharges and Electrical Insulation in Vacuum, 2008. ISDEIV 2008. 23rd International Symposium on. IEEE, 2008, 2: 553-556.

[16] R. Cimino et al., "Electron energy dependence of scrubbing efficiency to mitigate e-cloud formation in accelerators", in Proc. EPAC08, Genoa, Italy, 23-27 June 2008, paper TUPP027, pp.1592–1594.

[17] R. Valizadeh, O. B. Malyshev, S. Wang et al., "Low secondary electron yield engineered surface for electron cloud mitigation". Applied Physics Letters, 2014, 105(23): 231605.

[18] F. L. Pimpec, R.E. Kirby, F. King et al., Properties of TiN and TiZrV thin film as a remedy against electron cloud, Nucl. Instrum. Meth. Phys. Res. Sect. A 551 (2–3) (2005) 187–199.

[19] P. He, B. Henrist, F. L. Pimpec et al., "Secondary electron emission measurements for TiN coating on the stainless steel of SNS accumulator ring vacuum chamber". No. EPAC-2004-WEPKF085. 2004.

[20] K. Yamamoto, T. Shibata, N. Ogiwara et al. "Secondary electron emission yields from the J-PARC RCS vacuum components". Vacuum, 2007, 81(6): 788-792.

[21] P. Dawson, "Secondary electron emission yields of some ceramics", J. Appl. Phys. 37(9) (1966) 3644–3645.

[22] M. Commisso, P. Barone, A. Bonanno et al. "Angular dependence of secondary electron emission from Cu surfaces induced by electron bombardment". Journal of Physics: Conference Series. IOP Publishing, 2008, 100(9): 092013

[23] E. M. Baroody. "A theory of secondary electron emission from metals". Physical Review, 1950, 78(6): 780.

[24] J. L. H. Jonker, "The angular distribution of the secondary electrons of nickel". Philips Research Reports, 1951, 6(5): 372-387.

[25] T. Koshikawa, R. Shimizu. "Secondary electron and backscattering measurements for polycrystalline copper with a spherical retarding-field analyser". Journal of Physics D: Applied Physics, 1973, 6(11): 1369.

[26] H. Seiler. "Secondary electron emission in the scanning electron microscope". Journal of Applied Physics, 1983, 54(11): R1-R18.

[27] R. Cimino, I. R. Collins. "Vacuum chamber surface electronic properties influencing electron cloud phenomena". Applied surface science, 2004, 235(1-2): 231-235.

[28] T. Koshikawa, R. Shimizu. "Secondary electron and backscattering measurements for polycrystalline copper with a spherical retarding-field analyser". Journal of Physics D: Applied Physics, 1973, 6(11): 1369.

[29] R. Larciprete, D. R. Grosso, M. Commisso et al. "The chemical origin of SEY at technical surfaces". arXiv preprint arXiv:1308.1290, 2013.

[30] V. Baglin, "The Secondary Electron Yield of Technical Materials and its Variation with Surface Treatments," LHC-Project-Report-433, Proc. 7th European Particle Accelerator Conference, Vienna, Austria, 26 - 30 Jun 2000, pp. e-proc. 217 (2000).

[31] V. Baglin, I. Collins, B. Henrist, N. Hilleret, G. Vorlaufer, "A Summary of Main Experimental Results Concerning the Secondary Electron Emission of Copper," LHC-Project-Report-472 ; CERN-LHC-Project-Report-472 (2001).

SEY FROM NOBLE METALS*

L. A. Gonzalez, M. Angelucci, R. Larciprete[1] and R. Cimino†
LNF-INFN, 00044 Frascati (Roma), Italy
[1]also at CNR-ISC Istituto dei Sistemi Complessi, 00185 Roma, Italy.

Abstract

The detailed study of the secondary electron yield of technical surfaces for very low electron landing energies (LE-SEY) is a very important parameter to be taken into account to ensure the correct operation of particle accelerators [1]. Despite such interest, LE-SEY (0-30eV) curve has been rarely addressed due to the intrinsic experimental complexity to control very low energy electrons. In this paper, we present an experimental SEY and LE-SEY study carried out on a number of materials of interest for multipacting and electron cloud (e-cloud) mitigation. We also compare here the SEY curves of clean polycrystalline noble metals with those measured on their technical surface.

INTRODUCTION

The accurate determination of the Secondary Electron Yield (SEY) of the materials exposed to radiation is a key issue in the technical design of new particle accelerators [1–8]. The prediction and the minimization of SEY is a strict requirement to limit electron cloud phenomena favoring the stability of machine performances [9–10]. Analogous criticalities concern microwave and RF components for space applications that find one of their most important functional limitations in the multipactor and corona breakdown discharges [11]. In this work we show an experimental study of the SEY and LE-SEY of Au, Ag and Cu which, due to their secondary electron emission properties, are of relevant interest for the realm of e-cloud mitigation and space applications. The comparison of the LE-SEY curves measured from different samples before (as received) and after (clean) UHV surface cleaning qualifies this technique as a tool to characterize the state of the samples surface.

EXPERIMENTAL DETAILS

The experiments were performed at the Material Science INFN-LNF laboratory of Frascati, Roma, with the equipment described elsewhere [1,2,8,10,12]. For the measurements, the samples were inserted in a μ-metal chamber with less than 5mGauss residual magnetic field at the sample position, under ultra high vacuum (UHV) conditions, with a background pressure below $2\text{x}10^{-10}$ mbar. The system is equipped with spectroscopic techniques capabilities such as X-Ray (XPS) and ultraviolet (UPS) photoelectron spectroscopy. A preparation chamber enabling sputtering preparation of the samples is also connected to the main analysis chamber.

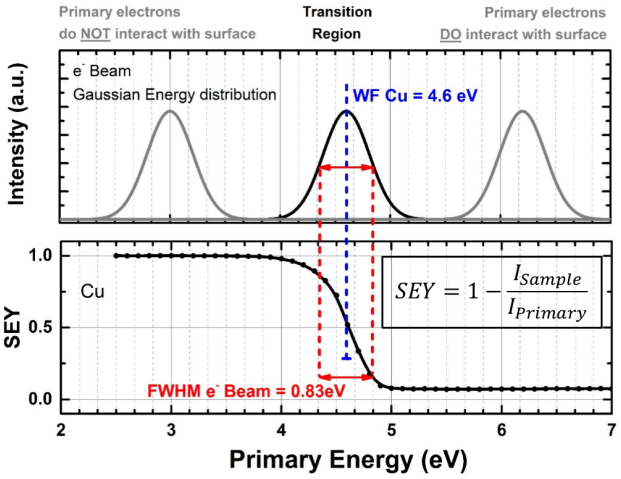

Figure 1: Upper panel: Energy distribution of impinging electrons for primary beam energy set above or below (grey curves) or coincident (back curve) with the sample work fuction. Lower panel: LE-SEY curve measured on the clean Cu sample.

The Secondary Electron Yield is defined as the ratio of the number of electrons leaving the sample surface (I_{out}) to the number of incident electrons (I_p) per unit area. I_p is measured by applying a positive bias on a Faraday cup, in order to prevent backscattered reemission out to the vacuum. To evaluate I_{out} we measure the sample current to ground I_s . Since $I_{out} = I_p - I_s$, then:

$$SEY = 1 - \frac{I_s}{I_p} \tag{1}$$

For this study, electrons were emitted from the cathode by means of thermionic emission. Their energetic distribution can be assumed to have a Gaussian shape with an energy width FWHM related to the cathode temperature. Such FWHM can play a critical role when the elctron primary energy E_p, becomes comparable to it. Fig. 1 shows the LE-SEY measured on polycrystalline clean Cu in the primary energy range 2 eV < E_p < 7 eV above the Fermi level. It can be observed that, for energies E_p < Ws - FWHM/2, primary electrons have not enough energy to overcome the sample work function (Ws) and interact with the sample, hence $I_s \sim 0$ and SEY is artificially calculated from (1) to be unity. On the other hand, when E_p > Ws + FWHM/2 all the electrons emitted from the gun have enough energy to interact with the surface, and hence the SEY is calculated with the relation (1). However, when Ws - FWHM/2 < E_p < Ws + FWHM/2,

* Work supported by the European Unions Horizon 2020 Research and Innovation Programe under Grant 654305, EuroCirCol Project, and by INFN Group V MICAproject
† roberto.cimino@lnf.infn.it

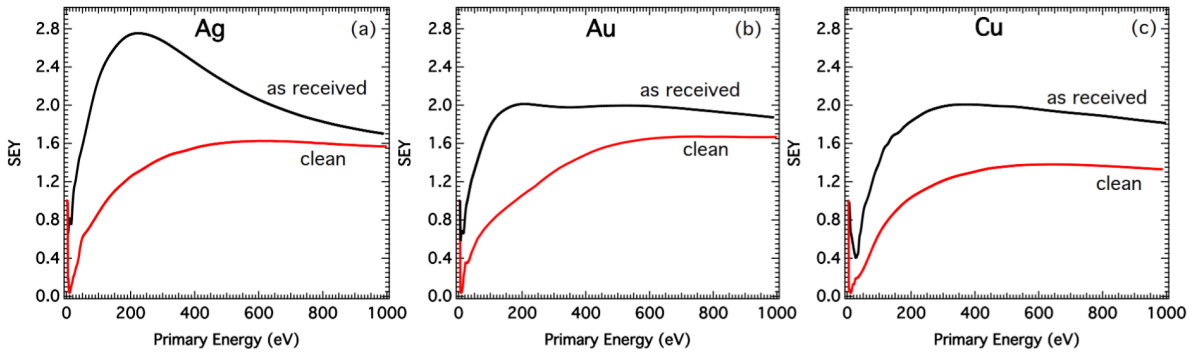

Figure 2: Comparisons between the SEY curves measured for clean (red line) and as received (black line) surfaces of a) Ag b) Au c) Cu polycrystalline samples. In all cases the primary energy is referred to the Fermi level [13].

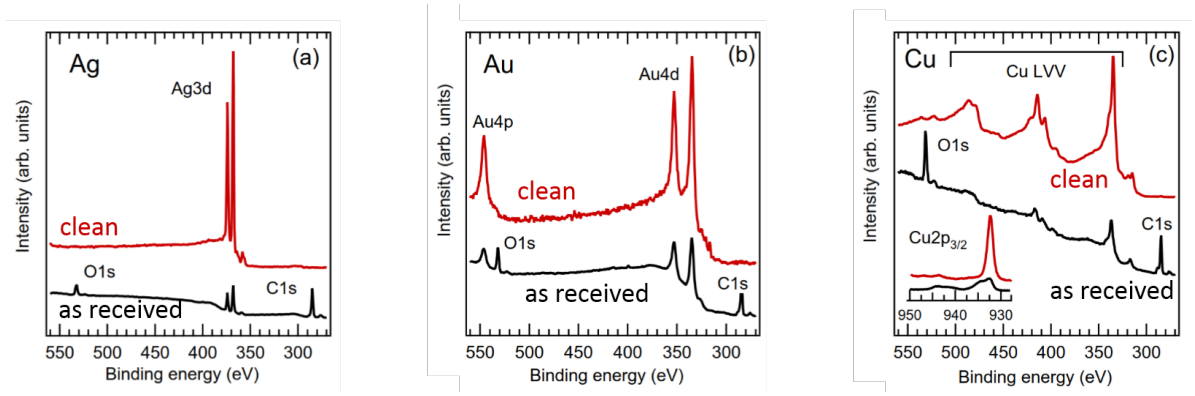

Figure 3: XPS spectra measured on "as received" (red lines) and Ar+ sputtered (black lines) a) Ag, b) Au and c) Cu polycrystalline samples. The inset in Fig.3c compares the high resolution spectra measured in the $Cu2p_{3/2}$ spectral region [13].

the number of electrons reaching the surface is not the same as measured by the Faraday cup since, due to the beam energy width, only some of them will have enough energy to interact with the solid. We can affirm that the width of this transition region is equal to FWHM. Nevertheless, this is a "blind region", where some of the impinging electrons interact with the surface and some are repelled, therefore in the region between Ws and Ws + FWHM/2 SEY cannot be accurately determined.

RESULTS

The SEY curves measured on "as received" Au, Ag and Cu samples are shown by the black lines in the upper panel of Fig.2. The SEY_{max} values measured for Ag, Au and Cu are 2.7, 2.0 and 2.1, respectively. In all cases the XPS spectra (black lines in Fig.3) exhibit very intense O1s and C1s core level peaks, which are determined by the presence of surface contamination on the samples. After surface cleaning by Ar^+ sputtering the level of contamination is brought below the XPS detection limit and correspondingly the SEY decreases for all three metals (red lines in Fig.3). SEY_{max} values measured for clean Ag, Au and Cu are 1.6, 1.7 and 1.3 respectively (red lines in Fig.2). Fig.4 shows LE-SEY measured on all the samples. It can be observed that all clean metals (red lines) show a sharp drop from 1 to values close to zero within an energy region smaller than 1 eV. The sharp transition gives the vacuum level position for each sample. The measured Ws values measured for Ag, Au and Cu are 4.4 eV, 5.3 eV and 4.6 eV respectively, in good agreement with the literature [14]. When moving to the "as received" samples, the black lines in Fig 4 show that for E_p above the transition region, the SEY remains higher than 0.5 for all metals. In the case of Ag and Au, the LE-SEY shows a minimum in proximity of the transition region followed by a 6 eV wide maximum and by a second minimum, suggesting the presence of a similar contaminating layer on both surfaces which dominates the overall sample behavior. In the case of Cu a continuous SEY decrease together with a net increase of the work function suggests a different chemical environment. This effect can be confirmed by analyzing the XPS O1s/C1s intensity ratio of each surface. It is of the order of 0.6-0.8 for Au and Ag, while it rises to 1.4 in the case of Cu, in agreement with the occurrence of metal oxidation, further confirmed by the $Cu2p_{3/2}$ line shape, which shows a dominating oxide phase (see inset in Fig.3c). The XPS analysis did not show any indication of oxidation on Ag and Au surfaces, suggesting that surface contaminants have a dominating effect on the SEY, even in the absence of surface oxidation.

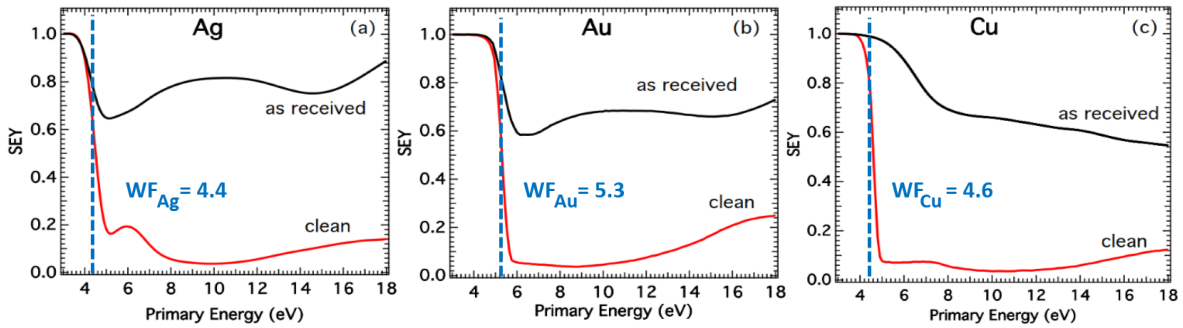

Figure 4: Comparisons between the LE-SEY curves measured for clean (black line) and as received (red line) surfaces of a) Ag b) Au c) Cu polycrystalline samples. In all cases the primary energy is referred to the Fermi Level [13].

In order to analyze the importance that surface contaminants have on SEY, the clean Cu sample was cooled down to 10K and dosed with CO. Fig 5 shows the LE-SEY (a) and SEY (b) measured on the cold Cu sample at CO coverages of 0.5 ML and 1 ML. Results measured at RT are also presented for comparison. The results show that cooling down does not change the SEY behavior of the sample. Fig 5 also shows the SEY results measured on the cold Cu exposed to the UHV residual gas molecules for a prolonged time. The coverage of the sample with contaminating molecules was estimated to be <0.3ML. The presence of such contaminants modifies only the LE-SEY which slightly increases with respect to the clean surface. It can be observed that SEY_{max} dicreases with increasing CO coverage whereas the inverse behavior is observed at the LE-SEY region. The fine structures which appear in the LE-SEY curve measured at CO coverage of 1 ML indicate that the signal is dominated by the adsorbed CO and will be the subject of a future investigation. The comparison between the curves taken with and without adsorbed CO indicates that a coverage of 1 ML is sufficient to deeply modify the LE-SEY curve proving the high surface sensitivity of this technique.

CONCLUSION

We have shown that the surface chemical state is a key factor in determining the metal SEY and LE-SEY curves. Whereas clean metals exhibit SEY values that do not exceed 1.6 and are even lower in the case of copper, the presence of a contaminating layer can rise SEY_{max} well above 2. More interestingly, the LE-SEY curves show heavy changes in the presence of adsorbates even at submonolayer coverage. Our results demonstrate that for very slow electrons the LE-SEY curve allows an easy measurement of the sample work function. Then SEY and LE-SEY are valid spectroscopic tools, that, with a limited experimental requirement, can be used both to determine the response of materials to external excitation in terms of secondary electrons emission and also as flexible and sensitive diagnostics to state surface cleanliness and to follow surface reactions, desorption and ultrathin layer growth.

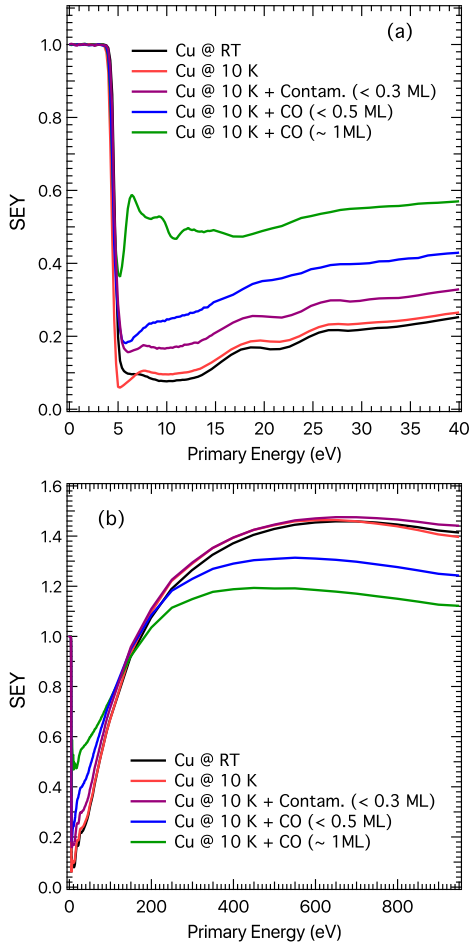

Figure 5: a) LE-SEY and b) SEY curves measured at 10 K on a polycristalline Cu sample clean (red) and in the presence of 0.3 ML of adsorbed residual gases (purple) and of about 0.5 ML (blue) and 1 ML (green) of adsorbed CO. The LE-SEY and SEY curves measured on the clean sample at RT are shown for comparison (black). In all cases the primary energy is referred to the Fermi level [13].

ACKNOWLEDGEMENTS

The authors would like to thank staff of Dafne-light for technical support.

REFERENCES

[1] R. Cimino, L.A. Gonzalez, R. Larciprete, A. Di Gaspare, G. Iadarola, and G. Rumolo Phys. Rev. ST Accel. Beams 18, 051002 (2015)

[2] R. Cimino, A. Di Gaspare, L.A. Gonzalez, R. Larciprete, IEEE Transactions on Plasma Science 43(9):1-1 (2015)

[3] A. W. Chao, K. H. Mess, M., and F. Zimmermann, eds., Handbook of Accelerator Physics and Engineering: 2nd Edition (World Scientific Publishing Co Pte Ltd, 2013).

[4] F. Zimmermann, Phys. Rev. ST Accel. Beams 7, 124801 (2004)

[5] R. Cimino, I. Collins, M. A. Furman., M. Pivi, F. Ruggiero, G. Rumolo, and F. Zimmermann, Phys. Rev. Lett. 93, 014801 (2004).

[6] O. Domınguez, K. Li, G. Arduini, E. M etral, G. Rumolo, F. Zimmermann, and H. M. Cuna, Phys. Rev. ST Accel. Beams 16, 011003 (2013)

[7] Proc. ECLOUD12 (La Biodola, Isola d'Elba, Italy), http://ecloud12.web.cern.ch/ecloud12/ (2012).

[8] R. Cimino and T. Demma, Int. J. Mod. Phys. A 29, 1430023 (2014).

[9] M. Pivi, G.Collet, F.King, R.E.Kirby, T.Markiewicz, T.O.Raubenheimer, J. Seeman, and F.LePimpec, Nucl.Instr. and Meth.A 621, 47 (1995).

[10] R. Cimino, D. Grosso, M. Commisso, R. Flammini, and R. Larciprete, Phys. Rev. Lett. 3, 2098 (2012).

[11] S. T. Lai, Fundamentals of Spacecraft Charging: Spacecraft Interactions with Space Plasmas (Princeton, NJ, 2002).

[12] R. Cimino, Nucl. Instrum. Methods Phys. Res., Sect. A 561, 272 (2006).

[13] L.A. Gonzalez, M. Angelucci, R. Larciprete and R. Cimino, AIP Advances 7, 115203 (2017)

[14] A. Kawano, Progr. Surf. Sci. 83, 1 (2008).

THE EFFECT OF THE STRUCTURAL PROPERTIES ON THE SEY OF C MATERIALS.

L. A. Gonzalez, M. Angelucci, R. Larciprete[1] and R. Cimino LNF-INFN, 00044 Frascati (Roma), Italy
[1]also at CNR-ISC Istituto dei Sistemi Complessi, 00185 Roma, Italy.

Abstract

We review here the dependence of the secondary electron yield (SEY) of carbon materials on the structural ordering of the C lattice and surface damage. We followed the SEY evolution during the thermal graphitization of thin amorphous carbon layers and during the amorphization of highly oriented pyrolytic graphite by means of Ar^+ bombardment. C1s core level and valence band spectroscopy, used to follow the structural modification, were measured in parallel with SEY curves. In the first case the SEY decrease observed with the progressive conversion of sp^3 hybrids into six-fold aromatic domains was related to the electronic structure of the C-films close to the Fermi level. We found that a moderate structural quality of the C layer, corresponding to aromatic clusters of limited size, is sufficient to obtain a SEY as low as ~ 1. For the bombarded graphite, the strong lattice damaging remains limited to the near surface layer, where the high density of defects reduces the transport of incoming and secondary electrons. Then, the SEY curves resulted differently modified in the low and high primary energy regions, but their maximum values remained favorably low. Our findings demonstrate that SEY, besides being an indispensable means to qualify technical materials in many technological fields, can be also used as a flexible and advantageous diagnostics to probe surfaces and interfaces.

INTRODUCTION

Secondary Electron Yield (SEY) is an ubiquitous property of matter determining the actual behavior of a surface in a device and/or in technologically relevant applications. In general, an efficient SEY reduction for materials exposed to high radiation doses might rely on the use of specific low emitting coatings, especially based on C, as it has been recently proposed for the baseline design of the high luminosity large hadron collider (HL-LHC) [1] and, potentially, for future circular colliders (FCC-hh) [2]. The beneficial effect of carbon coatings is usually related to the moderate SEY of the sp^2 C hybridization, lower with respect to other hybridization states [3], as it has been ascertained for several nanographitic materials as fullerene [4], nanotubes [5], graphene [6, 7] and graphene nanoplatelets [8]. The relevance of this issue makes the knowledge of the relation between microstructural and electronic properties of C materials and their macroscopic SEY highly desirable. On the other hand, C layers deposited on large areas, with techniques compatible with the geometry of accelerator components, may lack of high structural quality. Furthermore, even good graphitic layers, once exposed to electron, photon and ion fluxes during machine operation, might result severely damaged. It is therefore important to validate the SEY properties of graphitic films while their structural quality is altered by external factors.

In order to shed light on these points, in the last years we investigated the effect that the structural ordering of the C lattice has on the macroscopic SEY properties of ultrathin C layers. To this aim in a first study [9] we deposited amorphous C films on copper substrates and used x-ray (XPS) and ultraviolet (UPS) photoelectron spectroscopy to follow *in situ* the $sp^3 \rightarrow sp^2$ structural reorganization and the coalescence of the sp^2 clusters into nanocrystalline graphite induced by thermal annealing, while probing in parallel the SEY properties of the samples. In order to explore the opposite process, in a second study [10] we introduced controlled densities of crystal defects in a highly oriented pyrolytic graphite (HOPG) sample by subsequent cycles of Ar^+ ion bombardment at low kinetic energy (500 eV). Also in this case the effects of the lattice defects on the electronic, structural and secondary emission properties were monitored by measuring *in situ* UPS and XPS spectra together with SEY curves. Special attention was paid not only to the variation of the maximal SEY value, but also to more subtle changes on the entire curve, with a particular attention to the low energy secondary electron yield LE-SEY at low (<40 eV) primary electron energy [11]. In the following we summarize the results and elucidate the discordant behavior observed for the two systems.

EXPERIMENTAL

The experiments were performed in the Material Science Laboratory of the INFN-LNF at Frascati (Rome, Italy), in an ultra-high vacuum (UHV) system consisting of a preparation chamber and an analysis chamber, both having a base pressure of $2–5\times10^{-10}$ mbar.

Carbon films were grown on polycrystalline Cu substrates at room temperature by radiofrequency magnetron sputtering using a power of 50 W and Ar pressure of 6×10^{-2} mbar. The thickness of the films used for this experiment was estimated to be of the order of 20 nm. Thermal annealing was performed in steps, by heating for 30 minutes the sample at a fixed temperature up to 1070 K. The temperature was measured by a calibrated pyrometer.

The HOPG sample was cleaved with adhesive tape before being loaded into the UHV system. Prolonged thermal annealing at temperatures of $\sim$ 1000 K was carried out to desorb contaminants, whose absence was crosschecked by XPS. The HOPG was Ar^+ ion bombarded at 500 eV and Ar pressure of 5×10^{-6} mbar for increasing doses up to 4.5×10^{14} $\pm$ 0.1 Ar^+/cm^2. After each ion dose, UPS and XPS analysis

of the surface, as well as SEY measurements were carried out.

XPS and UPS measurements were performed by using an Omicron EA125 analyzer to reveal the photoelectrons excited by the non monochromatic radiation of Al Kα (hν = 1486.7 eV) or Mg Kα (hν = 1254.6 eV) and He II (hν =40.8 eV) sources, respectively.

The SEY(δ) is defined as $SEY=I_{out}/I_p=(I_p-I_s)/I_p$, where I_p is the current of the primary electron beam hitting the sample, I_{out} is the current of the electrons emerging from the sample and I_s is the sample current to ground, as measured by a precision amperometer. SEY is measured as described in detail in Refs. [12, 13]. In brief I_p (some tens of nA) was measured by means of a Faraday cup positively biased, whereas I_s was determined by biasing the sample at -75 V. SEY curves as a function of the primary energy E_p are characterized by a maximum value (δ_{max}) reached in correspondence of a certain energy (E_{max}).

RESULTS AND DISCUSSION

In the first study [9] we deposited amorphous C films on copper substrates and followed *in situ* the $sp^3 \rightarrow sp^2$ structural reorganization induced by thermal annealing , while acquiring at each step the SEY curve . Figures 1a and 1b show the evolution of the C1s and valence band spectra. The C1s spectrum measured on the as-deposited a-C layer (upper curve in Fig.1a) is peaked at 284.65 eV and exhibits a FWHM of 1.8 eV. The shift of 0.35 eV with respect to the position of the graphitic carbon indicates the presence a consistent fraction of sp^3 hybridized atoms. Accordingly, the valence band measured on the as-deposited layer (top curve in Fig.1b) shows only a broad unstructured peak centered at 7.7 eV related to the σ bonds, consistent with the presence of sp^2 chains and limited aromatic domains coexisting with the sp^3 phase. In the Fermi level region the VB spectrum reveals the presence of an energy gap of $\sim$ 0.4 eV. With thermal annealing, the main σ peak progressively narrows and the feature related to the π band in graphite appears at $\sim$ 3 eV, indicating a rising concentration of the six-fold coordinated rings. In parallel, the density of states in the region close to the Fermi level increases and in the sample annealed at 1070 K resembles the quasi metallic character typical of the graphitic structures. Also the C1s peak manifests the occurrence of graphitization. The BE of C1s photoelectrons in C materials is related to the hybridization state of the emitting atoms and is a useful mean to estimate the sp^3/sp^2 ratio, since typically the sp^3 and sp^2 fingerprint components are found with a separation of 0.8-0.9 eV [14]. The spectra in Fig.1a show that, with increasing annealing temperature, the C1s peak shifts to lower BE due to the progressive decrease of the sp^3 component, and after the annealing at 1070 K is peaked at 284.3 eV. However, even if this change indicates a substantial $sp^3 \rightarrow sp^2$ conversion, the wide spectral FWHM of the C1s peak (1.5 eV) reveals a low structural quality of the sp^2 network. The evolution of the SEY and LE-SEY curves with thermal annealing is summarized in Figs.2a and 2b. The slight δ_{max} decrease from 1.25 to 1.16 induced by the annealing to 710 K is followed by a more substantial reduction to 1.03 for the film annealed at 900 K, whereas after the last annealing step δ_{max} decreases to 0.99 and E_{max} shifts to 250 eV. The same trend indicating the SEY reduction is evident in the low energy region (Fig.2a).

Among the factors that might be at the origin of the observed behavior we can disregard the variation of the work function, which for nanographitic C has been shown to decrease with graphitization [15], and would then correspond to an increase of SEY. Instead, the behavior in the vicinity of the Fermi level can play a role. In a-C the presence of a gap at the Fermi level, setting a prohibited energy interval, reduces the probability for secondary electrons to lose energy through electron-electron collisions [4]. With the expansion of the graphitic domains induced by thermal annealing, the disappearance of the energy gap and the increasing number of electronic states close to the Fermi level likely raise the energy dissipation channels and reduce the diffusion length, thus effectively contributing to lower the yield of the secondary electrons emerging from the sample surface. Then the decrease in the SEY is directly related to the extent of graphitization. It is worth noting that Raman spectroscopy (not shown) has established that the average dimension of the graphitic crystallites, which is of the order of 1.3 nm in the pristine a-C layer, after annealing does not exceed $\sim$ 3.8 nm, confirming the moderate crystalline quality of the annealed film indicated by the width of the C1s peak. Then, it turns out that the presence or aromatic clusters of a few nanometers in size is sufficient to lower the macroscopic SEY to the level of graphitic carbon with much higher structural ordering [9]. It is likely that in materials with small graphitic grains the enhanced scattering at the grain boundaries provides an additional contribution to reduce the number of secondary electrons emerging from the surface.

In the second part of this study we started with a HOPG sample and introduced controlled amounts of defects in the crystalline lattice by subsequent cycles of Ar^+ ion bombardment at low kinetic energy (500 eV). Low energy ion bombardment can produce interstitial defects created by trapping incident ions underneath the carbon planes and generate vacancies in the graphitic network. The structural defects are expected to change the electronic and structural properties of HOPG and consequently to affect its secondary emission properties.

The extent of Ar^+ induced HOPG amorphization was monitored by C1s and valence band spectroscopy. Figure 1c shows that the C1s peak, which for HOPG is located at BE of 284.2 eV, after Ar^+ bombardment remains centered at the same BE and exhibits a broader line shape. Hence, ion bombardment ruins the crystalline network without inducing a real change in the hybridization of the C atoms. Similar indications are provided by the valence band spectra shown in Fig.1d. The spectrum of the intact HOPG exhibits sharp features at 4.3 (σ band) and 7.5 eV (π band) [16] (the peak

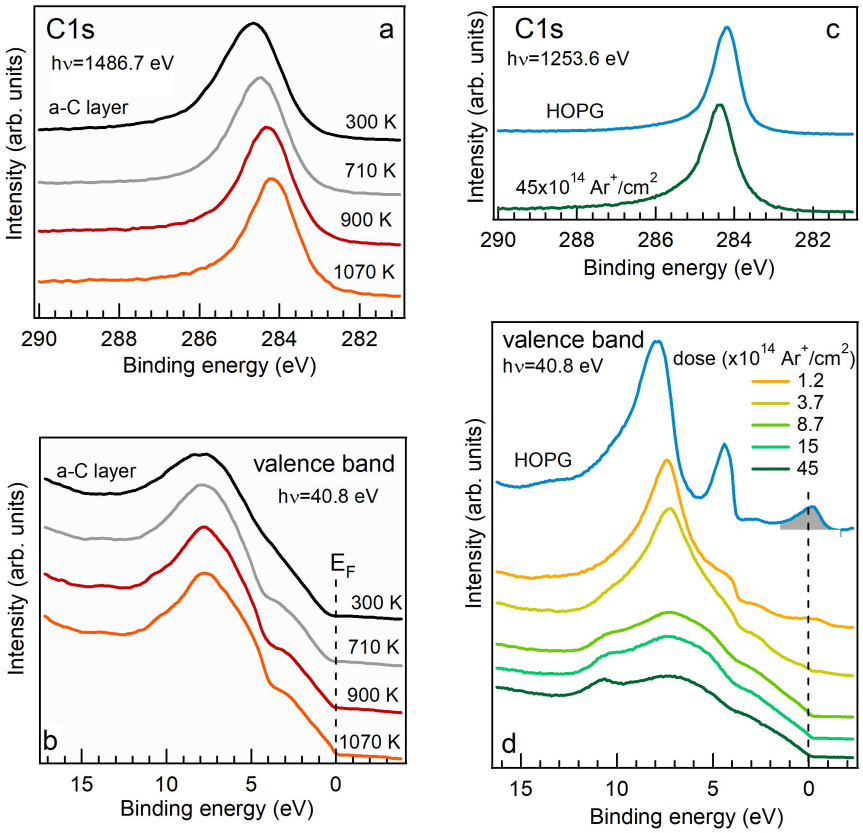

Figure 1: a) C1s and b) valence band spectra measured on the as-prepared a-C layer (black curves) and as function of the annealing temperature. c) C1s and d) valence band spectra measured on the pristine HOPG sample and after the exposure to increasing doses of Ar^+ ions with kinetic energy of 500 eV.

just above the Fermi Level is related to photoelectron emission excited by the He II satellite at hν=48.4 eV). Both bands progressively weaken and the broad unstructured features observed for doses higher than 5.0×10^{13} Ar^+/cm^2 reveal a total amorphization of the crystalline structure. The indications provided by the valence band spectra are paralleled by the evolution of the LE-SEY curves measured as a function of the ion dose (Fig.2d). The curve measured on pristine HOPG shows features related to the elastic and inelastic electron-solid interactions, which provide direct information on the unoccupied band structure [17, 18]. Such structured line shape is progressively canceled as the ion dose increases, due to the loss of crystalline ordering after the nucleation of lattice defects. At dose of 1.5×10^{14} Ar^+/cm^2 the smooth curve profile is clearly indicative for the presence of strong disorder in the probed sample depth. Complementary information is provided by the extended SEY curves shown in Fig.2e. The intact HOPG exhibits a maximum value of 1.0 for E_p in the 220-400 eV range. With rising ion dose, for $E_p > 200$ eV the SEY progressively decreases up to the ultimate value of 0.6. On the other hand in the low E_p region, δ_{max} rises to 1.1 for doses of the order of 15×10^{13} Ar^+/cm^2. We can then conclude that graphite maintains favorable secondary emission properties even when significantly defected. However the contrasting SEY behavior, which with increasing lattice defectivity rises at low E_p and decreases at high E_p, deserves a clarification.

It is interesting to compare this trend to the behavior observed in the previous paragraph during the graphitization of the a-C films. As can be seen in Figs.2b and 2e, whereas in the first case thermal annealing determines a nearly constant SEY reduction in the whole E_p region, ion bombardment modifies selectively the SEY of HOPG. The discordant behavior is made more evident by plotting in Fig.2c the δ_{max} values vs. annealing temperature measured for the first experiment, which show a trend consistent with the homogeneous graphitization of the whole layer, and in Fig.2f the SEY values measured at E_p=175 and 800 eV in the second experiment, showing at high, but not at low E_p, the SEY drop with increasing sputtering dose.

In order to explain the observed results one must consider that the localized states which appear near the defect sites act as scattering centers for electron waves, which affect the transport properties of the damaged HOPG surface layer, decreasing the electron mean free path with respect to defect-free lattice. The ion bombardment produces a "bi-layered" structure, with a ~2 nm thick damaged layer [10] on top of the pristine HOPG bulk. Consequently, the transport of

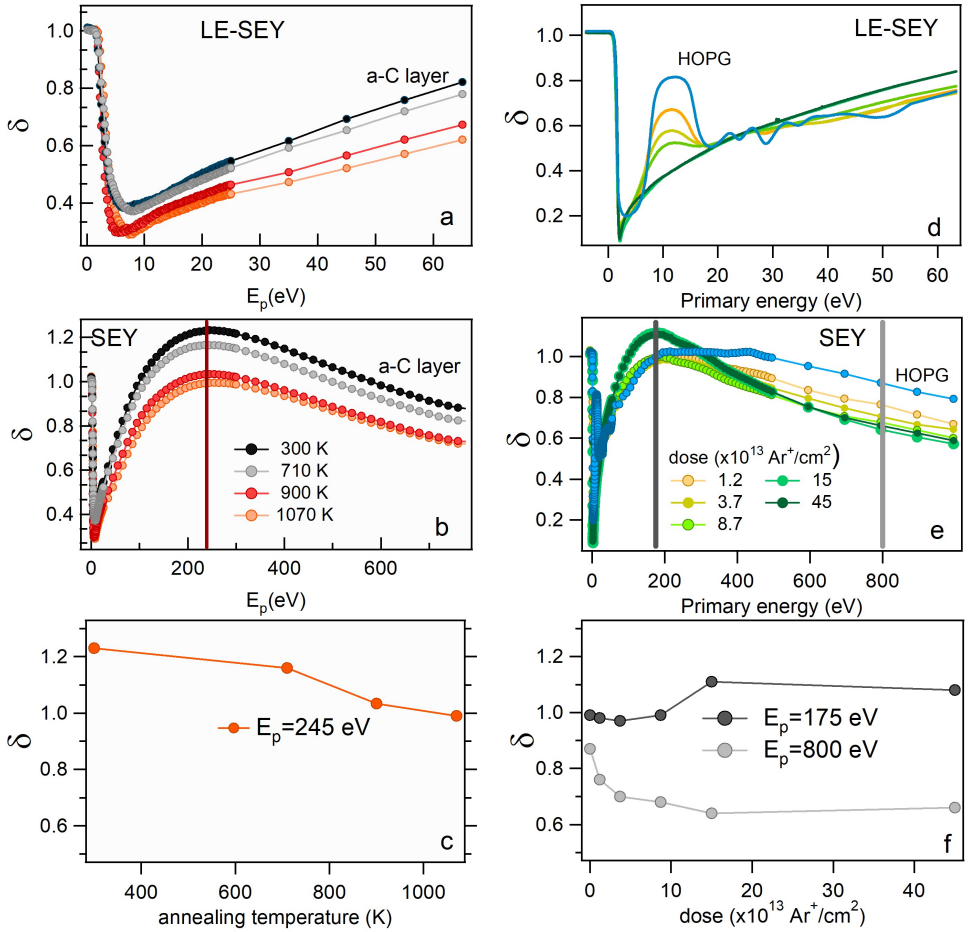

Figure 2: a) LE-SEY and b) SEY curves measured on the as-prepared a-C layer (black curves) and as function of the annealing temperature. d) LE-SEY and e) SEY curves measured on the pristine HOPG sample and after the exposure to increasing doses of Ar^+ ions with kinetic energy of 500 eV. c) δ_{max} values (E_p=245 eV) vs. annealing temperature measured during the graphitization of the a-C films (cfr. Fig.2b); f) δ values measured at E_p=175 and 800 eV vs. the Ar^+ dose during the amorphization of HOPG (cfr. Fig.2e).

primary and secondary electrons depends on whether they move through the defected or through the intact graphitic lattice [10]. The primary electron penetration depth λ, which for 40 eV $\geq E_p \geq$ 200 eV is $\leq$ 1 nm [19], decreases in the presence of defects, which means which *i)* primary electrons penetrate less than in the case of crystalline HOPG and *ii)* secondary electrons are produced in regions closer to the surface and escape more effectively to vacuum. Such effects finally determine the observed increase of SEY at Ep=200 eV after very high Ar^+ doses. At E_p=800 eV the kinetic energy of the primary electrons is sufficiently high that they will cross the damaged surface barrier. In that case the secondary electrons generated within the undamaged underlying HOPG, when traveling towards the surface with kinetic energies below 50 eV, suffer a significant mobility reduction [20], which hampers their escape into vacuum. This effect becomes more significant with increasing defect density at high ion doses.

CONCLUSIONS

We have shown that for C materials the SEY behavior and the structural properties are closely related. For amorphous C thin films the secondary emission decreases with the conversion of sp^3 hybrids to six-fold aromatic domains and the reason of that has been identified in the strong correlation between the electronic structure close to the Fermi level and the yield of secondary electrons. What is relevant is that a moderate structural quality of the C layer is sufficient for a considerable SEY decrease as aromatic clusters of limited size approach the secondary emission properties of graphite.

Amorphization of HOPG has been proved to modify the SEY curve, whose δ_{max}, however, remains stable and low ($\leq$1.1) even in the presence of a high defect density. The resulting LE-SEY curves strongly depend on the lattice ordering, which may have significant implications on simulations where SEY and LE-SEY curves are parametrized.

In conclusion we can remark that SEY and LE-SEY are valid tools, which, with a limited experimental requirement,

can be used as flexible diagnostics sensitive to chemical and structural properties of materials.

ACKNOWLEDGEMENTS

This work was supported by LNF through the grV project "MICA" . The authors wish to thank the DAFNE-L technical team for continuous assistance during the experiments.

REFERENCES

[1] G. Apollinari and I. Béjar–Alonso and O. Brüning and P. Fessia and M. Lamont and L. Rossi and L. Tavian, *High Luminosity Large Hadron Collider (HL-LHC): Technical Design Report V.0.1*, CERN Yellow Reports: Monographs; 4/2017

[2] R. Cimino, V. Baglin, and F. Schäfers, Phys. Rev. Lett. 115, 264804 (2015)

[3] M. Nishiwaki and S. Kato, J. Vac. Soc. Jap. 118, 48 (2005)

[4] J. M. Ripalda, I. Montero, L. Vázquez, D. Raboso, and L. Galán, J. Appl. Phys. 99, 043513 (2006)

[5] M. K. Alam, P. Yaghoobi, M. Chang, and A. Nojeha, Appl.Phys. Lett. 97, 261902 (2010)

[6] J. Luo, P. Tian, C.T. Pan, A. W. Robertson, J. H. Warner, E. W. Hill, and G. A. D. Brigg, ACS Nano 5, 1047 (2011)

[7] H. Hiura, H. Miyazaki, and K. Tsukagoshi, Appl. Phys. Expr. 3, 095101 (2010)

[8] I. Montero, L. Aguilera, M. E. Davila, V. C. Nistor, L. A. Gonzalez, L. Galan, D. Raboso, and R. Ferritto, Appl. Surf. Sci. 291, 74 (2014)

[9] R. Larciprete, D. Grosso, A. D. Trolio, and R. Cimino, App. Surf. Sci. 328, 356 (2015)

[10] L. Gonzalez, R. Larciprete, and R. Cimino, AIP Advances 6, 095117 (2016)

[11] R. Cimino, L. Gonzalez, R. Larciprete, A. Di Gaspare, G. Iadarola, and G. Rumolo, Phys. Rev. ST Accel. Beams 18, 051002 (2015)

[12] R. Larciprete, D. Grosso, M. Commisso, R. Flammini, and R. Cimino, Phys. Rev. ST Accel. Beams 16, 011002 (2013)

[13] R. Cimino and T. Demma, Int. J. Mod. Phys. A 29, 1430023 (2014)

[14] J. Diaz, G. Paolicelli, S. Ferrer, and F. Comin, Phys. Rev. B 54, 8064 (1996)

[15] A. Ilie, A. C. Ferrari, T. Yagi, S. E. Rodi, J. Robertson, E. Barborini, and P. Milani, J. Appl. Phys. 90, 2024 (2001)

[16] S. Y. Zhou, G.-H. Gweon, C. D. Spataru, J. Graf, D.H. Lee, S. G. Louie, and A. Lanzara, Phys. Rev. B 71, 161403 (2005)

[17] P. J. Mølert and M. H. Mohamed, J. Phys. C: Solid State Phys. 15, 6457 (1982)

[18] R. F. Willis, B. Fitton, and G. S. Painter, Phys. Rev. B 9, 1926 (1974)

[19] M. P. Seah and W. A. Dench, Surf. Interf. Analysis 1, 1 (1979).

[20] A. Lherbier, B. Biel, Y.-M. Niquet, and S. Roche, Phys. Rev. Lett. 100, 036803 (2008)

PHOTO REFLECTIVITY AND PHOTO ELECTRON YIELD FROM TECHNICAL SURFACES *

A. Liedl[1†], M. Angelucci[1], E. La Francesca[1,3], F. Schäfers[2], M.G. Sertsu[2], F. Siewert[2], A. Sokolov[2] and R. Cimino[1]
[1] *LNF-INFN, 00044 Frascati, Italy*
[2] *Helmholtz-Zentrum-Berlin, 12489 Berlin, Germany*
[3] *University of Rome "La Sapienza", 00185 Rome , Italy*

Abstract

The knowledge of material properties is an essential step to design particle accelerators and High Energy Colliders. During operation of these machines, the walls of the vacuum chambers are subjected to bombardment of photons and electrons. The detrimental interactions may be followed by issues related to vacuum and beam instability. Hence, it becomes crucial to obtain experimental data about these interaction in conditions as close as possible to the operative ones. Among others properties, Reflectivity (both specular and total component) and photoyield are of particular interest. These data will be used in numerical simulations to design vacuum systems. In an experimental campaign, carried out at the OPTICS beamline of BESSYII, we investigated the Reflectivity and the Photon Yield of technical materials of interest for the High Luminosity LHC upgrade and Future Circular Collider-hh design.

INTRODUCTION

The design of vacuum systems for future charged particle accelerators must face and solve issues related to beam induced effects [1]. Particularly, the High Energy Colliders and the positively charged particles accelerators may incur into important limitations due to the Synchrotron light interaction with vacuum chambers walls. This interaction can induce gas desorption and photoelectrons from the walls surface with detrimental consequences to vacuum stability, heat load and e-cloud build up. The scientific community has developed solutions to mitigate such effects and their consequences [1] but the development of a new generation of High Energy Collider, pushing forward the characteristics of these machines (energy, performances, size), increases the impact of beam induced effects. [2]
The Future Circular Collider (FCC-hh) considers to reach an energy of 100 TeV in the center of mass operating with a up to 16 T Dipole magnet field. These objective enhances the design constraints already present in LHC such as the maintenance of superconductive temperature on the dipole walls, vacuum and beam stability. During the LHC design and development, these problems have been solved by the construction of a beam screen (BS) compliant with all these requirements. BS of LHC represents the starting point of the new FCC-hh BS design [2].
Simulations of the various solutions proposed for the BS design are the tool for the forecasting of the performances in terms of heat load, beam induced multipacting and molecular density behavior [3-4]. To simulate such phenomena, the codes need some input parameters including photon Reflectivity (R), photoyield (PY, e- produced per incident photon), secondary electron yield (SEY), photon and electron stimulated desorption (PSD and ESD) and their dependencies on photon energy distribution and angle of incidence [5-12]. Calculations, modelling the effect of these parameters on the machine performance, are often based on the assumption of ideal material surface or trying to suppose characteristic of the operating ones. We show here, that only measurements on real representative samples can give the right input parameters[9]. In this context, this work presents some results of the experimental campaign conducted at OPTICS beamline at BESSYII on different technical surfaces.

EXPERIMENTAL

OPTICS beamline at BESSYII is a dedicated laboratory for "at wavelength" metrology of x-ray optical elements, reflectometry for nondestructive characterization and depth-profiling of microstructures, layered systems and buried interlayers [13-14]. There are many techniques for characterization of surface quality and finish of optical systems (Atomic Force Microscopy, White Light Interferometry, X-ray Diffraction and others..) and at-wavelength metrology for reflectivity and diffraction efficiency represent the final test bench. OPTICS beamline has been upgraded in the last years as described in details in [15]. The average spot size at the sample is 0.2x0.3 mm^2 size with a divergence of 0.5 mrad x 3.6 mrad. These features are sufficient to avoid any significant increase of beam size up to the detector positioned 310mm further downstream. The photon beam energy interval used for the experiment ranges from 35 to 1800 eV. The lower limit was determined to avoid second or higher orders of radiation, since above 35 ev, we can use second order suppression filters. The upper limit is the result of an optimization of radiation flux, available beam time and experimental specifications. Thus, the energy range

* This work was supported by INFN National committee V trough the "MICA" project. We thank HZB for the allocation of synchrotron radiation beamtime. Research leading to these results has also received funding by the project CALIPSOplus, under the Grant Agreement 730872 from the EU Framework Programme for Research and Innovation HORIZON 2020. We thank R. Valizadeh and O. Malyshev for providing us with the LASE sample. M.A. acknowledges the support of the WP4 "EuroCirCol" project, the European Union's Horizon 2020 research and innovation programme under grant agreement No. 654305.
† andrea.liedl@lnf.infn.it

covers perfectly the HILUMI-LHC spectrum (ϵ_{cr}≈50 eV) and also a useful interval for the understanding of beam induced effects in FCC-hh (ϵ_{cr}=4.3 keV). The endstation of the beamline is the UHV-Reflectometer, equipped with a four circle goniometer: two for samples and two for the detector. Furthermore, the sample position can be adjusted by using a UHV tripod systems (six degrees of freedom) that allows the fine alignment of the sample. The resolution and the range of such movements are extremely precise and allow to work at as grazing incidence as possible close to the working SR incident angle in LHC and FCC, respectively 0.28° and 0.07°. Thus, the energy range and the geometrical conditions, provided at the end-station, guarantee the reliability of the obtained data as input for the simulation codes and indicate the necessity of specialized experimental layout for such benchmark measures. For our experiments we define:

- θ_i:as the angle of incidence between photon beam and sample surface;
- θ_r:as the detector angle that identifies the position of the detector from the optical axis;
- ϕ:as the detector off-plane position defined as the distance from the plane normal to sample surface and containing the optical axis (ϕ=0).

Downstream, a series of detectors with variable apertures, obtained by the use of different pinholes, are available as described in ref [12-14]. The use of the specialized instrumentation of the OPTICS beamline allows to measure the different optical properties. Specular Reflectivity (R) is measured in the configuration shown in Fig.1-Left. The reflected beam is collected by a 4x4mm^2 detector placed at the specular position θ_r=2θ_i. The acceptance angle of the detector is 0.37° both in θ_r and in ϕ. This large aperture ensures the detection of the specular reflected signal and also some scattered radiation by rougher surface. R was measured either keeping fixed the photon beam energy and scanning over the different incident angles, or keeping fixed the geometry and scanning over the photon beam energy. The minimum angle of incidence was determined by the length of the sample and the beam size, so can change case by case. PY is measured in the same configuration measuring the photoelectrons by the current read through a Keythley picoamperometer connected to ground. During the measurement, the sample is insulated and without any bias in order to avoid possible noise. In the same way of R, PY was measured as function of incident angles and as function of photon energy. Total Reflectivity (R_t) is measured in the configuration shown in Fig.1-Right. The reflected and scattered radiation are collected by the detector, scanning over θ_r and keeping fixed the photon energy and the incident angle. The acquisition is repeated for other two different off-plane ϕ values in the positive verse. Assuming a symmetrical behavior on the two sides of the sampe, the angular distribution of the scattered radiation over a solid angle Ω is measured and R_t is obtained by this full solid angle integration.

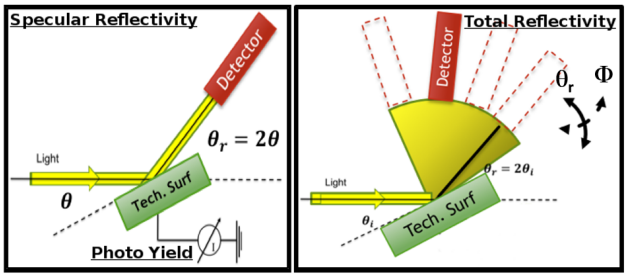

Figure 1: Two experimental configurations. (Left) $\theta/2\theta$ geometry for the measurement of R and PY keeping fixed beam energy scanning over different angles or keeping fixed geometry scanning over different beam energies. (Right) Measurement of angular distribution of reflected and scattered radiation keeping fixed beam energy and angle of incidence θ_i

SAMPLES

In this work we present results of some samples representative of materials of interest for the FCC-hh design (Fig.2). In particular we have analyzed:

- Flat Copper (Cu): Commercial Copper. Four samples distinguished by different surface treatments and different roughness (Fig.2a);
- LHC Copper (Cu-LHC): Representative sample of copper colaminated material used in LHC (Fig.2b);
- LHC Copper Saw Tooth (ST): Representative sample of copper used in the LHC with a Saw Tooth profile (40 µm high and 500µm pitch) (Fig.2c);
- Laser Treated Copper (LASE): a Representative sample of Copper treated by laser ablation process. This treatment gives to the surface particular morphology constituted by different scale structures, micrometrical grooves with coral-like sub-micron agglomeration of nano-spheres. (Fig.2d). The sample was processed at ASTeC, STFC Daresbury Laboratory, by R. Valizadeh within the WP4 EuroCirCol using the following Laser Parameters: Scan Speed 180mm/s; Power 50W: Waveform 30; Pitch 20um and Wavelength 1064nm; [16]

These four families of samples differ firstly for the roughness e for the surface aspect due to the surface treatments. The roughness was measured by the use of AFM microscopy in various metrology laboratories (HZB, CERN, INFN, CNIS-Rome1) investigating an area of 20x20 um^2. The samples Cu and Cu-LHC present similar values of R_a, respectively ≈10 nm and ≈ 15 nm, but different enough to have an impact on the optical properties. On the other hand, the design of the ST was specific to avoid the forward Reflection [17] while the LASE's hard processed surface was particularly designed for the reduction of emission of produced secondary electrons [16].

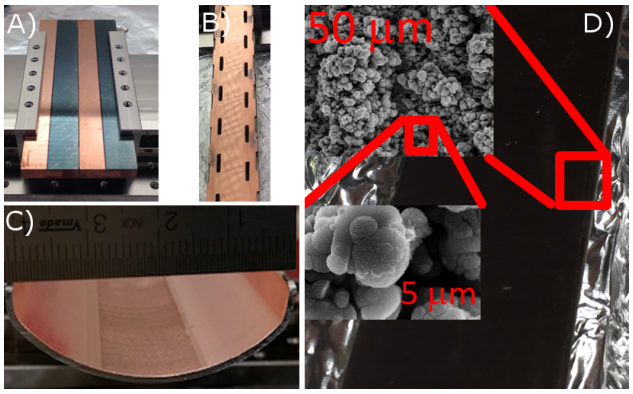

Figure 2: Investigated samples: a) Flat Copper (Cu), b) LHC Copper (Cu-LHC), c) LHC Copper Saw Tooth (ST), d) Laser Treated Copper (LASE)

RESULTS

SR metrology and experiments on real samples and in real conditions, is proved to be essential in order to provide useful input for the simulation codes during design phase of accelerators. In this section only some of the obtained results and discussions are presented. More specific and deeper analysis will be addressed in dedicated paper [18] In Fig.3, the experimental results for R are shown as a function of photon energy for three different incident angles: 0.25°, 0.5° and 1°. By a first analysis is possible to assess general features:

- R is higher for lower photon energies and at lower incident angles;
- The Cu $L_{2\text{-}3}$ absorption edge (≈930eV) is visible within the spectra as a drop of R. This feature is less evident for LASE;
- In all spectra the absorption K-edges of O and C (≈ 530eV and ≈280eV) are visible. These elements are present as contaminants on the surface;
- Values of R largely differ for the different samples. Cu and Cu-LHC present values from 0.9 to 0.3 and the low R_a of Cu implicates higher specular reflectivity. On the other hand, R for ST is always below 0.05 and below 0.01 for LASE;

Contemporary to the acquisition of R, the PY has been acquired and its dependence on the beam energy is plotted in Fig.4. Looking at the results it is possible to identify several features:

- The PY is higher for higher photon energies. The PY is strongly connected to the effective interaction with absorbed photons, hence it will be higher where R is lower;
- The PY is higher for higher incident angles. This statement is true only for a limited range of θ_i. In fact, higher incident angles generally increase the absorption and the production of photoelectrons. At the same time, beyond a certain value of θ_i the radiation penetrates too deep within the bulk and the produced photoelectrons could not be emitted. This phenomenon will be better discussed in [18];

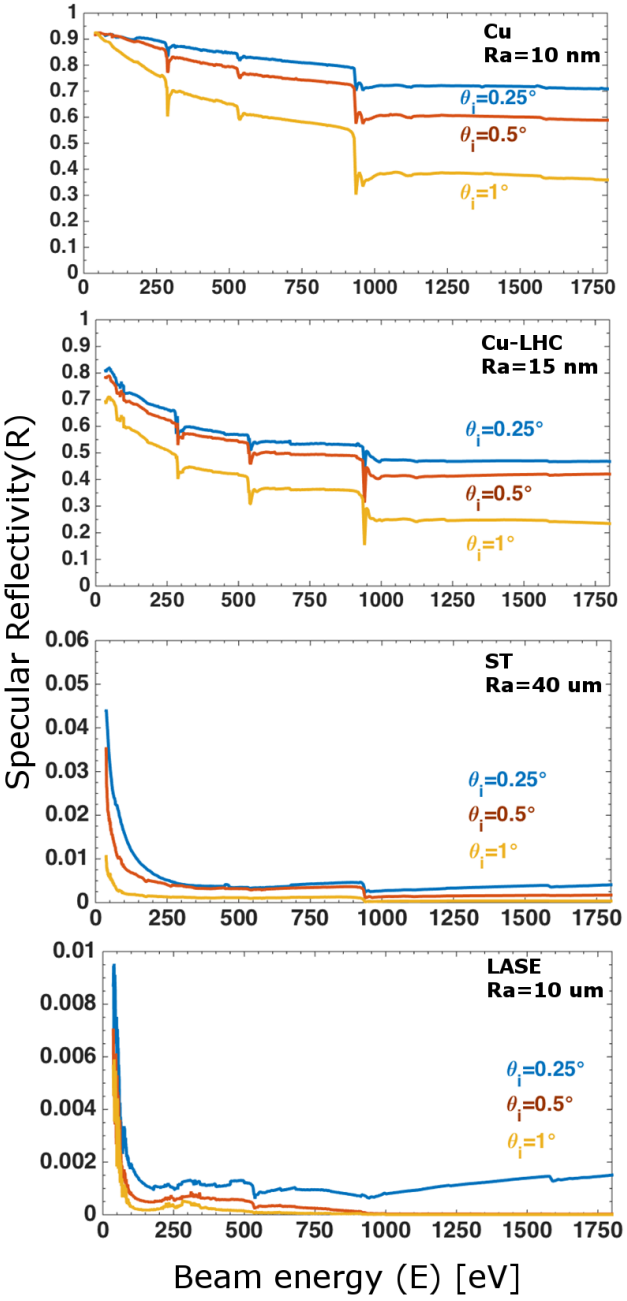

Figure 3: Specular R of different samples. From top to bottom Cu, Cu-LHC, ST and LASE

- The Cu $L_{2\text{-}3}$ absorption edge is visible and causes an increase of the PY due to the increment of the number of absorbed photons interacting with the material;
- The absorption K-edges of O and C are present. These elements are contaminant on the surface and their pres-

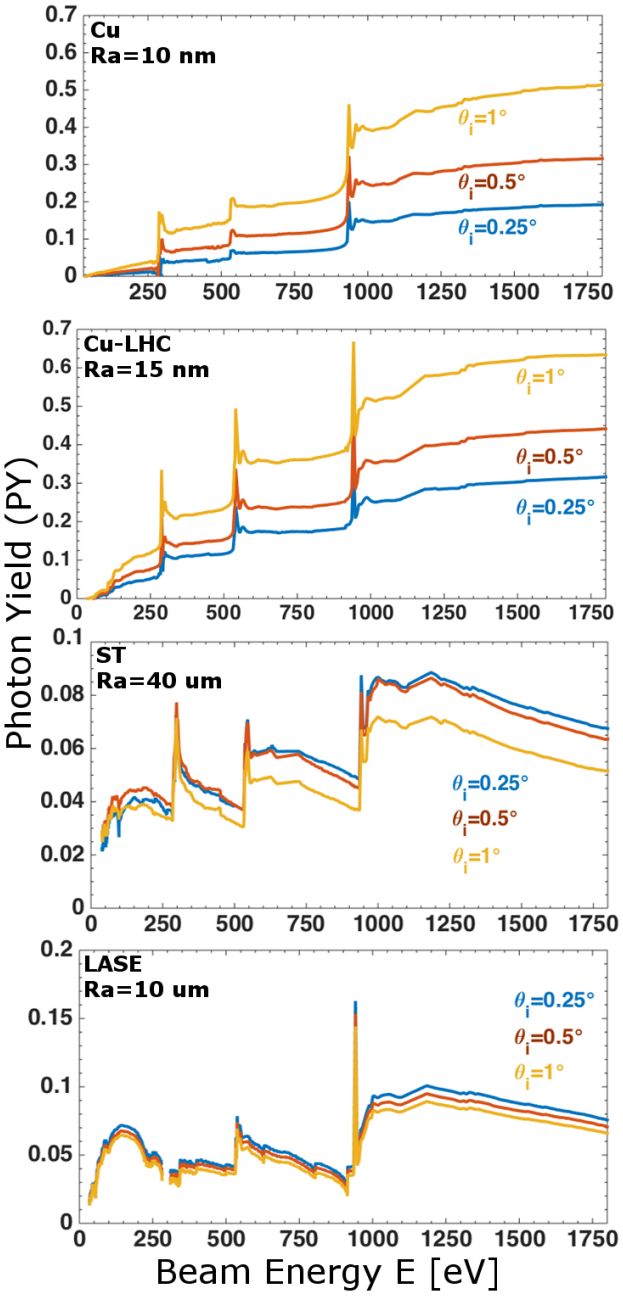

Figure 4: PY of four different samples. From top to bottom: Cu, Cu-LHC, ST and LASE

ence causes an increment of PY at the corresponding edges;

- The roughness and the surface aspect influence PY. For the moderate difference of R_a between Cu and LHC-Cu, the PY slightly changes. Otherwise, in the case of ST and LASE the PY results strongly reduced by a factor 5 or more;

The experimental results relative to the angular distribution of reflected radiation are shown in Fig.5. In particular, Fig.5 top panel is an example of angular distribution for a fixed incident angle and fixed photon energy from a Cu

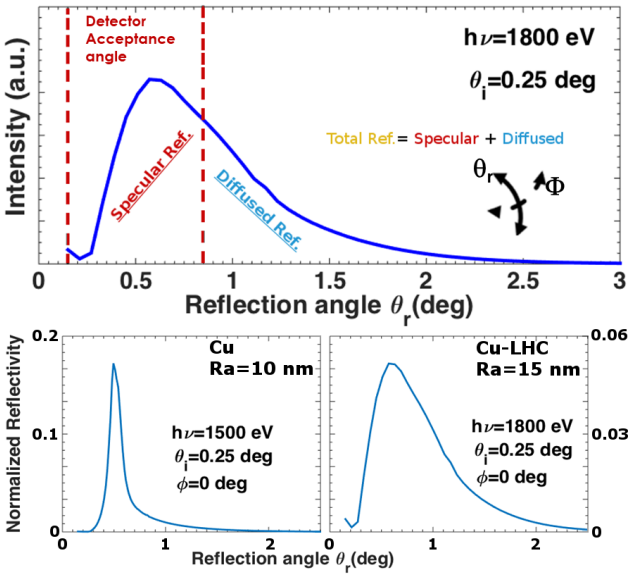

Figure 5: Total Reflectivity analysis. Top: Distinction between Specular Reflectivity area and Diffused Reflectivity during the angular scanning. Bottom: Comparison between Cu and Cu-LHC samples.

sample. The distribution presents a maximum around the geometrical specular reflection position and a tail for higher detector angular positions. The width of such distribution is correlated to the quantity of scattered radiation. Thus, R_t takes into account also this part of the reflected signal and will be calculated integrating the angular distribution. In Fig.5 bottom panel the angular distributions for Cu and Cu-LHC samples are shown. Looking at the data it is possible to conclude how lower roughness causes a reflection more focused around the $\theta_r=2\theta_i$ detector position while higher R_a are correlated to a broader distribution. However, R_t for these two samples are very similar (Table1). This result points out how the two samples reflect the same quantity of radiation but spread on different solid angle. Table 1 is a summary of the measured optical properties for a given beam energies and some incident angles.

Table 1: Optical Parameters of investigated Samples at hν=1500eV

Sample	θ_i**(deg)**	**Spec. Reflec.** ±2%	**Total. Reflec.** ±5%	**PY** ±2%
Cu	0.25°	0.61	0.74	0.18
Cu	0.5°	0.57	0.67	0.30
Cu-LHC	0.25°	0.47	0.72	0.32
Cu-LHC	0.5°	0.42	0.63	0.44
ST	0.25°	0.004	0.054	0.07
ST	0.5°	0.0017	0.006	0.06
LASE	0.25°	0.0015	0.007	0.08
LASE	0.5°	2.5e-05	0.0003	0.07

CONCLUSION

Experiments at the BESSYII OPTICS beamline allow the optical characterization of different samples of interest for FCC-hh and LHC-HL BS design. A first general analysis of the results pointed out various features to be deeper addressed in successive works [18]. Generally, the value of reflectivity used into the simulation codes is a simple average parameter obtained by analytical estimations. The experimental results demonstrate how R strongly depends on photon energy and the R(E,θ_i) function should be taken into account for the different SR emission spectra. Furthermore, it is known that roughness reduces the reflectivity of the surface. However, the simple consideration of specular reflectivity could bring, into simulations and ray tracing codes, to an underestimation of the reflected radiation due to the scattered component. In fact, for technical surfaces such component can be the dominant contribution on the total reflected radiation.

REFERENCES

[1] R. Cimino and T. Demma, "Electron cloud in accelerators," *Int. J. Mod. Phys. A*, vol. 29, no. 17, p. 1430023, 2014

[2] G. Apollinari, I. Béjar Alonso, O. Brüning, M. Lamont, and L. Rossi, "High-Luminosity Large Hadron Collider (HL-LHC): Technical Design Report V.0.1" *Cern Yellow Report:Monographs*, vol. 4, 2017.

[3] R. Kersevan, M. Ady, "Molflow+, Sinrad+", *CERN 2018, http://cern.ch/molflow*

[4] L. Boon, W. Lafayette, J. Crittenden, and K. Harkay, "Application of the SYNRAD3d Photon-Tracking Model to Shielded Pickup Measurements of Electron Clound Buildup at CesrTA," *Proceedings of IPAC2011*, pp. 5–7.

[5] R. Cimino, V. Baglin, and F. Schäfers, "Potential Remedies for the High Synchrotron-Radiation-Induced Heat Load for Future Highest-Energy-Proton Circular Colliders," *Phys. Rev. Lett.*, vol. 115, no. 26, pp. 1–5, 2015.

[6] N. Mahne et al., "Photon Reflectivity distributions from the LHC beam screen and their Implications on the Arc Beam Vacuum System," *Appl. Surf. Sci.*, vol. 235, pp. 221–226, 2004.

[7] F. Schäfers and R. Cimino, "Soft X-ray reflectivity: from quasi-perfect mirrors to accelerator walls,", *Proceedings of ECLOUD12*, 2013.

[8] V. Baglin et al., "Measurements At Epa of Vacuum and Electron-Cloud Related Effects Electron-Cloud," *Proceedings of Chamonix XI* no. September 2013, pp. 141–143, 2001.

[9] R. Cimino, V. Baglin, and I. R. Collins, "VUV synchrotron radiation studies of candidate LHC vacuum chamber materials," *Vacuum*, vol. 53, no. 1–2, pp. 273–276, 1999.

[10] R. Cimino, F. Schäfers, "Soft X-ray Reflectivity and Photoelectron Yield of technical Materials: Experimental input for instability simulations in High intensity accelerators," *Proceeding of IPAC2014*, pp. 2335–2337.

[11] R. Cimino, I. R. Collins, V. Baglin, and I. Introduction, "VUV photoemission studies of candidate Large Hadron Collider vacuum chamber materials," *Phys.Rev.Spe.Top.*, vol. 2, no. January, pp. 1–18, 1999.

[12] G. F. Dugan, K. G. Sonnad, R. Cimino, T. Ishibashi, and F. Schäfers, "Measurements of x-ray scattering from accelerator vacuum chamber surfaces, and comparison with an analytical model," *Phys. Rev. Spec. Top. - Accel. Beams*, vol. 18, no. 4, p. 040704, 2015.

[13] A. Sokolov, M. G. Sertsu, A. Gaupp, M. Luttecke, and F. Schäfers, "Efficient high-order suppression system for a metrology beamline", *J. of Synch. Rad.*, vol. 25, pp 100, 2018.

[14] A. Sokolov et al., "An XUV optics beamline at BESSY II," *Proceeding of SPIE2014*, no. February 2015, p. 92060J, 2014.

[15] Sokolov et al., "At-wavelength metrology facility for soft X-ray reflection optics," *Rev. Sci. Instrum.*, vol. 87, no. 5, 2016.

[16] R. Valizadeh, O. B. Malyshev, S. Wang, T. Sian, M. D. Cropper, and N. Sykes, "Reduction of secondary electron yield for E-cloud mitigation by laser ablation surface engineering," *Appl. Surf. Sci.*, vol. 404, pp. 370–379, 2017.

[17] F. Zimmermann, "Electron-Cloud Effects in past and future machines - walk through 50 years of Electron-Cloud studies" *ECLOUD12*, p. 9, 2013.

[18] E. La Francesca, M. Angelucci, A. Liedl, L. Spallino, L.A. Gonzalez, I. Bellafont, F. Siewert, M.G. Sertsu, A. Sokolov, F. Schäfers and R. Cimino, "Photo Reflectivity and Photoelectron Yield from Copper Technical Surfaces": to be published.

RECENT SECONDARY ELECTRON MODELING AT PRINCETON PLASMA PHYSICS LABORATORY

C. Swanson*, Princeton Satellite Systems, Plainsboro, New Jersey 08536, USA
I. D. Kaganovich†, Princeton Plasma Physics Laboratory, Princeton, New Jersey 08543, USA

ABSTRACT

Over the past 5 years, researchers at Princeton Plasma Physics Laboratory (PPPL) have been engaged in research to theoretically characterize Secondary Electron Emission (SEE) from complex surfaces. We have used both a Monte Carlo numerical method and an analytic integral model to study the phenomenon. We have studied the specific shapes of velvet, foam, and a feather-like fractal surface using these methods, including parametric dependence (aspect ratio, packing density, angle of incidence). We have found that the Secondary Electron Yield (SEY) of a velvet surface can be significantly smaller ($< 10\%$) than a flat surface, but only for electrons which are normally incident. We have found that the SEY of foam surfaces is much more isotropic with respect to angle of incidence, but that the minimum SEY does not approach that of velvet ($\sim 30\%$). Using the understanding gleaned from analysis of velvet, we proposed a primary velvet with a smaller secondary velvet grown onto it, which we called "feathered" because of its resemblance to down feathers. We have found that a feathered surface exhibits isotropic *and* dramatic SEY reduction.

INTRODUCTION

The interest in Secondary Electron Emission (SEE) at Princeton Plasma Physics Laboratory (PPPL) initially resulted from research into Hall Thrusters. Materials with low Secondary Electron Yield (SEY) were considered a way to reduce near-wall conductivity and to increase the potential profile favourably [15–17]. More broadly, the interest at PPPL is from the effect of SEE on plasma, such as its critical role in maintaining a DC discharge, [11] determining the potential in sheaths, [4] and causing plasma instabilities [19, 25]. The SEY of the Tungsten divertor in the ITER tokamak experiment is expected to be near unity [7, 28].

That said, we are aware of those non-plasma applications which are known to be sensitive to SEE, like accelerators [32] and RF amplifiers [26].

The technique of reducing SEY through the geometry of a surface was mostly confined to regular grooves until this decade [14, 20, 29]. Carbon velvets were early contenders for a surface, receiving both theoretical and experimental attention, both at PPPL and elsewhere [1, 10, 13, 21]. Foams, of the kind that are spontaneously generated when Helium plasma is incident on Tungsten, [28] are also surfaces of interest both at PPPL and elsewhere [5, 12, 23].

Other common structures under consideration are dendritic structures, [3] micro-pores, [31] and micro-spears and -nodules [6]. These micro-architectured materials may often be grown in-place via chemical processes.

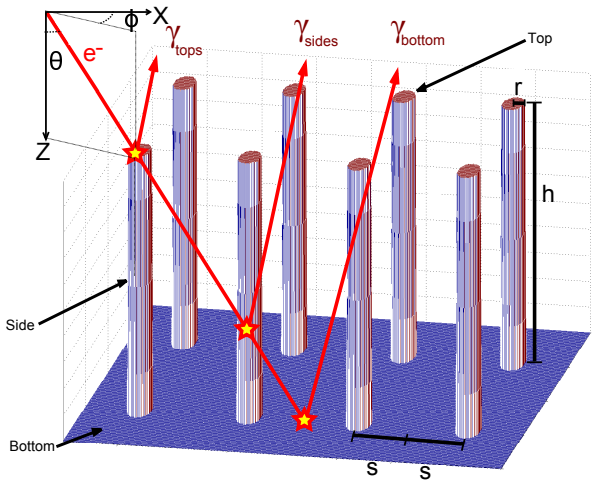

Figure 1: Velvet geometry, including secondary electrons produced on the velvet tops, sides, and bottom substrate

Here at PPPL we attempt via modeling to determine the parametric dependencies of the SEY, for example on aspect ratio, packing density, layer thickness, angle of incidence, etc. Other researchers have also analyzed geometries in this way [27, 30, 31]. Other groups also use a Monte-Carlo tool [2, 8, 9].

THE MECHANISM OF SEY SUPPRESSION

For the mechanism of SEY suppression, see Figure 1. Some incident electrons penetrate deep into the architectured layer. There, they produce secondary electrons. These secondary electrons are typically only a few eV of energy. At this energy, if they hit a surface again, they produce no more secondary electrons and are suppressed.

MONTE CARLO MODEL

The Monte Carlo model we have coded in MATLAB is described in detail by several of our papers [21–23]. It implements geometry as an iso-surface function of space, where $F_{iso}(\vec{x}) > 0$ is outside the geometry and $F_{iso}(\vec{x}) < 0$ is inside the geometry. It initializes 10^5 particles at the top of the simulation and allows them to follow ballistic, straight-line trajectories until they collide with the geometry.

When a collision occurs, the empirical models of Scholtz [18] and Vaughan [24] are used to determine the energy, ve-

* charles.swanson@psatellite.com
† ikaganov@pppl.gov

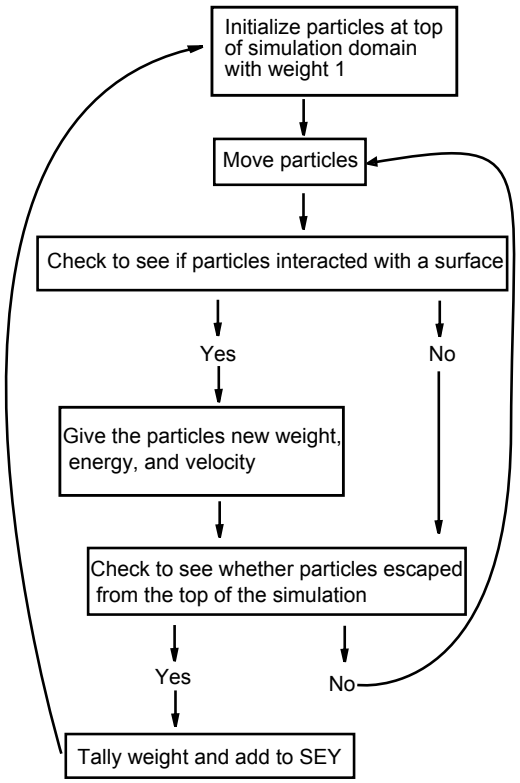

Figure 2: Flowchart of the algorithm used in the Monte Carlo tool

locity angles, and "weight" of the newly emitted secondary electron. Elastically scattered, inelastically scattered ("rediffused"), and "true" secondary electrons are considered. This process is described in more detail in our papers. If a particle escapes the top of the simulation, its weight is counted and it contributes to the SEY. The process is continued until all particles have escaped or their weight diminishes past a threshold. The process of starting with 10^5 particles and changing their weights produces similar ($\sim \sqrt{N}$) counting statistics to the process of starting with some number of particles and having them produce more or fewer daughter particles until 10^5 are reached and counted.

Figure 2 shows a flow chart depicting the algorithm.

VELVET

A velvet is a lattice of long whiskers grown onto a flat substrate. For the Monte Carlo calculation, this lattice was assumed to be rectangular, but real velvets are not. This geometry is depicted in Figure 1. We find that velvet is well suited to suppressing secondary electrons from primary electrons which are normally incident, and find the geometric quantities to optimze for minimum SEY [21].

We characterize the velvet by dimensionless functions of its geometry. From its radius, height, and the areal density of the whiskers (r, h, n), we consider velvets of specific aspect ratio $A = h/r$ and packing density $D = \pi r^2 n$.

We have developed an integral model which treats the probability of an electron-whisker impact as a continuous

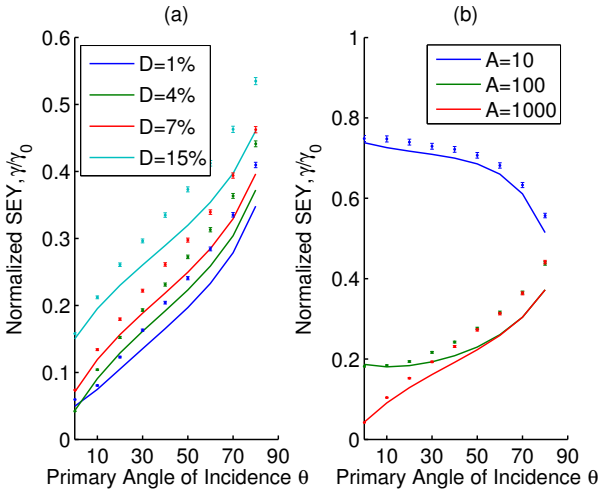

Figure 3: Results of the analyses for velvet: Monte Carlo and integral model. a) $A = 1000$. b) $D = 4\%$

scattering problem, assumes electron trajectories are straight-line between collisions, considers only one generation of secondary electrons, and considers only "true" secondary electrons. The details of this model are given in our velvet paper [21]. Determining the SEY of a single velvet (A, D) requires an integral over the polar velocity angle of the secondary electron population.

The result of the Monte Carlo and integral calculations are depicted in Figure 3. Agreement between the Monte Carlo and integral model can be as poor as 20% discrepancy. This is due to the approximation of the integral model that only one generation of secondaries is produced; in actuality, tertiary electrons from high-energy secondary electrons contribute to the SEY.

Some trends are worth discussing in Figure 3. First, it is apparent that increasing the length of the whiskers, or equivalently the aspect ratio A, decreases the SEY. For SEY reduction from velvet, longer is better.

Second, it is clear that, for the aspect ratios of the most interest to SEY reduction, velvet is best suited to suppressing SEY from primary electrons which are normally incident ($\theta = 0$). Velvet does not suppress SEY from shallowly incident ($\theta \to \pi/2$) electrons to better than 50%.

The integral model reduces to a simple geometric dependence.

$$\gamma_{eff} = \gamma_{flat}[D + (1 - D) f(u, \theta)] \quad (1)$$

where γ_{eff} is the secondary electron yield from the velvet surface, γ_{flat} is the secondary electron yield from a flat surface, D is the packing density, $f(u, \theta)$ is a function which is depicted in Figure 4, θ is the primary angle of incidence, and u is a dimensionless parameter characteristic to the velvet:

$$u = 2rhn = (2/\pi)AD \quad (2)$$

The condition to maximally suppress SEY is found to be

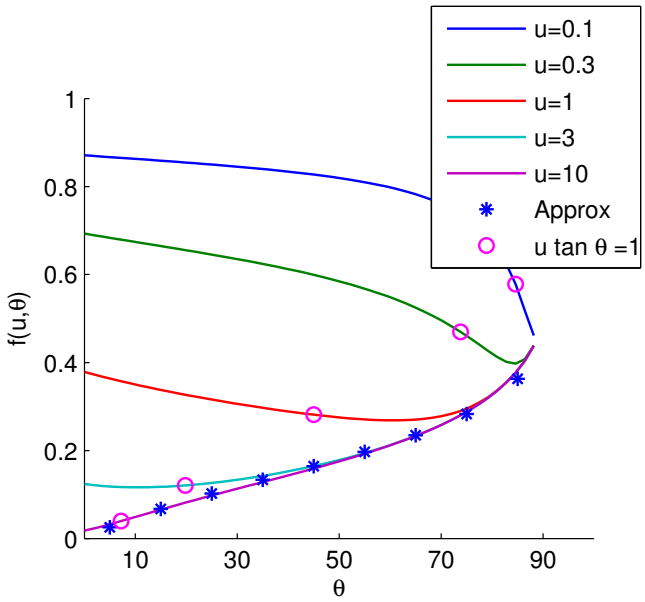

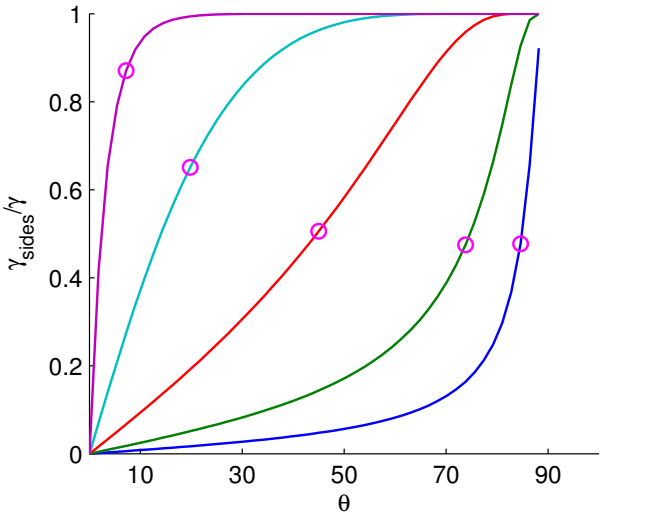

Figure 4: Quantities of interest and location of $u \tan\theta = 1$ point, showing a change in parameter regime for velvet at this point. Top: The dimensionless function $f(u,\theta)$ for several values of u. Bottom: The proportion of SEY which comes from the sides of the whiskers, indicating that $u \tan\theta = 1$ is generally a point at which the SEY behavior becomes dominated by the sides of the whiskers.

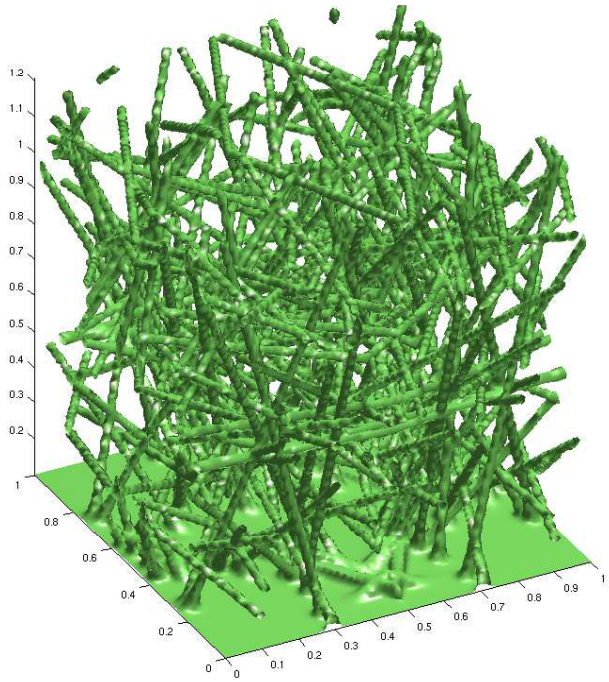

Figure 5: Foam geometry

$$u \to \infty, D \to 0 \tag{3}$$

However even in this limit, there is still finite SEY from all primary angles of incidence except the normal. We have developed an approximate formula for the SEY of velvet in the limit $u \to \infty$:

$$\lim_{u\to\infty} \gamma_{eff} \approx \gamma_{flat} D + \frac{1}{2}\gamma_{flat}(1-D) \times \left[1 - \frac{1}{(1.39\tan\theta + 1)^{0.45}}\right], \tag{4}$$

with average deviation of 0.5% from the exact result. This function is depicted in Fig. 4 (blue symbols).

FOAM

A foam is an array of whiskers which are disordered, and whose axes are aligned isotropically rather than all in the same direction. An example foam geometry can be seen in Figure 5. Foams can occur naturally in plasma applications [28]. We find that foam is much more isotropic with respect to the effect of primary angle of incidence on SEY. However, we also find that the minimum SEY possible from foam is $\sim 0.3\gamma_{flat}$ [23].

The Monte Carlo model was applied to the foam geometry seen in Figure 5. Also, an integral model was formulated with the same approximations as the velvet model: that electrons follow a ballistic, straight-line trajectory between collisions, that collisions follow a continuous-scattering mean-free-path law, that only true secondary electrons are produced, and that only one generation of secondary electrons is produced.

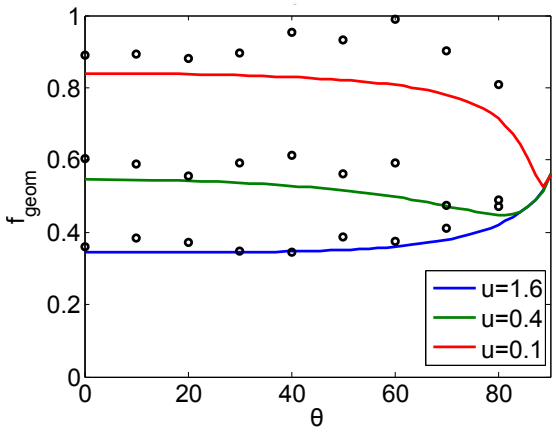

Figure 6: Results of the analyses for foam: Monte Carlo and integral model

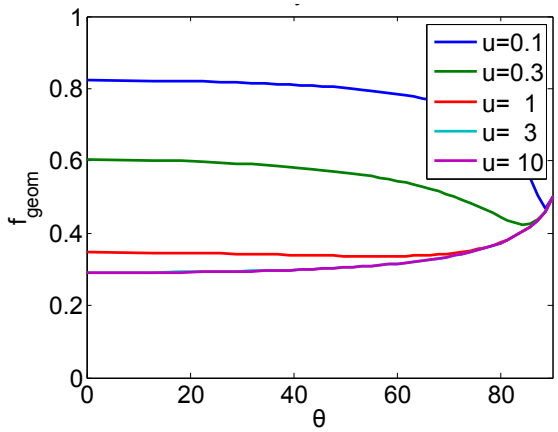

Figure 7: Results of integral foam model, including very high $\bar{u}$ parameter showing asymptote

As in the case of the velvet model, we found helpful dimensionless parameters to be: D, the volume fill fraction of the foam, $A = h/r$, the aspect ratio (ratio of foam layer thickness to whisker radius), and $\bar{u} = AD/2$, a parameter characteristic to the foam. Again like the velvet case, we found that for foam,

$$\gamma_{eff} = \gamma_{flat}[D + (1 - D)f(\bar{u}, \theta)] \quad (5)$$

The comparison between Monte Carlo and integral model is depicted in Figure 6. More values of $f(\bar{u}, \theta)$ appear in Figure 7.

We had initially hoped that foam would have the beneficial properties of velvet without the drawbacks. Indeed, the SEY from foam behaves more isotropically with respect to primary angle of incidence than the SEY from velvet. However, foam has a minimum SEY of around $0.3\gamma_{flat}$, even for the case that $\bar{u} \to \infty, D \to 0$.

We have developed an approximate formula in this limit:

$$\lim_{\bar{u}\to\infty} \gamma_{eff} \approx \gamma_{flat}[D + (1 - D)(C_1 e^{-C_2 \cos\theta} + C_3)] \quad (6)$$

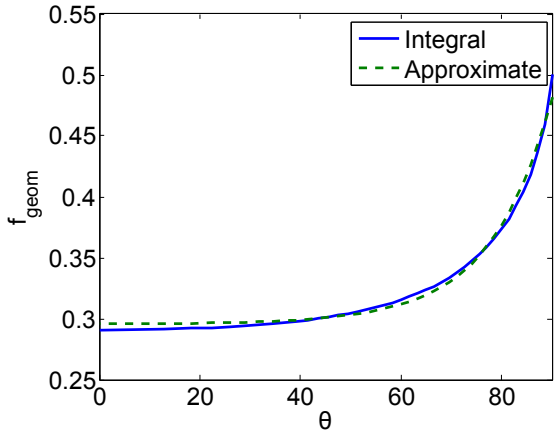

Figure 8: Comparison between approximate foam SEY and full integral model

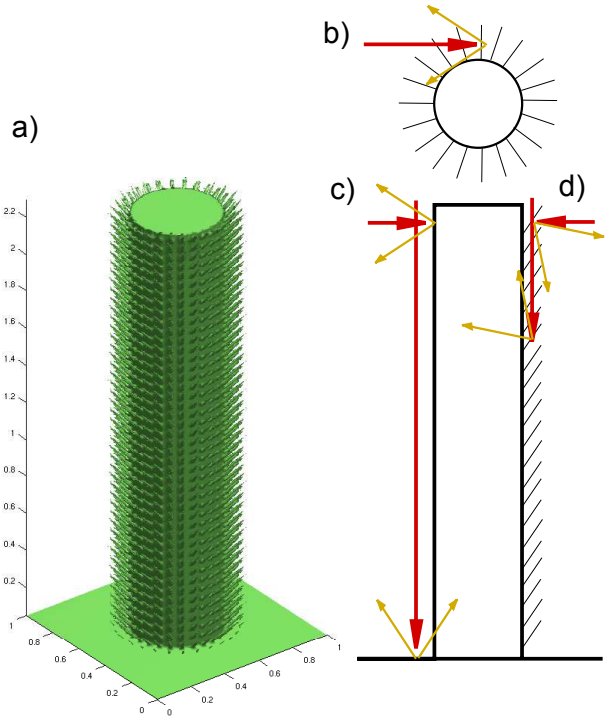

Figure 9: Feather geometry. This depicts $A = 10$, $D = 16\%$ primary and secondary whiskers, which are shorter and fatter than those simulated.

where $C_1 = 0.1887, C_2 = 4.8196, C_3 = 0.2947$. The root-mean-square error of this approximate formula is 0.46%. This fit is depicted in Fig. 8.

FEATHERS

From the lessons of both the velvet and the foam, we attempted to develop a geometry which would overcome the limitations of both. We settled on a feathered geometry, which is a large primary velvet with a small secondary velvet grown onto it. Such a geometry is depicted in Figure 9. The full analysis of this shape can be found in our paper [22].

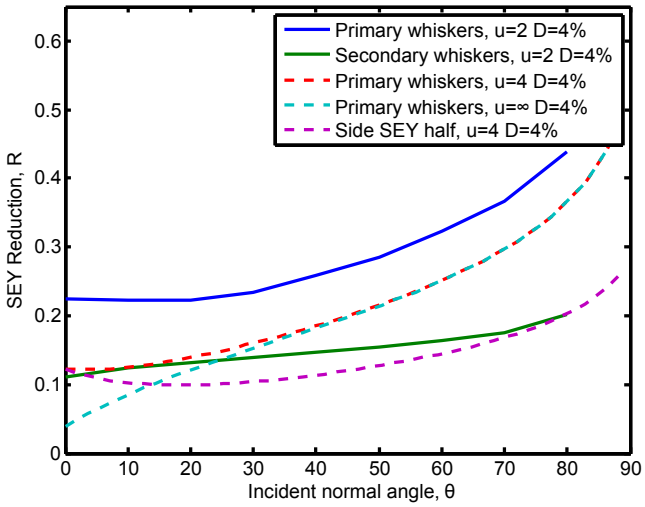

Figure 10: Results of the analyses for feathers: Monte Carlo (solid) and integral (dashed) models

Because of the dynamic range of length scales involved, from the length of the primary whisker to the radius of the secondary whisker, we could not use the Monte Carlo method to simulate the kinds of $A = 1000$ aspect ratios which can be made in the lab. Instead, we considered only a modest $D = 4\%$, $A = 80$ case for both the primary and secondary whiskers. This gives a $u = 2$, by the definition of the velvet u-parameter.

The results of two Monte Carlo and three integral calculations are depicted in Figure 10. "Side SEY half" refers to the case in which we computed the SEY for a velvet of the specified u, D, and reduced the SEY from the whisker sides by one-half.

The green solid line in Figure 10 depicts the feathered case. It lies below the blue solid line, which depicts the primary velvet only. This was expected. Crucially, the green line also lies below the cyan dashed line, which is the integral calculation's result for the SEY of an infinitely long velvet. Thus, feathers are capable of suppressing SEY in the shallow-incidence regime in which velvet can not.

CONCLUSION

PPPL has had a modeling effort over the past 5 years to characterize secondary electron emission (SEE) from complex surfaces. This effort was instigated at least in part by the prospect of using materials with low secondary electron yield (SEY) to improve the performance of Hall thrusters.

We have used a Monte Carlo code and an integral model to examine the SEY properties of velvet, foam, and feathers. Velvet, which is a lattice of whiskers grown onto a flat surface, is found to be suitable for reducing SEY by a large amount ($< 10\%$ the flat SEY), but only for primary electrons which are normally incident. Foam, which is a layer of whiskers which have their axes isotropically aligned, is found to be very isotropic with respect to primary angle of incidence, but suppress SEY by a much less extreme amount (to about $\sim 30\%$ of the flat SEY). We have determined a shape which we calculate to have extreme reduction for normal and shallow incidence; it is a primary velvet with a smaller secondary velvet grown onto the sides of the whiskers.

REFERENCES

[1] L. Aguilera, I. Montero, M. E. Dávila, A. Ruiz, L. Galán, V. Nistor, D. Raboso, J. Palomares, and F. Soria. CuO nanowires for inhibiting secondary electron emission. *Journal of Physics D: Applied Physics*, 46(16):165104, 2013.

[2] A. Alvarado, H.-Y. Chang, W. Nadvornick, N. Ghoniem, and J. Marian. Monte Carlo Raytracing Method for Calculating Secondary Electron Emission from Micro-Architected Surfaces. *arXiv:1806.00205 [cond-mat, physics:physics]*, June 2018. arXiv: 1806.00205.

[3] V. Baglin, J. Bojko, O. Grobner, B. Henrist, N. Hilleret, C. Scheuerlein, and M. Taborelli. The Secondary Electron Yield of Technical Materials and its Variation with Surface Treatments. In *Proceedings of the European Particle Accelerator Conference (EPAC)*, pages 217–221, Austria Center, Vienna Austria, June 2000.

[4] M. D. Campanell, A. V. Khrabrov, and I. D. Kaganovich. Absence of Debye Sheaths due to Secondary Electron Emission. *Physical Review Letters*, 108(25):255001, June 2012.

[5] Cimino. Search for new e-cloud mitigator materials for high intensity particle accelerators (PDF Download Available), 2014.

[6] N. M. Ghoniem, Y. Raitses, R. Shaefer, D. Goebel, I. D. Kaganovich, and B. Williams. Micro-Architectured Materials for Electric Propulsion and Pulsed Power. page 27, 2011.

[7] J. P. Gunn. Evidence for strong secondary electron emission in the tokamak scrape-off layer. *Plasma Physics and Controlled Fusion*, 54(8):085007, 2012.

[8] C. E. Huerta, M. I. Patino, and R. E. Wirz. Secondary electron emission from textured surfaces. *Journal of Physics D: Applied Physics*, 51(14):145202, 2018.

[9] C. E. Huerta and R. E. Wirz. Surface Geometry Effects on Secondary Electron Emission Via Monte Carlo Modeling. In *52nd AIAA/SAE/ASEE Joint Propulsion Conference*. American Institute of Aeronautics and Astronautics, 2016.

[10] C. Jin, A. Ottaviano, and Y. Raitses. Secondary electron emission yield from high aspect ratio carbon velvet surfaces. *Journal of Applied Physics*, 122(17):173301, Nov. 2017.

[11] F. Paschen. Ueber die zum FunkenÃijbergang in Luft, Wasserstoff und KohlensÃdure bei verschiedenen Drucken erforderliche Potentialdifferenz. *Annalen der Physik*, 273(5):69–96, 1889.

[12] M. Patino, Y. Raitses, and R. Wirz. Secondary electron emission from plasma-generated nanostructured tungsten fuzz. *Applied Physics Letters*, 109(20):201602, Nov. 2016.

[13] M. I. Patino and R. E. Wirz. Electron emission from carbon velvet due to incident xenon ions. *Applied Physics Letters*, 113(4):041603, July 2018.

[14] M. Pivi, F. K. King, R. E. Kirby, T. O. Raubenheimer, G. Stupakov, and F. Le Pimpec. Sharp reduction of the secondary electron emission yield from grooved surfaces. *Journal of Applied Physics*, 104(10):104904, Nov. 2008.

[15] Raitses. Electron Emission from Nano- and Micro-Engineered Materials Relevant to Electric Propulsion. 2013.

[16] Y. Raitses, I. D. Kaganovich, A. Khrabrov, D. Sydorenko, N. J. Fisch, and A. Smolyakov. Effect of Secondary Electron Emission on Electron Cross-Field Current in $E times B$ Discharges. *IEEE Transactions on Plasma Science*, 39(4):995–1006, Apr. 2011.

[17] Y. Raitses, D. Staack, A. Dunaevsky, and N. J. Fisch. Operation of a segmented Hall thruster with low-sputtering carbon-velvet electrodes. *Journal of Applied Physics*, 99(3):036103, Feb. 2006.

[18] J. J. Scholtz, D. Dijkkamp, and R. W. A. Schmitz. Secondary electron emission properties. *Philips Journal of Research*, 50(3):375–389, Jan. 1996.

[19] A. I. Smolyakov, W. Frias, I. D. Kaganovich, and Y. Raitses. Sheath-Induced Instabilities in Plasmas with ExB Drift. *Physical Review Letters*, 111(11):115002, Sept. 2013.

[20] G. Stupakov and M. Pivi. Suppression of the effective secondary emission yield for a grooved metal surface. In *Proceedings of the 31st ICFA Advanced Beam Dynamics Workshop on Electron-Cloud Effects*, Napa, CA, USA, 2004.

[21] C. Swanson and I. D. Kaganovich. Modeling of reduced effective secondary electron emission yield from a velvet surface. *Journal of Applied Physics*, 120(21):213302, Dec. 2016.

[22] C. Swanson and I. D. Kaganovich. "Feathered" fractal surfaces to minimize secondary electron emission for a wide range of incident angles. *Journal of Applied Physics*, 122(4):043301, July 2017.

[23] C. Swanson and I. D. Kaganovich. Modeling of reduced secondary electron emission yield from a foam or fuzz surface. *Journal of Applied Physics*, 123(2):023302, Jan. 2018.

[24] D. Sydorenko. *Particle-in-cell simulations of electron dynamics in low pressure discharges with magnetic fields*. PhD thesis, June 2006.

[25] D. Sydorenko, I. Kaganovich, Y. Raitses, and A. Smolyakov. Breakdown of a Space Charge Limited Regime of a Sheath in a Weakly Collisional Plasma Bounded by Walls with Secondary Electron Emission. *Physical Review Letters*, 103(14):145004, Oct. 2009.

[26] J. R. M. Vaughan. Multipactor. *IEEE Transactions on Electron Devices*, 35(7):1172–1180, July 1988.

[27] D. . Wang, Y. . He, M. . Ye, W. . Peng, and W. . Cui. Secondary electron emission characteristics of nanostructured silver surfaces. *Journal of Applied Physics*, 122(15):153302, Oct. 2017.

[28] K. Wang, R. P. Doerner, M. J. Baldwin, F. W. Meyer, M. E. Bannister, A. Darbal, R. Stroud, and C. M. Parish. Morphologies of tungsten nanotendrils grown under helium exposure. *Scientific Reports*, 7:42315, Feb. 2017.

[29] L. Wang, K. Bane, C. Chen, T. Himel, M. Munro, M. Pivi, T. Raubenheimer, and G. Stupakov. Suppression of secondary electron emission using triangular grooved surface in the ILC dipole and wiggler magnets. In *2007 IEEE Particle Accelerator Conference (PAC)*, pages 4234–4236, June 2007.

[30] M. Ye, W. Dan, and H. Yongning. Mechanism of total electron emission yield reduction using a micro-porous surface. *Journal of Applied Physics*, 121(12):124901, Mar. 2017.

[31] M. å. é. Ye, Y. N. è. He, S. G. è. Hu, R. ç. Wang, T. C. è. Hu, J. æ. Yang, and W. Z. å. Cui. Suppression of secondary electron yield by micro-porous array structure. *Journal of Applied Physics*, 113(7):074904, Feb. 2013.

[32] F. Zimmermann. A Simulation study of electron cloud instability and beam induced multipacting in the LHC. Technical Report CERN-LHC-PROJECT-REPORT-095, 1997.

FACETS OF SPACECRAFT CHARGING; CRITICAL TEMPERATURE AND DEPENDENCE ON AMBIENT ELECTRON DENSITY

Shu T. Lai, MIT, Cambridge, MA, 02139, USA, and
Boston College, Newton, MA, 02457, USA

Abstract

Spacecraft charging is important. Space plasmas, secondary and backscattered electrons, and surface conditions, are some of the main factors controlling spacecraft charging. At geosynchronous altitudes with Maxwellian space plasma, there are two properties for the onset of spacecraft charging. They are (1) existence of critical ambient electron temperature, and (2) independence of the ambient electron density. In space plasmas of Kappa or cut-off Maxwellian distributions, the two properties persist. In monopole-dipole configuration of dielectric spacecraft charging in sunlight, the high-level potential contours on the dark side wrap to the sunlit side and, as a result, the two properties also persist. However, the two properties do not apply to the following situations. They are charging by double-Maxwellian plasmas, charging by charged particle beam emissions, charging of plasma probes on spacecraft, low-level charging in the ionosphere, and low-level positive voltage charging of spacecraft in sunlight. We will summarize the various facets in a table, which, hopefully, will be very useful.

INTRODUCTION

Spacecraft charging [1,2,3] is caused by spacecraft-plasma interactions. High-level spacecraft charging at hundreds of electron volts (eV) or more, may affect scientific measurements onboard and, in severe cases, may terminate the mission.

When an object is put in space plasmas, or even laboratory plasmas, it intercepts more electrons than ions because electrons are much lighter and faster. This property alone leads to a naïve belief: - (1) not only a spacecraft must charge to negative potentials, but also (2) the magnitude of the spacecraft potential increases with the ambient electron density.

But, nature is not so naïve. For every incoming electron of energy E, there are δ(E) secondary electrons [4-10] and η(E) electrons [11-14] going out from the surface. Here, δ(E) and η(E) are the secondary electron yield (SEY) and backscattered electron yield (BEY) respectively. Depending on the surface properties, the SEY δ(E) > 1 for $E_1 < E < E_2$, where E_1 and E_2 are the crossing points [4-10]. For $E > E_2$, δ(E) < 1. This property suggests that, at sufficiently high energies E, there are more incoming electrons than outgoing secondary electrons.

The BEY η(E) << 1 at all E, except when E is very small [11-14] and therefore BEY does not an important role for spacecraft charging at high levels.

ONSET OF CHARGING

At equilibrium, the incoming and outgoing electron currents balance each other. The current balance equation determines the spacecraft potential ϕ.

For normal incidence, the current balance equation [Appendix in Ref.15] is as follows.

$$\int_0^\infty dEE\, f(E) = \int_0^\infty dEE\, f(E)\left[\delta(E)+\eta(E)\right] \qquad (1)$$

At equilibrium, the Maxwellian distribution function f (E) is given by

$$f(E) = n(m/2\pi kT)^{3/2} \exp\left(-E/kT\right) \qquad (2)$$

Substituting eq(2) into eq(1), one finds that the electron density n cancels out on both sides. For more electrons coming in, more secondary and backscattered electrons are going out. Eq(1) yields the solution T = T*. When the electron temperature exceeds the critical temperature T*, spacecraft charging occurs [16-22] and the occurrence is independent of the electron density n [21-23]. For a table of T* for various surface materials, see, for example, Ref.[3].

We have therefore obtained two important properties. Property I: The onset of charging is independent of the electron density n. Property II: For a given surface material, the solution T* of eq(1) is the critical electron temperature for the onset of spacecraft charging.

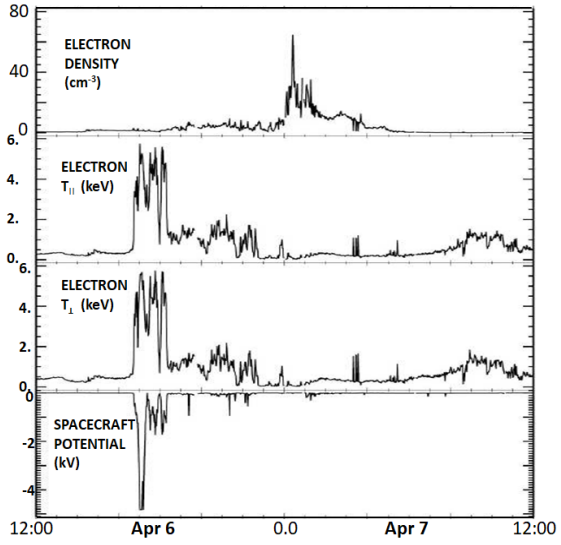

Figure 1 Spacecraft charging on the LANL 1994-084 satellite. The spacecraft potential rises to -5 kV at 17:00 UT, Apr 6, whereas the electron density rises to 65 cm^{-3} at 01:00 UT, Apr 7, 2000. Adapted from Ref.[23].

KAPPA DISTRIBUTION

The kappa distribution is often a good description of the ambient plasma in non-equilibrium [24,25]. The Kappa temperature T_κ is related to the usual temperature T as

$$f_\kappa(E) = n\frac{\Gamma(\kappa+1)}{\Gamma(3/2)\Gamma(\kappa-1/2)}\left[\left(\kappa-\frac{3}{2}\right)T_\kappa\right]^{-\frac{3}{2}}\left[1+\frac{E}{(\kappa-3/2)T_\kappa}\right]^{-(\kappa+1)} \quad (3)$$

where $T_\kappa = \frac{\kappa}{(\kappa-3/2)}T$ and $3/2 < \kappa < \infty$

For onset of spacecraft charging, the current balance equation is solved by using $f_\kappa(E)$.

$$\int_0^\infty dEE\, f_\kappa(E) = \int_0^\infty dEE\, f_\kappa(E)\left[\delta(E)+\eta(E)\right] \quad (4)$$

yielding the critical kappa temperature T_κ^* [23].

Again, the density n on both sides of eq(4) cancels out [23]. There exists critical T_κ^*, but the values are different from those of T* of the Maxwellian distribution.

CUT-OFF DISTRIBUTION

If the distribution f(E) has cut-offs at E_L and E_U. The current balance eq(1) becomes [17]

$$\int_{E_L}^{E_U} dEE\, f(E) = \int_{E_L}^{E_U} dEE\, f(E)\ \delta(E)+\eta(E) \quad (5)$$

where E_L and E_U are the lower and upper cutoff energies respectively [26].

The solution T=T* of the current eq(6) is the critical temperature for the onset of spacecraft charging. The values of T* [17,27] are different from those for the Maxwellian case. Again, the density n is cancelled on both sides in eq(5).

DOUBLE MAXWELLIAN DISTRIBUTION

Sometimes a double Maxwellian distribution f_D(E) may happen if a plasma moves into the region of another plasma and it takes time to reach equilibrium.

$$f_D(E) = f_1(E) + f_2(E) \quad (6)$$

$$f_1(E) = n_1\left(m/2\pi kT_1\right)^{3/2}\exp\left(-E/kT_1\right) \quad (7)$$

$$f_2(E) = n_2\left(m/2\pi kT_2\right)^{3/2}\exp\left(-E/kT_2\right) \quad (8)$$

In eq(6), there are two densities (n_1 and n_2) and two temperatures (T_1 and T_2). The spacecraft potential depends on all of them. They form parametric domains in which there exist single and triple roots of spacecraft potential. The resulting critical temperatures are not simple, as triple roots can suddenly change to single root [28-32].

MONOPOLE-DIPOLE POTENTIAL

For spacecraft with dielectric surfaces, the surface potentials can be different at different positions. Photoemission occurs on the sunlit side but not on the dark side. At geosynchronous altitudes, although the photoelectron current exceeds the ambient electron current, the photoelectron energy is typically a few eV only. The dark side can charge to hundreds of negative volts or more, because there is no photoelectron current involved. The high negative voltage contour can wrap to the sunlit side and block the photoelectrons, resulting in a monopole-dipole potential configuration [33-35]. The charging of the spacecraft is controlled by the charging of the dark side, where properties I and II apply.

LOW-LEVEL CHARGING IN SUNLIGHT

Photoelectron current I_{ph} from spacecraft at geosynchronous altitudes exceeds the ambient electron current [33-36]. The main solar ultraviolet line is at about 10.2eV in energy. There are some higher energy spectral lines. The work function of typical surface materials is 3 to 4 eV. The charging level ϕ(>0) in sunlight depends on the ambient electron current $I_e(\phi)$. For a conducting sphere, the current balance equation is as follows.

$$I_e(0)\left(1-\frac{q_e\phi}{kT_e}\right) - I_i(0)\exp\left(-\frac{q_i\phi}{kT_i}\right) = I_{ph}(\phi) \quad (9)$$

For $\phi > 0$, the ambient ion current $I_i(\phi)$ is small and so are the secondary electron currents. As $I_e(0)$ varies, the potential ϕ varies accordingly [37,38]. In this case, ϕ depends on the ambient electron density n. The charging level is low because of the low energies of the solar spectral lines.

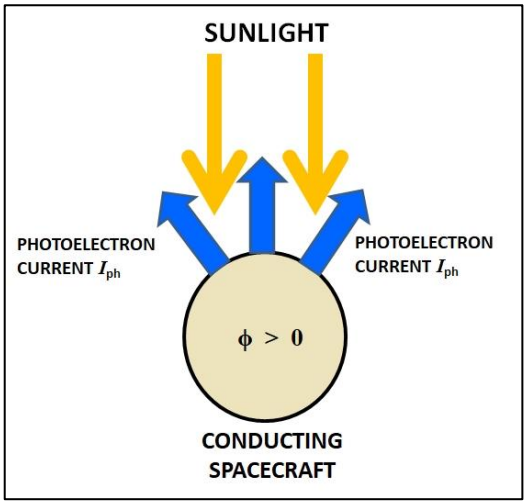

Figure 2. Low-level charging to positive potentials in sunlight.

PLASMA PROBES ON SATELLITE

Plasma probes are sometimes used on spacecraft [39,40]. In this case, does the spacecraft potential depend on the ambient electron density? Take, for example, the current balance equation for a spacecraft charged to a negative potential ϕ. The spacecraft current balance equation is as follows.

$$\int_{E_L}^{E_U} dEE\, f(E) = \int_{E_L}^{E_U} dEE\, f(E)\ \delta(E)+\eta(E)\ + I_p \quad (10)$$

where I_p is the current applied to the plasma probe.

With the addition of the applied current I_p, the density n of the incoming and outgoing electron current terms cannot be cancelled on both sides of eq(10). Therefore, ϕ depends on n. The onset of charging depends not only on the ambient currents but also the applied current. The above argument also applies to a positively charged spacecraft with a plasma probe on it.

CHARGED PARTICLE BEAM FROM SPACECRAFT

For a positive ion beam emitting from a negatively charged spacecraft, the current balance equation is

$$\int_0^\infty dEE f(E) = \int_0^\infty dEE[\delta(E)+\eta(E)]f(E) + I_B(E_B)\Theta(E_B - q\phi) \quad (11)$$

where $I_B(E_B)$ is the current of the ion beam of energy E_B and Θ is a step function (= 1 if $E_B > q\phi$, and = 0 if $E_B < q\phi$). If the beam has an energy distribution, one has to integrate over the beam energy [41]. If the returning beam generates secondary and backscattered electron currents, they should be included in the balance. The electron density terms do not cancel in eq(11). Thus, ϕ depends on the electron density. The critical temperature is more complicated. It depends on beam energy, beam current, and other parameters. For electron beam emissions [42], the charge signs are changed.

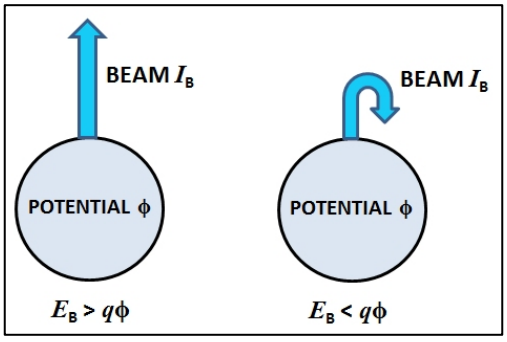

Figure 3. Charged particle beam emission. The beam returns if the beam energy is less than the spacecraft charging potential energy.

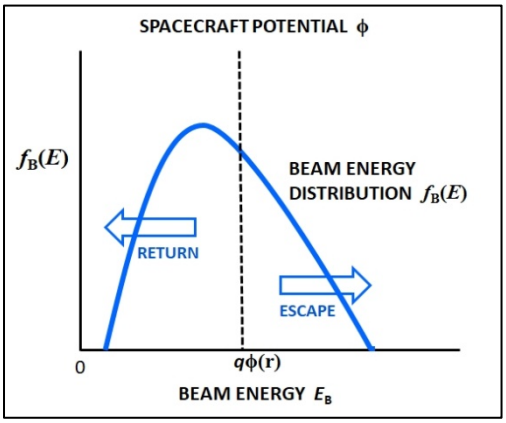

Figure 4. Partial return of a beam with an energy distribution. The partition is at the spacecraft charging potential energy at the location r.

SUMMARY AND DISCUSSION

We summarize the facets of spacecraft charging discussed above in Table 1 as follows.

Table 1: Facets of Spacecraft Charging

Situation	Electron Density	Critical Temperature
Maxwellian	Independent	T*
Double Maxwellian	Dependent	No
Kappa	Independent	T*
Cutoff Maxwellian	Independent	T*
Monopole-Dipole Model in Sunlight	Independent	T*
Low-Level Charging in Sunlight	Dependent	No
Plasma Probe on Spacecraft	Dependent	No
Charged Particle Beam Emission	Dependent	No

High-level spacecraft charging is important because it may affect the electronics and scientific measurements onboard. The natural cause of spacecraft charging is the result of spacecraft/plasma interaction.

Electrons are faster than ions because of the mass difference. An object put in plasmas would intercept more electrons than ions. It does not mean that the object must charge to negative volts, because the outgoing secondary and backscattered electrons play important roles in the current balance.

Since secondary electrons are of low energy (a few eV) and backscattered electrons are nearly negligible in most circumstances, high-level negative charging does not occur unless the energy E of the incoming electrons exceeds the second crossing point, $\delta(E)=1$, which depends on the material properties. With an energy distribution, one has to integrate over the energies in eq(1). As a result, two properties I and II emerge. They are (I) existence of critical temperature for the onset of spacecraft charging, and (II) independence of ambient electron density. The physics of (I) is that there are more high energy electrons in a high-temperature plasma, and therefore high temperature favours charging to negative voltages. The physics of (II) is that as more electrons are coming in, more secondary electrons are going out proportionally. These two important properties have been observed easily and repeatedly on the LANL geosynchronous satellites.

It is necessary to know that under certain conditions, these two properties do not apply. In this paper, we have discussed various situations. For example, in a double Maxwellian distribution, there are two densities and two temperatures. One needs to use parametric domains to delineate the properties of charging, and the results are not simple.

Sometimes, a kappa distribution is more appropriate to describe the space plasma deviating from equilibrium. In this situation, the critical temperature T* still exists but the values are not the same as those for the Maxwellian case. Since the electron density *n* is cancelled on both sides of eq(4), property II is valid.

Some other times, the distribution can be modelled as a cut-off Maxwellian. In this case, the critical temperature still exists but the values of T* are different. Again, property II also holds.

For a dielectric spacecraft in sunlight, the potential on the sunlit side is affected by photoemission while the dark side can charge to high levels by the energetic ambient electrons without photoemission. The high-level potential contours can wrap to the sunlit side blocking the photoelectrons. The charging of the sunlit side is greatly influenced by the charging of the dark side. The charging of the dark side is governed by both properties I and II.

Despite the persistence of property I and II in the above cases and the successful confirmations on all the LANL geosynchronous satellites, one must bear in mind that there are cases where these two properties do not apply. For example, if one has a conducting spacecraft charging by photoemission in sunlight. Although the charging level is low (10 V or less usually) because the sunlight spectral lines have low energies, the photoemission current exceeds the ambient electron current and therefore controls the spacecraft charging. Although low-level charging does practically no harm to the electronics onboard, we should discuss it because it is very common. In this case, the current balance is essentially between the photoelectrons and the ambient electrons, because most of the secondary electrons cannot leave and the ambient ions are repelled. Obviously, as the ambient electron density *n* varies in eq(9), so do the ambient electron current I_e and the spacecraft potential ϕ.

Another common case is using plasma probes on spacecraft. In this case, one applies an artificial sweeping current to a probe. As a result, the current balance is no longer between the incoming electrons and the outgoing electrons only. In similar modern physics language, the symmetry between the natural currents is broken in the balance equation. Therefore, the property of density cancellation does not apply.

Beam emission is gaining attention not only for spacecraft charging mitigation but also for space propulsion. A beam emitted can partially return depending on the beam energy distribution and the spacecraft charging level. Again, the symmetry between the natural currents is broken by the artificial beam current, rendering the property of density cancellation invalid. With the broken symmetry, a simple critical temperature is impossible because it depends on beam current, beam energy distribution, and other parameters.

Finally, we stress that both properties I and II are important. They have been derived theoretically and confirmed by space observation. One must be careful that there are situations where I and II do not apply.

A note added in proof: in the literature, there are other charging onset indicators such those without using SEY or with electron energies well above the second crossing point of SEY. Such approaches are outside the scope here and will not be discussed at this time.

ACKNOWLEDGMENT

The author thanks Dr. Roberto Cimino for inviting this paper. It was presented at MIT Space Propulsion Laboratory, May, 2018. The author thanks Professor Paulo Lozano for his encouragement.

REFERENCES

[1] DeForest, S.E., Spacecraft charging at synchronous orbit, *J. Geophys. Res.*, (1972), 77, 3587-3611.

[2] Hastings, D. and H. B. Garrett, Spacecraft-Environment Interactions, Cambridge Univ. Press, Cambridge, UK, (1997).

[3] Lai, S.T., Fundamentals of Spacecraft Charging, Princeton University Press, Princeton, NJ, USA. ISBN: 9780691129471, (2011).

[4] Sternglass, E. J., "Theory of secondary electron emission," Scientific Paper 1772, Westinghouse Research Laboratories, Pittsburgh, PA, (1954).

[5] Sanders, N.L. and G.T. Inouye, "Secondary emission effects on spacecraft charging: energy distribution consideration," in Spacecraft Charging Technology 1978, ed. R.C.Finke and C.P. Pike, NASA-2071, ADA 084626, (1978), pp.747-755.

[6] Scholtz, J. J., D. Dijkkamp, and R.W.A. Schmitz, *Philips J. Res*., (1996), 50(3-4), 375–389.

[7] Cazaux, J., *J. Phys. D: Appl. Phys*., (2005), 38, 2433-2441.

[8] Lin, Y. and D. G. Joy, *Surf. Interface Anal.,* (2005), 37: 895–900.

[9] Cimino, R., M. Commisso, D.R. Grosso, T. Demma, V. Baglin, R. Flammini, R. Laciprete, *Phys. Rev. Lett*., (2012), 109, 10.1103, doi: 109.064801.

[10] Larciprete, R., D.R. Grosso, M. Commisso, R. ammini, and R. Cimino, *Phys. Rev. Special Topics*, (2013), 16, 011002.

[11] Sternglass, E. J., *Phys. Rev.* (1954), 95: 345–358.

[12] Darlington, E. H., and V. E. Cosslett, *J. Phys. D: Applied Phys*. (1972), 5: 1969–1981.

[13] Jabonski, A., and P. Jiricek, *Surf. Interface Anal.*, (1996), 24: 781–785.

[14] Cazaux, J., *J. Applied Phys.*, (2012), 111, 064903.

[15] Lai, S.T., Spacecraft charging: Incoming and outgoing electrons, in Proceedings of ECLOUD'12: Joint INFN-CERN-EuCARD-AccNet Workshop on Electron-Cloud Effects, eds. R. Cimino, G. Rumolo, and F. Zimmermann, (CERN-2013-002, Geneva, 2013), pp.165-168, doi:10.5170/ CERN-2013-002.

[16] Lai, S.T., M.S. Gussenhoven, and H.A. Cohen, Range of electron energy spectrum responsible for spacecraft charging, presented at *AGU Spring Mtg*., Philadelphia, PA, May, (1982).

[17] Lai, S.T., M.S. Gussenhoven, and H.A. Cohen, The

concepts of critical temperature and energy cutoff of ambient electrons in high-voltage charging of spacecraft, in *Spacecraft/Plasma Interactions and Their Influence on Field and Particle Measurements*, eds. A. Pedersen, D. Guyenne and J. Hunt, European Space Agency (ESA), Noordwijk, the Netherlands (1983), pp.169-175.

[18] Laframboise, J.G., R. Godard, and M. Kamitsuma, Muliple floating potentials, threshold temperature effects, and barrier effects in high-voltage charging of exposed surfaces on spacecraft, in *Proceedings of Intn'l Symposium on Spacecraft Materials in Space Environment*, Toulouse, France, ESA Report ESA-178, ESA, Noordwijk, the Netherlands, (1982), pp.269-275.

[19] Laframboise, J. G., and M. Kamitsuma, "The threshold temperature effect in high voltage spacecraft charging," in *Proceedings of Air Force Geophysics Workshop on Natural Charging of Large Space Structures in Near Earth Polar Orbit*, eds. R. C. Sagalyn, D. E. Donatelli, and I. Michael, AFRL-TR-83-0046, ADA-134-894, Air Force Geophysics Laboratory, Hanscom AFB, MA, (1983), pp.293–308.

[20] Lai, S.T., *IEEE Trans. Nucl. Sci.*, Vol.19, pp.1629-1634, (1991).

[21] Lai, S.T. and D. Della-Rose, *J. Spacecraft & Rockets*, Vol.38, No.6, 922-928, (2001).

[22] Lai, S.T. and M. Tautz, *J. Geophys. Res*., Vol 111, A09201, doi:10.1029/2004JA010733, (2006).

[23] Lai, S.T., M. Martinez-Sanchez, K. Cahoy, M. Thomsen, Y. Shprits, W. Lohmeyer, and F. Wong, *IEEE Trans, Plasma Sci*., Vol.45(10), pp.2865-2884, (2017). doi:10.1109/TPS.2017.2751002.

[24] Vasyliunas, V.M., *J. Geophys. Res*., Vol. 73, pp. 2839-84, (1968).

[25] Meyer-Vernet, N., *Eur. J Phys*.,Vol.20, pp.167-176, (1999).

[26] Thomsen, M. F., H. Korth, and R. C. Elphic, *J. Geophys. Res*., 107(A10), 1331, doi:10.1029/ 2001JA000148, (2002).

[27] Lai, S.T., *J. Geophys. Res*.- *Space Phys.*, Vol.110, A01, pp.204-215, doi:10.1029/2002JA009447, (2005).

[28] Besse, A.L., *J. Geophys. Res*., (1981), Vol.86, pp.2443-2446.

[29] Lai, S.T., *J. Geophys. Res.*, (1991), 96, No.A11, pp.19269-19282.

[30] Lai, S.T. and M. Tautz, *J. Geophys. Res*., (2008), 113, A11211, doi:10.1029/2008JA01361.

[31] Huang, J.G., G.Q. Liu, and L.X. Jiang, *J. Geophys. Res*., 120, doi:10.1002/2015JA021173, (2015).

[32] Huang, J., G. Liu, and L. Jiang, *J. Geophys. Res.*, Vol.120, pp.10,404–10,414, doi: 10.1002/2015JA 021820, (2015).

[33] A. L. Besse and A. G. Rubin, *J. Geophys. Res.*, 85(A5), pp.2324–2328, (1980).

[34] Lai, S.T. and M. Tautz, *IEEE Trans. Plasma Sci*., Vol.34, No.5, 2053-2061, doi: 10.1109/TPS.2006 .883362, (2006).

[35] Lai, S.T. and K. Cahoy, *IEEE Trans. Plasma Sci*., Vol.43, No.9, pp.2856-2860, doi: 10.1109/TPS.2015 .2453370, (2015).

[36] Feuerbacher, B. and B. Fitton, *J. Appl. Phys.*, vol. 43, no. 4, (1972), pp.1563–1572.

[37] Knott, K., A. Korth, P. Décréau, A. Pedersen, and G. Wrenn, 'Observations of the GEOS Equilibrium Potential and its Relation to the Ambient Electron Energy Distribution', in *Spacecraft Plasma Interactions and Their Influence on Field and Particle Measurements, Proceedings of the 17th ESLAB Symposium*, ESA SP-198, (1983), p.19.

[38] Escoubet, C.P., A. Pedersen, R. Schmidt, and P.A. Lindquist, *J. Geophys. Res*., Vol.102, (1997), pp.17595-17609, doi:10.1029/97/JA00290

[39] Garnier, P., M.K.G. Holmberg, J.-E. Wahlund, G.R. Lewis, S. Rochel Grimald, M.F. Thomsen, D.A. Gurnett, A.J. Coates, F.J. Crary, and I. Dandouras, *J. Geophys. Res*., Vol.118, no.11, (2013), pp.7074-7073, doi: 10.1002/2013JA019114

[40] Kurth, W.S., S. De Pascuale, J.B. Faden, C.A. Kletzing, G.B. Hospodarsky, S. Thaller and J.R. Wygant, *J. Geophy. Res*., 120, (2004), pp.904-914, doi:10.1002/2004JA020857

[41] Lai, S.T., *IEEE Trans. Nuclear Sci.,* Vol.36, No.6, (1989), pp.2027-2032.

[42] Lai, S.T., *J. Geophys. Res.,* Vol.99, (1994), pp.459-468.

EXPERIMENTS WITH STABLE CONFINED ELECTRON COLUMNS

K. I. Thoma*, V. Britten, M. Droba, O. Meusel, H. Podlech, B. Scheible, K. Schulte
Goethe-University Frankfurt

Abstract

Gabor Lenses were invented for focusing ion beams by the electric field of a confined electron column. In synchrotrons spontaneously occurring electron clouds have an influence on the beam dynamics. Instabilities of single or multi bunches, emittance growth, excessive energy deposition, particle losses, interferences with diagnostic and gas desorption from chamber walls can appear. As a consequence of these interactions between ions and electrons, the beam is deflected or, in worst case, lost. If an ion beam bunch passes a confined electron column in a Gabor Lens these impacts can be studied as well. Collisions of the ions with the electron ensemble will lead to oscillation effects on the cloud and have an influence on the bunch train. These interaction effects will be increased by the number of bunches and their frequency and can be modified by the plasma parameters, temperature and density, of the electron column. If it is possible to damp the excitation of the confined electron column space charge compensation could be provided.
To study these impacts and interactions Gabor Lenses are built. In 2018 a new lens called Gabor Lens 2000 is constructed. This 2 m long lens can hold an electron column with an aspect ratio smaller than 0.1. Single pass experiments with ion beams will be performed under different temperature and density of the plasma and also different frequencies of the train.

INTRODUCTION

The development of the Gabor Lens (GL) by Dennis Gabor in 1947 opened up a new field of research for the investigation and usage of statically enclosed electron clouds. These electron clouds are plasmas of a single particle species – the so-called non-neutral plasma (NNP).
In Gabor Lenses a homogenous magnetic field created by a solenoid confines electrons in transverse direction, while a potential well created by a cylindrical electrode system confines them longitudinally (see picture 1).

Research with the Gabor Lens

Experiments with Gabor Lenses were done for several reasons. It is possible to inject an ion beam into the Gabor Lens and observe interactions between electron clouds and ion beams. The focal length of the lens as well as the charge exchange and recombination of the particles can be determined.
With the Gabor Lens it is possible to focus highly intensive ion beams. Improving the focusing quality and reducing the emittance growth is the main emphasis in the application of this electron trap. It is also possible to achieve space charge compensation with correctly adjusted lenses.
Furthermore, the non-neutral plasma is examined with the Gabor Lens. The plasma parameters, density distribution and temperature, can be determined.

* thoma@iap.uni-frankfurt.de

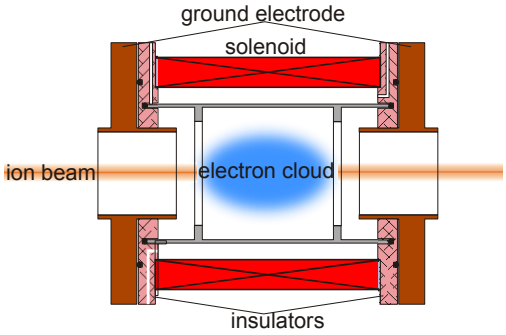

Figure 1: Basic principle of a Gabor Lens.
red: solenoid for magnetic field, brown: ground electrode, grey: anode for applying a potential, blue: electron column, orange/red: positive ion beam [**2**]

DIFFERENT GABOR LENSES UNDER INVESTIGATION

Several concepts of Gabor Lenses have been designed [**2**]-[**5**]. Here, the aspect ratio of the GL is a decisive parameter for the confinement behaviour of the non-neutral plasma. Different sizes of lenses have been tested and correspondingly different radius to length ratios were assumed. The following table will give an overview of the GL tested so far:

Name	Radius	Length	r/l	Ref.
small GL	0.054 m	0.16 m	0.3375	[**2**]
3-segmented GL	0.054 m	0.4 m	0.135	[**3**]
HSI-GL	0.085 m	0.340 m	0.25	[**4**]
Toroid-GL	0.1 m	0.68 m	0.147	[**5**]
GL2000	0.075 m	2 m	0.0375	(*)

Table 1: Aspect ratio of the Gabor Lenses designed by the NNP Group
(*) under construction

The first four GL's in the table have already been tested at NNP Group. Following the research results are briefly presented:

- small GL: The lens has a maximum potential of $\phi_{A,max} = 6\,kV$ and a maximum magnetic field of $B_{max} = 30\,mT$. The magnetic field is created by

solenoidal windings. With this lens it was possible to focus Ar- and He-beams up to 30 keV and space charge compensation in the transport channel has been reached.

- 3-segmented GL: This GL is a 3-segmented lens for the creation of a longitudinal gradient in the magnetic field. It has three separated ports for the potential and also three independent magnetic solenoids. With the feed-throughs through the anode tube optical diagnostics is possible and advanced diagnostic concepts have been developed.
- HSI-GL: The maximum potential of the anode is $\phi_{A,max}$ = 50 kV and the maximum of the magnetic field is B_{max} = 160 mT. With this lens a plasma radius of r = 5 cm is created. A segmentation in radial direction of the potential makes it possible to get an asymmetric confinement. This lens was tested at GSI/FAIR Darmstadt and focused intense Ar^1 – beams in accelerators up to 130 keV and 35 mA. With HSI-GL the effective focusing quality of a GL has been proofed and possible reduction of emittance growth has been observed (under assumption of 100 % transmission) (see picture 2).

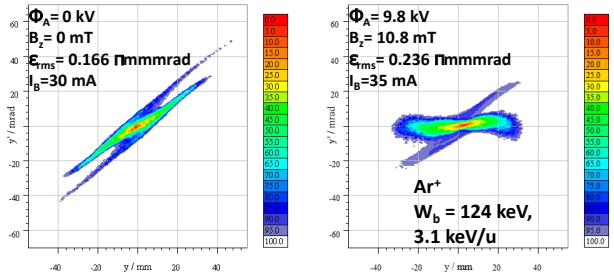

Figure 2: Focusing an ion beam with a Gabor Lens – Emittance growing factor 1.38 [**4**].

- Toroid-GL: This type consists of a toroidal magnetic confinement and a 30 degree-bent anode. With the Toroid-GL electron trapping in an asymmetric potential and magnetic field is possible. The experiments found that the light density distribution of the excited residual gas atoms at the inner edge of the anode tube was significantly more intensive (see picture 3). Thus, a shifted electron density distribution towards the higher magnetic field could be confirmed. A next step could be an application of the toroid GL as a toroidal ion beam guiding device.

GL2000 has the lowest aspect ratio with longest on-axis distance of all lenses designed to date. GL2000 is under construction right now and will be tested till the end of 2018.

GL2000

GL2000 opens up a new field in research with Gabor Lenses. It is planned to confine the largest stable electron column.

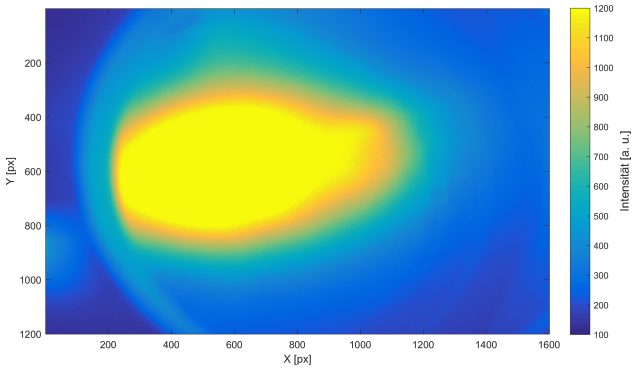

Figure 3: Shift of the light density distribution - the light density distribution is more intensive towards the inner edge of the beam tube [**5**].

The anode of the lens is a 2 m long stainless steel tube with a radius of 75 mm. The copper made electrodes are grounded and the potential well is up to 30 kV. The magnetic field of the lens is created by 23 water-cooled copper coils in pancake configuration. The coils are held by a manufactured frame and can therefore be aligned radially to the anode tube and moved longitudinally to it.

Plasma diagnostics such as emittance measuring systems, Faraday Cups, CCD cams, monochromators, momentum spectrometers and also insitu diagnostic will help to determine the plasma parameters in the lens. It is provided with six feed-throughs for various measurements.

Due to the aspect ratio of 0.0375, the confinement of the electron plasma will be a challenge. Because of the long anode tube, the resulting electric field in the tube is nearly zero and the electrons have a lower kinetic energy. Consequently, there are less impact ionizations and less electron productions. The formation of an electron cloud in the GL2000 is expected to take at least longer than in the previously investigated lenses.

Possible applications of GL2000

GL2000 was developed to confine a long and stable electron cloud. The subsequent diagnostics will characterize the electron plasma as comprehensively as possible and determine the plasma parameters and formation of the longitudinal plasma instabilities.

In the next step, pencil beam experiments will be performed to determine the focal length of the lens. Then beam experiments with highly intense positive ions will be implemented. These ion beams are dominated by space charge and will provide information about the space charge compensation by passing the electron column. The emittance growth can be estimated transversal and longitudinal.

The interaction between electron cloud and ion beam gives information about optimal GL settings for ion beam guiding without losses.

Also new physical effects are expected compared to a series of many small lenses. The shorter, already characterized and functional Gabor Lenses can also be used for beam focusing.

However, the disadvantage is that much more electronics would be required, as each laboratory lens would have to be equipped with its own power supplies and magnets. Furthermore and much more important, the electron cloud would always be constant in density only within the respective lens. Thus, there would be no constant focusing effect on the ion beam due to a chain of Gabor Lenses.

Focusing a positive Ion Beam with GL2000

The transit time of a relativistic ion beam through the 2 m long Gabor Lens is with v=c according to $v = \frac{l}{t}$ about $t_r = 6,67 \cdot 10^{-9}$ s.
The plasma frequency of the electron plasma inside the lens is $\omega_{PE} = 2\pi f = \sqrt{\frac{n_e \cdot e^2}{\epsilon_0 \cdot m_e}} = 564,15$ MHz $T_P = \frac{2\pi}{\omega_{PE}} = 1,7 \cdot 10^{-9}$ s, if the density is assumed to be $n_e = 1 \cdot 10^{14}$ m^{-3}.
If the transit time t_r of the ion beam is equal to the response time of the electron cloud, expressed by the plasma frequency ω_{PE} and the beam bunch frequency is below ω_{PE}, the focusing of space charged and emittance dominated beam transport should be possible.

PRESENT STATUS AND OUTLOOK

GL2000 has been designed since the beginning of 2018 and is currently being assembled. The status of the experimental setup can be seen in Figure 4. The lens is adjusted on a frame and mounted on a rack. The frame can be moved on the rack and later holds not only the lens but also the 23 longitudinally movable copper coils.

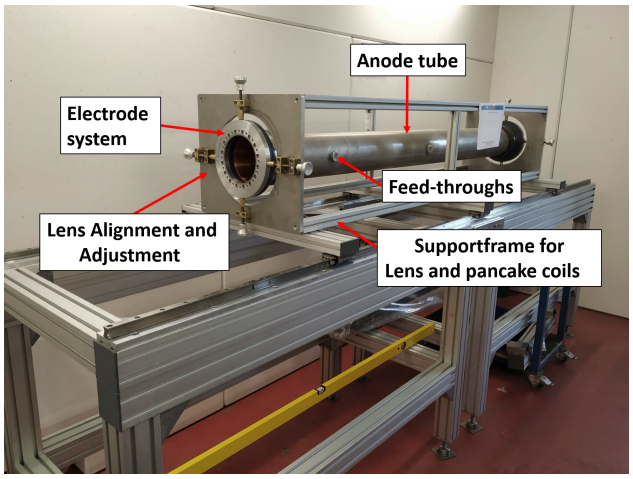

Figure 4: Picture of the present experimental setup of GL2000 (October 2018).

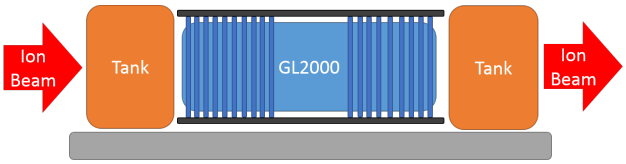

Figure 5: Schematic structure of the experimental setup

After the coils have been mounted on the experiment, the tanks for pumps and diagnostic instruments are to be connected. Following, the first experiments will be carried out at the beginning of 2019. Figure 5 shows a schematic representation of the finished setup. The red arrows represent the ion beam, which passes through the first tank before it is guided through the Gabor Lens and can then be detected in the second tank.

ACKNOWLEDGEMENTS

We appreciate our thank to Aries collaboration (work-package 2016: "Electron lenses for synchrotrons").

REFERENCES

[1] Davidson, R.C., Physics of nonneutral plasmas, Imperial College Press, London, 2001.

[2] Oliver Meusel, Focussing and transport of ion beams using space charge lenses, Goethe University, Frankfurt a. M., Germany, 2005, urn:nbn:de:hebis:30-28283.

[3] Kathrin Schulte, Research of diagnostic techniques on a nonneutral plasma, Goethe University, Frankfurt a. M., Germany, 2008, urn:nbn:de:hebis:30-62446.

[4] Kathrin Schulte, Studies on the focusing performance of a Gabor lens depending on nonneutral plasma properties, Goethe University, Frankfurt a. M., Germany, 2013, urn:nbn:de:hebis:30:3-334310.

[5] Katrin Isabell Thoma, Investigation of a nonneutral plasma in a toroidal confinement, Goethe University, Frankfurt a. M., Germany, 2017, urn:nbn:de:hebis:30:3-462936.

SYNCHROTRON RADIATION INTERACTION WITH CRYOSORBED LAYERS FOR ASTROCHEMICAL INVESTIGATIONS

R. Dupuy[1], M. Bertin[1], G. Féraud[1], X. Michaut[1], T. Putaud[1], L. Philippe[1], P. Jeseck[1], R. Cimino[2], V. Baglin[3], C. Romanzin[4], and J.-H. Fillion[1]

[1]Sorbonne Université, Observatoire de Paris, Université PSL, CNRS, LERMA, F-75005, Paris, France
[2]Laboratori Nazionali di Frascati (LNF)-INFN I-00044 Frascati
[3]CERN, CH-1211 Geneva 23, Switzerland
[4]Laboratoire de Chimie Physique, CNRS, Univ. Paris-Sud, Université Paris-Saclay, 91405, Orsay, France

Abstract

Photon-stimulated desorption (PSD) is a process of interest for the two seemingly unrelated topics of accelerator vacuum dynamics and astrochemistry. Here we present an approach to studying PSD of interstellar ice analogs, i.e. condensed films of molecules of astrophysical interest at cryogenic temperatures, using synchrotron radiation. We present results obtained in the VUV range on various pure and layered ices, focusing on elucidating the desorption mechanisms, and results in the X-ray range for H_2O.

INTRODUCTION

Photon-stimulated desorption, the process by which an adsorbed molecule on a surface is detached by a photon, is one example of a surface science process whose study has applications in different fields. In the context of accelerators, the synchrotron radiation generated by the circulating beams of charged particles hits the walls and releases molecules into the gas phase, thus limiting the vacuum and potentially hindering beam stability. During beam operations (in the presence of photons, electrons and energetic ions), the vacuum in an accelerator becomes orders of magnitude higher owing to non-thermal processes, which are thus completely dominant [1, 2]. Studies of photon-stimulated desorption and its impact on the vacuum dynamics of accelerators have been made in this context.

Studies of photodesorption have also been made in a very different context: astrochemistry of the cold interstellar medium (see [3–8] and references therein). The cold interstellar medium and accelerators present interesting similarities in this context. As will be detailed in part 2, the cold interstellar medium also features very low densities, molecules (similar to those composing the residual gases of vacuum chambers) adsorbed on low temperature surfaces (relevant for accelerators such as the LHC operating at cryogenic temperatures), and the presence of photons and energetic particles.

The general context of astrochemistry will be briefly introduced, then our approach to the study of photodesorption, which makes use of synchrotron radiation to uncover fundamental mechanisms, will be presented in both the VUV photon range and in the more recently explored X-ray photon range.

ASTROCHEMICAL CONTEXT

In the interstellar medium, molecules are found in many different regions [9]. Observational spectroscopy spanning from the centimeter to the far UV region of the spectrum allowed the identification of more than 200 molecules. Radioastronomy, which identifies molecules through their rotational lines, has probably been the most fruitful method for identifying molecules so far. Aside from gas phase molecules, in all these regions tiny, carbonaceous and/or silicated dust grains (<1 μm) are also found, which can act as reaction catalysts for the formation of molecules. Of particular interest here are the cold (<100K) and dense (>10^3 molecules cm^{-3}) regions. These regions typically start off as so-called molecular clouds. Some parts of these molecular clouds can form denser clumps which through gravitational collapse end up more and more dense, and also colder and colder as they become completely shielded from external irradiation. These "dense cores" then evolve as the gravitational collapse forms a protostar, with its protostellar envelope. Next is the formation of a young star, with creation of a surrounding disk of matter called a protoplanetary disk, which will eventually evolve into a system of planets, asteroids and comets [10].

In all these stages, the aforementioned dust grains can be cold enough to act as molecular sinks: molecules that form at their surface or that accrete from the gas phase stay cryosorbed. Thus in parallel of the gas phase, there is a solid phase, usually called the ice mantles. The typical content of these ice mantles is known mainly thanks to mid-infrared spectroscopy, although it is much harder to constrain than the content of the gas phase. The main component by far is H_2O. Following are CO and CO_2 with a few tens of percent with respect to H_2O, and CH_3OH, NH_3, CH_4 and a few molecules at the few percent level. These numbers can vary a lot depending on the observed source [11].

In regions where these grains are exposed to heat, the interaction between this solid phase and the gas phase can happen through thermal desorption of molecules. However, when the temperature stays cold, this interaction can only happen

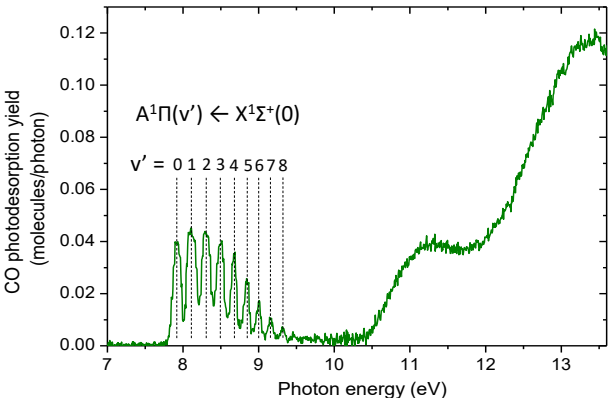

Figure 1: Photodesorption yield of CO as a function of photon energy, for a 20 ML thick CO ice at 10 K. Adapted from Ref. [15]

through non-thermal desorption mechanisms. In these cold regions, observations of molecules in the gas phase that could only have formed on the grains, or of molecules that should be completely frozen out on the grains and absent from the gas, showed that such mechanisms should be at play. Energy coming from cosmic rays, exothermic chemistry, shocks or photons can cause desorption of molecules. This is why photon-stimulated desorption is of interest here.

The importance for astrochemistry of the photodesorption process and of its study with dedicated laboratory experiments has been demonstrated by astrochemical models implementing it. Astrochemical models aim to help the interpretation of astronomical observations of molecules and to extract meaningful information from them. They include a physical modeling of the considered region and a chemical network of up to thousands of reactions to try to reproduce the observed abundances of molecules. For example, in a typical model of protoplanetary disk [12], if the photodesorption process is turned off, the prediction is that there is no water in the gas phase in the cold, outer part of the disk, which contradicts observations [13]. The inclusion of photodesorption is necessary to reproduce the observations. Another example in protoplanetary disks is the detection of CH_3CN, the first moderately complex organic molecule to be detected in this kind of astrophysical object [14]. The current hypothesis is that this molecule forms at the surface of cold grains, and is then released by photodesorption in the gas phase where it is detected.

In order to implement the photodesorption process in astrochemical models, laboratory studies are mandatory to obtain quantitative inputs (number of desorbed molecules per incident photon) and their dependence on various parameters (most importantly the nature of the molecule, but also the temperature, ice morphology, thickness, etc...).

METHODS

The experiments were performed in the SPICES set-up and its upgraded version, the SPICES 2 set-up. These set-ups are described in more detail elsewhere [16,17]. Briefly, they consist of an ultra-high vacuum chamber with a rotatable sample holder cooled down to 10-20 K by a closed-cycle helium cryostat. The sample holder has several surfaces that can be used. The experiments were typically performed on either polycristalline gold or OFHC copper. In SPICES 2, a copper surface is electrically isolated from the sample holder, allowing to measure the current at the sample, which is used for total electron yield measurements during X-ray irradation. A gas injection line connected to a dosing tube inside the chamber allows depositing molecular films of controlled thicknesses [16] (0.2 - 200 monolayers). The films deposited can be probed using an infrared spectrometer (RAIRS-FTIR). During irradiation, the desorption of molecules is monitored by a quadrupole mass spectrometer (QMS). In SPICES 2, two different mass spectrometers can be used, one dedicated to the detection of neutral species, and the second one also being able to detect positive and negative ions and to filter them as a function of their kinetic energy using a 45° deflector.

The set-ups are mobile and can be connected, among other possibilities (lasers, etc) to beamlines at the SOLEIL synchrotron. Experiments in the VUV range were performed at the DESIRS beamline, and experiments in the X-ray range at the SEXTANTS beamline. On the DESIRS beamline the output of the undulator is monochromatized with a resolution of ~0.04 eV and scanned continuously between 7 and 14 eV. The second harmonics is suppressed by a Krypton gas filter. The typical flux in this mode is 10^{13} photons s^{-1}. On the SEXTANTS beamline, similarly the output is monochromatized with a resolution of ~0.15 eV and scanned continuously between 520 and 600 eV, around the O 1s edge. The flux is about 10^{13} photons s^{-1}. More details on the beamlines [18,19] and their use in our experiments [17,20] can be found elsewhere.

The results we obtain are "photodesorption spectra", which is the desorption signal of a given molecule as a function of photon energy. The signal on the relevant mass channel of the QMS, which is proportional to the desorption flux of the molecule, is divided by the photon flux. This is then calibrated to an absolute number of molecules desorbed per incident photon [17,20]. More details on the specific experiments mentioned later can be found in the corresponding papers (see citations below).

VUV PHOTODESORPTION

A prototypical example of the kind of information obtained through the photodesorption spectrum of a molecule, thanks to synchrotron radiation, is the CO molecule. Its photodesorption spectrum is shown in Fig. 1. The spectrum is taken between 7 and 13.6 eV. The upper limit of 13.6 eV comes from the astrophysical context: in astrophysical media photons above 13.6 eV are absorbed by atomic hydrogen, which is by far the most abundant element, and thus they do not need to be considered. The photodesorption yield varies wildly as a function of photon energy, and the spectrum is very structured. These structures can be readily

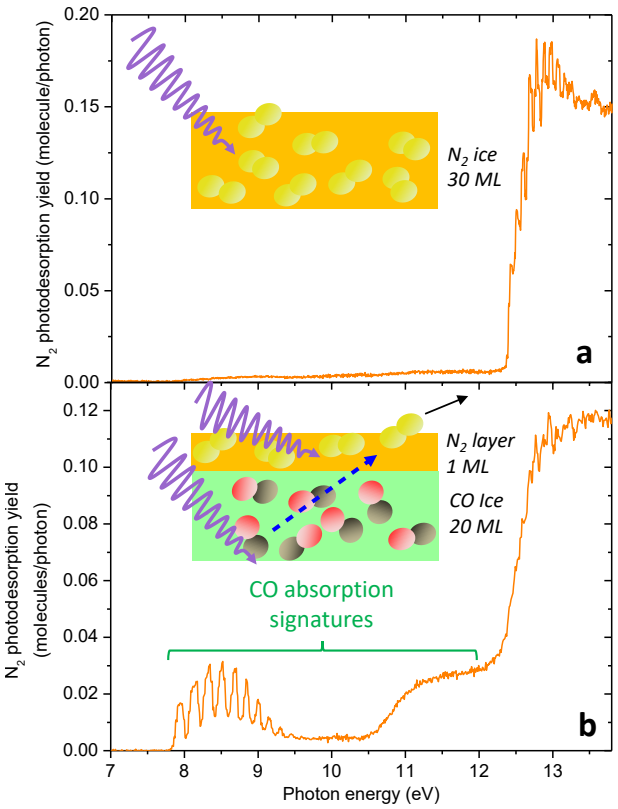

Figure 2: a. Photodesorption yield of N_2 as a function of photon energy, for a 30 ML thick N_2 ice at 18 K. b. Photodesorption yield of N_2 as a function of photon energy, for 1 ML of N_2 layered on a 20 ML CO ice. Adapted from Ref. [21]

identified with the electronic transitions of condensed CO: for example, the peaks between 8 and 9 eV correspond to the vibrational progression of the A-X transition. These molecular signatures give a first basic information, which is that the initial step of desorption is the absorption of the photon by a CO molecule (and not e.g. the substrate), and that a single-photon process is involved (otherwise, for multi-photon processes, the structures would be deformed when compared to the absorption spectrum). This is usually termed Desorption Induced by Electronic Transitions (DIET). How the electronic energy is converted into a desorption event is the more difficult question. More details on CO photodesorption can be found in Ref. [20].

The signal on the mass spectrometer allows to identify which species desorbs in the end, while the spectral information tells which species initially absorbed a photon. The desorbed molecule need not be the same as the one which absorbed a photon, however. This can be shown for a system with different species, such as a layer of one molecule on a substrate of another molecule. It has been shown by layering isotopically labeled ^{13}CO on a ^{12}CO ice that the desorbed molecules are the uppermost ^{13}CO molecules, but that they can be desorbed following absorption of photons

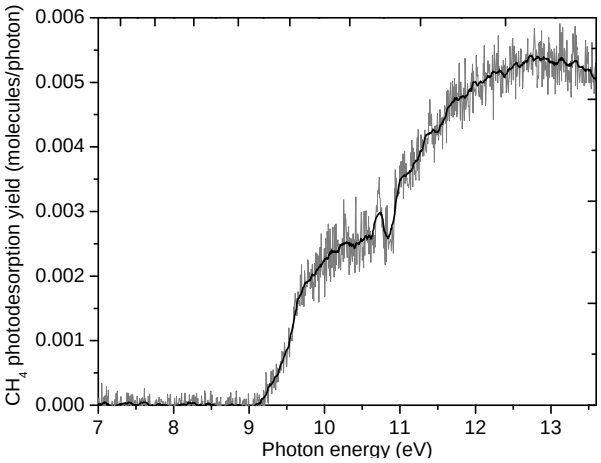

Figure 3: Photodesorption yield of CH_4 as a function of photon energy, for a 20 ML pure CH_4 ice at 10 K. Adapted from Ref. [15]

by sub-surface ^{12}CO molecules, as the spectral signatures of the isotopes slightly differ [22]. The result is even more striking for N_2 layered on a CO ice [23]. Fig 2a shows the photodesorption spectrum of pure N_2 ice. The first allowed electronic transition of N_2 is rather high in energy and thus strong photodesorption is only observed above 12 eV. When one monolayer of N_2 is layered on top of a CO ice, however, monitoring the desorption of N_2 we can see appearing in the spectrum peaks between 8 and 9 eV that are the molecular signature of CO absorption (Fig. 2b). While a N_2 molecule desorbs, the photon was initially absorbed by a CO molecule. Thus an energy transfer of some sort occurs. This process has been termed "indirect DIET" before [22].

The aforementioned molecules, CO and N_2, are not or not efficiently dissociated by VUV irradiation in the considered energy range. When molecules that dissociate are considered, many new possibilities for photodesorption open. Photochemistry and photodissociation can lead to the desorption of not just the parent molecule, but also other molecules and fragments, as in the case of methanol for example [24]. For the parent molecule, new channels of desorption are also opened. The example taken here is the CH_4 molecule (more details are found in Ref. [15]). The photodesorption spectrum of CH_4 is shown in Fig. 3 and features the electronic signature of the molecule, with the electronic states being this time dissociative. Dissociation of methane creates many fragments in the ice (CH_3, CH_2, H, etc) which can subsequently react. Reactions that lead back to the CH_4 molecules are usually exothermic, and the excess energy can be used for desorption (for example, the $CH_3 + H \rightarrow CH_4$ liberates ~4.5 eV). Another possibility is that the fragments themselves can be energetic: in particular, the light H fragments can carry a lot of kinetic energy and could "kick" CH_4 molecules out of the ice. The kick out mechanism was initially proposed and studied in simulations of the photodesorption of water [25].

These examples illustrate some of the complexity of photon-stimulated desorption processes: even in the case of a

simple, pure ice like CO, the mechanism of desorption is not exactly well known, and as soon as different molecules and chemistry are involved the degree of complexity increases. Indirect desorption changes the picture of photodesorption in a realistic astrophysical ice, which contains many molecules.

X-RAY PHOTODESORPTION

The UV range is particularly interesting for astrophysics as UV photons up to 13.6 eV are ubiquitous in the interstellar medium. But some regions, such as protoplanetary disks, also see considerable X-ray irradiation. Photodesorption by X-rays in an astrophysical context has been little studied so far and it is not yet taken into account in models. Therefore we performed experiments on X-ray photodesorption from pure water ice, for which some results are presented here. More details on both the results and the astrophysical context can be found in Ref. [17].

X-ray photodesorption, like UV photodesorption, is initiated by an electronic transition, except instead of exciting valence electrons, the core electrons of a molecule are excited. In the case of water the O 1s electrons are excited, in the 520-600 eV range. A core excitation for low atomic number atoms relaxes almost entirely through Auger decay. Auger decay leaves the molecule in a highly excited state that can give rise to dissociation pathways not accessible for single valence electron excitations. The desorption of some species will occur predominantly through such dissociation pathways. For other species, the dominant process will be the X-ray induced Electron Stimulated Desorption (XESD). The Auger electron, with about 500 eV of kinetic energy in the case of water, will be scattered in the ice, causing many secondary electrons and excitations. These secondary events, which are similar to the low-energy valence excitations in the VUV range, will be responsible for the desorption of certain species. In fact, since most of the energy of the initial photon goes into the XESD channel and creates many secondary events, XESD is expected to dominate the desorption of species which are also seen for low-energy excitations.

Fig. 4 shows the photodesorption spectrum of the intact H_2O molecule around the O 1s edge, as well as the Total Electron Yield (TEY), i.e. the number of electrons escaping the surface per incident photon. The number of escaping electrons is proportional to the number of Auger decays occuring in the ice and thus to the number of absorbed X-ray photons. The TEY therefore represents the X-ray absorption spectrum (XAS). We can see that the photodesorption of H_2O follows the absorption. This is also the case for the other detected desorbing neutral species, O_2 and H_2 [17]. The contribution of the XESD mechanism, i.e. the electrons, to desorption should follow the total electron yield. The fact that the desorption spectra of neutrals follow exactly the TEY hints that XESD probably dominates. This is further compounded by the argument developed above, as neutral species are desorbed by low-energy excitation. The estimation of the photodesorption yield per absorbed photon of H_2O is also similar to the electron-stimulated desorption yield (see [17]), which is another argument for the dominance of XESD.

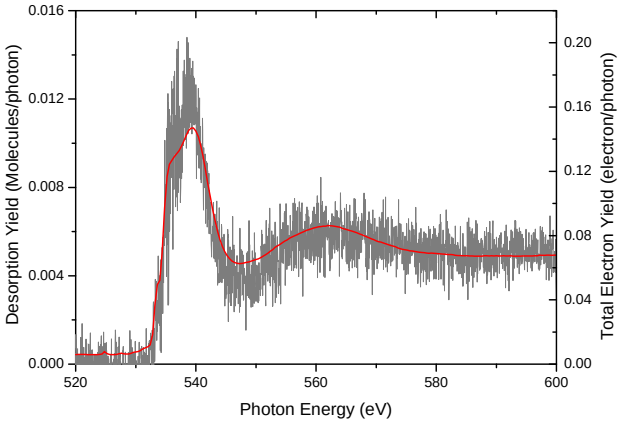

Figure 4: Photodesorption yield of H_2O for a 100 ML compact amorphous solid water (c-ASW) ice at 90K (grey trace). Also shown is the TEY (red trace). Adapted from Ref. [17]

One example of a species whose desorption does not follow the TEY, and where XESD thus does not play a dominant role, is O . The photodesorption yield of O is shown in Fig. 5. In fact, the features observed between 530 and 536 eV in the spectrum do not correspond to resonances of water: instead, the peaks can be identified to resonances of H_2O_2. This molecule is a product of the photolysis of water by the X-rays, present at the few percent level in the ice. The observations of the H_2O_2 peaks dominating the photodesorption spectrum of O indicate that (i) O is not dominated by secondary electrons and (ii) it is efficiently produced by direct excitation of H_2O_2, and not by excitation of H_2O. The differences in efficiency must be very large, as H_2O_2 is only a minor product in the irradiated ice, which is still mostly made of water. A similar behaviour is also observed for other O-bearing ionic fragments. One simple reasoning that can help explain this observation is the following: when dissociating a water molecule to form an oxygen-bearing fragment, an O-H bond (or two) are broken. In this dissociation process, the much lighter H or H fragment will carry most of the kinetic energy, as the energy partition is expected to depend on the mass ratio of the fragments. Thus not enough kinetic energy is left for the oxygen-bearing fragment to desorb. Conversely, when dissociating H_2O_2, an O-O bond is broken, yielding a roughly similar amount of energy to both fragments, which then have the required energy to desorb. Confirming such an explanation will require further experiments.

Besides these two species, many more are seen desorbing [17]. The neutral species are by far the most abundant desorption products, but as shown in the example of O , ion desorption can provide interesting information as well. Even in the case of a pure ice of a molecule like water, where the chemical network is not very complex, the number of different species desorbing is high and distinct desorption pathways exist.

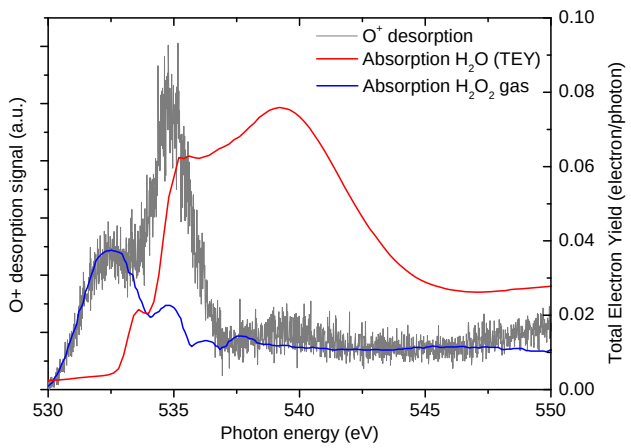

Figure 5: Photodesorption yield of O for a 100 ML c-ASW ice at 90K (grey trace). Also shown are the TEY (red trace) and the gas phase absorption of H_2O_2 [26] (blue trace), shifted to match the O yield.

CONCLUSION

Photon-stimulated desorption by UV and X-ray photons is relevant for both astrochemistry and accelerator vacuum dynamics. Focusing here on multilayer physisorbed molecules, we showed that photodesorption yields depend strongly on (i) wavelength (5×10^{-2} to $< 1 \times 10^{-3}$ molecule/photon for CO over the VUV range) and (ii) molecules (a few 10^{-2} for CO to $< 1 \times 10^{-5}$ molecule/photon for methanol [24]), but also depends on other factors like the presence of different molecules through indirect desorption. Comparing yields at the maxima of absorption in the VUV and X-ray ranges, X-ray desorption yields are higher (for H_2O, 1×10^{-2} for X-rays to 3×10^{-4} molecule/photon for UV). The variety of mechanisms that can be involved has been introduced.

As shown with the example of photon-stimulated desorption, surface science studies can be of interest to vastly different fields like astrochemistry and accelerator vacuum dynamics. While the exact systems that are of interest for each field may differ, efforts to develop experimental techniques and knowledge can be shared. In particular, here we focused on attempts to unravel some fundamental mechanisms that can be more general than the particular examples presented, and from which conclusions can be drawn that are of broader interest.

REFERENCES

[1] O. Gröbner, "Dynamic Outgassing," 1999.

[2] N. Hilleret, "Non-thermal outgassing," 2007.

[3] M. S. Westley, R. A. Baragiola, R. E. Johnson, and G. A. Baratta, "Photodesorption from low-temperature water ice in interstellar and circumsolar grains," *Nature*, vol. 373, no. 6513, pp. 405–407, Feb. 1995.

[4] K. I. Öberg, E. F. van Dishoeck, and H. Linnartz, "Photodesorption of ices I: CO, N2 , and CO2," *Astronomy and Astrophysics*, vol. 496, no. 1, pp. 281–293, Mar. 2009.

[5] A. Yabushita, T. Hama, and M. Kawasaki, "Photochemical reaction processes during vacuum-ultraviolet irradiation of water ice," *Journal of Photochemistry and Photobiology C: Photochemistry Reviews*, vol. 16, pp. 46–61, Sep. 2013.

[6] C. Arasa, J. Koning, G.-J. Kroes, C. Walsh, and E. F. van Dishoeck, "Photodesorption of H2O, HDO, and D2O ice and its impact on fractionation," *Astronomy & Astrophysics*, vol. 575, p. A121, Mar. 2015.

[7] R. Martín-Doménech, J. Manzano-Santamaría, G. M. Muñoz Caro, G. A. Cruz-Díaz, Y.-J. Chen, V. J. Herrero, and I. Tanarro, "UV photoprocessing of CO2 ice: A complete quantification of photochemistry and photon-induced desorption processes," *Astronomy & Astrophysics*, vol. 584, p. A14, Dec. 2015.

[8] R. Dupuy, G. Féraud, M. Bertin, X. Michaut, T. Putaud, P. Jeseck, L. Philippe, C. Romanzin, V. Baglin, R. Cimino, and J.-H. Fillion, "The efficient photodesorption of nitric oxide (NO) ices: A laboratory astrophysics study," *Astronomy & Astrophysics*, vol. 606, p. L9, Oct. 2017.

[9] A. G. G. M. Tielens, "The molecular universe," *Reviews of Modern Physics*, vol. 85, no. 3, pp. 1021–1081, Jul. 2013.

[10] E. F. van Dishoeck, "Astrochemistry: Overview and challenges," *arXiv preprint arXiv:1710.05940*, 2017.

[11] A. A. Boogert, P. A. Gerakines, and D. C. Whittet, "Observations of the Icy Universe," *Annual Review of Astronomy and Astrophysics*, vol. 53, no. 1, pp. 541–581, Aug. 2015.

[12] I. Kamp, W.-F. Thi, G. Meeus, P. Woitke, C. Pinte, R. Meijerink, M. Spaans, I. Pascucci, G. Aresu, and W. R. F. Dent, "Uncertainties in water chemistry in disks: An application to TW Hydrae," *Astronomy & Astrophysics*, vol. 559, p. A24, Nov. 2013.

[13] M. R. Hogerheijde, E. A. Bergin, C. Brinch, L. I. Cleeves, J. K. Fogel, G. A. Blake, C. Dominik, D. C. Lis, G. Melnick, D. Neufeld *et al.*, "Detection of the water reservoir in a forming planetary system," *Science*, vol. 334, no. 6054, pp. 338–340, 2011.

[14] K. I. Öberg, V. V. Guzmán, K. Furuya, C. Qi, Y. Aikawa, S. M. Andrews, R. Loomis, and D. J. Wilner, "The comet-like composition of a protoplanetary disk as revealed by complex cyanides," *Nature*, vol. 520, no. 7546, pp. 198–201, Apr. 2015.

[15] R. Dupuy, M. Bertin, G. Féraud, X. Michaut, P. Jeseck, M. Doronin, L. Philippe, C. Romanzin, and J.-H. Fillion, "Spectrally-resolved UV photodesorption of CH4 in pure and layered ices," *Astronomy & Astrophysics*, vol. 603, p. A61, Jul. 2017.

[16] M. Doronin, M. Bertin, X. Michaut, L. Philippe, and J.-H. Fillion, "Adsorption energies and prefactor determination for CH3OH adsorption on graphite," *The Journal of Chemical Physics*, vol. 143, no. 8, p. 084703, Aug. 2015.

[17] R. Dupuy, M. Bertin, G. Féraud, M. Hassenfratz, X. Michaut, T. Putaud, L. Philippe, P. Jeseck, M. Angelucci, R. Cimino, V. Baglin, C. Romanzin, and J.-H. Fillion, "X-ray photodesorption from water ice in protoplanetary disks and X-ray-dominated regions," *Nature Astronomy*, vol. 2, no. 10, pp. 796–801, Oct. 2018.

[18] L. Nahon, N. de Oliveira, G. A. Garcia, J.-F. Gil, B. Pilette, O. Marcouillé, B. Lagarde, and F. Polack, "DESIRS: A state-of-the-art VUV beamline featuring high resolution and variable polarization for spectroscopy and dichroism at SOLEIL," *Journal of Synchrotron Radiation*, vol. 19, no. 4, pp. 508–520, Jul. 2012.

[19] M. Sacchi, N. Jaouen, H. Popescu, R. Gaudemer, J. M. Tonnerre, S. G. Chiuzbaian, C. F. Hague, A. Delmotte, J. M. Dubuisson, G. Cauchon, B. Lagarde, and F. Polack, "The SEXTANTS beamline at SOLEIL: A new facility for elastic, inelastic and coherent scattering of soft X-rays," *Journal of Physics: Conference Series*, vol. 425, no. 7, p. 072018, Mar. 2013.

[20] E. C. Fayolle, M. Bertin, C. Romanzin, X. Michaut, K. I. Öberg, H. Linnartz, and J.-H. Fillion, "CO ice photodesorption: A wavelength-dependent study," *The Astrophysical Journal*, vol. 739, no. 2, p. L36, Oct. 2011.

[21] E. C. Fayolle, M. Bertin, C. Romanzin, H. A. M Poderoso, L. Philippe, X. Michaut, P. Jeseck, H. Linnartz, K. I. Öberg, and J.-H. Fillion, "Wavelength-dependent UV photodesorption of pure N2 and O2 ices," *Astronomy & Astrophysics*, vol. 556, p. A122, Aug. 2013.

[22] M. Bertin, E. C. Fayolle, C. Romanzin, K. I. Öberg, X. Michaut, A. Moudens, L. Philippe, P. Jeseck, H. Linnartz, and J.-H. Fillion, "UV photodesorption of interstellar CO ice analogues: From subsurface excitation to surface desorption," *Physical Chemistry Chemical Physics*, vol. 14, no. 28, p. 9929, 2012.

[23] M. Bertin, E. C. Fayolle, C. Romanzin, H. A. M. Poderoso, X. Michaut, L. Philippe, P. Jeseck, K. I. Öberg, H. Linnartz, and J.-H. Fillion, "Indirect Ultraviolet Photodesorption From CO:N2 Binary Ices — an Efficient Grain-gas Process," *The Astrophysical Journal*, vol. 779, no. 2, p. 120, Dec. 2013.

[24] M. Bertin, C. Romanzin, M. Doronin, L. Philippe, P. Jeseck, N. Ligterink, H. Linnartz, X. Michaut, and J.-H. Fillion, "UV photodesorption of methanol in pure and CO-rich ices: Desorption rates of the intact molecules and the photofragments," *The Astrophysical Journal*, vol. 817, no. 2, p. L12, Jan. 2016.

[25] S. Andersson and E. F. van Dishoeck, "Photodesorption of water ice," *Astronomy and Astrophysics*, vol. 491, no. 3, pp. 907–916, Dec. 2008.

[26] J. Berkowitz, *Atomic and Molecular Photoabsorption: Absolute Total Cross Sections*. Academic Press, 2002.

SEY AND OTHER MATERIAL PROPERTIES STUDIED AT CRYOGENIC TEMPERATURES

L.Spallino*, M. Angelucci, R. Larciprete[1] and R. Cimino, LNF-INFN, Frascati (Roma), Italy.
[1]also at CNR-ISC Istituto dei Sistemi Complessi, Roma, Italy.

Abstract

A very low secondary electron yield is confirmed to be the fingerprint of laser treated copper substrates. In future high energy particle accelerators, this feature offers unquestionable advantages for electron cloud mitigation purposes. Thermal programmed desorption between 20 and 70 K by dosing Ar multilayers of different thicknesses on a laser treated copper substrate and on its flat counterpart are here reported. The results show that, as a consequence of their nanostructured porous morphology, the desorption of gas from the laser treated substrates occurs in a much broader and higher temperature range with respect to what is observed from the flat substrates. These findings suggest that vacuum transient effects against temperature fluctuations should be better evaluated, if such surfaces would be included as cryogenic vacuum components in accelerators.

INTRODUCTION

The secondary emission yield (SEY) is an intrinsic property of materials, accounting for the capability to produce secondary electrons when an electron impacts the surface. From plasma physics to satellite and radio-frequency applications, SEY determination is therefore of paramount importance. SEY could play a fundamental role in governing, for example, space-charge effects and/or radio-frequency break down [1–3]. In the same way, SEY is a crucial parameter for all modern high-energy positively charged particle accelerators for which, as a consequence of the strong coupling between the charged particle beam and the cloud of low energy electrons, electron-cloud effects (ECE) may cause machine and beam instabilities [4–10]. Efficient ECE mitigation strategies are nowadays considered as a priority for the commissioning of the High Luminosity-Large Hadron Collider (HL-LHC) [19,20] and for the proton-proton Future Circular Collider (FCC-hh) [21]. These strategies have the objective to reduce SEY [8, 11–14]. Surface geometrical modifications have been proved to be quite effective [1–3, 12, 15, 16] and recently an engineering method based on laser ablation (LASE) has been proposed to this purpose. LASE can modify the surface at the nanoscale. It ensures an impressive reduction of SEY down to values even less then 1, depending on the detailed process and substrate material [18, 38]. The advantageous results of laser processing have brought laser treated copper (LASE-Cu) surfaces to be proposed to be used in future accelerator technology. LASE-Cu is a potential candidate to mitigate ECE expected to occur on the beam screen (BS) in the cold bore of the dipoles of HL-LHC [19, 20] and FCC-hh [21]. However, before definitely including LASE-surfaces in the machine design, the consequences of having a rough rather than a flat wall in the cryogenic ultra high vacuum (UHV) should be carefully evaluated.

At cryogenic temperature, even small and unavoidable temperature (T) fluctuations of the accelerator vacuum components may cause undesirable vacuum transient. If T is low enough, residual gas molecules like H_2, CO, CO_2, H_2O, CH_4, etc. may be adsorbed on the cryogenic walls. Any T increase may induce their desorption and an unwanted pressure increase. [22]. High p, even if only for a short time or in a small section of the accelerator, may indeed have significant detrimental effects on machine performances. Therefore, a cryogenic vacuum system should avoid vacuum transient and pressure excursions [23, 24]. For this reason, the BS in the cold bore of LHC is efficiently working at T~20 K. Whereas, for costs reasons and available cooling budget, the cold bore of FCC-hh has been proposed to operate in a temperature range between 40 K and 60 K [25]. At these temperatures, indeed, the saturated vapor pressure curves of the residual gas species adsorbed on the BS flat surfaces [26] are compatible with the operational pressure range planned for these machines [27]. This could not be the case for strongly *modified* surfaces. In the case of any porous structure and, specifically, for laser treated samples, the nanostructure surface may trap more efficiently adatoms even in presence of adsorbed contaminants. Shifts of the desorption T at higher values in respect to the one foreseen by the saturated vapor pressure curve and a significant spread of the desorption T have been already observed in various porous systems [28–31]. Therefore, in case of strongly morphologically *modified* surfaces in the cryogenic vacuum system, the evaluation of the saturated vapor pressure curves may not be sufficient to assess the absence of vacuum transient during small temperature fluctuations. The investigation of the behavior of adsorbates on the artificially roughed surfaces as a function of temperature is then mandatory.

Here, the SEY characteristic of the LASE-Cu sample is presented, confirming the unquestionable advantages offered by such substrates as ECE mitigators. In accordance with our previous work [32], the thermal desorption characteristics of Ar dosed on the LASE-Cu are also reported and compared to the ones coming from the flat counterpart. These results, intimately connected with the nanostructured porous morphology of the LASE-Cu materials, show possible troubling consequences that could arise by exploiting them as cryogenic vacuum components of accelerators.

* luisa.spallino@lnf.infn.it

EXPERIMENTAL

Experiments were performed at the Material Science Laboratory of the LNF-INFN (Frascati, Italy), in a μ-metal UHV chamber, having base pressure $p<1\cdot10^{-10}$ mbar and equipped with a close cycle He cooled cryogenic manipulator at the end of which the sample holder is mounted. The temperature of the samples can be increased in the range 15-400 K by a resistive heater controlled by a diode with a 0.2 K precision. The sample is electrically insulated, therefore sample drain current can be measured and, with it, Secondary Electron Yield. SEY is the ratio of the number of electrons leaving the sample surface (I_{out}) to the number of incident electrons (I_p) per unit area. Experimental details are reported elsewhere [5, 8, 32–35]. SEY was determined by measuring I_p and the total sample current I_s. Since I_{out}= I_p-I_s, then:

$$SEY = \frac{I_{out}}{I_p} = 1 - \frac{I_s}{I_p} \quad (1)$$

I_p is measured by means of a Faraday cup positively biased in order to prevent back-scattered re-emission to vacuum, whereas a negative bias voltage of V_s=-75 V is applied to the sample to determine I_s. SEY is measured as a function of the primary electron energy coming from an Omicron electron gun using a standard LaB_6 cathode. The electron beam was set to be smaller than 0,5 mm^2 in transverse cross-sectional area at the sample surface. The SEY measurements were performed at normal incidence, by using electron beam currents of a few nA to induce minimal electron-desorption during data acquisition.

Desorption was studied as a function of T, performing Thermal Programmed Desorption (TPD) measurements by using a quadrupole mass spectrometer (Hiden, HAL 3F PIC) while heating the sample with a rate of 0.005 K/s. Gas was delivered on the substrate held at 15-18 K through a specially designed gas-dosing system. This system has chicanes to reduce the speed of the impinging particles and it ends up with an 8×8 mm^2 dosing square, which nearly exactly matches the sample size. The doser can be inserted very close (< than 1 mm) to the sample surface or retracted away from it. The first configuration allows to reduce the gas adsorbed on the cold manipulator and then the background signal in the TPD measurements. In the retracted position the amount of gas seen by the sample is the same as the one measured by the pressure gauge and mass spectrometer, therefore a dose calibration can be performed. The gas was dosed through a leak valve at a pressure $p\sim1.2\cdot10^{-9}$ mbar. The dosing unit are given in Langumir (1L=$1.33\cdot10^{-6}$ mbar·s). A 1 L dose (performed with the retracted doser) on the *flat* polycrystalline surface can be approximately assumed to be 1 monolayer (ML), where 1 ML≈10^{15} atoms/cm^2. This conversion is obtained by considering a mean density of Cu atoms on a polycrystalline surfaces lacking crystalline order and assuming an Ar sticking coefficient close to 1 [36]. This equivalence has been used when calibrating the coverage on the *flat* sample by using SEY. LASE-Cu has an actual surface available for sticking Ar significantly larger than its sample geometrical surface. Therefore, the thickness of an Ar layer could be different on the porous and on the *flat* substrates even for nominally equal doses. Moreover, the assumption that the Ar pressure seen by the *flat* surface is homogeneous in all the porous fractals of the LASE-Cu cannot be considered to be valid. Therefore, the number of atoms deposited onto the LASE-Cu may depend on the actual sample nanostructure and coverages in ML on LASE-Cu results ill-defined. Since the task is to compare the behavior of LASE and *flat* Cu, we use Langmuir unit as common variable for both cases.

Two categories of Cu sample were considered for the present investigation: a *flat* Cu substrate and a representative sample of the LASE-Cu materials. The *flat* substrate is a polycrystalline Cu (poly-Cu) and was investigated both as received and Ar^+ sputtered at 1 keV with a current of ∼15 μA measured on the sample at a pressure of p_{Ar}=8×10^{-6} mbar. These sputtering parameters are consistent with a cleaning procedure which does not increase the pristine roughness of the surface [37]. The Ar multilayer TPD results coming from it is anyway independent of the surface cleanliness. The LASE-Cu consists in copper colaminated stainless steel. Its surface is engineered by pulsed laser ablation [38] and its morphology was probed by Scanning Electron Microscopy (SEM) using a SNE-3200M Tabletop SEM.

RESULTS AND DISCUSSION

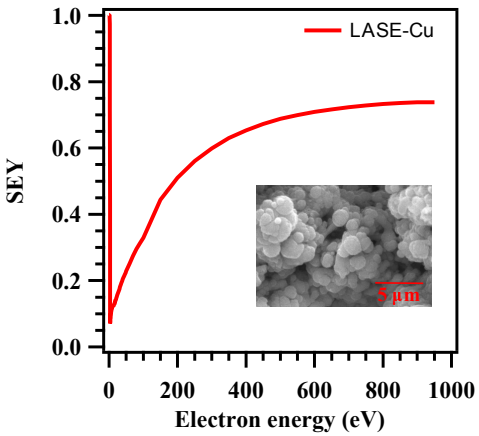

Figure 1: SEY curve at room temperature of the LASE-Cu sample under investigation. A SEM micrograph of the sample is reported in the inset.

Figure 1 shows a typical secondary emission curve acquired at room temperature from the LASE-Cu sample under investigation. In accordance with literature [38], it is characterized by an impressive low SEY (≈0.74 at 900 eV) determined by the peculiar morphological features represented by the SEM micrograph shown in the inset. It is worth to note that the low energy region of the SEY curve is measured in the LASE-Cu sample by us for the first time. A clear decrease towards SEY≈0.1 is observed for impinging electron energies close to 0 eV, as in the case of clean metallic

surfaces [35, 37]. The submicrometric highly porous network acts as a trap both for the incoming primary electrons and for secondary electrons. This qualifies such class of materials as ECE mitigators. When held at cryogenic temperature, the SEY properties of the LASE-Cu sample do not significantly change in the energy range over ~100 eV, while small SEY variations are observed in the low energy region (curve not reported). It is known, indeed, that keeping the sample at low temperature for some time determines the progressive adsorption of residual gas molecules (mainly H_2O, CO, CO_2 and CH4) [37], slightly modifiyng the low energy SEY region.

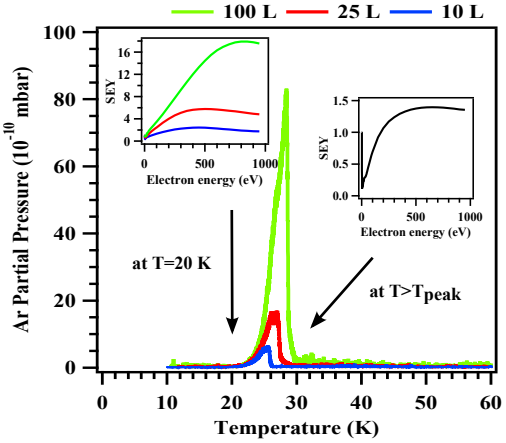

Figure 2: TPD from poly-Cu after dosing 10, 25 100 L of Ar. The SEY curves related to the given doses are reported in the inset, below (left) and after (right) the desorption peak.

To evaluate the vacuum behavior of LASE-Cu against temperature fluctuations by TPD, a preliminary study has been carried out on the poly-Cu sample to be used as reference system and to properly set the parameters for all the TPD measurements. Three increasing Ar doses were considered, namely 10, 25 and 100 L. Such high doses on the flat sample correspond to have multilayers on the substrate. This is the coverage typically expected to occur in long exposures to residual gasses in an accelerator cryogenic environment [23].

In Fig. 2 the Ar TPD results from the poly-Cu sample are shown. The curves show a sharp peak at T~28-30 K, having a Full Width at Half Maximum FWHM~4 K. The TPD area linearly increases with the Ar dose. This single peak corresponds to the desorption of a condensed thick Ar layer, as evidenced by the SEY curves acquired for each coverage below (left panel) and above (right panel) the relative desorption peak. Indeed, at T=20 K (below the desorption peaks), SEY characteristics depend on the actual Ar thickness, in good agreement with literature results [39]. Just above each desorption peak (right panel), the SEY curve is the one of the bare poly-Cu substrate for all cases, thus indicating the transition temperatures at which the gas multilayer desorbs from the surface [26, 40].

It is worth to note how sensitive is SEY to variations in Ar coverages, showing the effectiveness of using this simple spectroscopy as a technique capable to estimate them. By doing so, we can precisely (±10%) estimate the effective dose seen by the samples when dosing close to its surface even if, in this latter case, the pressure measured by the gauge and quadrupole is not representative of the Ar pressure seen by the surface. Moreover, the remarkable sensitivity of SEY to the presence of any overlayer allows also to calibrate the temperature read on the manipulator diode against the real surface temperature and to address the transition temperatures at which the gas multilayer desorbs to the multilayer desorption temperature as foreseen by literature.

The TPD data shown in Fig. 2 for the flat poly-Cu are in agreement with previous literature findings [41–43]. This single peak corresponds to the desorption of a condensed thick Ar layer. Its temperature is determined by the weak Ar-Ar Van der Waals interaction energies [26, 40]. Above this peak, a ~10, 25, 100 times smaller signal is expected to appear due to the desorption of the first monolayer [42, 43]. At present, our set-up does not allow to observe it since not only it is too small, but probably hidden below the manipulator background signal which has been set to zero. However, at this stage, the investigation of the monolayer/submonolayer regime is out of the scope of the present work.

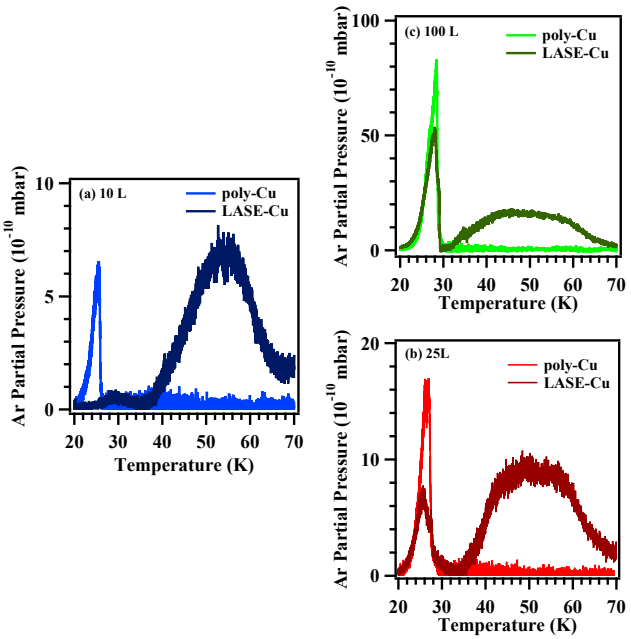

Figure 3: TPD curves obtained monitoring the desorption of 10 L (a), 25 L (b), and 100 L (c) of Ar dosed on the LASE-Cu sample (dark color lines) and on flat Cu substrate (light color lines).

The desorption curves measured on the Ar dosed LASE-Cu surface are reported in Fig. 3). For the sake of comparison the TPD profiles obtained from the flat counterpart at equal Ar doses are reported in each panel. The Ar TPD curves from LASE-Cu are characterized by broad profiles, whose peak temperatures and widths depend on the Ar dose. On increasing the Ar coverage by dosing 10 (a), 25 (b) and 100 L (c), the almost bell-shaped curves are centered at T~56 K, T~52 K and T~50 K, and have FWHM of about 15, 20

and 25 K, respectively. Moreover, after 25 and 100 L, the Ar desorption at T~28-30 K is also observed.

The Ar desorption behavior from the LASE surfaces indicates a significant dependence of the process on the surface morphology. On one hand, micro and nano-structuring dramatically increases the specific surface, making the area accessible to atomic/molecular species much larger than the one available in the flat sample. On the other hand, such a nanostructured morphology determines a local increase of the adsorption energy for the Ar atoms in correspondence of under-coordinated sites and defects [44–46]. The desorption of the Ar atoms close to defected surfaces and/or trapped in the pores of the LASE-Cu surface is shifted to higher temperature. The progressive occupation of all available adsorption sites (pores wall included) could then explain the gradual broadening of the TPD peak above 30 K observed for the LASE-Cu with increasing Ar dose. On the contrary, multilayer Ar atoms which basically feel only the Ar-Ar forces, desorb around 28-30 K, as in the case of the flat sample.

Those results are better discussed in [32]. Similar results were observed by dosing the two different Cu surfaces with gasses typically expected to be part of the residual gas composition of any accelerator vacuum system (H_2, CO and CH_4) [32, 47]. This confirms the validity of using Ar as a paradigmatic system to investigate the vacuum behaviour of the porous surfaces.

CONCLUSION

In summary, the intrinsic morphological structure confers to the LASE-Cu samples a very low SEY (SEY<1 in the energy range 0-1000 eV), both at room and cryogenic temperature. This makes such a class of materials optimal e^--cloud suppressors and, then, promising components of the future high energy particle accelerators. On the other hand, Ar TPD measurements from LASE-Cu sample have evidenced that, as a consequence of the nanostructured porous morphology, the gas desorption occurs at a higher than expected temperature and spreads over a broad range. Therefore, their vacuum behaviour at cryogenic conditions against temperature fluctuation could give rise to troubling consequences on the usually very stringent vacuum requirements of most cryogenic accelerators. In conclusion, while the use and optimization of LASE surfaces to mitigate SEY is quite advanced, a significant additional experimental campaign is necessary to validate their use in future accelerators. In particular, since non-thermal desorption processes are acknowledged to markedly contribute to accelerator vacuum behavior, photo and electron induced desorption yield should also be carefully studied.

ACKNOWLEDGEMENTS

This work was supported by The European Circular Energy- Frontier Collider Study (EuroCirCol) project (Grant No. 654305) and by the MICA project funded by INFN Scientific National Committee 5. We thank V. Baglin, P. Chiggiato, R. Kersevan, O. Malyshev, and R. Valizadeh for useful discussions and for the LASE samples. The DAΦNE-L team is acknowledged for technical assistance.

REFERENCES

[1] C. Swanson and I. D. Kaganovich, J. Appl. Phys. 120, 213302 (2016)

[2] C. Swanson and I. D. Kaganovich, J. Appl. Phys. 122, 043301 (2017)

[3] V. Nistor, L. A. Gonzalez, L. Aguilera, I. Montero, L. Galan, U. Wochner, and D. Raboso, Appl. Surf. Sci. 315, 445 (2014)

[4] G. Rumolo, A. Z. Ghalam, T. Katsouleas, C. K. Huang, V. K. Decyk, C. Ren, W. B. Mori, F. Zimmermann, and F. Ruggiero, Phys. Rev. Spec. Top. Accel. Beams 6, 081002 (2003)

[5] R. Cimino, I. Collins, M. Furman, M. Pivi, F. Ruggiero, G. Rumolo and F. Zimmermann, Phys. Rev. Lett. 93, 014801 (2004)

[6] F. Zimmermann, Phys. Rev. Spec. Top. Accel. Beams 7, 124801 (2004)

[7] ECLOUD'12: Joint INFN-CERN-EuCARD-AccNet Workshop on Electron-Cloud Effects, CERN Yellow Reports: Conference Proceedings, edited by R. Cimino, G. Rumolo, and F. Zimmermann (CERN, Geneva, 2013)

[8] R. Cimino and T. Demma, Int. J. Mod. Phys. A 29, 1430023 (2014)

[9] G. Rumolo and G. Iadarola, in CERN Yellow Reports: School Proceedings (2017), Vol. 3, p. 411

[10] K. Ohmi, F. Zimmermann, L. Mether, and D. Schulte, "Study of electron cloud instabilities in fcc-hh," Technical Report CERN-ACC-2015-285 (2015)

[11] Y. Suetsugu, K. Kanazawa, K. Shibata, and H. Hisamatsu, Nucl. Instrum. Methods Phys. Res., A 556, 399 (2006)

[12] M. Pivi, F. King, R. Kirby, T. Raubenheimer, G. Stupakov, and F. Le Pimpec, J. Appl. Phys. 104, 104904 (2008)

[13] Y. Suetsugu, H. Fukuma, L. Wang, M. Pivi, A. Morishige, Y. Suzuki, M. Tsukamoto, and M. Tsuchiya, Nucl. Instrum. Methods Phys. Res., A 598, 372 (2009)

[14] C. Yin Vallgren, G. Arduini, J. Bauche, S. Calatroni, P. Chiggiato, K. Cornelis, P. C. Pinto, B. Henrist, E. Metral, H. Neupert, G. Rumolo, E. Shaposhnikova, and M. Taborelli, Phys. Rev. Spec. Top. Accel. Beams 14, 071001 (2011)

[15] A. Krasnov, Vacuum 73, 195 (2004)

[16] M. Ye, D. Wang, and Y. He, J. Appl. Phys. 121, 124901 (2017)

[17] R. Valizadeh, O. B. Malyshev, S. Wang, S. A. Zolotovskaya, W. Allan Gillespie, and A. Abdolvand, Appl. Phys. Lett. 105, 231605 (2014)

[18] R. Valizadeh, O. Malyshev, S. Wang, T. Sian, M. D. Cropper, and N. Sykes, Appl. Surf. Sci. 404, 370 (2017)

[19] See http://hilumilhc.web.cern.ch/ for for details on the project

[20] G. Apollinari, I. B. Alonso, O. Br€uning, P. Fessia, M. Lamont, L. Rossi, and L. Tavian, High-Luminosity Large Hadron Collider (HL-LHC): Technical Design Report (CERN, 2017)

[21] See http://fcc.web.cern.ch/ for details on the project

[22] C. Benvenuti, J. Cazeneuve, P. Chiggiato, F. Cicoira, A. E. Santana, V. Johanek, V. Ruzinov, and J. Fraxedas, Vacuum 53, 219 (1999)

[23] V. Baglin, "Vacuum transients during LHC operation," in 1st LHC Project Workshop, Chamonix, France, 19–23 January (2004), p. 275

[24] W. C. Turner, J. Vac. Sci. Technol., A 14, 2026 (1996)

[25] F. J. P. Rodriguez, P. Chiggiato, C. Garion, J. F. Topham, and on behalf of EuroCirCol WP4, "Preliminary beam screen and beam pipe engineering design: Deliverable D4.3," Technical Report No. CERN-ACC-2019-0023 (CERN, Geneva, 2017)

[26] R. E. Honig and H. O. Hook, RCA Rev. 21, 360 (1960)

[27] V. Baglin, L. Tavian, P. Lebrun, and R. van Weelderen, "Cryogenic beam screens for high-energy particle accelerators," Technical Report CERN-ATS- 2013-006 (2013)

[28] J. Thrower, M. Collings, F. Rutten, and M. McCoustra, Mon. Not. R. Astron. Soc. 394, 1510 (2009)

[29] A. Paldor, G. Toker, Y. Lilach, and M. Asscher, Phys. Chem. Chem. Phys. 12, 6774 (2010)

[30] A. Clemens, L. Hellberg, H. Gr€onbeck, and D. Chakarov, Phys. Chem. Chem. Phys. 15, 20456 (2013)

[31] T. Suhasaria, J. Thrower, and H. Zacharias, Mon. Not. R. Astron. Soc. 472, 389–399 (2017)

[32] L. Spallino, M. Angelucci, R. Larciprete and R. Cimino, Appl. Phys. Lett. 114, 153103 (2019)

[33] R. Cimino, M. Commisso, D. R. Grosso, T. Demma, V. Baglin, R. Flammini and R. Larciprete, Phys. Rev. Lett. 109, 064801 (2012)

[34] R. Larciprete, D. R. Grosso, M. Commisso, R. Flammini and R. Cimino, Phys. Rev. Spec. Top. Accel. Beams 16, 011002 (2013)

[35] R. Cimino, L. A. Gonzalez, R. Larciprete, A. Di Gaspare, G. Iadarola, and G. Rumolo, Phys. Rev. Spec. Top. Accel. Beams, 18, 051002 (2015)

[36] L. L. Levenson, J. Vac. Sci. Technol. 8, 629 (1971)

[37] L. Gonzalez, M. Angelucci, R. Larciprete, and R. Cimino, AIP Adv. 7, 115203 (2017)

[38] R. Valizadeh, O. B. Malyshev, S. Wang, S. A. Zolotovskaya, W. Allan Gillespie and A. Abdolvand, Appl. Phys. Lett. 105, 231605 (2014)

[39] J. Cazaux, Y. Bozhko, and N. Hilleret, Phys. Rev. B 71, 035419 (2005)

[40] A. Ferreira and L. Lobo, J. Chem. Thermodyn. 40, 1621 (2008)

[41] M. Stichler, P. Zebisch, M. Weinelt, and H.-P. Steinr€uck, Surf. Sci. 348, 370 (1996)

[42] W. Berthold, P. Feulner, and U. H€ofer, Chem. Phys. Lett. 358, 502 (2002)

[43] A. Damm, K. Schubert, J. G€udde, and U. H€ofer, Phys. Rev. B 80, 205425 (2009)

[44] J.Y. Park, S.J. Kahng, U. Ham, Y. Kuk, K. Miyake, K. Hata, and H. Shigekawa, Phys. Rev. B 60, 16934 (1999)

[45] P. Ayotte, R. S. Smith, K. P. Stevenson, Z. Dohnalek, G. A. Kimmel, and B. D. Kay, J. Geophys. Res. Planets 106, 33387 (2001)

[46] L. Baker, B. Holsclaw, A. E. Baber, H. L. Tierney, E. C. H. Sykes, and A. J. Gellman, J. Phys. Chem. C 114, 18566 (2010)

[47] L. Spallino, M. Angelucci, R. Larciprete and R. Cimino, article in preparation.

Characterisation of technical surfaces at cryogenic temperature under electron bombardment.

B. Henrist†, V. Baglin, M. Haubner, CERN, 1211 Geneva, Switzerland

Abstract

The vacuum chambers of the LHC's arcs operate in a temperature range between 1.9 K, *i.e.* the temperature of the superconducting magnets, and 20 K. At such low temperatures, most of the residual gas species are efficiently adsorbed on the cold surface.

LHC's proton beam emits synchrotron radiation inside its bending magnets and, consequently, electrons are extracted from the surrounding walls by the photoelectric effect. The successive proton bunches accelerates the photoelectrons, building-up an "electron cloud" which generates gas desorption from the vacuum chamber and heat load for the cryogenic system. This phenomenon might become a limiting factor for the operation of the High Luminosity LHC upgrade, where more intense proton bunches will circulate.

In order to study the electron interaction with gas adsorbed at cryogenic temperature, a new facility has been designed and built at CERN. It reproduces in the laboratory the typical conditions of a cryogenic ultra-high vacuum surface present in the accelerator.

In this paper, the first results obtained with selected accelerator materials at different surface gas coverages are presented.

EXPERIMENTAL

A sample representing the inner surface of the accelerator is mounted on a 4-axis manipulator able to regulate the temperature between 10 K and 250 K. Known quantities of gas can be adsorbed on the sample surface that can be bombarded by an electron beam at different energies.

The experimental vacuum system is composed of three parts shown in Fig. 1: the main chamber made of mumetal to shield against earth magnetic field, the storage chamber to keep the samples under ultra-high vacuum and the load-lock to insert new samples.

Three linear feedthroughs and two gate valves, allows to transfer the sample, in less than half an hour, from the atmosphere to the ultra-high vacuum around 2.10^{-10} mbar, passing through the sample storage rack kept under 10^{-9} mbar.

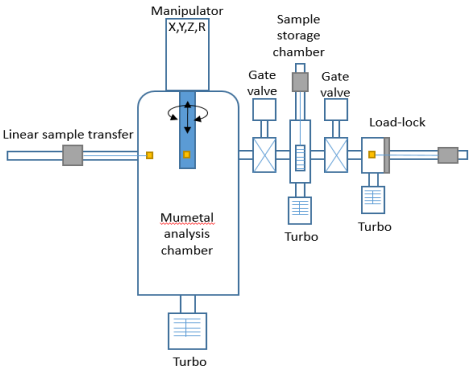

Fig. 1: Experimental setup.

The manipulator, shown in Fig. 2, controls the sample position with the help of four motorized axis. It has one thermo-regulated sample holder able to set a temperature between 10 K and 500 K using liquid helium and a thermo-coax heater. A front cover, closed, while using a wobble stick, minimise the ambient radiation towards the sample.

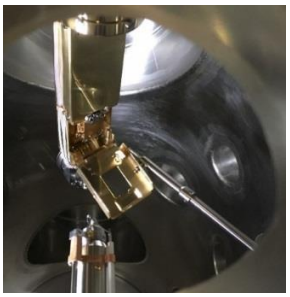

Fig. 2: Sample on the manipulator, thermal shield opened using the wobble stick and electron gun.

A second sample holder is installed just under the main one. It is not thermo-regulated, but can be used for example to hold a phosphor target to monitor the electron beam shape. The beam size is typically smaller than 2 mm and can be measured with a digital microscope installed in front of a viewport. The microscope also provides a mean to insure the reproducibility of the sample position.

Finally, on the back of the manipulator is also placed a Faraday cup to measure the intensity of the electron beam.

Pure gas can be injected inside the vessel through a diaphragm of known conductance C. According to equation (1), the injected flux, Q_{inj}, can be determined from the pressure difference across either side of the conductance, Δp_{cond}.

$$Q_{inj} = C \cdot \Delta p_{cond} \quad (1)$$

† Bernard.Henrist@cern.ch

Knowing the injected flux, the pumping speed of the system, S, is computed with equation (2). This value depends on the nature of the gas, the temperature of the sample and must be known to estimate the molecular desorption rate.

$$S = \frac{Q_{inj}}{p} \quad (2)$$

The gas can also be injected into the vessel using a calibrated volume, V. Injecting via this volume allows to compute the number of injected molecules, n, by recording the variation of the pressure in the volume, Δp_V, and using equation (3), where k is the Boltzmann constant and T the temperature.

$$n = \frac{\Delta p_V \cdot k \cdot T}{V} \quad (3)$$

The injection from the calibrated volume to the sample surface is performed through a retractable injector, as shown in Fig. 3. Doing so, the ice layer thickness can be controlled.

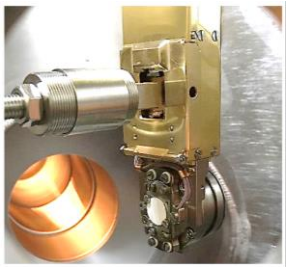

Fig. 3: Retractable gas injection device.

SEY MEASUREMENT

The secondary electron yield (SEY) of a material is defined by the ratio of the number of emitted secondary electrons to the number of incoming electrons. Thus, to quantify the SEY, the electron beam current and the secondary electron current must be measured.

Three different methods can be used to measure the electron beam current:

1. A Faraday cup set in front of the electron gun as shown on the right side of Fig. 4 could measure the current exiting the gun.
2. A Faraday cup placed at the back of the manipulator as shown on the left side of Fig. 4 is used to check the beam profile.
3. The use of a positive bias on the sample as shown on the right side of Fig. 5. This method is used to perform electron-conditioning measurement.

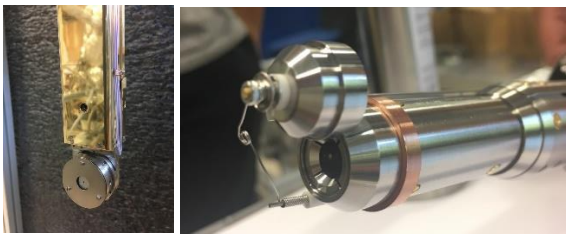

Fig. 4: Faraday cups on the manipulator and on the electron gun.

On the left side of Fig. 5, a negative voltage is applied to the sample to repel the secondary emitted electrons (I_{out}). This mode is called "SEY mode" and the measured current I_s is the difference between I_{out} and I_{beam}.

On the right side of Fig. 5, the bias is positive to prevent the escape of the secondaries and in this configuration the measured current I_s is equal to the beam current I_{beam}. It is called "Beam Mode".

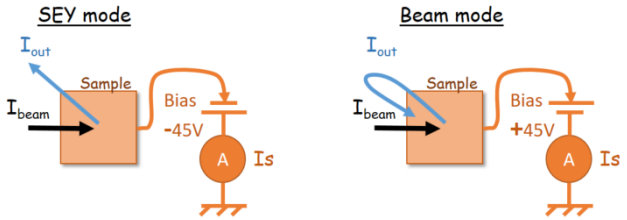

Fig. 5: SEY measurement mode (left) and Beam measurement mode (right)

After the determination of the beam current done in "Beam mode", the value of the SEY, δ, can be deduced using the "SEY mode" and the following formula (4).

$$\delta = \frac{emitted\ current}{incident\ current} = \frac{I_{out}}{I_b} = 1 - \frac{I_s}{I_b} \quad (4)$$

ICE LAYER PREPARATION

As described before, a known quantity of gas can be injected on the cold surface using the injector to condense the desired number of monolayer (ML). For a metallic technical surface like a copper sheet, the layers are supposed to be stacked homogeneously and the molecular surface density is assumed to be 1 ML=8.10^{14} molecules/cm^2. This assumption could be wrong for rough or porous material.

ELECTRON CONDITIONING

Electron bombardment is a well-known method to reduce the SEY of a surface [1, 8]. For example, this method is routinely used for RF conditioning and for beam scrubbing in the LHC ring.

In this paper, the electron conditioning and the SEY measurement are done at fix energy of 300 eV with an electron beam impinging at normal incidence on unbaked samples held at either room temperature (RT) either at 10 K.

The measurement consists to determine the beam current, I_b, using the "Beam mode" and to switch in "SEY mode" monitoring the current, I_s, to compute δ using equation (4). Some hours are necessary to reach a total electron dose of about 10^{-2} C/mm^2. The electron beam current is measured every hour to guarantee its stability during the process.

The measurements were done on Oxygen Free Electronic (OFE) copper, Deoxidized High Phosphorus (DHP) copper, laser treated DHP copper and amorphous carbon coated (a-C) copper.

OFE Copper

OFE copper, also called C10100, is a 99.99% pure copper with an amount of 0.0005% oxygen. It is a commonly used material in vacuum systems. It minimises the presence of oxygen, which deteriorate the thermal and electric properties of the copper and may cause cracks at welds.

Fig. 6 shows the conditioning curves at 300 eV of OFE Cu at RT and at 10 K.

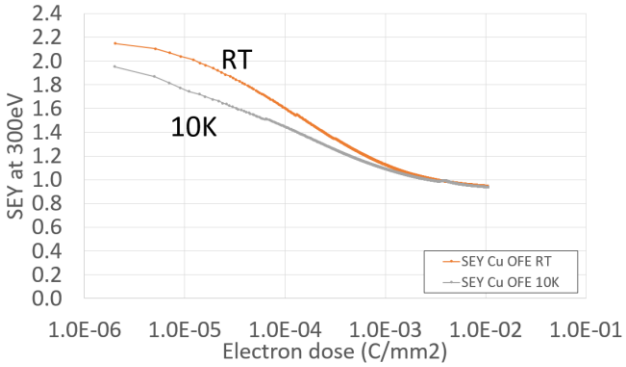

Fig. 6: Conditioning curves of OFE copper with 300 eV electrons at RT and at 10 K.

At RT, the initial SEY at 300 eV is 2.2 and 2 at 10 K. The difference may be attributed to the physisorption at 10 K of some molecules. The conditioning with 300 eV electrons leads, in both cases, to the same final SEY value of 0.9 at a dose of 10^{-2} C/mm^2. These results are in agreement with published data [1, 2, 3].

DHP Copper

DHP copper, also called C12200, is a 99.9% pure copper deoxidized by addition of phosphorus (0.015% to 0.040% P). It is an alternative to the OFE copper used in other technologies than vacuum.

Fig. 7 compares the conditioning curves at RT of DHP and OFE Cu under 300 eV electron bombardment.

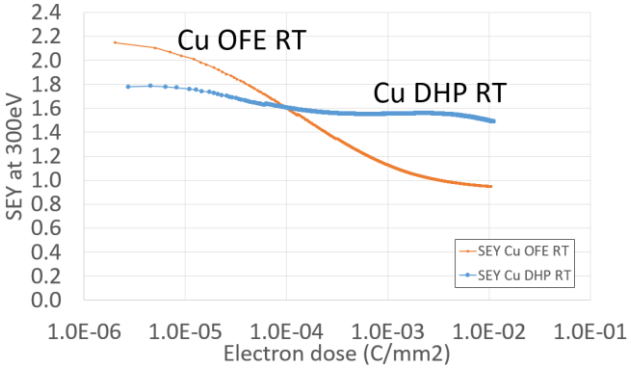

Fig. 7: Conditioning of DHP copper with 300 eV electrons at room temperature compared with OFE Cu.

The result obtained with DHP copper is different from the OFE copper. Although the initial SEY is lower for DHP (1.8) than OFE (2.2), the 300 eV conditioning rate of DHP is smaller. Thus, a final SEY of 1.5 is reached after a dose of 10^{-2} C/mm^2, suggesting a different surface state of DHP from OFE Cu. Preliminary XPS analyses have revealed some silicon traces which origin and impact on the SEY are not clear today [4].

a-C coating on DHP Copper

a-C coating is proposed for the upgrade of the LHC (*i.e.* the High Luminosity LHC) to reduce the SEY of a surface. Since carbon has a low SEY, and since the coating morphology is rough, the SEY of the surface is reduced as compared to metallic samples.

The a-C coating was carried out at CERN by dc pulsed Magnetron Sputtering at 10 kHz under Ar atmosphrere on a DHP copper with a sublayer of 500 nm of titanium, to provide adherence, and a top layer of 50 nm of carbon.

Fig. 8 shows the conditioning curves at 300 eV a-C coating at RT and 10 K.

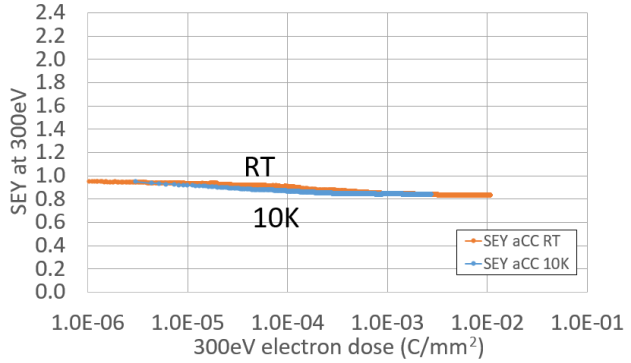

Fig. 8: Conditioning curves of a-C coated copper with 300 eV electrons at room temperature and at 10 K.

Although the Cu bulk is of different nature than stainless steel, since at 300 eV, the electron penetration depth is less than 10 nm; the initial SEY value equals 0.9, in agreement with previous data [5]. The SEY decreases to 0.8 after a 300 eV electron dose of 10^{-2} C/mm^2. The temperature of the sample has no effect on the conditioning level and rate.

Laser treated DHP Copper

Laser treatment is a recent technology that modifies the geometry and the surface state of the material by ablation of matter [6]. Beside the surface modification, it increases the roughness allowing trapping the outgoing electrons to reduce the SEY. This treatment was applied on a DHP copper sample by the University of Dundee using laser parameters similar to the COLDEX samples [7].

The laser surface structuring was performed using a linearly polarized pulsed (10 ps) laser system operating at a wavelength of 532 nm and at a repetition rate of 200 kHz. The diameter of the focused spot was ~13 µm.

The treatment was performed with N_2 flowing at the laser focus point. The structures were obtained by a raster scanning speed of 10 mm/s and 240 pulses per spot using Line Hatch (LH) pattern. The distance between consecutive spots was kept at ~24 µm. The treatment was performed at average laser pulse energy of 5 µJ (laser beam intensity of ~0.4 TW·cm^{-2}).

Fig. 9 shows the conditioning curves at 300 eV of the laser treated DHP Cu at RT and at 10 K.

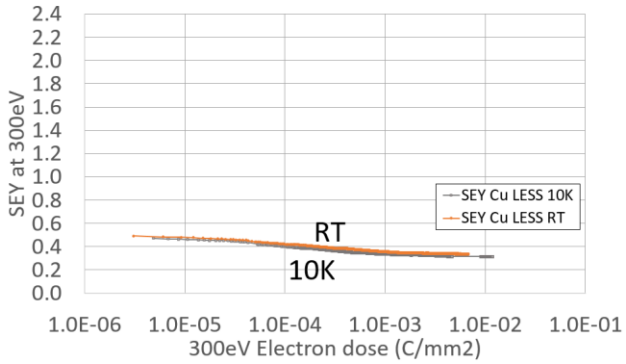

Fig. 9: Conditioning curves of laser treated DHP copper (COLDEX like) with 300 eV electrons at RT and 10 K.

For both temperature, the SEY starts at 0.5. This value is smaller than the one obtained with OFE copper [6]. Beside different laser parameters, a possible origin of this lower value is the use of a DHP copper bulk instead of OFE. Indeed, as shown in Fig. 7, DHP has an initial SEY lower than OFE Cu.

The conditioning rate is weak with a decrease from 0.5 to 0.3 at 10^{-2} C/mm^2. The temperature has no effect on the conditioning rate.

Gas coverage

In order to study the impact of a large air leak, 500 ML of nitrogen was condensed on an OFE Cu sample held at 10 K. It was observed that the conditioning behaviour of this surface is strongly different from the uncovered metallic surfaces.

As shown in Fig. 10, image 1, when a 300 eV electron beam impinges on the ice layer, the solid nitrogen phosphorescence is observed as a green spot. During the irradiation, a "dark stain" appears (image 2). Further bombardment is enlarging the diameter of the "dark stain" as shown in images 3 and 4. The "dark stain" is attributed to the removal of the N_2 layer by the continuous electron bombardment

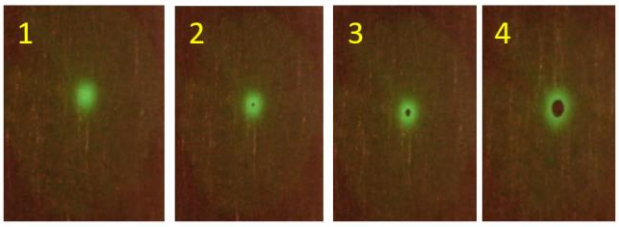

Fig. 10: Evolution under electron bombardment of the green phosphorescent spot due to 300 eV electrons irradiating 500 ML of condensed N_2.

The increase of the N_2 partial pressure due to the impact of electrons was recorded with a calibrated residual gas analyser. The molecular desorption rate was deduced from this measurement. At 10 K for 300 eV electrons, the molecular desorption yield equals 1.8 N_2/e^-.

Fig. 11 shows the time evolution of a typical N_2 residual gas analyser signals for masses 14 and 28 superposed with the measured SEY of the surface. The apparent SEY equals 1 (label 1). Since the surface is an insulator, no electron can reach the surface to neutralise the charge during the bombardment. This leads to a zero current measured on the sample. Thus, according to equation (4), when I_s=0, δ=1.

When the "dark stain" appears (image 2, Fig. 10), label 2, the amount of desorbed gas decreases and in the same time, the measured SEY reach a maximum of about 1.4. After this time, the beam can influence directly the substrate, the conditioning is effective and the SEY decrease again towards 1.

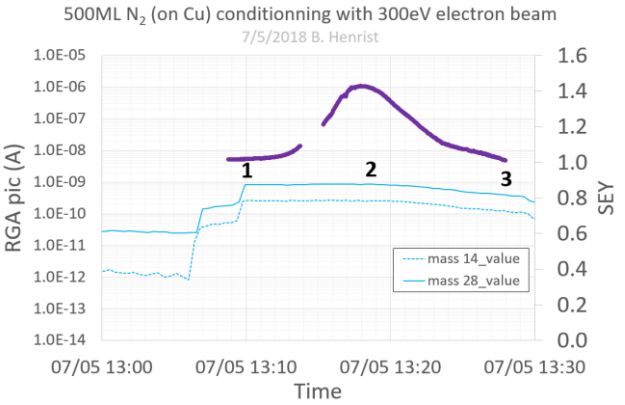

Fig. 11: Conditioning and desorption of 500 layers of N_2 ice on copper with 300 eV electrons at 10 K.

CONCLUSION

A new experimental set-up to measure ESD and SEY of samples held at cryogenic temperature was successfully commissioned at CERN. Electron conditioning studies were performed at a fix energy of 300 eV for which SEY and removal coefficient of N_2 were measured.

At 10 K, the initial SEY of OFE Cu is smaller than at RT. However, after an electron dose of a few 10^{-3} C/mm^2, the difference disappears and both SEY at 300 eV reaches 1. Irrespectively of the sample temperature, the as received SEY of a-C coated and laser treated Cu is below 1. Electron beam conditioning does not trigger temperature difference either. DHP copper has a much different as received SEY and conditioning behaviour than OFE copper, underlying the importance of the material and surface specificities.

A thick layer (500 ML) of condensed N_2 at 10 K is phosphorescent when exited by 300 eV electron. This ice layer is charging like an insulator with a molecular removal coefficient of 1.8 N_2/e^-.

ACKNOWLEDGEMENTS

The authors would like to acknowledge Remi Dupuy who participates to the fine-tuning of the commissioning and Antoine Benoit who build all the required interfaces with LabVIEW® to control and record all the data.

REFERENCES

[1] , V. Baglin, J. Bojko, O. Gröbner, B. Henrist, N. Hilleret *et al*., "The secondary electron yield of technical materials and its variation with surface treatments", CERN LHC Project Report 433, Proc. of EPAC 2000, Vienna, Austria, June 2000.

[2] A. Kuzucan, H. Neupert, M. Taborelli, H. Störi, "Secondary electron yield on cryogenic surfaces as a function of physisorbed gases", J. Vac. Sci. Technol. A 30(5), 051401 (2012).

[3] V. Baglin., "The LHC vacuum system: commissioning up to nominal luminosity", Vacuum 138 (2017) 112-119.

[4] V. Petit, private communication, September 2018.

[5] P. Costa Pinto, S. Calatroni, H. Neupert, D. Letant-Delrieux, P. Edwards *et al*., "Carbon coating with low secondary electron yield", Vacuum 98 (2013) 29-36.

[6] R. Valizadeh, O.B. Malyshev, S. Wang, S. Zolotovskaya, W. Gillespie *et al.*, "Low secondary electron yield engineered surface for electron cloud mitigation", Appl. Phys. Lett. 105, 231605 (2014).

[7] R. Salemme, V. Baglin, S. Calatroni, P. Chiggiato, B. Di Girolamo, E. Garcia-Tabares Valdivieso *et al.*, "First beam test of laser engineered surface structures (LESS) at cryogenic temperature in CERN SPS accelerator", Proc. of IPAC 2018, Vancouver, BC, Canada, May 2018.

[8] G. Iadarola and G. Rumolo, "Scrubbing: expectations and strategy, long range perspective", Proceedings of Chamonix 2014 Workshop on LHC Performance

COLDEX: A TOOL TO STUDY COLD SURFACES IN ACCELERATORS

V. Baglin
CERN, Geneva, Switzerland

Abstract

With the advent of more and more accelerator machines based on superconducting technology, the detailed understanding of the cryogenic vacuum system is of primary importance for the design and operation of modern machines. COLDEX was built to study the beam / cold surfaces interactions in LHC in the context of the electron cloud build-up. This paper reviews the main results obtained with COLDEX for Cu, the LHC material and a-C coating the proposed anti-multipacting surface for the LHC upgrade. It presents also recent results obtained with a laser treated surface, a potential anti-multipacting material for the next generation of colliders operating at cryogenic temperature.

INTRODUCTION

In the last decades, there have been an increasing number of projects or studies, which are based on the use of superconducting technologies. Thus, unless and anti-cryostat is included in the design, the associated vacuum system shall operate at cryogenic temperature. This is the case of superconducting RF cavities and superconducting magnets installed in synchrotrons or linacs and storage rings. Some examples of built machines are the Hadron Electron Ring Accelerator (HERA) and the European X-Ray Free ELectron Laser facility (XFEL) both at Desy, the Tevatron at Fermilab, the Relativistic Heavy Ion Collider (RHIC) at Brookhaven, the Large Hadron Collider (LHC) at CERN and the synchrotron SIS-100 of the Facility for Antiproton and Ion Research (FAIR) at Darmstadt. Examples of past or future projects are the Superconducting Super Collider (SSC), the International Linear Collider (ILC), the Future Circular hadron-hadron Collider (FCC-hh) and the Super Proton Proton Collider (SPPC).

When operating with cryogenic machines, the molecules can be physisorbed or condensed on the vacuum chamber wall. In some circumstances, these molecules are therefore available for subsequent desorption in the gas phase, leading to potential limitation of the machine operation.

The LHC is one of the first superconducting storage ring which operation can be potentially limited by the desorption of molecules from the cryogenic beam tube [1]. For this reason, the LHC arc vacuum system is made of a cold bore into which is inserted a perforated beam screen to control the gas density level [2]. The molecules desorbed from the beam screen under synchrotron radiation and beam induced electron cloud bombardments, can either be physisorbed on the 5-20 K beam screen surface or pumped through the beam screen's holes towards the 1,9 K cold bore which almost acts as a perfect sink for all gases except He. The detailed understanding of the beam interaction, via synchrotron radiation and beam induced electron cloud, with this innovative concept of perforated beam screen / cold bore vacuum system was of primary importance for the success of the LHC project.

The COLD bore EXperiment (COLDEX), was built, in collaboration with the NIKHEF institute of Amsterdam, to study the interaction of the synchrotron radiation with an LHC type vacuum system. After 2 years of construction, the cryostat was delivered at CERN by Nov. 1997 and, following commissioning, installed in the Synchrotron Light Facility 92 of the Electron Positron Accumulator (EPA) in Feb. 1998 during the Large Electron Positon (LEP) collider shutdown [3]. Until Apr. 2001, 69 runs were performed at EPA out of which 11 were conducted with the COLDEX cryostat installed in the accumulator where e^- and e^+ beams circulated through a 2.2 m long Cu beam screen with 1 % transparency and 70 mm inner diameter. The remaining studies were performed with the cryostat removed from within the accumulator and installed on a tangential synchrotron radiation beam line. In this way, it was possible to irradiate COLDEX with synchrotron radiation of 45 and 194 eV critical energies, in the range of the LHC machine. Unperforated and perforated, stainless steel, Cu, Cu-colaminated on stainless steel and cryosorbers equipped beam screens were deeply characterised under synchrotron radiation for the detailed design of the LHC machine. Irradiations were performed at 11 mrad grazing incidence on a 2.2 m long beams screens of 50 mm inner diameter with, when applicable, 1 % transparency [4, 5, 6, 7]. Specific studies using gas injections to characterise the beam screen equipped with cryosorbers were then conducted till Dec. 2001 [7].

Later, the COLDEX cryostat was installed during the 2002 shutdown in a bypass system of the SPS ring in BA4. An intense study campaign with perforated Cu beam screens started with the SPS scrubbing week of June 2003. In the context of the "electron cloud crash program", until Nov. 2004, 11 runs with LHC type beams using different beam structures, intensities and with several surface conditions were performed in 18 months before the LHC ring installation [8, 9, 10, 11, 12]!

In 2014, after the successful operation of the beam screen for the LHC exploitation, the cryostat was refurbished to house an amorphous carbon (a-C) coated Cu beam screen to study the proposed design for the LHC upgrade, the High-Luminosity LHC (HL-LHC) [13, 14, 15, 16]. For 2 years, 6 dedicated machine developments periods were held to study the a-C coating at cryogenic temperature which was already proven to be an efficient back-up to beam conditioning for the electron cloud mitigation of the room temperature SPS ring [17].

With the recent development of new technologies to mitigate the electron cloud build and their potential implication for the HL-LHC or Future Circular Colliders, a laser treated beam screen was installed for first tests in 2017 [18].

This paper gives an overview of the main results obtained with the COLDEX system when used to study the electron cloud interaction with Cu, a-C coated, and laser treated surfaces. Details discussions, available for the interested reader, are given in the references.

EXPERIMENTAL

The COLDEX cryostat is mounted in a bypass of the SPS ring, located in BA4. When in "OUT" position, the beams circulate through a standard SPS vacuum chamber. During the studies, the system is placed in IN position where the proton beams circulate through the 2.8 m long cryostat, as shown in Figure 1. The system can move, within one hour from one position to another, while the cryostat is held at cryogenic temperature. Due to the reduced beam pipe aperture, the extraction kickers, towards the LHC injection tunnel, TI8, are interlocked with the "IN" position. Two sector valves placed upstream and downstream to the cryostat, define the vacuum sector 41737, which decouples the cryogenic vacuum sector from the SPS ring. This decoupling allows to cool down and warm up the cryostat without perturbing the routine operation of the machine.

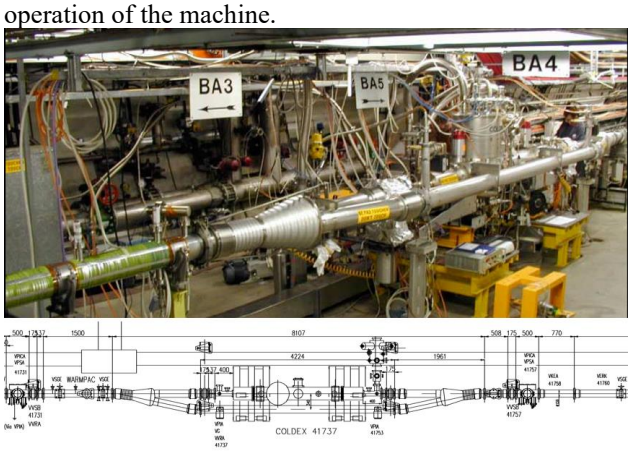

Figure 1: Top, picture of the device and, bottom, layout of the COLDEX cryostat installed in the bypass of the SPS ring.

As shown in Figure 2, many instruments are used with the COLDEX cryostat to monitor the interaction of the proton beam with the tested surface. The total and partial pressure are recorded along the system with calibrated instruments: a Bayard-Alpert gauge and a residual gas analyser (BA and RGA respectively). Measurement ports are provided upstream, downstream and in the middle of the cryostat. Electrodes are placed along the beam screen to collect charges, signatures of the beam-vacuum system interactions. The beam induced heat load is measured with additional room temperature calorimeters, WArm MultiPAC calorimeters, WAMPAC, and with the temperature increase along the cold beam screen [19]. The WAMPAC is made of a liner inserted into the vacuum pipe. From the measurement difference between the liner temperature and its surrounding tube, ΔT, the beam induced heat load, $\dot{Q}$, dissipated onto it can be derived in dynamic and steady state conditions using equations (1) and (2) respectively.

$$\dot{Q} = C\frac{\mathrm{d}\Delta T_{Eq}}{dt} \quad (1)$$

Where C is the thermal capacity of the liner.

$$\dot{Q} = \frac{\Delta T_{Eq}}{R} \quad (2)$$

Where R is the thermal resistivity and ΔT_{Eq} the temperature difference, at equilibrium, between the liner and its surrounding tube.

The WAMPAC is calibrated by applying a known heat, in an insulated cable welded along the liner, to measure the thermal parameters, C and R.

In COLDEX, the heat load on the beam screen, $\dot{Q}_{BS}$ is derived from the enthalpy (h_{He}), difference of the gaseous helium between the downstream and upstream beam screen temperatures and the He mass flow measurement, $\dot{m}$, see equation (3).

$$\dot{Q}_{BS} = \dot{m}\left[h_{He}(T_{down}) - h_{He}(T_{up})\right]C\frac{\mathrm{d}\Delta T_{Eq}}{dt} \quad (3)$$

Using an insulated powered cable stretched along the beam screen, the measurement system could be cross calibrated by applying a known heat load and the detection limit was estimated to be ~ 100 mW/m.

A gas injection system is used to dose the beam screen surface with known quantities of gas while monitoring the pressure drop of a calibrated volume with a capacitance gauge. By changing the pressure over the helium bath, the cold bore temperature is controlled from the lambda point (2.17 K) until 5 K. The bore can operate also in a "warm mode" from 200 to 300 K. The beam screen temperature is controlled using gaseous helium from 10 to 120 K. In static mode, a controlled helium flow along the beam screen maintains a temperature difference across the extremities from 2 to 10 K. Solenoids are placed at the cryostat extremity to supress the beam induced multipacting in these areas.

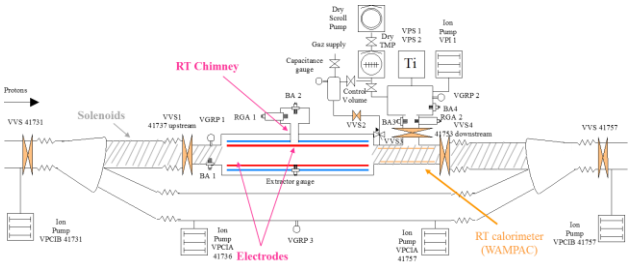

Figure 2: Schematic of the COLDEX bypass.

One of the difficulties to evaluate the pressure in a cryogenic vacuum system is due to the potential re-adsorption on the cold surface of the desorbed molecules before their detection by the vacuum instruments. Another limitation is due to the possible detection by the instruments of the molecules desorbed from the external parts of the cold beam screen. For this reason, the axial conductance shall be minimised and the beam screen long enough to ensure that the pressure rise observed at the central part is only due to the interaction of the beam with the beam screen surface. Moreover, the production of holes along a beam screen with optimised dimensions, similar to the ones used in this study, reduces to zero the impact on the vacuum measurements of these end effects. A chimney, held at room temperature, placed as close as ~ 1 mm to the beam screen's middle port, collected all the molecules from the cryogenic system for their detection with Bayard-Alpert (BA) vacuum gauge BA2 and residual gas analyser (RGA) 1. Figure 3 shows, on the left, a picture of the beam screen central part, and, on the right the Cu chimney during its introduction. A stainless-steel grid is placed at the beam screen's middle port to allow the passage of the image current and to avoid the development of high order modes in the chimney volume.

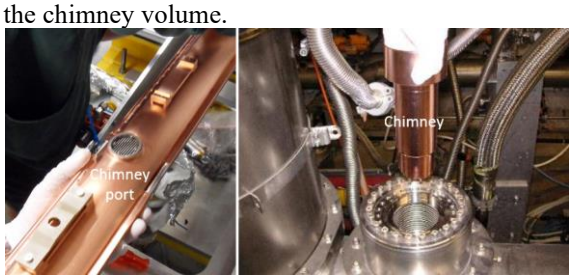

Figure 3: Left, central part of the beam screen, right, Cu chimney. Courtesy of R. Salemme.

The direct detection of electrons presence is of primary importance to support the observation of electron cloud formation. For this purpose, two electrodes are used in COLDEX, one located at the beam screen extremity and one located in the chimney, as shown in Figure 4. The beam screen electrode is located behind the beam screen holes at ~ 20 cm from the beam screen extremity and the chimney electrode is placed behind the beam screen grid (Figure 3), in the middle of the cryostat. These electrodes can be biased from – 1kV to + 1 kV with a detection limit of 0.1 nA.

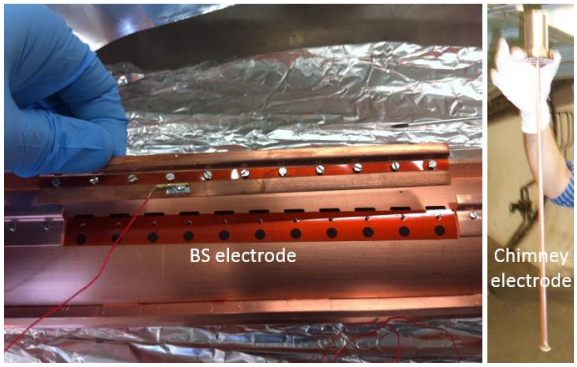

Figure 4: Left, beam screen electrode, right, chimney electrode. Courtesy of R. Salemme.

The impedance of the whole set up was optimised to guarantee a negligible contribution of it to the total heat load measured by the beam screen [11, 12]. The beam screen's aperture continuity is ensured by cold to warm transitions, see Figure 5. The design is very similar to the LHC one. It uses a Cu plated stainless steel to minimise the beam power loss and heat load onto the beam screen. A thermal anchoring to the COLDEX thermal screen, held at ~ 90 K, was produced to define the temperature gradient along the transition. A set of RF fingers, placed externally and at each extremity of the transition, allow the passage of the image current along the vacuum chamber pipe. Tapers are used to adjust the shape of the beam screen to its surrounding pipes.

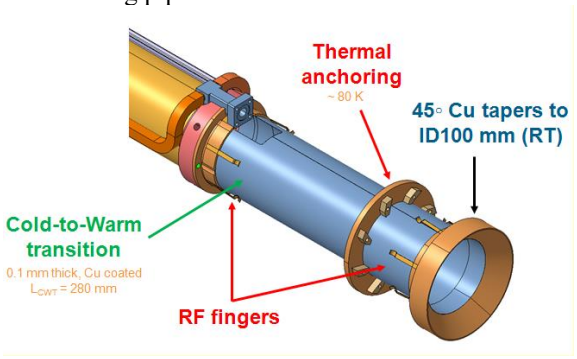

Figure 5: The COLDEX cold to warm circular transition.

Opposite to the LHC, which is a storage ring which collide proton beams at 7 TeV, the SPS ring is used to accelerate beams for end users such as fix target experiments or for the LHC injection. For this reason, during a SPS cycle of ~ 20-30 s, the proton beam is injected at 26 GeV in several batches from the PS and may be accelerated to 450 GeV before being extracted.

Table 1 shows the main SPS parameters and compares them with the LHC nominal parameters. During the studies described below, the typical proton bunch population was in the range of 10^{11} with a spacing of 25 ns between bunches, both parameters being strictly equal to the LHC ones.

However, the SPS beam energy (thus the beam emittance) is much lower than in the LHC and it is limited

to 450 GeV. Moreover, the SPS filling factor is restrained to 31 % for impedance reasons. A direct extrapolation of the results presented below to the LHC, relies therefore on some assumptions. For example, neglecting the impact of the beam emittance and the filling factor on the observed phenomena, an estimate of the LHC heat load can be done by multiplying the measured heat load by the COLDEX apparatus by the ratio of the respective filling factors (×0.79/0.31 for 4 SPS batches). On the other hand, the results presented here can still be used as inputs to simulation codes for extrapolation to other cryogenic machines.

Table 1: LHC & SPS machine parameters.

Parameters	LHC	SPS	
Beam energy (GeV)	7 000	26	450
Bunch length (ns)	1	2.8	1.7
Revolution period (μs)	89	23	
Batch spacing (ns)	-	225	
Beam current (mA)	560	55/110/165/220	
Number of batches	-	1/2/3/4	
Number of bunches	2808	72/144/216/288	
Filling factor (%)	79	9/16/24/31	
Bunch current (proton/bunch)	$1.1\ 10^{11}$		
Bunch spacing (ns)	25		

COPPER SURFACE

The interaction of an electron cloud with copper, the surface material of the LHC arcs, was studied from May 2002 until November 2004.

Two types of beam screens were produced, an oval-shape beam screen with H84-V66 dimensions [8, 11] was used the first year to gain experience with the SPS beams and a circular beam screen (ID67) was then used [9, 10, 12]. Both beam screens with 1% transparency were made of OFE copper. In the first version, the perforations were made of 2 × 73 circular holes of 7 mm diameter located in the horizontal plane. In the second version, the perforations were made of 2 × 131 rounded slots. The slots were 2 mm wide and 7.5 mm long. An electron shield to protect the cold bore from unwanted heat load towards the cold bore was placed behind each slot (see Figure 4).

Electron cloud signatures

The observation of electron cloud with the COLDEX set-up was confirmed by pressure & heat load increase concomitant with electron detection.

A bunch intensity scan with 4 SPS batches was done with the beam screen held at 12 K and the cold bore at 3 K. Figure 6 shows the heat load measured on the 12 K beam screen as a function of the bunch population. The curve has a threshold at $7\ 10^{10}$ proton/bunch above which the heat load increases linearly with the bunch population. Such behaviour is a typical signature of the electron cloud formation.

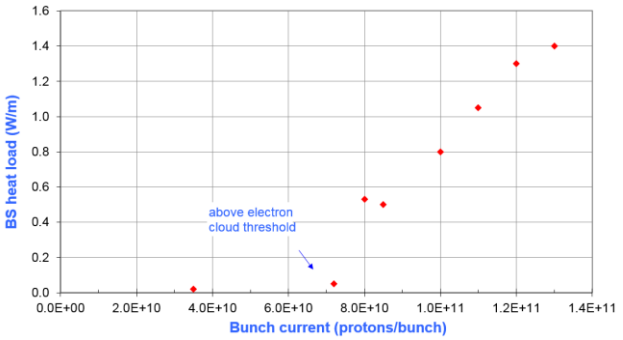

Figure 6: Electron cloud induced heat load vs bunch intensity for the circular Cu beam screen held at 12 K.

As shown in Table 2, in agreement with the observation of an electron cloud when increasing the bunch spacing from 25 ns to 75 ns, the electron current measured by the chimney electrode and the heat load on the beam screen are strongly reduced by ~ a factor 10. Other values measured at the beam screen and chimney electrodes for different configurations and conditioning are discussed in detail in Ref. [20].

Table 2: Electron cloud activity and heat load for 25 and 75 ns bunch spacing.

Bunch spacing (ns)	Electron cloud activity (μA)	Heat load (W/m)
75	1.6	0.2
25	20	1.4

Long-term behaviour

The long-term behaviour could be observed during dedicated SPS scrubbing which lasted typically 1-2 weeks. Figure 7 and Figure 8 are showing the evolution of the heat load on the beam screen due to beam induced electron cloud and the partial pressure evolution.

To avoid the scattering due to different filling factor inherent to a scrubbing period, the data of Figure 7 were normalised to 4 batches of SPS. Following beam conditioning to 12 A.h, and an estimated electron dose of 20 mC/mm^2, the final heat load was ~ 1.5 W/m [9]. According to simulations performed for WAMPAC 3, a Cu calorimeter with the same circular geometry as the COLDEX beam screen, the corresponding maximum secondary electron yield was estimated to be ~ 1.3 in agreement with a scrubbed surface [21].

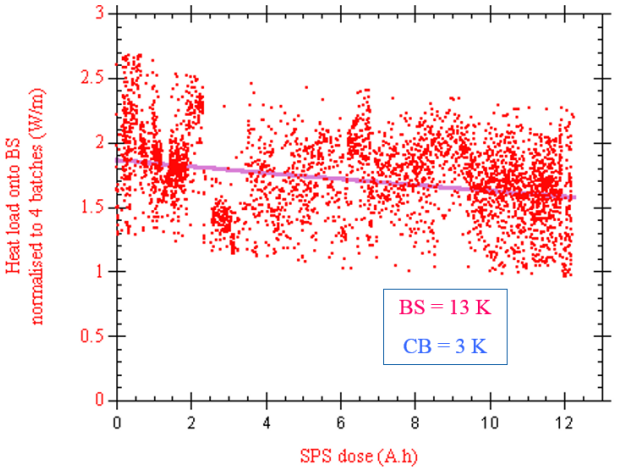

Figure 7: Heat load on the circular beam screen due to beam induced electron cloud [9].

In the presence of an electron cloud, the vacuum chamber wall is subjected to electron bombardment. Although the pumping speed of a cryogenic system held in the range 5-20 K, like LHC, can be very large (several thousand litre per sec per meter of beam tube), the electron irradiation stimulates the molecular desorption of tightly bound molecules.

Of primary importance for superconducting machines, is the hydrogen desorption. Indeed, as shown in Figure 8, the desorbed hydrogen can be physisorbed and accumulated on the beam screen surface at 8 K leading to a pressure increase due to the subsequent recycling of the weakly bounded hydrogen. This phenomenon is the LHC beam screen perforation raison d'être. As shown in Figure 8, the hydrogen partial pressure levels off after 1 h thanks to the beam screen's slots through which hydrogen can be pumped on the cold bore, and then decrease following beam conditioning. The hydrogen desorption yield was estimated to be ~ 5×10^{-2} H_2/e.

The electron bombardment stimulated also the desorption of other molecular species. However, their pressure level is two order of magnitude lower than hydrogen indicating a much lower recycling capability. For this reason, only the sum of the primary desorption, η, and recycling desorption, η', over the sticking coefficient, σ, was measured. The measured values range from 2×10^{-2} to 2×10^{-1} molecules/e.

It must be stressed that longer electron bombardment results to a surface conditioning associated with the reduction of the desorption yield for all gases as shown in [9] and observed for LHC which has a vacuum life time much larger than 100 h despite the presence of an electron cloud in the arcs [22].

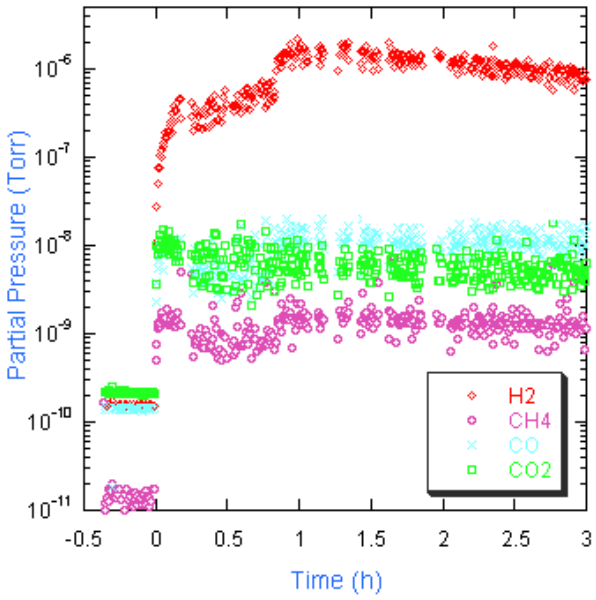

Figure 8: Partial pressure evolution during electron cloud irradiation of the oval beam screen held at 8 K with a cold bore at 4.2K [8].

Effects on pressure of physisorbed and condensed gases

As shown above, the accumulation of molecules on the cryogenic surface may lead to molecular recycling. In a real machine, gas molecules may accumulate at specific location during cool down or temperature excursion and accumulate during beam operation under electron cloud bombardment triggering pressure transients after modification of the beam parameters such as bunch intensity, filling scheme etc. [23].

Hence, several studies were performed with H_2, CO and CO_2 to investigate the interplay and the impact on the LHC design of the gas physisorption and condensation. To do so, with the extremity valves closed and the cold bore temperature held above 100 K, a known quantity of gas was injected into the system after which the beam screen temperature was increased to maintain a pressure level along the beam screen length in the range of 10^{-5} mbar. This method allowed the molecules to be uniformly distributed on the beam screen thanks to the very large impingement rate. The temperature was then slowly set back to below 15 K to allow gas cryosorption and finally the cold bore cooled down to 3 K.

Figure 9 shows the hydrogen recycling under electron cloud bombardment for 10^{15} H_2/cm^2 condensed on the beam screen held at 5 K. A large pressure increases up to 6×10^{-8} Torr followed by a fast decrease is seen. The derived recycling yield, η'/σ, equals 3 H_2/e. This large yield provokes a fast flushing of the hydrogen molecules trough the holes towards the cold bore. Thus, the pressure remains for a very short time (0.005 A.h) above the 100 h life time limit of LHC (~ 10^{-8} Torr for H_2). However, during this

process, no significant heat load increase on the beam screen (larger than 0.1 W/m) as compared to the bare surface was observed.

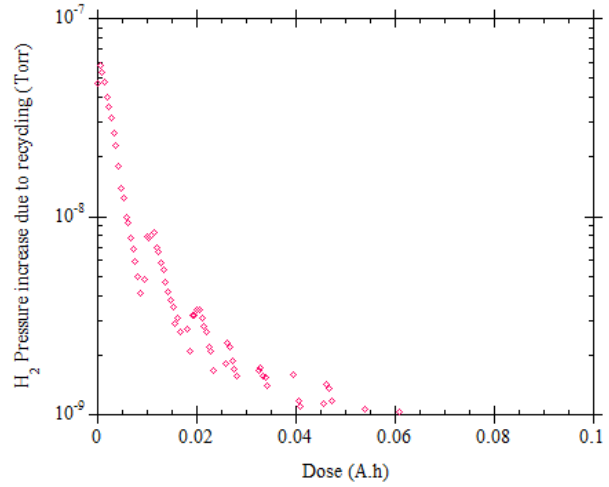

Figure 9: Hydrogen recycling under electron cloud irradiation when two SPS batches circulated with 10^{15} H_2/cm^2 condensed on the beam screen [10].

Figure 10 shows the result of a similar experiment with carbon monoxide recycling under electron cloud bombardment when 5×10^{15} CO/cm^2 are condensed on the beam screen held at 5 K. A pressure increases up to 1.5×10^{-8} mbar followed by a slow flushing of the CO molecules towards the cold bore is observed. The computed recycling yield, η'/σ, equals 0.4 CO/e. This value is much lower than for hydrogen, thereby the CO partial pressure remained above the 100 h life time limit for LHC (~ 10^{-9} Torr of CO) for a much longer period of at least 0.5 A.h. In this case also, the heat load increase on the beam screen associated with the amount of condensed gas was negligible.

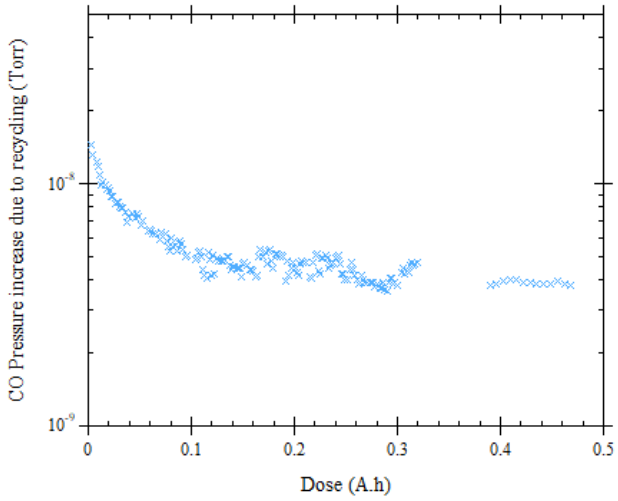

Figure 10: Carbon monoxide recycling under electron cloud irradiation when one SPS batches circulated with 5 10^{15} CO/cm^2 condensed on the beam screen [10].

The condensation of 15×10^{15} CO_2/cm^2 on the beam screen held at 15 K revealed a similar behaviour as carbon monoxide. However, as shown in Figure 11, the carbon dioxide molecule was cracked into carbon monoxide and oxygen under the electron bombardment: the resulting partial pressure of CO was seven times the partial pressure of CO_2. A slow flushing of the molecules towards the cold bore was observed with a computed recycling yield, η'/σ, of 0.01 CO_2/e. Again, for 1 circulating batch, the pressure increases remained above the 100 h life time limit of LHC for several hours with a negligible heat load increase.

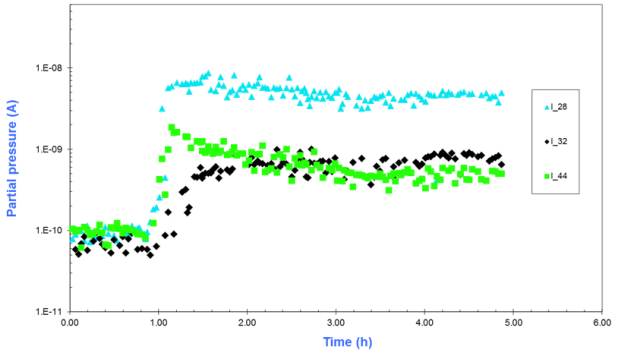

Figure 11: Carbon dioxide recycling and dissociation under electron cloud irradiation.

Impact of thick layers of condensates

In the event of the condensation of thick layers of gas, after *e.g.* a redistribution of molecules from the cold bore to the beam screen following a magnet quench, the impact on the machine operation may be dramatic as anticipated in [23]. A very similar scenario was unfortunately recently observed with the LHC following a probable air inlet in one interconnect of the 16L2 half-cell [24, 25].

Figure 12 shows the heat load induced by the electron cloud when 60×10^{15} CO/cm^2 is condensed on the beam screen. Due to the modification of the surface's secondary electron yield by the condensate, the observed heat load increased above 5 W/m for a long period. In the meantime, the hydrogen and carbon monoxide partial pressures reached 10^{-6} and 10^{-7} Torr respectively.

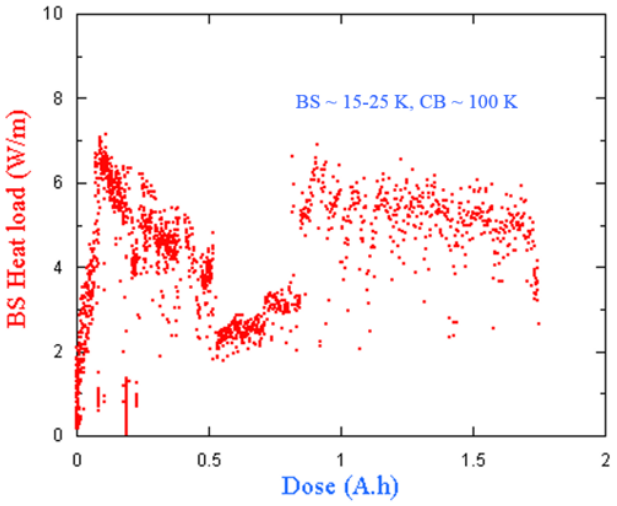

Figure 12: Beam screen heat load when 1, 2, 3 and 4 batches circulated with 60 10^{15} CO/cm^2 condensed on the beam screen [10].

Thus, the condensation of many monolayers of gas can be harmful for the operation of a superconducting machine. Figure 13 shows the computed carbon monoxide partial pressure using desorption yield data measured in the laboratory [26]. The curves are calculated for two values of heat load dissipated on the beam screen.

As shown, for 25×10^{15} CO/cm^2 condensed on the LHC beam screen, in the presence of electron cloud, the CO partial pressure is well above the 100 h life time limit. The lower the electron cloud activity, the longer the time is required to flush the carbon monoxide molecules from the beam screen to the cold bore. Several hours of beam circulation are needed at a low electron cloud activity (P = 0.1 W/m)

The removal of the carbon monoxide molecules can be speeded up by increasing the electron cloud activity. However, a too large electron cloud activity will stimulate a too high pressure level which may ultimately lead to a magnet quench. This is the case when 1.5 W/m is dissipated on the beam screen by the electron cloud.

To mitigate the above effect, beam screen heaters were integrated into the LHC design. Without beam operation, the heaters allows to warm up the beam screen above 80 K while maintaining the cold bore below 4.5 K, thereby flushing most of the gases towards the cold bore, with the exception of the water molecules [2].

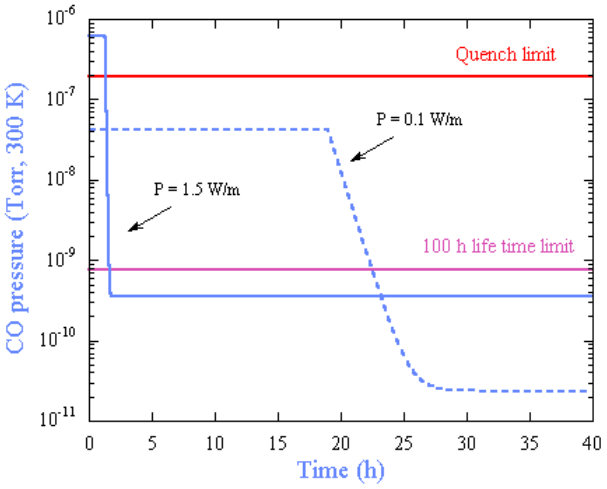

Figure 13: Vacuum transient due to the condensation of 25 10^{15} CO/cm^2 on the beam screen [10, 23].

At cryogenic temperature, although there is no thermal desorption of water, the H_2O desorption can be stimulated by electron bombardment. This is the case of unbaked surfaces or surfaces previously exposed to humidity. For this reason, it is recommended to pump down as long as possible an unbaked beam pipe before its cooling down to evacuate the maximum of water from the pipe. To do so, 5 weeks of pump down are required in the LHC machine before cooling.

Figure 14 shows the total pressure and the beam screen heat load for 2×72 circulating bunches. In the first part of the study, the pressure decreased by one order of magnitude until 10^{-5} Pa (10^{-7} Torr), conversely, the heat load increase up to 8 W/m while the beam screen temperature was drifting from 8 to 20 K due to the large beam induced heat loads! At t=100h, the beam screen was warmed up to 240 K while keeping the cold bore at 120 K with the beam circulating for a couple of hours during which a further vacuum conditioning was observed. A t=150h, the beam screen and cold bore were once again cooled down to 10 and 4.2 K respectively. The pressure continued to decrease further by one order of magnitude while the measured heat load on the beam screen was ~ 0.5-1 W/m.

Clearly, the temperature excursion up to 240 K together with the beam circulation contributed to the strong reduction of the heat load. Previous studies have shown that condensed water modifies the secondary electron yield of a surface. Indeed, a maximum secondary electron yield as large as 2.3 was measured in the laboratory with 150 monolayers [27]. Since water is desorbed from a Cu beam screen above 200 K, the origin of the previously described heat load is attributed to the water condensation. Indeed, before the experiment, the extremities of the experimental system were baked while the beam screen was kept at room temperature. Although the thermally desorbed gas was evacuated by the turbomolecular pumping, some molecules, in particular water, were sorbed on the beam screen. In the LHC, this undesirable situation

is avoided by adding a sector valve at each cold to warm transition to decouple the room temperature vacuum system from the cryogenic temperature vacuum system.

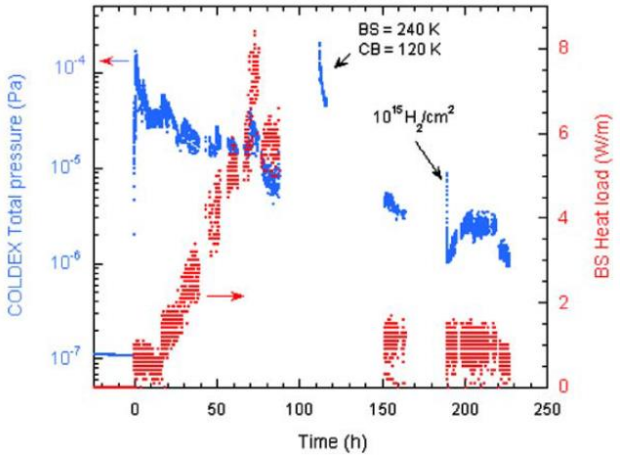

Figure 14: Total pressure and heat load on the beam screen for 2x72 circulating bunches of 0.8 – 1.1 10^{11} protons/bunch [8].

Other observations

In the presence of electron cloud, the heat load measured on the beam screen held at cryogenic temperature was compared to the heat load measured on a room temperature Cu pipe using the WAMPAC located upstream to COLDEX [19]. As expected, both equipment showed the same results indicating that both secondary electron yield were the same for both systems irrespective of their operating temperature [9, 22]. Obviously, as shown above, the presence of physisorbed and condensed gas may modify the secondary electron yield of the cryogenic surface leading to difference between heat loads measured at cryogenic and room temperature.

Several experiments were led to investigate further the behaviour of a cryogenic system in the presence of electron cloud and its impact on operation:

1. The COLDEX was kept under vacuum (P ~ 10^{-8} Torr) at RT for 2 months. After cooling down, no significant increase of the total pressure nor the heat load was noticed.
2. Similar observations were also made when, while held at RT, COLDEX was vented to air and pumped back before cooling down.
3. Finally, the COLDEX was kept to atmospheric pressure for 2 weeks and pumped down to 10^{-4} Torr before valving off the turbomolecular pump. Then, the beam screen was cooled down to 10 K and finally the cold bore to 3 K. This protocol gave the same observations as above.

CARBON COATED SURFACE

Since 2010, CERN is preparing the LHC upgrade: the High-Luminosity LHC (HL-LHC), a project which was approved by the CERN council in June 2016. This project consists in multiplying by 5 the LHC luminosity with an objective of 3 000 fb^{-1} accumulated in the mid 2030ies which corresponds to the production of more than 1 million Higgs bosons! [13].

For this purpose, the optics and the LHC matching section are modified by an entire production of new final focussing quadrupole magnets around ATLAS and CMS experiments. Table 2 shows the LHC and HL-LHC main parameters. The reduction of the normalised emittance and the doubling of the bunch population will be obtained after Long Shutdown 2 following the LHC Injector Upgrade (LIU) program [17]. The installation of the new focussing magnets and the deployment of the upgraded matching section will allow, after Long Shutdown 3, in the 2nd semester of 2026, to start a new era for the LHC employing the full capability of the Achromatic Telescopic Squeeze optic to further reduce the beam size at the collision point thereby increasing further the luminosity.

The expected high luminosity will be levelled to ~ 5×10^{34} Hz/cm^2 in order to maintain, at an acceptable level for the experimental detectors, the number of collisions at the interaction point. Although the detector experiments encapsulated as much as possible the collision point, a large amount of the produced debris will escape from the collision point towards the focussing superconducting quadrupoles. For this reason, the HL-LHC beam screen is shielded with tungsten, on its external side, to protect the cold mass from premature ageing ensuring the desired life time for the superconducting magnets [28, 13].

In order to mitigate electron multipacting thereby reducing the heat load on the cryogenic system and the background to the experiments, a-C coating, of the inner beam screen side, is proposed as a second major upgrade of the LHC-like beam screen design. This technology was recently successfully deployed for the CERN SPS machine to mitigate electron cloud [29]. Indeed, this coating acts as an anti-multipactor since the maximum secondary electron yield measured in the laboratory equals 1+/- 0.1 at a primary electron energy of 200 eV [30]. However, this coating was never evaluated at cryogenic temperature. For this reason, the COLDEX experiment was refurbished and equipped with a a-C coated (~ 400 nm thick) beam screen as shown in Figure 15 [14].

Table 3: LHC and HL-LHC beam parameters.

Parameters	LHC		HL-LHC
	Nominal	Ultimate	Nominal
Energy (TeV)	7		
Luminosity (x10^{34} Hz/cm^2)	1.0	2.3	5*
Current (mA)	584	860	1090
Proton per bunch (x10^{11})	1.15	1.7	2.2
Number of bunches	2808		2736
Bunch spacing (ns)	25		
Minimum β* (m)	0.55		0.15
Normalised emittance (μm)	3.75		2.5

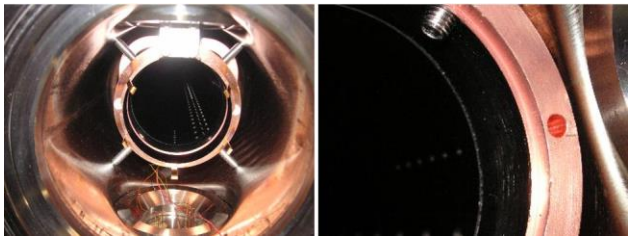

Figure 15: Picture of COLDEX extremity with a-C coated beam screen. Courtesy of B. Jenninger.

For 2 years, several important studies were conducted without and with protons beams [31]. The first observation was the demonstration of the large porosity of the ~ 400 nm thick coating. Indeed, at cryogenic temperature, the cryosorption capacity of hydrogen, measured with an adsorption isotherm, was estimated to be larger than 2×10^{17} H_2/cm^2 below 10 K *i.e.* more than 100 time the Cu capacity! A second observation, linked to the molecular capacity of the coating, was the thermal desorption of molecules at high temperature. Low coverage of hydrogen desorbs until ~ 60 K whereas other gases desorbed above 80 K.

Therefore, the working operating temperature of the HL-LHC beam screen needs to be studied in detail in a specific experimental set-up equipped with a 500 nm thick a-C coated sample to identify an acceptable temperature window [32]. Table 4 shows a compilation of the obtained results for the main gas species in the temperature range of interest for the HL-LHC inner triplets. As said above, in the 40-60 K temperature range, hydrogen is thermally desorbed for any surface coverage. Therefore, any temperature variation of the HL-LHC beam screen may lead to unwanted pressure oscillations thereby provoking beam induced background to the experiment or magnet quench in the ultimate case of very large pressure excursion. For this reason, and for this type of coating, an acceptable temperature range would be 60-80 K in which no hydrogen is physisorbed, thereby not available for desorption. In this temperature range, the other gases are available for desorption only when condensed in large quantities thus after several month of beam operation. An appropriate warm up at regular intervals will then suffice to guarantee a low enough surface coverage [33].

Table 4: Temperature range of desorption peaks from a 500 nm thick a-C coating [33].

T	H_2	CH_4	CO	CO_2
40-60 K	Any coverage	$> 10^{17}$ CH_4/cm^2	$> 2\times10^{16}$ CO/cm^2	$> 10^{18}$ CO_2/cm^2
60-80 K	No coverage	$> 5\times10^{16}$ CH_4/cm^2	$> 5\times10^{15}$ CO/cm^2	$> 10^{17}$ CO_2/cm^2

Long term operation of the SPS beams during scrubbing runs, with an accumulated beam dose till 10 A.h, were conducted to study the interaction of the LHC-like proton beam (4×72 bunches, 25 ns, up to 1.5×10^{11} protons/bunch) with the a-C coating held at cryogenic temperature. The studied beam screen temperatures were at 10, 50 and 80 K with the cold bore held at 3 - 4.5 K. No pressure rise larger than a few 10^{-10} mbar, no significant heat load larger than 0.2 W/m (opposed to 1.5 W/m for Cu, as shown in Figure 7) and no significant current on the central electron pick-up larger than 0.1 nA (opposed to a few µA for Cu, see Table 2) were observed. Unfortunately, the beam screen electrode was not available during the a-C coating qualification phase.

The impact of operating temperature and gas absorption were studied during dedicated machine development periods. Hydrogen was condensed on the beam screen with 3×10^{16} H_2/cm^2 and studied at 10, 15, 20, 25 and 50 K. Carbon monoxide was condensed on the beam screen with 2×10^{16} CO/cm^2 and studied at 10 and 50 K. Finally, carbon dioxide was condensed on the beam screen with 3×10^{16} CO_2/cm^2 and studied at 10 and 60 K with the cold bore held, in all cases, at 3 – 4.5 K. Similar to the long term studies of a bare surface, no dynamic pressure attributed to the electron stimulated desorption larger than 10^{-9} mbar, nor electron multipacting activity above 0.1 nA were observed. The measured dynamic heat load was 0.2 +/- 0.1 W/m in all cases.

Given the difficulty to trigger and observe a signature signal of electron cloud, in complement to the standard calibration of the instruments, a specific protocol was developed to assess the detection limit of the electron probes. Using the pumping and desorption properties of the a-C coating, the temperature of the beam screen was increased up to 60 K during the beam circulation. Around 40-60 K, the natural hydrogen thermal desorption, lead to an escalation of the beam gas ionisation modifying the collection current at the chimney electrode [31]. Figure 16 shows a superposition of three plots with: top, the SPS beam intensity, middle, the pressure at the COLDEX extremities (VG1, VG3) and COLDEX centre (VG2) and bottom, the electron current measured at the COLDEX chimney located at the same position as VG2. The hydrogen thermal desorption, up to 5×10^{-8} mbar, induced by the beam screen temperature increase from 40 to 60 K, provoked a current read at the chimney electrode from 0.1 to 1.5 nA modulated by the passage of the SPS batches through the beam screen. This observation confirmed a detection limit of 0.1 nA for our electrode.

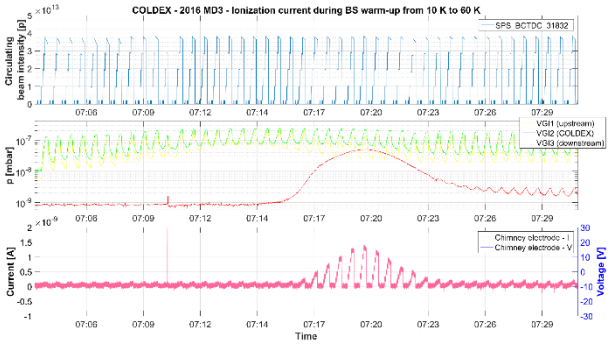

Figure 16: Top, SPS beam intensity, middle, total pressure along COLDEX, bottom, electron current at the COLDEX chimney, while increasing the a-C coated beam screen temperature from 10 to 60 K [31].

To assess the maximum secondary electron yield of the studied a-C coating, several PyCloud simulations were done. They demonstrated that the electron current detection was more sensitive than the heat load detection [15]. Figure 17 shows the simulation results using a model of the a-C secondary electron yield curve derived from laboratory measurements [31]. A maximum secondary electron yield of 1.1 can be derived from the electrical measurements (< 0.1 nA), in agreement with pressure and heat loads observations. This value is consistent with published a-C data [29] and recent measurement in the laboratory at cryogenic temperature [34].

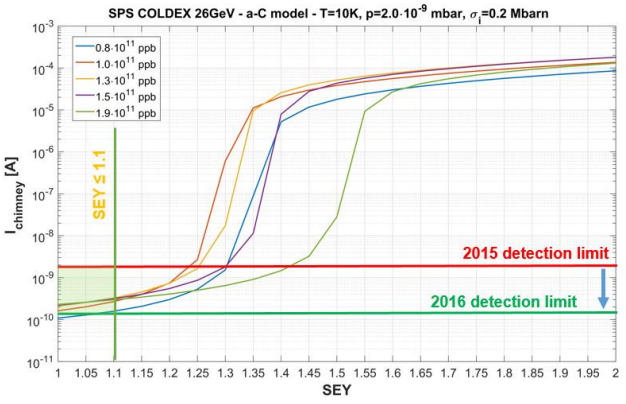

Figure 17: PyCloud simulation of the electron activity at the COLDEX chimney [31].

The above results confirmed the appropriate choice of a-C coating for the HL-LHC base line providing the coating is operated in appropriate conditions. Together with the use of the coating as an anti-multipactor technology the SPS upgrade [30] and its good behaviour in the LHC at room temperature [35], the technology will be deployed during the Long Shutdown 2 for a validation test in the LHC standalone magnets Q5R2, Q6R2, Q6L8 and Q5R8 during RUN3 before HL-LHC construction.

LASER TREATED SURFACE

Laser engineering surface were recently developed to lower the secondary electron yield of materials much below 1 [36, 37]. First studies at room temperature were successfully conducted in a short test section of the SPS showing results as good as a-C coating [38]. For this reason, with the objective to develop an alternative base line for the HL-LHC and to investigate the potential use with Future Circular Colliders, a laser treated beam screen was constructed for COLDEX [18].

Due to technological constraints, this laser treated beam screen was built out of 9 segments which were produced in collaboration with CERN – STFC and the University of Dundee, and finally assembled and tested at CERN, see Figure 18. The final beam screen was of the same dimensions as the ID 67 Cu and a-C coated beam screens.

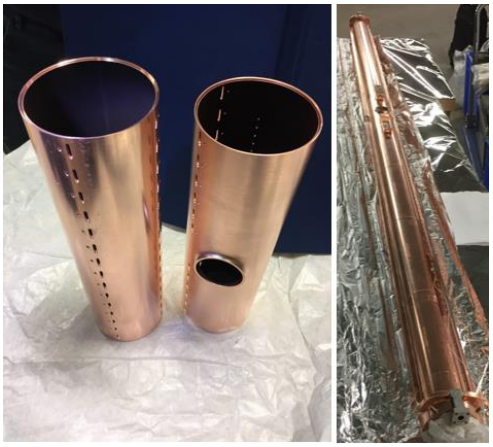

Figure 18: Left, segments of laser treated tube before their assembly at CERN, right assembled laser treated tubes to form a beam screen before its insertion into COLDEX [18].

Each segment was laser treated under nitrogen atmosphere at the University of Dundee with the following laser parameters: a wavelength of 532 nm (2.3 eV), a repetition rate of 200 kHz, a pulse length of < 15 ps, a focal spot diameter of 12 µm, an intensity of 0.4 TW/cm^2 (10^{30} ph/s/cm^2), a rotating speed of 10 mm/s and an advancing speed of 1-2 µm/s. The laser treatment lasted 3 days per segment. During the treatment, the laser head was fixed around which the ~ 25 cm long segment to be treated was rotating. Figure 19 shows the scanning electron microscope photography of a laser treated segment. The laser treatment produces groove, of 10 µm depth, located along the diameter of the segment and spaced by ~ 23 µm. A closer look to the surface shows a "cauliflower" like structure of ~ 3 µm size. X-ray Photoelectron Spectroscopy analysis indicates the presence of Cu and copper oxide, CuO, on the surface following the treatment. The maximum secondary electron yield measured in the laboratory is ~ 0.87 at a primary electron energy of 861 eV [38, 18]. As compared to standard Cu and a-C secondary electron yield curves, the curve of the laser treated surface has a maximum at much higher primary energies.

Therefore, the electron energy distribution resulting from interaction of the electron cloud with the surface will greatly differ from the interaction of the cloud with Cu or a-C surfaces.

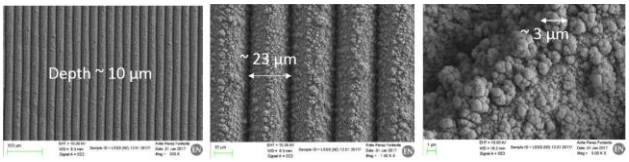

Figure 19: Scanning electron microscope photography of a laser treated beam screen segment. Courtesy A. Perez Fontenla, CERN EN-MME.

For 2 years, several studies were conducted without and with LHC-like beams, the main findings are summarised below. Detailed analysis and discussions will be published in a future report.

As shown in Figure 20, temperature programmed desorption (TPD) studies showed that H_2 is desorbed in the range 20-35 K, N_2 and CO in the range 20-40 K and CO_2 in the range 110-150 K. These values are strongly different from the one obtained with a-C coating and Cu surface underlying the fact that the TPD characterisation of materials is required to select the proper material for future applications [39].

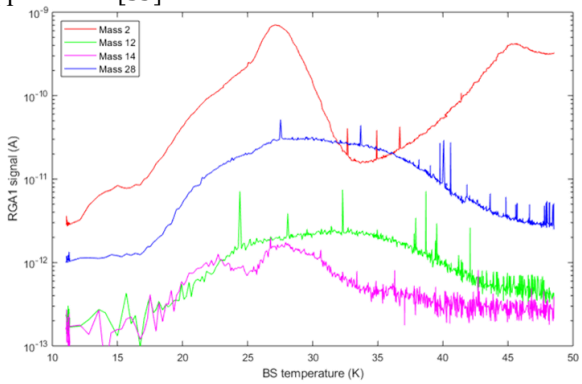

Figure 20: Temperature programmed desorption spectra from 10 to 50 K of the laser treated COLDEX beam screen. Courtesy of V. Badin.

Hydrogen transmission studies through the beam screen held at 20 K and the cold bore at 3 K, were also conducted showing the development of a pressure wave similar to the LHC case for He [40]. For a hydrogen flux of 2×10^{-3} mbar.ℓ/s, the measured speed of the H_2 wave was 12 cm/min and a pressure of 10^{-7} mbar at the beam screen centre. Of course, a lower hydrogen flux would reduce proportionally the wave speed and pressure level.

Six periods of 24 h were devoted to study the interaction of the LHC-like beam (4×72 bunches, 25 ns bunch spacing, 0.9 – 1.4 10^{11} proton/bunch, 26 GeV) with the laser treated surface.

With the COLDEX cold bore held at 3 K, the beam screen temperature was set at 10 and 50 K. At 10 K, no pressure rises larger than 10^{-10} mbar were observed in the centre of COLDEX although electron induced pressure rise in the 10^{-7} mbar range were present in the room temperature vacuum chambers upstream and downstream to COLDEX. At 50 K, the hydrogen was no pumped anymore by the laser treated beam screen and a pressure increase of ~ 10^{-9} mbar was noticed. When acting on the solenoids at the extremity, the pressure increase was slightly reduced, as expected, but not cancelled. This residual pressure increase may be attributed to the electron cloud generated in the COLDEX cold to warm transitions. Indeed, an electron current was measured on the beam screen electrode (0.1 µA for 50 V applied), whereas no electron signal was measured at the central chimney electrode.

Several studies were made with CO_2 condensed on the surface prior beam circulation. Although condensed quantities were as large as $1\div3\times10^{17}$ CO_2/cm^2, no pressure or beam induced heat load increases nor electron signals as compared to the bare surface situation were observed underlying the robustness of the material against gas condensation.

Specific studies with different beam structures were also performed to address the origin of the dynamic heat load observed with the laser treated surface. As shown in Figure 21, a dynamic heat load was measured in the warm laser treated calorimeter when the beam was dumped (ΔT = 0.3 K). When LHC-type beams circulated (4 batches with 1.3 10^{11} protons/bunch), this quantity amounts to ~ 80 mW/m opposed to 420 mW/m for the Cu surface. Although a signal was noticeable, the same quantity was barely measurable with enough accuracy for the laser treated beam screen held at cryogenic temperature. Operating the SPS with different bunch structure increasing the spacing from 200 ns to 2500 ns between batches or using 8b4e beams to supress the electron cloud build up indicated that the major part (if not all) of this heat load was due to the power losses attributed to the sample impedance. Indeed, beside the surface morphology of a laser treated surface which may affect its impedance, the present sample had grooves perpendicular to the beam path by construction which may further increase the power loss due to impedance.

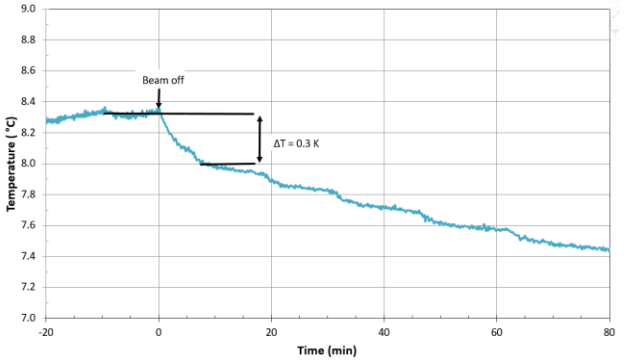

Figure 21: Observation of dynamic heat load at the warm laser treated calorimeter when LHC-type beams circulated. Courtesy B. Jenninger.

Finally, a specific run was held to study the behaviour of a laser treated beam screen in the presence of "large partial pressure". To this end, H_2 and N_2 were injected up to ~ 10^{-8} mbar inside the beam screen (held from 10 to 65 K) during beam circulation. Apart for the electron signal collected at the chimney electrode due to beam-gas ionisation (similar to Figure 16), no significant heat load increases were observed, demonstrating the robustness of the laser treatment in the presence of "large partial pressure".

CONCLUSIONS

The experimental modelling of cryogenic vacuum system is of paramount importance for the design and operation of superconducting machines.

For this reason, during the LHC design phase, the COLDEX experiment was installed in a bypass of the SPS ring to study the electron-cloud interaction with an LHC type beam screen. Data obtained with Cu material in laboratories could be then complemented by observations with beams on an LHC type mock-up. The studies confirmed the beam conditioning effect and the control of the gas density level by the beam screen perforation but highlighted the impact of the physisorbed and condensed gas on the machine operation leading to the setting-up of specific procedures for the LHC machine cool down and beam screen regeneration [2].

With the upgrade of the LHC machine, the HL-LHC, to be commissioned by mid-2026, the evaluation of the recently developed anti-multipacting surfaces such as a-C coating was needed [29, 13]. Qualifications at cryogenic temperatures with COLDEX showed no major showstopper for the use of a-C coating in superconducting machines, apart from a specific definition of the operating temperature owing to the material porosity [15, 16, 33]. These studies led to the pilot deployment of the a-C coating in four superconducting magnets of the LHC matching section for final validations during Run 3 before a full deployment during the HL-LHC construction phase.

A recently developed anti-multipacting surface such as laser treated beam screen was also evaluated at cryogenic temperature with COLDEX as an alternative to the a-C coating. The studies showed that this material has a very good behaviour and robustness against multipacting when LHC-type beams circulates. However, more detailed studies are still needed to assess the impact of the surface morphology on the beam performances together with studies at cryogenic temperature and room temperature evaluation in the LHC [35] before integrating such material in the HL-LHC vacuum system.

ACKNOWLEDGMENTS

I would like to warmly acknowledge the constant commitment and expertise of B. Jenninger during the design, installation(s) and operation of the COLDEX apparatus. I would like also to underline the skills of R. Salemme, the Beam Vacuum Operation section, in charge of the SPS vacuum operation, and the CRG group for their cryogenic expertise and support during the refurbishment and re-commissioning of the COLDEX system. Results with a-C coating and laser treated beam screens were mainly obtained by R. Salemme and V. Badin respectively, two fellows I had the pleasure to supervise during these studies. I am delighted to underline their ability to operate COLDEX and analyse the data. The a-C coating was successfully performed thanks to the talent of P. Costa Pinto. The laser treated beam screen fabrication, produced under the collaboration between CERN, STFC and the University of Dundee, was successfully coordinated by R. Salemme despite the tight schedule. I want to underline also the quality of the LHC-type beams delivered by the SPS operators and warmly acknowledge the HL-LHC project office and the TE department for their constant support during the a-C coating and the laser treated surface studies.

REFERENCES

[1] O. Gröbner. Overview of the LHC vacuum system. Vacuum 60 (2001) 25-34.

[2] The LHC design report. CERN-2004-003, CERN, Geneva, June 2004.

[3] J.P. Potier, L. Rinolfi. The LEP Pre-Injector as a multipurpose facility. Proc. of EPAC'98, Stockholm, Sweden, 22-26 June 1998.

[4] V. Baglin, I.R. Collins, C. Grünhagel, O. Gröbner and B. Jenninger. First from COLDEX applicable to the LHC cryogenic vacuum system. Proc. of EPAC'00, Vienna, Austria, 26-30 June 2000.

[5] V. Baglin, I.R. Collins, C. Grünhagel, O. Gröbner and B. Jenninger. Molecular desorption by synchrotron radiation and sticking coefficient at cryogenic temperatures for H_2, CH_4, CO and CO_2. Vacuum 67 (2002) 421-428.

[6] V. Baglin, I.R. Collins, C. Grünhagel, O. Gröbner and B. Jenninger. Synchrotron radiation studies of the LHC dipole beam screen with COLDEX. Proc. of EPAC'02, Paris, France, 3-7 June 2002.

[7] V. Baglin, I.R. Collins, C. Grünhagel, O. Gröbner and B. Jenninger. Cryosorbers studies for the LHC long straight section beam screens with COLDEX. Proc. of EPAC'02, Paris, France, 3-7 June 2002.

[8] V. Baglin, I.R. Collins, B. Jenninger. Performance of a cryogenic vacuum system (COLDEX) with an LHC type beam. Vacuum 73 (2004) 201-2016.

[9] V. Baglin, B. Jenninger. Pressure and heat load in a LHC type cryogenic vacuum system subjected to electron cloud. Proc. of ECLOUD'04, Napa, Ca, USA, April 2004.

[10] V. Baglin, B. Jenninger. Gas condensate onto a LHC type cryogenic vacuum system subjected to electron cloud. Proc. of EPAC'04, Lucerne, Switzerland, July 2004.

[11] B. Spataro et al. Impedances of the cold bore experiment, COLDEX, installed in the SPS machine. Nucl. Instr. And Meth. A 564 (2006) 38-43.

[12] B. Spataro et al. Coupling impedance studies and power loss measurement of the COLDEX upgraded vacuum chamber. Nucl. Instr. And Meth. A 581 (2007) 885-889.

[13] High Luminosity Large Hadron Collider (HL-LHC), Technical Design Report. CERN 2017-007-M, July 2017.

[14] R. Salemme, V. Baglin, F. Bellorini, G. Bregliozzi *et al.* Recommissioning of the COLDEX experiment at CERN. Proc. of IPAC 2015, Richmond, VA, USA, May 2015.

[15] R. Salemme, V. Baglin, G. Bregliozzi, P. Chiggiato. Amorphous carbon coatings at cryogenic temperatures with LHC type beams: first results with the COLDEX experiment. Proc. of IPAC 2015, Richmond, VA, USA, May 2015.

[16] R. Salemme, V. Baglin, G. Bregliozzi, P. Chiggiato. Vacuum performance of amorphous carbon coating at cryogenic temperature with presence of proton beams. Proc. of IPAC 2016, Busan, Korea, May 2016.

[17] LHC Injector Upgrade, Technical Design Report, CERN-ACC-2014-0337, CERN, Geneva, December 2014.

[18] R. Salemme, V. Baglin, S. Calatroni, P. Chiggiato *et al.* First beam test of laser engineered surface structures (LESS) at cryogenic temperature in CERN SPS accelerator. Proc. of IPAC 2018, Vancouver, Canada, May 2018. J. Phys.: Conf. Ser. **1067** 082017.

[19] V. Baglin, B. Jenninger. CERN SPS electron cloud heat load measurements and simulations. Phys. Rev. STAB, 6, 063201 (2003).

[20] V. Baglin, B. Jenninger. Preliminary results of June 2004 scrubbing run. Presented at the Accelerator Performance Committee, 18th June 2004.

[21] D. Schulte and F. Zimmermann. Electron cloud build up simulations using ECLOUD. Proc. of ECLOUD'04, Napa, Ca, USA, April 2004.

[22] V. Baglin. The LHC vacuum system: commissioning up to nominal luminosity. Vacuum 138 (2017) 112-119.

[23] V. Baglin. Vacuum transients during LHC operation. Proc. of LHC Project Workshop - Chamonix XIII, Chamonix, January 2004.

[24] J. M. Jimenez, S. Antipov, G. Arduini, A. Bertarelli, N. Biancacci *et al.* Observations, analysis and mitigation of recurrent LHC beam dumps caused by fast losses in arc half-cell 16L2. Proc. of IPAC 2018, Vancouver, Canada, 2018.

[25] B. Salvant, S. Antipov, G. Arduini, N. Biancacci, X. Buffat *et al.* Experimental characterisation of a fast instability linked to losses in the 16L2 cryogenic half-cell in the CERN LHC. Proc. of IPAC 2018, Vancouver, Canada, 2018.

[26] H. Tratnik, N. Hilleret, H. Störi. The desorption of condensed noble gases and gas mixtures from cryogenic surfaces. Vacuum 81 (2007) 731-737.

[27] V. Baglin, B. Henrist, N. Hilleret, E. Mercier, C. Scheurlein. Ingredients for the understanding and the simulation of multipacting. Proc. of the 10th Chamonix SPS&LEP performance workshop, Chamonix, January 2000.

[28] V. Baglin, A. Ballarino, F. Cerutti, R. Denz, P. Fessia et al. Conceptual design of the LHC interaction Upgrade – Phase – I. LHC Project Report 1163, Nov 2018.

[29] P. Costa Pinto, S. Calatroni, H. Neupert, D. Letant-Delrieux, P. Edwards *et al.* Carbon coatings with low secondary electron yield. Vacuum 98 (2013) 29-36.

[30] C. Yin Vallgreen, G. Arduini, J. Bauche, S. Calatroni, P. Chiggiato *et al.* Amorphous carbon coatings for the mitigation of electron cloud in the CERN Super Proton Synchrotron. Phys. Rev. ST Accel. Beams 14, 071001 (2011).

[31] R. Salemme. Space charge compensation and electron cloud effects in modern high intensity proton accelerator. PhD thesis, Universita di Roma Sapienza, October 2016.

[32] A.-L. Lamure, V. Baglin, P Chiggiato, B. Henrist. Adsorption/desorption from amorphous carbon coatings at cryogenic temperatures. Presented at AVS 64th International Symposium & Exhibition, Oct. 29 – Nov. 3, 2017, Tampa, FL, USA

[33] V. Baglin. Towards final validation of new temperature of BS triplets. Presented at the 8Th HL-LHC Collaboration Meeting, CERN, 15-18th October 2018.

[34] B. Henrist, V. Baglin, M. Haubner. Characterisation of technical surfaces at cryogenic temperature under electron bombardment. These proceedings.

[35] E. Buratin, V. Baglin, B. Henrist. Preliminary results obtained with the LHC Vacuum Pilot Sector. These proceedings.

[36] R. Valizadeh, O.B. Malyshev, S. Wang, S.A. Zolotovskaya, W.A. Gillespie, A. Abdolvand. Low secondary electron yield engineered surface for electron cloud mitigation. Appl. Phys. Lett. 105, 231605 (2014).

[37] R. Valizadeh, O.B. Malyshev, S. Wang, T. Sian, M.D. Cropper, N. Sykes. Reduction of secondary electron yield for E-cloud mitigation by laser ablation surface engineering. Appl. Surf. Sci. 404 (2017) 370-379.

[38] S. Calatroni, E. Garcia-Tabares Valdivieso, H. Neupert, V. Nistor *et al.* First accelerator test of

vacuum components with laser-engineered surfaces for electron cloud mitigation. Phys. Rev. Accel. Beams 20, 113201 (2017).
[39] V. Baglin, Ph. Lebrun, L. Tavian, R. van Weelderen. Cryogenic beam screens for high-energy particle accelerators. Proc. of ICEC24-ICMC2012, Fukuoka, Japan, 2012. CERN-ATS-2013-006.
[40] E. Wallen. Experimental test of the propagation of a He pressure front in a long, cryogenically cooled tube. J. Vac. Sci. & Technol. A15, 2949 (1997).

ELECTRON CLOUD EFFECTS IN SUPERKEKB COMMISSIONING

K. Ohmi *, J. Flanagan, H. Fukuma, H. Ikeda, E. Mulyani, K. Shibata, Y. Suetsugu, M. Tobiyama,
KEK, Tsukuba, Japan, also at Soken-dai, Tsukuba, Japan

Abstract

A vertical emittance growth (beam size blow-up) due to electron cloud has been observed in the positron low energy ring (LER) in Phase-I commissioning (2016) of SuperKEKB. The emittance growth is caused by fast head-tail instability due to wake force induced by electron cloud. The emittance growth was suppressed by weak permanent magnets generating longitudinal field, which cover the drift space of the ring in Phase-II (2018). The emittance growth has been studied during the commissioning with measuring electron cloud density in the beam chamber. We discuss threshold of the electron density for the instability.

INTRODUCTION

The electron cloud instabilities, vertical fast head-tail instability [1] and fast coupled bunch instability [2], were key issues in KEKB. The instabilities have also been regarded as a problem in SuperKEKB. In SuperKEKB, cure of electron cloud was one of the highest priority issue. A target electron cloud density to manage the instability has been evaluated theoretically and numerically, and the vacuum system has been designed to realize the target density. Antechambers with TiN coating and grooved surface were adopted in arc section. TiN coating was applied also in straight section chambers [3].

Beam commissioning of Phase-I was performed in February to June in 2016 without interaction region and Phase-II commissioning was performed in March to July 2018 after installation of IR magnets and the BELLE-II detector. Study of electron cloud effects in the positron ring (LER) was important subject in the commissioning. Vertical emittance growth due to electron cloud has been observed in the positron ring (LER) in Phase-I commissioning. The emittance growth was suppressed by weak permanent magnets, which cover the drift space of the ring in Phase-II commissioning. Electron cloud density has been monitored during the commissioning and the threshold for the electron cloud instability has been studied in various operating beam conditions. Electron cloud has been monitored at an aluminium test chamber w and w/o TiN coating. Table 1 summarizes parameters of SuperKEKB LER. Bunches were filled by 3 bucket (6 ns spacing) in the commissioning, while they are filled by 2 bucket (4ns spacing) in the design. Maximum operating current 1 A was achieved at the total number of bunches 1576, to be compared with 3.6 A for 2500 bunches in the design.

* ohmi@post.kek.jp

Table 1: Parameter list of SuperKEKB LER

	Phase I, II	Design
Circumference, L (m)	3016.3	
Energy, E (GeV)	4	
Current, I (A)	1	3.6
Number of bunch, N_b	1576	2500
Bunch population, N_p (10^{10})	≤ 5	9
Emittance, $\varepsilon_{x/y}$ (nm/pm)	2.1/15	3.2/9
Bunch length, σ_z (mm)	6	
Synchrotron tune, ν_s	0.02	0.022

PREDICTION FOR ELECTRON CLOUD INSTABILITIES IN SUPERKEKB

Threshold of electron density was evaluated by a simulation code PEHTS. Electron cloud is generated at 16 points in the LER ring. Beam motion is integrated over 16 steps per revolution interacting with electron cloud. Figure 1 presents simulation results for single bunch instability caused by electron cloud. Top plot shows evolution of vertical beam size for various electron density. The threshold density is estimated as $\rho_{e,th} = 3.8 \times 10^{11}$ m^{-3} at the design parameters of SuperKEKB. Bottom plot shows vertical position ($y_e(t = z/c)$) of electron cloud during interaction with a bunch and vertical position ($y(z)$) and size ($\sigma_y(z)$) of the bunch at 400-th turn for the density $\rho_e = 4.2 \times 10^{11}$ m^{-3}. Clear signal of head-tail instability and collective motion of electron cloud are seen. This head-tail motion appears as vertical emittance growth of positron beam.

The single bunch instability is caused by a vertical wake force induced by electron cloud. The wake force is expressed by [4].

$$W(z) = c\frac{R_S}{Q} e^{\omega_c z/(2cQ)} \sin\frac{\omega_c z}{c} \tag{1}$$

where

$$c\frac{R_S}{Q} = K\frac{2\sqrt{2}\pi^{3/2}\rho_e L}{N_p}\frac{\omega_c\sigma_z}{c}. \tag{2}$$

ω_c is coherent frequency of vertical motion of electron cloud with the same transverse size as beam ($\sigma_x \times \sigma_y$),

$$\omega_c^2 = \frac{N_p r_e c^2}{\sqrt{2\pi}\sigma_z\sigma_x\sigma_y} \tag{3}$$

where the positron beam is flat, $\sigma_x \gg \sigma_y$. A small frequency shift $\omega_c\sqrt{1 - 1/(4Q^2)} \approx \omega_c$ is neglected. Incoherent frequency for an electron is $\omega_e = \sqrt{2}\omega_c$.

Two particle model is available for $\omega_c\sigma_z/c \sim 1$. Coasting beam model is desirable for $\omega_c\sigma_z/c > 1$. The stability

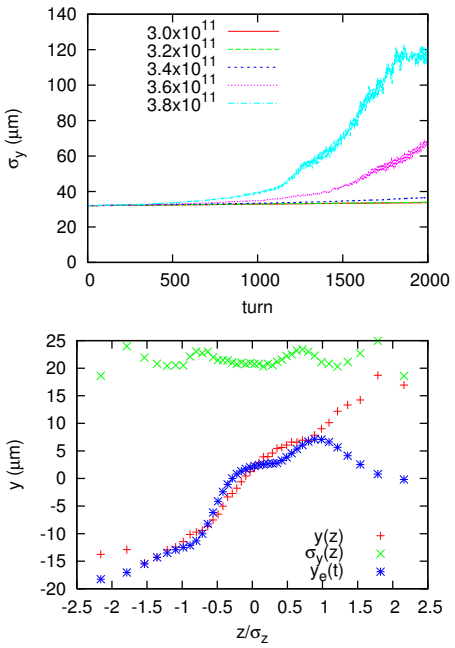

Figure 1: Simulation of single bunch instability caused by electron cloud. Top plot shows evolution of vertical beam size, and bottom plot shows intra-bunch oscillation and electron motion.

condition by a coasting beam model determines the threshold of electron density as [5]

$$\rho_{e,th} = \frac{2\gamma\nu_s\omega_c\sigma_z/c}{\sqrt{3}KQr_e\langle\beta_y\rangle L}. \quad (4)$$

The quality factor Q is characterized by nonlinear interaction of beam and electron cloud. The nonlinear component of Q is evaluated by a numerical simulation as $Q_{nl} \approx 5-15$ depending on the cloud size and beam shape (flat or round). One typical value is $Q_{nl} = 6.3$ for interaction of flat beam and electron cloud with the size of $10\sigma_x \times 10\sigma_y$ [4]. Wake force with longer range than the bunch length does not contribute to the instability. Therefore Q is effectively described by

$$Q = min(Q_{nl}, \omega_c\sigma_z/c). \quad (5)$$

The frequency of the wake force is 25% larger than ω_c for the typical case. It is between ω_c and ω_e.

K characterizes enhancement of wake force strength depending on how much electrons contribute the instability. For KEKB, $K \approx 3$ for $\omega_c\sigma_z/c \approx 3$ [4]. We assume $K \approx \omega_c\sigma_z/c$, because the number of electrons, which contribute to the instability, is proportional to $\omega_c\sigma_z/c$.

For low emittance ring, $\omega_c\sigma_z/c$ is large. It is larger than $Q_{nl} = 6.3$ for $N_p > 1.3\times10^{10}$ for Phase-I, II parameters. The effective Q is constant $Q = Q_{nl} = 6.3$. The threshold is constant assuming $K = \omega_e\sigma_z/c$,

$$\rho_{e,th} = \frac{2\gamma\nu_s}{\sqrt{3}Q_{nl}r_e\langle\beta_y\rangle L} = 2.8\times10^{11}\ \mathrm{m}^{-3}, \quad (6)$$

where the averaged vertical beta function $\langle\beta_y\rangle = 12$ m.

VERTICAL EMITTANCE GROWTH DUE TO ELECTRON CLOUD INSTABILITY

In the early stage of Phase-I commissioning, a vertical emittance growth had been observed. The reason why the instability arose was that 5% of the LER ring were not coated by TiN [6]. The 5% area is near joint of chambers with bellows. Fortunately the appearance of the emittance growth was a good opportunity for studying threshold behavior of the single bunch electron cloud instability.

We studied the emittance growth for bunch train with various filling. Figure 2 shows the vertical beam size, measured by the X-ray monitor [7], as a function of beam current for several bunch filling, 2, 3, 4, 6 bucket spacing, where the total number of bunches is 600. Thresholds of the beam

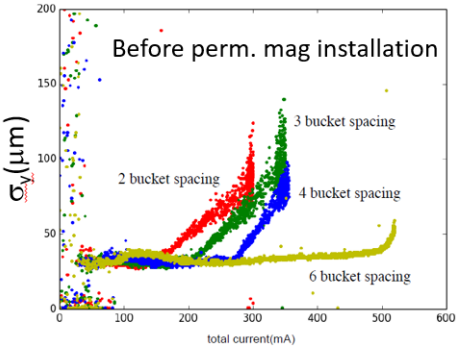

Figure 2: Beam size as a function of beam current.

current for each bunch spacing are obtained from the figure. They are 160, 200, 260 and 500 mA for 2, 3, 4 and 6 bucket spacing, respectively. Corresponding bunch populations are 1.6, 2.0, 2.7 and 5.2×10^{10}, respectively.

Simulations using the beam parameters were executed to evaluate threshold of electron density. Figure 3 presents simulation results for $N_p = 1.6, 2.0, 2.7$ and 5.2×10^{10}. The threshold density is summarized in Figure 4. The threshold density is weakly dependent on the bunch population, $\rho_{e,th} = 3 \sim 4\times10^{11}$ m^{-3}.

The electron density at area with/without the TiN coating is measured using a test chamber [8]. Figure 5 presents the measured electron density as a function of beam current in various bunch filling at the test chamber. Top and bottom plots show electron density without and with TiN coating, respectively. The density without TiN coating is very high and rapidly increases as function of the beam current. The density at the region without TiN coating is 2.0, 3.2, 4.3 and 8.1×10^{12} m^{-3} at the threshold for fillings with 2, 3, 4, 6 bucket spacing, respectively, in Figure 2. The corresponding densities with TiN coating are 2.5, 2.0, 2.0 and 2.3×10^{11} m^{-3}.

The joint area, 5% of the ring, was not coated by TiN. The contribution to whole ring is 1.0, 1.6, 2.2 and 4.1×10^{11} m^{-3}. In the early stage of Phase-I commissioning, no cure had been applied in the joint area. On average, beam expe-

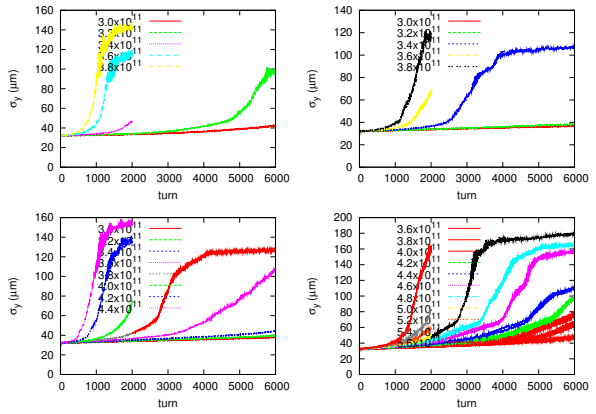

Figure 3: Vertical emittance growth in simulation PEHTS. Top left, top right, bottom left and bottom right are evolution of the vertical beam size for $N_p = 1.6, 2.0, 2.7$ and 5.2×10^{10}, respectively.

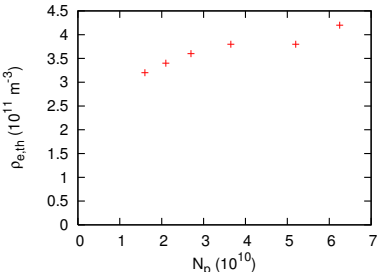

Figure 4: Instability threshold of electron density determined by the simulation using PEHTS.

riences electron cloud with the density 3.4, 3.5, 4.1 and 6.3×10^{11} m^{-3} at the threshold of each filling.

The emittance growth was suppressed by installation of permanent magnets at the joint area, The magnets produce an axial field ($B_z \sim 100$ G) at the chamber surface effectively. Figure 6 shows measured beam size after installation of the magnets. Threshold beam currents of the emittance growth were 200 and 330mA for 2 and 3 bucket spacing , respectively, and higher than 600 mA for 4 or more bucket spacing. The threshold electron density is evaluated from the bottom (with TiN coating) of Figure 5, if electrons at the joint area are perfectly cleared.

Table 2 summarizes the threshold current and electron density at the threshold for each bunch spacing. Top 4 lines and bottom 3 lines correspond to conditions before and after the permanent magnet installation, respectively.

The threshold of 2 bucket spacing ($N_p = 2.1 \times 10^{10}$) is serious for the design bunch population (9×10^{10}). For Phase-II commissioning, further permanent magnets were attached at most (86%) of the beam chambers in drift space. The emittance growth has not been observed in Phase-II until $N_p = 4.5 \times 10^{10}$ with 2 bucket spacing.

Table 2: Summary of threshold of the vertical emittance growth.

$N_{p,th}$ 10^{10}	$\omega_e\sigma_z/c$	$\rho_{e,sim}$	$\rho_{e,mon}$ 10^{11} m^{-3}	spacing	$I_{p,th}$ mA
1.6	6.8	3.2	3.4	2	160
2.1	7.8	3.2	3.5	3	200
2.7	8.9	3.6	4.1	4	260
5.2	12.3	3.8	6.3	6	500
2.1	7.8	3.2	3.0	2	200
3.65	10.3	3.8	3.0	3	350
6.25	13.5	4.2	2.0	4	>600

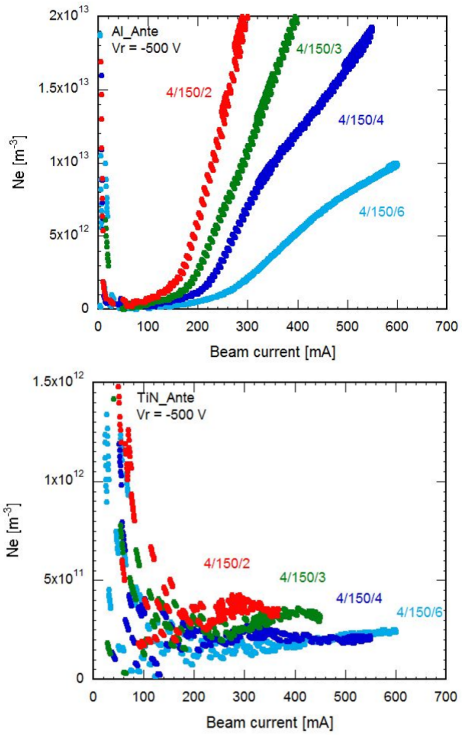

Figure 5: Measured electron density at a test chamber. Top and bottom are density without and with TiN coating, respectively, as a function of beam current in various bunch filling.

TUNE SHIFT DUE TO ELECTRON CLOUD

Electron cloud causes a positive tune shift due to the attractive force between beam and electron cloud. The tune shift depends on the electron density and distribution. For a static round charge distribution, tune shift is expressed by

$$\Delta\nu_x = \Delta\nu_y = \frac{\rho_e r_e \langle\beta_{x,y}\rangle}{2\gamma} C \qquad (7)$$

For flat distribution along x,

$$\Delta\nu_x = 0, \qquad \Delta\nu_y = \frac{\rho_e r_e \langle\beta_{x,y}\rangle}{\gamma} C \qquad (8)$$

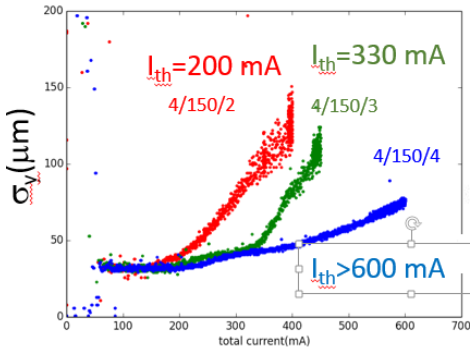

Figure 6: Measured vertical beam size after permanent magnet installation.

Transverse tune was measured along the bunch train for 3 bucket spacing filling. Figure 7 shows horizontal (top) and vertical (bottom) tune of bunches at 0, 150,300 and 450-th bucket.

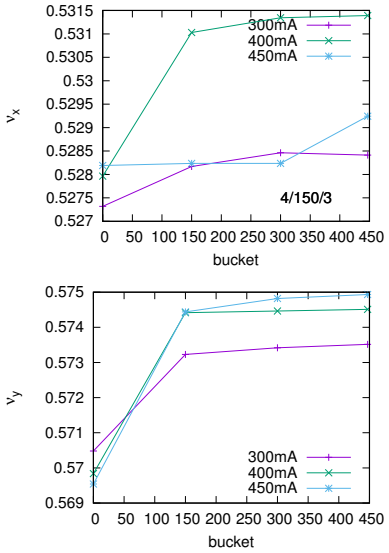

Figure 7: Tune shift along bunch train for 3 spacing filling.

The horizontal tune shift depends on the beam current (I): i.e., $\nu_x = 0.003$ for $I = 400$ mA and $\nu_x = 0.001$ for $I = 300$ and 450 mA. The horizontal tune shift seems to be ambiguous. The vertical tune shift is $\nu_y = 0.005$. The electron density is estimated to be $\rho_e = 4 \times 10^{11}$ m^{-3}, if only the vertical tune shift is considered. For $\nu_x + \nu_y = 0.006 - 0.008$, the density is $\rho_e = 5 - 6 \times 10^{11}$ m^{-3}. The density is in good agreement with that directly measured in the test chamber with/without TiN coating.

CONCLUSION

Beam commissioning of Phase-I was performed in February to June in 2016 without interaction region and Phase-II commissioning was performed in March to July 2018 after installation of IR magnets and the BELLE-II detector. Study of electron cloud effects was one of the highest priority issue in the commissioning. Fast head-tail instability due to electron cloud was observed at the predicted density, and was suppressed by axial field in uncoated bellows area of TiN as expected. Electron density were measured during the commissioning progress. The measured tune shift was consistent with the threshold value of the electron density. Further permanent magnets, which produce axial field, were attached at most (86%) of the beam chambers for Phase-II commissioning. The emittance growth has not been observed in Phase-II until $N_p = 4.5 \times 10^{10}$ with 2 bucket spacing.

ACKNOWLEDGEMENT

The authors thank SuperKEKB team for the commissioning and operation and help for machine experiments.

REFERENCES

[1] K. Ohmi, F. Zimmermann, Phys. Rev. Lett. 85, 3821 (2000).

[2] K. Ohmi, Phys. Rev. Lett. 75, 1526 (1995).

[3] Y. Suetsugu et al., Phys. Rev. AB 19, 121001 (2016).

[4] K. Ohmi, F. Zimmermann, E. Perevedentsev, Phys. Rev. E 65, 016502 (2001).

[5] A. W. Chao, *Physics of Collective Beam Instabilities in High Energy Accelerators*, Wiley-Interscience Publication, New York, 1993), and references therein.

[6] Y. Suetsugu et al., proceedings of IPAC17, WEPIK008 (2017).

[7] E. Mulyani, J. Flanagan, H. Ikeda, H. Fukuma, M. Tobiyama, proceedings of IPAC18, THPML074.

[8] Y. Suetsugu et al., in this proceedings (2018).

SIMULATIONS OF SYNCHROTRON-RADIATION-INDUCED ELECTRON PRODUCTION IN THE CESR VACUUM CHAMBER WALL

J.A. Crittenden, S. Poprocki, D.L. Rubin and D. Sagan
CLASSE, Cornell University, Ithaca NY 14853

Abstract

We report on calculations of electron production by synchrotron radiation absorbed in the vacuum chamber walls of the Cornell Electron Storage Ring (CESR). These photoelectrons are the source of electron clouds which limit the performance of storage rings by causing betatron tune shifts, instabilities and emittance growth. Until now, cloud buildup modeling codes have used ad hoc models for the production of the seed electrons. We have employed the photon scattering code Synrad3D developed at Cornell University to quantify the pattern of absorbed photons around the CESR ring, including the distribution in azimuthal location on the wall of the beampipe. The reflectivity of the wall, including its dependence on photon incident angle and energy, is modeled for various materials using online look-up tables. Micro-groove structure in the vacuum chamber wall is also accounted for. The resulting absorbed photon energy and incident angle information are used as input to Geant4-based simulations of electron emission from the walls, in which the material composition of the wall is also taken into account. The quantum efficiency is found to vary dramatically with the location of the absorption site, owing to the distribution in photon impact energies and angles. The electron production energy spectrum plays an important role in the modeling of electron cloud buildup, where the interplay of production energy and acceleration by the beam bunches determines the time structure and multipacting characteristics of the cloud.

INTRODUCTION

The buildup of high densities of low-energy electrons has been recognized as an important operational limitation in a variety of accelerator facilities since the 1960s [1]. In positron storage rings such as KEKB and the Cornell Electron Storage Ring (CESR), as well as in the proton rings at the Large Hadron Collider, a primary source of electron production is synchrotron-radiation-induced photon absorption processes in the vacuum chamber walls. Thus the incident photon rate and quantum efficiency for producing electrons are critical factors in the time dependence of the electron densities and their interaction with the beam bunches. The quantum efficiency depends strongly on the wall material and surface properties, as well as on the incident photon energy and angle. The photon absorption rates, energies, and angles of incidence determine the azimuthal electron production locations on the vacuum wall surface around the ring, and in the various magnetic field environments, on which the subsequent evolution of the cloud depends. In addition, the cloud dynamics depend crucially on the photoelectron production energies, since, together with the momentum kicks imparted by the beam bunches, they determine the cloud density profile present at the arrival time of succeeding bunches.

Joining a multi-decade collaborative effort, the CESR Test Accelerator (CESRTA) project [2] has undertaken a series of measurements, both local and ring-wide, to quantify, characterize and model the buildup of electron clouds, with the goal of extending the predictive power of the models to include betatron tune shifts and emittance growth and contributing to the robust design of future accelerator facilities. Recent experimental and modeling work on tune shifts increasing along a train of positron bunches has motivated the present study of photoelectron production in the CESR vacuum chamber walls throughout the entire circumference of the ring.

This paper first describes recent improvements in the photon tracking simulation. The physics of reflection from grooved surfaces and thin surface layers has been incorporated. We then present the results of the Geant4 code used to generate 10^5 events in each of 720 bins in transverse azimuthal photon absorption site location on the vacuum chamber wall, using samples of individual photon energies and incident angles collected from the photon tracking summed over the field-free and dipole regions of the ring. In the following, we refer to the electrons produced inside the beampipe volume via photoelectric effect and atomic de-excitation processes as photoelectrons. We show as well the dependence on vacuum chamber wall material used as input to the Geant4 simulation. The CESR vacuum chamber wall material is modeled as 3 mm of aluminum 6061 alloy with a 5-nm layer of CO, a choice consistent with reflectivity measurements of material samples in X-ray beams [3]. These Geant4 simulations provide the electron production rate in units of electrons per meter per beam particle per radian in the 720 bins around the transverse perimeter of the beampipe separately for the field-free and dipole regions of the ring. The electron production energy spectrum from 1 eV to 5 keV is provided separately in three regions of azimuthal production location, again separately for the field-free and dipole regions. These distributions in electron production location and energy are provided to the cloud buildup code, which uses them in separate simulations for the field-free and dipole cases, as described in Refs. [4, 5].

The results presented below concern primarily modeling for a 5.3 GeV positron beam, with a summary of results for the 2.1 GeV and 6.0 GeV modeling included in tabular form for comparison.

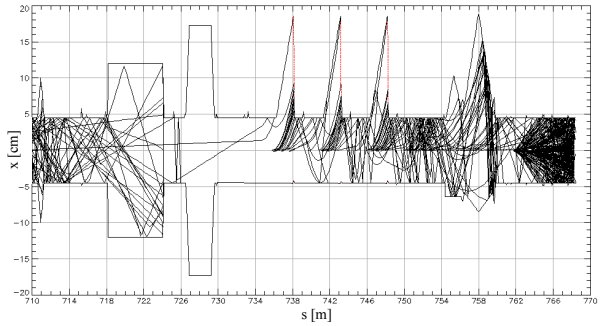

Figure 1: Top down view (x vs. s) for a portion of the CESR ring, showing photon tracks (black lines). The red vertical lines represent X-ray beam line exit ports, and any photon hitting those surfaces are terminated and excluded from the absorbed photon rate.

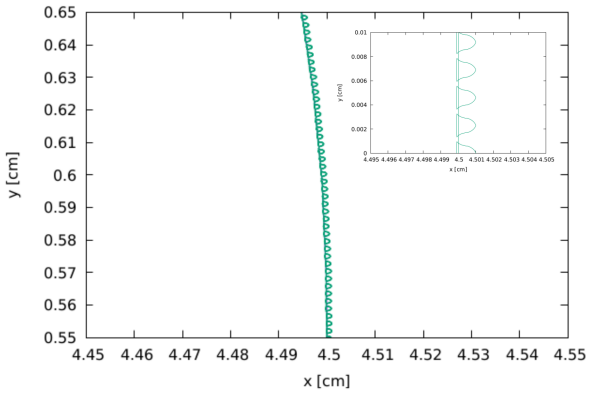

Figure 2: Schematic diagram of the 10-micron grooves on the CESR vacuum chamber wall used in the photon reflectivity model.

SYNCHROTRON RADIATION PHOTON TRACKING CALCULATION

An essential tool in this study is the photon-tracking calculation Synrad3D [6]. It provides for the generation of individual photons radiated by the positron beam, and incorporates a user-defined 3D model of the vacuum chamber to model the reflection and absorption of photons using the Bmad library [7] and X-ray data from an LBNL database [8]. Figure 1 shows a plan view of photon trajectories in a region of the CESR ring which includes X-ray beamline exit windows at which incident photons are not included in the tally of electron-producing photon strikes.

Photon reflectivity plays a crucial role in electron cloud buildup, since it determines the distribution of photon absorption sites around the ring. Absent photon reflectivity, few photons could be absorbed on the top and bottom of the beampipe, where photoelectron production is the primary source of cloud generation in the vertical plane containing the beam.

A micro-groove structure on the surface of the vacuum chamber, arising from the beampipe extrusion process, has been measured using atomic force microscopy and studied in X-ray beams as well [3]. These grooves are roughly parallel to the beam axis and understood to be caused by the beampipe extrusion process. Their effect is taken into account separately from the 100-nm surface roughness used in the diffuse scattering in Synrad3D, by incorporating the groove structure into the beampipe model. Figure 2 shows a diagram of the modeled grooves used in the photon-tracking simulation, and Fig. 3 shows the effect of the grooves on the photon tracks.

Figure 4 shows the result of the enhancement in larger reflection angles. The absorbed photon rate on the top and bottom of the beampipe increases by a factor of about three.

The reflectivity is also critically dependent on the material composition of the vacuum chamber wall. Figure 5 shows the fraction of photons reflected as a function of photon energy for a 5° grazing angle for aluminum with or without

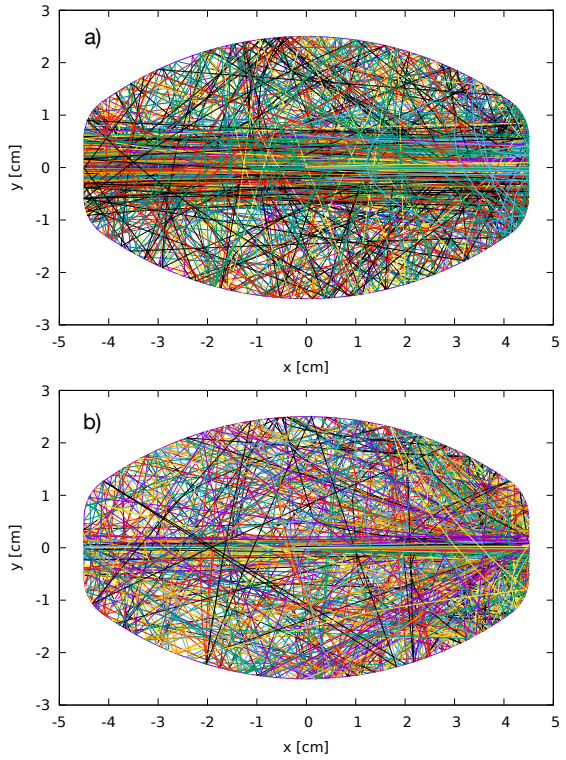

Figure 3: Photon tracking a) without and b) with grooves. The groove pattern results in greatly enhanced scattering out of the horizontal mid-plane. The apparent curvature in the tracks is a consequence of the longitudinal bend in the reference trajectory in the dipole.

C and CO surface layers. In validating our modeling studies, we have chosen to use the 5-nm CO layer, as in Ref. [3].

The photon tracking simulation identifies 10^6 locations around the CESR ring where photons are absorbed, along with the energy and incident angle of the photon. Figure 6 shows the linear density of absorption sites around the 768-m-circumference CESR ring,as well as the energy distribution of the absorbed photons and the number of reflections prior to absorption.

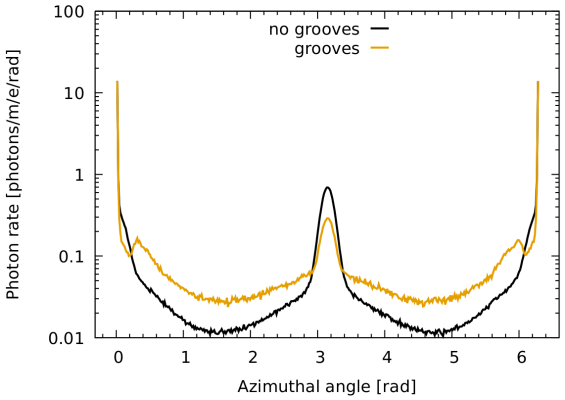

Figure 4: Comparison of the azimuthal absorption location of the absorbed photons when the micro-grooves are introduced in the CESR vacuum chamber geometry. The azimuthal angle is defined to be 180° in the midplane on the inside of the ring.

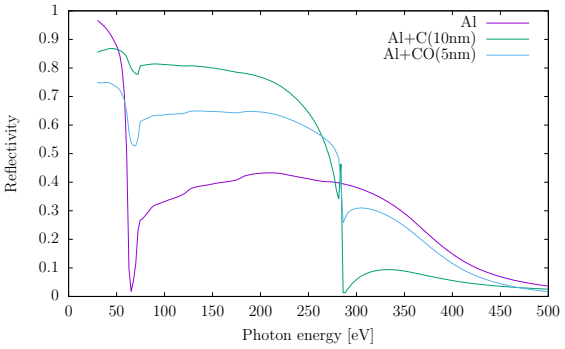

Figure 5: Smooth-surface photon reflectivity versus photon energy for aluminum, aluminum with a 10-nm carbon layer, and aluminum with a 5-nm carbon monoxide layer, for photons incident at a 5° grazing angle. The data were obtained from the LBNL database [8].

Only reflected photons strike the top, bottom and inner walls of the vacuum chamber. The typical number of reflections before absorption depends on the transverse azimuthal Φ_{180} angle of the absorption site location, where Φ_{180} ranges from $-180°$ to $+180°$ with its origin in the mid-plane on the outside of the ring. Figure 7 a) shows the dependence of the average number of reflections prior to absorption on this angle. Figure 7 b) shows the average number of prior reflections of the photons absorbed on the outer wall of the chamber. Figures 7 c), d) and e) show the distributions in the number of prior reflections for the azimuthal ranges $|\Phi_{180}| < 1.5°$, $1.5 < |\Phi_{180}| < 165°$, and $|\Phi_{180}| > 165°$, respectively. For $|\Phi_{180}| < 1.5°$, 83% of the photons were not reflected prior to absorption.

Due to the correlation of azimuthal angle with number of reflections, and the energy dependence of the photon reflectivity, we anticipate a correlation of photon energy with azimuthal angle. The dependence of absorbed photon energy on azimuth is shown in detail in Fig. 8. And since the probability for electron emission depends on photon energy,

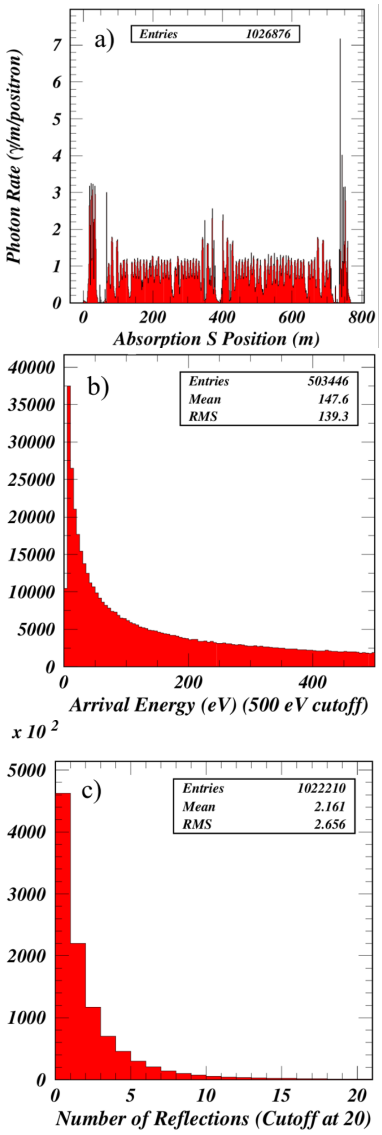

Figure 6: Distributions of absorbed photons in a) location along the CESR ring, b) photon energy and c) number of prior reflections.

we find that the effective quantum efficiency can depend strongly on azimuthal angle.

Figures 8 d), e), and f) illustrate the reasoning for choosing three distinct azimuthal regions when providing electron production energy distributions to the electron cloud buildup simulation. The average energy of the absorbed photons in the azimuthal ranges $|\Phi_{180}| < 1.5°$, $1.5° < |\Phi_{180}| < 165°$ and $|\Phi_{180}| > 165°$ is 2987 eV, 195 eV and 343 eV, respectively, averaged over the full ring.

We will see below in the section on the Geant4 simulations that the photoelectron production energy depends strongly on the angle of incidence of the photon on the chamber wall. Figures 9 and 10 show details of the photon angle distributions as functions of azimuthal impact location, summed over the field-free and dipole regions of the ring, respectively. The distributions in photon angle of incidence on

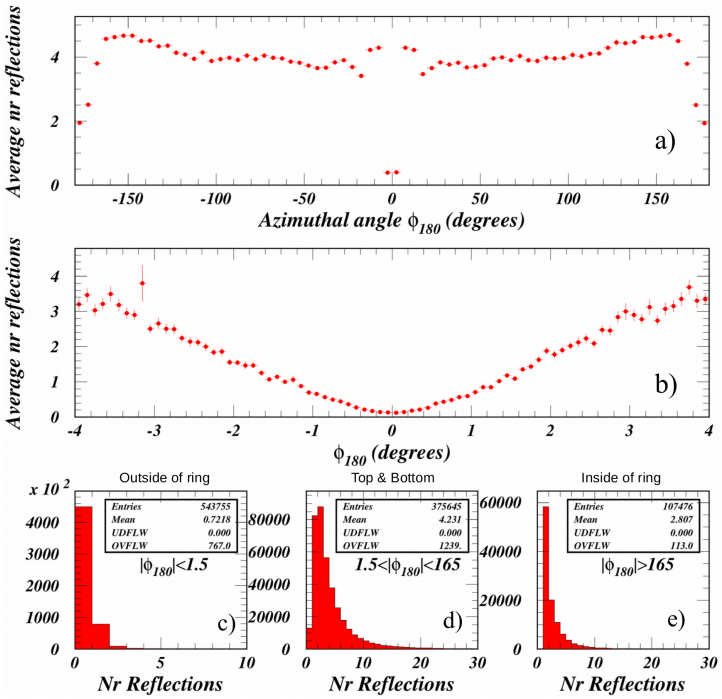

Figure 7: Average number of prior reflections for absorbed photons summed over the full ring a) as a function of the azimuthal location on the vacuum chamber wall, Φ_{180}, b) in the narrow range $\Phi_{180} < 4°$. The distribution in the number of reflections are shown for the three azimuthal regions c) $|\Phi_{180}| < 1.5°$, d) $1.5 < |\Phi_{180}| < 165°$, and e) $|\Phi_{180}| > 165°$.

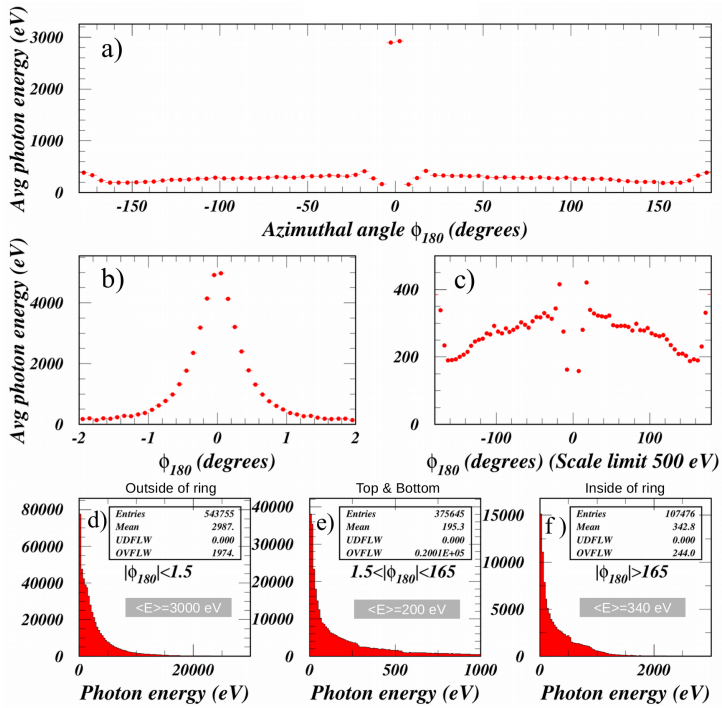

Figure 8: Average energy of the absorbed photons summed over the full ring a) as a function of the azimuthal location on the vacuum chamber wall, Φ_{180}, b) in the narrow range $\Phi_{180} < 2°$, a region rich in unreflected photons, and c) the full azimuthal range, but with the vertical scale limited to a maximum of 500 eV in order to show details of the energy distribution for multiply reflected photons. The photon energy distributions are also shown for the three azimuthal regions for which electron energy distribution were provided to the electron cloud buildup simulation: d) $|\Phi_{180}| < 1.5°$, d) $1.5 < |\Phi_{180}| < 165°$, and f) $|\Phi_{180}| > 165°$.

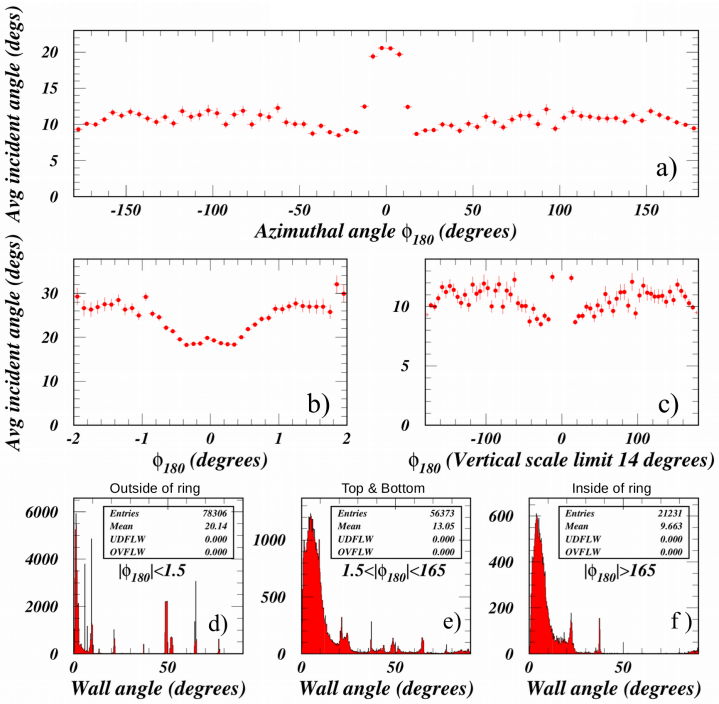

Figure 9: Average angle of incidence $<\theta_\gamma^{inc}>$ of the absorbed photons summed over the field-free regions of the CESR ring a) as a function of the azimuthal location on the vacuum chamber wall, Φ_{180}, b) in the narrow range $\Phi_{180} < 2°$, and c) the full azimuthal range, but with the vertical scale limited to a maximum of 14° in order to show details of the angular distribution for multiply reflected photons. These distributions are also shown for the three azimuthal regions c) $|\Phi_{180}| < 1.5°$, d) $1.5 < |\Phi_{180}| < 165°$, and f) $|\Phi_{180}| > 165°$.

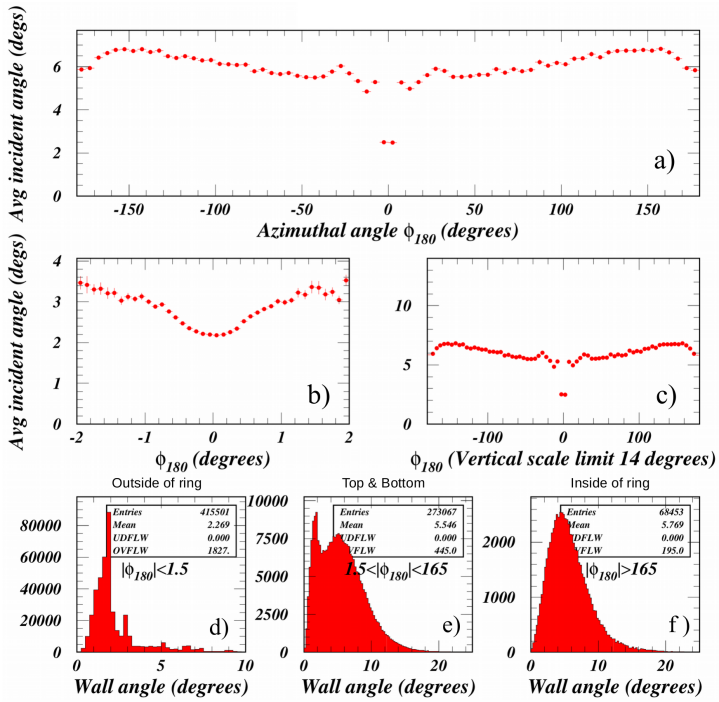

Figure 10: Average angle of incidence $<\theta_\gamma^{inc}>$ of the absorbed photons summed over the dipole regions of the CESR ring a) as a function of the azimuthal location on the vacuum chamber wall, Φ_{180}, b) in the narrow range $\Phi_{180} < 2°$, and c) the full azimuthal range, but with the vertical scale limited to a maximum of 14° in order to show details of the angular distribution for multiply reflected photons. These distributions are also shown for the three azimuthal regions c) $|\Phi_{180}| < 1.5°$, d) $1.5 < |\Phi_{180}| < 165°$, and f) $|\Phi_{180}| > 165°$.

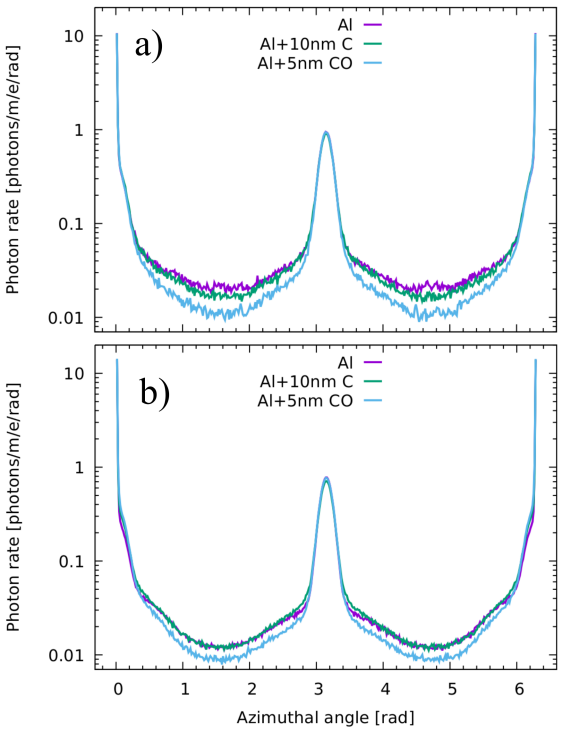

Figure 11: Azimuthal distribution of photon absorption rate averaged over a) field-free and b) dipole regions of the CESR ring.

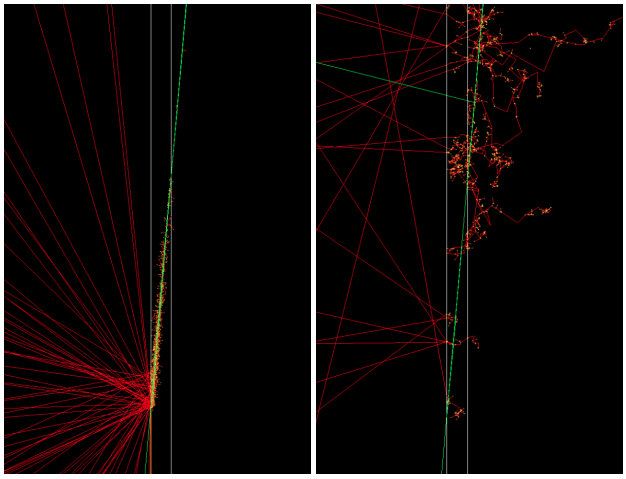

Figure 12: Tracks from incident photons (green), initially traveling left to right, and subsequently generated electrons (red) in the Geant4 simulation for photon energies of 30 eV (left) and 2 keV (right). Low-energy photons interact primarily with the 5-nm CO layer, while the higher energy photons interact in the aluminum. Electrons produced by photoeffect reach the interior of the vacuum chamber via rescattering, while those produced radially symmetrically by atomic de-excitation processes can exit the wall more directly.

the vacuum chamber wall are very different for dipole and field-free regions, with dramatic consequences for the average quantum efficiency. Generally the photons absorbed in the field-free regions have been multiply reflected and are of lower energy, which enhances the quantum efficiency. However, details of the vacuum chambers, such as gate valves, sliding joints and exit windows result in a complicated pattern of photon incident angles around the ring.

The photon tracking simulation thus provides the longitudinal and transverse location, and incident angle and energy on a photon-by-photon basis. Figure 11 shows the distribution in transverse azimuthal location of absorbed photons, averaged separately over the field-free and dipole regions of the ring.

GEANT4 SIMULATION RESULTS

Significant progress in simulating low-energy electromagnetic processes has been achieved over the past decade in the Geant4 simulations toolkit [9, 10], including both photoeffect and atomic de-excitation processes in a wide variety of materials [11].

Quantum efficiency

In order to determine the azimuthal dependence of the quantum efficiency, we subdivide the vacuum chamber wall into 720 azimuthal bins. The distribution of photons absorbed in each bin is determined by the photon tracking code. Given a sample of photon energies and angles of incidence, the Geant4 code is used to generate 10^5 photoabsorption events, determining the rate of emitted electrons summed over the bin. Examples of such events are shown in Fig. 12.

We thus obtain a value for the electron production rate specific to the photon incident angle and energy distribution in each azimuthal bin, including (relatively rare) multi-electron production events. Figure 13 shows the detail with which Geant4 calculates average electron production rates for various wall materials.

The dependence of the quantum efficiency on the incident angle of the absorbed photon is very strong in the Geant4 modeling, as illustrated in Fig. 14, favoring more grazing angles. We recall that the average incident angle of the absorbed photons in the azimuthal ranges $|\Phi_{180}| < 1.5°$, $1.5° < |\Phi_{180}| < 165°$ and $|\Phi_{180}| > 165°$ is 20.14°, 9.66°, and 13.05° (2.27°, 5.77°, and 5.55°), in the field-free (dipole) regions, respectively.

Figure 15 shows azimuthal distributions in average quantum efficiency obtained from the Geant4 simulations for the 5.3 GeV positron beam. The resulting distributions in electron production rate in the 720 azimuthal bins provided to the electron cloud buildup simulation code for the case of the aluminum chamber with the 5-nm CO layer are shown in Fig. 16. The integrated rates are 0.0454 and 0.0839 electrons/m/positron for the field-free and dipole regions, respectively. Prior to this work, these two quantities and two values for effective average reflectivity around the ring served as input to the cloud buildup simulations.

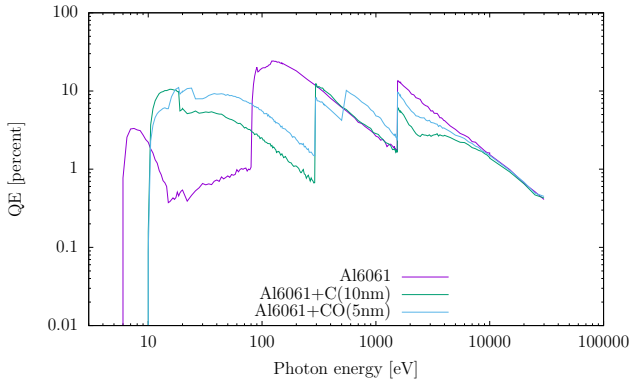

Figure 13: Quantum efficiency versus photon energy for photons incident at a 5-degree grazing angle, for the aluminum alloy 6061, aluminum with carbon layer, and aluminum with carbon monoxide layer. The quantum efficiency is sharply enhanced at photon energies above various atomic shell transition energies, such as aluminum L_{II} and L_{III} (73 eV), carbon K (284 eV), oxygen K (543 eV), and aluminum K (1560 eV).

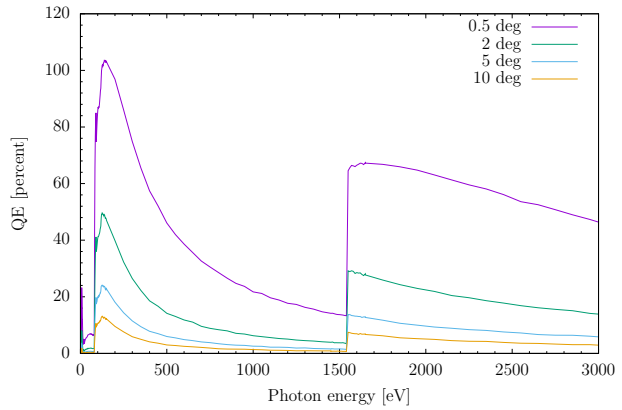

Figure 14: Quantum efficiency versus photon energy for photons incident at grazing angles between 0.5° and 10° for the aluminum alloy 6061 as modeled in Geant4.

Photoelectron energy distributions

In addition to the determination of quantum efficiencies, we obtain energy distributions of the photoelectrons in each of the three azimuthal regions $|\Phi_{180}| < 1.5°$, $1.5 < |\Phi_{180}| < 165°$ and $|\Phi_{180}| > 165°$ by simulating 10^6 events in each region, again using absorbed photons from the photon tracking code. These distributions are shown for the CESR dipole regions in Fig. 17. Within each of these three angular regions, electron energy distribution is roughly independent of azimuthal angle. The quantum efficiency values and photoelectron energy distributions are obtained separately for the field-free and dipole regions of the ring, so a total of 1.5×10^8 simulated events are obtained for use in the electron cloud buildup simulations.

The simulation results for the photoelectron energy distributions show substantial high-energy tails, resulting in an average energy in the azimuthal ranges $|\Phi_{180}| < 1.5°$,

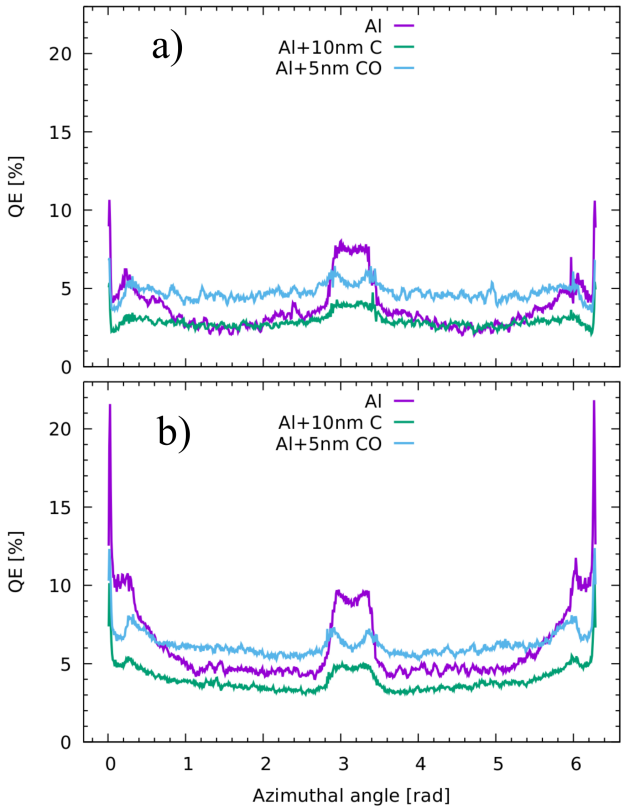

Figure 15: Azimuthal dependence of quantum efficiency for a) field-free regions and b) dipole regions of the CESR ring for aluminum and aluminum with a carbon or carbon monoxide layer.

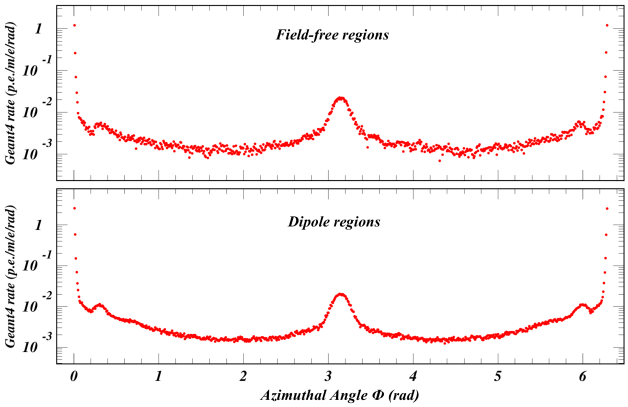

Figure 16: Electron production rates as a function of azimuthal production location on the vacuum chamber wall for a) field-free regions and b) dipole regions in units of electrons/m/positron/radian.

$1.5° < |\Phi_{180}| < 165°$ and $|\Phi_{180}| > 165°$ of 761 eV, 99 eV and 120 eV (662 eV, 78 eV and 110 eV), for the field-free (dipole) regions, respectively. These three energy distributions, as well as the average electron production rates in 0.5 degree azimuthal bins are provided separately for the field-free and dipole regions of the CESR ring as input to the electron cloud buildup calculations described in [4]. Our modeling has shown that it is important and, to an accu-

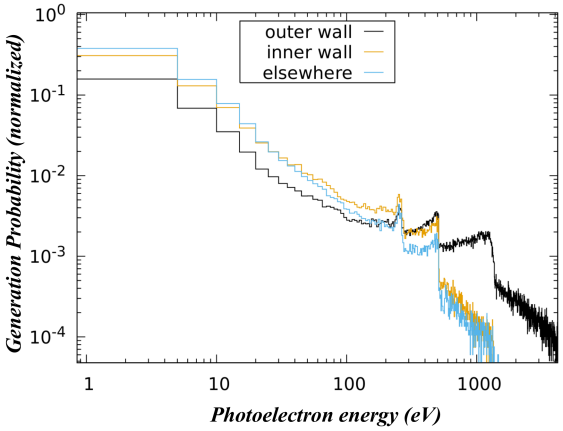

Figure 17: Electron energy distributions for production locations on the outside wall, inside wall, and elsewhere along the vacuum chamber summed over the dipole regions. Since lower energy photons are more likely to be reflected, the inner wall and elsewhere (including top & bottom) are struck by lower energy photoelectrons than is the outer wall at the midplane. These distributions are used as input to the electron cloud build-up simulations [4].

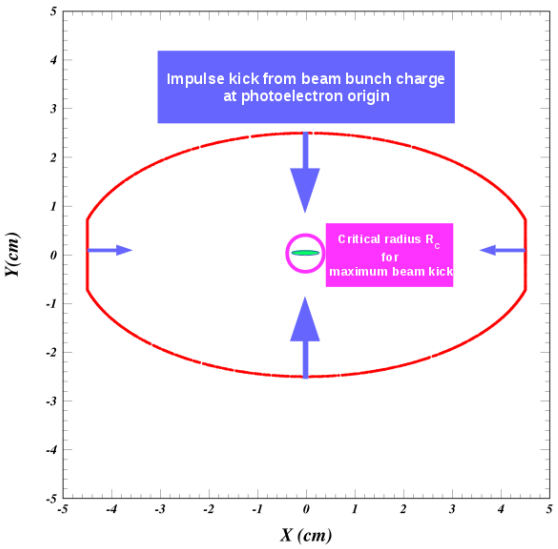

Figure 18: Schematic diagram of the laterally truncated elliptical CESR vacuum chamber illustrating the beam kicks for an electron produced at the wall and the radius R_C at which an electron receives the maximum kick.

racy acceptable for comparing to measurements, sufficient to differentiate between the field-free and dipole-occupied regions, comprising 17% and 66% of the ring, respectively. The contribution to the simulated tune shift values from the remaining 17% of the ring are at the level of a percent.

The electron production energy distribution is of particular importance, since the dependence of, for example, betatron tune shifts varies dramatically, with beam bunch population between 0.6×10^{10} and 9.5×10^{10} positrons/bunch. The associated beam kicks for electrons produced at the wall can be comparable to the electron production energies. These Geant4 simulations show that the primary sources of high-energy electrons (>100 eV) are atomic de-excitation processes, such as the Auger effect. The contribution of such electrons to cloud development is greater at lower bunch population, since their kinetic energies provide for higher subsequent secondary yields, replacing the effect of strong momentum kicks from the beam bunches. Figure 18 shows a schematic diagram of the CESR vacuum chamber illustrating the beam kick quantities in Table 1. In an impulse approximation, the beam bunch charge integrated over the bunch passage gives a momentum kick to an electron produced at the wall [13]. An electron generated simultaneously with the passage of the longitudinal center of the bunch, for example, receives half of this kick. We present the kick as the kinetic energy gained by the electron during the bunch passage. The elliptical shape of the vacuum chamber results

Table 1: Parameters for the acceleration provided by a positron bunch to a cloud electron located at the vacuum chamber wall on the X or Y axes. These examples correspond to the CesrTA measurements of betatron tune shifts [4] as well as for the predictions for the 6.0 GeV upgrade of CESR [5, 12]. The total kick values are given as the kinetic energy of the electron following acceleration by the positron bunch in the impulse approximation. The direct and image kick values are signed according to whether they add or subtract from the total kick.

Beam energy (GeV)		2.085		5.289			6.000
Beam size $\sigma_X \times \sigma_Y \times \sigma_Z$ (mm)		$0.735 \times 0.030 \times 9.2$		$1.44 \times 0.139 \times 15.8$			$1.44 \times 0.139 \times 15.8$
Bunch population (10^{10})		0.64	1.12	3.25	6.66	9.54	3.52
Critical radius R_C (mm)		0.73	0.96	2.14	3.1	3.7	2.2
Maximum kick (keV)		1.2	2.5	3.5	9.0	14.1	3.9
X=4.5 Y=0 cm	Direct kick (eV)	0.16	0.5	41.8	17.6	36	4.9
	Image kick (eV)	-0.14	-0.44	-41.3	-15.6	-32	-4.3
	Total kick (eV)	0.02	0.06	0.5	2.0	4	0.6
X=0 Y=2.5 cm	Direct kick (eV)	0.50	1.6	13.4	56	115	15.8
	Image kick (eV)	0.60	1.6	13.9	59	120	16.3
	Total kick (eV)	1.10	3.2	27.3	115	235	32.1

an increased (reduced) kick in the vertical (horizontal) plane from the image charges ensuring the boundary conditions at the wall. The transverse beam size determines the critical radius R_C at which a cloud electron receives the maximum kick during bunch passage. Table 1 shows these values for the bunch populations and beam sizes for which CESRTA betatron tune shift measurements are available, and also for the parameters of the upgraded Cornell High Energy Synchrotron Source to be commissioned at 6 GeV in 2019 [14]. Since the time interval between bunch passages is 14 ns, the kick corresponding to the horizontal (vertical) wall-to-wall traversal prior to the arrival of the succeeding bunch is 36 eV (9 eV). Another relevant consideration in this regard is that the secondary yield curve is maximum for an electron at perpendicular incidence carrying an energy of about 300 eV.

The wide range of beam kick values causes a great variation in the cloud dynamics as a function of bunch population and transverse beam size as evidenced in the patterns of tune shifts observed along a train of positron bunches [4]. The interplay between these kicks and the electron production energy distribution is an important aspect of the cloud buildup modeling.

Summary table

Table 2 compares the results of the photon tracking and photoelectron generation simulations for the 2.1, 5.3, and 6.0 GeV CESR lattices.

SUMMARY

We have implemented a Geant4-based post-processor for the Synrad3D photon-tracking code in order to obtain accurate values for the dependence of quantum efficiency on production location and a realistic photoelectron energy spectrum. We find that the quantum efficiency and electron production kinematics depend strongly on the vacuum chamber wall characteristics as well as on the location of photon absorption sites around the ring and on the incident photon grazing angles and energies. The coding tools provided by this work can be generalized to a wide variety of accelerators and vacuum chamber geometries and materials. For example, an initial study of the 97-km-circumference Future Circular Collider operating at 45.6 GeV with a NEG-coated copper chamber finds high quantum efficiencies (typically 20%, but reaching 70% in some regions) due to the small grazing angles of the photon wall strikes. More work is needed to assess quantitatively the effectiveness of the antechambers and the photon stops. The results of this study can be used to provide important input to electron cloud buildup modeling codes used at a wide variety of accelerators for purposes of understanding phenomena including betatron tune shifts, emittance growth, RF phase shifts, heat loads, and various types of instabilities.

ACKNOWLEDGMENTS

We thank E. Belli for useful information on the Future Circular Collider and K. Oide for making the FCC lattice available. We also wish to acknowledge important contributions from the technical staffs of the Wilson Laboratory. This work is supported by National Science Foundation and by the US Department of Energy under contract numbers PHY-0734867, PHY-1002467 and DE-FC02-08ER41538 and DE-SC0006505.

Table 2: Results from the photon tracking and photoelectron generation simulations for the CESRTA tune shift measurements at 2.1 and 5.3 GeV and for the 6.0 GeV CESR upgrade, where the new combined-function (C-F) magnet and undulator regions are modeled separately in addition to the field-free and dipole regions.

Beam energy (GeV)	2.085				
	Entire ring	Field-free	Dipole	C-F magnet	Undulator
Ring fraction (%)		16.5	65.6		
Number of photons	1064932	171987	710002		
Photon absorption rate (γ/m/e+)	0.765	0.378	0.370		
Number of electrons		3653092	4536786		
Electron production rate (p.e./m/e+)		0.02137	0.03144		
$\langle\theta_\gamma^{\rm inc}\rangle$ on outside of ring (eV)	3.02	24.4	2.71		
$\langle\theta_\gamma^{\rm inc}\rangle$ on top and bottom (eV)	5.99	12.26	5.59		
$\langle\theta_\gamma^{\rm inc}\rangle$ on inside of ring (eV)	6.08	10.55	6.32		
$\langle E_\gamma\rangle$ on outside of ring (eV)	1443	867	1434		
$\langle E_\gamma\rangle$ on top and bottom (eV)	132	121	121		
$\langle E_\gamma\rangle$ on inside of ring (eV)	297	319	202		
$\langle E_{\rm electron}\rangle$ on outside of ring (eV)		416	331		
$\langle E_{\rm electron}\rangle$ on top and bottom (eV)		118	110		
$\langle E_{\rm electron}\rangle$ on inside of ring (eV)		352	115		

Beam energy (GeV)	5.289				
	Entire ring	Field-free	Dipole	C-F magnet	Undulator
Ring fraction (%)		16.5	65.6		
Number of photons	1026876	155910	757021		
Photon absorption rate (γ/m/e+)	1.604	0.728	0.876		
Number of electrons		3740767	4552831		
Electron production rate (p.e./m/e+)		0.0454	0.0839		
$\langle\theta_\gamma^{\rm inc}\rangle$ on outside of ring (eV)	2.40	20.14	2.27		
$\langle\theta_\gamma^{\rm inc}\rangle$ on top and bottom (eV)	6.18	9.66	5.77		
$\langle\theta_\gamma^{\rm inc}\rangle$ on inside of ring (eV)	5.93	13.05	5.55		
$\langle E_\gamma\rangle$ on outside of ring (eV)	2987	3079	2929		
$\langle E_\gamma\rangle$ on top and bottom (eV)	195	172	198		
$\langle E_\gamma\rangle$ on inside of ring (eV)	343	340	342		
$\langle E_{\rm electron}\rangle$ on outside of ring (eV)		761	662		
$\langle E_{\rm electron}\rangle$ on top and bottom (eV)		99	78		
$\langle E_{\rm electron}\rangle$ on inside of ring (eV)		120	110		

Beam energy (GeV)	6.000				
	Entire ring	Field-free	Dipole	C-F magnet	Undulator
Ring fraction (%)		60.4	16.7	3.7	2.9
Number of photons	5006978	764360	3264221	336558	78187
Photon absorption rate (γ/m/e+)	3.77	0.833	0.973	1.655	0.3076
Number of electrons		3881357	4583462	4650963	4493193
Electron production rate (p.e./m/e+)		0.0603	0.0956	0.1241	0.0317
$\langle\theta_\gamma^{\rm inc}\rangle$ on outside of ring (eV)	2.10	11.91	2.00	2.32	1.08
$\langle\theta_\gamma^{\rm inc}\rangle$ on top and bottom (eV)	5.85	11.55	5.50	4.05	6.17
$\langle\theta_\gamma^{\rm inc}\rangle$ on inside of ring (eV)	6.00	8.46	5.62	5.99	5.40
$\langle E_\gamma\rangle$ on outside of ring (eV)	3961	4346	3506	5949	7867
$\langle E_\gamma\rangle$ on top and bottom (eV)	200	174	206	181	151
$\langle E_\gamma\rangle$ on inside of ring (eV)	388	376	365	434	526
$\langle E_{\rm electron}\rangle$ on outside of ring (eV)		889	747	809	1291
$\langle E_{\rm electron}\rangle$ on top and bottom (eV)		108	86	287	218
$\langle E_{\rm electron}\rangle$ on inside of ring (eV)		136	115	168	187

REFERENCES

[1] F. Zimmermann, "Electron-Cloud Effects in Past & Future Machines—Walk through 50 Years of Electron-Cloud Studies," in *Proceedings of ECLOUD 2012: Joint INFN-CERN-EuCARD-AccNet Workshop on Electron-Cloud Effects, La Biodola, Elba, Italy*, R. Cimino, G. Rumolo & F. Zimmermann, Eds., CERN, Geneva, Switzerland (2013), CERN-2013-002, p. 9–17.

[2] "The CESR Test Accelerator Electron Cloud Research Program: Phase I Report," Tech. Rep. CLNS-12-2084, LEPP, Cornell University, Ithaca, NY (Jan. 2013).

[3] G. F. Dugan *et al.*, "Measurements of X-Ray Scattering from Accelerator Vacuum Chamber Surfaces, and Comparison with an Analytical Model," *Phys. Rev. ST Accel. Beams* **18**, 040704 (Apr. 2015).

[4] S. Poprocki *et al.*, "Measurements and simulations of electron-cloud-induced tune shifts and emittance growth at CesrTA," in *Proceedings of ECLOUD 2018: Joint INFN-CERN-EuroCirCol-ARIES-APEC Workshop on Electron-Cloud Effects, La Biodola, Elba, Italy*.

[5] K. Rowan, "Revised Stability Predictions for CHESS-U due to Electron-Cloud-Based Tune Shifts," Tech. rep.

[6] G. Dugan & D. Sagan, "Simulating synchrotron radiation in accelerators including diffuse and specular reflections," *Phys. Rev. Accel. Beams* **20**, 020708 (Feb. 2017).

[7] D. Sagan, "Bmad: A Relativistic Charged Particle Simulation Library," *Nucl. Instrum. Methods Phys. Res.* **A558**, p. 356–359 (Mar. 2006).

[8] B. L. Henke, E. M. Gullikson & J. C. Davis, "X-Ray Interactions: Photoabsorption, Scattering, Transmission, and Reflection at E = 50–30,000 eV, Z = 1–92," *At. Data Nucl. Data Tables* **54**, p. 181–342 (Jul. 1993).

[9] S. Agostinelli *et al.*, "Geant4—a simulation toolkit," *Nuclear Instruments and Methods in Physics Research Section A: Accelerators, Spectrometers, Detectors and Associated Equipment* **506**, p. 250 – 303 (2003).

[10] J. Allison *et al.*, "Recent developments in Geant4," *Nuclear Instruments and Methods in Physics Research Section A: Accelerators, Spectrometers, Detectors and Associated Equipment* **835**, p. 186 – 225 (2016).

[11] S. Incerti *et al.*, "Simulation of Auger electron emission from nanometer-size gold targets using the Geant4 Monte Carlo simulation toolkit," *Nuclear Instruments and Methods in Physics Research Section B: Beam Interactions with Materials and Atoms* **372**, p. 91 – 101 (2016).

[12] J. Crittenden *et al.*, "Electron Cloud Simulations for the Low-Emittance Upgrade at the Cornell Electron Storage Ring," in *NAPAC2016: Proceedings of the North American Particle Accelerator Conference, Chicago, IL* (2016), Paper TUPOB23.

[13] J. S. Berg, "Energy Gain in an Electron Cloud During the Passage of a Bunch," LHC Project Report 97 (Jul. 1997), `https://cds.cern.ch/record/692004/files/project-note-97.pdf`.

[14] J. Shanks *et al.*, "Accelerator Design for the CHESS-U Upgrade," (Oct. 2018), `https://arxiv.org/abs/1810.06557`.

PRELIMINARY RESULTS OBTAINED WITH THE LHC VACUUM PILOT SECTOR

E. Buratin[1], V. Baglin, B. Henrist, CERN, Geneva, Switzerland
[1]also at EPFL, Lausanne, Switzerland

Abstract

The Large Hadron Collider (LHC) is affected by electron cloud that reduces the quality of the beam, provokes instabilities, and increases the residual-gas pressure and heat load in the vacuum chambers. Synchrotron radiation, via photoelectron emission, plays also an important role in the electron cloud build-up. An innovative room temperature Vacuum Pilot Sector (VPS) was installed in a straight section of the LHC to investigate these phenomena *in situ* [1]. The VPS is instrumented to monitor the electron cloud and its interaction with different surfaces. Currently the system is testing technical surfaces such as copper, amorphous carbon coating, and NEG thin films.

INTRODUCTION

The objective of the VPS system is to investigate the electron cloud (EC) and synchrotron radiation (SR) effects on the LHC's vacuum system.

Free electrons are generated in the beampipe by several mechanisms. Primary electrons can be produced by protons impinging on both beam pipes and residual gas. These primary electrons are accelerated by the electric field of the bunched beam towards the vacuum chamber walls. While impinging on the surfaces, depending on their energy and direction, the primaries can be reflected and/or release secondary electrons. The amount of secondary electrons is defined by a surface property, called secondary electron yield (SEY). If the SEY is larger than one, the number of free electrons inside the beam pipe increases.

Also, the beam structure and parameters play an important role for the electron cloud build-up. With short bunch spacing and high bunch population, free electrons can survive between bunches. Due to this, the electron density grows at each bunch passage and the first free electrons produce a cloud. This process is called multipacting [2, 3].

During the energy ramp-up, the impinging SR generates photoelectrons from the beam pipe material that contributes to the EC build-up. Depending on the photoelectron yield (PEY) and the SEY of the surface, these additional electrons can be the only measurable electron signal, trigger the multipacting process, or simply sustain the existing EC.

We examine the dynamics of the EC and SR by measuring electrical signals, pressures, and temperatures in a dedicated system. The measurements have been performed with proton beams at energies ranging from 450 GeV at injection to the present LHC collision value (6.5 TeV). We also present some preliminary time dependent data of the electron cloud build-up as measured by an oscilloscope.

VPS SYSTEM

The 18 m long VPS is a room temperature vacuum system installed in a field free area of the LHC long straight section (Fig. 1). In this part of the accelerator, the LHC protons beams circulate in opposite directions inside two separated beam pipes of 80 mm inner diameter.

The system consists of four stations, each composed by a vacuum vessel into which a liner is inserted. Surface modifications can be applied to the internal wall of the liners. In the first station, a 1.5-2 μm thick non-evaporable getter (NEG) thin film, deposited on Cu, is studied. This film was activated in the laboratory at 230°C for one day, vented with nitrogen, and finally installed in the VPS after a limited exposure time to the air without any subsequent activation. For this reason, it is called in this context *ex situ* NEG, where *ex situ* means that the film was not activated *in situ* as the usual practice for such a material would require. The Cu liners of the second station are coated with a-C, 400-600 nm thick, deposited by magnetron sputtering. The liners of the last two stations are made of uncoated copper OFE tubes.

All liners were mildly baked at 80° C to degas part of the water adsorbed on the walls and in the Kapton wires of the in-vacuum instruments. Distributed and localised pumping systems are installed to reduce the mutual pressure influence between consecutive stations. Five activated NEG coated buffers are inserted in order to pump hydrogen, carbon monoxide and dioxide. Localised ion pumps with additional NEG cartridges are embedded at the extremities of each station to increase the pumping speed for the above-mentioned species and to pump methane and noble gasses, which are not pumped by the NEG.

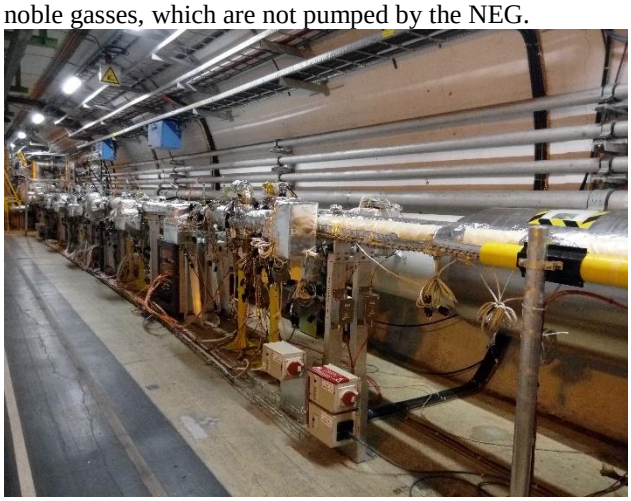

Figure 1: VPS installation in the LHC tunnel.

In each station, several detectors are installed in order to characterise the EC. Shielded and unshielded pick-ups are used to monitor the electrical signals of the EC and the beam structure. Ion-trap mass spectrometers (Vacuum Quality Monitor) and ionization gauges (Bayard-Alpert gauges) are installed to measure the partial and total pressures. Calorimeters mounted along the liners are used to quantify the power deposition due to the impedance, EC and SR contributions. Each calorimeter is made of a thin copper plate onto which temperature sensors (PT100) are welded. Kapton coated wires are used to carry the electrical signals to the vacuum feedthrough. Cables are used to transport all the signals in a service gallery where the control and monitoring instruments are protected from the LHC radiation. A LabVIEW program acquires simultaneously the pick-ups currents, the pressures, the temperatures and the beam parameters.

DYNAMIC OF ELECTRICAL SIGNALS

The typical LHC filling scheme is made in three consecutive steps. First, the beam is injected from the SPS into the LHC in bunches of 10^{11} protons. The bunches are spaced by either 25 or 50 ns. A batch is then formed by a maximum of 72 bunches. The batches are in turn assembled in trains. A maximum of 4 batches can be injected from the SPS into the LHC. Second, when the LHC machine is filled with bunches, the beam energy is ramped up from 450 GeV to 6.5 TeV. Finally, the beam is set in a stable mode during which the protons collide for physics studies.

The analysis presented below compares the case of a copper OFE station, installed into the external beam pipe, with 50 ns and 25 ns bunch spacing. Table 1 gives the main beam parameters of the two fills considered in this study.

Table 1: Beam parameters of the two LHC fills.

Fill name	5980	5979
Bunch spacing [ns]	50	25
Number of bunches	1284	2556
Protons per bunch	$9.13 \cdot 10^{10}$	$1.22 \cdot 10^{11}$
Beam current [A]	0.25	0.51

50 ns bunch spacing

With 50 ns bunch spacing, no EC build up is expected at injection. Free electrons, generated by beam gas ionisation and proton losses, are accelerated during the bunch passage but the distance between bunches is so large that the number of survival electrons is negligible and no multipacting is taking place.

As shown in Figure 2, the measurements during a fill with 50 ns bunch spacing confirm the expectations: no EC current is observed at injection energy. However, above 2.8 TeV, photoelectrons are detected because a significant fraction of impinging photons has an energy above the work function of Cu (4 ÷ 5 eV).

In the absence of multipacting, the electron current measured at 6.5 TeV corresponds to the number of photo-electrons generated and is directly related to the PEY of the surface.

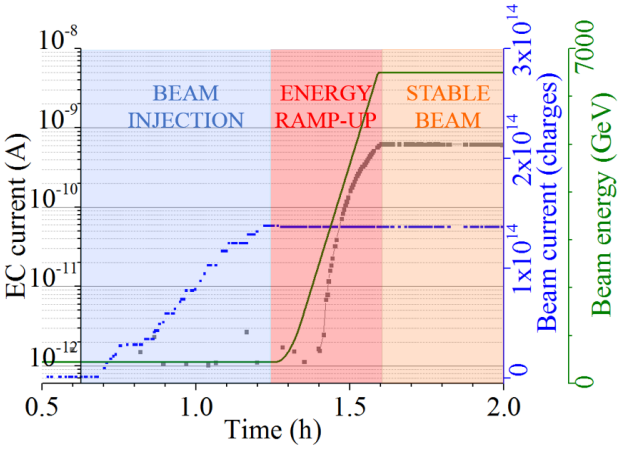

Figure 2: The photoelectron signal of a 50 ns bunch spacing beam, for a copper surface, is displayed in grey in logarithmic scale. The current of beam 1 and the beam energy are displayed in dark blue and dark green, respectively.

25 ns bunch spacing

With 25 ns bunch spacing, EC build-up due to multipacting is expected for a copper surface. During the beam injection, once the multipacting regime starts, the EC current is proportional to the beam current (Figure 3). When the beam injection finishes, the EC signal decreases because the proton beam intensity is reduced by losses.

In order to understand the behaviour of the EC current at the beginning of the energy ramp-up, one must take into account the bunch length parameter, which is inversely proportional to the square root of the beam energy [4]. When the energy ramp-up starts, the bunch length decreases. In LHC, when the bunch length reaches a value below 8 10^{-10} s, longitudinal instabilities arises. Thus, as shown in Figure 3, a RF noise is injected inside the superconducting cavities to increase the bunch length. In the meantime, the beam energy continues to increase, still contracting the bunch. The effect of the bunch length dynamic is also observed on the EC current. Indeed, the shorter the bunch length the higher the energy gained by the electrons kicked by the bunch. Above an energy of few hundreds eV, the electrons tends to penetrate into the surface so deeply that the number of secondary electrons decreases, consequently reducing the multipacting effect.

As previously explained with 50 ns bunch spacing, above 2.8 TeV, photoelectrons provide an additional contribution to the ecloud signals.

At the collision energy, once the LHC is tuned and the parameters set, the proton-proton collisions start. Then, the EC current behaviour is mainly driven by the beam losses.

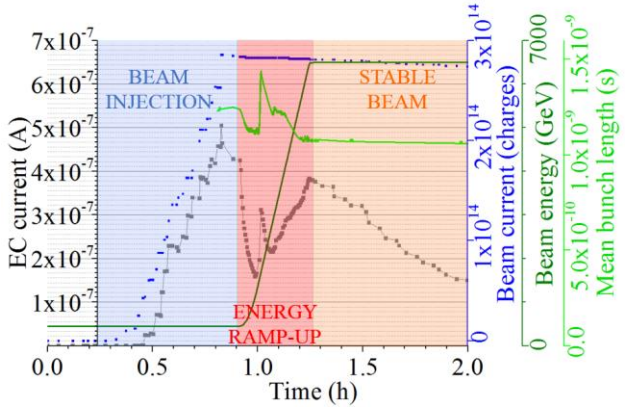

Figure 3: The EC current of a 25 ns bunch spacing beam, for a copper surface, is displayed in grey in linear scale. The current, energy and bunch length of the beam are presented in dark blue, dark green and light green, respectively.

DYNAMICS OF PRESSURE AND TEMPERATURE

Pressure trend

As shown in Fig.4, pressure and the EC current have a similar behaviour. During the beam injection, the pressure increases due to electron stimulated desorption (ESD). During the energy ramp-up, two other sources of gas are added: one due to photon stimulated desorption (PSD) and one caused by the contribution of photoelectrons to ESD.

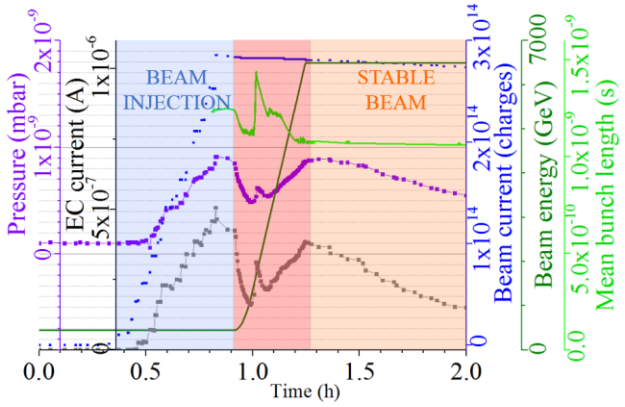

Figure 4: The pressure behaviour of a copper surface for a 25 ns beam is displayed in purple in linear scale. In grey the EC current of the corresponding pick-up is shown. The current, energy and bunch length of the beam are presented in dark blue, dark green and light green, respectively.

Temperature trend

The temperature change, shown in Figure 5, can be understood by taking into account the wall impedance, EC and SR. The calorimeter signal requires about ten minutes to reach a steady state value.

During the injection of a 25 ns spaced beam, EC and resistive wall heat loads are present and they increase linearly with the number of bunches.

The resistive wall power due to surface impedance is given by Eq. (1):

$$P_{RW} = \frac{1}{2\pi R}\Gamma\left(\frac{3}{4}\right)\frac{M}{b}\left(\frac{N_b e}{2\pi}\right)^2\sqrt{\frac{c\rho Z_0}{2}}\sigma^{-\frac{3}{2}} \qquad (1)$$

where $2\pi R$ is the LHC circumference, Γ is the Gamma function, M is the number of bunches, b is the radius of the beam pipe, $N_b e$ is the bunch charge, ρ is the liner resistivity, Z_0 is the free space impedance, σ is the bunch length [5].

However, during the energy ramp-up, below 2.8 TeV, the bunch length dynamic has a big impact on the temperature behaviour. During the bunch length contraction (see between 0.9 h and 1 h in the time axis of Fig. 5), the resistive wall heat load increases. But, the EC heat load resulting from a given electron flux (*i.e.* EC current), and its time evolution, cannot be predicted without a dedicated simulation. Actually, the thermal balance between the impedance and the EC heat loads is, in this case, positive yielding to a temperature increase.

During the energy ramp-up, above 2.8 TeV, there is an additional heat load related to SR and to photoelectrons impinging on the wall.

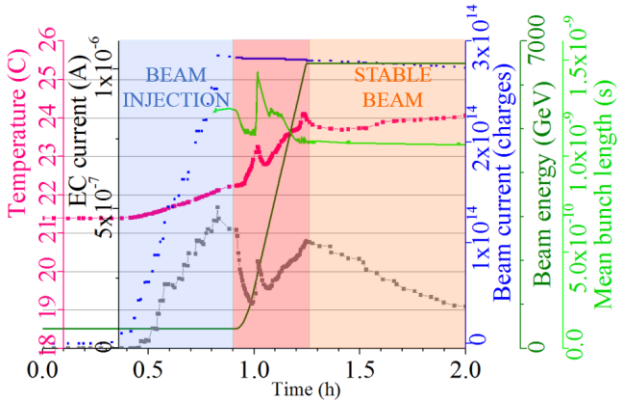

Figure 5: The temperature of a copper surface for a 25 ns bunch spacing beam is displayed in pink. In grey the EC current of the corresponding pick-up is also shown. The current, energy and bunch length of the beam are presented in dark blue, dark green and light green, respectively.

SURFACES COMPARISON

The following analysis compares 50 ns and 25 ns bunch spacing beams for the three surfaces installed in the VPS, i.e. *ex situ* NEG, a-C coating and OFE copper.

50 ns bunch spacing

With 50 ns bunch spacing, in the three samples no EC signal is measured during the beam injection (Figure 6). However, similarly to Figure 2, photoelectrons are detected above 2.8 TeV. Assuming the same SR flux and reflectivity, one concludes that among the three materials a-C coating has a lowest PEY.

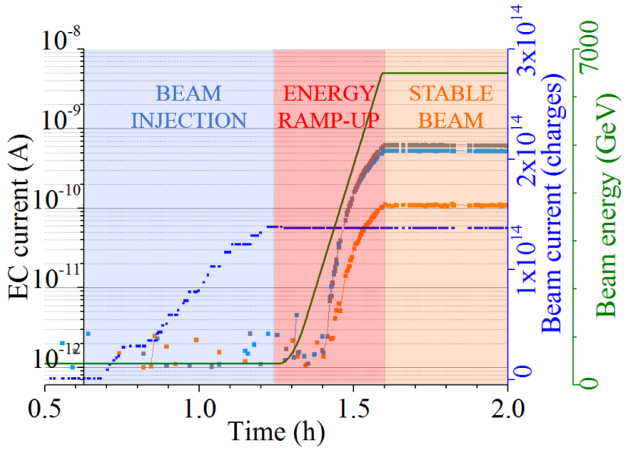

Figure 6: Photoelectrons signals of a 50 ns bunch spacing beam are displayed in logarithmic scale for different surfaces. The electrical signal measured for the copper surface is shown in grey, *ex situ* NEG in light blue, a-C coating in orange. The current of beam 1 and the beam energy are presented in dark blue and dark green, respectively.

25 ns bunch spacing

With 25 ns bunch spacing, during the beam injection at 450 GeV (Figure 7), the EC signal for the copper surface due to beam-induced multipacting is the highest. Due to its larger SEY, the copper surface has an enhanced multipacting effect than *ex situ* NEG coating. For a-C coating, no EC is visible; this confirms that this coating has a much lower SEY than the one of the other two surfaces.

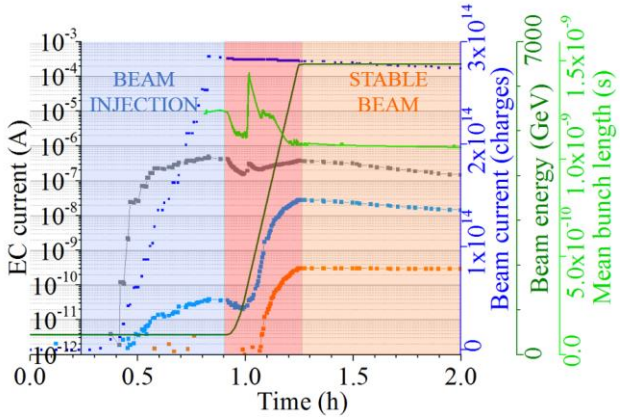

Figure 7: EC signals of a 25 ns bunch spacing beam are displayed in logarithmic scale for different surfaces. The electrical signal read on the copper surface is shown in grey, *ex situ* NEG in light blue, amorphous carbon coating in orange. The current, energy and bunch length of the beam are presented in dark blue, dark green and light green, respectively.

At the beginning of the energy ramp, the bunch length decreases. The aforementioned bunch length dynamic is observed on the pick-ups current when the electron cloud is already present in the vacuum chamber. This is the case for the copper and the *ex situ* NEG sample.

Above 2.8 TeV, the SR generates measurable photoelectrons in each station. In the copper station, the photoelectrons contribute to the existing EC multipacting resulting in a signal above $10^{-7}A$. In the *ex situ* NEG station, photoelectrons largely contribute to the electron cloud, reaching a current of $10^{-8}A$. For a-C coating, only photoelectrons are measurable and the signal reaches $10^{-10}A$.

EC AND SR CONTRIBUTIONS

In order to estimate the contribution of photoelectrons during a fill with 25 ns bunch spacing, a simple calculation has been carried out. The model assumes that the whole current measured with a 50 ns bunch spacing is only due to photoelectrons. Therefore, it is possible to estimate the SR contribution to the total electron current with a 25 ns standard beam.

As shown in Figure 8 and 9 for copper and *ex situ* NEG, after ten hours of circulating beams, the recorded current is mainly due to photoelectrons and tends asymptotically to the photoelectron contribution computed from data of 50 ns bunch spacing beams.

For the a-C coated surface (Figure 10), no EC signal is observed at injection energy with 25 ns bunch spacing. Only the photoelectrons contribution due to SR is observed at 6.5 TeV. The slight discrepancy between the data and the computed photoelectron contribution may be due to the simplicity of our model and measurement accuracy.

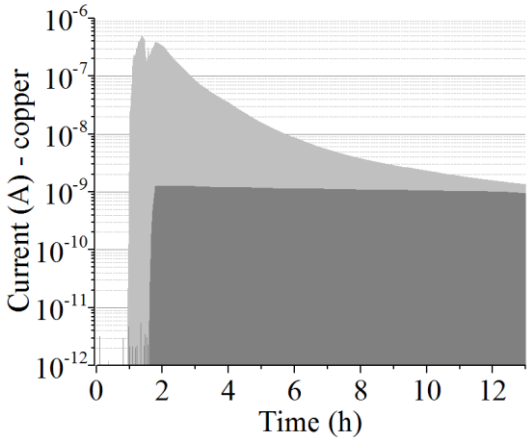

Figure 8: In light grey the EC signal and in dark grey the photoelectrons component of a 25 ns beam for the copper surface.

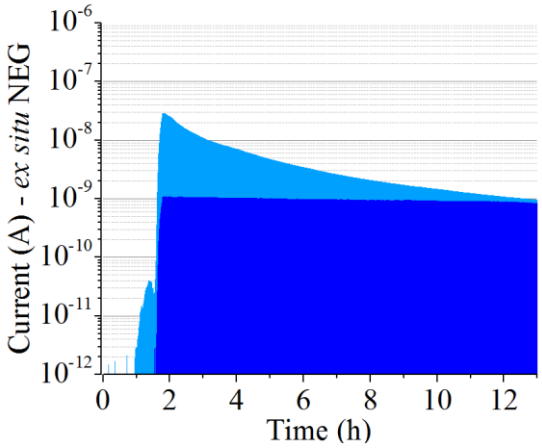

Figure 9: In light blue the EC signal and in dark blue the photoelectrons component of a 25 ns beam for the *ex situ* NEG surface.

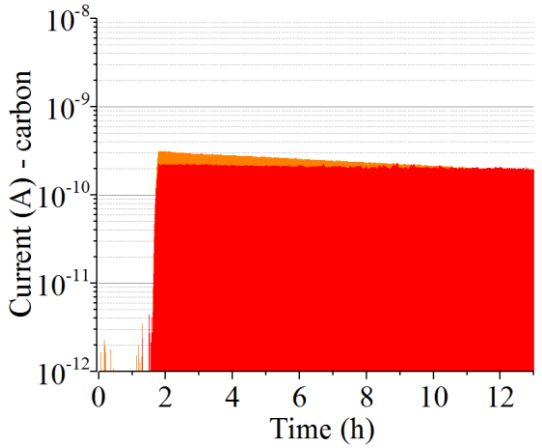

Figure 10: In orange the electron signal and in red the photoelectrons component of a 25 ns beam for the carbon surface.

OSCILLOSCOPE MEASUREMENTS

In addition to the use of a picoammeter that integrate the signal, a fast measurement was also carried out with an oscilloscope coupled with amplifiers and filters.

With unshielded pick-ups, the beam structure signal is then observed (dark blue curve in Figure 11). Here, 12 pilot bunches and 3 batches are shown at injection energy with 25 ns bunch spacing. In light blue, the EC signal of the *ex situ* NEG surface is shown.

The EC signal starts when the first bunch passes in front of the pick-up. Due to the surface reflectivity, some free electrons, called "survivals", remain in the beam pipe in between two bunches. With the passage of the second bunch, the electron density increases. Along the batch, after a few bunches, the EC density grows up to a quasi-stable value.

Between two batches, the EC signal totally disappears and it is restored with the next batch.

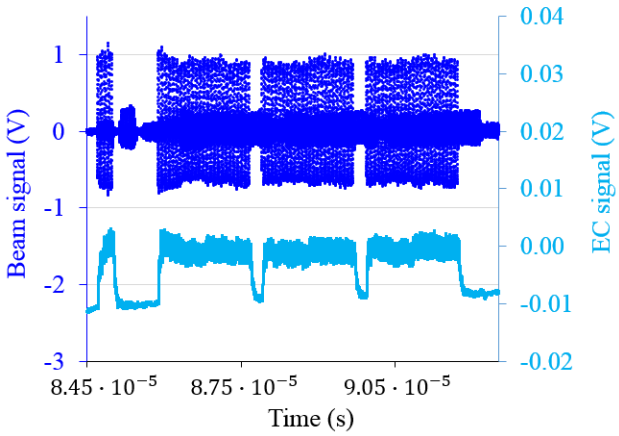

Figure 11: The beam signal recorded by the oscilloscope is displayed in dark blue, while the EC signal for the *ex situ* NEG surface is in light blue.

CONCLUSIONS

In the LHC vacuum system, primary electrons can be generated by beam-gas ionisation or by proton losses. These electrons are accelerated by the beam EM field towards the vacuum chamber wall. Secondary electrons can then be generated on the surface and, if the SEY is above one, the number of free electrons increases. When the LHC bunch spacing is set to 25 ns, the electrons density is amplified at each bunch passage, resulting in a multipacting regime.

The EC dynamics was studied for typical LHC fills, comparing different bunch spacing and surface materials. The EC behaviour is closely linked to the beam current, the beam losses, the bunch length dynamic and the beam energy. The SR generates photoelectrons above 2.8 TeV that have an additional effect on the EC. These two contributions can be disentangled by a simple method. The vacuum behaviour is dominated by EC multipacting when the SEY is high, as for copper, or by photoelectrons if no multipacting is taking place, as for the a-C coating case.

For the first time in the LHC, EC observations were also done in their time domain with an oscilloscope.

Due to its low SEY, the a-C coating results to be the best sample, among the three installed, with no EC multipacting. The only recorded electron current signal is generated by SR via the extraction of photoelectrons.

ACKNOWLEDGMENTS

The authors would like to thanks J. Wenninger, for the support on understanding the bunch length dynamic of the beam; M. Gasior and M. Wendt, for the contribution to the upgrade of the EC pick-ups; Professor A. Fasoli from EPFL university for his support and the help with the analyses. A big thank also to all the people that cooperated for the design, the installation and the maintenance of the VPS.

REFERENCES

[1] B. Henrist et al., Proceeding of IPAC2014, Dresden, Germany.

[2] J.M. Jimenez et al., LHC Project Report 632, Geneva, 2003.

[3] G. Bregliozzi et al., Proceeding of IPAC2011, San Sebastian, Spain.

[4] W. Pirkl, Longitudinal Beam Dynamics, Proceedings of CERN Accelerator School - Fifth Advanced Accelerator Physics Course, Rhodes, Greece, 1993.

[5] G. Iadarola et al., "Beam induced heat load on the beam screens of the twin-bore magnets in the IRs of the HL-LHC", CERN, Geneva, Switzerland, Rep. CERN-ACC-2016-0112, Sept. 2016.

Electron Cloud Effect and Its Cures in the SuperKEKB Positron Ring

Y. Suetsugu†, H. Fukuma, K. Ohmi, M. Tobiyama, K. Shibata
High Energy Accelerator Research Organization (KEK), 305-0801, Tsukuba, Japan

Abstract

Various countermeasures against the electron cloud effect (ECE) were adopted for the positron ring of SuperKEKB. During Phase−1 commissioning from February to June 2016, however, the ECE was observed, such as a blow up of the vertical beam size. The electron clouds at high beam currents were in the beam pipes at drift spaces in the ring, where antechambers and titanium nitride (TiN) film coating were prepared as countermeasures against ECE. Before starting the next commissioning, permanent magnets and solenoids to generate a magnetic field in the beam direction were attached to the beam pipes as additional countermeasures. Consequently, in the experiment at the end of May during Phase−2 commissioning from March 2018, it was found that the threshold current linear density for exciting ECE increased by a factor of at least 1.5 when compared to that during Phase−1 commissioning.

INTRODUCTION

The SuperKEKB is an electron-positron collider with asymmetric energies in KEK that aims for an extremely high luminosity of 8×10^{35} cm^{-2} s^{-1} (Fig.1) [1]. The main ring (MR) consists of two rings, i.e. the high-energy ring (HER) for 7-GeV electrons and the low-energy ring (LER) for 4-GeV positrons. Each ring has four arc sections and four straight sections, as shown in Fig.2.

The single-bunch instability caused by the electron cloud, i.e. the electron cloud effect (ECE), is a serious problem for the SuperKEKB LER [2]. More effective countermeasures than ever before were required. From elaborate simulations, the average density of electrons in the ring should be less than ~3×10^{11} m^{-3} in order to avoid the excitation of ECE [3]. Hence, various types of countermeasures were adopted in the SuperKEKB LER, which are summarized in Table 1 [4].

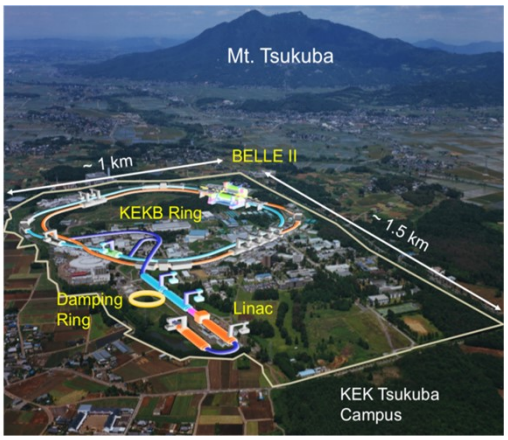

Figure 1: SuperKEKB at KEK Tsukuba campus.

† yusuke.suetsugu@kek.jp

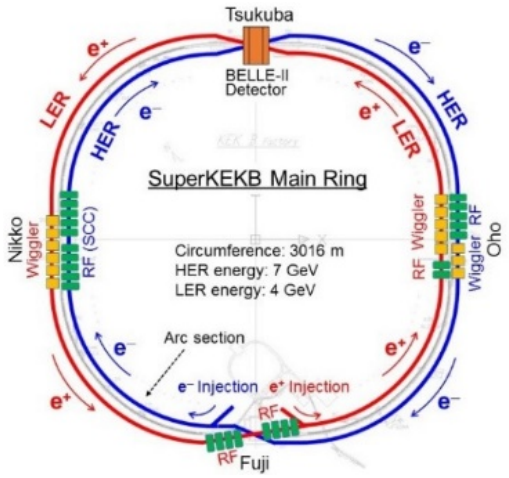

Figure 2: Layout of the SuperKEKB Main Ring (MR). One ring consists of four arc sections and four straight sections.

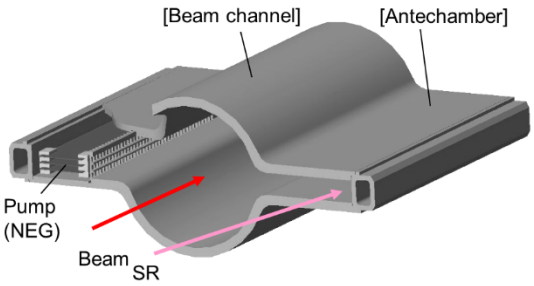

Figure 3: Typical cross section of a beam pipe at arc sections for LER.

An antechamber helps to minimize the effects of photoelectrons, since most of synchrotron radiation (SR) is directly irradiated at the side wall of it. A schematic of a beam pipe with antechamber is shown in Fig. 3. In the high-bunch-current regime, however, secondary electrons play a major role in forming the electron cloud. A magnetic field in the beam direction (B_z [G]) generated by solenoids or permanent magnets around the beam pipe is very effective to suppress the emission of electrons from the inner wall. However, these are available only in the drift spaces (field-free regions) between electromagnets, such as quadrupole and sextupole magnets. Most of the beam pipes for the SuperKEKB LER were made of aluminum (Al) -alloy, and the beam channel was coated with a TiN film to reduce the secondary electron yield (SEY). A grooved surface was adopted for the beam pipes in bending magnets in the arc sections. A grooved surface geometrically reduces the SEY. A TiN film was subsequently applied to the grooved surface. Clearing electrodes were installed in the beam pipes for wiggler magnets instead of the TiN film coating. A clearing electrode absorbs the electrons around the beam orbit by a static electric field. These beam pipes also have

Table 1: Countermeasures used to minimize the ECE in the SuperKEKB LER. The circular dots indicate the countermeasures applied for each main section in the ring.

Sections	Length [m]	n_e (circular) [m^{-3}]	Countermeasures: Antechamber (1/5)	TiN coating (3/5)	Solenoid (B_z) (1/50)	Groove (1/2)	Electrode (1/100)	n_e (expected) [m^{-3}]
Drift space (arc)	1629	8×10^{12}	●	●	●			2×10^{10}
Corrector mag.	316	8×10^{12}	●	●	●			2×10^{10}
Bending mag.	519	1×10^{12}	●	●		●		6×10^{10}
Wiggler mag.	154	4×10^{12}	●	●*			●	5×10^{9}
Quadrupole and Sextupole mag.	254	4×10^{10}	●	●				5×10^{9}
RF cav. section	124	1×10^{11}		●	●			1×10^{9}
IR	20	5×10^{11}		●	●			6×10^{9}
Total	3016							
Average		5.5×10^{12}						2.4×10^{10}

*Except for beam pipes with clearing electrodes.
Abbreviations;
RF cav. section: Beam pipes around RF cavities, IR: Interaction region
n_e (circular): Density of electrons expected for circular beam pipe (copper)
n_e (expected): Density of electrons expected after applying countermeasures
Antechamber: Antechamber scheme, Solenoid: Solenoid winding, but actually applying a magnetic field (B_z) in the beam direction
Groove: Beam pipe with grooves, Electrode: Beam pipe with clearing electrodes

antechambers and are made of copper. As a result, approximately 90% of the beam pipes in the ring have the antechambers and TiN coating.

The circular dots in Table 1 indicate the countermeasures applied in each main section in the ring. The density of electrons (n_e [m^{-3}]) expected in the case of circular beam pipes (copper) and those with the above countermeasures are presented in the table. Here, the efficiencies in reducing n_e for the antechamber scheme, TiN coating, solenoid (i.e. B_z), grooved surface, and clearing electrode are assumed to be 1/5, 3/5, 1/50, 1/2, and 1/100, respectively, on the bases of the experimental results obtained thus far [4]. With these all countermeasures, an n_e [m^{-3}] value of approximately 2×10^{10} m^{-3} was expected at the designed beam parameters, i.e. a beam current of 3.6 A at a bunch fill pattern of one train of 2500 bunches, with a bunch spacing of 2 RF-buckets (referred to as 1/2500/2RF hereafter). Here, one RF-bucket corresponds to 2 ns. This value of n_e is sufficiently lower than the threshold density of electrons ($n_{e,th}$ [m^{-3}]), at which the ECE is excited, 3×10^{11} m^{-3}. It should be noted that the B_z at drift spaces were not prepared before Phase–1 commissioning, since the expected beam current was not particularly high during the commissioning, i.e. approximately 1 A at the maximum.

The n_e around the circulating beam in an Al-alloy beam pipe with antechambers was measured via electron current monitors, which were also used in the previous KEKB experiments [5]. These two electron monitors were set up at the bottom of the beam channel. The voltage applied to the electron collector was 100 V, while that applied to the grid (repeller) varied from 0 V to –500 V. These two electron monitors were attached to the same beam pipe: one in the region with TiN film coating (as in the other typical beam pipes in the ring) and one in the region without the TiN film coating (i.e. bare Al surface). The test beam pipe was placed in an arc section of the ring. The line density of photons of the synchrotron radiation (SR) is 1×10^{15} photons s^{-1} m^{-1} mA^{-1}. This line density is almost same as the average value of arc sections.

ECE IN PHASE–1 COMMISSIONING

First observation

The ECEs, such as a blow up of vertical beam size and a non-linear pressure rise with beam current, were firstly observed during Phase–1 commissioning from a beam current (I [mA]) of approximately 600 mA at a bunch fill pattern of 1/1576/3.06RF in despite the implementation of the various countermeasures described above [6, 7]. This value of I corresponds to the current line density (I_b [mA $bunch^{-1}$]), i.e. the bunch current divided by the bunch spacing, of 0.1–0.12 mA $bunch^{-1}$ RF-$bucket^{-1}$. The typical behavior of the average pressure (P [Pa]) in an arc section divided by I, P/I [Pa mA^{-1}], is presented in Fig. 4(a) ([without PM at bellows]). Note that the high P/I at low I is due to the effect of base pressures. If the gas load comes from only the photodesorption by the SR, the P/I should be a constant, since the number of photons is proportional to I. As shown in Fig. 4(a), however, the P/I increased with an increase in I. This increase in P/I was attributed to the electron-stimulated gas desorption caused by multipactoring of high-density electrons in the beam pipe.

The vertical beam size began to blow up at almost the same I where the increase in P/I occurred, as shown in Fig. 4(b) ([without PM at bellows]). The emittance control knob (ECK), which is a tool to adjust the beam emittance using two skew-type quadrupole magnets, was active in this case. However, the behavior of the vertical beam size at $I \geq 600$ mA was independent of it. Since the B_z was not applied to beam pipes in Phase–1 commissioning, as described

before, the excitation of the ECE was an undeniable possibility. However, the threshold of beam current for exciting ECE was lower than expected.

A dedicated machine study to investigate the phenomena found that the threshold of I_d (I_{d_th} [mA bunch^{-1} RF-bucket^{-1}]) where the blow up of beam size begins was almost irrespective of the bunch fill pattern as shown in Fig. 5(a). This is a typical characteristic of ECE. The I_{d_th} was 0.1–0.12 mA bunch^{-1} RF-bucket^{-1}.

The modes of coupled-bunch instability were also found to be typical modes for ECE due to the electrons in drift spaces. Furthermore, the n_e was measured at the region without TiN film coating in the test beam pipe. The result at a bunch fill pattern of 1/1576/3.06RF is shown in Fig. 6(a). Note here that high n_e values at a low I_d are not reliable, since the volume used in the calculation of n_e is so small that the estimation method is no longer valid in principle [5]. The n_e value was over 20 times higher than the expected n_{e_th}, ~3×10^{11} m^{-3}, at an I value of 600 mA, which corresponds to I_d ~ 0.12 mA bunch^{-1} RF-bucket^{-1}.

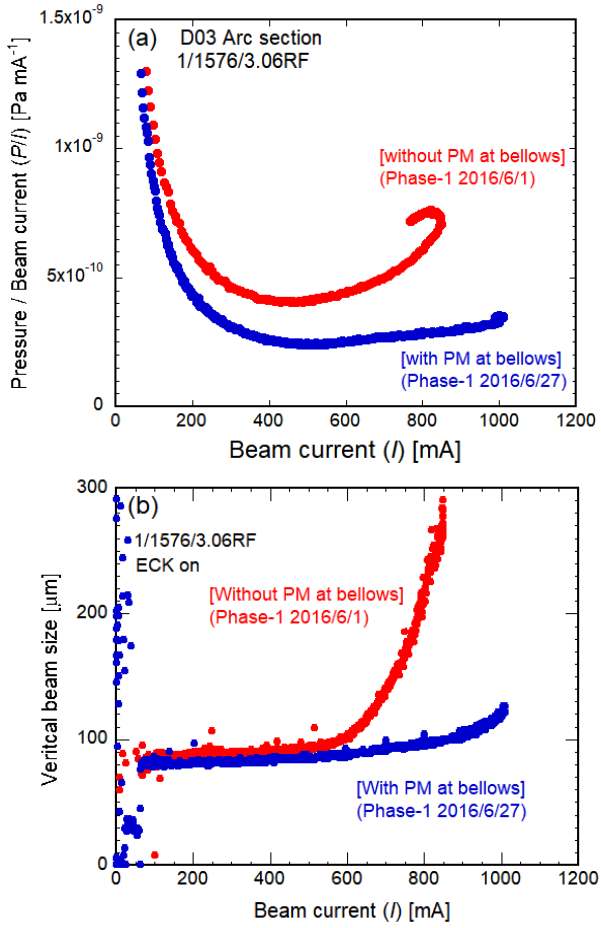

Figure 4: Behaviors of (a) average pressure in an arc section and (b) vertical beam size versus beam current without and with permanent magnets (PM) on Al-alloy bellows chambers for a bunch fill pattern of 1/1576/3.06RF.

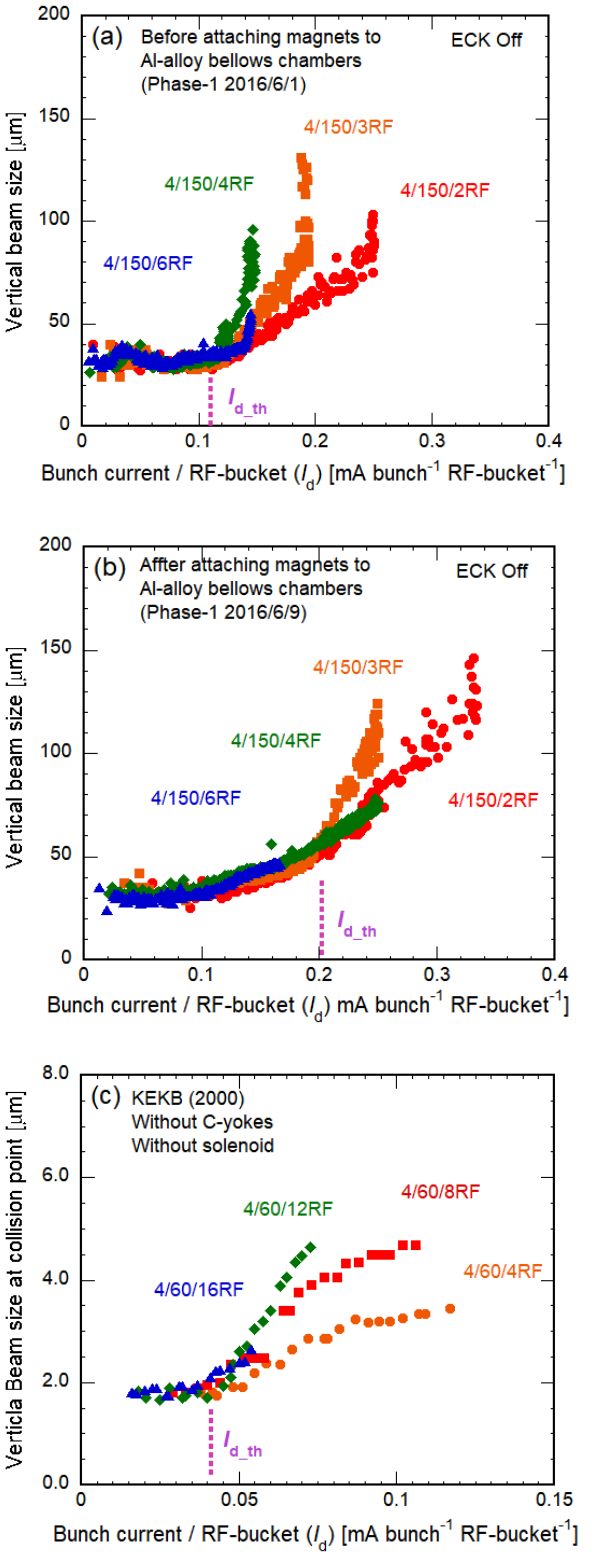

Figure 5: Vertical beam sizes as a function of the current line density (I_d) for several bunch fill patterns measured (a) before and (b) after attaching PM units to Al-alloy bellows chambers during Phase–1 commissioning of SuperKEKB, and (c) in the early stage of KEKB era.

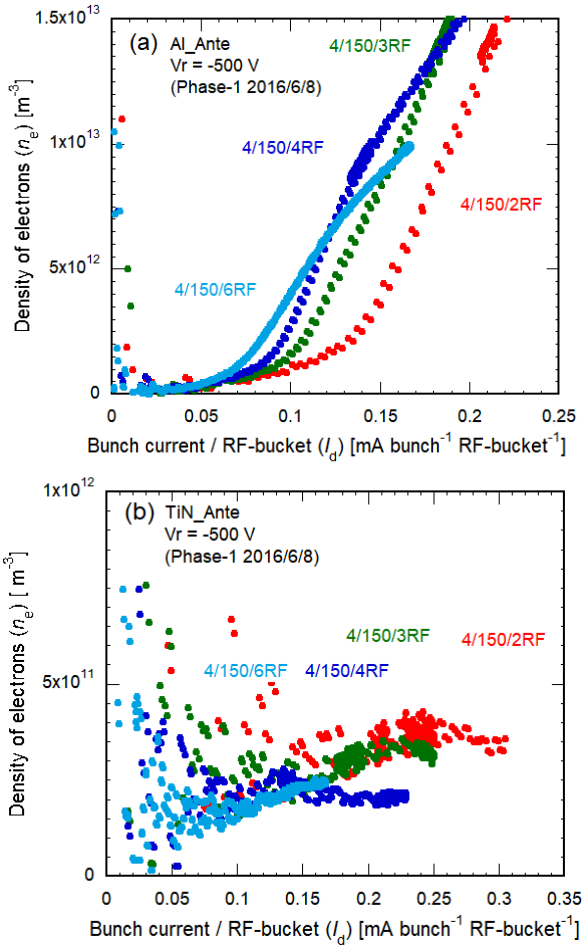

Figure 6: Measured densities of electrons (n_e) in the test beam pipe at the region (a) without and (b) with TiN film coating as functions of the current linear density (I_d) for various bunch fill patterns, where the grid voltage of the electron monitor was –500 V.

On the other hand, the n_e in the TiN-coated region of the test beam pipe, in Fig. 6(b), was still slightly lower than I_{d_th} at the same I_d, although the values of n_e are scattered at a low I_d because of the measurement errors at small monitor currents. From these facts, it was suspected that the ECE was excited owing to the electrons at the Al-alloy region without coating in the ring.

It was finally found that this ECE was caused by the electrons in the Al-alloy bellows chambers without TiN film coating. They are 200 mm long and are located at an average of every 3 m around the ring as shown in Fig. 7(a). There are approximately 830 bellows chambers in total, and their total occupied length is ~5% of the circumference of the ring. Therefore, if the n_e in the Al-alloy bellows chambers is 20 times that in the other TiN-coated regions, the ECE is likely to be excited.

To counteract the ECE, two units of permanent magnets (PM), where PM were attached to C-shaped iron plates (yokes), were placed at the top and bottom of each Al-alloy bellows chamber, as shown in Fig. 7(b). Each PM has a diameter of 30 mm, and the intensity of magnetic field at the surface is approximately 850 G. A B_z of approximately 100 G is formed in most regions in the PM units, although the polarity reverses locally near the magnets.

After attaching the PM units to all Al-alloy bellows chambers, the non-linear increase in P/I relaxed substantially as shown in Fig. 4(a) ([with PM at bellows]), and the blow up of vertical beam size was not evident until I value reached approximately 800 mA, as shown in Fig. 4 (b) ([with PM at bellows]). Thus, the ECE was successfully suppressed by applying B_z using PM units on the Al-bellows chambers. The measurement of the vertical beam size for bunch fill patterns of 4/150/2RF, 4/150/3RF, 4/150/4RF and 4/150/6RF showed that the I_{d_th} shifted from 0.1–0.12 mA bunch RF-bucket^{-1} to 0.18–0.2 mA bunch^{-1} RF-bucket^{-1}, as indicated in Fig. 5 (b).

At this point, approximately 90 % of the beam pipes in the LER have antechambers and TiN coating. It should be noted that the I_{d_th} is much higher than that in the case of the KEKB at the early stage [8], where most beam pipes were circular copper without any coating and solenoid windings. The I_{d_th} was approximately 0.04 mA RF-bucket^{-1} at the early stage of the KEKB, as shown in Fig. 5(c). On the other hand, after applying PM units to Al-alloy bellows chambers in the SuperKEKB, the I_{d_th} is 0.18 – 0.2 mA bunch^{-1} RF-bucket^{-1} (Fig. 5 (b)), which is approximately 5 times that in the KEKB. This indicates that the antechambers and the TiN coating of the beam pipes effectively suppress the ECE.

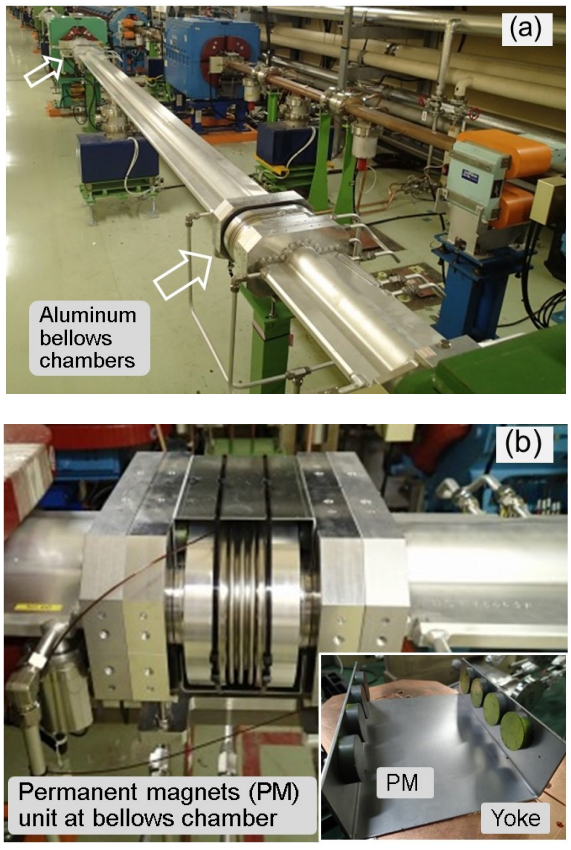

Figure 7: (a) Al-alloy bellows chambers in the LER, (b) PM and yokes (PM units) attached to them.

ECE at higher beam current

The ECE observed from an I value of approximately 600 mA caused by electrons in Al-alloy bellows chambers were successfully suppressed, as described above. However, as anticipated from Fig. 5(b), the ECE began to appear at an I value of approximately 900 mA at a bunch fill pattern of 1/1576/3.06RF. This I value corresponds to the I_d value of approximately 0.2 mA bunch^{-1} RF-bucket^{-1}. The blow up of vertical beam size reappeared at the same I as shown in Fig. 4 (b) ([with PM at bellows]). Furthermore, the n_e measured in the region with TiN film coating in the test beam pipe approached the value of n_{e_th} at the I_d of 0.2 mA bunch^{-1} RF-bucket^{-1} for 3RF-buckets and 2RF-buckets spacing as seen in Fig. 6(b). The growth rates of the transverse coupled bunch instabilities were measured using a bunch-by-bunch feedback system [9]. The modes caused by the electrons at the drift spaces were detected.

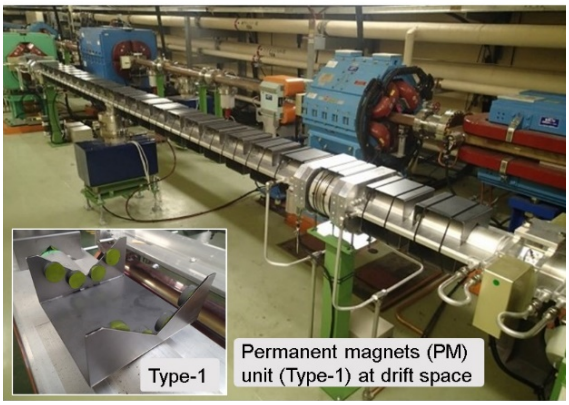

Figure 8: PM units (Type–1) attached to the beam pipes at drift spaces for test.

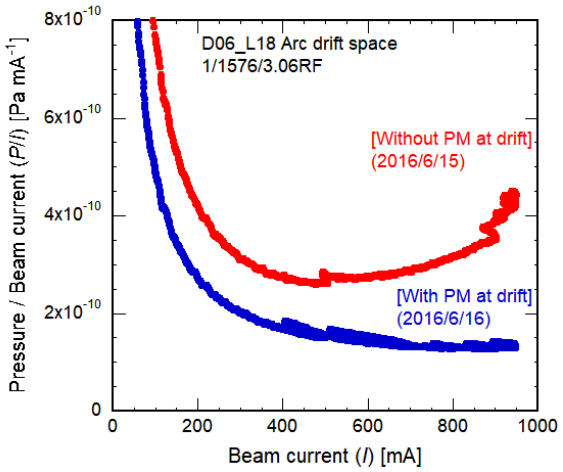

Figure 9: Behaviors of pressures in an arc section divided by the beam current (P/I) against the beam current (I) before and after attaching PM units to the beam pipes at drift spaces,

As a test, PM units similar to those used for the Al-alloy bellows chambers were attached to some beam pipes at drift spaces of approximately 20 m in an arc section (Fig. 8). The B_z value of over 60 G was obtained along the beam pipe, except for the polarity reversal points. After that, the P/I in this test region became flat and almost constant against I, as shown in Fig. 9 ([with PM at drift]). This meant that the ECE was excited by the electron cloud formed in the beam pipes with antechambers and TiN film coating at drift spaces.

The excitation of ECE meant that the countermeasures in Phase–1 commissioning were still insufficient. Additional countermeasures, that is, application of B_z by using PM units and solenoids to most drift spaces in the ring was required before starting the next commissioning.

Note here that the simulation of ECE indicates that the average value of the maximum SEY (δ_{max}) in the ring should be larger than 1.3 – 1.4 to excite ECE for the present condition of the LER. Here the ratio of the number of photoelectrons in the beam channel to the total number of those in the beam pipe was assumed to be 0.01 on the bases of the experimental result in KEKB [10]. On the other hand, the δ_{max} measured in the laboratory was 0.9 – 1.2 at the estimated electron dose of 5×10^{-4} C mm^{-2} [11], where the energy of incident electrons was 250 eV. The reason of the difference in the expected δ_{max} has not been clarified. Some possibilities are; (1) The dose of electrons with sufficient energies is still low, that is, the aging of the surface is insufficient. However, little decrease in n_e at the region with TiN film coating was observed during Phase–2 commissioning relative to that in Phase–1 commissioning. (2) The pressure is still high in the beam pipe. It was found in an experiment at the laboratory that the maximum SEY was high if the samples were not baked and the pressure in the test chamber was high. (3) The number of photoelectrons is larger than expected in the beam channel of the real beam pipes with antechambers, due to scattering of photons and the vertical spread of SR. In any way, the investigations on this discrepancy in the δ_{max} are in progress through simulations and experiments.

ADDITIONAL COUNTERMEASURES

As additional countermeasures against the ECE for the next Phase–2 commissioning, PM units and solenoids were attached to most of the beam pipes at drift spaces in LER. The PM units with iron yokes (Type–1unit), similar to those used for Al-alloy bellows chambers, were placed in series around the beam pipe as shown in Fig. 10(a), which produced a B_Z of approximately 60 G. A simulation by the code CLOUDLAND [12] showed that the n_e around the beam orbit reduced to approximately 1/10th of the n_{e_th} even for the designed beam parameters, as shown in Figs. 11 (a) and (b). However, the Type–1 unit cannot be used near electromagnets, such as quadrupole and sextupole magnets, because the iron yokes affect their magnetic field. Therefore, another type of PM units (Type–2 unit), which consists of Al-alloy cylinders with permanent magnets

inside and Al-alloy supports, was placed close to the electromagnets, as also shown in Fig. 10(a). The B_z inside the Type–2 unit was approximately 100 G. For the beam pipes that had been used since the KEKB era, solenoid windings were revived as shown in Fig. 10(b) [8]. Before starting Phase–2 commissioning, approximately 86% of the drift spaces (approximately 2 km) was covered with a B_z higher than approximately 20 G. Note that a simulation indicated that the n_e around the beam orbit in a B_z value higher than 10 G is lower than 1×10^{11} m^{-3} even for the designed beam parameters.

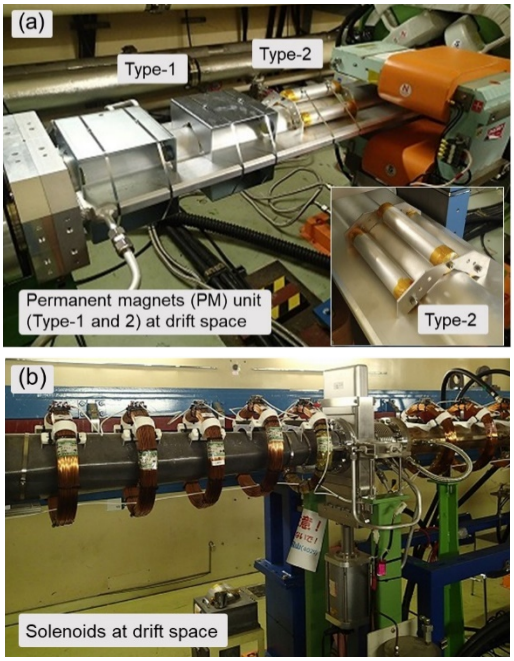

Figure 10: (a) Type–1 and Type–2 units and (b) solenoids at drift spaces.

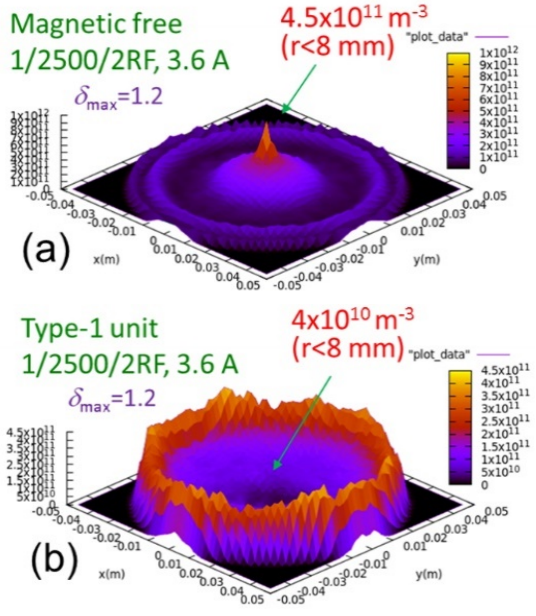

Figure 11: Density of electrons (n_e) in a beam pipe (a) without magnetic field and (b) with Type–1 PM units calculated by CLOUDLAND simulation code for a beam current of 3.6A at a bunch fill pattern of 1/2500/2RF.

ECE IN PHASE–2 COMMISSIONING

The Phase–2 commissioning started in March 2018. The vertical beam sizes and the P/I were measured at the end of May as in the case during Phase–1.

Figure 12 shows the behavior of P/I at arc sections against I, for a bunch fill pattern of 2 RF-buckets spacings during Phase–1 and Phase–2 commissioning. As shown in Fig. 12, the P/I increased with I when the I value was higher than 300 mA in the case of Phase–1. On the other hand, the P/I is almost constant against I in the case of Phase–2 commissioning. This indicated less multipactoring of electrons. Note here that the P itself decreased in Phase–2 commissioning when compared to that in Phase–1 commissioning due to vacuum scrubbing [13].

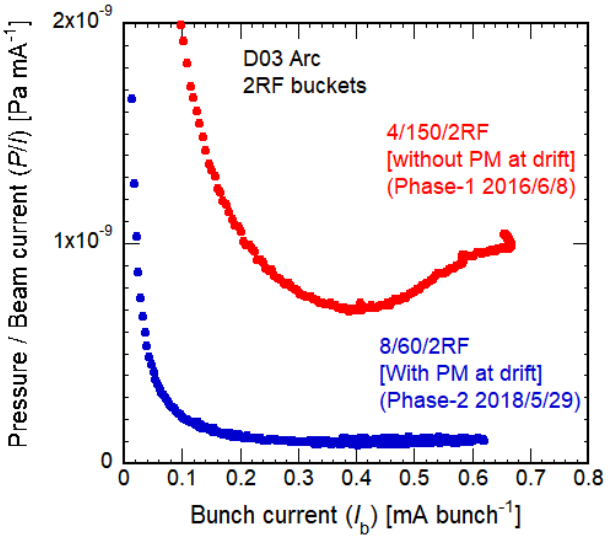

Figure 12: Behaviors of pressures at an arc section divided by the beam current (P/I) against the bunch current (I_{bunch}) in Phase–1 and Phase–2 commissioning (May 2018).

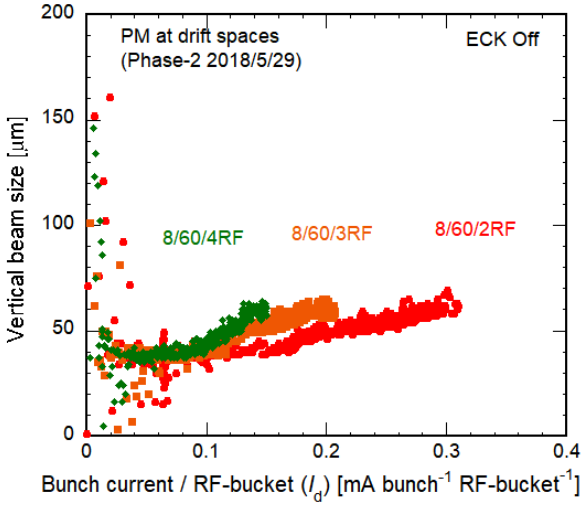

Figure 13: Vertical beam sizes as a function of current linear density (I_d) for several bunch fill patterns during Phase−2 commissioning (May 2018).

Figure 13 shows the dependence of the vertical beam size on I_d for bunch fill patterns of 4/120/2RF, 4/120/3RF and 4/120/4RF. As shown in Fig. 13, the blow up was not observed until the I_d value of 0.3 mA bunch^{-1} RF-bucket^{-1}. The I_{d_th} increased by at least 1.5 times when compared to the case of Phase−1 commissioning (Fig. 5(b)).

The modes and growth rates of the transverse coupled bunch instabilities were measured and analysed again. The modes caused by the electrons at near the inner wall trapped by B_z was observed, instead of the modes caused by the electrons in drift spaces. Furthermore, the growth rates were much slower than those measured during Phase−1 commissioning.

On the other hand, the measured n_e in the test beam pipe at the region with TiN film coating without Bz did not change from that observed in Phase−1 commissioning.

From these observations, it can be concluded that the additional countermeasures, i.e. a B_z generated by PM units and solenoids at drift spaces, contributed towards suppressing the ECE in Phase−2 commissioning.

SUMMARY

The ECE was observed in the SuperKEKB LER during Phase−1 commissioning. The ECE due to Al-alloy bellows chambers was successfully suppressed by applying PM units which produced a B_z of several ten gausses in the bellows chambers. The ECE due to beam pipes at drift spaces, however, was still observed at higher current regions, although the beam pipes had antechambers and TiN film coating as countermeasures against ECE. The antechambers and TiN film coating seemed to be functioning to some extent, but further countermeasures were required for the next commissioning. As additional countermeasures, two types of PM units and solenoids were prepared for beam pipes at drift spaces before Phase−2 commissioning. The Phase−2 commissioning started on March 2018. The experiment at the end of May 2018 found that the I_{d_th} increased by at least 1.5 times when compared to that in Phase−1 commissioning. The non-linear increase in P/I with an increase in I also disappeared. The B_z for the beam pipes at drift spaces functioned well with regards to suppressing ECE. Further studies on the ECE are planned at higher beam currents. The re-evaluation of the effectiveness of antechambers and TiN film coating is also planned to check whether they are functioning as expected to explain the discrepancy between the δ_{max} estimated in the ring and that obtained in the laboratory.

ACKNOWLEDGEMENTS

The authors would like to thank all the staff of the KEKB accelerator division for their cooperation and continuous encouragement during the commissioning phase.

REFERENCES

[1] Y. Ohnishi, "Report on SuperKEKB phase 2 commissioning," in Proc. IPAC'18, Vancouver, Canada, April 29 – May 4, 2018, pp. 1–5.

[2] K. Ohmi and F. Zimmermann, "Head-Tail Instability Caused by Electron Clouds in Positron Storage Rings," Phys. Rev. Lett. 85, p. 3821, 2000.

[3] Y. Susaki et al., "Electron cloud instability in SuperKEKB low energy ring", in Proc. IPAC'10, Kyoto, May 23–28, 2010, pp.1545–1547.

[4] Y. Suetsugu et al., "Results and problems in the construction phase of the SuperKEKB vacuum system," J. Vac. Sci. Technol. A, 34, p. 021605, 2016.

[5] K. Kanazawa et al., "Measurement of the electron cloud density around the beam," in Proc. PAC'05, Knoxville, USA, May 16–20, 1995, pp. 1054–1056.

[6] Y. Suetsugu et al., "Achievements and problems in the first commissioning of SuperKEKB vacuum system," J. Vac. Sci. Technol. A, 35, p. 03E103, 2017.

[7] Y. Suetsugu et al., "First Commissioning of the SupeKEKB Vacuum System," Phys. Rev. Accel. Beams, 19, p. 121001, 2016.

[8] H. Fukuma et al., "Status of Solenoid System to Suppress the Electron Cloud Effects at the KEKB", AIP Conference Proceedings 642, 2002, pp.357–359.

[9] K. Ohmi, et al., "Electron cloud studies in SuperKEKB phase I commissioning," in Proc. IPAC2017, Copenhagen, Denmark, May 14–19, 2017, pp. 3104–3106.

[10] Y. Suetsugu *et al*., "R&D of copper beam duct with antechamber scheme for high current accelerators," Nucl. Instrum. Method Phys. Res. A, 538, p. 206, 2005.

[11] K. Shibata *et al*., "Development of TiN coating system for beam ducts of KEK B-factory," in Proc. EPAC'08, Genoa, Italy, June 23–27, 2008, pp. 1700–1702.

[12] L. Wang *et al*., "A perfect electrode to suppress secondary electrons inside the magnets," in Proc. EPAC 2006, Edinburgh, Scotland, June 26 – 30, 2006, pp.1489–1491.

[13] Y. Suetsugu *et al*., "Beam scrubbing of beam pipes during the first commissioning of SuperKEKB," Appl. Surface Sci., 432, p. 347, 2018.

Laser Ablated Surface Engineering: From Discovery to Machine Application

R. Valizadeh[1], O.B. Malyshev[1], T. Sian[1,2], J.S.Colligon[1], Q. Li[3], W. Perrie[3],

[1]ASTeC, STFC Daresbury Laboratory, Warrington, WA4 4AD, UK
[2]The Photon Science Institute, University of Manchester, Manchester M13 9PL, UK
[3]Laser group, University of Liverpool, L69 3BX, UK

Abstract

In the past few years we have established that Laser Ablation Surface Engineering (LASE) is a very effective way of producing surfaces which have Secondary Electron yields (SEY) < 1. These can be achieved with a variety of laser pulse durations from nano- to pico seconds. Unfortunately the features (i.e. moderately deep grooves and nano-particulates) that help to reduce the SEY also produce undesirable effects such as an increase in surface impedance and loose particulates. In this paper we have examined several techniques to minimise these unwanted effects. For reducing the depth of the surface altered layer femtosecond laser pulses are used which generate wavelength-scale surface structures with directionality and periodicity, known as laser-induced periodic surface structure (LIPSS). The reduction in SEY in most cases has been less effective, but a few laser processing parameters have produced reasonable SEY values (less than 1 for primary electron energy below 400 eV). The role of processing atmosphere has also been examined where the processing in inert gas (Ar) resulted in a non-stoichiometric oxide surface as compared with air laser treated surfaces that resulted in fully oxidised state. The latter inhibited the growth of carbon on the surface but still aged with time and yielded a higher SEY after several months of exposure to air.

INTRODUCTION

In particle accelerators such as the LHC [1-3], KEKB [4], DAΦNE [5], RHIC [6] and others, the secondary electron emission (SEE) can cause an electron cloud build-up inducing an increase in beam instability, beam losses, emittance growth, vacuum pressure increase, a reduction in the beam lifetime, or, it can lead to additional heat loads on a cryogenic vacuum chamber. It was specifically highlighted in many scientific presentation that the high luminosity upgrade for the LHC (known as HL-LHC) requires complete elimination of the electron cloud which would be only possible when the beam screen surface SEY could be reduced, ideally to less than unity.

SEE is a phenomenon that negatively affects particle accelerators. It can be described as follows: initial electrons appear from residual gas ionisation by beam particles or due to photoelectron emission (PEE) from beam pipe walls, from synchrotron radiation emitted by accelerated particles in the dipoles and quadrupoles. These primary electrons are accelerated in the electric field of the passing bunches and can acquire kinetic energies up to several hundreds of eV. In turn, upon colliding with the wall of the chamber, they can cause SEE. Electron multipacting can be triggered in the case of resonant conditions generated by the electromagnetic field of the beam train. Although the primary photon-induced emission and gas ionisation could be a significant source of electrons, the electron-wall impact, with energies in the range of 100 to 300 eV, can significantly increase the electron density by several orders of magnitude over the primary electron density.

It has been shown both theoretically and experimentally [3] that the e-cloud density build-up depends on the SEY function δ(E) and to minimize the effects of e-cloud, the δmax value should be less than a certain threshold value, but in all cases δmax<1 would be a sufficient condition [3,7]. Since the secondary electron yield is influenced by the wall material, surface chemistry, topography and electron energy, any deliberate mitigation mechanism is based on engineering the first three of these parameters. There are a few ways of reducing the SEY:

(a) Choice of material with low SEY (for example, Cu has lower SEY than Al);
(b) Modifying surface geometry (e.g. making grooves) [3,8];
(c) Coating with low SEY materials (such as TiN [9], Non-Evaporable Getters (NEG) [10] and amorphous carbon (a-C) [11]);
(d) Coating with low SEY microstructure (eg.: copper black, gold black;
(e) columnar NEG is better than dense) [12,13];
(f) Various combinations of above.

Recently, a low SEY < 0.9 for as-received metal surfaces modified by a nanosecond pulsed laser was reported for the first time by Valizadeh et.al. [14-16]. The technique involves rapid surface micro- and nano- restructuring at room temperature using a high power pulsed laser at various wavelengths for processing of aluminium, stainless steel and copper surfaces. The average laser energy fluence is at the ablation threshold of the substrates. The process of low SEY laser treated surfaces is the most promising solution as it is technically simple and cost effective. The influence of micro- and nano-structures induced by laser surface treatment in air of copper samples as function of various laser irradiation parameters such as peak power of laser, number of pulses per point (scan speed and repetition rate) and fluence, on the SEY has been discussed at length in our previous paper [17]. The effectiveness of the LASE has also been discussed in detail after test carried out on a section of the

SPS accelerator at CERN where the section was equipped with an e-cloud monitor [18].

The results in this paper are primarily focused on the effect of surface texturing created by the interference between the incident polarized laser light and the light scattered from the irradiated surface. The light is scattered due to surface impurities or defects, and the interference induces periodic energy density undulation on the surface. This generates wavelength-scale surface structures with directionality and periodicity, known as laser-induced periodic surface structure (LIPSS) [19-21]. This allows for formation of features in the nano-scale which is significantly smaller than achievable by direct ablation. Hence it may result in reducing the increase of surface impedance after laser treatment.

It also examines the effect of process atmosphere, effect of aging on SEY as well as the size of particle generated after laser ablation.

EXPERIMENTAL PROCEDURES

Production of LIPSS and periodic structure on stainless steel and copper

A standard Omicron sample holder fabricated from 314 SS and oxygen free copper was used as substrate for this study. A Ti-sapphire (Clark-MXR CPA 2010), of τ = 180 fs, repetition rate of f = 1 kHz and maximum average power of 30 W at λ = 775 nm was utilized for irradiation of the samples in an air atmosphere at room temperature. The diameter of the focused laser spot on each target between the points where the intensity has fallen to $1/e^2$ of the central value was varied between 10 µm. The laser beam had a Gaussian intensity profile ($M_2 \sim 1.1$) and was focused on to the target surfaces using a Nutfield scan head with 100 mm f theta lens system which is a specialised lens system in which the focal plane of the deflected laser beam is a flat surface. Figure 1 and Table 1 show the sample process identification and process laser parameters.

A facility for SEY and surface chemistry studies

A dedicated facility was designed, built and operated for SEY studies. The facility consists of three chambers as shown in Fig. 2 1: a load-lock chamber, the SEY measurement chamber, the surface treatment and the analysis chamber. After placing a sample into the load lock chamber, it was pumped there for at least 12 hours using a 210 l/s turbo-molecular pump (TMU 261, PFEIFFER Vacuum).

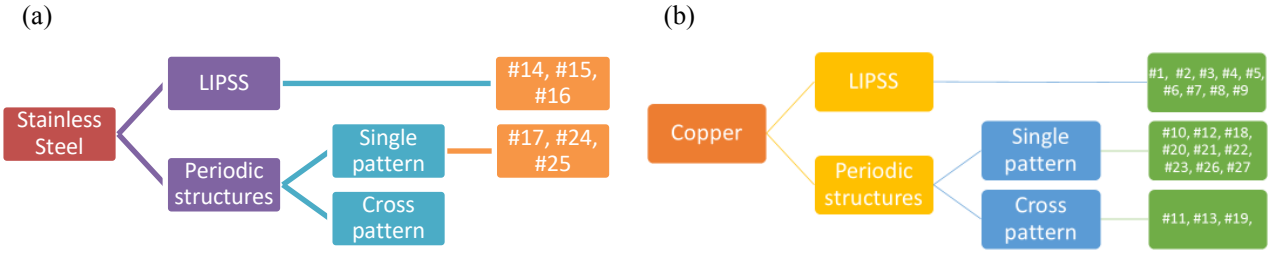

Figure 1: Sample processing identification and their maximum SEY: (a) stainless steel and (b) copper substrates.

Table 1: Laser parameters for LIPSS and periodic structure production: (a) stainless steel and (b) copper substrates.

Sample	Energy (µJ)	Hatch (µm)	Speed (mm/s)	Overscan	Ra (nm)	Width *w* (µm)	Depth *d* (µm)	*d/w*	δ_{max}
	(a) Stainless steel								
Pristine					200				
14	123	120	7.5	1	247				1.67
15	123	180	7.5	1	224				1.60
16	123	70	7.5	1	219				1.59
17	50	30	5	3	1210	13	4	0.31	1.34
24	50	30	5	5	899	14	3.5	0.25	1.51
25	50	30	5	15	1200	15	4	027	1.52
	(b) Copper								
Pristine					70				
18	20	30, 60	5	1	586	15	2.5	0.17	1.51
19	20	30, 60	5	1	666	14	3	0.21	1.56
20	50	30, 60	5	1	1120	18	4.5	0.25	1.50
21	50	30	7.5	1	483	22	2	0.09	1.65
22	20	30	10	1	179	14	0.7	0.05	1.57
23	50	30	10	1	365	20	1.5	0.08	1.60
26	75	42	5	10	9000	25	23	1.04	1.54
27	75	30	5	6	5700	18	15	0.83	1.46

The pressure of 2×10^{-9} mbar, measured using an MKS Pirani and inverted magnetron gauges, is routinely reached after overnight pumping from atmosphere. The sample is then transferred into the UHV SEY measurement chamber. The SEY measurement chamber is equipped with a combined NEG and sputter ion pump (NEXTORR® D100-5, SAES Getters), which enables a pressure of 2×10^{-10} mbar to be obtained without electron bombardment and of (2-5) $\times10^{-9}$ mbar during electron bombardment. The pressure is measured using a Leybold extractor gauge.

The schematic layout of the SEY measurements is shown in Figure 2. The electron beam with energy ranging from 80 to 1000 eV is generated by the Kimball electron gun (ELG-2/EGPS-2). The Faraday cup is made of 304L stainless steel and is a 85 mm long and 50 mm diameter cylinder with two plates on the top and bottom. The electrons enter the Faraday cup through the top 8-mm diameter hole passing through to the opposite site of the Faraday cup and bombard the sample placed in front of the 10-mm diameter hole in the Faraday cup. The beam size at the sample (full width half maximum - FWHM) has been measured with a phosphor screen and wire scanner for different electron gun parameters and electron beam energies before performing the SEY experiments. The spot size during the SEY measurements was 0.28 cm^2.

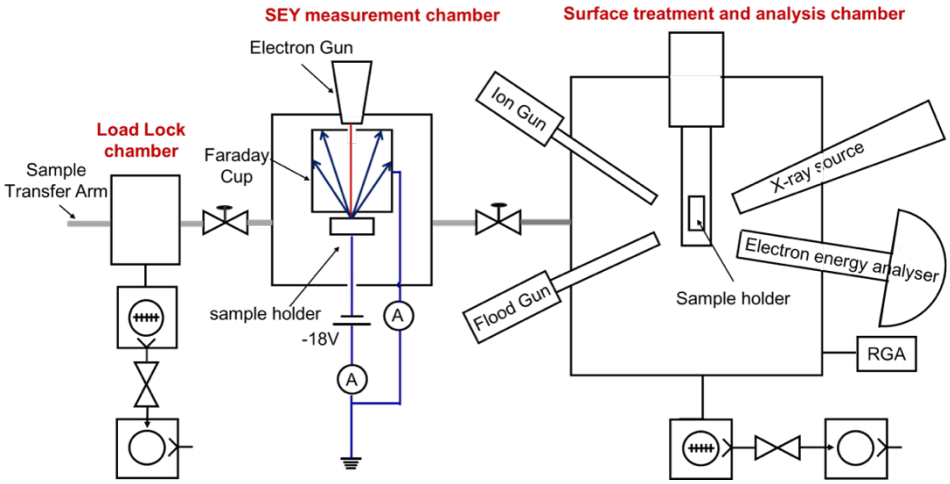

Figure 2: Schematic layout of the facility for SEY studies.

The secondary electrons are collected by the Faraday cup. The currents flowing through the sample and the Faraday cup are recorded for the SEY measurement.

The total SEY (or δ) is defined as

$$\delta = \frac{I_f}{I_\rho} = \frac{I_f}{I_s + I_f} \quad (1)$$

where I_s is the secondary electron current (including both elastic and inelastic processes) measured at the sample, I_f is the current on the Faraday cup and I_p is the primary beam current. In these experiments the net current at the sample biased at –18 V and the Faraday cup at ground potential were measured with two current amplifiers (Keithley 6517A and Keithley 6485, accuracy ±0.01%). As the SEY is very sensitive to the electron dose, the total electron dose during the SEY measurements, as a function of primary energy, was not allowed to exceed 10^{-6} C·mm^{-2}. The accuracy of the SEY measurements was estimated to be within 1% for primary electron energies between 80 and 800 eV and about 6% for primary electron energies above 800 eV.

After SEY measurements the sample can be transferred to the surface treatment and analysis chamber which is equipped with a flood gun (AG 31F, VG) used for electron conditioning (electron energy 485 eV and the accuracy of the electron dose was within 10%), an argon ion gun (PSP, ISIS 3000) with energy of 1.5 keV for surface etching and a sample heater which allows sample heating up to 300 °C. In addition the sample surface composition and chemical bonding energies can be analysed using an X-ray gun and an electron energy analyser. XPS measurements are carried out using a hemispherical analyser fitted with a five channeltron detector. Power supplies are for the spectrometer a PSP Resolve Control and, for the detectors, a PSP #705. The spectrometer was operated at 20 eV pass energy at all times and the angle between the X-ray source and electron analyser is 70 degree. Photo-electrons are excited by a non-monochromatic Al Kα X-ray source ($h\nu$ = 1463 eV) using a VG twin anode. The Al anode used at all times operated at 10 keV, 20 mA.

The surface treatment and analysis chamber is equipped with a 340 l/s turbo-molecular pump (Leybold 340M) and 1000 l/s getter pump (CapaciTorr® D-1000 Pump, SAES Getters). The base pressure of about 10^{-9} mbar was measured by a Leybold extractor gauge and the residual gas composition was monitored using a residual gas analyser (RGA, VG Thermo, VGQ).

A typical experimental procedure could involve SEY measurement of the as-received sample, followed by XPS measurement, conditioning using the diffuse-beamed

electrons from the flood gun, ion bombardment, or, thermal treatment, followed by another XPS measurement and another SEY measurement..

Particle size measurement set-up

Particle size counting measurements were carried out in an ISO 3 clean room at ETC?. Laser treated samples were exposed to nitrogen with two different pressures of 1.5 bar and 5 bar. Particle size counting measurements were performed using a particle counter situated in the clean room (Figure 3) by counting for 60 seconds for each pressure and sample. Background data was also checked before performing measurements and was found to be quite low for both the pressures of 1.5 and 5 bar.

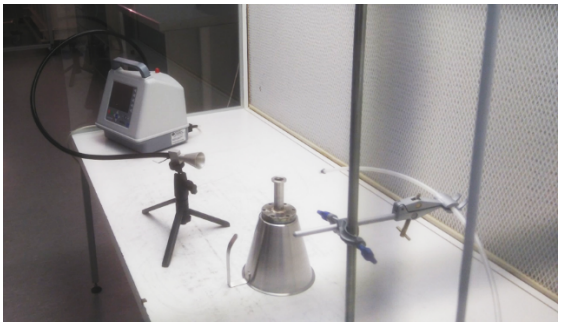

Figure 3: Particle size measurement set-up.

RESULTS AND DISCUSSION

SEY of LIPSS

Figure 4 depicts the SEY counts per second of the laser-treated SS sample with scan values higher than 1. In all cases the SEY has decreased over all the primary electron range and the δ_{max} (at E_p =300 eV), observed for the as-received untreated sample, is replaced by slowly increasing slope. The SEY rises initially for primary electron energies below 200 eV. For energies 200 eV < E_p < 400 eV the rate of increase reduces and flattens off with gradient towards the higher primary electron energy.
The decrease in SEY is not as large as the one reported previously [14-15-16] where deeper grooves (100 to 10 µm) were formed by laser ablation at higher pulse length of (τ in pico and nanosecond).

It has been shown that the reduction in SEY is due to the presence of deep grooves and the nanoparticle location on the surface [16]. For LIPSS the grooves are a factor 10 shallower and hence the reduction in SEY is not sufficiently suppressed. The value of δ_{max} for all the laser process parameters are tabulated in Table 1 for the stainless steel and copper samples.

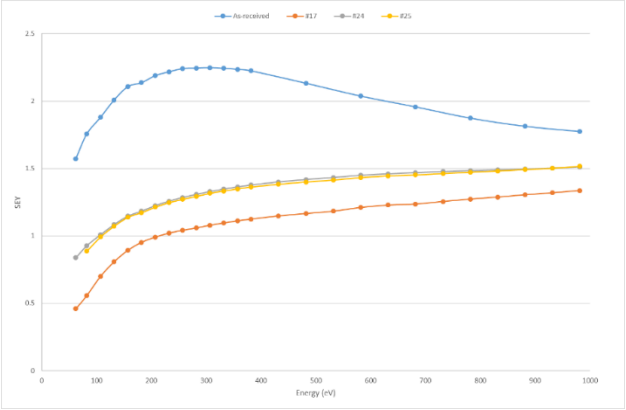

Figure 4: SEY as a function of incident electron energy for the untreated and the laser treated stainless steel samples 17, 24 and 25.

Process atmosphere

Copper substrates were laser treated in argon and air atmosphere with identical laser processing parameters. Figure 5 represents the XPS spectra of a copper substrate laser treated in an argon atmosphere for as-received and after electron bombardment for various doses at 500 eV. It can be seen that the as-received surface is in a Cu(I) oxide state and the surface is covered by a thick carbon layer. However further electron scrubbing has reduced the oxide state and promotes further carbon growth at the surface. Table 2 depicts the atomic percent of copper, oxygen and carbon at the surface for as-received and the data after each electron fluence. It can be seen that the atomic percent of copper is increasing while the oxygen atomic percent is decreasing and, at the same time, the carbon atomic percent is steadily increasing.

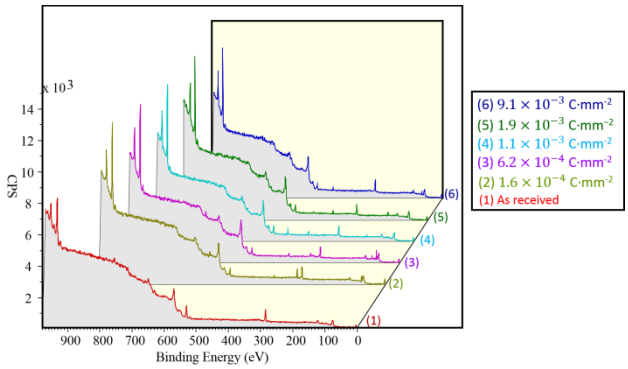

Figure 5: XPS survey spectra of as receive and electron beam scrubbing of copper sample laser treated in argon atmosphere.

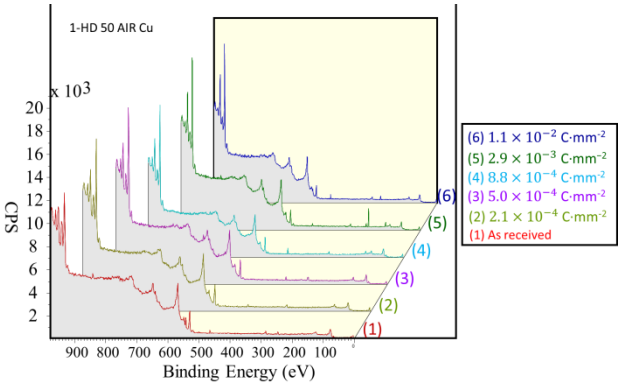

Figure 6: XPS survey spectra of as receive and electron beam scrubbing of copper sample laser treated in air atmosphere.

Figure 6 represents the XPS spectra of a copper substrate laser treated in air atmosphere for as-received and after electron bombardment for various dose at 500 eV. It can be seen that the as- received sample surface is in the Cu(II) oxide state (note the presence of satellite at biding energy of 943 eV) and the surface is covered by a thinner carbon layer.

Further electron scrubbing has lesser influence in reducing the oxide state and no further carbon growth takes place at the surface.

Table 3 depicts the atomic percent of copper, oxygen and carbon at the surface for as-received and after each experience of electron fluence. It can be seen that the overall atomic percentage of individual species (Cu, C, O) at the surface remains the same even after long electron scrubbing.

Table 2: Atomic percent of surface composition as receive and electron beam scrubbing of copper sample laser treated in argon atmosphere.

Electron dose (C/mm^2)	O1s			C1s			Cu2p		
	position	FWHM	At%	position	FWHM	At%	position	FWHM	At%
As received	531	3.11	26.6	285	2.56	63.3	932	2.49	10.1
1.6×10^{-4}	531	2.58	15.4	285	2.43	67.9	932	2.08	16.7
6.2×10^{-4}	530	2.78	22.6	285	2.43	59.6	932	2.12	17.8
1.1×10^{-3}	530	2.04	16.3	284	2.41	65.5	932	2.09	18.1
1.9×10^{-3}	530	2.16	14.7	284	2.39	69.2	932	2.07	16.1
9.1×10^{-3}	530	2.47	14.8	284	3.29	70.1	932	2.09	15.1

Table 3: Atomic percent of surface composition as receive and electron beam scrubbing of copper sample laser treated in air atmosphere.

Electron dose (C/mm^2)	O1s			C1s			Cu2p		
	position	FWHM	At%	position	FWHM	At%	position	FWHM	At%
As received	530	3.65	47.5	285	2.44	20.6	934	3.83	32.0
2.1×10^{-4}	530	2.96	58.6	285	4.58	20.0	933	2.76	21.5
5.0×10^{-4}	530	2.68	37.6	285	4.75	30.1	933	2.80	32.3
8.8×10^{-4}	530	2.71	52.1	284	2.62	22.2	932	2.09	25.7
2.9×10^{-3}	530	2.61	45.9	284	2.06	18.6	932	2.51	35.4
1.1×10^{-2}	530	2.58	44.6	284	2.81	20.0	932	2.37	35.5

Effect of sample aging on SEY

Figure 7 represents the effect of ultrasonic cleaning in acetone and data for the same sample aged for 10 months on the SEY of the copper sample laser treated with the parameters tabulated in Table 4. It can be seen that the shape of the curve stays almost the same but the SEY is shifted to a higher value for all the primary electron energies with the shift becoming larger with increasing primary electron beam energy and remaining almost constant for $E_p > 400$ eV.

Figure 8 is the SEM image of the as-received laser treated copper sample. The ten 10 to 15 µm deep grooves formed under laser treatment are completely covered with nanoparticles. The increase of SEY after the acetone cleaning is attributed to the loss of loose nanoparticles at the surface which have become separated due to ultrasonic agitation. The increase of SEY is hypothesised to be due to the build of a hydrocarbon layer while the sample was exposed to air.

Table 4: The laser processing parameters for the copper Sample 1.

Pulse duration	ps	5
Scan speed	mm/s	30
Wavelength	nm	1064
Pitch spacing	µm	5
Repetition	kHz	1.25
Power	W	5

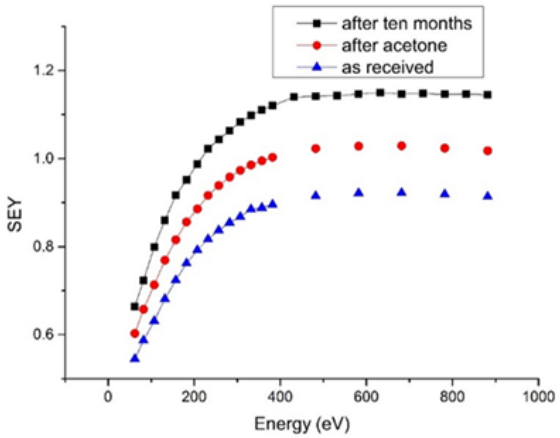

Figure 7: Effect of acetone cleaning and aging on SEY as a function of incident electron energy.

Hence extra steps should be taken to ensure the surface chemistry is not modified after laser treatment. One way of achieving such goal is to keep the surface either in vacuum or in an inert gas atmosphere.

During electron scrubbing, the process of carbon build up is done in vacuum, the carbon layer is composed of amorphous carbon which is known to have low SEY, however when the sample is exposed to air the carbon layer is composed of hydrocarbon which has high SEY.

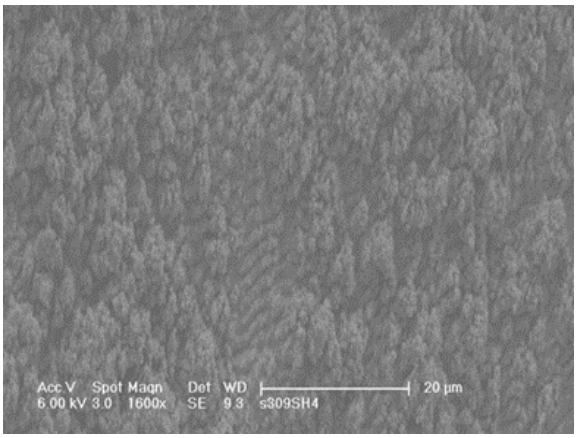

Figure 8: SEM image of as-received of a laser treated copper substrate.

Particle size determination

One of the by-products of the laser ablation is production of particulates which, if not attached strongly enough to the surface, have the potential of causing serious damage during beam delivery in particle accelerators. Hence it is vitally important to assess the size and quantity of loose particles generated after laser processing. The assessment was done using two different methods:

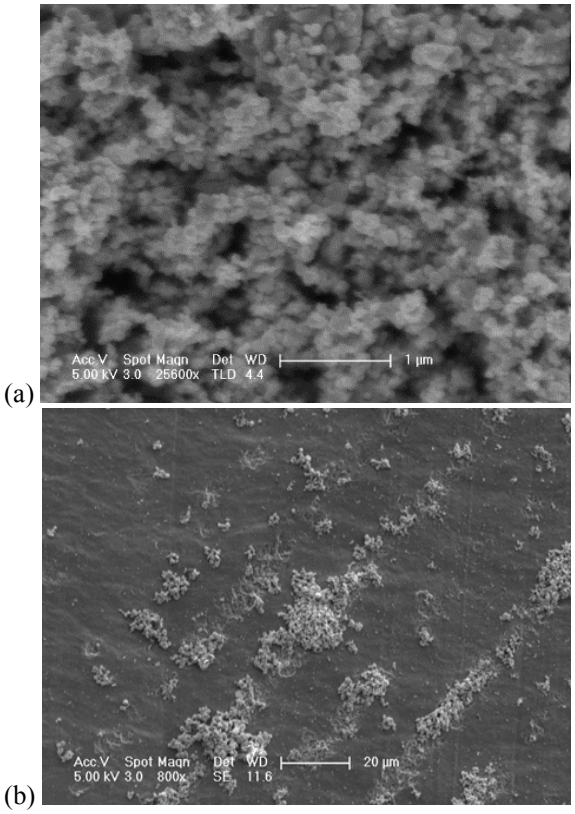

Figure 9: SEM images of laser processed copper substrate, after ultrasonic bath agitation (a), and the remaining residual at the bottom of the bicker.

(1) Ultrasonic bath agitation

Figure 9 depicts the SEM image of a copper sample, laser-irradiated with pulse length t = 5 ps and wavelength of λ = 1064 nm, scanned over with spot size of 15 µm and scan pitch of 5 µm, after ultrasonic agitation in acetone (Fig. 9a).The residual material left at the bottom of the beaker is shown in Figure. 9b. As it can be seen, although the surface has stayed to some extent intact nevertheless there is a small amount of particulates that have been detached during the agitation.

The effect of such loss of material from the surface on SEY is shown in Fig. 10 for two different scan speeds. As can be seen in both cases, the SEY has increased and more so for the higher scan speed. As mentioned above the increase can be attributed to two factors:

- Loss of particulate shown in Fig. 9b;
- Built up an hydrocarbon layer on the surface.

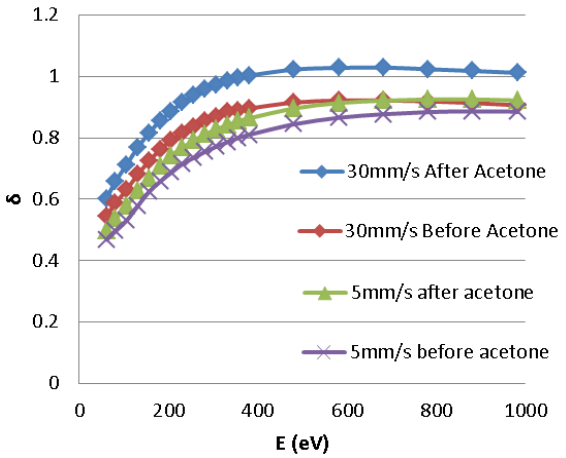

Figure 10: SEY as a function of incident electron energy for laser processed copper for as received samples and samples after ultrasonic agitation for two different scan speeds.

(2) Particle count

Figure 11 shows the the amount and the size of particles between 0.3 to 0.5 μm and 0.5 to 1 μm for samples treated in air at two different scan speeds (30 and 5 mm/s) and in an Ar atmosphere at scan speed of 5 mm/s. Polished and untreated samples were used as reference baseline samples. The detector could measure up to a particle size of 25 μm, however the largest particle observed was 1 μm in size. The largest quantity was for 5mm/s scan in air. The lowest quantity was for the sample treated in Ar which most probably is due to extra flow during laser ablation that has helped to remove any loose particles. Based on this finding it is recommended that the laser ablation should be always carried out with a flow of some kind of gas to remove the execess unwanted particulates.

CONCLUSIONS

In a previous papers we have demonstrated that reduction of SEY with laser ablation surface engineering (LASE) is very effective to produce surfaces with the lowest SEY reported up to date These are easy to achieve (as compared with other already existing techniques), is reasonably scalable since the technology already exists for other sectors and can be easily adapted. The process can be very cost-effective, especially with the availability of new more powerful and low cost lasers offered by industry.

However, several small problems still remain such as surface impedance, loose particles and effect of aging that need to be addressed. The results in this paper have gone some way in addressing these problems and offer applicable solutions either, to completely overcome or partially reduce them.

Using a femtosecond laser, where the surface engineering is more confined to the sample surface, it will be possible to reduce the increase in the RF surface resistance induced by laser ablation. A gas flow with adequate pressure will reduce the concentration of loose particles. It may also help to change the surface chemistry at the same time. By keeping the threated surface in either vacuum or inert gas atmosphere the effect of ageing can be reduced considerably.

There is a need for more study on LASE to determine the induced increased impedance both quantitatively and qualitatively.

(a)

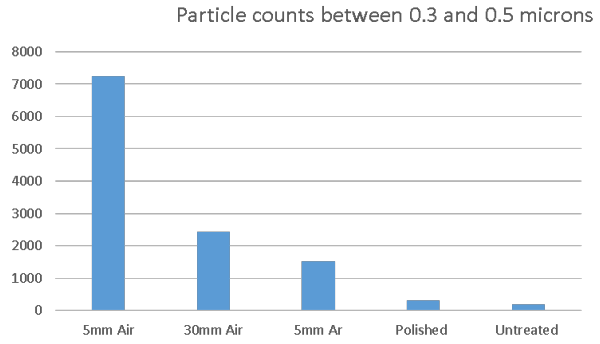

(b)

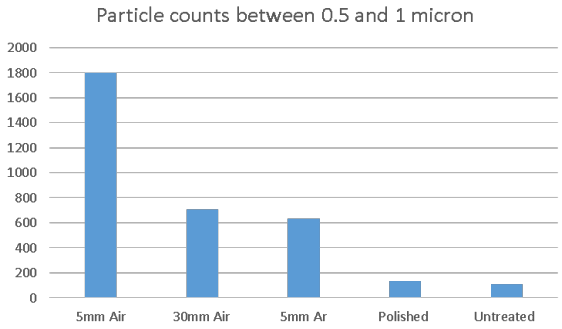

Figure 11: Particle counts for two different size range (a) 0.3 to 0.5 μm and (b) 0.5 to 1 μm.

REFERENCES

[1] G. Rumolo, G. Arduini, V. Baglin, H. Bartosik, N. Biancacci, et al. Electron cloud observations in LHC. Proc. of IPAC2011, San Sebastián, Spain (2011) p. 2862.

[2] [1] G. Rumolo, G. Arduini, V. Baglin, H. Bartosik, N. Biancacci, et al. Electron cloud observations in LHC. Proc. of IPAC2011, San Sebastián, Spain (2011) p. 2862.

[2] J. A. Crittenden, J. V. Conway, G. Dugan, M.A. Palmer, D.L. Rubin, K. Harkay, L. Boon, M.A. Furman, S. Guiducci, M.T.F. Pivi and L. Wang. Investigation into electron cloud effects in the ILC damping ring design. Proc. of IPAC-2012, New Orleans, Louisiana, USA, p. 1963 (2012).

[3] F. Zimmermann. Review of single bunch instabilities driven by an electron cloud. Phys. Rev. ST Accel. Beams 7, 124801 (2004).

[4] S. Kato, M. Nishiwaki. e-Cloud Activity of DLC and TiN Coated Chambers at KEKB Positron Ring. Proc. of Ecloud'10, Ithaca, New York, USA (2010), p. 37.

[5] D. Alesini, T. Demma, A. Drago, A. Gallo, S. Guiducci, C. Milardi, P. Raimondi, M. Zobov, S. De Santis, T. Demma, P. Raimondi. Experimental measurements of e- -2012, New Orleans, Louisiana, USA, p.1107 (2012).

[6] W. Fischer, U. Iriso. Bunch patterns and pressure rise in RHIC. Proc. of EPAC'04, Lucerne, Switzerland, July 2004, p. 914.

[7] H. Fukuma. Electron Cloud Observations and Predictions at KEKB, PEP-II and SuperB Factories. Proc. Of Ecloud'12, 5-9 Jun 2012, La Biodola, Isola d'Elba, Italy, p. 27 (2012).

[8] G. Stupakov and M. Pivi. Suppression of the effective SEY for a grooved metal surface, Proc. of ECLOUD'04, Napa, California, 19-23 April 2004, p.139 (2004).

[9.] P. He, H.C. Hseuh, M. Mapes, R. Todd and D. Weiss. Development of titanium nitride coating for SNS ring vacuum-chambers. Proc. PAC01, p.2159 (2001).

[10] W W. Fischer, M. Blaskiewicz, J. M. Brennan, H. Huang, H.-C. Hseuh, V. Ptitsyn, T. Roser, P. Thieberger, D. Trbojevic, J. Wei, S. Y. Zhang, and U. Iriso. Electron cloud observations and cures in the Relativistic Heavy Ion Collider. Phys. Rev. ST Accel. Beams 11, 041002 (2008).

[11] C. Yin Vallgren, G Arduini, J.Bauche, S. Calatroni, P. Chiggiato, K. Cornelis, P. Costa Pinto, E. Metral, G. Rumolo, E. Shaposhnikova, M. Taborelli, G. Vandoni. Amorphus carbon coatings for mitigation of electron cloud in the CERN SPS. Proc. IPAC'10, Kyoto, Japan, paper TUPD048, p. 2033 (2010).

[12] S. Wang. PhD Thesis. Loughborough University, UK, July 2016.

[13] I. Montero, L. Aguilera, M.E. Dávila, et al. Novel types of anti-ecloud surfaces. In proc. of E-CLOUD12 workshop, ELBA, Italy, 2012, p. 153.

[14] R. Valizadeh, O.B. Malyshev, S. Wang, et al. Low secondary electron yield engineered surface for electron cloud mitigation. App. Phys. Lett. 105, 231605 (2014).

[15] R. Valizadeh, O. Malyshev. Apparatus and methods relating to reduced photoelectron yield and/or secondary electron yield. Patent publication number WO2015189645 A1. 17th Dec 2015.

[16] R. Valizadeh, O.B. Malyshev, S. Wang, T. Sian, L. Gurran, P. Goudket, M.D. Cropper, N. Sykes. Low secondary electronyield of laser treated surfaces of copper, aluminium and stainless steel. In Proc. of IPAC'16, 8-13 May 2016, Busan, Korea (2016), p. 1089.

[17] R. Valizadeh, O.B. Malyshev, S. Wang, T. Sian, M. D. Cropper and N. Sykes. Reduction of Secondary Electron Yield for E-cloud Mitigation by Laser Ablation Surface Engineering. Appl. Surf. Sci. 404, 370–379 (2017).

[18] S. Calatroni, E. Garcia-Tabares Valdivieso, H. Neupert, V. Nistor A. Perez Fontenla, et al. First accelerator test of vacuum components with laser-engineered surfaces for electron-cloud mitigation. Phys. Rev. Accel. Beams 20, 113201 (2017).

[19] M. Birnbaum, Semiconductor surface damage produced by ruby lasers, J. Appl. Phys. 36 (1965) 3688.

[20] J. E. Sipe, J. F. Young, J. S. Preston, H. M. van Driel, Laser-induced periodic surface structure. I. theory, Phys. Rev. B 27 (1983) 1141–1154.

[21] S. A. Akhmanov, V. I. Emel'yanov, N. I. Koroteev, V. N. Seminogov, Interaction of powerful laser radiation with the surfaces of semiconductors and metals: nonlinear optical effects and nonlinear optical diagnostics, Sov. Phys. Uspekhi 28 (1985) 1084–1124.

Complex Technological Solutions For Particle Accelerators

Oleg B. Malyshev* and Reza Valizadeh

ASTeC, STFC Daresbury Laboratory, Warrington, WA4 4AD, UK

Abstract

An advantage of complex technological solutions that address a few problems is demonstrated on two examples: laser ablation surface engineering (LASE) and non-evaporable getter (NEG) coated surfaces. NEG coating is not only the best vacuum solution for UHV/XHV accelerator vacuum chamber but can also provide electron cloud mitigation. LASE surface can provide not only SEY <1 (which is sufficient for e-cloud elimination but also reduces thermal and particle stimulated gas desorption). Both LASE and NEG has been characterised for their surface resistance and its impact on a beam wakefield impedance. It has been demonstrated that the surface resistance for both LASE and NEG can be reduced to meet the specification on the required surface resistance and provide the required vacuum and e-cloud mitigation properties.

INTRODUCTION

In a design of particle accelerators there are many specifications. Sometimes, the best solution to meet one specification can make it difficult or even impossible to meet another specification. For example, a small aperture of beam chamber allow to reach stronger magnetic field at reduced cost but could be too small for the beam aperture, cause beam impedance and make it challenging to meet the vacuum specifications. Rough surfaces may be efficient for e-cloud mitigation but increase the beam emittance.

The ASTeC team working on technological solutions for a beam vacuum chamber that address these problem in a complex approach, i.e. developing complex technological solutions to solve a few problems in the most optimum way for the particle accelerator performance. These approached are demonstrated below with two technologies: non-evaporable getter (NEG) coating and laser ablation surface engineering (LASE).

INTERACTION BETWEEN A BEAM AND A VACUUM CHAMBER

A primary role of vacuum chamber is providing a specified level of vacuum in order to minimise the interactions between the beam particles and the residual gas molecules. Thus, accelerator vacuum chamber should meet a number of vacuum specification: on leak tightness, thermal outgassing, photon and electron stimulated desorption (PSD and ESD), etc.

Additional specification may relate to interaction of synchrotron radiation generated by the beam and vacuum chamber or its components: photon reflectivity or absorption, thermal conductivity, photoelectron emissivity.

Finally, there is a direct interaction between the beam and vacuum chamber. Beam aperture defined the beam chamber transversal dimensions. Vacuum chamber material and its geometry defines a resistive wall wakefield impedance which, in turn, may lead to increase of the beam energy spread. Residual gas, photo- and secondary electron emission yield are key parameters for the build up of an electron cloud, which drives both single and multi-bunch instabilities, leading to the betatron tune shift and energy spread as well as an emittance growth.

NEG COATING

NEG coating technology, originally invented in CERN as a vacuum technology, is thin film of transitional metals (Ti, Zr and V) covering an entire surface of vacuum chamber and providing distributed pumping [1-4]. This allows reaching pressures below 10^{-13} mbar in vacuum chambers without synchrotron radiation, and significantly lower pressure in presence of SR than in uncoated chambers [5-6]. Presently, NEG coated chambers are widely used in many particle accelerators [7-14].

Vacuum properties

Over the last 20 years the NEG coating was further developed many focusing in these directions: (1) to increase sticking probability and sorption capacity, (2) to reduce an activation temperature, and (3) to reduce PSD and ESD.

The progress in increasing sticking probability and sorption capacity was achieved by employing an alloy target instead of twisted wires and depositing quaternary Ti-Zr-Hf-V films instead of ternary Ti-Zr-V [15-16]. Thus, the NEG coating pumping properties can be described as: sticking probabilities are $\alpha_{co} \le 0.4$, $\alpha_{co2} \le 0.6$, $\alpha_{H2} \le 0.02$, and sorption capacities are $\Theta_{co} \le 3$ ML, $\Theta_{co2} \le 10$ ML.

The NEG coating activation temperature was reduced from 180 °C for Ti-Zr-V to 150-160 °C for Ti-Zr-Hf-V.

Reduction in PSD and ESD was achieved by careful cleaning of substrate before deposition, in-situ bakeout before deposition, and low background in a deposition chamber as well as high purity of discharge gas [17]. Vacuum firing of substrates allows to further reduce PSD and ESD by an order of magnitude [18].

All these studies were originally focused on columnar structure of the NEG coating. It was shown later that PSD and ESD can be further reduced with dense structure of the NEG coating because it effectively reduces the gas atoms diffusion from the substrate to the beam vacuum, but at the cost of reduced pumping properties [15-18].

* submitting author, e-mail: oleg.malyshev@stfc.ac.uk

Finally, a dual layer NEG coating consisting of dense NEG coating on a substrate followed by a columnar NEG film allow to combine the best properties of both [19].

PSD and pumping properties were reported in [20].

Secondary electron yield

An additional benefit of NEG coating is that its secondary electron yield (SEY or δ) could reach $\delta_{max} < 1$ [21-22]. Combined with vacuum properties described above it becomes an ideal solution for many applications, see Fig. 1.

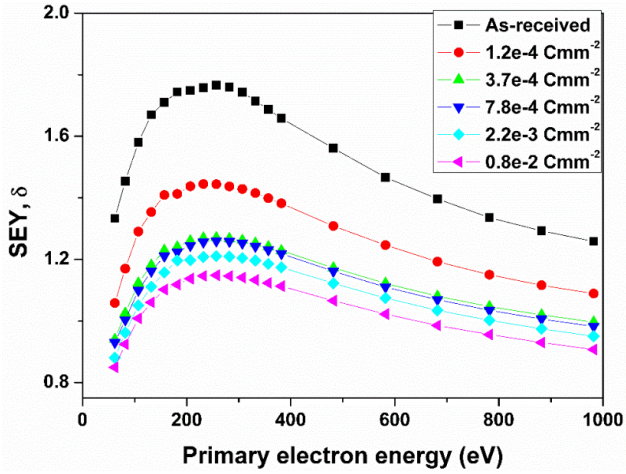

Figure 1: SEY of Ti-Zr-V NEG coating [22].

Photoelectron emission is another important characteristic of NEG; it was shown that it is approximately proportional to SEY [23]; more studies are still required.

Surface resistance

In short bunch accelerators a resistive wall wakefield impedance should be considered very seriously. The electric conductivity of NEG coating was experimentally studied at 7.8 GHz [24], on a facility shown in Fig. 2, and the main results are shown in Fig. 3.

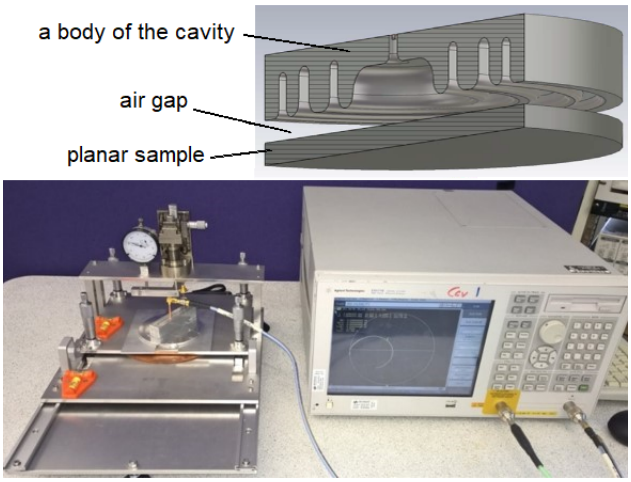

Figure 2: A facility for surface resistance measurements.

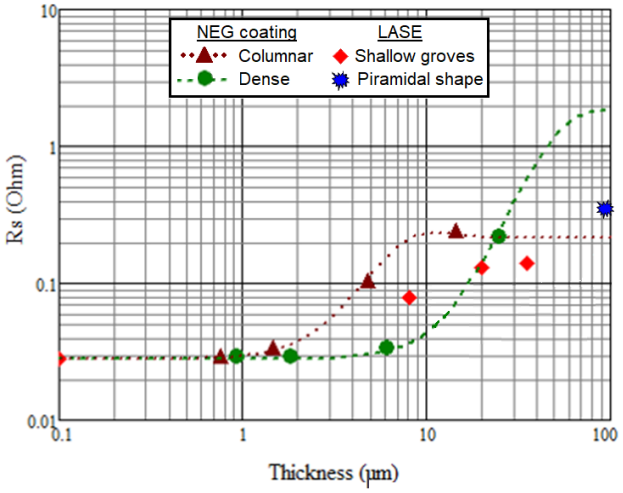

Figure 3: Surface resistance at 7.8 GHz for LASE and NEG coating on a copper substrate.

It was shown that electric conductivity of NEG coating depends on film morphology and varies between σ_d = 1.4×10⁵ S/m for columnar NEG coating and σ_d = 8×10⁵ S/m for dense NEG coating.

Thus, the surface resistance of NEG coatings depends not only on film morphology but also on substrate material, film thickness and RF frequency [25] as demonstrated on Fig. 4.

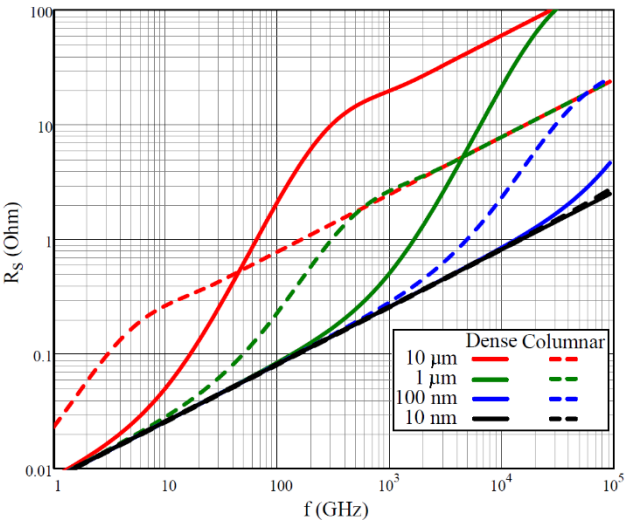

Figure 4: A calculated surface resistance of NEG coated copper as a function of RF frequency for different thickness of dense and columnar films.

Limitations

Physical vapour deposition (PVD) is a well-developed technology for film coating. It was demonstrated that vacuum chamber of different geometries can be successfully coated. However, it is still challenging to coat narrow vacuum chambers with a cross sectional size smaller than 5 mm.

LASE

Laser surface engineering is a technology that has been intensively developing over last ~25 years. Various structures or an hierarchy of structures could be formed as desired, using varied types of lasers [25-28].

Secondary electron yield

In 2014, it was discovered that the LASE surface can provide the surface with $\delta_{max} < 0.8$ on copper, aluminium and stainless steel surfaces [29,30]. Figure 5 shows an example of LASE surface obtained with a 355-nm laser with 40-kHz repetition rate, 10-μm pitch and 15 μm beam sport size. Figure 6 shows SEY for four samples obtained with different power and scan speed.

Further development allows reducing SEY to $\delta_{max} < 0.6$ [31-32]. The main advantage of this technology is that the laser surface treatment does not require vacuum, LASE can be done in air or in controlled gas atmosphere at atmospheric pressure.

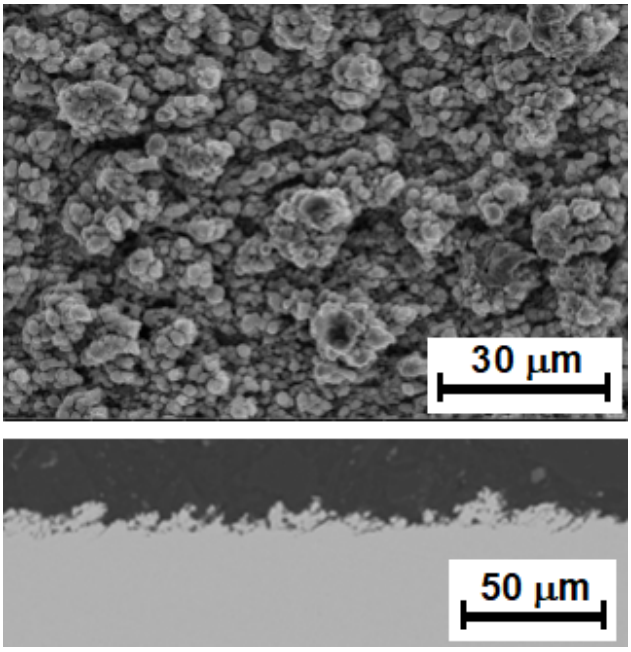

Figure 5: SEM images of LASE surface of Cu sample.

Over 100 structures were created and tested by ASTeC team, and more than 60% provide a surface with $\delta_{max} < 1$ [33]. An experimental study of a LASE treated screens on SPS confirmed the efficiency of e-cloud mitigation [34].

Vacuum properties

Thermal outgassing of Cu and 316LN surfaces with LASE is not greater than without LASE.

It is interesting that ESD of Cu surface with LASE treated in air and Ar is an order of magnitude lower than untreated Cu surface [35].

There still no data for PSD from LASE surface; however a PSD experiment will be performed in a few months on KARA with the H2020 EuroCirCol collaboration.

More vacuum evaluation testing should be done in the future for each material (different types of stainless steel, Cu and Al and their alloys, other materials of interest) and after various LASE procedures; this incudes effect of different cleaning procedures, bakeout, vacuum firing, etc.

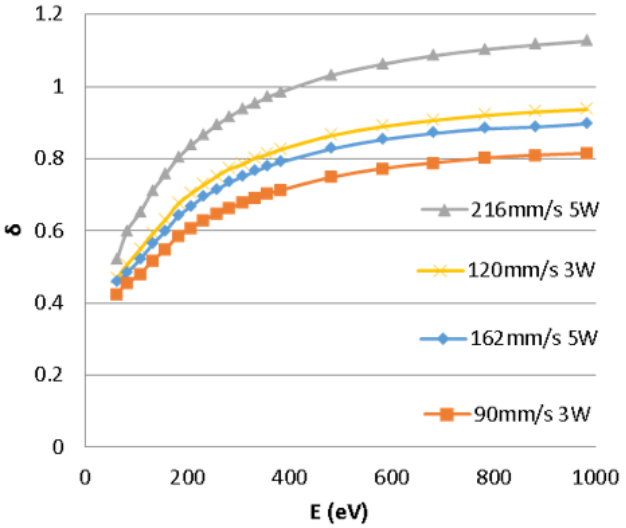

Figure 6: SEY as a function of incident electron energy for cupper samples after LASE treatment with laser power of 3 and 5 W and various laser scan speeds.

Surface resistance

LASE surface consist of a superposition or an hierarchy of few structures [31,32]: grooves with a depth between a few and 100 μm, submicron structures and ~100 nm structures. All these types of structures could increase the surface resistance. Calculating the surface resistance with surface roughness parameters does not provide correct results. Therefore, the surface resistance must be obtained experimentally. The surface resistance of the LASE surfaces shown in Fig. 3 was measured at 7.8 GHz on the same facility as NEG coating [31,35]. A Horizontal (Thickness) axis corresponds to the depth of surface layer affected by LASE (it is visible on cross sectional SEM images). The thinner this layer the lower the surface resistance of LASE surface.

Limitations

There are still a few problems that should be addressed. One of the main problems is particulate generation during LASE process. There is ongoing work to reduce particulate generation by varying laser parameters, applying gas flow, cleaning, etc., and to calculate a possible impact on the beam quality.

COMPARISON OF IMPACT OF E-CLOUD MITIGATION ON OTHER SYSTEMS

A comparison of impact of e-cloud mitigation with NEG coating and LASE on other systems is simplistically summarised in Table 1. Although the table is not complete, it

allows to see that the characterisation of both NEG coatings and LASE surfaces has targeted a possible impact on other systems. Many experimental data have been obtained and published.

However, some data has been already obtained but not published yet, there are a few ongoing experiments to obtain the data and some important data are still missing.

The available information is sufficient to conclude that both technologies are, in general, compatible with particle accelerators; however, further characterisation of these technologies is still required for more confidence and for obtaining more data for a specific type of NEG coating or LASE surface in application to an upgraded or a new machine.

Table 1: Impact of e-cloud mitigation on other systems.

	LASE	**NEG coating**
SEY	$\delta_{max} < 0.6$	$\delta_{max} < 1$
PEY	PEY likely to scale with SEY.	PEY scaled with SEY [23]
Vacuum		
Thermal outgassing	Low	Negligible
PSD	To be studied (for example in the KARA experiment)	Lower than for 316LN • BINP and ESRF data, • experience from many machines
ESD	Much lower than for Cu	Much lower than for 316LN
Bakeout/activation temperature	150 – 300 °C	150 – 250 °C
Cryogenic vacuum system	Talks at this workshop: R. Cimino and a team (INFN); T. Sian (ASTeC);	BINP data [20]; A facility is under development in ASTeC
Beam wakefield impedance	Low R_s LASE surface development [36]	Low R_s NEG coating development (A. Hannah's talk at this workshop)
UFO	Particulate generation measurements and control [36]	Film delamination is negligible

CONCLUSIONS AND FUTURE DEVELOPMENT

The NEG coating originally developed as a vacuum solution and the LASE surfaces originally developed as a e-cloud mitigation solution have been developed to meet more specifications and become complex solutions for solving a few problems: UHV/XHV vacuum, e-cloud mitigation and wakefield beam impedance. An attention is paid to multiple specification and avoid the creation of new problems to other systems.

REFERENCES

[1] C. Benvenuti. Non-Evaporable Getters: From Pumping Strips To Thin Film Coatings. Proc. of EPAC'98, 22-26 June 1998, Stockholm, Sweden, p. 200 (1998).

[2] C. Benvenuti, P. Chiggiato, F. Cicoira and V. Ruzinov. Decreasing surface outgassing by thin film getter coatings. Vacuum 50, 57 (1998)

[3] C. Benvenuti, J.M. Cazeneuve, P. Chiggiato, F. Cicoira, A. Escudeiro Santana, V. Johanek, V. Ruzinov, J. Fraxedas. A novel route to extreme vacua: the non-evaporable getter thin film coatings. Vacuum 53, 219-225 (1999).

[4] C. Benvenuti, A. Escudeiro Santana and V. Ruzinov. Ultimate pressures achieved in TiZrV sputter-coated vacuum chambers. Vacuum 60, 279 (2001).

[5] P. Chiggiato and R. Kersevan. Synchrotron radiation-induced desorption from a NEG-coated vacuum chamber. Vacuum 60, 67 (2001).

[6] V.V. Anashin, I.R. Collins, R.V. Dostovalov, N.V. Fedorov, A.A. Krasnov, O.B. Malyshev and V.L. Ruzinov. Comparative study of photodesorption from TiZrV coated and uncoated stainless steel vacuum chambers. Vacuum 75, 155 (2004).

[7] R. Kersevan. Performance of a narrow-gap, NEG-coated, extruded aluminium vacuum chamber at the ESRF. Proc. of EPAC-2000, 26-30 June 2000, Vienna, Austria, p. 2291 (2000).

[8] F. Mazzolini, J. Miertusova, F. Pradal, L. Rumiz. Performance of Insertion Device Vacuum Chambers at ELETTRA. Proc. of EPAC 2002, 2-7 June 2002, Paris, France, p. 2577 (2002).

[9] C. Herbeaux , N. Béchu and J-M. Filhol. Vacuum Conditioning of the SOLEIL Storage Ring with Extensive Use of NEG Coating. Proc. of EPAC'08, 23-28 June 2008, Genoa, Italy, p. 3696 (2008).

[10] J.D. Herbert, O.B. Malyshev, K.J. Middleman and R.J. Reid. Design of the Vacuum System for Diamond, the UK 3rd Generation Light Source. Vacuum 73, 219 (2004).

[11] D. J. Wang, J. R. Chen, G. Y. Hsiung, J. G. Shyy, J. R. Huang, S. N. Hsu, K. M. Hsiao, and Y. C. Liu. Vacuum chamber for the wiggler of the Taiwan Light Source at the Synchrotron Radiation Research Center. J. Vac. Sci. Technol. A 14, 2624 (1996).

[12] G. Bregliozzi, V. Baglin, S. Blanchard, J. Hansen, J.M. Jimenez and K. Weiss. Achievement and Evaluation of the Beam Vacuum Performance of the LHC Long Straight Sections. Proc. of EPAC'08, 23-28 June 2008, Genoa, Italy, p. 3685 (2008).

[13] M.C. Bellachioma, J. Kurdal, M. Bender, H. Kollmus, A. Krämer, H. Reich-Sprenger. Thin film getter coatings for the GSI heavy-ion synchrotron upgrade, Vacuum 82, 435-439 (2007).

[14] S. Calatroni, P. Chiggiato, P. Costa Pinto, et al. NEG thin film coating development for the MAX IV vacuum system. Proc. IPAC2013, Shanghai, China, p. 3385 (2013)

[15] R. Valizadeh, O.B. Malyshev, J.S. Colligon, A. Hannah and V.M. Vishnyakov. Comparison of Ti-Zr-V non–evaporable getter films deposited using alloy or twisted wire sputter-targets. J. Vac. Sci. Technol. A 28, 1404-1412 (2010).

[16] O.B. Malyshev, R. Valizadeh and A. Hannah. Pumping properties of Ti-Zr-Hf-V non-evaporable getter coating. Vacuum 100, 26-28 (2014).

[17] O.B. Malyshev, R. Valizadeh, R.M.A. Jones, A. Hannah. Effect of coating morphology on the electron stimulated desorption from Ti-Zr-Hf-V nonevaporable-getter-coated stainless steel. Vacuum 86, 2035 (2012).

[18] O.B. Malyshev, R. Valizadeh, B.T. Hogan and A. Hannah. Electron-stimulated desorption from polished and vacuum fired 316LN stainless steel coated with Ti-Zr-Hf-V. J. Vac. Sci. Technol. A 32, 061601 (2014).

[19] O.B. Malyshev, R. Valizadeh and A. Hannah. Pumping and electron-stimulated desorption properties of a dual-layer non-evaporable getter. J. Vac. Sci. Technol. A 34, 061602 (2016).

[20] V.V. Anashin , R.V. Dostovalov , A.A. Krasnov , V.L. Ruzinov. Adsorption and desorption properties of TiZrV getter film at different temperatures in the presence of synchrotron radiation. Journal of Physics: Conference Series 100, 092027 (2008).

[21] B. Henrist, N. Hilleret, C. Scheuerlein, M. Taborelli. The secondary electron yield of TiZr and TiZrV non-evaporable getter thin film coatings. Appl. Surf. Sci. 172, 95-102 (2001).

[22] S. Wang. Secondary electron yield measurements of anti-multipacting surfaces for accelerators. PhD thesis, Chapter 5, Loughborough University, March 2016.

[23] Y. Suetsugu, K. Kanazawa, K. Shibata, H. Hisamatsu, K. Oide, F. Takasaki, R.V. Dostovalov, A.A. Krasnov, K.V. Zolotarev, E.S. Konstantinov, V.A. Chernov, A.E. Bondar, A.N. Shmakov. First experimental and simulation study on the secondary electron and photoelectron yield of NEG materials (Ti–Zr–V) coating under intense photon irradiation. Nucl. Instrum. Methods Phys. Res., A 554, 92-113 (2005).

[24] O.B. Malyshev, L. Gurran, P. Goudket, K. Marinov, S. Wilde, R. Valizadeh and G. Burt. RF Surface Resistance Study of Non-Evaporable Getter Coatings. Nucl. Instrum. Methods Phys. Res. A 844, 99-107 (2017).

[25] A.Y. Vorobyev and C. Guo. Femtosecond laser nanostructuring of metals. Optics Express Vol. 14, Issue 6, pp. 2164-2169 (2006).

[26] A.Y. Vorobyev, C. Guo. Femtosecond laser blackening of platinum. J. Appl. Phys. 2008, 104, 053516

[27] Frank Siegel, Ulrich Klug and Rainer Kling. Extensive micro-structuring of metals using picosecond pulses – ablation behavior and industrial relevance. JLMN-Journal of Laser Micro/Nanoengineering 4(2), 2009, 104-110.

[28] J. Byskov-Nielsen, J.-M. Savolainen, M. S. Christensen, P. Balling. Ultra-short pulse laser ablation of metals: threshold fluence, incubation coefficient and ablation rates. Appl. Phys. A 101 (2010) 97-101.

[29] R. Valizadeh, O. Malyshev. Apparatus and methods relating to reduced photoelectron yield and/or secondary electron yield. Patent publication number WO2015189645 A1. 17th Dec 2015.

[30] R. Valizadeh, O.B. Malyshev, S. Wang, S. Zolotovskaya, A. Abdolvand. Low secondary electron yield engineered surface for electron cloud mitigation. App. Phys. Lett. 105, 231605 (2014).

[31] R. Valizadeh, O.B. Malyshev, S. Wang, T. Sian, L. Gurran, et al. Low secondary electron yield of laser treated surfaces of copper, aluminium and stainless steel. Proc. of IPAC 2016, Busan, Korea, 2016, p.1089.

[32] R. Valizadeh, O.B. Malyshev, S. Wang, T. Sian, M. D. Cropper and N. Sykes. Reduction of Secondary Electron Yield for E-cloud Mitigation by Laser Ablation Surface Engineering. Appl. Surf. Sci. 404, 370–379 (2017).

[33] 157. T. Sian, R. Valizadeh, O. Malyshev. LASE surfaces for mitigation of electron cloud in accelerators. In Proc. of IPAC'18, Vancouver, British Columbia, Canada, 29th April – 4th May 2018, paper THPAL133, p. 3958 (2018).

[34] S. Calatroni, E. Garcia-Tabares Valdivieso, H. Neupert, V. Nistor A. Perez Fontenla, et al. First accelerator test of vacuum components with laser-engineered surfaces for electron-cloud mitigation. Phys. Rev. Accel. Beams 20, 113201 (2017).

[35] R. Valizadeh, O.B. Malyshev, S. Wang, et al. "Efficient electron cloud mitigation with novel low SEY laser-engineered surface structures (LESS)". A&T seminar, CERN, Geneva, 26 Feb 2015.

[36] R. Valizadeh, O.B. Malyshev, T. Sian, L. Qianliang, W. Perrie. Laser Ablated Surface Engineering: From Discovery To Machine Application. In Proc. of eclous'18 workshop.

Intra-bunch feedback system developments at DAFNE*

A. Drago, INFN-LNF, Frascati and Tor Vergata University, Rome, Italy

D. Alesini, S. Caschera, A. Gallo, INFN-LNF, Frascati, Italy

J.D. Fox, Stanford University, Stanford, USA

J. Cesaratto (Toohig Fellow), J. Dusatko, J. Olsen, C. Rivetta, O. Turgut, SLAC, Menlo Park, USA

W. Hofle, G. Iadarola, K. Li, E. Metral, E. Montesinos, G. Rumolo, CERN, Geneva, Switzerland

S. De Santis, M. Furman, J-L Vay, LBNL, Berkeley, USA

M. Tobiyama, KEK, Tsukuba, Japan

Abstract

This paper presents history and evolution of the intra-bunch feedback system for circular accelerators. This project has been presented by John D. Fox (SLAC/Stanford Un.) at the IPAC2010 held in Kyoto. The idea of the proposal is to build a flexible and powerful instrument to mitigate the parasitic e-cloud effects on the proton (and potentially positron) beams in storage rings. Being a new and ambitious project, the financial issues have been quite important. US LHC Accelerator Research Program (LARP) and other institution funding sources have assured the development of the design for implementing the feedback in the SPS ring at CERN. Here the intra-bunch feedback system has been installed and tested in the frame of the LIU (LHC Injector Upgrade) program.

After the end of the LARP funding, a possible new interesting chance to continue the R&D activity, could be by implementing the system in a lepton storage ring affected by e-cloud effects. For achieving this goal, a possible experiment could be carried out in the positron ring of DAFNE at Frascati, Italy. The feasibility of the proposal is evaluated in the following sections. In case of approval of the experiment, indeed the project could be inserted in the DAFNE-TF (DAFNE Test Facility) program that is foreseen after the 2020 for the following 3-5 years.

INTRODUCTION

As it is well known, in a storage ring the photons emitted by the beams and hitting the vacuum chamber form electron clouds. These negatively charged clouds affect the beam dynamics of the positively charged beams with several undesired effects.

Many mitigation techniques are studied and developed. One of these is the "intra-bunch feedback", that has been often called "e-cloud feedback" or "wide band feedback system" (WBFS), too.

The intra-bunch feedback definition derives from the fact that it is a kind of system that treats the bunch of particles not as a rigid body as in the bunch-by-bunch feedback but considering each bunch split in several slices. Hence, the system applies an individual correction signal kick to each bunch slice. It is noteworthy to underline that a standard bunch-by-bunch system working on the centroid of the bunch is still usually necessary.

Quite the opposite, the wideband name has been chosen for the fundamental importance to have a wide frequency band for this kind of feedback. By using this definition, the main technological feature and challenge is reported in the name.

The e-cloud feedback definition just remembers the main goal of the system, i.e. to mitigate the e-cloud effects on the beams.

A LARGE COLLABORATION

After the year 2009, John Fox started to ask funds to the LARP program in USA for research on a new type of feedback, able to damp bunch slices independently and to be implemented in SPS/LHC. The LARP (U.S. LHC Accelerator Research Program) consists of four laboratories, Brookhaven National Laboratory (BNL), Fermi National Accelerator Laboratory (FNAL), Lawrence Berkeley National Laboratory (LBNL) and Stanford Linear Accelerator Center (SLAC).

They collaborate with CERN and other institutions in the context of the High Luminosity LHC program (HL_LHC) on the Large Hadron Collider in order to:

a) Make more luminosity, in an early stage.
b) Collaborate in interaction region upgrades, to make more luminosity, in a subsequent stage.
c) Use, develop, and preserve unique U.S. resources and capabilities.

Unfortunately, the LARP funding to the WBFS ended on September 2017.

The first general talk on the project was presented at the IPAC'10 conference held at Kyoto and John Fox proposed an "SPS E-cloud Feedback" [1]. Along the following years, a large collaboration grew with the interest of experts from many laboratories around the world, as reported in the Annex A.

The first goal of the project was to implement the new feedback in SPS ring at CERN as part of the LIU (LHC

Injector Upgrade) program. A prototype of the WBFS was developed and tested on the SPS proton beam and the proof of principle was achieved with single bunch as shown in Figure 1, and reported in [2].

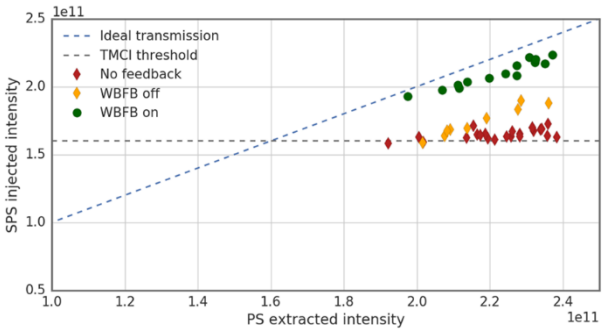

Figure 1: The effect of the WBFS on SPS beam current, from K. Li talk at LIU MD Days, 15/3/2018 [2].

The main R&D activities are outlined in the following points:

a) to characterize the pickups installed in the SPS ring in the past to figure out if they showed the needed frequency band and flatness for the bunch signals.
b) To develop a new feedback digital unit able to process 8 or 4 Gsamples/s [3-4] and to output the computed correction signal for each slice, see Figure 2.
c) To identify power amplifiers with a bandwidth of 1 GHz and showing a correct 2 ns impulse response.
d) To carry on R&D efforts to evaluate the best wide band kicker (1 GHz) to which applying the correction signal.
e) To install and test the new WBFS on the SPS proton beam.

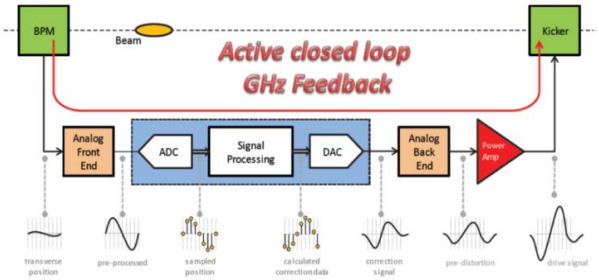

Figure 2: Layout of the WBFS, from [3].

The main efforts of the collaboration were shared between the interested laboratories depending on the skill of the researchers. However, the b) and d) activities have requested the more important R&D manpower. The b) task, to develop the digital processing unit, was carried on mainly by the SLAC team, while the d) activity, kicker studies, were shared between LBNL, CERN, SLAC and INFN/LNF teams. Regarding the c) task (power amplifier), the Japanese contribution was relevant to identify the best solution. Of course the e) task, installation and test at SPS, required big efforts from the CERN feedback team.

It is important to highlight for the following discussion, that in the SPS storage ring the intra-bunch feedback processes proton bunches having a length of 1.7 ns and divides the bunch in 16 slices. These features are reported in the O. Turgut's talk and paper for the IPAC16 [5-6].

DAFNE TEAM CONTRIBUTIONS

At LNF, the Italian laboratory, from the end of 2011, some researchers and engineers of the DAFNE team start to collaborate with the SLAC/CERN/LBNL task force as participating to Hi-Lumi-LHC collaboration funded by EU (November 2011-2015, within the FP7, seventh Framework Programme) to increase the LHC luminosity.

In particular efforts were carried on to evaluate the more suitable kicker to be implemented considering the large frequency bandwidth of the signals. Several designs were considered [7].

In particular, three different kicker types were studied and compared:

a) 10 cm long stripline kicker designed to have a large frequency bandwidth by S. De Santis at ALS Berkeley (installed in SPS in 2016);

b) the slotted kicker studied at the beginning mainly by J. Cesaratto;

c) an approach based on several RF cavities proposed by A. Gallo from LNF.

The LNF team was involved only in the b) and c) cases.

Indeed, John M. Cesaratto spent few weeks at LNF in 2013 working on the slotted kicker and funded by the FAI ("Fondo Affari Internazionali") program of INFN. The work done analysed three different designs versus performance and impedance of the kicker [8], see Figure 3.

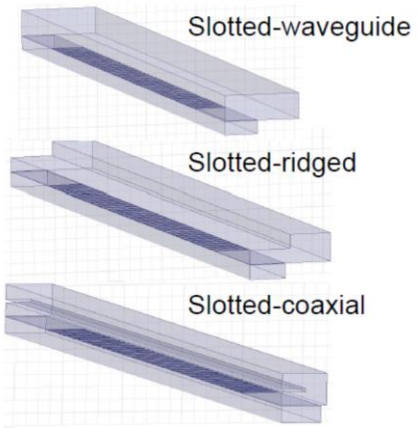

Figure 3: Quarter models of three slotted kickers studied.

The slotted-type kicker geometries, evaluated by HFSS, are similar to that used for the stochastic cooling:

a) the slotted-waveguide kicker consists of a waveguide coupled to a beam pipe via slots.

b) The slotted-ridged waveguide is an extension of the slotted-waveguide kicker where the ridge concentrates the field.

c) The slotted-coaxial kicker has a coaxial transmission line within the waveguide.

In the Figure 3 the quarter model geometries of three slotted kickers are presented.

The study brought eventually to an engineered version of the c) option, having 1 m of length, later designed at CERN to be installed in SPS ring in the June 2018. In this case, the slotted kicker frequency band is complementary to the one of the stripline kickers, already installed in the past in SPS. Indeed, the slotted kicker achieves a better response at the higher frequency, between 0.7 and 1 GHz.

Going to the c) option, the RF cavities based, it has remained at a preliminary stage up to now. This approach proposed by A. Gallo [9-10] wishes to operate on the bunch by splitting the correction signal in several frequency bands that need to be applied at RF cavities and stripline kickers.

Even if it is a very interesting approach, this design was not carried on up to now most likely for the difficulty to equalize and to time the different frequency bands of the bunch correction signal as well as for the impedance added to the ring. Nevertheless, it could be developed and installed in the next years in SPS if funded by a new R&D program.

As shown in the Figure 4, the correction signal, after the equalization and the Fourier transform expansion, is split and applied respectively to a cavity or stripline kicker working up to f0 (400 MHz) and to other two cavities working around 2f0 (800 MHz) and 3f0 (1200 MHz), both using the TM110 deflecting mode.

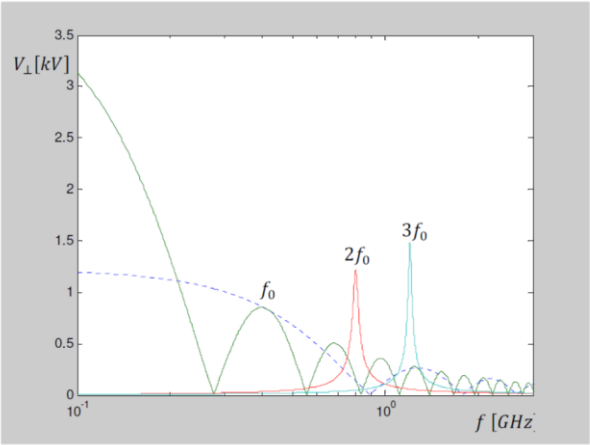

Figure 4: Deflecting voltages delivered by striplines and TM010 single cell cavities excited with 1 kW RF power.

A FEASIBILITY STUDY FOR DAFNE-TF

Even if at the present no funds from SLAC and LNF are available for new activities, at LNF in the December 2018, an ICFA and ARIES Mini-Workshop on DAFNE as Open Accelerator Test Facility (DAFNE-TF) will be held [11].

The workshop is intended to discuss the interest from scientists to access the DAFNE e+ e- complex, which will conclude its physics program as collider in 2020. An infrastructure almost unique, that could open as test facility to the international community for studies of accelerator technologies and beam physics, for small experiments, and to be used as a test bed for enterprises active in the sector of components for accelerators.

Given that the intra-bunch feedback up to now has never been implemented for lepton storage rings, a proposal for DAFNE-TF can be drawn up. Of course, in case of approval, it needs to be funded.

The interest in a lepton storage ring would be not only in the e+ ring to cope the e-cloud effects but also in the e- ring for a possible application to mitigate the Transverse Mode Coupling Instability (TMCI).

The main limitation for using an intra-bunch feedback in DAFNE is in the too short length of the bunch. With the present configuration, this is about 300 ps. Given that the main RF frequency is ~368 MHz, each bucket is ~2.7 ns, with a semi-period of 1.35 ns. From a comparison with the SPS bunch length seen above, it is necessary to stretch the DAFNE bunch as more as possible.

With respect to SPS beam using the intra-bunch feedback in the vertical plane, at DAFNE the e-cloud effects require a system in the horizontal plane where the instability is stronger than in the vertical plane [12-13]. The intra-bunch feedback could help to store more beam current than the 1.2A that has been achieved for the e+ ring in DAFNE up to now.

A beam dynamics simulation study needs to be carried on in order to be able to store in the ring a very long bunch (~1.0-1.3 ns). This value for the bunch length seems feasible, most likely by using a third harmonic cavity to stretch the bunches. An issue could arise to find space for the new cavity. It most likely should be placed in the second interaction region.

Going to the feedback design, it has to be added to the other three systems (horizontal, vertical and longitudinal). At the present in the DAFNE e+ ring there is a second horizontal feedback with a stripline kicker. This complementary system could be taken off and a slotted kicker can be placed where now is located the second horizontal stripline kicker. The available space is about one meter.

A 4 GSamples/s processing unit is necessary and maybe it can be borrowed from SLAC or from CERN.

Otherwise it needs to be designed again partially or fully. At LNF there are other data acquisition systems that can be adapted reprogramming the FPGA code and making some small hardware modifications [14]. See in Figure 5 the eight data acquisition systems working in parallel for the experiment 3+L in DAFNE e+ ring.

As third option, a completely new digital system should be designed. This solution would have the advantage to use state-of-art components, even if it will be more expensive.

As starting point, a number of 8 slices (8 channels for each bunch) seems to be sufficient as processing power. However, the SPS system implements the double, 16 channels, as reported above.

Furthermore, for budget reasons, it is necessary to foresee the necessary power. The power amplifiers are the most expensive items in the feedback. At the present, in the DAFNE e+ ring the bunch-by-bunch systems have last stage amplifiers of 2x250W in the horizontal plane, and the same in the vertical one. A second horizontal bunch-by-bunch feedback is ready but still to be tested with the beam, being equipped with 2x500W amplifiers. For the intra-bunch, 250 W power seems reasonable to begin the experiment, even if it could be useful to foresee a later increment of the power up to 1kW.

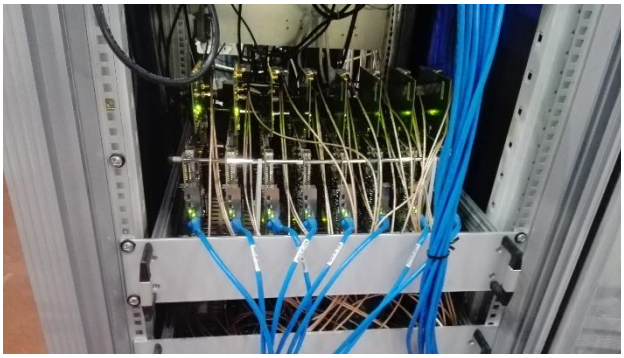

Figure 5: DAFNE 3+L data acquisition system based on 8 FPGA based boards working in parallel.

After all the previous considerations, the funds to implement the WBFS in DAFNE e+ ring would be of the order of 300k euro, without considering the costs for the manpower.

CONCLUSION

Transverse instabilities produced by e-cloud effect can limit both beam and single bunch currents in proton and positron beams. The wideband feedback has already been demonstrated at SPS that it is a powerful instrument to mitigate the intra-bunch instabilities.

Nevertheless, there is no more funding from LARP and Hi-Lumi-LHC to continue the R&D activities.

After the year 2020, DAFNE-TF could offer the occasion to implement a wideband feedback system in a positron ring. Given the beam current limits in DAFNE for the e-cloud effects in the horizontal plane, it would be more interesting to design it for this plane.

As consequence, the kicker design should be different from SPS where it is working in the vertical plane.

At a first attempt, the budget for the experiment could be limited to about 300k€. In case of approval of the project, studies for understanding how to stretch the bunches should be carried on as soon as possible to have a correct evaluation of the beam characteristics, remembering that a too short bunch cannot be useful for the intra-bunch feedback system.

ACKNOWLEDGEMENT

This work was supported in part by the European Commission under the HORIZON2020 Integrating Activity project ARIES, grant agreement 730871.

REFERENCES

[1] J.D.Fox, *et al.* "SPS Ecloud Instabilities – Analysis of machine studies and implications for Ecloud", IPAC'10 Proceedings, 2010.

[2] K.Li *et al.*, "Wideband feedback demonstrator system – selected results from 2017", talk presented at the LIU MD Days – 15.03.2018.

[3] J.D.Fox *et al.*, "Performance of the wide band feedback demonstrator system –Recent results", talk presented at the HL-LHC workshop, November 2016.

[4] J.Dusatko *et al.*, "A 4 Gsa/s instability feedback processing system for intra-bunch instabilities", poster and proc. of IPAC2013, Shanghai, China. WEPME059. May 2013.

[5] O.Turgut *et al.*, "Identification of intra-bunch transverse dynamics for model-based wideband feedback control at CERN Super Proton Synchrotron", talk presented at the IPAC2016, thoaa01, May,12, 2016, Busan, Korea.

[6] O.Turgut *et al.*, "Identification of intra-bunch transverse dynamics for model-based control purposes at CERN Super Proton Synchrotron", Proc. of IPAC2016, thoaa01, May,12, 2016.

[7] J.M.Cesaratto *et al.*, "SPS wideband transverse feedback kicker: design report", CERN-ACC-NOTE-2013-0047, SLAC report number: SLAC-R-1037. 20-12-2013.

[8] J.M.Cesaratto *et al.*, "A wideband slotted kicker design for SPS transverse intra-bunch feedback", poster and proc. of IPAC2013, Shanghai, China. WEPME061. May 2013.

[9] A.Gallo, "On the required bandwidth for an intra-bunch feedback system. Preliminary considerations", private communication, January 2012.

[10] A.Gallo (on behalf of the INFN Frascati HL-LHC fbk team), LIU review talk, CERN, 30/7/2013.

[11] DAFNE-TF Workshop 2018, LNF, 17/December/2018. https://agenda.infn.it/event/16334/overview

[12] A.Drago, "Fast Horizontal e+ instability measurements in DAFNE", PAC'09, TH5RFP057. Vancouver, Canada, 2009.

[13] A. Drago et al., "Mitigation and control of instabilities in DAFNE positron ring". Apr 2012. 3 pp. e-Print: arXiv:1204.5016 [physics.acc-ph]. Presented at 2012 Beam Instrumentation Workshop (BIW12), April 15-19, 2012, Newport News, USA. Task 2.4 meeting, CERN, 13/06/2012: http://emetral.web.cern.ch/emetral/Task2point4OfHLLHCWP2/3rdMeeting_05-09-12/TUPG001_talk_r1.pdf

[14] A.Drago, *et al.*, "Bunch-by-bunch profile diagnostics in storage rings by infrared array detection". Meas. Sci. Technol. 26 (2015) 094003 (10pp). Published in Measur.Sci.Tech. 26 (2015) 094003. DOI: 10.1088/0957-0233/26/9/09400.

ANNEX A:

THE WBFS COLLABORATION*

J.D. Fox, J. Cesaratto (Toohig fellow), J. Dusatko, J. Goldfield, J. Olsen, M. Pivi, K. Pollock, N.Redmon, C. Rivetta, O. Turgut, S. Uemura, SLAC, 2575 Sand Hill Rd, Menlo Park, CA 94025, USA
D. Aguilera, G. Arduini, H. Bartosik, S. Calvo, W. Hofle, G. Iadarola, G. Kotzian, K. Li, E. Metral, E. Montesinos, G. Rumolo, B. Salvant, U. Wehrle, M. Wendt, C. Zanini, CERN, 1211 Geneva 23, Switzerland
S. De Santis, M. Furman, H. Quian, M. Venturini, J-L Vay, LBNL, Lawrence Berkeley National Laboratory, 1 Cyclotron Rd, Berkeley, CA 94720, USA
D. Alesini, A. Drago, A. Gallo, F. Marcellini, M. Zobov, INFN-LNF, Via Enrico Fermi 40, 00044 Frascati, Italy
M. Tobiyama, KEK, Tsukuba, Ibaraki 305-0801, Japan

ECLOUD'18 SUMMARY*

R. Cimino, LNF-INFN, Frascati, Italy
F. Zimmermann†, CERN, Geneva, Switzerland

Abstract

This article reports some highlights from the joint INFN/ARIES workshop ECLOUD'18. We focus on electron-cloud effects in the LHC and at SuperKEKB, predictions for future machines like FCC-hh, HE-LHC and FCC-ee, models and parameters for the secondary-emission yield, recent trends in electron-cloud simulations, mitigation measures, and novel phenomena. Some workshop statistics and a brief outlook conclude the paper.

INTRODUCTION

ECLOUD'18 [1] was held at La Biodola, Isola d'Elba, from 3 to 7 June 2018. It was jointly organized by INFN [2], CERN [3], the FCC study [4], EuroCirCol [5] and ARIES Work Package 6 APEC [6]. ECLOUD'18 surveyed the state-of-the-art of global electron-cloud research. Topics ranges from electron-cloud build up and effects in particle accelerators and space applications, over beam-induced multipactoring, secondary emission yield models, and surface properties, to mitigation measures and electron-cloud diagnostics. The ECLOUD'18 workshop offered world experts a platform to present and discuss many recent and new electron-cloud observations at the LHC, SuperKEKB, CESR-TA and DAΦNE, and to report and compare electron-cloud predictions for future facilities like FAIR, NICA and the FCC. ECLOUD'18 also showcased and examined electron-cloud mitigation measures, such as clearing electrodes, graphite/carbon coatings, and chemically or laser treated surfaces. In addition, the workshop reviewed the modeling of incoherent electron-cloud effects, self-consistent simulations, and it explored the synergies with other communities like the Valencia Space Consortium and the European Space Agency. Only selected highlights can be presented in the following.

ELECTRON CLOUD IN THE LHC

A big mystery is the unexplained heat-load difference between LHC arc sectors during LHC Run 2 [7], which had not been visible in LHC Run 1 (2010–2012); see Fig. 1. Figure 2 illustrates that the heat load differences appeared between LHC Runs 1 and 2, with four of the LHC sectors showing up to four times higher heat loads after the Long Shutdown 1, which separated Run 1 and Run 2. No correlation had yet been found with any of the shutdown activities. Detailed analyses of local heat loads revealed, in high-load sectors, large differences from cell to cell, and a high heat load in some of the dipole magnets [7, 8]. From simulations, the LHC electron cloud is predicted to be most violent in the quadrupole magnets [9]; for these quadrupoles the presence or absence of photoelectrons does not matter for the heat load [9]. The differences in the heat load could be potentially explained by different surface coverages with CO molecules. Already half a mono-layer of CO can significantly alter the secondary emission yield and its variation with the primary electron energy, as is illustrated in Fig. 3 [10].

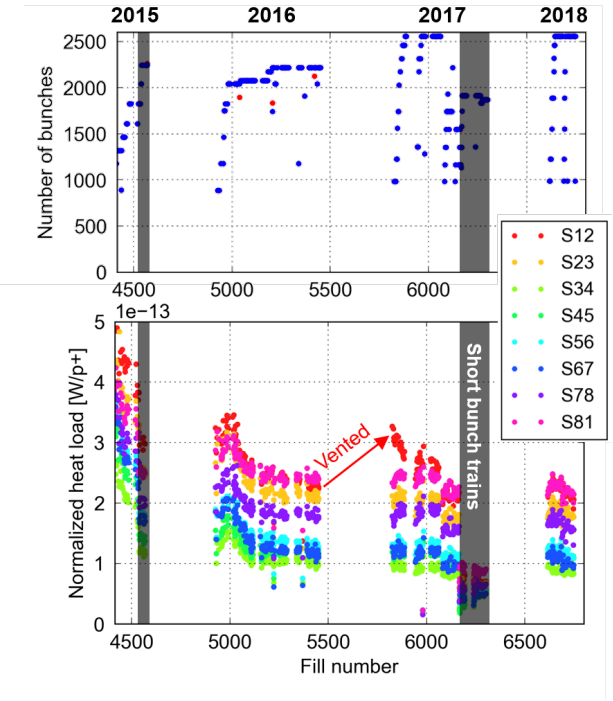

Figure 1: Beam intensity (top) and normalized heat load in the eight LHC arc sectors (bottom) as a function of fill number during almost 4 years of LHC Run 2 operation [7]

The secondary emission yield of LHC beam screens exposed to the proton beam was examined as a function of position [11]. Surprisingly almost no azimuthal dependence is seen, despite the presence of a strong dipole field [11]; the uniformity of the secondary emission yield may also indicate that photoelectrons do not significantly contribute to the surface conditioning. However, these measurements had been taken after keeping the beam screen in air for 1–2 months, which may have resulted in significant deconditioning and/or additional contamination. Measurements during and after white light SR conditioning at a DAΦNE XUV beam line (photon energies 5–1000 eV) show a significant decrease of the secondary electron emission yield (SEY) as a function of photon dose [12], as is documented in Fig. 4. Simulations studies indicate that changes in the orientation and detailed shape of the "sawtooth" surface, on the hori-

* This work was supported in part by the European Commission under the HORIZON 2020 project ARIES no. 730871.
† frank.zimmermann@cern.ch

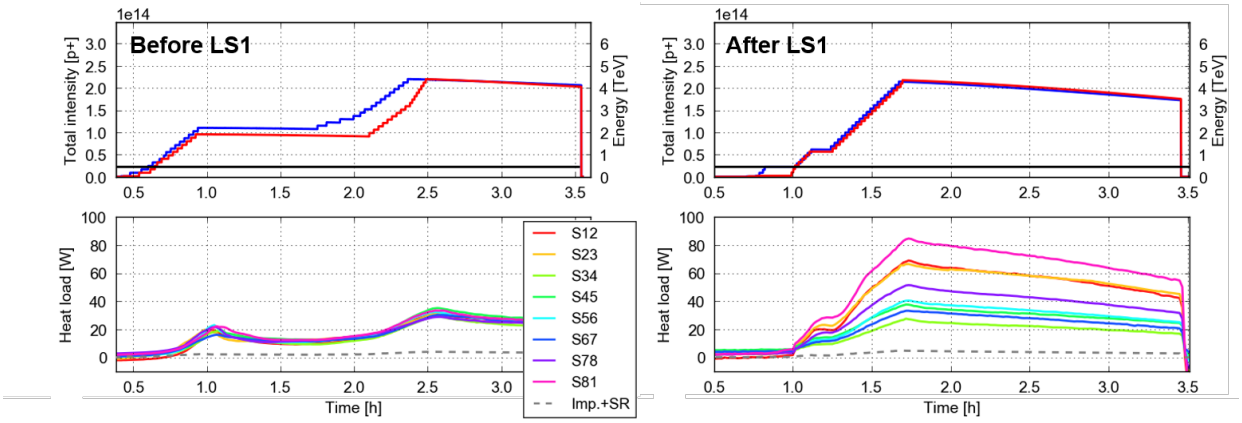

Figure 2: Beam intensity (top) and normalized heat loads (bottom) in the eight LHC arc sectors as a function of time for similar beam parameters before the Long Shutdown 1 (LS1) during Run 1 (left) and after the LS1 in Run 2 (right) [7]

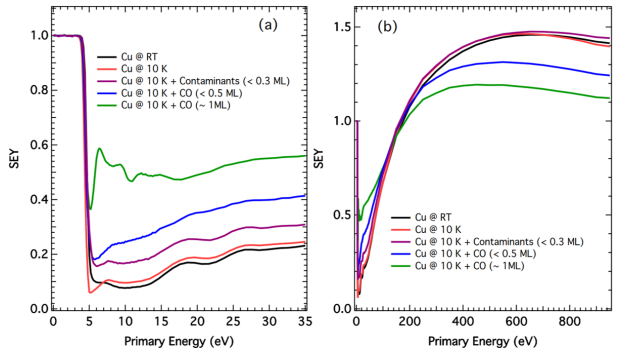

Figure 3: Low-energy (left) and regular secondary emission yield (right) at room temperature (RT) and 10 K, as a function of primary electron energy, for varying surface coverage with contaminants or carbon monoxide of up to one mono-layer (ML) [10].

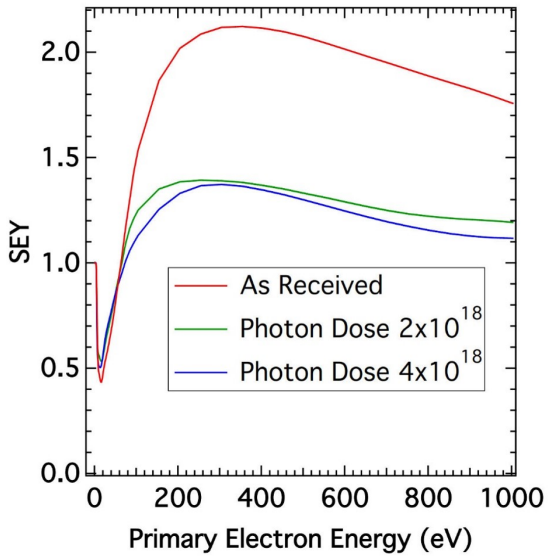

Figure 4: Secondary emission yield for perpendicular incidence of primary electrons as a function of primary energy before, during and after photon conditioning with a total dose of 4×10^{18} mm^{-2} [12].

zontal outward side of the LHC beam screen, can greatly affect the reflectivity and azimuthal distribution of absorbed photons and the resulting electron-cloud heat load [14, 15]. Measurements carried out in the LHC vacuum pilot sector allow discriminating between electron-cloud components caused by synchrotron radiation and due to secondary emission [13]. For a copper surface the secondary emission can contribute two or three orders of magnitude more electrons than primary photoelectrons liberated by synchrotron radiation [13]. These studies also confirmed the electron-cloud reduction by ex-situ NEG coating, and the complete suppression of any electron-cloud build up by amorphous carbon coating [13]

"Post-electron-cloud" simulations include both electrons and ionized molecules, explaining the local beam losses at LHC location "16L2", which is attributed to a local air in-leakage during cooldown. Figure 5 shows the evolution of the simulated ion and electron density during the passage of two successive 48-bunch trains [16]. Synergies of the newly developed multi-specie simulation tool with ITER and other fusion projects [17] and possible applications to muon colliders [18] were highlighted.

SECONDARY EMISSION YIELD STUDIES FOR CSNS

Comprehensive measurements of the angular distribution of the secondary electrons were performed at the CSNS [19]. This complements earlier studies at CERN [20, 21] and at SLAC [22,23]. Figure 6 shows some of the results for various materials. The angular distribution of the secondaries can be parametrised as

$$f(\theta) = \cos\theta(1 + a\sin^2\theta + b\sin^4\theta)\ . \qquad (1)$$

The fitted parameters a and b for different surface materials are summarised in Table 1.

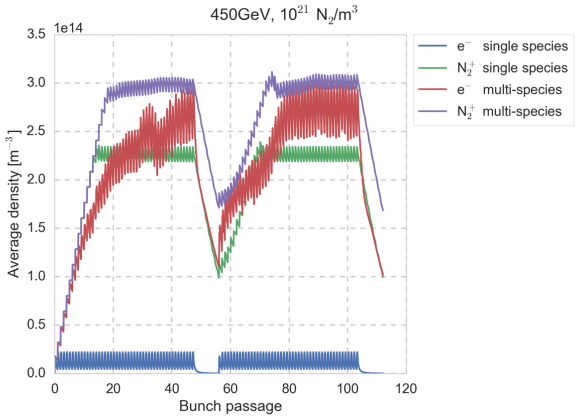

Figure 5: Density of electrons and singly-ionized nitrogen molecules as a function of time in units of bunch passages (the nominal bunch spacing is 25 ns). [16].

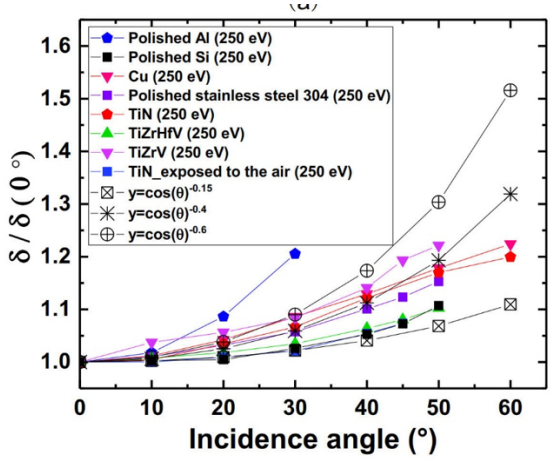

Figure 6: Variation of the secondary emission yield δ with incident angle θ (with respect to the surface normal) [19].

Table 1: Fit parameters characterizing the variation of the secondary emission with the angle of incidence of the primary electron according to Eq. (1), for different surface materials [19].

	a	b
Cu	−2.10	1.63
TiN	−1.24	1.91
TiZrHfV	−1.09	2.03
TiZrV	−0.06	1.99

CLEARING ELECTRODES AT DAΦNE

At DAΦNE, clearing electrodes affected the electron cloud as expected from simulations. Predictions and measurements are compared in Fig. 7. In later times the DAΦNE clearing electrodes were operated with a negative bias voltage [25].

SUPERKEKB

The residual electron cloud in SuperKEKB has been suppressed by many countermeasures, the latest one being permanent-magnet units in any small drift spaces between Phases 1 (2016) and 2 (2018). As far as electron cloud is concerned, SuperKEKB appears well on track towards the design performance. Growth rates measured by the multibunch feedback system [26], vertical beam sizes for close bunch spacing at high positron beam current, up to 600 mA [27], and the pressure rise against the beam current (Fig. 8) [28, 29] all indicate a complete, or nearly complete suppression of electron-cloud build up.

The Phase 2 of SuperKEKB commissioning started in March 2018 [27]. One important ingredient was the squeezing of $\beta^*_{x,y}$ (β^*_x = 200 mm, β^*_y = 4 mm was reached in May 2018). Electron-cloud driven coupled-bunch and single-bunch instabilities were studied in dedicated machine experiments on 29 May. A solenoid-type coupled-bunch instability was observed with a growth time of about 4 ms, that is well suppressed by the bunch-by-bunch feedback system. No single bunch instability (beam size blow-up) was seen up to 0.6 mA/bunch with the design bunch spacing of 4 ns. For comparison, the design bunch current is 1.4 mA. The electron cloud appears to be well controlled [28]. However, the design current is more than a factor two higher than achieved so far and the vertical emittance will be decreased from now 2–3% to the design value of 0.3% during the next year (commissioning phase 3).

Electron-cloud effects in the interaction region (IR) with very high beta is another concern. For the nominal β^* squeeze, the electron density in the IR area should be less than 8×10^{10} m^{-3} to avoid both coherent instability and incoherent emittance growth [27]. Based on a detailed modelling of SuperKEKB synchrotron radiation, including photon scattering, and associated electron-cloud simulations, the electron density in the final superconducting quadrupole QCS was estimated to be as high as, or higher than, 10^{14} m^{-3} [31–33]. Such an electron density could result in a strong instability and emittance growth for the squeezed optics of SuperKEKB.

ELECTRON CLOUD IN FCC-ee

Electron cloud build up in the arcs of the FCC-ee positron ring can be critical, as is illustrated in Fig. 9 [34]. If no care is taken the average heat load due to electron cloud can become comparable to, or exceed, the heat load from synchrotron radiation (about 500 W/m). A maximum secondary emission yield (SEY) below about 1.4–1.5 is required to avoid strong multipacting and to maintain an acceptable load. Such a

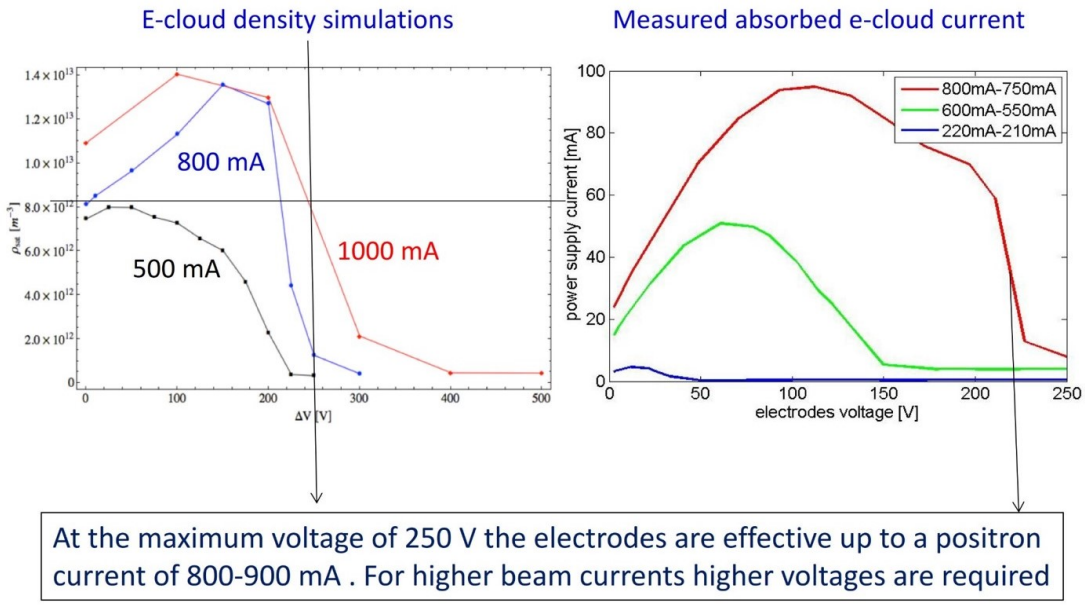

Figure 7: Simulated electron-cloud density (left) and measured electron current (right) as a function of clearing-electrode voltage for different positron beam current in DAΦNE [25].

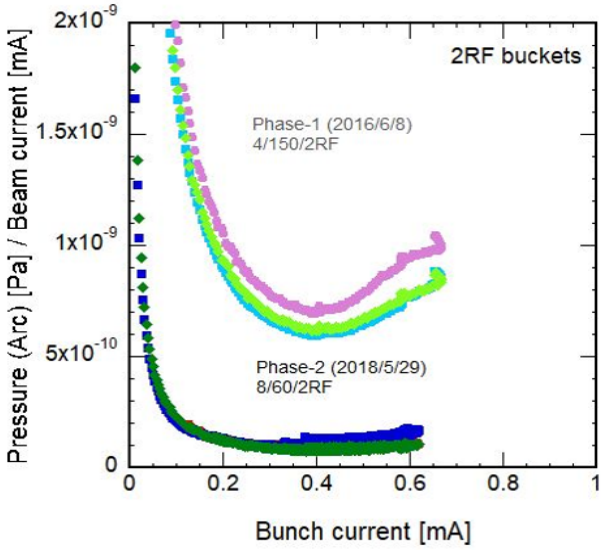

Figure 8: Arc pressure normalised to beam current as a function of beam current in SuperKEKB commissioning phases 1 (2016) and 2 (2018) [28].

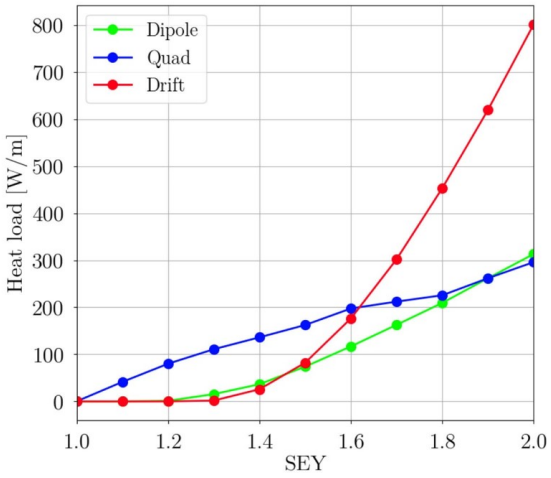

Figure 9: Electron-cloud inducted heat load per unit length for the FCC-ee positron beam in arc dipoles, quadrupoles, and drift spaces [34, 35].

secondary emission yield can be obtained by a NEG coating of the vacuum chamber. On the other hand, the thickness of the NEG coating determines the resistive-wall impedance, and thinner coatings are preferred. The measurements in Fig. 10 shows that novel NEG coatings with a thicknes of only about 100 nm provide the required SEY value even after multiple NEG activations [34, 35].

ELECTRON CLOUD IN HE-LHC AND FCC-hh

The electron cloud in both HE-LHC and FCC-hh is more benign than at the present LHC. Table 2 shows simulated multipacting thresholds in HE-LHC dipoles magnets and drift spaces for the nominal 25 ns bunch spacing, at three different beam energies. Figure 11 shows the simulated heat load in FCC-hh at top energy, as a function of the maximum secondary emission yield, for dipoles, quadrupoles, and drift

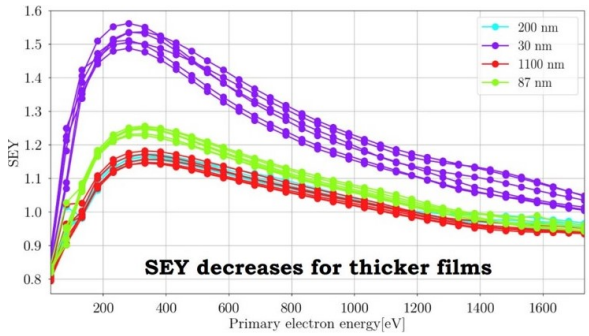

Figure 10: Secondary emission yield, after the fourth NEG activation cycle, as a function of primary electron energy for NEG coating of varying thickness [34, 35].

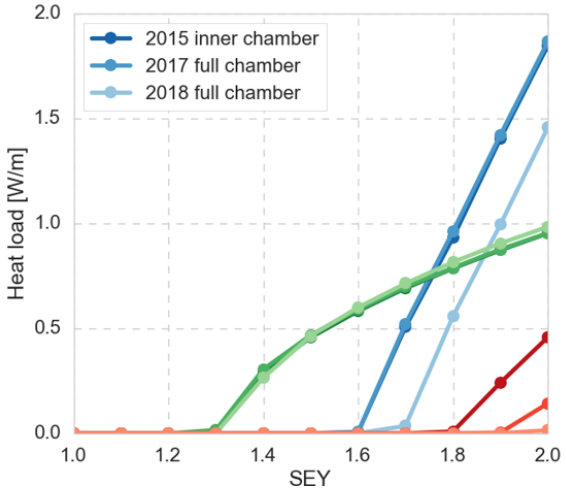

Figure 11: Simulated heat load per unit length in the FCC-hh at top energy (50 TeV per beam) as a function of the maximum secondary emission yield for dipoles (blue), quadrupoles (green), and drift spaces (red) [36].

spaces, considering three different version of the FCC-hh beamscreen.

Table 2: Multipacting thresholds in the HE-LHC arcs from build-up simulations; the threshold is defined as highest SEY without build-up [36].

SEY_{thr}	1.3 TeV inj.	13.5 TeV	13.5 TeV (int. scan)
dipole	1.55	1.45	1.40
drift	1.40	1.45	1.10

A new 2D simulation tool "openEcloud" for electron-cloud studies was developed in Darmstadt [37–39]. The electromagnetic field is calculated with a finite integration technique, using a 2D LU Poisson Solver with arbitrary cut-cell boundaries. A standard particle-in-cell method is employed for the simulation the electron motion, including boundary interaction models. Figure 12 illustrates the de-

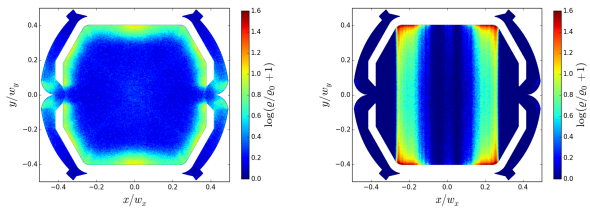

Figure 12: Simulated electron-cloud density for an FCC-hh vacuum chamber with beam screen inside a drift space (left) and a dipole magnet (right) [37].

tailed modelling of the vacuum chamber and shows some example electron distribution for the FCC-hh beam screen in a drift space and inside a dipole magnet,

A transition from Python to Cython programming was advertised [37]. Table 3 summarises simulated multipacting thresholds in LHC and FCC-hh dipole magnets, quadrupole magnets, and drift spaces comparing two different models for the secondary emission. The threshold values in terms of maximum SEY vary greatly with the model. For either model the situation for FCC-hh is more benign than at the LHC, which is consistent with the results of L. Mether [36]. No significant difference is seen between injection and top energy.

Table 3: Multipacting thresholds in the LHC and FCC-hh arcs from build-up simulations comparing the Furman/Pivi [40] and the Cimino/Collins models [21] for the secondary emission yield; the threshold is defined as highest SEY without build-up [37].

	Furman/Pivi		Cimino/Collins	
SEY_{thr}	FCC-hh	LHC	FCC-hh	LHC
dipole	1.25	1.1	1.56	1.32
drift	1.3	1.23	1.6	1.3

A series of thermal desorption spectroscopies has been performed, comparing different levels of surface coverage for common gases [41, 42]. The results in Fig. 13 reveal that the larger the coverage, the lower is the desorption temperature. Binding energies are in the range 100–500 meV and decrease with surface coverage. The question was raised if, given these results, the 60–80 K temperature window is an appropriate choice for the beam screens of HL-LHC, HE-LHC and FCC-hh [42].

LORENTZ BOOSTED FRAME

A frame of reference exists which minimises an aggregate measure of the range of space and time scales for electron-cloud studies [45]. Simulations in a Lorentz boosted frame [44, 45] are illustrated in Fig. 14. This Lorentz boost to an optimised frame allows for much faster and more accurate algorithms and can offer three orders of magnitude

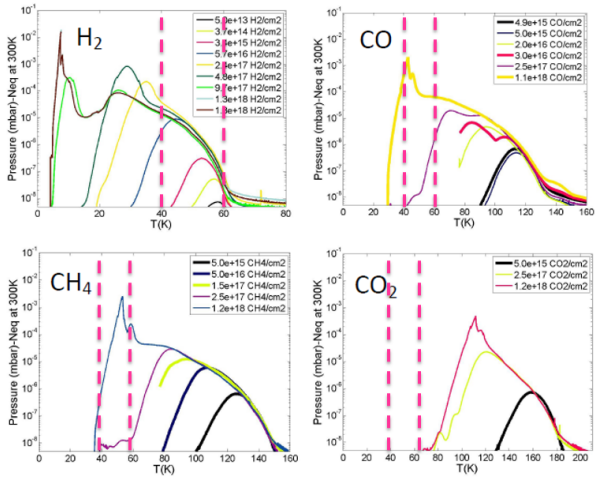

Figure 13: Simulated electron-cloud density for an FCC-hh vacuum chamber with beam screen inside a drift space (left) and a dipole magnet (right) [41, 42].

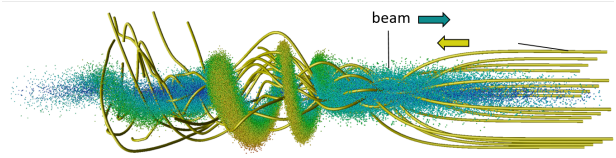

Figure 14: Illustration of an electron-cloud simulation in a Lorentz-boosted frame [44, 45].

gain in computing speed, for a frame with $\gamma^2 = 512$. An arbitrary-order Maxwell solver offers flexibility in accuracy, on centered or staggered grids.

ELECTRON-CLOUD RADIATION

Perhaps inspired by Vay's presentation [44], it was pointed out that in the frame of the beam electrons colliding with protons should lose energy by bremsstrahlung [46]. Photons with energies of order 10–100 keV could be expected in the LHC. With a bremsstrahlung cross section of, for example, $\sigma_{\text{brems}} \approx 10$ mbarn, a proton bunch intensity N_b, and transverse rms beam sizes σ_x and σ_y, the emission probability is of order $\sigma_{\text{brems}} N_b/(\pi\sigma_x\sigma_y) \approx 10^{-9}$ per electron and per proton bunch. An electron cloud line density of order 10^9/m (in the beam rest frame multiplied by γ) with a 25 ns bunch spacing (in the beam rest frame again multiplied by γ) would, back in the laboratory frame, lead to a photon rate of order 50 MHz per meter divided by γ, or 10 kHz per metre. Such "electron-cloud radiation" might be important for the LHC or for the next generation of high-energy hadron colliders.

WORKSHOP STATISTICS

The ECLOUD'18 workshop was attended by 64 experts from around the world. Figure 15 shows the geographical distribution of the ECLOUD'18 participants. In particular, 31% of the participants hailed from the hosting country, Italy, 26% came from nearby Switzerland, and here mostly CERN.

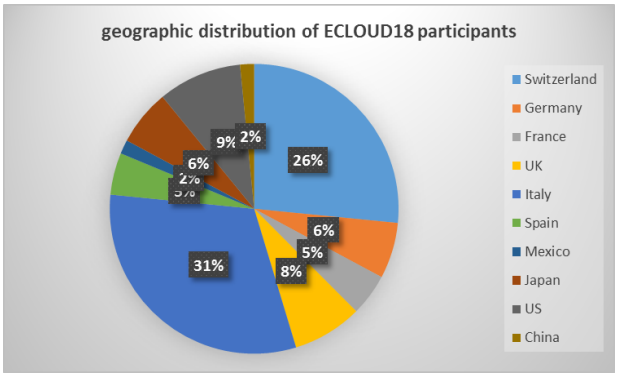

Figure 15: Geographical distribution of ECLOUD'18 participants.

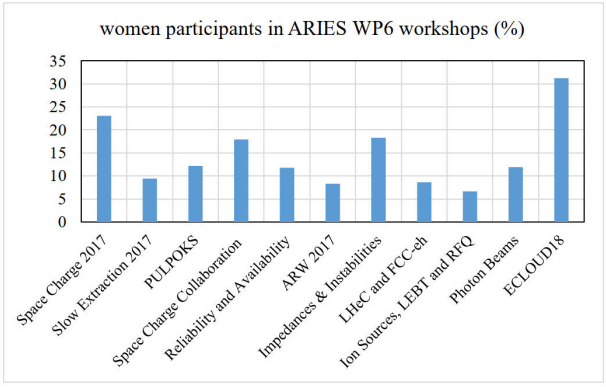

Figure 16: Percentage of women participants for all workshops organized till summer 2018 by ARIES Work Package 6 APEC.

The United States, Japan, UK, Germany and France contributed between 9% and 5% of the participants each. China and Mexico sent 2% each. Figure 16 reveals a rather high fraction of women participants in this workshop devoted to electron-cloud studies, compared with earlier ARIES workshops, which had addressed other topics.

EPILOGUE

ECLOUD'18 presented a superb overview of the present state-of-the-art in electron-cloud modelling and understanding. The remaining challenges, outstanding open questions, and several new approaches were carved out. Electron cloud remains important for the LHC and its upgrade HL-LHC, for SuperKEKB, and for all future high-energy colliders. Another electron-cloud workshop in three years' time (2021) would surely be warranted.

REFERENCES

[1] https://agenda.infn.it/event/13351/

[2] http://www.infn.it

[3] http://www.cern.ch

[4] http://www.cern.ch\fcc

[5] http://eurocircol.eu/

[6] http://aries.web.cern.ch/content/wp6

[7] G. Iadarola, "An Overview on Heat Loads in the LHC", ECLOUD'18, La Biodola, these proceedings.

[8] B. Bradu, "How does a cryogenic system cope with e-cloud induced heat load?", ECLOUD'18, La Biodola, these proceedings.

[9] P. Dijkstal, "Investigating the role of photoemission in the e-cloud formation at the LHC", ECLOUD'18, La Biodola, these proceedings.

[10] L.A. Gonzalez Gomez, "SEY from noble metals", ECLOUD'18, La Biodola, these proceedings and L.A. Gonzalez Gomez, M. Angelucci, R. Larciprete, R. Cimino, "The secondary electron yield of noble metal surfaces", AIP Advances 7, 115203 (2017).

[11] V. Petit, "Characterisation of beam screens extracted from LHC magnets", ECLOUD'18, La Biodola, these proceedings.

[12] M. Angelucci, "Photon Interaction with Technical Surfaces", ECLOUD'18, La Biodola, these proceedings.

[13] E. Buratin, "Preliminary results obtained with the LHC Vacuum Pilot Sector", ECLOUD'18, La Biodola, these proceedings.

[14] G. Guillermo, D. Sagan, and F. Zimmermann, "Examining mitigation schemes for synchrotron radiation in high-energy hadron colliders", Phys. Rev. Accel. Beams 21, 021001 (2018).

[15] G. Guillermo, "Effect of synchrotron radiation and chamber properties on LHC electron-cloud heat load", ECLOUD'18, La Biodola, these proceedings.

[16] G. Iadarola, L. Mether, K. Poland, G. Rumolo, "Post-ecloud regime, challenges for multi-species simulations in beam dynamics", ECLOUD'18, La Biodola, these proceedings.

[17] I. Kaganovich, comment at ECLOUD'18, La Biodola, these proceedings.

[18] R. Cimino, comment at ECLOUD'18, La Biodola, these proceedings.

[19] S. Liu, "SEY studies at CSNS" , ECLOUD'18, La Biodola, these proceedings.

[20] B. Henrist et al., "Secondary Electron Emission Data for the Simulation of Electron Cloud", in Proc. ECLOUD'02, CERN, Geneva, 15–18 April 2002, edited by G. Rumolo and F. Zimmermann, CERN-2002-001 (2002) p. 75.

[21] R. Cimino et al., "Can Low-Energy Electrons Affect High-Energy Physics Accelerators?", Phys. Rev. Lett. 93, 014801 (2004).

[22] M.A. Furman, "The Electron-Cloud Effect in the Arcs of the LHC", LHC-Project-Report-180 (1998).

[23] R.E. Kirby and F.K. King, "Secondary electron emission yields from PEP-II accelerator materials", Nucl. Instrum. Methods Phys. Res. A 469 (2001) 'pp. 1–12.

[24] E. Buratin, "Preliminary results obtained with the LHC Vacuum Pilot Sector" , ECLOUD'18, La Biodola, these proceedings.

[25] C. Milardi, "DAΦNE&ecloud: observations and prospective", ECLOUD'18, La Biodola, this workshop, and D. Alesini D et al. "DAΦNE Operation with Electron-Cloud-Clearing Electrodes" Phys. Rev. Lett. 110 124801

[26] M. Tobiyama, "Coupled-bunch instabilities and related effects due to electron cloud in SuperKEKB LER,", ECLOUD'18, La Biodola, these proceedings.

[27] K. Ohmi, "E-cloud challenges at SuperKEKB and future colliders", ECLOUD'18, La Biodola, these proceedings.

[28] Y. Suetsugu, "ECE and its cures in the SuperKEKB positron ring", ECLOUD'18, La Biodola, these proceedings.

[29] Y. Suetsugu et al., "Mitigating the electron cloud effect in the SuperKEKB positron ring", Phys. Rev. Accel. Beams 22, 023201 (2019).

[30] S.S. Win et al., "Effect of Electron Cloud on the Coupled Bunch Instability in KEKB LER", in Proc. ECLOUD'02, CERN, Geneva, 15–18 April 2002, edited by G. Rumolo and F. Zimmermann, CERN-2002-001 (2002) p. 199.

[31] J. Crittenden, comment at ECLOUD'18, La Biodola, these proceedings.

[32] J.A. Crittenden, D.C. Sagan, T. Ishibashi and Y. Suetsugu, "Synchrotron Radiation Analysis of the SuperKEKB Positron Storage Ring", Proc. IPAC2015 Richmond (2015), p. 2222, http://accelconf.web.cern.ch/AccelConf/IPAC2015/papers/tupty080.pdf

[33] J.A. Crittenden, "Initial Modeling of Electron Cloud Buildup in the Final-Focus Quadrupole Magnets of the SuperKEKB Positron Ring', Proc. IPAC2015 Richmond (2015), p. 2218, http://accelconf.web.cern.ch/AccelConf/IPAC2015/papers/tupty079.pdf

[34] E. Belli, "SEY measurements of coated surfaces with different coating thickness", ECLOUD'18, La Biodola, these proceedings.

[35] E. Belli et al., "Electron cloud buildup and impedance effects on beam dynamics in the Future Circular e+e- Collider and experimental characterization of thin TiZrV vacuum chamber coatings", Phys. Rev. Accel. Beams 21, 111002 (2018).

[36] L. Mether et al., "Electron cloud challenges for future circular machines", ECLOUD'18, La Biodola, these proceedings.

[37] D. Astapovych et al., "E-Cloud Studies for FCC-hh," ECLOUD'18, La Biodola, these proceedings.

[38] https://github.com/openecloud

[39] F. Petrov, O. Boine-Frankenheim, O. Haas, "Interaction of relativistic short proton bunches with space charge limited electron clouds", Phys. Rev. ST Accel. Beams 17, 121001 (2014).

[40] M.A. Furman and M.T.F. Pivi, ÃğProbabilistic model for the simulation of secondary electron emission", Phys. Rev. ST Accel. Beams 5, 124404 (2002).

[41] A.L. Lamure et al., "Adsorption/Desorption from Amorphous Carbon Coating at Cryogenic Temperatures", American Vacuum Society 64th International Symposium and Exhibition (AVS64), Tampa, Florida (2017).

[42] V. Baglin, "Coldex: A tool to study cold surfaces in Accelerators", ECLOUD'18, La Biodola, these proceedings.

[43] L. Spallino, "SEY and other material properties studies at cryogenic temperatures", ECLOUD'18, La Biodola, these proceedings and L. Spallino, M. Angelucci, R. Larciprete and R. Cimino,"On the compatibility of porous surfaces with cryogenic vacuum in future high-energy particle accelerators", Applied Physics Letters 114(15), p. 153103, (2019)

[44] J.-L. Vay, "Progress with 3D modelling of beam dynamics in presence of electron cloud", ECLOUD'18, La Biodola, these proceedings.

[45] J.-L. Vay, "Noninvariance of Space- and Time-Scale Ranges under a Lorentz Transformation and the Implications for the Study of Relativistic Interactionsm", Phys. Rev. Lett. 98, 130405 (2007).

[46] A. Hershcovitch, comment at ECLOUD'18, La Biodola, these proceedings.

List of Participants to the sixth electron-cloud workshop, ECLOUD'18 Held from 3 to 7 June, 2018 at La Biodola (isola d'Elba) Italy			
Name	Affiliation	City	Country
Adrian Hannah	STFC ASTeC	Daresbury	UK
Ady Hershcovitch	BNL	Upton	USA
Alessandro Drago	INFN/LNF	Frascati	Italy
Andrea Ghigo	LNF - INF	Frascati	Italy
Andrea Liedl	LNF	Frascati	Italy
Andrea Mostacci	Sapienza, University of Rome	Rome	Italy
Annalisa Romano	CERN	Geneva	Switzerland
Benjamin Bradu	CERN	Geneva	Switzerland
Benoit Salvant	CERN	Geneva	Switzerland
Bernard Henrist	CERN	Geneva	Switzerland
Bhagat-Taaj Sian	STFC	Daresbury	UK
Catia Milardi	INFN - LNF	Frascati	Italy
Christina Yin Vallgren	CERN	Geneva	Switzerland
Daria Astapovych	TU Darmstadt	Darmstadt	Germany
Elena Buratin	CERN	Geneva	Switzerland
Eleonora Belli	INFN ROMA1	Rome	Italy
Eliana La Francesca	LNF	Frascati	Italy
Frank Zimmermann	CERN	Geneva	Switzerland
Gerardo Guillermo	CERN (BE)	Geneva	Switzerland
Gimeno Martinez Benito	University of Valencia	Valencia	Spain
Giovanni Iadarola	CERN	Geneva	Switzerland
Giovanni Rumolo	CERN	Geneva	Switzerland
Igor Kaganovich	PPPL	Princeton	USA
Isabel Montero	CSIC- ICMM	Madrid	Spain
James Crittenden	Cornell University	Cornell	USA
Jean-Luc Vay	LBNL	Berkeley	USA
Jonathan Smith	Tech-X UK Ltd	Daresbury	UK
Katrin Isabell Thoma	Goethe Universität Frankfurt	Frankfurt	Germany
Kazuhito Ohmi	KEK	Tsukuba	Japan
Luca Sabato	CERN	Geneva	Switzerland
Lucia Lilli	INFN - Pisa	Pisa	Italy
Luis Antonio Gonzalez Gomez	LNF	Frascati	Italy
Luisa Spallino	LNF	Frascati	Italy
Makoto Tobiyama	KEK Accelerator Laboratory	Tsukuba	Japan
Marco Angelucci	LNF	Frascati	Italy
Maria Rita Ferrazza	LNF	Frascati	Italy
Maria Rosaria Masullo	NA	Naples	Italy
Martina Azzolini	ECT* -FBK-Università degli studi di Trento	Trento	Italy
Mauro Taborelli	CERN	Geneva	Switzerland
Mirko Simeoni	Consorzio C.R.E.O.	L'Aquila	Italy
Mohamed Belhaj	ONERA	**To**ulouse	France
Mu-Lee Yao	KEK	Tsukuba	Japan
Nasrin Nasresfahani	CERN	Geneva	Switzerland
Oleg Malyshev	STFC Daresbury Laboratory	Daresbury	UK
Pedro Costa Pinto	CERN	Geneva	Switzerland
Philipp Dijkstal	Paul Scherrer Institut	Villigen	Switzerland
Rafael Estrada	CSIC	Madrid	Spain
Rainer Wanzenberg	DESY	Hamburg	Germany
Rémi Dupuy	LERMA (Sorbonne Université, Obs. Paris)	Daresbury	UK
Reza Valizadeh	ASTeC, STFC	Frascati	Italy
Roberto Cimino	LNF	Rome	Italy
Rosanna Larciprete	CNR-ISC/LNF-INFN	Paris	France
Sandro Mengali	CREO Centro Ricerche Elettro-Ottiche	L'Aquila	Italy
Sergey Antipov	CERN	Geneva	Switzerland
Shenghua Liu	Institute of High Energy Physics, Chinese Academy of Sciences	Beijin	China
Stephen Poprocki	Cornell University	Cornell	USA

Suheyla Bilgen	CNRS & Paris Sud University	Paris	France
Valentine Petit	CERN	Geneva	Switzerland
Vincent Baglin	CERN	Geneva	Switzerland
Vinicio Tullio	LNF	Frascati	Italy
Virginia Britten	Goethe-Universität Frankfurt	Frankfurt	Germany
Vittorio Giorgio Vaccaro	NA	Neaples	Italy
Xiaofeng Gu	Brookhaven National Lab	Brookhaven	USA
Yusuke Suetsugu	High Energy Accelerator Research Organization	Tsukuba	Japan


e-CLOUD'18
3 - 7 June, 2018 La Biodola (Isola d'Elba) Italy